REVIEW • OPEN ACCESS

Geodesic acoustic modes in magnetic confinement devices

OPEN ACCESS
IOP Publishing | International Atomic Energy Agency Nuclear Fusion
Nucl. Fusion **62** (2022) 013001 (149pp) https://doi.org/10.1088/1741-4326/ac0dd1

Review

Geodesic acoustic modes in magnetic confinement devices

G.D. Conway[1,*], A.I. Smolyakov[2] and T. Ido[3]

[1] Max-Planck-Institut für Plasmaphysik, Boltzmannstraße 2, 85748 Garching, Germany
[2] Department of Physics and Engineering Physics, University of Saskatchewan, Saskatoon, Saskatchewan, S7N 5E2 Canada
[3] Research Institute for Applied Mechanics, Kyushu University, Kasugakoen, Kasuga, Fukuoka 816-8580, Japan

E-mail: Garrard.Conway@ipp.mpg.de

Received 5 October 2020, revised 30 April 2021
Accepted for publication 23 June 2021
Published 14 December 2021

Abstract

Geodesic acoustic modes (GAMs) are ubiquitous oscillatory flow phenomena observed in toroidal magnetic confinement fusion plasmas, such as tokamaks and stellarators. They are recognized as the non-stationary branch of the turbulence driven zonal flows which play a critical regulatory role in cross-field turbulent transport. GAMs are supported by the plasma compressibility due to magnetic geodesic curvature—an intrinsic feature of any toroidal confinement device. GAMs impact the plasma confinement via velocity shearing of turbulent eddies, modulation of transport, and by providing additional routes for energy dissipation. GAMs can also be driven by energetic particles (so-called EGAMs) or even pumped by a variety of other mechanisms, both internal and external to the plasma, opening-up possibilities for plasma diagnosis and turbulence control. In recent years there have been major advances in all areas of GAM research: measurements, theory, and numerical simulations. This review assesses the status of these developments and the progress made towards a unified understanding of the GAM behaviour and its role in plasma confinement. The review begins with tutorial-like reviews of the basic concepts and theory, followed by a series of topic orientated sections covering different aspects of the GAM. The approach adopted here is to present and contrast experimental observations alongside the predictions from theory and numerical simulations. The review concludes with a comprehensive summary of the field, highlighting outstanding issues and prospects for future developments.

Keywords: GAM, magnetic confinement, zonal flows, review

(Some figures may appear in colour only in the online journal)

* Author to whom any correspondence should be addressed.

1. Introduction and background

Geodesic acoustic modes (GAMs) are ubiquitous oscillatory flow phenomena observed in toroidal magnetic confinement fusion devices, such as tokamaks and stellarators. They have long been recognized as the non-stationary branch of turbulence driven zonal flows (ZFs) and are understood to play a consequent critical regulatory role in cross-field edge turbulent transport, via enhanced velocity shearing of turbulent eddies, or by providing an additional sink for the turbulence energy dissipation through damping. Their role in moderating turbulence is thus important for understanding the general behaviour of turbulent transport in magnetically confined plasmas, and hence they are a topic of high interest in fusion research.

Although the outpouring of publications on GAMs is a relatively recent phenomenon, their story begins with the 1968 paper of Winsor [1] which introduced a simple magnetohydrodynamic (MHD) model describing low frequency electrostatic $n = 0$ (toroidal mode number) acoustic modes in a toroidal axisymmetric magnetically confined plasma—which was originally sought as an explanation for oscillations observed in the model C stellarator. Winsor's fluid model (for a low temperature, large aspect ratio $r \ll R_0$, circular cross-sectional plasma of radius r) gives a local frequency for the GAM

$$\omega_{\rm GAM}^2 = c_{\rm s}^2 k_\parallel^2 (1 + 2q^2) = \frac{2c_{\rm s}^2}{R_0^2}\left(1 + \frac{\iota^2}{8\pi^2}\right) = \frac{2c_{\rm s}^2}{R_0^2}\left(1 + \frac{1}{2q^2}\right), \qquad (1)$$

where $k_\parallel = 1/(qR_0)$ with toroidal major radius R_0, local safety factor (inverse rotational transform) $q = 2\pi/\iota$, sound speed $c_{\rm s} = \sqrt{\gamma p_0/\rho_0} = \sqrt{\gamma(T_{\rm e} + T_{\rm i})/m_{\rm i}}$, plasma pressure p_0, plasma density ρ_0, electron (ion) temperature $T_{\rm e,(i)}$, ion mass $m_{\rm i}$, and $\gamma = 5/3$ the specific heat ratio (adiabatic index) for a monoatomic gas.

A critical aspect of the mode is the geodesic curvature (i.e. the surface component) of the confining magnetic field lines in a toroidal device, which gives a compressible plasma response to poloidal rotation. This means that a $\tilde{\mathbf{v}}_\perp = \tilde{\mathbf{E}}_{\rm r} \times \mathbf{B}/B^2$ flow perturbation compresses the plasma creating a $\tilde{p}$ pressure disturbance, which is compensated by an induced $v_\parallel$ parallel flow. This is the situation for the classic zero-frequency ZF which takes an $m = n = 0$ flow structure, without forming a pressure mode. However, in the case of the GAM the $\tilde{v}_\perp$ perturbation is too fast for the parallel flow to fully compensate the $\tilde{p}$ perturbation, resulting in an $n = 0, m = \pm 1$ pressure mode (called a sideband, i.e. a higher mode due to modulation) linearly coupled to the $m = 0$ flow via the radial diamagnetic current. This sideband is also responsible for the coupling to an $m = 1$ parallel ion sound mode $\omega_{\rm SW} = c_{\rm s} k_\parallel$. In equation (1) the ion sound mode appears in the term $(1 + 1/2q^2)$, while the $1/R_0$ is the result of the geodesic curvature. In short, the GAM oscillation is supported by the plasma compressibility due to the toroidal geodesic curvature, similar to sound waves (SWs)—hence the name GAM.

The basic features of what was to become known as the GAM were laid out in some detail in [1], which were supported by early numerical MHD simulations [2, 3]. The model predictions for the GAM can be summarized as follows:

- It has a poloidal mode number $m = 0$ plasma displacement within the magnetic surface, i.e. an oscillatory poloidal rotation flow $\tilde{\mathbf{v}}_\perp$ due to the radial electric field $\tilde{E}_{\rm r}$/potential $\tilde{\phi}$ perturbation.
- It has an $m = \pm 1$ pressure disturbance (sideband) with an up–down anti-symmetric $\tilde{p} \propto \sin\theta$ structure (tokamak), induced by plasma compressibility via $\nabla \cdot \tilde{\mathbf{v}}_\perp \neq 0$. This is a defining feature of the GAM which distinguishes it from the classic ZF which has no sideband.
- In axisymmetric magnetic systems the flow and sidebands have an $n = 0$ toroidal mode number structure.
- It has a local (continuum) frequency in the low kHz acoustic range scaling with the local sound speed $c_{\rm s}$, but higher than the parallel compressional SW $\omega_{\rm SW}$.
- It may exist in any magnetic system with geodesic curvature and closed flux surfaces.

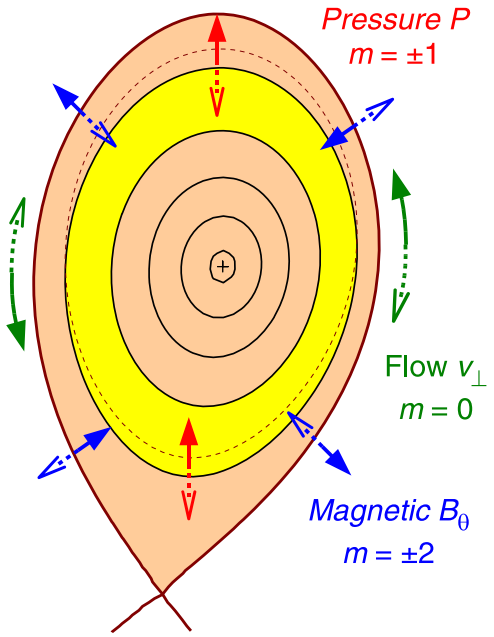

Figure 1. Schematic of the GAM poloidal structure in a diverted tokamak plasma configuration. The principle components are: green = $v_\perp$ flow ($m = 0$); red = pressure (up–down asym. $m = \pm 1$), blue = magnetic B_θ ($m = \pm 2$ up/down & in/out asym.).

Figure 1 shows schematically the zonal/poloidal structure of the GAM components: the $m = 0$ perpendicular flow in green; the up–down $m = \pm 1$ pressure/density $\tilde{n}_{\rm e} \propto \sin\theta$ in red, and the up–down, in–out $m = \pm 2$ magnetic halo/zonal $\tilde{B}_\theta \propto \sin 2\theta$ field in blue. The predicted ideal modal (toroidal and poloidal) structure of the GAM flow and its sidebands, together with its zonal radial nature have been verified experimentally. Real experimental devices generally do not have ideal circular flux surfaces, but are often elongated, triangular, and have field-nulls (X-points). These shape effects introduce structure distortions as well as corrections to the GAM frequency and damping.

The original Winsor paper [1] used ideal single-fluid MHD theory to obtain the basic GAM dispersion relation. Independently, a much more general GAM dispersion relation was obtained a little later in 1973 in the context of the finite m and n electromagnetic (EM) drift wave instabilities, including Alfvén waves, temperature gradients and ion finite Larmor radius (FLR) effects [4], such that the basic GAM mode of Winsor, equation (1), is only a special limit case of the dispersion relation obtained in [4]. Along similar lines, the GAM dispersion relation was later derived as a special limit case of the general kinetic theory of Alfvén waves in inhomogeneous plasmas [5]. Note that neither [4] nor [5] refer to the original Winsor paper, nor used the name GAM for this mode.

As the GAM is a mode of plasma rotation it was natural that GAM physics was discussed along the somewhat parallel studies of plasma rotation in a tokamak, in particular, mechanisms of spontaneous poloidal spin-up [6], where the GAM basic dispersion relation was explicitly derived as part of the Stringer spin-up mechanism (1969) [7], again without the reference to [1]. It was realised later that the oscillatory GAM eigenmode is an inherent part of the relaxation process for establishing the equilibrium neoclassical rotation [8, 9] at which point the connection to the original work [1] was firmly established.

The MHD dispersion relation gives a local frequency, which, for experimental conditions with radial gradients ('system non-uniformities') in the temperatures and q, means the frequency varies continuously with the plasma radius giving a continuum mode spectrum. As with other types of continuum modes (e.g. Alfvénic) observed in plasmas [10], the GAM experiences phase-mixing (PM), continuum damping, as well as FLR and finite orbit width (FOW) effects which result in frequency corrections and are important for radial propagation and localization of the GAM. Nevertheless, there are also some important differences to Alfvénic continua, particularly concerning resonances and mode conversions. In addition to PM and continuum damping, the GAM is also subject to collisionless damping, which requires a kinetic description. In the literature the term kinetic GAM (KGAM/GAM) [11] is applied to the GAM dispersion relation derived from kinetic based models, as an extension to the local continuum GAM at the short wavelength regime and/or when wave-particle resonances are involved—situations where MHD models are not valid.

While many experimental observations conform to the GAM continuum behaviour, there are, however, plasma conditions where the GAM has a constant frequency extending radially over a significant portion of the plasma cross-section (although the GAM amplitude may still vary with radius). The GAM may also form a series of radial steps with a staircase-like behaviour. In these cases the GAM structure is often referred to as global or eigenmode. Note in the literature the use of global and eigenmode terminology varies, especially between experiments and theory. For example, the term global GAM (GGAM) eigenmode [12, 13] specifically refers to conditions when the GAM continuum frequency has an off-axis maximum, which can occur in reversed shear configurations of so-called 'advanced tokamak scenarios' with raised q^2 in the core, or at high plasma core pressures where the GAM frequency is reduced by $\omega^2 = \omega_G^2/(1+\beta)$ when $\beta = c_s^2/v_A^2$ becomes significant. Here, the GGAM eigenmode has a constant frequency close to that of the continuum mode at the maxima location. Such eigenmodes can have substantial $m = 2$ flow and magnetic components that extend over large distances—thus allowing their easy detection. Generally eigenmode GAMs are not fully understood, but there are several theory mechanisms, including (linear) eigenmodes forming where the GAM continuum crosses ion-sound [14] or Alfvén branches [15]. Another concept is the radially propagating wave-packet eigenmode. This GAM does not have a specific radial position but has a radial width in the so-called 'mesoscale' range (between turbulence and system dimensions) determined by FLR/FOW and temperature gradient length scale parameters [11, 16].

Thus, from later observations and theory one can add to the list of characteristics:

- Its local (continuum) frequency has equilibrium shape (elongation, Shafranov shift, etc) dependencies.
- It is dispersive, i.e. radially propagating.
- It experiences continuum, collisional and collisionless (parallel ion Landau and toroidal resonance) damping.
- It is generally radially localised with a finite k_r, i.e. zonal-like, with a radial width much less than the plasma minor radius a.
- It can develop an extended radial structure with a fixed frequency.
- It can develop $m = \pm 2$ sidebands which appear in pressure and magnetic field, in particular at high plasma β. The $m = 2$ magnetic field extends outside the plasma facilitating the mode detection.
- It requires drive, typically from drift-wave (DW) turbulence or energetic particles (EPs).

The basic GAM is generally stable [17] and therefore needs to be driven. The most universal drive sources are related to drift turbulence [via turbulent Reynolds stress (RS) or transport modulations] and EPs. Developments in the theory of plasma turbulence driven RS in the early 1990s [18], as well as gyrofluid and gyrokinetic (GK) numerical simulations in the mid to late 1990s, revealed the presence of turbulence driven ZFs (both stationary and oscillatory) and their role in turbulence and transport control [19–24]. Together with the detection of GAMs as a result of the relaxation of the poloidal rotation in numerical simulations [22, 24] this stimulated further interest in GAMs as finite frequency ZF structures, leading eventually to serious attempts to measure ZFs and GAMs in experiments.

The first clear observation of (declared) GAMs in a toroidal device was around 2002 with reports from the HT-7 [27], DIII-D [28, 29], and TEXT [30] tokamaks, followed closely with measurements from ASDEX Upgrade (AUG) [31], JFT-2M [32], CHS [33], T-10 [34], TUMAN-3M [35], JIPPT-IIU [36] devices. Two typical edge GAM spectra from HL-2A and AUG are shown in figure 2, respectively with and without a

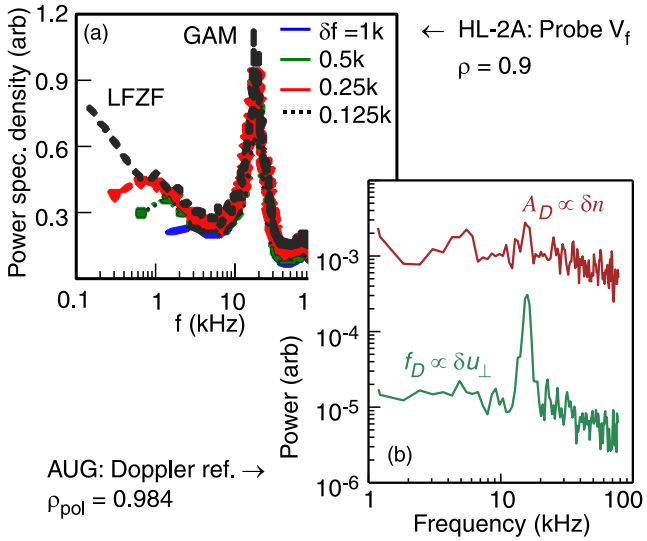

Figure 2. Typical edge GAM spectra: (*a*) HL-2A Langmuir probe (LP) $\tilde{V}_f$. Reprinted figure with permission from [25], Copyright (2009) by the American Physical Society. (*b*) AUG Doppler reflectometer flow. Reproduced from [26]. © IOP Publishing Ltd. All rights reserved.

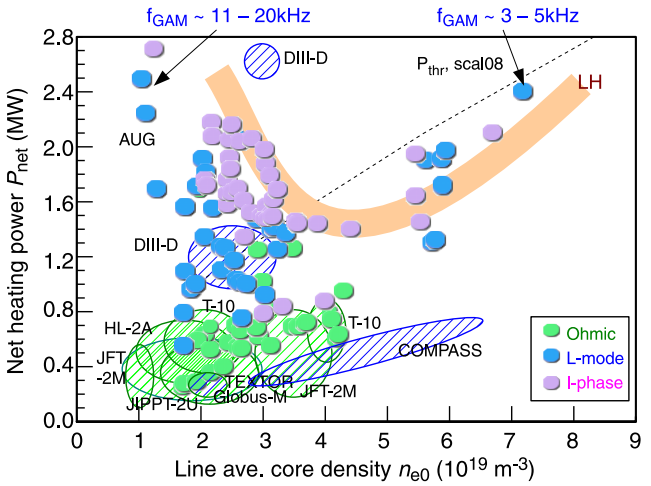

Figure 3. GAM measurement (existence) diagram in terms of net heating power $P_{net} = P_{ohm} + P_{heat} - dW/dt$ and line average core density $\bar{n}_{e0}$ for different confinement regimes (colours) from various devices (points = AUG). The thick line represents the typical L–H power threshold for AUG. Reproduced with permission from [43].

concurrent stationary (zero-frequency) ZF. Subsequently several early observations of coherent flow and plasma potential oscillations were either retrospectively identified as possible GAMs, cf in the core (mid-radius) region of the H-1 heliac stellarator [37, 38], or in the case of early observations of plasma potential modes in TEXT [39] and JIPP T-IIU tokamaks by implication of later measurements [40, 41].

Turbulence driven GAMs have now been ubiquitously observed in ohmic and low-confinement L-mode plasmas in many devices, but not in strong high-confinement H-mode plasmas—although recent results suggest GAMs may form in weak H-modes where the edge turbulence level has recovered sufficiently [42]. The detection of GAMs also requires suitable diagnostics with sufficient sensitivity, and of course GAMs of measurable amplitude. The GAM amplitude is essentially a balance between the strength of the drive mechanism—which can include a variety of linear and nonlinear sources—and the various damping mechanisms, such as continuum, collisional and collisionless Landau damping. The latter is sensitive to the safety factor, $\gamma \propto \exp(-q^2)$, therefore making the radial profile of q an important factor in distinguishing the edge turbulence GAM from the more core localized ZF.

Figure 3 shows a measurement diagram of reported GAMs as functions of net absorbed heating power P_{net} (representing drive) and line-averaged core density $\bar{n}_{e0}$ (representing damping) for a range of discharge conditions, such as ohmic heated, additional heated low confinement L-mode and intermediate (between L and H-mode) I-phase, in various devices. A large majority of GAM studies have been performed in relatively small devices with low ohmic or additional heating power, hence the observations tend to cluster at low densities (low collisionality and weak damping). Such devices tend to have easier diagnostic access. The higher density regions have been probed in some of the larger tokamaks, such as DIII-D, JET and AUG which have greater capacity for additional heating. In general, higher densities tend to result in lower temperatures, thus reducing the GAM frequency to the low kHz, as well as stronger damping.

While turbulence has been clearly established as the main driving mechanism for the GAM excitation, directly via nonlinear RS or indirectly via transport and pressure modulations, it is not the only drive mechanism. EPs with anisotropic or inverted slope velocity distributions can also drive GAMs via inverse Landau damping mechanisms. Furthermore, EPs can lead to the excitation of new (additional) GAM-like modes—EGAMs.

The first observations of EP driven GAM modes dates from the mid 2000s with chirping modes observed in both JET [12, 13] and DIII-D [44] tokamaks. The modes observed in JET were due to energetic ions (several hundred keV) generated by ICRF minority heating. The inverted energy distribution of the ion beam excited a global eigenmode GGAM via inverse Landau damping. Numerically it was shown [12, 13] that the GGAM was formed as a result of an off-axis maximum in the GAM frequency in a reversed magnetic shear equilibrium. The EM component (halo) of the GGAM made it particularly easy to detect with external pick-up coils. New GGAM-like modes in DIII-D [44] were observed well below the ideal GAM frequency and were identified as non-perturbative modes excited by anisotropic distributions of EPs due to transit resonances. These modes had radial widths determined by the EP orbits and were termed EGAMs [45]. Generally the EGAM appears as repetitive bursts of large up and down frequency chirping (in the tens of kHz range) due to the formation of phase space structures (a kinetic effect) interacting with the fluid ZF. Geodesic-like oscillations associated with EPs have now been observed in the core plasma region of numerous tokamaks and stellarators.

The GAM interaction with EPs has many facets and makes for a rather complex, and sometimes confusing, story where an EP effect can vary depending on competing parameters.

Nevertheless, in the GAM/EGAM picture a more or less definitive divide can be established between two main situations:

(a) Perturbative modes where the excitation is by EPs while retaining the basic feature of the standard GAM as a linear eigenmode structure, which would exist even in the absence of EPs. The JET observations of a reversed shear GGAM driven by EPs would belong to this category;
(b) Non-perturbative modes whose existence, eigenmode structure and localization is determined by the EP source.

In general, EP related GAM modes are of particular interest due to the generation of energetic alpha particles in future burning plasmas.

Finally, GAMs may even be pumped by external modulation mechanisms, such as biased limiters, or theoretically by localised plasma heating, or by magnetic field perturbation coils. These possibilities open-up potential GAM applications for plasma diagnosis, or even the control of the edge turbulence which may be used to facilitate confinement mode transitions.

Already in the late 1990s the impact of coherent and incoherent random flow shearing on turbulence moderation was studied [46–48]. Indeed the significance of the GAM's role in moderating turbulence [48] and transport control [24] either via turbulence shearing effects or direct energy sink for ZFs [24, 49] is one of the main reasons for the intense interest in GAMs. In addition to turbulence and transport effects, GAM/EGAMs have also been associated with ion heating—the so-called GAM energy and momentum channelling effects [50, 51].

GAMs are essentially part of the larger ZF and turbulence picture. The flow spectrum can be divided into distinct components:

(a) Zero-mean-frequency stationary zonal flows (SZF), sometimes referred to as the Rosenbluth–Hinton residual (RHR) in theory papers [52]. SZFs may have spectral widths of the order of the ion–ion collision frequency, i.e. a few kHz [53]. They are generally damped by collisions, but can also be damped by other linear and nonlinear mechanisms such as Kelvin–Helmholtz (KH) instabilities as well as by collisionless Landau resonances in the plateau collisionality regime. SFZs do not have pressure sidebands.
(b) Low frequency ZF oscillations (ZFOs) with frequencies typically an order of magnitude smaller than GAMs, e.g. low kHz. ZFOs include modes driven by linear mechanisms such as plasma rotation, or equilibrium pressure anisotropy, or diamagnetic drift (gradient) effects. ZFOs can be viewed as an non-zero-mean-frequency oscillatory version of the SZF (no pressure sideband) but, with increasing frequency may convert to a GAM (with pressure sideband). Radial drifts of trapped ion orbits can also drive a radial current with a low frequency oscillatory (LFO) response. For stellarator geometries they may be particularly prominent [54, 55]. ZFOs may also result from nonlinear interactions between a KH instability, SZF and trapped ion modes in a tokamak [56].
(c) Standard GAMs with a frequency of the order of the ion sound speed over the toroidal curvature length scale, c_s/R_0. GAMs can be considered as the geodesic counterpart of the ion acoustic wave (IAW in cylindrical geometry) due to the magnetic geometry of the tokamak/helical device.
(d) EGAMs. EPs may couple to an existing GAM/GGAM branch or drive an EGAM. These GAMs typically frequency chirp around the EP ion transit frequency. In other situations they are set by the EP resonances, so practically the EGAM frequency is lower than (often around half), but also as high as twice that of the standard GAM.

An example of this rich fluctuation spectrum is shown in figure 6 of [57] (cf figure 114 in section 16) from a numerical simulation of a large helical device (LHD) configuration with a simultaneous SZF, trapped particle driven ZFO/LFO, and a GAM. ZFOs are important to the GAM story. In stellarator or helical-field configurations trapped particle driven ZFOs are predicted to be stronger than GAMs in certain conditions. Their frequency and damping being intrinsically related to the magnetic geometry via $\bar{\omega}_d = k_r \bar{v}_d$ (bounce averaged drift velocity) [57]. In a tokamak the trapped particle response is behind the neoclassical polarization (equivalently, neoclassical inertia enhancement) that defines the Rosenbluth–Hinton (RH) residual [52] and collisional ZF damping. Strong magnetic field ripple and externally applied resonant magnetic perturbations (RMPs) may be a source of other trapped particle resonances. Of equal interest are the effects of plasma rotation, pressure anisotropy and diamagnetic drifts which may open-up a low frequency GAM-like branch in the dispersion relation, which bridges into the SZF. Since ZFOs and GAMs are effectively in competition for the turbulent energy there is the deeper issue of their interaction and transformation, particularly when approaching confinement mode transitions.

In recent years there have been major advances in all areas of GAM research with many hundreds of papers published. This review assesses the status of these developments and the progress made to-date towards a unified understanding of the GAM behaviour and its role in plasma transport and confinement. The focus is on the oscillatory flows in magnetic confinement devices—principally GAMs, but extending to the low frequency ZFOs and the transitions between them. The pure zero-mean-frequency stationary ZFs are not discussed directly as they have been extensively covered elsewhere, for example in the wide-ranging review of [53] and the more focussed reviews [58–61] of some ten years ago. There is also a collection of papers on ZFs in a special section of the April 2006 issue of *Plasma Physics and Controlled Fusion* [62]. More recently there have been a couple of brief reviews of GAMs with emphasis on kinetic theory [63] and its application to experiment [64].

The review begins with general tutorial-like introductions to the basic linear theory of turbulence driven GAMs in section 2 and EGAMs in section 3. The focus is on the basic

concepts of the GAM formation, structure and damping mechanisms using MHD/fluid and kinetic models in simple toroidal geometry. Some additional specific elements of theory relating to particular aspects of the GAM behaviour, such as equilibrium shaping and rotation effects, are introduced in the subsequent topic sections together with the experimental measurements. The theory introductions are supplemented by two brief reviews focussing on the theory of GAM generation and non-linear effects in section 4, and on GK numerical simulations and benchmarking studies in section 5.

The GAM experimental results are presented in the second part of the review, which begins with an overview of the current status of experimental observations and diagnostic capabilities in section 6 in the form of tables. Then follows a series of topic orientated sections which review, first the basic GAM characteristics and its identification in section 7—including the effects of pressure anisotropy, isotope, and impurities as well as plasma shaping—then the GAM modal structure and sidebands in section 8, and the GAM radial structure and propagation in section 9. Most GAM studies have been made in stationary plasmas, but the effects of plasma rotation on the GAM frequency and amplitude can be significant. These effects are discussed in section 10.

The approach adopted here is to present and contrast the experimental evidence against the theory predictions and numerical simulations. Each section contains an introduction and a summary with the intention that each topic can be read independently, allowing the reader to dip into the review at will. Nevertheless, the GAM has many overlapping and interlinked elements, which are brought together via cross-referencing.

After the basic characteristics it is logical to address the GAM drive and damping. Section 11 reviews the various GAM drive mechanisms; including turbulence threshold effects as well as external drive mechanisms such as modulation and biasing. This is followed by GAM damping mechanisms in section 12. EGAMs are the topic of section 13. This leads into the role of the nonlinear coupling between the turbulence and the GAM in section 14, and then to the impact of GAMs on plasma transport in section 15. The effects of non-axisymmetric field configurations are addressed in section 16, which includes the special feature of stellarator LFOs, and the driving and suppression of GAMs by MHD islands and externally applied RMPs. Section 17 addresses the formation of finite frequency ZFOs and their transition into GAMs. The specific ZFO generation mechanisms include: rotation, which was addressed in section 10; pressure anisotropy in section 2.3 and diamagnetic drifts in section 2.13. The last topic of the review, in section 18, is the role of GAMs in plasma confinement mode transitions. Finally, conclusions are drawn in section 19 with an outlook to future prospects and developments.

2. Overview of GAM theory

In this section an overview of theoretical developments in linear GAM theory and its components is given. To simplify exposition, different effects are considered separately, progressing from basic MHD model to more advanced formulations with two-fluid, kinetic and GK theories and include dispersion, drift, and wave–particle interactions effects. The collation of the linear effects of plasma rotation is presented separately, in section 10. Table 1 provides a high level synopsis of various effects discussed in this section.

The GAM oscillation is based on the balance and feedback of two mechanisms for the radial current: one induced by the inertial plasma response related to the time derivative of the $m = 0$ component of the radial electric field $E_r = -\partial\tilde{\phi}_0(r)/\partial r$, and the other one, the diamagnetic current $\mathbf{J}_\perp = -\left(c/B_0^2\right)\mathbf{B}_0 \times \nabla\hat{p}_1$, due to the $m = 1$ poloidal oscillations of plasma pressure $\hat{p}_1$.[4]

In toroidal geometry these two mechanisms are coupled via feedback when the poloidal plasma flow $\tilde{\mathbf{v}}_\perp = c\mathbf{B} \times \nabla\tilde{\phi}_0/B^2$ induces oscillations of plasma pressure due plasma compressibility, $\nabla \cdot \tilde{\mathbf{v}}_\perp \neq 0$. Additional contribution is also provided by ion sound perturbations propagating along the total magnetic field.

The dispersion relation for the GAM obtained from simple MHD theory [1], as described in section 2.1, is quantitatively different from the later result obtained in the kinetic theory [9]. Such a difference is not expected nor natural as the GAM is a low frequency mode to which the fluid (MHD) theory should be well applicable. The above discrepancy is corrected when one takes into the account the anisotropy of plasma pressure perturbations [65] in the low frequency MHD as described in section 2.2.

The coupling of the diamagnetic current (due to poloidal perturbations of plasma pressure) and radial inertial current also exists for modes with a finite toroidal mode number n. Such coupling of the finite m and n, EM (Alfvén) modes with GAMs result in the so-called beta-induced Alfvén eigenmodes (BAE) which have been ubiquitously detected in experiments [66–69]. The BAE dispersion relation is closely related to the GAM for modes with $m \approx nq$ as outlined in section 2.12. The GAM contribution to the BAE dispersion relation becomes a minimum frequency of the Alfvén continuum (achieved for $k_\parallel = 0$). The GAM related plasma pressure effects are important for Alfvén cascades (ACs) and q-profile diagnostics [67, 70–73].

The GAM inherently involves an $m = 1$ poloidal harmonic of pressure perturbations and, as a result, is coupled to the $m = 1$ ion sound mode. The ion sound corrections $\sim c_s^2/q^2R_0^2$ to the GAM dispersion can be obtained in the fluid theory (section 2.1), however, due to anisotropy of the *pressure perturbations*, the exact expressions are different from those obtained from a single fluid (isotropic pressure) MHD. More accurate expressions can be obtained either from two-pressure MHD or from the kinetic theory as described in section 2.5. A finite electron temperature provides additional contributions

[4] In what follows, unless stated otherwise, the notation X_0 denotes the equilibrium values, $\tilde{X}$—general perturbations, $\tilde{X}_0$—the perturbed $m = 0$ quantities, and $\hat{X}_m$—$m \neq 0$ sidebands, CGS notation is also used throughout the theory sections.

Table 1. Overview of GAM theoretical models and effects.

Model	Effects	Notes
MHD fluid	Compressibility $\tilde{p} \sim \nabla \cdot \tilde{\mathbf{v}}_\perp \neq 0$ & diamag. current due to $\tilde{p}$ sideband	Basic GAM, $\gamma = 5/3$, equation (1)
	Anisotropy of pert. $\tilde{p}_\perp \neq \tilde{p}_\parallel$	$\gamma_\mathrm{i} = 7/4$, equation (15)
	Anisotropy of equilib. $p_{\perp 0} \neq p_{\parallel 0}$	Additional ZFO branch/instability, equation (22)
	Rotation effects	Additional ZFO/GAM branch(s) and instability, equation (265)
	EM effects and finite β	$m = 2\tilde{B}_\theta$ sideband, GGAM, BAE degeneration, equations (112) and (110)
Two-fluid	Ion sound Larmor radius dispersion	Equation (26)
	Drift effects & GAM instability	Two ω roots, equation (119)
	Geodesic oscillations of $\tilde{T}_\mathrm{i}$	Short wavelength mode, equation (127)
	Convective damping	Equation (106)
	Ion–ion collisional damping & freq. modifications	Equation (93)
Drift-kinetic	Ion transit (Landau) damping	Equation (50)
	Ion sound coupling	Equation (53)
	EGAM drive, reactive EGAM	Equation (183)
Gyro-kinetic	Transit & toroidal resonances	$p = 2$ resonance damping, equation (88)
	Dispersion & radial propagation	Equation (84)
	EGAMs	Equations (143)–(151)

to the GAM frequency. These modifications can be described within the two-fluid theory as presented in section 2.4.

In the lowest order, the basic dispersion relation for the GAM has no dispersion as the GAM frequency is independent of the wave vector of the perturbations. The higher order effects introduce a dependence on the radial wave vector—GAM dispersion. The GAM dispersion $\omega_\mathrm{GAM}(k_\mathrm{r})$ induces the radial propagation $\partial\omega_\mathrm{GAM}/\partial k_\mathrm{r} \neq 0$ and is important for the global eigenmode structure. There are several sources of dispersive corrections to the GAM frequency. GAM dispersion, related to the effects of ion inertia and finite electron temperature (the so-called ion sound Larmor radius effects $\sim k_\mathrm{r}^2\rho_\mathrm{s}^2$, $\rho_\mathrm{s}^2 = T_\mathrm{e}/m_\mathrm{i}\omega_\mathrm{ci}^2$) can be investigated within the basic two-fluid theory with a finite electron temperature. Other dispersion effects, such as finite ion Larmor radius $\sim k_\mathrm{r}^2\rho_\mathrm{i}^2$, $\rho_\mathrm{i}^2 = v_{T\mathrm{i}}^2/\omega_\mathrm{ci}^2$, and finite magnetic gradient drift $\sim \omega_\mathrm{d}^2/\omega^2$, where $\omega_\mathrm{d} = k_\mathrm{r}v_\mathrm{d} = k_\mathrm{r}\left(v_\perp^2/2 + v_\parallel^2\right)/\omega_\mathrm{ci}R_0$, generally require FLR kinetic (GK) theory, as described in section 2.5. Note that with $\omega_\mathrm{d} \sim k_\mathrm{r}v_{T\mathrm{i}}^2/(\omega_\mathrm{ci}R_0)$ and GAM frequency $\omega \sim v_{T\mathrm{i}}/R_0$, the finite magnetic drift frequency effects scale similar to the FLR effects, $(\omega_\mathrm{d}/\omega)^2 \simeq k_\mathrm{r}^2v_{T\mathrm{i}}^2/\omega_\mathrm{c}^2 \simeq k_\mathrm{r}^2\rho_\mathrm{i}^2$. Although these two effects formally look similar and both scale as $\sim k_\mathrm{r}^2\rho_\mathrm{i}^2$, they have different origins.

The terms due to the finite ratio $\omega_\mathrm{d}^2/\omega^2$ come from the radial excursion of particles due to the magnetic drift v_d and are sometimes called finite orbit width (FOW) effects. They appear in the second order expansion in a small parameter $\omega_\mathrm{d}^2/\omega^2 < 1$ and are related to the higher ($m \geqslant 2$) poloidal sidebands of plasma pressure, density and potential. Numerically, they have large factors related to $\sim \left\langle\omega_\mathrm{d}^{2m}\right\rangle$ moments of the distribution function and are different from the standard ion FLR term $\sim 3k_\mathrm{r}^2\rho_\mathrm{i}^2/4$. It is interesting that the sign of the finite ion sound Larmor radius dispersion $k_\mathrm{r}^2\rho_\mathrm{s}^2 = k_\mathrm{r}^2T_\mathrm{e}/\left(m_\mathrm{i}\omega_\mathrm{ci}^2\right)$ is negative while the ion FLR and FOW are positive, so that for high electron temperature $T_\mathrm{e} > 5.45\,T_\mathrm{i}$ [74], the dispersion may change sign to negative. The kinetic and $m = 2$ effects on the GAM dispersion are described in section 2.6.

In the literature, another expansion parameter $\omega_\mathrm{d}/(v_{T\mathrm{i}}/qR_0) \sim k_\mathrm{r}\rho_\mathrm{i}q$ is also referred to as the FOW effect. For the basic GAM the natural small parameters are $\omega \gg \omega_\mathrm{d}$ and $\omega \gg v_\parallel/qR_0 \sim v_{T\mathrm{i}}/qR_0$, but ω_d can be of the same order as the transit frequency $v_\parallel/qR_0$, $\omega_\mathrm{d} \sim v_\parallel/qR_0$. Thus the parameter $\omega_\mathrm{d}/(v_{T\mathrm{i}}/qR_0) \sim k_\mathrm{r}\rho_\mathrm{i}q$ does not need to be small and only occurs as a result of the specific method of the solution of the kinetic equation, see section 2.6. This parameter, however, defines the relative contribution of the transit and toroidal resonances to the mode damping as discussed below and further in section 2.6.

The various GAM driving mechanisms compete against the GAM damping, and their competition eventually determines the GAM occurrence and its amplitude for a particular set of plasma parameters. The collisionless GAM damping occurs due to collisionless wave–particle interactions. Typically, and for $q > 1$, the GAM frequency is larger than the particle transit $\omega_\mathrm{t} = v_\parallel/qR_0$ and toroidal drift ω_d frequencies, $\omega_\mathrm{GAM} > (\omega_\mathrm{t}, \omega_\mathrm{d})$. For a small fraction of particles, however, in the tail of the distribution function, the ω_t and ω_d could be of the same order as ω_GAM resulting in the effective energy exchange between particles and waves $\mathrm{d}\mathcal{E}/\mathrm{d}t = e(v_\parallel\mathbf{b} + \mathbf{v}_\mathrm{d}) \cdot \mathbf{E}$, where $\mathbf{v}_\mathrm{d} = \omega_\mathrm{c}^{-1}(v_\perp^2/2 + v_\parallel^2)\mathbf{B} \times \nabla \ln B/B$. Note that the contributions of both, the poloidal, $v_\parallel B_\theta E_\theta/B_0$, and the radial components of the electric field, $v_\mathrm{dr}E_\mathrm{r}$ are important. Respectively, both resonances $\omega \simeq v_\parallel/qR_0$, and $\omega \simeq \omega_\mathrm{d}$ are responsible for collisionless GAM damping. We will refer to the condition $\omega \simeq v_\parallel/qR_0$ as the transit (Landau) resonance and the condition $\omega \simeq \omega_\mathrm{d}$ as a toroidal resonance. Interaction with $m = 1$ components of the electric field, $\omega \simeq v_\parallel/qR_0$, results in the damping rate $\sim \exp(-\omega^2q^2R_0^2/v_{T\mathrm{i}}^2)$ and for $\omega^2 = \omega_\mathrm{GAM}^2 \simeq$

v_{Ti}^2/R_0^2, leads to the damping rate scaling as $\gamma \sim \exp(-q^2)$ which is considered as one of the factors responsible for the typical absence of GAMs in the tokamak core region. Often, due to the GAM eigenmode structure $k_r > 1/r$, the contribution of the poloidal drift velocity $v_d\theta E_\theta$ is neglected, however, it could be important for the global modes if $k_r \simeq 1/r$. The energy exchange due to the interaction of circulating particles with parallel electric field, $v_\parallel B_\theta E_\theta/B_0$, is also important for energetic particle (EP) driven modes. This is discussed further in sections 2.5 and 3.4.

The second order, $m = 2$ sidebands are often detected with GAMs. Indeed, these are often instrumental in GAM detection since $m = 2$ appear as magnetic signals that can be measured externally (see sections 13.3 and 8.4). It has been noted [54, 75–77] that the second order resonances $\omega \simeq 2v_\parallel/qR_0$ related to the $m = 2$ sidebands could provide damping rates comparable to those from the $m = 1$ harmonics. The higher order Landau resonances occur at lower velocities $\omega \simeq mv_\parallel/(qR_0)$, so that more particles participate. This effect however competes with the smaller amplitudes of the higher order sidebands which enter with a small dispersion factor $k_r^2\rho_i^2 < 1$. It was shown numerically that, generally, several harmonics have to be included in the analytic expressions to fully match the GAM damping results from full kinetic simulations [78, 79]. In general, the transit and toroidal resonances are coupled, e.g. the resonance condition for the first order resonance has the form $\Delta = \omega^2 - v_\parallel^2/q^2R_0^2 - \omega_d^2/2 = 0$, so that both transit and toroidal drift resonances have to be considered.

The collisionless wave–particle interaction may also result in GAM excitation due to EPs with non-Maxwellian distributions leading to the inverse Landau damping (mode growth) of GAMs. Furthermore, a strong contribution of EPs may result in a significant modification of the eigenmode structure and the appearance of new types of modes (see section 3), EGAMs. In this case, the higher m sidebands and FOW effects can be even more important due to larger values of the $k_r\rho q$ parameter for EPs, also leading to GAM excitations via the fractioanal resonances at large amplitudes, as discussed in section 13.5.

The GAM is also subject to collisional damping due to ion–ion collisions, ν_{ii}, which results in neoclassical viscosity damping of poloidal rotation [9, 80], $\gamma_c \simeq \nu_{ii}/\epsilon^\alpha$, where the value of α depends on the collisionality regime and whether passing or trapped particles are considered. The ion–ion collisions also result in a modification of the GAM real frequency [80] towards the isotropic MHD result, due to the equilibration of the *perturbed* plasma pressure resulting in the isotropic perturbations, $(\tilde{p}_\perp - \tilde{p}_\parallel) \sim \exp(-\gamma_c t)$, see section 2.10.

2.1. Basic mechanisms

The basic physics of GAM oscillations can be presented within a rather simple MHD model. Though it misses on many important questions, e.g. the GAM dispersion, the radial eigenmode structure, as well as damping and particle Landau resonance effects, the MHD model presented in [1] is an appropriate starting point of GAM theory providing a local MHD dispersion relation and giving the GAM frequency scaling with plasma pressure. Additional effects will gradually be introduced in subsequent sections for a more complicated and complete GAM theory.

The single-fluid ideal MHD equations have the form

$$\rho\frac{d\mathbf{v}}{dt} = \frac{1}{c}\mathbf{J}\times\mathbf{B} - \nabla p, \tag{2}$$

$$\mathbf{E} + \frac{1}{c}\mathbf{v}\times\mathbf{B} = 0, \tag{3}$$

$$\frac{dp}{dt} + \gamma p\nabla\cdot\mathbf{v} = 0. \tag{4}$$

The poloidal plasma rotation is a critical element of the GAM. Within the ideal MHD model the plasma flow velocity $\mathbf{v}$ is determined by the frozen-in condition (3). Then, in the lowest order, the $m = 0$ perturbation of the electrostatic potential $\phi_0(r, t)$ produces the radial electric field $\mathbf{E}_r = -\nabla\tilde{\phi}_0$, and, subsequently, the poloidal plasma flow within the magnetic flux surfaces, $\mathbf{v}_E = c\mathbf{E}_r\times\mathbf{B}/B^2$. For simplicity, one can use the circular geometry and the radial coordinate r as a magnetic flux surface label. Finite plasma compressibility, $\nabla\cdot\mathbf{v}_E \neq 0$, is another inherent element in the GAM picture. As the plasma moves poloidally in the nonuniform toroidal field, compressibility results in volume changes generating the $m = 1$ pressure/density sidebands. In the linear approximation one has

$$\frac{\partial\hat{p}_1}{\partial t} = -\gamma p_0\nabla\cdot\tilde{\mathbf{v}}_E. \tag{5}$$

Here, $\hat{p}_1$ means the $m = 1$ harmonic of the *perturbed pressure*. In low temperature (low β) plasmas, $\nabla\cdot\mathbf{v}_E = -2\mathbf{v}_E\cdot\nabla\ln B$, which emphasises that it is the poloidal plasma flow which generates the $m = 1$ pressure sidebands $\hat{p}_1$.

The restoring feedback that results in oscillations is provided via quasi-neutrality and the radial polarization current compensating the compressible part of the diamagnetic current from the $\hat{p}_1$ perturbations. The expression for the perpendicular current has the form

$$\mathbf{J}_\perp = \frac{en}{\omega_{ci}}\mathbf{b}\times\frac{d\mathbf{v}_E}{dt} + \frac{c}{B^2}\mathbf{B}\times\nabla p, \tag{6}$$

$d/dt = \partial/\partial t + \mathbf{v}_E\cdot\nabla$. The quasi-neutrality $\nabla_\perp\cdot\mathbf{J}_\perp = 0$ leads to the equation

$$-2\frac{c}{B}\mathbf{b}\times\nabla\hat{p}_1\cdot\nabla\ln B - \frac{en_0c}{B_0\omega_{ci}} \times\left(\frac{\partial}{\partial t}\nabla_\perp^2\tilde{\phi}_0 + \frac{c}{B_0}\left(\mathbf{v}_E\cdot\nabla\nabla_\perp^2\phi\right)_0\right) = 0. \tag{7}$$

The last term in this equation is the $m = 0$ component of the nonlinear inertial term Reynolds stress (RS) that will be discussed in section 4. Neglecting the nonlinear effects and using in (7) the expression for the perturbed pressure from (5) one has a basic GAM dispersion relation

$$\omega^2 = 4c_s^2\overline{(\nabla\ln B)^2} = \frac{2c_s^2}{R_0^2} \tag{8}$$

where $c_s^2 = \gamma p_0/n_0m_i$, and $\overline{(\nabla\ln B)^2} = \left(2R_0^2\right)^{-1}$ for the large aspect-ratio and circular cross-section used. In what follows,

Table 2. Summary of model predictions for the GAM modal structure and sidebands.

Parameter	Mode	Notes
Flow	$m=0, n=0$	$\tilde{v}_\perp$ magnitude follows RS strength
		$v_\parallel \propto (1/R_0)\partial\tilde{p}/\partial\theta$
	$m\neq 0, n\neq 0$	Non-axisymmetric equilib. + rotation, section 16.4
Pressure	$m=\pm 1, n=0$	$\tilde{p}\propto p_0\tilde{E}_\mathrm{r}\ \sin(\theta)$, up–down asymmetric
		$\propto \tilde{\phi}\ \sin(\theta)$, one-fluid MHD
Magnetic	$m=\pm 2, n=0$	$\tilde{B}_\theta \propto \sin(2\theta_\mathrm{s})$, up–down & in–out asymmetric
	$m=\pm 1$	$T_\perp \neq T_{\mathrm{i}\parallel}$ section 2.3, T_e dispersion, section 2.12, equation (111)
	$m=\pm 4$	Shape & EGAM, section 8.4

$B=B_0(1-r/R\cos\theta)$ is assumed. Note that $\gamma=5/3$ for a monoatomic gas.

Plasma flow along the magnetic field line couples the GAM with an $m=1$ ion sound mode. This can be simply included by adding the parallel flow $v_\parallel$ to the pressure perturbation equation

$$\frac{\partial\hat{p}_1}{\partial t}=-\gamma p_0\nabla\cdot\tilde{\mathbf{v}}_E-\gamma p_0\nabla_\parallel\hat{v}_{\parallel_1}. \tag{9}$$

Respectively, the parallel flow is driven by the pressure gradient force

$$m_\mathrm{i}n_0\frac{\partial\hat{v}_{\parallel_1}}{\partial t}=-\nabla_\parallel\hat{p}_1, \tag{10}$$

where $\nabla_\parallel=\mathbf{B}\cdot\nabla/B_0$.

The effect of the parallel flow $\hat{v}_{\parallel_1}$ modifies the $\hat{p}_1$ response in equation (5) bringing in the finite $1/qR_0$ effects

$$-\mathrm{i}\omega\left(1+\frac{c_\mathrm{s}^2\nabla_\parallel^2}{\omega^2}\right)\hat{p}_1=-\gamma p_0\nabla\cdot\tilde{\mathbf{v}}_E. \tag{11}$$

The quasi-neutrality condition (7), which is the equation for the $m=0$ harmonic, is not affected by the $\hat{v}_{\parallel_1}$. Thus from (7) and (11), and using $\nabla_\parallel=(qR_0)^{-1}\left(\partial/\partial\theta\right)$, the dispersion relation, modified to take account of the $m=1$ ion sound harmonic $\hat{v}_{\parallel_1}$, becomes

$$-\omega^2+\frac{\omega^2c_\mathrm{s}^2}{R_0^2\left(\omega^2-q^2c_\mathrm{s}^2\right)}=0, \tag{12}$$

which results in equation (1).

These simple arguments also highlight the polarization properties of the basic GAM which involve the $m=0$ harmonic of the potential $\tilde{\phi}_0$ and the radial electric field $\tilde{E}_{\mathrm{r}0}$, and the $m=1, \sim\sin\theta$ sideband of the pressure perturbation

$$\hat{p}_1=-\frac{2\mathrm{i}\gamma c}{\omega B_0R_0}p_0\tilde{E}_{\mathrm{r}0}\ \sin\theta, \tag{13}$$

and the $m=1, \sim\cos\theta$ sideband of the parallel velocity $\hat{v}_{\parallel_1}$

$$\hat{v}_{\parallel_1}=-\frac{\mathrm{i}}{\omega m_\mathrm{i}n_0qR_0}\frac{\partial}{\partial\theta}\hat{p}_1. \tag{14}$$

The poloidal $\sin\theta$ distribution of density fluctuations has been detected experimentally—see section 8.1. Table 2 summarizes the predicted modal structure for the flow and the accompanying sidebands.

It is worth noting that the dispersion relation (12) also shows the presence of the degenerate mode $\omega=0$. This degeneration can be removed by the nonlinear RS, plasma temperature gradient, anisotropy, or rotation, so that the $\omega=0$ mode becomes a low frequency ZF mode (termed ZFO). These details are described in sections 4.2, 2.13, 2.3, and 10 respectively.

2.2. GAM frequency in kinetic theory and two-pressure (CGL) model

This section describes how the superficial discrepancy between the kinetic and fluid calculations of the GAM frequency is resolved when taking into account the anisotropy of the perturbed pressure.

The first kinetic derivation of the GAM frequency making a direct connection to the original paper [1] was probably in [9] in the context of the relaxation of the poloidal rotation in tokamaks. There, the drift-kinetic equation (DKE) was used to obtain the expression

$$\omega_\mathrm{GAM}^2=\left(\frac{7}{4}+\tau_\mathrm{e}\right)\frac{v_{T\mathrm{i}}^2}{R_0^2}, \tag{15}$$

where the term with $\tau_\mathrm{e}=T_\mathrm{e}/T_\mathrm{i}$ describes the electron contribution, and $v_{T\mathrm{i}}^2=2T_\mathrm{i}/m_\mathrm{i}$. Thus, the kinetic theory predicts the factor 7/4 for the ion term compared to the factor γ from the single-fluid MHD. Noting that $\gamma=5/3$ for a monoatomic gas, the factor 5/3 of the fluid theory should be compared with 7/4 of the kinetic theory. Although the actual difference is not large, it is discomforting as the basic low frequency GAM should be fully amenable to the fluid description. The discrepancy between the GAM frequency obtained from the ideal MHD in [1], giving equation (8), and the results of kinetic calculations [5, 9, 81] that give (15), is not natural. The discrepancy is resolved by realizing that in general the *pressure perturbations* due to the compressibility of the poloidal flow are anisotropic even when the *equilibrium pressure* is isotropic. In other words, the compressibility indices for the parallel $\tilde{p}_\parallel$ and perpendicular pressure $\tilde{p}_\perp$ are different. The two-pressure fluid model that takes into account the anisotropy of the *perturbed* pressure fully removes [65, 82] the discrepancy between fluid (8) and kinetic results (15). The two-pressure ((Chew–Goldberger–Low (CGL)) model [83] with $p_\parallel$ and $p_\perp$ is equivalent to the equations for the evolution of isotropic pressure p and the parallel viscosity tensor $\Pi_\parallel=3\pi_\parallel(\mathbf{bb}-$

$\mathbf{I}/3)/2$, which defines the pressure anisotropy, $3\pi_\parallel/2 = p_\parallel - p_\perp$. The equation for the evolution of the parallel viscosity tensor can be obtained from Grad type moment equations [65, 84]. For a monoatomic gas the perturbed pressure and parallel viscosity are [65]

$$\frac{3}{2}\frac{\mathrm{d}p}{\mathrm{d}t} - 5p_{0\mathrm{i}}\mathbf{v}_E\cdot\nabla\ln B = 0, \tag{16}$$

$$\frac{\mathrm{d}}{\mathrm{d}t}\pi_\parallel - \frac{2}{3}p_{0\mathrm{i}}\mathbf{v}_E\cdot\nabla\ln B = 0. \tag{17}$$

The anisotropic part of the diamagnetic current due to $\Pi_\parallel$ has to be added to the perpendicular current that takes the form

$$\mathbf{J}_\perp = \frac{en_0}{\omega_{\mathrm{ci}}}\mathbf{b}\times\frac{\mathrm{d}\mathbf{v}_E}{\mathrm{d}t} + \frac{c}{B}\mathbf{b}\times\nabla p + \frac{c}{B}\mathbf{b}\times\nabla\cdot\boldsymbol{\Pi}_\parallel. \tag{18}$$

Then, the quasi-neutrality equation $\nabla\cdot\mathbf{J}_\perp = 0$ (7) is modified as follows:

$$\frac{2c}{B}\nabla\left(\hat{p}_1 + \frac{1}{4}\hat{\pi}_{\parallel 1}\right)\cdot\mathbf{b}\times\nabla\ln B - \frac{en_0c}{B_0\omega_{\mathrm{ci}}}\frac{\partial}{\partial t}\nabla_\perp^2\widetilde{\phi}_0 = 0. \tag{19}$$

Using the $m = 1$ components of the pressure $\hat{p}_1 \sim \sin\theta$ and parallel viscosity $\hat{\pi}_{\parallel 1} \sim \sin\theta$ from (16) and (17) one obtains the kinetic result of (15) with a 7/4 factor for the ion part of the GAM frequency. Note that the electron contribution with the τ_e factor in (15) is obtained by the addition of the electron pressure to the diamagnetic current in equation (18), assuming isothermal electrons, which is justified due to the condition $\omega < v_{Te}/qR_0$.

2.3. Anisotropic plasmas — GAM and the low frequency (zonal flow) instability

The GAM frequency is modified when an anisotropic equilibrium is considered. But what is more important is that the anisotropic pressure induces a coupling of the GAM and the ZF (zero-mean-frequency, degenerate mode) so that the ZF acquires a finite frequency. The latter low frequency branch may become unstable when the anisotropy is sufficiently large. This phenomena, and relevant results from the literature, are reviewed in this section.

The effect of anisotropy in the background or equilibrium plasma pressure $\chi = p_\perp/p_\parallel \neq 1$ on the ZF and GAM behaviour has been studied in a number of recent works [85–88]. These studies were performed within the MHD framework with the two-pressure CGL model (see section 2.5) from which a general GAM dispersion relation was obtained in the form [87]

$$\omega^4 - \left(\omega_{\mathrm{GAM}}^2 + \frac{c_\parallel^2}{q^2R_0^2}\right)\omega^2 + \frac{\chi c_\parallel^4}{6q^2R_0^4}\left\langle\frac{\partial}{\partial\theta}\ln\frac{1}{B^2}\frac{\partial}{\partial\theta}\ln\left(\frac{s_\perp}{s_{\parallel}^{1/3}}\right)\right\rangle = 0, \tag{20}$$

where

$$\omega_{\mathrm{GAM}}^2 = \frac{c_\parallel^2}{2R_0^2}\left\langle\frac{\partial}{\partial\theta}\ln\frac{1}{B^2}\left[\frac{\partial}{\partial\theta}\ln\left(\frac{\rho s_\parallel^{1/3}}{B^2}\right) + \frac{\chi}{3}\frac{\partial}{\partial\theta}\ln\left(\frac{\rho s_\perp}{B^2}\right)\right]\right\rangle, \tag{21}$$

and a poloidal average over the magnetic surface defined as $\langle f\rangle \equiv \left(R_0^2/2\pi r^2\right)\int_0^{2\pi} f\,\mathrm{d}\theta$, $c_\parallel^2 = 3p_\parallel/\rho$. The entropy functions are defined as in the CGL model: $s_\parallel = p_\parallel B^2/\rho^3$ and $s_\perp = p_\perp/\rho B$. From equations (20) and (21) one sees that for anisotropic pressure, the value of the GAM mode, which involves $m = 0$ and $m = \pm 1$ sidebands, depends not only on the average of the poloidal oscillations of the magnetic field B but also involves poloidal oscillations of plasma pressures $p_\perp, p_\parallel$ and density ρ, which enter via the $s_\parallel$, $s_\perp$ functions. Thus, the application of equations (20) and (21) requires specification of $p_\perp, p_\parallel$ and ρ profiles. The latter cannot be fully determined from CGL theory, and in general require solution of the Grad–Shafranov equation for the equilibrium.

However, an important result is that there now exist two branches for ω^2: ω_+^2 and ω_-^2, with $\omega_+^2 \gg \omega_-^2$ for $q \gg 1$. Using the anisotropic pressure equilibrium conditions for a tokamak with circular magnetic surfaces gives the following expressions [87]

$$\omega_\pm^2 = \frac{c_\parallel^2}{R_0^2}\frac{G_1 \pm \sqrt{G_0}}{2}, \tag{22}$$

where

$$G_1 = \frac{1}{2} + \frac{2\chi}{3} + \frac{\chi}{3}\lambda_\perp + \frac{1}{q^2}, \tag{23}$$

$$G_0 = \left(\frac{1}{2} + \frac{2\chi}{3} + \frac{\chi}{3}\lambda_\perp - \frac{1}{q^2}\right)^2 + \frac{2}{q^2}\left(1 + \frac{\chi}{3}\right)^2, \tag{24}$$

with

$$\lambda_\perp = \left\langle\left(\frac{\partial}{\partial\theta}\ln\frac{1}{B^2}\right)^2\right\rangle^{-1}\left\langle\frac{\partial}{\partial\theta}(\ln p_\perp)\frac{\partial}{\partial\theta}\ln\frac{1}{B^2}\right\rangle. \tag{25}$$

Note that the result depends significantly on the poloidal variation of the perpendicular pressure—which remains a free parameter in the CGL equilibrium. The low frequency mode ω_- was called the zonal mode as it merges into the zero-frequency ZF at $\chi = 1$, while the high frequency mode ω_+ was called the GAM mode. For a plasma equilibrium with a homogeneous average pressure ($p_\parallel + p_\perp = p(\psi)$) then $\lambda_\perp = (1-\chi)/2\chi$ and one obtains the earlier ideal MHD model [85, 86]. An interesting result is that the ω_- mode can become aperiodically unstable for certain equilibria [85, 87]. Lakhin *et al* [87] give the following condition for the instability: $\lambda_\perp < \chi/6 - 1$.

In general, the MHD/CGL results [85, 87, 89] show the GAM frequency increasing with the χ (anisotropy) and $\lambda_\perp$

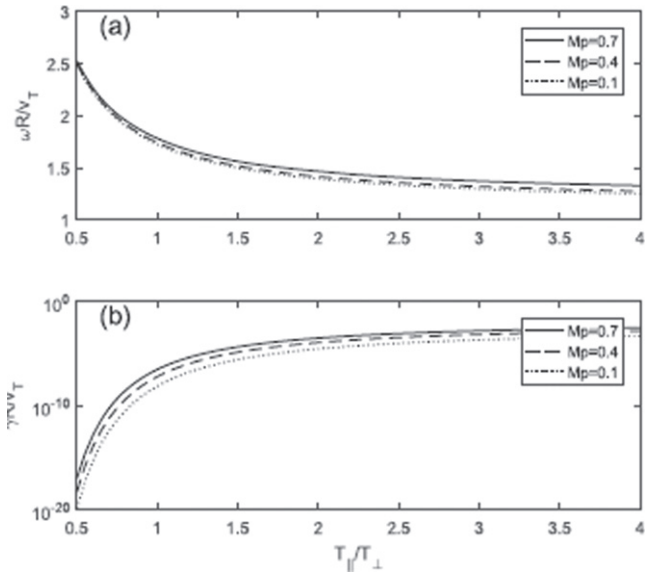

Figure 4. Normalized GAM frequency $\omega R_0/v_T$ and damping rate $\gamma R_0/v_T$ vs (ion) temperature anisotropy $T_\parallel/T_\perp$ from GK simulations of standard GAM in a low β, circular plasma, with $qR_0\omega/v_T \gg 1$. Reproduced from [90]. © 2018 Hefei Institutes of Physical Science, Chinese Academy of Sciences and IOP Publishing. All rights reserved.

parameters. Similar behaviour was obtained from GK theory [86, 90], and from an extended fluid model with Grad type evolution equations for the heat flux [89, 91]. The effects of plasma anisotropy in combination with toroidal rotation have also been considered [88, 92]. Centrifugal and Coriolis forces further modify the plasma equilibria, thus affecting the perturbations. A general low-frequency continuous MHD spectrum in a toroidally rotating plasma with anisotropic pressure was derived in [88] giving expressions for GAM frequencies, equivalent to (22)–(25), generalized for a rotating plasma.

The effect of an anisotropic *ion* distribution on the GAM frequency and damping was also studied by numerically solving the GK equation [90]. As shown in figure 4, the GAM frequency decreases with increasing ion $\chi^{-1} = T_\parallel/T_\perp$, while the damping rate increases. For $T_\parallel/T_\perp > 1.5$ the variation in frequency and damping are less dramatic.

Finally, the GAM magnetic components in a collisionless plasma with a weakly anisotropic ion distribution have been investigated [93]. An $m = 1$ perpendicular magnetic perturbation is discovered to be proportional to the relative difference between the perpendicular and parallel ion temperatures, in addition to an $m = 2$ perpendicular magnetic perturbation which always exists due to the $m = 2$ parallel return current. That is, a small temperature imbalance, of the order of 10%, can induce an $m = 1$ magnetic component of comparable amplitude to the $m = 2B_\theta$ component.

2.4. GAM dispersion due to ion sound Larmor radius effects

A finite electron temperature provides an additional correction to the GAM frequency that depends on the radial wavenumber so that GAM becomes dispersive and, as a result will propagate radially. The dispersion due to finite T_e is in fact due to the ion transverse inertia, similar to, for example, the dispersion of drift waves. This is the so-called ion sound Larmor radius effect and is easily described within the two-fluid theory as presented below.

The one-fluid MHD model for GAMs does not distinguish separate contributions of the electron and ion temperature to the GAM frequency. As discussed above, due to anisotropy of the *perturbed* ion pressure, the ion temperature enters the expression for the GAM frequency with a specific coefficient $\gamma_i = 7/4$, instead of the standard $\gamma = 5/3$ for a monoatomic gas. In the main order, neglecting non-adiabatic contributions, e.g. due to electron–ion collisions, the electron temperature remains constant due to the condition $\omega \ll v_{Te}/R_0$, thus resulting in the electron contribution corresponding to the isothermal ion sound velocity (with respect to the electron temperature), $\omega^2_{GAM} = 2(7T_i/4 + T_e)/m_iR_0^2$.

The electron contributions to the GAM can be described by a simple two-fluid model with cold ions. Such a model also instructively highlights another important effect: the GAM dispersion due to the finite electron temperature, or the so-called ion sound Larmor radius, $\rho_s^2 = T_e/m_i\omega_{ci}^2$. The GAM dispersion lowers the mode frequency and is responsible for radial GAM propagation due to the finite group velocity $\partial\omega_{GAM}/\partial k_r \neq 0$. The GAM dispersion is critical for the eigenmode structure and determines the radial length scale of the localized GAM eigenmodes. For cold ions the local GAM frequency is

$$\omega^2 = \frac{2T_e}{m_iR_0^2}\left(1 - \frac{1}{2}k_r^2\rho_s^2\right). \tag{26}$$

The dispersion corrections to the GAM frequency require accounting for the second order sidebands of pressure and potential, that need to be included in addition to the first order sidebands $\phi_s \sim n_s \sim \sin\theta$. Such effects can be easily illustrated within the two-fluid model.

The main constitutive equations in two-fluid model are the ion and electron continuity

$$\frac{\partial n}{\partial t} + \mathbf{v}_E\cdot\nabla n - 2n\mathbf{v}_E\cdot\nabla\ln B + \nabla_\parallel\left(nv_{\parallel i}\right) - \frac{cn_0}{B_0\omega_{ci}}\frac{\partial}{\partial t}\nabla_\perp^2\phi = 0, \tag{27}$$

$$\frac{\partial n}{\partial t} + \mathbf{v}_E\cdot\nabla n - 2n\mathbf{v}_E\cdot\nabla\ln B - 2n\mathbf{v}_{pe}\cdot\nabla\ln B + \nabla_\parallel\left(nv_{\parallel e}\right) = 0, \tag{28}$$

supplemented by the electron momentum balance (Ohm's law)

$$-eE_\parallel - T_e\nabla_\parallel n = 0. \tag{29}$$

The equation for the ion parallel velocity can be added to include the ion sound effects.

It is often convenient to use the current closure equation instead of the ion (or the electron) continuity equation. From the quasi-neutrality condition one has

$$2n\mathbf{v}_{pe}\cdot\nabla\ln B + \nabla_\parallel\left(nv_{\parallel i} - nv_{\parallel e}\right) - \frac{cn_0}{B_0\omega_{ci}}\frac{\partial}{\partial t}\nabla_\perp^2\phi = 0. \tag{30}$$

The $m = 0$ components of the current closure and density evolution are separated from (27) and (28) by the averaging in

poloidal angle, $\overline{(\ldots)} = (2\pi)^{-1}\int_0^{2\pi}(\ldots)\mathrm{d}\theta$, giving

$$2n\overline{\hat{\mathbf{v}}_{pe}\cdot\nabla\ln B} - \frac{cn_0}{B_0\omega_{ci}}\frac{\partial}{\partial t}\nabla_\perp^2\tilde{\phi}_0 = 0. \tag{31}$$

$$\frac{\partial\overline{n}}{\partial t} - 2n\overline{\hat{\mathbf{v}}_E\cdot\nabla\ln B} - \frac{cn_0}{B_0\omega_{ci}}\frac{\partial}{\partial t}\nabla_\perp^2\tilde{\phi}_0 = 0. \tag{32}$$

Here, the oscillating (sideband) harmonics are defined as $\hat{(\ldots)} = (\ldots) - \overline{(\ldots)}$; note that $\overline{X} = X_0$ will be used below for $m = 0$ perturbations.

For the adiabatic sideband, when $\hat{n} = e\hat{\phi}/T_e n_0$, and $\overline{\hat{\mathbf{v}}_{pe}\cdot\nabla\ln B + \hat{\mathbf{v}}_E\cdot\nabla\ln B} = 0$, one can see from equations (31) and (32) that the $m = 0$ component of the perturbed density is zero, $\overline{n} = 0$, while the $m = 0$ potential perturbation is finite, $\overline{\phi} \neq 0$. The equations for the oscillating sidebands follow from the density equations (27) and (28)

$$\left(2n\hat{\mathbf{v}}_{pe}\cdot\nabla\ln B - \overline{(\ldots)}\right) - \frac{cn_0}{B_0\omega_{ci}}\frac{\partial}{\partial t}\nabla_\perp^2\hat{\phi} = 0, \tag{33}$$

$$\frac{\partial\hat{n}}{\partial t} - 2\left(n\hat{\mathbf{v}}_E\cdot\nabla\ln B - \overline{(\ldots)}\right) - \frac{cn_0}{B_0\omega_{ci}}\frac{\partial}{\partial t}\nabla_\perp^2\hat{\phi} = 0. \tag{34}$$

Here, the parallel ion density contribution is neglected, so the coupling to the ion sound modes is omitted.

As follows from equations (33) and (34) the dispersive effects in the two-fluid model with cold ions originate from the transverse ion inertia (ion sound Larmor radius effect), described by the last terms in (33) and (34). One has to require the small parameter, $k_r^2\rho_s^2 < 1$, to justify neglecting the higher sidebands. Therefore, considering $\hat{X} = \hat{X}_{(s)}\sin\theta + \hat{X}_{(2c)}\cos 2\theta$, for $\hat{X} = (\hat{n}, \hat{\phi})$, one has the full system:

$$-\mathrm{i}\omega\hat{n}_{(s)} - \mathrm{i}\omega_D\overline{\phi} - \mathrm{i}\omega k_r^2\rho_s^2\hat{\phi}_{(s)} + \frac{\mathrm{i}}{2}\omega_D\hat{\phi}_{(2c)} = 0, \tag{35}$$

$$-\mathrm{i}\omega\hat{n}_{(2c)} + \frac{\mathrm{i}}{2}\omega_D\hat{\phi}_{(s)} - \mathrm{i}\omega k_r^2\rho_s^2\hat{\phi}_{(2c)} = 0 \tag{36}$$

$$-\mathrm{i}\omega k_r^2\rho_s^2\hat{\phi}_{(s)} - \mathrm{i}\omega_D\overline{n} + \frac{\mathrm{i}}{2}\omega_D\hat{n}_{(2c)} = 0 \tag{37}$$

$$-\mathrm{i}\omega k_r^2\rho_s^2\hat{\phi}_{(2c)} + \frac{\mathrm{i}}{2}\omega_D\hat{n}_{(s)} = 0. \tag{38}$$

Here, dimensionless $e\hat{\phi}_{(s,2c)}/T_e \to \hat{\phi}_{(s,2c)}$ and $\hat{n}_{(s,2c)}/n_0$ are used, and $\omega_D = 2k_r cT_e/(eB_R)$. The mean part of the current closure (31) in the form

$$-\mathrm{i}\omega k_r^2\rho_s^2\overline{\phi} - \mathrm{i}\frac{\omega_D}{2}\hat{n}_{(s)} = 0, \tag{39}$$

with equations (35)–(38) results in the GAM with the ion sound Larmor dispersion (26). The finite ion sound Larmor radius corrections to the GAM frequency are negative, while the finite ion temperature effects are positive as discussed in the section below.

2.5. Transit resonance (Landau) and coupling to the ion sound

The ion parallel motion in response to the $m = 1$ electric field perturbation is responsible for the GAM coupling to the ion sound branches and for the resonant Landau interactions due to the $\omega \simeq v_\parallel/qR_0$ resonance. In this section a basic theoretical framework required for the description of these effects is outlined.

Many significant GAM properties such as damping, dispersion and EP effects cannot be described within the fluid theory and thus require the kinetic theory. A simplest form of the drift-kinetic theory allows to highlight the main features of resonant GAM interactions leading to damping and GAM excitation as well as to obtain the ion-sound corrections to the GAM due to the inertial ion parallel motion. The lowest order drift-kinetic equation (DKE) can be written as [94]

$$\frac{\partial f}{\partial t} + v_\parallel\mathbf{b}\cdot\nabla f + \mathbf{v}_E\cdot\nabla f + \mathbf{v}_d\cdot\nabla f + \frac{q}{m}E_\parallel\frac{\partial f}{\partial v_\parallel} + \mathbf{v}_E\cdot\nabla\ln B\left(v_\parallel\frac{\partial f}{\partial v_\parallel} + v_\perp^2\frac{\partial f}{\partial v_\perp^2}\right) + \left(\frac{v_\perp^2}{2}\frac{\partial f_0}{\partial v_\parallel} - v_\parallel v_\perp^2\frac{\partial f_0}{\partial v_\perp^2}\right)\nabla\cdot\mathbf{b} = 0. \tag{40}$$

Here, $f = f\left(v_\parallel, v_\perp^2, \mathbf{r}, t\right)$ is the particle distribution function where $\mathbf{r}$ is the guiding centre coordinate; in this order (without the inertial drift) the difference between guiding centre and particle coordinates is not important. The low β limit, $\nabla\times\mathbf{B} \simeq 0$, is assumed so that the magnetic drift velocity $\mathbf{v}_d$ is

$$\mathbf{v}_d = \frac{1}{\omega_c}\left(\frac{v_\perp^2}{2} + v_\parallel^2\right)\mathbf{b}\times\nabla\ln B. \tag{41}$$

In the linear approximation and omitting the effects due to density and temperature gradients in the equilibrium, the $m = 1$ harmonics of the pressure $\hat{p}_1$ and viscosity $\hat{\pi}_{\parallel 1}$ (or alternatively $\hat{p}_{\perp 1}$ and $\hat{p}_{\parallel 1}$) can be calculated from the linearized form of the DKE (40) assuming the Maxwellian (isotropic) equilibrium function $f_0\left(v_\parallel, v_\perp^2\right)$

$$-\mathrm{i}(\omega - \hat{\omega}_d)\widetilde{f} + \frac{v_\parallel}{qR_0}\frac{\partial}{\partial\theta}\widetilde{f} + \frac{q}{m}E_\parallel\frac{\partial f_0}{\partial v_\parallel} + \mathbf{v}_E\cdot\nabla\ln B\left(v_\parallel\frac{\partial f_0}{\partial v_\parallel} + v_\perp^2\frac{\partial f_0}{\partial v_\perp^2}\right) = 0, \tag{42}$$

where

$$\hat{\omega}_d = -\frac{1}{\omega_c R_0}\left(\frac{v_\perp^2}{2} + v_\parallel^2\right)k_r\sin\theta. \tag{43}$$

From this equation, in the lowest order, $\omega \gg \left(\omega_d, v_\parallel/qR_0\right)$, the perturbed distribution function, $\widetilde{f}_1 \sim \sin\theta$, is due to the compressibility of the $\tilde{\mathbf{v}}_{E0}$ flow due to the $m = 0$ electrostatic potential $\tilde{\phi}_0$ as

$$\widetilde{f}_1 \simeq \mathrm{i}\left(2v_\parallel^2 + v_\perp^2\right)\frac{\tilde{\mathbf{v}}_{E0}\cdot\nabla\ln B}{\omega v_{Ti}^2}f_0. \tag{44}$$

Expression (44) clearly shows that the pressure perturbations are anisotropic even if the equilibrium distribution function f_0 is isotropic Maxwellian. The perturbed distribution function (44) can be used to find the total contribution of the ion diamagnetic current including the anisotropic pressure tensor in

equation (18):

$$\langle \mathbf{v}_{\rm d} f\rangle = \frac{1}{m\omega_{\rm c}}\left(p_\perp + p_\parallel\right)\mathbf{b}\times\nabla\ln B$$
$$= \frac{1}{m\omega_{\rm c}}\left(2p + \frac{1}{2}\pi_\parallel\right)\mathbf{b}\times\nabla\ln B$$
$$= \nabla\cdot\left(\frac{c}{B}\mathbf{b}\times\nabla p + \frac{c}{B}\mathbf{b}\times\nabla\cdot\mathbf{\Pi}_\parallel\right), \qquad (45)$$

where the pressure moments are

$$p_\perp = m\left\langle\frac{v_\perp^2}{2}f\right\rangle, \qquad (46)$$

$$p_\parallel = m\left\langle v_\parallel^2 f\right\rangle. \qquad (47)$$

Here, the angle brackets $\langle..\rangle$ means averaging over the full velocity space. Instead of $p_\perp$ and $p_\parallel$, one can use the isotropic pressure $p = \left(2p_\perp + p_\parallel\right)/3$ and the parallel viscosity $\pi_\parallel = 2(p_\parallel - p_\perp)/3$. The latter notations are convenient to make the connection to the standard neoclassical theory of plasma rotation in a tokamak.

The GAM oscillation feedback relies on the inertial polarization current, the first term in equation (18), which is absent in the lowest order DKE as given by equation (40). In other words, the first term in equation (18) cannot be obtained from (40). Therefore, the full quasi-neutrality condition has to be obtained either from the higher order kinetic equation with large flows [95–98] that amounts to adding the inertial term to equation (40), as it was done in [8], or from the full GK equation, as in [5]. Equivalently, one can use the current closure equation in the form (134), and use the DKE to find the perturbed distribution function for calculations of $p_1 + \pi_{\parallel 1}/4$. Using equations (19) and (44) one finds the ion contribution with the $7/4$ factor as in the dispersion relation (15).

The DKE (42) also clearly illustrates the nature of the resonant ion Landau damping that leads to collisionless damping of GAMs [9]. Here, we have to allow for the mode resonances with the ion transit motion so that $\omega \simeq v_\parallel/qR_0 \gg \omega_{\rm d}$. Then, one finds from (42) for the perturbed distribution function in the form $\widetilde{f} = \widetilde{f}_{\rm c}\cos\theta + \widetilde{f}_{\rm s}\sin\theta$:

$$\omega\widetilde{f}_{\rm c} - \frac{v_\parallel}{qR_0}\widetilde{f}_{\rm s} = 0, \qquad (48)$$

$$\omega\widetilde{f}_{\rm s} + \frac{v_\parallel}{qR_0}\widetilde{f}_{\rm c} + \frac{2c}{B_0R_0}k_{\rm r}\widetilde{\phi}_0\frac{v_\parallel^2 + v_\perp^2/2}{v_{Ti}^2}f_0 = 0, \qquad (49)$$

where radially localized perturbations are assumed so that $k_{\rm r} \gg 1/r$. Solving equations (48) and (49) one has the expression

$$\widetilde{f}_{\rm s} = \frac{2\omega}{\omega^2 - v_\parallel^2/q^2R_0^2}\frac{ck_{\rm r}\widetilde{\phi}_0}{B_0R_0}\frac{v_\parallel^2 + v_\perp^2/2}{v_{Ti}^2}f_0, \qquad (50)$$

which shows the resonance at $\omega \simeq v_\parallel/qR_0$ leading to the transient resonance damping.

The transient time damping is often approximated as $\gamma \propto \exp(-v_{\parallel{\rm r}}^2/v_{Ti}^2) \propto \omega_{\rm GAM}\exp(-q^2)$ [99], where $v_{\parallel{\rm r}} \simeq \omega_{\rm GAM}qR_0$. However, this simple estimate neglects a toroidal resonance since $\omega \simeq v_\parallel/qR_0 \gg \omega_{\rm d}$ was assumed. Since the effects of $\omega_{\rm d} = k_{\rm r}V_{\rm dr}$ correspond to the radial particle drift off the magnetic surface, such effects are often called FOW. FOW effects are important both for the GAM dispersion and GAM damping due to the toroidal resonance $\omega \simeq \omega_{\rm d}$. In general, the transit and toroidal resonances are coupled even in the lowest (non-dispersive) order, so they can be considered within the drift-kinetic approximation as given by equations (40) and (18). However, since the GAM requires an inertial current (omitted in the drift-kinetic theory) it is more convenient to discuss the transit and toroidal GAM damping in more general GK theory which fully takes into account all inertial and FLR effects. GK theory is also more convenient for the discussion of the second, $m = 2$, harmonics that are important both for the GAM damping and dispersion. This discussion is presented in section 2.6.

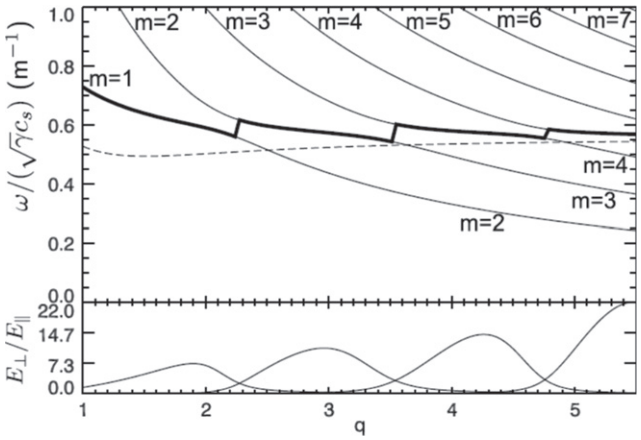

Figure 5. Frequency of SW branches (thin solid), GAM (thick), and pure GAM frequency (dashed) versus safety factor q. Reproduced from [14]. © IOP Publishing Ltd. All rights reserved.

As outlined in section 2.1, the GAM is inherently related with ion-sound perturbations due to plasma motion along the magnetic field, formally manifested via the $\hat{v}_{\parallel 1}$ and $\hat{p}_1$ coupling. Within the simple one fluid MHD, such coupling results in the $1 + 1/2q^2$ correction factor to the GAM frequency. In fact, the anisotropy of plasma pressure perturbations also affects the contribution of the ion sound coupling which can be accurately described by the full CGL model taking into account the parallel velocity. Alternatively, such corrections of the order of $\sim v_{Ti}^2/\left(\omega^2q^2R_0^2\right)$ can be obtained from kinetic theory. From equation (40) one finds

$$\hat{f}_1 = {\rm i}\left(2v_\parallel^2 + v_\perp^2\right)\left(1 - \frac{v_\parallel^2}{\omega^2q^2R_0^2}\right)\frac{\tilde{\mathbf{v}}_{E0}\cdot\nabla\ln B}{\omega v_{Ti}^2}f_0. \qquad (51)$$

Using this expression in (46) and (47), one obtains from (19)

$$\omega^2 = \frac{7}{4}\frac{v_{Ti}^2}{R_0^2}\left(1 + \frac{46}{49}q^{-2}\right). \qquad (52)$$

Finite electron temperature allows the excitation of the parallel electric field $\hat{E}_{\parallel 1}$ related to the $m = 1$ harmonic of the perturbed potential which also needs to be included into the calculation of the ion response. The dispersion relation (52) is then modified and additional terms of the order $v_{Ti}^2/\omega^2q^2R_0^2$

Table 3. Various model predictions for the GAM frequency, with $c_s^2 = \gamma p_0/\rho_0 \to (T_e + \gamma_i T_i)/m_i$, and $v_{Ti}^2 = 2T_i/m_i$, and $\tau_e = T_e/T_i$ and M = Mach number.

Formula ω^2	Model
$\omega^2 = 2c_s^2/R_0^2(1 + 1/2q^2)$	One-fluid MHD + ion sound, equation (1)
$\omega^2 = (\frac{5}{3} + \tau_e)v_{Ti}^2/R_0^2$	Two-fluid MHD with warm electrons
$\omega^2 = \left(\frac{7}{4} + \tau_e\right)_{Ti}^2/R_0^2$	Kinetic and two-pressure, equation (15)
$\omega^2 = (\gamma_i + \tau_e)_{Ti}^2/R_0^2(1+\beta)^{-1}$	Finite β correction, equation (110)
$\omega^2 = \left(\frac{5}{3} + \frac{1}{12}(1 + 6i\nu_i/5\omega)^{-1}\right) v_{Ti}^2/R_0^2$	Two-pressure + collisions, equation (93)
$\omega^2 = 2T_e/m_i R_0(1 - k_r^2\rho_s^2/2)$	Dispersive, $T_i = 0$, equation (26)
$\omega^2 = \beta(k_r^2\rho_i^2)v_{Ti}^2/R_0^2$	Ion temp. oscillations, equation (127)
$\omega^2 = c_s^2/R_0^2$ fnct.$(\kappa, \epsilon, ..)$	Non-circular, section 7.6
$\omega_\pm^2 = (G_1 \pm \sqrt{G_0})/2c_\parallel^2/R_0^2$	Equilib. pressure anisotropy, equation (22)
$\omega_\pm^2 = v_{Ti}^2/R_0^2$ fnct.(M^2)	Rotation effects, section 10, equations (265) and (266)

should be included [11, 74, 100]

$$\omega^2 = \frac{v_{Ti}^2}{R_0^2}\left(\frac{7}{4} + \tau_e\right) + \frac{v_{Ti}^4}{\omega^2 q^2 R_0^4}\left(\frac{23}{8} + \frac{2}{\tau_e} + \frac{1}{2\tau_e^2}\right). \quad (53)$$

The coupling to the parallel ion motion (effectively the ion sound modes) displayed in equations (52) and (53) was obtained as the corrections to the basic GAM mode frequency. It was suggested [14, 101] that crossing of the GAM continuum with ion-sound branches may result in non-perturbative modification of the mode frequency and formation of the radially localized eigenmodes. Figure 5 from [14] shows local GAM and ion-sound continua when higher m modes are included. FLR and FOW effects need to be included near the crossing point and it may be expected that the localized GAM eigenmodes occurs, squeezed, between the ion sound branches. It is interesting that somewhat similar localization of GAM eigenmodes was observed in nonlinear simulations in [102], see figure 26, and in [103], see figure 27.

Table 3 summarizes the various predictions for the GAM frequency from different models and effects.

2.6. Coupling of transit and toroidal resonances

Coupling of the $m = 0$ and higher $m = \pm 1, \pm 2, \ldots$ poloidal harmonics (sidebands) is a fundamental feature of the GAM dynamics. In general the truncation of the infinite series of harmonics $m = \pm 1, \pm 2, \pm 3, \ldots$ requires some small parameters. In this section we present two alternative approaches to dealing with such series, describing the various pitfalls, and review some of the literature results dealing with this problem. It is shown that even in the lowest order coupling to the $m = \pm 1$ order terms, the transient $\omega = v_\parallel/qR_0$ and toroidal $\omega = \omega_d$ resonances are coupled, in particular, affecting the mode damping and growth rates due to EPs.

GK theory provides the most complete description of GAM dynamics. GK formulation is required for the dispersion effects related to the higher order ($m \geqslant 2$) sidebands, in particular, those related to the ion Larmor radius effects, $\sim k_r^2\rho_i^2$. As is well known, in the linear GK theory, the FLR effects are manifested by the gyro-averaging operators represented by the Bessel functions, $\propto J_0^2(k_\perp v_\perp/\omega_{ci})$, which are not directly related to the magnetic gradient effects. For GAMs, there are additional dispersion effects directly related to the magnetic drifts, $\omega_d = k_r v_{dr}$. The FOW effects appear as second order corrections due to small terms of the order of $\omega_d^2/\omega^2 < 1$. These are obtained as the expansion of the solution of the GK equation in the $(\omega_d/\omega)^{2m}$ small parameter, and thus correspond to the higher moments of the distribution function $\sim \left\langle (v_\perp^2/2 + v_\parallel^2)^{2m} \right\rangle$ with $m \geqslant 2$. The dispersion due to the finite value of the ω_d^2/ω^2 (FOW) terms formally has a scaling similar to the finite ion Larmor radius, since $\omega_d^2/\omega_{GAM}^2 \sim k_r^2\rho_i^2$, though numerical values of the coefficient due to these terms greatly exceed the typical value $3/4$ that comes from the Bessel function expansion due to the ion FLR effects. In principle, following the Grad scheme, it is possible to devise a hierarchy of the higher order fluid moment equations that would capture the $(\omega_d/\omega)^4$ order terms, however, such equations are not easily available at the moment, and are not more compact and transparent compared to the direct GK formulations. The higher order terms $\omega_d^{2m}/\omega^{2m}$ can also be derived in the drift-kinetic approximation; the latter however misses the 'real' FLR effects.

A description of the dispersion and Landau damping is possible with full Vlasov equation as a starting point [104]. Effectively, the expressions for the dielectric permittivity tensor obtained in [104] correspond to the low frequency GK ordering: $\omega \ll \omega_{ci}$, with finite (but small) values of the ion Larmor radius, so that the dispersion effects due to $k_\perp^2\rho_i^2 < 1$ and higher order terms $(\omega_d^{2m}/\omega^{2m})$ are included. Here, the overview of the GAM dispersion and collisionless damping based on the GK approach is presented.

The standard GK equation in the form [105, 106] is used for ions

$$f_i = -\frac{e}{T_i}F_{0i}\phi + g_i, \quad (54)$$

$$\left(\omega - \hat{\omega}_{di} + \frac{iv_\parallel}{qR_0}\frac{\partial}{\partial\theta}\right) g_i = (\omega - \hat{\omega}_{*i})\frac{e}{T_i} \times \left(\phi - \frac{v_\parallel}{c}A\right) J_0^2(k_\perp v_\perp/\omega_i)F_{0i}, \quad (55)$$

where the harmonic time dependence $\exp(-\mathrm{i}\omega t)$ was assumed, and

$$\hat{\omega}_{*\mathrm{i}} = \omega_{*\mathrm{i}}\left(1+\eta_{\mathrm{i}}\left(\frac{v^2}{v_{T_{\mathrm{i}}}^2}-\frac{3}{2}\right)\right) \tag{56}$$

$$\hat{\omega}_{\mathrm{di}} = \mathrm{i}\frac{v_\perp^2/2+v_\parallel^2}{\omega_{\mathrm{ci}}}(\mathbf{b}\times\nabla\ln B)\cdot\nabla. \tag{57}$$

As standard in GAM theory, the normal magnetic curvature is neglected assuming that radial gradients are large compared to the poloidal, $\nabla_{\mathrm{r}} > \nabla_\theta$. Then for $\nabla \to \mathrm{i}\mathbf{k}$ one has

$$\begin{aligned}\hat{\omega}_{\mathrm{d}} \simeq k_{\mathrm{r}} v_{\mathrm{dr}} &= -\frac{v_\perp^2/2+v_\parallel^2}{\omega_{\mathrm{ci}}R_0}k_{\mathrm{r}}\ \sin\ \theta \\ &= -\overline{\omega}_{\mathrm{d}}\frac{v_\perp^2/2+v_\parallel^2}{v_T^2}\ \sin\ \theta \\ &= -\omega_{\mathrm{di}}\ \sin\ \theta,\end{aligned} \tag{58}$$

$$\omega_{*\mathrm{i}} = \frac{k_\theta c T_{\mathrm{i}}}{eB}\frac{n_0'}{n_0}, \tag{59}$$

where $\overline{\omega}_{\mathrm{di}} = k_{\mathrm{r}} v_{T\mathrm{i}}^2/(R_0\omega_{\mathrm{c}})$.

The GK equation (55) takes into account the EM perturbations (important for BAE modes) and drift effects and has been used to study kinetic properties of GAM and BAE modes in many works, e.g. [5, 74, 75, 107–109] and many others.

For the electrons FLR effects are not important, so the equations analogous to (54) and (55) can be used taking into account that $J_0^2(k_\perp v_\perp/\omega_{\mathrm{ce}}) \to 1$. In the limit $(\omega, \omega_{\mathrm{De}}) \ll v_{\parallel\mathrm{e}}/qR_0$, and neglecting the EM effects and all kinetic effects related to the damping due to electrons, the electron density response for the sidebands is Boltzmann in the main order, while the $m=0$ component of the density perturbation is zero. Thus, one can use $\hat{n}_m = e\hat{\phi}_m/T_{\mathrm{e}}n_0$, for $m=\pm1,\pm2$, and $\tilde{n}_0 = 0$ for $m=0$.

In the context of GAM theory there exist two approaches to the solution of the GK equation (55). In one approach, the exact solution of equation (55) is obtained by the method of integration over ion trajectories [110]. This method was widely used in many kinetic studies of GAMs. For example, [108] gives the formal solution of equation (55) for ions in the form $f_{\mathrm{i}} = \sum_{m=-\infty}^{\infty} f_m \exp(\mathrm{i}m\theta)$, where

$$\begin{aligned}f_m = -\frac{ef_0}{T_{\mathrm{i}}}\Bigg\{&\phi_m - J_0^2(kv_\perp/\Omega_{\mathrm{i}}) \\ &\times\sum_{n,l=-\infty}^{\infty}\mathrm{i}^{-l+m}\frac{\omega J_n(\xi)J_{n-l+m}(\xi)}{\omega+(n-l)\omega_{T\mathrm{i}}}\phi_l\Bigg\}.\end{aligned} \tag{60}$$

Here, $\xi = \omega_{\mathrm{di}}/\omega_{\mathrm{t}} = \omega_{\mathrm{di}}qR_0/v_\parallel$, and only passing ions are included.

Practical use of the expression (60) requires some care in handling the infinite series of Bessel functions. The basic GAM frequency has the ordering $\omega \gg (\omega_{\mathrm{di}}, v_\parallel/qR_0)$. However, the ratio of the magnetic drift frequency to the transit frequency does not have to be small, so the value of the parameter $\xi = \omega_{\mathrm{di}}/\omega_{\mathrm{t}}$ in the argument of the Bessel functions in (60) can be arbitrary. For large $\xi \geqslant 1$, the contribution of the terms $J_n(\xi)J_{n-l+m}(\xi)$ is not small for $n>1$, $n-l+m>1$, so that formally all terms in the series have to be included, even for $\omega \gg (\omega_{\mathrm{di}}, v_\parallel/qR_0)$. Moreover, small $\xi \ll 1$ expansions of the $J_n(\xi)J_{n-l+m}(\xi) \sim \xi^2$ terms formally contains singular $\sim 1/v_\parallel$ denominators that diverge for $v_\parallel \to 0$, e.g. see equation (1) in [76]. It was shown in [111] that these divergences are superficial and the diverging terms are cancelled with proper summation of all terms to the relevant order. A somewhat similar procedure to remove the $1/v_\parallel$ divergence was also used in [79]. Nevertheless, the most common approach was to expand the Bessel function in equation (60) for small ξ and retain only the first few terms in powers of $\xi = \omega_{\mathrm{di}}/\omega_{\mathrm{t}}$. As was shown in [111], this expansion becomes equivalent to the direct expansion of the GK equation in powers of $\omega_{\mathrm{d}}^2/\omega^2$.

The above noted technical difficulty becomes more severe when using the expression (60) for the calculation of the GAM damping due to passing ion resonances, with $\omega \simeq v_\parallel/qR_0$. Expression (60) directly shows the resonant contributions of passing ions at $\omega = pv_\parallel/qR_0$, where $p = \pm1, \pm2, \ldots$; and the magnitude of the $J_n(\xi)J_{p+m}(\xi)$ coefficients indicates the strength of the resonances at each value of p. For large $\xi = \omega_{\mathrm{di}}/\omega_{\mathrm{t}} \simeq qk_{\mathrm{r}}\rho_{\mathrm{i}} \geqslant 1$, the $J_n(\xi)J_{p+m}(\xi)$ coefficients do not decrease and all terms have to be formally included. Therefore, the FOW effects are even more important for the GAM damping in the regime $\omega_{\mathrm{di}}/\omega_{\mathrm{t}} \geqslant 1$. The importance of the higher order resonant term was pointed out in [76, 78, 112]. The higher order terms were handled numerically in [78, 112], where it was shown that many resonant terms, up to $p=10$, have to be included for larger values of q.

An alternative approach to the solution of the GK equation consists of a perturbative treatment of the coupling of various poloidal harmonics of the perturbed distribution function. This suggests directly solving the GK equation in the form of the series $f = f_0 + f_{\mathrm{c}}\cos\theta + f_{\mathrm{s}}\sin\theta + f_{2\mathrm{c}}\cos 2\theta + f_{2\mathrm{s}}\sin 2\theta\ldots$, assuming an analogous series for $\phi = \phi_0 + \phi_{\mathrm{s}}\cos\theta + \phi_{\mathrm{s}}\sin\theta + \phi_{2\mathrm{c}}\cos 2\theta + \phi_{2\mathrm{s}}\sin 2\theta\ldots$ Such an expansion is based on the fundamental small parameter that is required in the analytic theory of GAMs: $f_2/f_1 \sim \phi_2/\phi_1 \sim \phi_1/\phi_0 \sim \omega_{\mathrm{d}}/\omega \sim k_{\mathrm{r}}\rho < 1$. This approach was followed in [100, 107, 113, 114], in particular, for studies of the GAM dispersion [111]. Note that in this approach no restriction is placed on the value of the $\omega_{\mathrm{di}}/\omega_{\mathrm{t}}$ parameter.

To illustrate the main idea we consider the solution for the main order terms (all variables are for the perturbed quantities)

$$\phi = \phi_0 + \phi_{\mathrm{s}}\ \sin\ \theta, \tag{61}$$

$$f = f_0 + f_{\mathrm{s}}\ \sin\ \theta + f_{\mathrm{c}}\ \cos\ \theta, \tag{62}$$

which are sufficient for the basic electrostatic GAM including the $m=0$ and $m=1$ harmonics of the perturbed potential and $m=1$ density perturbations; one can show that the $\phi_{\mathrm{c}}\cos\theta$

component is decoupled in the absence of the drift effects and symmetric (in $v_\parallel$) equilibrium distribution function.

From equation (55) one obtains the following system of equations for (61) and (62)

$$\omega g_0 + \frac{1}{2}\omega_d g_s = \omega\phi_0 \frac{eF_{0i}}{T_i} J_0^2, \tag{63}$$

$$\omega g_s + \omega_d g_0 - i\frac{v_\parallel}{qR_0} g_c = \omega\phi_s \frac{eF_{0i}}{T_i} J_0^2, \tag{64}$$

$$\omega g_c + i\frac{v_\parallel}{qR_0} g_s = 0, \tag{65}$$

which has the following solution for g_0 and g_s

$$g_s = \frac{(\omega^2\phi_s - \omega\omega_D\phi_0)}{\omega^2 - v_\parallel^2/q^2R_0^2 - \omega_d^2/2} \frac{eF_{0i}}{T_i} J_0^2, \tag{66}$$

$$g_0 = \frac{\left(-\omega_D\omega\phi_s/2 + (\omega^2 - v_\parallel^2/q^2R_0^2)\phi_0\right)}{\omega^2 - v_\parallel^2/q^2R_0^2 - \omega_d^2/2} \frac{eF_{0i}}{T_i} J_0^2, \tag{67}$$

where

$$\Delta = \omega^2 - \frac{v_\parallel^2}{q^2R_0^2} - \frac{\omega_d^2}{2}, \tag{68}$$

is the resonance propagator.

Using $n_s = e\phi_s/T_e n_0$ and $n_0 = 0$ one easily gets from equations (66) and (67) the general dispersion relation in neglect of dispersion effects

$$\Gamma_0 - 1 + \frac{1}{2}\left\langle \omega_{di}^2 J_0^2/\Delta \right\rangle + \frac{\tau_e}{2}\left\langle \omega\omega_{di}^2 J_0^2/\Delta \right\rangle^2 = 0. \tag{69}$$

Note that this dispersion relation fully takes into account resonant effects due to the transient and toroidal resonances. In neglect of the resonances, $\Delta \to \omega^2$, and one has $\omega^2 = \left(7/4 + \tau_e\right)\overline{\omega}_{di}^2/k_r^2\rho_i^2$. In general, the resonance propagator shows coupling of transient (passing particles), $\omega \simeq \omega_t$ and toroidal, $\omega \simeq \omega_d/\sqrt{2}$ resonances, even in the main order.

One can represent the resonance function as a series

$$\frac{1}{\omega^2 - v_\parallel^2/q^2R_0^2 - \omega_d^2/2} = \frac{1}{\omega^2 - \omega_t^2}\left[1 + \frac{\omega_d^2/2}{\omega^2 - \omega_t^2} + \frac{\omega_d^4/4}{\left(\omega^2 - \omega_t^2\right)^2} + \cdots\right], \tag{70}$$

which illustrates that the toroidal resonance can be viewed as a series of multiple transient resonances of the higher orders, such as $1/\left(\omega^2 - \omega_t^2\right)^n$, as has been noted in [115].

In [115, 116], an approximate procedure was used with the expansion of the resonant denominator $1/\left(\omega - \omega_d\right) = 1/\left(\omega - \hat{\omega}_d \sin\theta\right)$ near the $\theta = \pm\pi/2$. Note that the sign of the magnetic drift term $\omega_d = k_r v_{Ti}\rho_{Ti}\left(v_\perp^2/2 + v_\parallel^2\right)\sin\theta$ in [115] and a number of other works, is opposite to what is used here in equation (58), which is the same convention as used elsewhere, e.g. [11, 116]. The representation in equations (66)–(68) directly captures the toroidal resonances effects $1/\left(\omega^2 - \omega_d^2/2\right)$ for the GAM mode involving the ϕ_0 and ϕ_s perturbations without any additional expansions. The addition of second harmonics makes the coupling more complicated; the expressions for f_s, f_c, f_{2c} and f_{2s} with the second order resonant propagator Δ_2 were obtained in [114]. It would be important to compare the GAM damping obtained with the full propagator Δ in equation (68), or Δ_2 from [114], with the results of the summation of multiple harmonics as in [78, 79, 112]. The representation (66)–(68) will also be useful in the EGAM theory discussed in section 3. It is also worth noting at this point that the above discussion of toroidal resonance only applies to passing particles. Effects of the toroidal drift of trapped ions are more involved and will be commented on later.

2.7. GAM dispersion and radial propagation

This section summarizes the literature results on the dispersive correction to the GAM frequency due to finite electron and ion temperatures.

As discussed above, in the expression for the perturbed density the terms leading to GAM dispersion appear as fourth order terms, $n \propto \left(e\phi_0/T\right)\omega_d^4/\omega^4$, therefore, the second order, $m = 2$, poloidal harmonics have to be included in the solution of the GK equation (55) for

$$\phi = \phi_0 + \phi_s \sin\theta + \phi_{2c}\cos 2\theta, \tag{71}$$

$$f = f_s \sin\theta + f_{2c}\cos 2\theta. \tag{72}$$

The higher order terms ϕ_{3s}, ϕ_{4c}, g_{3s},... do not contribute to this order.

In the limit of $\omega \gg v_\parallel/qR_0$, thus neglecting the ion Landau damping due to transit resonances, from equation (55) one finds the equations for g_0, g_s, and g_{2c}, cf with (63)–(65),

$$\omega g_0 + \frac{1}{2}\overline{\omega}_d g_s = \omega J_0^2(k_\perp v_\perp/\omega_{ci})\frac{e}{T_i} f_0\phi_0, \tag{73}$$

$$\overline{\omega}_d g_0 + \omega g_s - \frac{1}{2}\overline{\omega}_d g_{2c} = \omega J_0^2(k_\perp v_\perp/\omega_{ci})\frac{e}{T_i} f_0\phi_s, \tag{74}$$

$$-\frac{1}{2}\overline{\omega}_d g_s + \omega g_{2c} = \omega J_0^2(k_\perp v_\perp/\omega_{ci})\frac{e}{T_i} f_0\phi_{2c}. \tag{75}$$

The perturbation of the electron density with $m = 0$ component is absent, $n_0 = 0$ and the first and second poloidal harmonics follow Boltzmann distribution:

$$n_\mu = \frac{e}{T_e}\phi_\mu, \tag{76}$$

where $\mu = (s, 2c)$.

The perturbation of the ion distribution function is found from the coupled equations (73)–(75) solved for g_s and g_{2c} and expanded to the fourth order in ω_d/ω. Integration over the velocity space gives the perturbed ion density which is closed with the expressions for the perturbed electron density and quasineutrality conditions for each harmonic. After some algebra [100, 111] one eventually arrives at the dispersion relation

$$-1 + \frac{v_{Ti}^2}{\omega^2 R_0^2}\left(\frac{7}{4} + \tau_e\right) + \frac{1}{2}k_r^2\rho_i^2 D_1 = 0. \tag{77}$$

where the dispersive term D_1 has the form

$$D_1 \equiv \left[\frac{3}{4} - \frac{v_{Ti}^2}{R_0^2\omega^2}\left(\frac{13}{4} + 3\tau_e + \tau_e^2\right) + \frac{v_{Ti}^4}{R_0^4\omega^4}\left(\frac{747}{32} + \frac{481}{32}\tau_e + \frac{35}{8}\tau_e^2 + \frac{1}{2}\tau_e^3\right)\right]. \quad (78)$$

It has been shown [111] that the same results can be obtained using the exact solution in the form of equation (60). As was generally discussed above, the dispersive corrections in D_1 originate from several different sources. The $3/4$ term is a result of direct ion FLR effects, while both the last terms in round brackets, $\sim \tau_e^2 v_{Ti}^2/R_0^2\omega^2$ and $\tau_e^3 v_{Ti}^4/2R_0^4\omega^4$ are due to the ion sound Larmor radius related to the finite electron temperature (compare with equation (26)), and all other terms are the FOW effects due to a finite ratio of the magnetic drift frequency to the mode frequency, $\sim \omega_d^4/\omega^4$. Expression (77) is identical to that obtained previously with different methods [11, 74]. Also a general expression for shaped magnetic surfaces in [117] reduces to (77) in the absence of ellipticity when $\kappa = 1$.

It is worth noting that the form of the dispersion equation given by equation (77) may not be unique but depends on the way the initial equations are expanded in the small parameter $k_r^2\rho_i^2$. For instance an alternative derivation gives the following equation

$$-1 + \frac{v_{Ti}^2}{\omega^2 R_0^2}\left(\frac{7}{4} + \tau_e\right) + \frac{1}{2}k_r^2\rho_i^2 D_2 = 0, \quad (79)$$

where

$$D_2 \equiv \left[\frac{3}{4} - 2\tau_e + \frac{v_{Ti}^2}{R_0^2\omega^2}\left(-\frac{13}{4} + \frac{39}{8}\tau_e + \frac{3}{2}\tau_e^2\right) + \frac{v_{Ti}^4}{R_0^4\omega^4}\left(\frac{747}{32} + \frac{59}{8}\tau_e - \frac{7}{8}\tau_e^2\right)\right], \quad (80)$$

In fact, equations (77) and (79) are equivalent to the order of the terms $k_r^2\rho_i^2$. This can be seen by noting that the dispersion factors D_1 and D_2 in these equations are different by the term containing the lowest order dispersion equation:

$$D_2 = D_1 + \tau_e\left[-1 + \frac{v_{Ti}^2}{\omega^2 R_0^2}\left(\frac{7}{4} + \tau_e\right)\right] \times \left[2 - \frac{v_{Ti}^2}{\omega^2 R_0^2}\left(\frac{35}{8} + \frac{\tau_e}{2}\right)\right]. \quad (81)$$

As a result, the difference in D_1 and D_2 does not affect the first order dispersive corrections in $k_r^2\rho_i^2$ in the GAM frequency. Expanding (77) in the small parameter, $k_r^2\rho_i^2 < 1$, one obtains for the GAM frequency

$$\omega^2 = \omega_0^2\left(1 + \frac{1}{2}k^2\rho_i^2 D\right). \quad (82)$$

Here,

$$D \equiv \left[\frac{3}{4} - \left(\frac{7}{4} + \tau_e\right)^{-1}\left(\frac{13}{4} + 3\tau_e + \tau_e^2\right) + \left(\frac{7}{4} + \tau_e\right)^{-2}\left(\frac{747}{32} + \frac{481}{32}\tau_e + \frac{35}{8}\tau_e^2 + \frac{1}{2}\tau_e^3\right)\right]. \quad (83)$$

Equation (83) gives the following group velocity for the radial wave energy propagation

$$v_{gr} = \frac{\partial\omega}{\partial k_r} = \frac{1}{2}\omega_0 k_r\rho_i^2 D. \quad (84)$$

It is interesting that the dispersion effects due to ion sound Larmor radius are negative while those due to the finite ion temperature are positive. The latter are dominant in plasmas with $\tau_e \simeq 1$. The sign of the dispersion correction D changes to negative around $\tau_e = T_e/T_i \simeq 5.45$ [74, 118].

Analytic calculations of the GAM dispersion are cumbersome, and literature provides several conflicting expressions for the higher order effects, e.g. expressions in [63, 116] are different from those in [11], and respectively from equation (77). Other expressions [16, 101, 119, 120] miss some terms and have some incorrect coefficients. It is also noted that [118] presents an original method of the calculation of the GAM group velocity based on energy conservation and compare the results from the fluid and GK theory, which are in good agreement for large q.

2.8. Collisionless damping of GAMs

Here, the main results in the literature on the rate of collisionless damping of GAMs are summarized and the comparison with some numerical results are presented.

As was discussed above, in general, the collisionless damping of GAMs is a combination of the Landau (transit time) $\omega \simeq v_\parallel/qR_0$ and toroidal resonances $\omega \simeq \omega_{di}/\sqrt{2}$. The GAM damping due to the resonant contribution from Landau damping in equation (69), in neglect of the magnetic drift velocity, provides the scaling $\exp(-\omega^2 q^2 R_0^2/v_T^2) \sim \exp\left(-q^2\right)$ [9]. This basic scaling is behind the common view that strong Landau damping for smaller q values is the reason why GAMs are more often observed at the edge rather than in the core region. In [5], from the lowest order GK equation, neglecting the dispersive effects, coupling to the ion sound, and magnetic drift contribution to the resonance, the real part of the GAM frequency and damping were obtained as

$$\Omega_0^2 = \left(\frac{7}{4} + \tau_e\right)q^2, \quad (85)$$

$$\Omega = \Omega_0 - \mathrm{i}\frac{\sqrt{\pi}}{2}q^2\Omega_0^4\exp\left(-\Omega_0^2\right), \quad (86)$$

where $\Omega = qR_0\omega/v_{Ti}$. The same expression for the GAM damping was also obtained in [108, 121].

As noted above, the higher order transit resonances, $\omega \simeq pv_\parallel/qR_0$, $p = 2, 3, \ldots$, are also involved, and may even become more important, because the resonance parallel velocity is shifted to the lower values for larger p, so that the number of resonant particles is increased thus resulting in increased damping as pointed out by Sugama [75]. The expression for

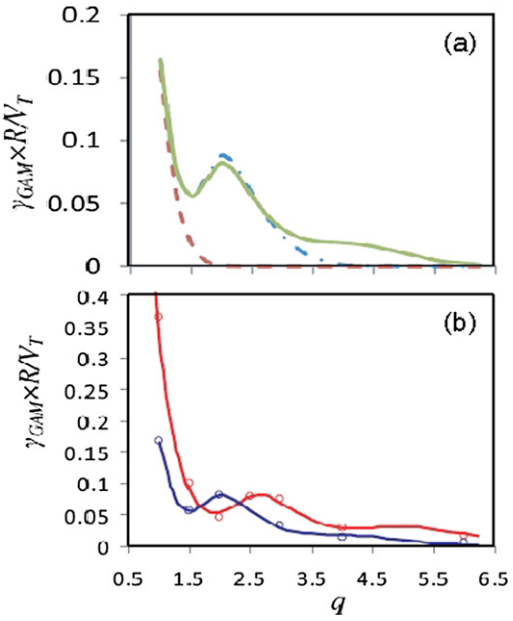

Figure 6. (*a*) Numerical solution for collisionless GAM relaxation rate corresponding to $k = k_\perp \bar{\rho}_i = 0.1375$ with $\tau = 1$. Number of poloidal harmonics retained in the asymptotic analysis are $N = 1$ (dashed curves), $N = 2$ (dotted-dashed curves), $N = 3$ (solid curves). (*b*) Decay rate as function of safety factor q. Dots are from COGENT simulations with lines from numerically evaluated analytic predictions with $N = 3$ transit harmonics with $Z_i = 1$, $\epsilon = 0.2$, $k_\perp \bar{\rho}_i = 2\pi\bar{\rho}_i/\Delta_r = 0.1375$, and $T_e/T_i = 1$ (blue), 0.1 (red). Reproduced courtesy of IAEA. Figure adapted from [79]. Copyright (2013) IAEA.

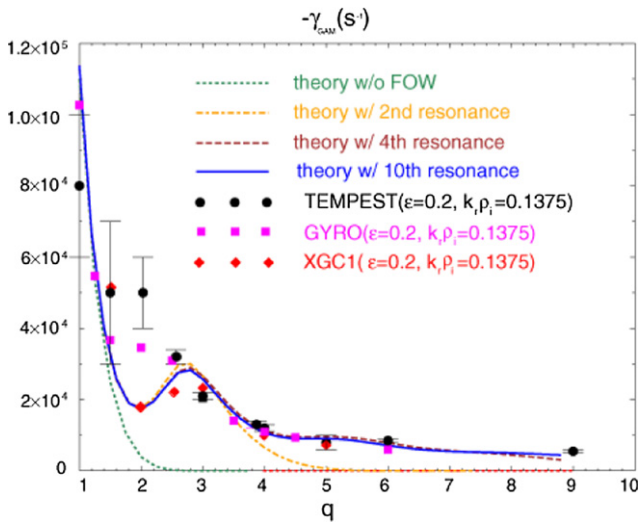

Figure 7. GAM damping rate versus q for $\epsilon = 0.2$ in homogeneous plasmas. Theoretical curves are from [108], points are from TEMPEST, squares GYRO, and diamonds XGC1 simulations. Reproduced courtesy of IAEA. Figure adapted from [112]. Copyright (2009) IAEA.

the GAM damping, taking into account the second order resonance with $p = 2$, and neglecting the toroidal resonances, was obtained in the form [75, 76],

$$\omega_{\rm GAM} = \frac{\sqrt{7+4\tau_e}}{2}\frac{v_{Ti}}{R_0}\left[1+\frac{2\left(23+16\tau_e+4\tau_e^2\right)}{q^2(7+4\tau_e)^2}\right] \quad (87)$$

$$\gamma_{\rm col} = -\frac{\pi^{1/2}\,v_{Ti}q}{2R_0}\left[1+\frac{2(23/4+4\tau_e+\tau_e^2)}{q^2(7/2+2\tau_e)^2}\right]^{-1} \times\left[\exp(-\hat{\omega}_G^2)\{\hat{\omega}_G^4+(1+2\tau_e)\hat{\omega}_G^2\}+\frac{1}{4}\left(\frac{k_r v_{Ti}q}{\Omega_i}\right)^2 \times\exp(-\hat{\omega}_G^2/4)\left\{\frac{\hat{\omega}_G^6}{128}+\frac{1+\tau_e}{16}\hat{\omega}_G^4 +\left(\frac{3}{8}+\frac{7\tau_e}{16}+\frac{5\tau_e^2}{32}\right)\hat{\omega}_G^2\right\}\right], \quad (88)$$

where $\hat{\omega}_G = \omega_{\rm GAM}\,qR_0/v_{Ti}$. The term $\exp\left(-\hat{\omega}_G^2\right)$ is responsible for $p = 1$ resonance, and the term with $\exp\left(-\hat{\omega}_G^2/4\right)$ describes the $p = 2$ resonance: $\omega \simeq 2v_\parallel/qR_0$. Expressions for helical systems were derived within the same approximation [54, 77]. Analytic calculations of the GAM damping including the $p = 2$ transit resonance are cumbersome as they have to be performed simultaneously with the calculations of the dispersive correction to the frequency, see section 2.7. There are several different expressions in the literature [11, 75, 76, 116, 120]. Comparison with numerical simulations [78, 79, 112] show that the inclusion of higher harmonics in the ion response, as in equation (60), improves agreement with results of direct simulations with GK codes such as TEMPEST [78, 112] and COGENTA [79]. The effect of adding higher transit harmonics to the numerical solution is shown in figure 6(*a*) [79] and in figure 6(*b*) with a comparison to results of COGENTA.

Similar numerical solutions with many transit harmonics following the theory of [108] were compared with results of GK simulations from TEMPEST, GYRO and XGC1 [78, 112]. It was shown that up to ten transit harmonics need to be included to achieve agreement with the results of direct kinetic simulations for larger values of the safety factor, $q > 4$. However for smaller $q \simeq 2$, the results from the different codes themselves and the theory disagree up to a factor of 2, figure 7.

Expression (88) well illustrates the technical difficulty, noted above in section 2.6, of using the parameter $\xi = \omega_{\rm di}/\omega_t = k_r\rho_i q$ as an expansion parameter. The contribution of the second order resonance, $p = 2$ to the growth rate in equation (88) has a pre-factor ξ^2, which in general, does not need to be small. Moreover the contributions of the second, and higher order resonances, are increasing with p due to the exponential factor $\exp(-\hat{\omega}_G^2/2p)$. Thus it is not obvious if the corresponding series will converge as commented in [122]. Nevertheless, numerical calculations in [79, 112] show the improvement of the agreement between the results of direct GK simulations and analytical expressions with large number of terms corresponding to the higher order transit resonances $\omega = pv_\parallel/qR$.

In the limit of large q and shorter radial wavelengths, when the ξ parameter is large $\xi = qk_r\rho_i > 1$, the resonance with the magnetic drift frequency $\omega \simeq \omega_d/\sqrt{2}$ becomes dominant, as was discussed in section 2.6. In this limit, the authors of [11, 116], using alternative expansion for resonant particles, have obtained a cumbersome expression for the damping rate due toroidal resonances, which has a general scaling of the

form

$$\frac{\gamma}{\omega} \sim \frac{\sqrt{2}}{k_r^2 \rho_{it}^2} \exp\left(-\frac{\omega}{\omega_d}\right). \quad (89)$$

This expression does not consider the trapped particles which may significantly affect the damping rates. Trapped particle effects were considered in [54, 55, 57, 123] where it was shown that additional trapping due to the ripples in helical toroidal systems enhances collisionless damping of GAMs.

A note on terminology: the limit when the toroidal resonance is dominant, $\omega_d \gg \omega_t$, or $\xi \gg 1$, corresponding to the expression (89), was referred to in [11, 116] as KGAM but also as FOW effects. The effects of the $p = 2$ resonances with the prefactor ξ^2 as in equation (88) were also termed as FOW effects in [76] and some later publications. In [117, 122], the case of $\xi \gg 1$, analogous to equation (89), was called large orbit drift width (ODW), while the expression analogous to equation (88) was called the low ODW limit. In this review, similar to other literature, we refer to FOW as an expansion in terms of the $\omega_d/\omega \simeq k_r \rho_i < 1$ small parameter, i.e. on par with the ion FLR effects, except section 12.2 where large and small ODW classification are used, as in original papers and subsequent comparison with experiments, to avoid confusion.

2.9. Electron contributions to GAM damping

The electron contribution to the damping is often neglected since, most commonly, the electron response in GAM theory is assumed in the Boltzmann form, or its natural generalization to the EM case. The natural justification is that the transit frequency of passing electrons is much higher than the GAM frequency, so generally it is expected that the electron contribution to damping is small [124, 125]

$$\frac{\gamma}{v_{Ti}/R_0} \sim \left(\frac{m_e}{m_i}\right)^{1/2}. \quad (90)$$

However, the trapped electrons can provide a larger contribution. This has been investigated analytically in [125] where it was shown that the boundary between barely trapped and passing electrons is most important and the electron damping was estimated in the form

$$\frac{\gamma R_0}{v_{Ti}} \simeq (0.315 + 0.30\varepsilon)\left(1 + \frac{2+\tau_e}{q^2\Omega_0^2}\right)^2 q\tau_e^{1/2} D\left(\sigma^*, \varepsilon\right)\left(\frac{m_e}{m_i}\right)^{1/2}, \quad (91)$$

where $D(\sigma^*, \varepsilon) \leqslant 1$ is some weight function.

It was concluded in [126] that the trapped electrons have negligible effect on the GAM frequency, but can be important for damping. Thus, for large values of $q \simeq 7$ the damping due to trapped electrons can reach that of due to circulating ions in the low q region.

The effects of kinetic electrons were investigated in global GK particle simulations with the GTC code [127] where it was shown that indeed kinetic electrons increase the GAM damping in the high q region, as shown in figures 8 and 9. It is noted that the GAM real frequency is weakly affected by kinetic electrons and generally follows the scaling from [75], as shown in figure 9. The GAM damping rate increase with the aspect ratio ϵ, as shown in figure 9, is an indication of the trapped electron contribution.

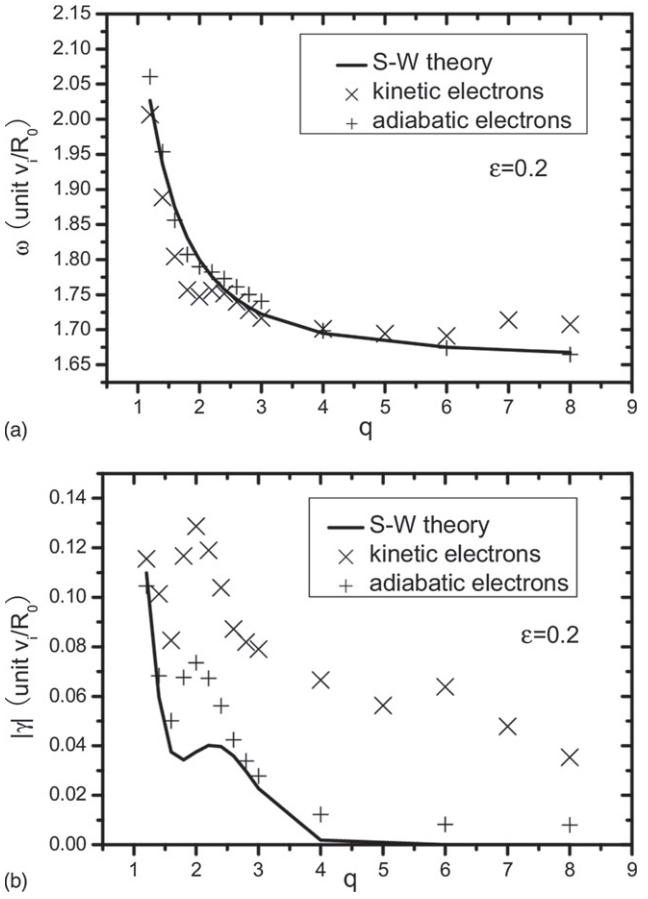

Figure 8. Comparison of GAM (*a*) frequency and (*b*) damping rate between adiabatic and kinetic electrons at different q; solid line from [75]. Reprinted from [127], with the permission of AIP Publishing.

The comparison of theoretical predictions on the role of barely trapped and passing electrons [125] with dedicated GK simulations was performed in [128] with full-f codes with kinetic electrons GYSELA and ORB5. These results confirm that the electron contribution to GAM damping is not negligible and that analytical results show good agreement with simulations. Similar to other works the GAM frequency is weakly affected by kinetic electrons.

2.10. Collisional effects and collisional damping

This section summarizes the effects of collisions, presenting, among others, the physical picture of GAM collisional damping and real frequency modification due to ion–ion collisions.

Collisions may affect GAMs in several different ways. In the main order, the electron–ion collisions are ambipolar in strongly magnetized plasma. While the electron–ion collisions cause plasma diffusion across the magnetic field, they do not produce any perpendicular current, and thus do not affect the GAM directly. The electron–ion collisions may also affect the parallel (to the magnetic field) electron current modifying the

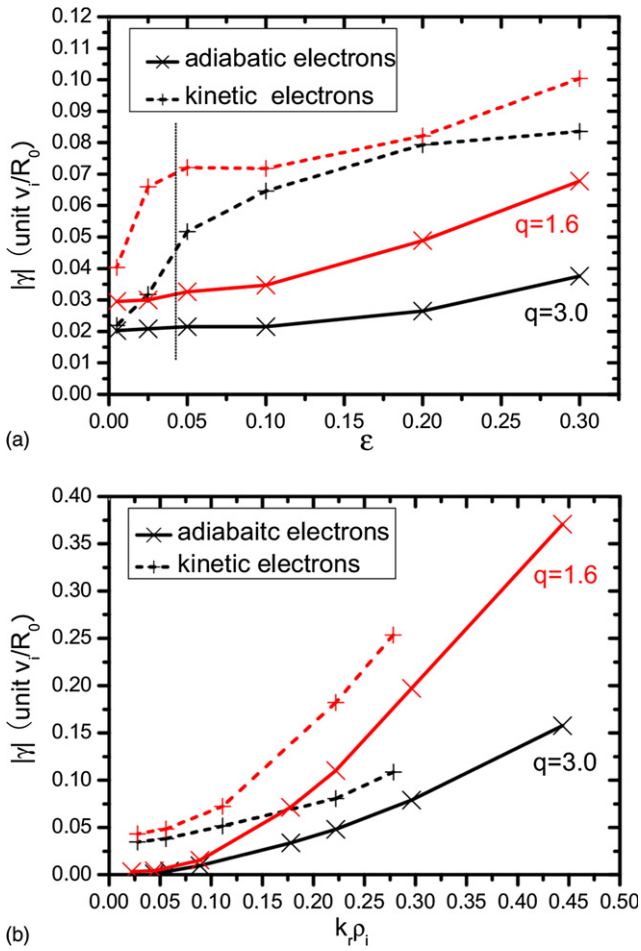

Figure 9. GAM damping rate vs (*a*) ε and (*b*) $k_r\rho_i$ at $q = 1.6$ and $q = 3$; solid line-adiabatic electrons, dashed line-kinetic. Reprinted from [127], with the permission of AIP Publishing.

Boltzmann relation between the sidebands of the electron density and potential and affect the electron temperature evolution due to the parallel heat flux as considered in [129] together with the EM effects. Therefore, the electron–ion collision effects will also appear in the next order, including $m = 2$ sidebands, together with the dispersion due to ion sound Larmor radius, finite ion Larmor radius, and finite $\langle\omega_D^2\rangle/\omega^2$ terms. To our knowledge, such higher order effects were not considered in the literature.

Contrary to the electron–ion collisions, the ion–ion collisions directly affects the GAM resulting in collisional damping and modification of the real part of the GAM frequency. Collisional GAM damping was studied in the drift-kinetic theory [8, 9, 130] and in fluid theory in [80]. Recently, results similar to [80] were obtained in GK theory using various forms of the collision operator [131, 132].

The basic behaviour of the GAM due to ion–ion collisions can be easily understood from fluid theory [80]. The key effect of the ion–ion collisions is the relaxation between parallel and perpendicular components of the perturbed pressure, the so-called magnetic pumping. The relaxation between the perturbed $p_\perp$ and $p_\parallel$ can be described by the evolution equation for the parallel viscosity, $\widetilde{\pi}_\parallel \sim \left(\widetilde{p}_\parallel - \widetilde{p}_\perp\right)$, equation (17), which is now modified as follows

$$\frac{\mathrm{d}}{\mathrm{d}t}\widetilde{\pi}_\parallel - \frac{2}{3}p_{0\mathrm{i}}\mathbf{v}_E^0\cdot\nabla\ln B = -\frac{6}{5}\nu_\mathrm{i}\widetilde{\pi}_\parallel. \tag{92}$$

Note that the isotropic part of the pressure $\widetilde{p}$ is not affected by ion–ion collisions in this order, and thus equation (16) remains unchanged. Note also that this means that GAM damping due to ion–ion collisions cannot be described within the standard MHD framework, but requires the extended two-pressure MHD model. The perturbation of the parallel viscosity adds to the diamagnetic current affecting the feedback in the quasi-neutrality equation as is shown in equation (134). Using equations (92), (16) and (7) one obtains the dispersion relation [80]

$$\omega^2 = \frac{v_{T\mathrm{i}}^2}{R_0^2}\left(\frac{5}{3} + \frac{1}{12}\frac{1}{1+6\mathrm{i}\nu_\mathrm{i}/5\omega}\right). \tag{93}$$

In the collisionless limit, $\nu_\mathrm{i}\to 0$, one obtains the collisionless result $\omega^2 = 7v_{T\mathrm{i}}^2/4R_0^2$, as in equation (15).

In general, equation (93) has three roots: two correspond to the GAM modes with damping, and the third is a strongly damped (aperiodic) root, $\omega\sim -\mathrm{i}\nu_{\mathrm{ii}}$. For weak collisions, $\nu_\mathrm{i}\ll v_{T\mathrm{i}}/R_0$, the GAM modes have the frequency

$$\omega \simeq \pm\sqrt{\frac{7}{4}}\frac{v_{T\mathrm{i}}}{R_0} - \frac{\mathrm{i}}{35}\nu_\mathrm{i}, \tag{94}$$

and the aperiodic root $\omega\simeq -8\mathrm{i}\nu_\mathrm{i}/7$. For high collisionality, $\nu_\mathrm{i}\gg v_{T\mathrm{i}}/R_0$, the complex GAM frequency is

$$\omega \simeq \pm\sqrt{\frac{5}{3}}\frac{v_{T\mathrm{i}}}{R_0} - \frac{5\mathrm{i}}{144}\frac{v_{T\mathrm{i}}^2}{R_0^2\nu_\mathrm{i}}, \tag{95}$$

and the aperiodic root is $\omega\simeq -6\mathrm{i}\nu_{\mathrm{ii}}/5$.

An interesting property is that in the high collisionality limit the GAM frequency decreases from the collisionless value, $\sqrt{7/4}\,v_{T\mathrm{i}}/R_0$, to the one-fluid value $\sqrt{5/3}\,v_{T\mathrm{i}}/R_0$ constant value, which does not depend on the collision rate ν_i. Therefore, GAMs 'survive' the collisional damping even when ν_i is large, albeit with a different frequency, see equations (94) and (95).

Equations (94) and (95) demonstrate a related interesting feature: the non-monotonic behaviour of the GAM collisional damping with collisionality. The damping is initially rising linearly at low ion collision rates ν_i but then decreasing inversely at high collision rates, $\sim v_{T\mathrm{i}}^2/R_0^2\nu_\mathrm{i}$. In both the low collisionality $\nu_\mathrm{i}\ll v_{T\mathrm{i}}/R$, and high collisionality $\nu_\mathrm{i}\gg v_{T\mathrm{i}}/R_0$, regimes the damping rate remains smaller than the real part of the frequency. The damping is maximal at $\nu_\mathrm{i}\simeq v_{T\mathrm{i}}/R$. In the regime of high collisionality, $\nu_\mathrm{i}\gg v_{T\mathrm{i}}/R_0$, the GAM frequency naturally reduces to the isotropic one-fluid MHD result, because in this limit collisions make pressure perturbations isotropic. This behaviour was also found in GK theory as illustrated in figure 10 obtained in [132] as discussed below.

Collisional damping was also studied directly with kinetic theory. Novakovskii [8], using a specific collision operator in the Hirshman–Sigmar–Clarke form, derived

$$\gamma_{\mathrm{col}} = -4/7\nu_\mathrm{i} \tag{96}$$

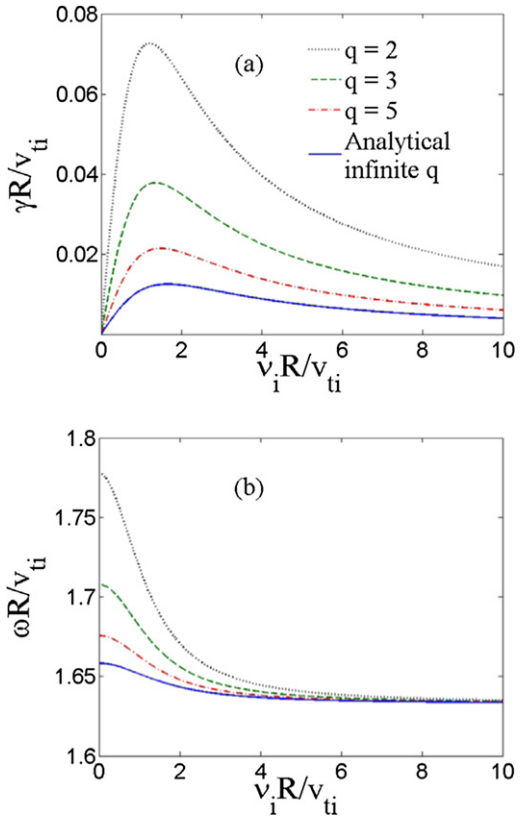

Figure 10. Normalized GAM (*a*) damping rate and (*b*) real frequency for Krook operator with number and energy conservation terms for $\tau = 1$. Reproduced courtesy of IAEA. Figure from [132]. Copyright (2015) IAEA.

Gao, starting from a GK model with a number-conserving Krook collision operator, derived [131]

$$(7/4 + \tau_e)\widehat{\gamma} + \frac{3\widehat{\nu}_i}{8} + \frac{\widehat{\gamma}}{q^2}(4\widehat{\gamma}^2 + 4\widehat{\gamma}\widehat{\nu}_i + \widehat{\nu}_i^2) = 0, \qquad (97)$$

where $\widehat{\nu}_i = \nu_i q R_0/v_{Ti}$ and $\widehat{\gamma} = \gamma q R_0/v_{Ti}$. For $\widehat{\nu}_i \ll 1$ and $\widehat{\gamma} \ll 1$ this simplifies to:

$$\gamma_{col} = \frac{3\nu_i}{14 + 8\tau_e} \qquad (98)$$

while for $\widehat{\nu} \geqslant q$ and $\widehat{\gamma} \ll 1$ one obtains

$$\gamma_{col} = \frac{3\nu_i}{(14 + 8\tau_e + 8\nu_i^2 R_0^2/v_{Ti}^2)}. \qquad (99)$$

Damping rates derived from a drift kinetic model with different collision operators, including Lorentz operators, Hirshmann–Sigmar–Clarke form, and Krook operators with and without energy conserving collision rates were compared by Li [132]. For a number only conserving Krook operator at low collisionality Li obtained Gao's equation (99), with a very weak ν_i dependence in the real frequency. However, with a number and energy conserving (NEC) operator the damping rate is a factor of 9 smaller:

$$\gamma_{nec} = \frac{\nu_i}{3\,(14 + 8\tau_e + 8\nu_i^2 R_0^2/v_{Ti}^2)} \qquad (100)$$

with real frequency

$$\omega_{nec} = \frac{v_{Ti}}{R_0}\left(\frac{7}{4} + \tau_e - \frac{\nu_i^2 R_0^2}{3\,(7v_{Ti}^2 + 4\tau_e v_{Ti}^2 + 4\nu_i^2 R_0^2)}\right)^{1/2}. \qquad (101)$$

The structure of the equation obtained in fluid theory (93) is similar to equations (97)–(101) obtained with kinetic approach. Note that the latter equations correspond to a pure fluid limit and any differences between them and fluid result (93) should come from the form of the collisional operators used in these calculations. Overall, the collisional GAM damping rate is non-monotonic, initially rising linearly at low ion collision rates ν_i but then decreasing inversely at high collision rates, as shown in figure 10. At the same time, the GAM frequency decreases from the collisionless (in the kinetic or two-pressure model) value, $\sqrt{7/4 + \tau_e}\, v_{Ti}/R_0$, to the isotropic perturbed pressure (one-fluid or two-fluid MHD) value, which does not depend on the collision rate. This effect has a simple explanation as it was discussed above: the primary role of ion–ion collisions is to mix parallel and perpendicular pressure, so the GAM frequency reduces to the isotropic pressure result. The conservation properties of the collision operator used in [132] affect the frequency in the limit of strong collisions. For the number-conserving-only operator the GAM frequency limit is $\sqrt{1 + \tau_e}\, v_{Ti}/R_0$ as $\nu_i \to \infty$, while for the NEC operator the limit is $\sqrt{5/3 + \tau_e}\, v_{Ti}/R_0$, corresponding to the isothermal and adiabatic behaviour of ions.

The GAM damping due to the ion–ion collisions originates in the relaxation of the parallel viscosity, $\widetilde{\pi}_\parallel \sim (p_\parallel - p_\perp)$, in other words from mixing parallel and perpendicular pressure, the process which conserves the total energy. One notes that the Krook operator, while still approximate but with energy conservation gives the result (100) closer to the value in (94) obtained with the collisional relaxation rate (in equation (92)) from the 13-moment Grad approach [84] with the collisional operator in the Landau form [133]. More accurate results can be obtained by using the 21-moment system [84], which also includes the relaxation of the higher order (energy weighted) viscosity tensor, ${\pi^*}_\parallel$ in notations of [84]. In the latter case, the coefficient 6/5 in equation (92), and respectively in (93), has to be replaced with another coefficient $6/5 \to 6 \times 178/(5 \times 205) = 1.042$, which will slightly modify the results (94) and (95). The accuracy of the fluid results obtained with Landau collision operator for the relaxation of the viscosity and energy weighted viscosity tensor is expected to be higher than those employing the reduced forms of the Krook collision operators [131, 132]. The accuracy of the Grad 21-moments system corresponds to the accuracy of the Braginskii transport equations employing the direct solution of the kinetic equation with Landau collision operator with two-polynomials expansion.

Additional collisional effects, such as due to the heat flux related to the ion–ion collisions [134], will appear in the higher order compared to the relaxation of the parallel viscosity. The electron–ion collisions also enter the GAM damping via the parallel electron current [129], which is, in general, related to the $m = 1$ magnetic perturbations.

Table 4. Model predictions for the various classes of GAM damping. Notes: zero orbit (drift) width $= k_r\rho_i q \to 0$.

Damping rate, γ	Model
Collisionless	
$\gamma = -q^5 \exp[-q^2(7/4+\tau_e)]$	Landau/Watari [99] zero OW, circular
$\gamma = -(k_r\rho_i)^{-2} \exp[-\sqrt{7/4+\tau_e}/(k_r\rho_i]$	Gao 2013 [131] large OW, circular
Equation (88)	Sugama [75] finite OW, circular
Equation (269)	Gao 2008 [108] small OW with shape
Equation (270)	Gao 2010 [117] large OW with shape
Collisional	
$\gamma \sim -\nu_i$	Lebedev [9], general collision operator
$\gamma = -4/7\nu_i$ equation (96)	Novakoskii [8], HSC operator
Equations (98) and (99)	Gao 2013 [131], number conserving Krook operator
Equation (100)	Li 2015 [132], number and energy conserving operator

The presence of impurities was found to enhance the collisional damping of ZFs by at least a factor of Z_{eff}, as it was shown in case of an additional single species of charged heavy impurity ion $Z > 1$ [135]. The enhancement increased with the aspect ratio R_0/a.

Table 4 summarizes the various model predictions for the GAM collisionless and collisional damping. In practice, expressions for the damping rates should be understood as qualitative estimates. In general, there are several mechanisms and distinct time scales in the damping rate: ν_i, ω_D and v_{Ti}/qR_0. The toroidal resonances and higher harmonics, as discussed in section 2.6, will also strongly affect the damping rates. At low frequencies the trapped ions will become important. Interaction of various mechanisms and sensitivity to initial conditions [136] is expected to create several different damping regimes [23], which also depend on magnetic surfaces shaping.

2.11. Convective, continuum damping and phase-mixing effects

Radial inhomogeneities (profile effects) of plasma parameters bring a number of new effects to the GAM dynamics such as GAM propagation and an effective GAM damping. Profile effects are also crucial for the GAM eigenmode formation. The main ideas and some literature results are discussed in this section.

In addition to the damping due to the wave–particle interactions and collisions, GAMs are also subject to an effective damping related to the radial propagation and associated phase-mixing (PM) [137–141]. Essentially, different mechanisms involved in such damping are all due to the non-eigenmode nature of the considered perturbations. Plasma inhomogeneities, giving rise to the radial dependence of the local GAM frequency, result in additional amplitude decay due to PM thus amplifying the wave damping due to the direct energy absorption related to collisions and wave–particle resonances. Nonlinear interactions also affect the radial propagation effects [142]. Here, we discuss some basic ideas illustrating convective and continuum damping, which are discussed further and contrasted with observations in section 9.6.

A simple deviation from the local theory in an inhomogeneous medium results in the convective damping. To illustrate this we consider a simple case of cold ions so that the radial diamagnetic current is only due to the electron pressure. Then the basic GAM equation (19) for the $m = 0$ component of the potential perturbation $\widetilde{\phi}_0$ has the form

$$-2\frac{c}{B_0}\mathbf{b}\times\nabla\hat{p}_e\cdot\nabla\ln B - \frac{en_0c}{B_0\omega_{ci}}\frac{\partial}{\partial t}\nabla_\perp^2\widetilde{\phi}_0 = 0, \qquad (102)$$

while the electron pressure perturbation is determined by the compressibility of the $\mathbf{v}_E$ plasma flow due to the ϕ_0 potential perturbation,

$$\frac{\partial\hat{n}}{\partial t} + n_0\nabla\cdot\mathbf{v}_E = \frac{\partial\hat{n}}{\partial t} - 2n_0\mathbf{v}_E\cdot\nabla\ln B_0 = 0. \qquad (103)$$

The electron temperature is assumed constant so that $\hat{p}_e = T_e\hat{n}$. One finds from (103)

$$\hat{p}_e = -\frac{2n_0T_ec}{RB_0\omega}q_r\widetilde{\phi}_0\ \sin\ \theta. \qquad (104)$$

Equation (102) takes the form

$$-\mathrm{i}\frac{en_0c}{B_0\omega_{ci}}\omega q_r^2\widetilde{\phi}_0 - \frac{2c}{B_0}\overline{\left(\frac{\partial\hat{p}_e}{\partial r}\frac{1}{r}\frac{\partial}{\partial\theta}\nabla\ln B - \frac{1}{r}\frac{\partial\hat{p}_e}{\partial\theta}\frac{\partial}{\partial r}\nabla\ln B\right)} = 0. \qquad (105)$$

Here, in addition to the standard term with radial derivative of the pressure $\partial\hat{p}_e/\partial r$, the second term with the poloidal pressure gradient is retained. Using (104) in equation (105) the GAM dispersion equation is obtained in the form

$$\omega^2 = \frac{2c_s^2}{R_0^2}\left(1 - \frac{\mathrm{i}}{q_r r}\right). \qquad (106)$$

The non-local (due to the deviation from the local Boussinesq approximation) term $\mathrm{i}/q_r r$ describes the radial propagation and, associated with this, a reduction of the amplitude of the wave packet in non-homogeneous medium. This expression (106) illustrates a simple example of convective damping due to the radial propagation. Such damping is a non-dissipative process that occurs due to the wave radial propagation.

The GAM dispersion makes these processes more complicated when the radial inhomogeneities of plasma density and,

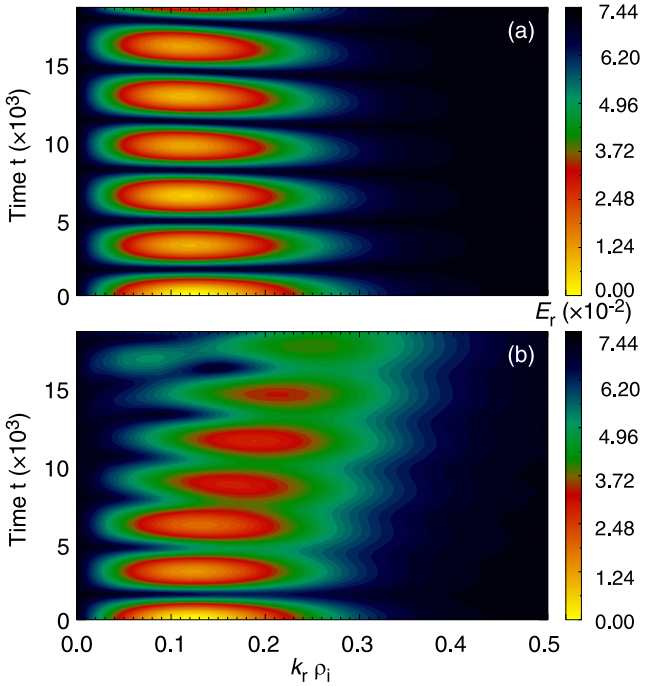

Figure 11. Contour plots of E_r as function of k_r and time t for (*a*) $ak_T = 0$ and (*b*) $ak_T = 7$. Adapted from [149]. CC BY 3.0.

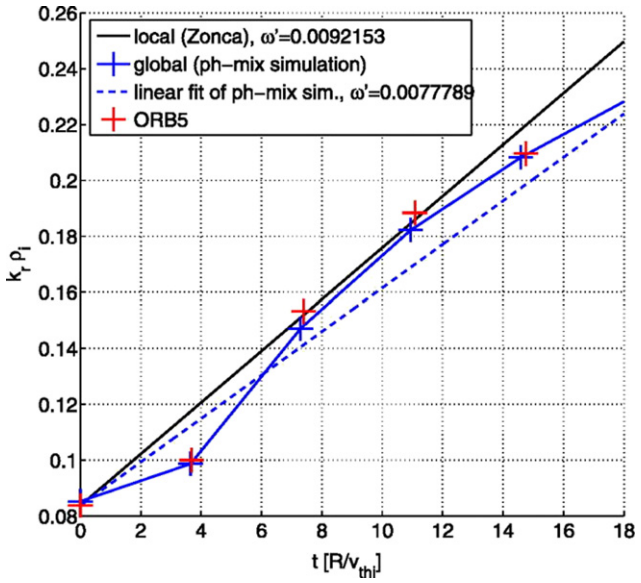

Figure 12. Wavenumber evolution from ORB5 (red crosses), analytic predictions in the local limit (black line) and with an initial-value code including first order global effects (blue crosses), for a case with $k_T = 4$. The linear fit of the effective wavenumber cascade is shown as dashed line. Adapted from [151], with the permission of AIP Publishing.

especially, temperature are included [140]. Radial GAM propagation is important for GAM coupling to turbulence and low frequency ZFs and also can be modified by turbulence and nonlinear interactions [142–148].

PM distorts the radial structure of the propagating GAM and, for a wave-packet, can be characterized by a radial wavevector $k_r(t)$ which increases in time as $k_r \propto -(\mathrm{d}\omega_{GAM}(r)/\mathrm{d}r)t$, i.e. proportional to the local radial derivative of the continuum frequency [11, 139, 150, 151]. The linear time evolution of the radial wavevector was directly shown in simulations [149, 151, 152], see figures 11 and 12. The variation of the local k_r results in the effective GAM amplitude decaying in time as $A \propto t^{-1}\exp[-i\omega_{GAM}(r)t]$, giving rise to the continuum damping. An approach based on the complex eikonal formulation was recently developed to study the two-dimensional propagation of the GAM in inhomogenous plasmas [153].

In the context of damping mechanisms, collisionless and collisional GAM damping are expected to be enhanced by the PM resulting in a stronger combined damping mechanism [139]. In particular, the damping increasing with the temperature gradient was demonstrated in [139, 151], cf figure 13. Estimates of the damping rates indicate that the combined PM/Landau damping (PL) mechanism can raise the effective damping in realistic tokamak conditions by an order of magnitude [139, 151].

It was suggested that continuum damping may also enhance other dissipation mechanisms, such as viscosity, leading to the damping factor of $\exp[-(t/t_0)^3]$ with $t_0 \sim \nu^{-1/3}$ where ν is viscosity [137].

The continuum damping in general disappears if a localized eigenmode is formed, though some residual damping may

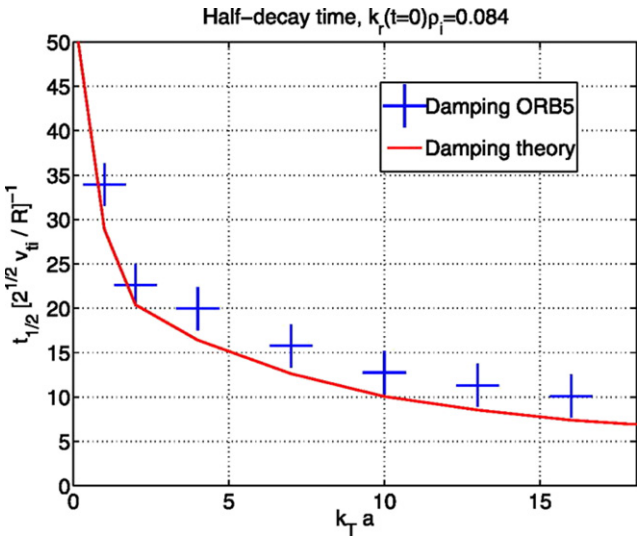

Figure 13. Half-decay time for simulations with different temperature gradients k_T. numerical simulations are shown with blue crosses, and the theoretical estimate with a red continuous line. Adapted from [151], with the permission of AIP Publishing.

still be present due to tunnelling and coupling to the continuous spectrum. A simple example of the stationary (non-damped) eigenmode in a plasma with strong pressure gradient was presented in [154]. In general, such inhomogeneous situations where plasma parameters (specifically the local GAM frequency) are functions of the radial coordinate, should be treated as an eigenvalue problem with appropriate boundary conditions. The eigenmode (the GGAM) that exists due to EM effects is discussed in the next section.

When the dispersive effects are included the GAM behaviour can be compared with the resonance and mode conversion for shear Alfvén waves [10]. The model differential equation used to describe this situation, as obtained from the GAM dispersion equation (83), has the form

$$\alpha\rho_{\rm i}^2\frac{{\rm d}^2}{{\rm d}r^2}\phi+\left(\frac{\omega^2}{\omega_{\rm GAM}^2(r)}-1\right)\phi=0, \tag{107}$$

where α is a numerical parameter characterising the FLR dispersive corrections to GAM, as in equation (83), and $\omega_{\rm GAM}(r)$ is the radial profile of the local GAM frequency. In neglect of the FLR effects, equation (107) describes the GAM continuous spectrum. It also shows that for $\alpha>0$ the propagating solution with $k_{\rm r}^2>0$ exists in the region $\omega>\omega_{\rm GAM}$, while for $\omega<\omega_{\rm GAM}$ one has a localized solution with $k_{\rm r}^2<0$. A point $r=r_0$ where the frequency of the external perturbation ω_0 matches the local GAM frequency, $\omega_0=\omega_{\rm GAM}(r_0)$, becomes a resonance point. Expanding equation (107) near the resonant point one has the eigenmode solution in the form of the Airy function with the characteristic length scale $\lambda\sim(\alpha\rho_{\rm i}^2L_\omega)^{1/3}$, where $L_\omega^{-1}=\omega_{\rm GAM}^{-2}\,\partial\omega_{\rm GAM}^2/\partial r$ is the characteristic length scale of the GAM frequency variation near the $r=r_0$ point [16, 155, 156]. For a typical situation with $\partial\omega_{\rm GAM}^2/\partial r<0$, one has the outward propagating solution in the region $r>r_0$, and decaying solution for $r<r_0$. Note that in the case of an electron dominated dispersion, when $\alpha<0$, see section 2.4, the regions of the decaying and propagating solutions (and the direction of propagation) reverse.

It is expected that a solution in form of the Airy function will carry a finite energy flux away/towards the resonant point $r=r_0$. One can envisage the situation when the GAM is generated near the local resonance and the wave packet propagates away from the generation region, or the case when the GAM is generated off the resonance and the wave packet propagates towards the resonance where the energy is absorbed (mode conversion). In both situations the mode frequency (and the location of the resonance) will be determined by the source frequency. The mode conversion process is similar to the shear Alfvén wave resonance [10]. Radial GAM propagation was observed experimentally, as discussed in section 9.6, but to our knowledge there was no clear indication of the nature (and frequency) of the external perturbations that would resonantly couple to the GAM via this linear process, nor a clear correlation of the generating source with the resonance point.

Note also that in the case of the Alfvén wave resonance the range of possible resonant frequencies is rather wide, from high frequency $k_\parallel v_{\rm A}\sim v_{\rm A}/qR_0$ to the very low values $\omega=k_\parallel v_{\rm A}\to0$ for $k_\parallel\to0$ in a sheared magnetic field, while for GAM it is limited by the range of the radial variation of $\omega_{\rm GAM}(r)$.

One can also readily see that in the case of the positive dispersion, $\alpha>0$, and with a non-monotonic GAM profile with an off-axis maximum $\omega_{\rm GAM}(r)=\omega_{\rm GAM}(r_0)+\omega''_{\rm GAM}(r_0)(r-r_0)^2/2$, $\omega''_{\rm GAM}(r_0)<0$ one can easily construct from equation (107) an eigenmode solution localized near $r=r_0$. This localization mechanism is purely electrostatic and not related to the $m=2$ magnetic component as discussed in section 2.12, but requires $m=2$ electrostatic components which are important for the dispersion.

Table 5 summarizes the various forms and model effects for the GAM radial structure.

2.12. Electromagnetic effects and relation to Alfvén eigenmodes

Finite plasma pressure couples the GAM with magnetic perturbations, modifying the GAM frequency. Coupling to the $m=2$ magnetic sideband results in the GGAM eigenmodes. These and related EM effects are described in this section.

Though the basic GAM is seen as an electrostatic mode, in general one expects finite magnetic fluctuations in finite β plasmas. The presence of the magnetic component is easily seen in the standard MHD model that show the coupling of Alfvén and SWs due to the geodesic curvature [12, 13, 158, 159].

$$\left[\frac{\omega^2}{v_{\rm A}^2}|\nabla\psi|^2+(\mathbf{B}_0\cdot\nabla)\frac{|\nabla\psi|^2}{B_0}(\mathbf{B}_0\cdot\nabla)\right]Y+\frac{c_{\rm s}^2}{v_{\rm A}^2}K_{\rm s}B_0^2Z=0, \tag{108}$$

$$\left[\omega^2\left(1+\frac{c_{\rm s}^2}{v_{\rm A}^2}\right)+c_{\rm s}^2(\mathbf{B}_0\cdot\nabla)\frac{1}{B_0}(\mathbf{B}_0\cdot\nabla)\right]Z+\omega^2K_{\rm s}Y=0. \tag{109}$$

Here, $Z=\nabla\cdot\boldsymbol{\xi}$ describes full plasma compressibility responsible both for the radial diamagnetic current that provides feedback for the GAM oscillations as well as for the SWs, ξ is the plasma displacement vector, and $Y=\left({\rm i}c/\omega\right)\partial\phi/\partial\psi$ is effectively the poloidal plasma velocity, ψ is the poloidal magnetic flux, and $K_{\rm s}=\left(2/B_0^2\right)\mathbf{K}\times\mathbf{B}_0\cdot\nabla\psi$ is the geodesic curvature operator, $\mathbf{K}=(\mathbf{b}\cdot\nabla)\,\mathbf{b}$.

The first and last terms in equations (108) and (109) are responsible for the local GAM eigenmode while the second terms in (108) and (109) describe the coupling to the ion-sound mode. One can already see that the first term in (109) has the $\beta=c_{\rm s}^2/v_{\rm A}^2$ correction to the basic GAM dispersion relation [160]

$$\omega^2=\frac{2c_{\rm s}^2}{R_0^2(1+\beta)}. \tag{110}$$

Such finite plasma pressure corrections arise from the perturbation of the parallel magnetic field due to the radial diamagnetic current. The perturbation of the parallel magnetic field can be found from the equation $\mathbf{B}_0\cdot\widetilde{\mathbf{B}}_\parallel+4\pi\widetilde{p}\simeq0$, which means the absence of compressible magnetic sound for low frequency modes. Therefore, within standard MHD theory, one can expect small $m=1$ magnetic perturbations of $\tilde{B}_\parallel$, correlated with pressure perturbations, $\tilde{B}_\parallel\simeq-4\pi\widetilde{p}_1/B_0$.

From equations (108) and (109) it is also easy to see the coupling to $m=2$ magnetic perturbations of the Alfvén type. The $m=2$ component is critical for the existence of the GGAM eigenmodes [12, 13, 161–163]. When the $m=2$ is artificially omitted from full MHD equations, no eigenmode occurs, even for profiles with a local maximum in the GAM frequency as shown numerically [164] and analytically [165].

Table 5. Summary of model predictions for the GAM radial structure.

Structure	Mechanism	Prediction
Continuum $\omega \propto c_s/R_0$	MHD (a) Non-linear DW turb. (b) EP v distribution	Exists with T_e & $T_i \neq 0$ Δ = narrow. Profiles set location of singular $r = r_0$ surface Δ & location set by EP
Eigenmode ω = const.	(a) MHD + EM, non-local (b) ISW/Alfvén resonances (c) Kinetic FLR/FOW $+\nabla T$	$m = 0$ & 1 flow coupling [157] Δ set by ω_{GAM} & ω_{SW} [14] or ω_A profiles [15] $\Delta \sim \lambda_{Airy} \propto \rho_i^{1/3} L_\omega^{2/3}$, $\rho_i \to 0$ converts to continuum, PM $\to$ propagation [11, 16, 108, 155]
Global ω = const.	Off-axis max. in ω_{GAM} $m = 2$ mag. coupling (1) reverse shear (2) high beta	(a) Turb.: Δ set by profiles (b) EP: Δ set by beam width $\omega_{GAM} \sim \omega_s(1 + 1/2q)$ [12, 13] $\omega_{GAM} \sim \omega_s/(1 + \beta)$ [158, 159]

In contrast to the $m = 0$ and $m = 1$ components, which are localized near the local frequency maximum, the $m = 2$ magnetic component has a tail (a halo) extending to the plasma edge [12, 13] and outside in the vacuum region [166, 167]. It is this tail that allows the detection of GAMs by external magnetic probes. These features of $m = 2$ magnetic signatures have been clearly demonstrated in numerical MHD simulations with CASTOR code [12, 13, 164]. Within the framework of the ideal MHD theory, several models including the $m = 2$ component for global eigenmodes with the local maximum of the GAM frequency have been developed [160, 162, 168–170] and in particular for profiles with monotonic temperature and positive magnetic shear [161, 163]. The coupling to the $m = 2$ component is in fact controlled by the value of the $q^2\beta$ parameter. The detailed theory of the poloidal mode coupling including the $m = 2$ and higher harmonics in plasmas with high beta, $q^2\beta \leqslant 1$, was presented in [160]. This analysis, based on MHD theory, was extended for non-circular magnetic surfaces [169] and to plasmas with energetic ions [168]. Simple expressions for GAM frequencies in various $q^2\beta$ regimes were proposed and verified numerically as well as with the solution of the Mathieu's equation that takes into account infinite coupling of Alfvén and sound harmonics [160].

The EM effects on GAMs were also studied with kinetic theory in which $m = 2$ [171] and $m = 1$ [100, 107, 114] sidebands were considered. It was noted from kinetic theory that the $m = 1$ magnetic component appears in the higher order in the $k_r\rho_i$ parameter compared to the $m = 2$ sideband [109]. Kinetic analysis reveals that the $m = 1$ magnetic component may be related to the anisotropy of the *equilibrium* ion temperature [93] and plasma rotation due to the equilibrium radial electric field [172]. The $m = 1$ component was also found in the ideal MHD analysis [173] and in two-fluid theory with dissipation and heat flux due to the electron–ion collisions [129].

The simple two-fluid model with cold ions shows [174] that the $m = 1$ magnetic component appears as a dispersive correction (therefore smaller as $k_r\rho_s$ compared to the magnetic $m = 2$) and inevitably related to the $m = 0$ density perturbation. The amplitude of the $m = 1$ poloidal magnetic field perturbation $\tilde{B}_\theta = \hat{B}^c_\theta \cos\theta$ and $m = 0$ density $\overline{n}$ are related as

$$\frac{\overline{n}}{n_0} = q\frac{\hat{B}^c_\theta}{B_0}. \tag{111}$$

The discussion above was concerned with the GAM mode which has an $m = 0$ perturbation as a principal component and zero toroidal number, $n = 0$. Another type of tokamak oscillation with finite m and n are the so-called BAE, which are closely related to GAMs. BAE modes are detected in many situations as being excited by energetic ion beams which lead to enhanced losses of energetic ions. Clearly EM, and with a cluster of different toroidal harmonics, their characteristic frequency is inside the beta-induced gap [175] and below the toroidicity-induced Alfvén eigenmode (TAE) frequency. They show both Alfvén mode type $\sim B/\sqrt{n}$ and ion-sound type $\sqrt{T}$ scaling, but '…A BAE is not necessarily an Alfvén eigenmode…' [176]. It is notable that the comprehensive BAE review [176] does not cite the Winsor paper and does not mention the possible relation of BAEs and GAMs. Similarly, some earlier fluid derivations of GAM-like dispersion relations were performed for the EM modes with finite poloidal-m and toroidal-n mode numbers [4], and the KGAM dispersion relation was obtained for low-frequency Alfvén modes in [5], again without the reference to the Winsor paper [1].

The relation of the BAE and GAM was explicitly realized in studies of the excitation of the AC eigenmodes by EPs [70], who have derived the following expression for the AC modes

$$\omega^2 = \left(\frac{7}{4} + \tau_e\right)\frac{v_{Ti}^2}{R_0^2} + \left(\frac{m - nq}{qR_0}\right)^2 v_A^2. \tag{112}$$

This dispersion relation can be easily derived from equations (108) and (109). The main harmonic, $m = nq$, is EM and the ideal MHD-like with approximately $E_{\parallel,mn} = -\nabla_\parallel\phi_{mn} - \frac{1}{c}\partial A_{mn}/\partial t \simeq 0$, while the pressure $\hat{p}_{m\pm1,n}$ and potential sidebands $\tilde{\phi}_{m\pm1,n}$ generated by the geodesic coupling are mostly electrostatic. In the limit $k_\parallel = (m - nq)/qR_0 \to 0$, the dispersion relation (112) is reduced to the GAM modes. This is the so-called BAE and GAM degeneracy, which at a certain level allows the treatment of the BAE and GAM modes within a unified formalism [11, 74]. The geodesic effects on Alfvén waves were further studied in the full (Vlasov) kinetic theory [104, 177]. The deformation of the Alfvén continuum due to the geodesic

effects results in the chirping modes that could be used for the q-profile diagnostic [72, 73]. A detailed analysis of the coupling of ion sound, EM effects and geodesic curvature in plasmas with magnetic shear reveals the global beta-Alfvén-acoustic-eigenmodes modes that can be destabilized by EPs and have been detected in experiments [15, 178–180].

2.13. Drift (diamagnetic) effects on GAMs

Density and temperature gradients mix parities of the GAM sidebands which, in particular, result in the excitation of the $\cos\theta$ sideband of density (temperature). As is discussed in this section, one of the possible consequences is the GAM destabilization due to the ion temperature gradient (ITG).

There are only a limited number of works that take into account the profile gradient (drift) effects on the GAM dynamics. The $m = 0$ component of the GAM is not subject to the drift effect, but the $m = 1$ components of the density and potential obviously may be affected by the gradients. Due to the frequency separation between the GAM mode and the $m = 1$ drift frequency, $\omega_{\rm GAM} \gg \omega_{1*}$, where $\omega_{1*} = -cT_{\rm e}n_0'/reB_0n_0$, and $k_\theta = m/r$ is taken as the wave vector of the drift mode, the drift effects are not commonly considered in the GAM theory, except in earlier work where GAMs were considered as a special case of more general EM drift and drift-Alfvén modes [4, 5]. Drift effects were also considered in the theory of the closely GAM related BAE [113, 179] with finite poloidal and toroidal mode numbers, m, n. Here, a simple model is presented which takes into account the drift effects on the GAM mode with $m = 0$ and $m = 1$ potential perturbations.

First, a simple model of cold ions is considered, thus neglecting any effects of the ITG. The basic $m = 0$ GAM equation (19), or (7) is not modified by the plasma density gradient n_0'. However, the density gradient has to be retained in the $m = 1$ equation (27), or (103), which now has the form

$$\frac{\partial \hat{n}}{\partial t} + \hat{\mathbf{v}}_E \cdot \nabla n_0 - 2n_0 \overline{\mathbf{v}}_E \cdot \nabla \ln B_0 = 0. \tag{113}$$

Here, $\hat{\mathbf{v}}_E$ and $\overline{\mathbf{v}}_E$ are respectively the $m = 1$ and $m = 0$ components of the $\mathbf{E} \times \mathbf{B}$ velocity. One can see that the drift term in (113) mixes the parity and couples to the $\cos\theta$ component of the density (potential) perturbations, which are usually not included in GAM theory. Thus, the general equation for the $m = 1$ density becomes

$$-\mathrm{i}\omega\hat{n} - \frac{c}{B_0 r}\frac{\partial \hat{\phi}}{\partial \theta} n_0' - \frac{2cn_0}{R_0 B_0}\frac{\partial \phi_0}{\partial r}\sin\theta = 0. \tag{114}$$

Here, the coupling to the higher order sidebands $\cos 2\theta$, $\sin 2\theta$, … has been neglected. These are important for the dispersion but can be omitted in the main (non-dispersive) order. Separating the density perturbation into the $\cos\theta$ and $\sin\theta$ components, $\hat{n} = n_{\rm s}\sin\theta + n_{\rm c}\cos\theta$, one finds

$$n_{\rm s} = -\left(\omega - \frac{\omega_{1*}^2}{\omega}\right)^{-1} \frac{2n_0 T_{\rm e} c}{R_0 B_0} q_{\rm r} \widetilde{\phi}_0. \tag{115}$$

Using this expression in the $m = 0$ equation (19), or (7), one obtains

$$\omega^2 = \omega_{1*}^2 + \frac{2c_{\rm s}^2}{R_0^2}. \tag{116}$$

Although the electron drift frequency ω_{1*} correction to the GAM frequency is generally small, it may contribute to the GAM local frequency in regions of large density gradients.

The effects of the ITG are more involved, and more interesting. The inclusion of such effects into the GAM theory is also straightforward within the two-fluid MHD model [181]. The ion pressure equation (16) is modified as follows

$$\frac{3}{2}\left(\frac{\partial \hat{p}_{\rm i}}{\partial t} + \hat{\mathbf{v}}_E \cdot \nabla p_0\right) - 5p_0 \overline{\mathbf{v}}_E \cdot \nabla \ln B_0 = 0, \tag{117}$$

while the equation for the ion parallel viscosity (17) remains unchanged. Now, the radial diamagnetic current in the $m = 0$ quasineutrality equation (19) should include both the electron and ion pressure contributions from (32), (115) and (117). The final dispersion equation has the form [181]

$$\omega^2 = \frac{v_{T\rm i}^2}{R_0^2}\left(\frac{7}{4} + \frac{\tau_{\rm i}^{-1} + (1+\eta_{\rm i})\,\omega_{*\rm i}^2/\omega^2}{\tau_{\rm i}^{-2} - \omega_{*\rm i}^2/\omega^2}\right), \tag{118}$$

where $\omega_{*\rm i} = -\omega_{1*}/\tau_{\rm i}$ with $\tau_{\rm i} = T_{\rm i}/T_{\rm e}$ and $\eta_{\rm i} = \partial \ln T_{\rm i}/\partial \ln n$. The solution of this equation has two branches:

$$\omega_\pm^2 = \frac{1}{2}\left(\omega_{\rm GAM}^2 + \omega_{1*}^2 \pm \sqrt{\left(\omega_{\rm GAM}^2 + \omega_{1*}^2\right)^2 + (4\eta_{\rm i} - 3)\,\omega_{1*}^2 v_{T\rm i}^2/R_0^2}\right), \tag{119}$$

where $\omega_{\rm GAM}^2 = \left(7/4 + \tau_{\rm i}^{-1}\right) v_{T\rm i}^2/R_0^2$.

The higher frequency branch is the usual GAM modified by the drift effects and the low frequency branch is related to the zero-frequency stationary ZF. It is interesting to note that the low frequency mode becomes unstable for $\eta_{\rm i} > 3/4$. This branch is possibly related to the low frequency ZF branch which is destabilized by pressure anisotropy or by plasma flow, etc—see sections 2.3 and 10. It is noted that the approach of [181] did not include the ion FLR corrections in the inertial term. For EGAMs (eigenmode GAMs) these may become particularly important. Further studies here are warranted.

To our knowledge there have been no attempts to include drift corrections into the comparison of theoretical predictions for the GAM frequency with those of experimental measurements.

2.14. Geodesic oscillations of ion temperature

Ion diamagnetic effects result in ion temperature oscillations which are similar in nature to GAMs. The same effects lead to the additional short-wavelength branch of GAMs due to a finite ion temperature. This section presents the fluid model of such effects.

The standard GAM does not induce an $m = 0$ component in the density. This is most easily seen from the electron density equation (28) which shows that for isothermal Boltzmann electrons the contributions of the electron pressure and potential exactly cancel each other and the $m = 0$ density perturbation is absent. Such a constraint is absent for the ion pressure. The

ion pressure equation can be written as [182]

$$\frac{3}{2}\frac{\partial}{\partial t}p - 5p\mathbf{v}_E\cdot\nabla\ln B - 5\frac{c}{eB}\mathbf{b}\times\nabla(pT)\cdot\nabla\ln B + \frac{5}{2}p\nabla\cdot\mathbf{v}_I + \nabla\cdot\mathbf{q}_I = 0. \quad (120)$$

This equation includes the additional inertial terms associated with finite ion temperature fluctuations, such as the inertial heat flux $\mathbf{q}_I$,

$$\mathbf{q}_I = \frac{1}{\omega_{ci}}\mathbf{b}\times\frac{\partial}{\partial t}\mathbf{q}^{(0)}, \quad (121)$$

where the collisionless diamagnetic heat flux

$$\mathbf{q}^{(0)} = \frac{5}{2}\frac{cp_i}{eB}\mathbf{b}\times\nabla T_i.$$

The ion polarization flux is also modified by the addition of the ion pressure

$$\mathbf{v}_I = \frac{1}{\omega_{ci}}\mathbf{b}\times\frac{\partial}{\partial t}\left(\mathbf{v}_E + \mathbf{v}_{pi}\right) = -\frac{c}{B_0\omega_{ci}}\frac{\partial}{\partial t}\left(\nabla_\perp\phi + \frac{1}{en}\nabla_\perp p_i\right), \quad (122)$$

where

$$\mathbf{v}_{pi} = \frac{c}{enB_0}\mathbf{b}\times\nabla p_i. \quad (123)$$

Separating now the ion pressure perturbations into the $m=0$ and $m=1$ parts, $\overline{p}$ and $\hat{p}$, respectively, so that $p = p_0 + \overline{p} + \hat{p}$, where p_0 is the equilibrium pressure, one has for the pressure evolution

$$\frac{3}{2}\frac{\partial}{\partial t}\hat{p} - 5p\overline{\mathbf{v}}_E\cdot\nabla\ln B - 5\frac{c}{eB}\mathbf{b}\times\nabla\left(\overline{pT}\right)\cdot\nabla\ln B + \frac{5}{2}p_0\nabla\cdot\hat{\mathbf{v}}_I + \nabla\cdot\hat{\mathbf{q}}_I = 0, \quad (124)$$

$$\frac{3}{2}\frac{\partial}{\partial t}\overline{p} - 5\overline{\hat{\mathbf{v}}_E\cdot\nabla\ln B} - 5\frac{c}{eB}\mathbf{b}\times\overline{\nabla(\hat{pT})\cdot\nabla\ln B} + \frac{5}{2}p_0\nabla\cdot\overline{\mathbf{v}}_I + \nabla\cdot\overline{\mathbf{q}}_I = 0. \quad (125)$$

One can observe the following important features in these equations: (a) the $m=1$ pressure oscillations, that were responsible for the $m=0$ radial diamagnetic current, now contribute to the $m=0$ pressure perturbation in equation (125); (b) the contribution of the $m=1$ pressure in equation (143) is not cancelled by the $m=1$ perturbation of the potential, as it happens for the $m=0$ density; (c) the $m=0$ ion pressure adds to the inertial ion response in equation (125) and also adds an additional driving term $\mathbf{b}\times\nabla\left(\overline{pT}\right)\cdot\nabla\ln B$ for the $\hat{p}$ excitation, in addition to $\overline{\mathbf{v}}_E\cdot\nabla\ln B$ in equation (124); (d) the radial ion polarization current in the quasineutrality equation is also modified by the $m=0$ ion pressure perturbation

$$2\overline{\left(n\hat{\mathbf{v}}_{pe} - n\hat{\mathbf{v}}_{pi}\right)\cdot\nabla\ln B} + n\nabla\cdot\overline{\mathbf{v}}_I = 0. \quad (126)$$

Thus coupling to the $m=0$ ion temperature (pressure) produces an additional geodesic type mode. This additional eigenmode, associated with oscillations of the ion temperature, in general, appears as a short wavelength mode with a frequency scaling as [183]

$$\omega_2^2 = \beta\frac{v_{Ti}^2}{R^2}k_r^2\rho_i^2 \sim \omega_{di}^2, \quad (127)$$

where β is a numerical coefficient of the order of unity. In [184] this coefficient was obtained from the two-fluid MHD theory (and neglecting the anisotropy of the perturbed pressure) in the form

$$\beta = \frac{5}{3}\frac{15+13\tau_e}{5+3\tau_e}, \quad (128)$$

where $\tau_e = T_e/T_i$.

The important feature of this short wavelength mode is its strong dispersion due to the linear dependence on $k_r\rho_i$, $\omega\sim\omega_{di}$. Note that here $k_r\rho_i$ appears not due the ion FLR effect but from the magnetic drift frequency due to the radial wave vector k_r, which is a result of the radial excursion of particles from the magnetic surface (FOW effects). The short wavelength geodesic oscillations were identified in nonlinear fluid simulations [183] where it was concluded that this branch is more effectively excited by ITG turbulence.

2.15. Electron GAM

Geodesic effects also affect the higher frequency turbulence modes, such as electron temperature gradient modes (ETG). Geodesic coupling via magnetic perturbations leads to a separate branch of unstable EM short wavelength ETG mode [185] and results in symmetry breaking of ETG in toroidal plasmas [186]. A higher frequency GAM type branch, the so-called electron GAMs (el-GAM), was also predicted [187]. Using simple fluid/MHD equations a high frequency GAM with a dispersion relation different from the conventional GAM is obtained:

$$\omega = \frac{\sqrt{2}\,v_{Te}}{R_0}\frac{k_r\rho_e(1+\tau_e)}{(\tau_e + k_r^2\rho_e^2)}, \quad (129)$$

where $v_{Te} = (T_e/m_e)^{1/2}$ and $\tau_e = T_e/T_i$ and k_r is the GAM radial wavenumber. It is interesting that the el-GAM frequency is a radially propagating mode and has a frequency scaling analogous to the short wavelength ion temperature oscillations—see section 2.14. They are also expected to be restricted to the plasma edge by Landau damping. Since the Landau damping rate scales as $\exp(-\omega^2q^2R_0^2/v_{Te}^2)$, thus for the el-GAM to have a non-negligible amplitude requires both $q>1$ and $\tau_e\sim 1$. The el-GAM is coupled to ETG modes and can be driven by ETG turbulence as modelled using the fluid description [188] and also including the finite β effects [189]. It should be noted that the ZF growth rate for ETG turbulence is slower than for DW/ITG due to a higher effective inertia [58] and thus weaker. No obvious experimental observations of el-GAMs have been reported to date.

3. Theory of energetic particle driven GAMs

Energetic particles (EPs) are a robust source of free energy leading to the appearance of geodesic acoustic-like modes as reported in experiments, cf [44] and section 13. EPs can drive

GAM modes, with frequencies close to the natural GAM frequency of the bulk thermal plasma, as well as excite modes with frequencies different from that of the bulk GAM mode. The physics of such modes is closely related to the physics of natural GAMs and both can be conveniently discussed within a uniform approach. One has to note however that the terminology in the literature differs, e.g. the often used term EGAMs may be used for the GAM-like and for GAM related modes of different types. In this review, and to emphasize the common physics, we refer to such modes as EP GAMs and EGAM/GAMs, while in reference to the original publications we will use the terminology of the authors to avoid the confusion. In this section, an overview of the main developments and results in EGAM/GAM theory are presented.

As is the case with many other instabilities in plasmas, some anisotropy in the population of the EP is required to excite GAM-like modes. The pressure anisotropy is an important feature of high energy particles, and the theory of GAMs in plasmas with anisotropic pressure provides a simple insight on the special case of GAMs driven by EPs. Equations (20)–(25) in section 2.3 illustrate that an anisotropic plasma pressure $p_\perp \neq p_\parallel$ may result in a significant modification of the natural GAM frequency and the appearance of an additional mode which may become unstable. As a matter of terminology, in the literature, such modes often are not discussed as EGAMs, though their physics have much in common with some types, in particular, with the so-called reactive EGAMs [190].

Another type of the anisotropy that may induce GAM modes is the presence of beams of high energy particles. Such instabilities may be viewed as analogous to plasma–beam instabilities. Furthermore, two types of EP related GAM modes discussed in the literature, dissipative (resonance) and reactive EGAMs [190, 191], are analogous to two regimes of plasma–beam instabilities, respectively to kinetic, or finite temperature plasma–beam instabilities, and to fluid, or cold plasma–beam instabilities. As is well known, plasma beam instabilities are driven by the population of particles with an inverse, or beam-like, derivative of the distribution function, $\partial f_0/\partial v > 0$, at the point of the resonance with some plasma eigenmode, $\mathbf{k}\cdot\mathbf{v} = \omega$. Formally, for a beam with a finite temperature (finite energy spread) the contribution of such particles is described by the pole (residue) resonance giving an imaginary contribution to the dispersion relation resulting in the instability. This is the mechanism of the so-called dissipative or resonant EGAMs which require a kinetic theory treatment. Alternatively, cold beams, with delta-function like distribution functions, result in real contributions to the dispersion equation, so that the full dispersion equation has all real coefficients. As a result, unstable eigenmodes appear in complex conjugate pairs, resulting in reactive instabilities. This is the mechanism of the so-called reactive EGAMs, which, in general, can be described by fluid theory. The actual conditions when the beam may be considered cold, and therefore lead to the reactive EGAMs, will depend on the type of anisotropy of EPs ('the beam shape'), and the relation of the beam temperature (energy spread in the beam distribution function) to the bulk plasma temperature.

Another aspect of EP driven GAMs is their relation to the GAM existing in the bulk thermal plasma. In some situations the contribution from high energy particles may be considered as a small perturbation to the initially stable (without EP) GAM that existed in the bulk plasma. In other cases the effect of the EPs is large and result in the appearance of modes with significantly different frequencies from that of the bulk plasma GAM mode. This suggests the distinction of perturbative and non-perturbative solutions. Perturbative and non-perturbative solutions are understood here as regular and singular perturbations: regular perturbations modify the old solution, while singular perturbations result in the appearance of new solutions.

A simple classification of reactive and dissipative EGAMs may be transparent and attractive but it has some limitations. Essentially such a classification is based on the reduced fluid theory where the GAM dispersion relation (in the absence of EPs) is described by the polynomial in ω (typically of the second order in the absence of dispersive effects), and the notion that the contribution of high energy particles is real (for reactive EGAMs) or imaginary (for dissipative EGAMs). In fully kinetic theory, and in regimes when both bulk and high energy ions have finite temperature, the dispersion equation is transcendental and there are multiple solutions even in the absence of high energy particles [192–194]. Thus, in kinetic theory, in addition to the basic fluid GAM mode with weak damping, there exist heavily damped modes. With addition of high energy particles the basic fluid GAM may acquire a positive imaginary part of the frequency, turning it into an EGAM, in the terminology of [194]—EGAM from GAM. Alternatively, a heavily damped mode may become unstable leading to a Landau EGAM [194]. Typically, the latter show a stronger modification of the real part of the frequency compared to the case of EGAM from GAM [192, 194]. Therefore, it is also possible that the reactive contribution of EPs modifies the real part of the GAM frequency without making it unstable, and additional effects may also be at work resulting in the instability. Table 6 provides a basic classification of the EGAM/GAM excitation mechanisms and the dominant mechanism defining its radial structure.

It is generally thought that the destabilization of GAM modes by EPs is related to the sign of the derivative of the EP distribution function at a resonant point, and, that the condition for the instability can be determined by the sign of the energy exchange term, i.e. the mode becomes unstable when the energy input from EPs (due to the inverted distribution function) exceeds the energy losses due to the damping in the thermal ions [192]. The situation may become more complicated when the contribution of the EPs have both a cold beam-like reactive part and the pole-like resonant part. The presence of the equilibrium flow due to the beam may create the condition for the existence of a negative energy mode excitation which can be made unstable by positive dissipation, i.e. the EGAM can be excited when the resonant energy exchange is negative, that is the total energy losses are positive. Such a situation of the EGAM instability of the negative energy mode induced by the positive dissipation was considered in [195].

Table 6. Simplified classification of EP driven GAMs by: (1) excitation mechanisms and (2) radial structure.

1. Excitation mechanisms
A: Dissipative EGAM
- Full kinetic theory—multiple solutions
- Warm-beam—imaginary contribution to the dispersion relation
- Inverse Landau damping [45]
A-1: EGAM from GAM (from weakly damped/stable modes) [192, 194]
A-2: Landau EGAM (from heavily damped modes) [194]
B: Reactive EGAM
- Reduced fluid theory
- Cold-beam—real contribution to the dispersion relation
- Two stream instability [190, 191]
2. Radial structure
i. Fast ion distribution
ii. Local GAM continuum maxima (GGAM)

Despite that the discussed classification is somewhat simplified, and that more complex realistic scenarios may occur, it is still useful for highlighting different physics and regimes of EGAM/GAM instabilities that depend on the type of the distribution function of the EPs as they are produced by various sources in fusion plasmas, such as neutral beam injection (NBI), RF heating, and fusion products.

The analysis of GAMs in plasmas with anisotropic pressure well illustrates another point often missed or neglected in the existing literature on EGAMs. As noted in the brief account of the pressure anisotropy effects in section 2.3, the pressure anisotropy is a part of the plasma equilibrium and the conclusions on the GAM modifications and possible instability are sensitive to the details of the equilibrium and the nature of the anisotropy. The quantitative analysis of the conditions for EGAM instabilities should include a consideration of the equilibrium constraints taking into account the contribution the EPs, which is rarely (if ever) done in the EGAM theory. This could be especially important in situations when EPs provide a large fraction of the total plasma pressure. The main ideas and equations of EGAM/GAM theory can be presented within the fluid and kinetic frameworks as similar to those presented in sections 2.2 and 2.5. This will be done in the next sections.

3.1. Hybrid MHD-kinetic formulation for the EGAM/GAMs

The presence of high energy particles modifies the basic constituent equation—the quasineutrality condition

$$n_{\mathrm{e}} = n_{\mathrm{i}} + n_{\mathrm{h}}, \tag{130}$$

where n_{e}, n_{i}, and n_{h} are the electron, bulk ions, and high energy particle density, respectively. One of the approaches in the theory of EP related GAMs is based on the fluid like reformulation of the quasineutrality condition (130) in the form of the current conservation, $\nabla \cdot \mathbf{J} = 0$, which is often more transparent. Using continuity equations for all species,

$$\frac{\partial n_\alpha}{\partial t} + \nabla \cdot (n_\alpha \mathbf{v}_\alpha) = 0, \tag{131}$$

where $\alpha = (\mathrm{e}, \mathrm{i}, \mathrm{h})$, the current conservation, equivalent to the condition (130), becomes

$$\nabla \cdot (n_{\mathrm{i}} \mathbf{v}_{\mathrm{i}} + n_{\mathrm{h}} \mathbf{v}_{\mathrm{h}} - n_{\mathrm{e}} \mathbf{v}_{\mathrm{e}}) = 0. \tag{132}$$

As in the basic GAM theory, it is most convenient to use the $m = 0$ component (by averaging over the poloidal angle) as the main equation: $\langle \nabla \cdot \mathbf{J}_\perp \rangle = 0$. In the next steps the calculation of the transverse currents in (132) proceeds with some simplifications, as in the original work [45]. Formally, it is based on the strong magnetic field expansion when the velocities of all species can be written in the form

$$\mathbf{v}_\alpha = \mathbf{v}_E + \mathbf{v}_{p_\alpha} + \mathbf{v}_{I\alpha}, \tag{133}$$

where respectively $\mathbf{v}_E$, $\mathbf{v}_{p_\alpha}$ and $\mathbf{v}_{I\alpha}$ are the electric, diamagnetic, and inertial drifts. Upon summation over all species in equation (132), the electric drift contributions cancel out due to the quasineutrality, and the diamagnetic drifts sum up into the diamagnetic current due to the total pressure from all plasma components. The inertial currents are also added together producing the $m = 0$ equation

$$\frac{c}{B} \left\langle \nabla \left(\hat{p}_\parallel + \hat{p}_\perp + \hat{p}_{\parallel \mathrm{h}} + \hat{p}_{\perp \mathrm{h}} \right) \cdot \mathbf{b} \times \nabla \ln B \right\rangle - \left(\frac{e n_{0\mathrm{i}} c}{B_0 \omega_{\mathrm{ci}}} + \frac{e n_{0\mathrm{h}}}{B_0 \omega_{\mathrm{ch}}} \right) \frac{\partial}{\partial t} \nabla_\perp^2 \widetilde{\phi}_0 = 0. \tag{134}$$

Note that the diamagnetic current has to be calculated taking into account full pressure anisotropy as in equation (18). Here, $\hat{p}_\parallel$ and $\hat{p}_\perp$ are the $m = 1$ components of the bulk plasma pressure (electron + ion), and $\hat{p}_{\parallel \mathrm{h}}$ and $\hat{p}_{\perp \mathrm{h}}$ are the $m = 1$ components of the parallel and perpendicular pressure of high energy particles, and $e n_{0\mathrm{i}} c/B_0 \omega_{\mathrm{ci}} + e n_{0\mathrm{h}} c/B_0 \omega_{\mathrm{ch}} = c^2 \rho / B_0$, where $\rho = n_{0\mathrm{i}} m_{\mathrm{i}} + n_{0\mathrm{h}} m_{\mathrm{h}}$ is the total plasma density, $\omega_{\mathrm{ch}} = e B_0 / m_{\mathrm{h}} c$. An equation in the form of (134) was obtained in [45]. Note that equations (133) and (134) respectively, neglect the effects of FLR for thermal and high energy ions.

Kinetic effects and resonances are generally important for EPs and are included in the kinetic calculations of the high

energy particles pressure

$$\hat{p}_{\|\mathrm{h}} + \hat{p}_{\perp\mathrm{h}} = \int m\left(v_\|^2 + v_\perp^2/2\right)\widetilde{f}_\mathrm{h}\,\mathrm{d}^3\mathbf{v}, \tag{135}$$

where $\widetilde{f}_\mathrm{h}$ is found from the kinetic equation, e.g. either from the reduced DKE (40) or from the full GK equation (55). When the pressure perturbations of the thermal ions is found in the MHD limit, equation (134) together with (135) and the kinetic equation for the EPs form the so-called pressure coupled MHD-kinetic formulation.

As was discussed in section 2.1, the GAM dispersion relation is defined by the balance of the inertial current (last term in equation (134)) with the radial diamagnetic current (the first term in equation (134)). Assuming that the response of the pressure of the EP is similar to that of the bulk plasma pressure, $(\hat{p}_{\|\mathrm{h}} + \hat{p}_{\perp\mathrm{h}}) \sim (\hat{p}_\| + \hat{p}_\perp)n_{0\mathrm{h}}T_\mathrm{h}/(n_\mathrm{eq}T_\mathrm{i}) \sim (\hat{p}_\| + \hat{p}_\perp)(v_{0\mathrm{h}}/v_\mathrm{th})^2 n_{0\mathrm{h}}/n_\mathrm{eq}$ one gets a simple estimate for the GAM frequency modified by the presence of the EPs [193]

$$\omega = \sqrt{\omega_\mathrm{G}^2\left(1 + C_\mathrm{h}\left(v_{0\mathrm{h}}/v_\mathrm{th}\right)^2 n_{0\mathrm{h}}/n_\mathrm{eq}\right)} \tag{136}$$

where $v_{0\mathrm{h}}$ is the characteristic 'beam' velocity of the EPs, $m_\mathrm{h}v_{0\mathrm{h}}^2 \sim T_{0\mathrm{h}}$, and $T_{0\mathrm{h}}$ is their characteristic temperature. The numerical coefficient C_h depends on the type of the EP distribution function [50, 193]. The response of the EPs, however, can be very different from that of the thermal plasma due to kinetic resonances so that the estimate (136) would not apply, and the EP modified GAM frequency is below that of the natural GAM.

3.2. Local kinetic theory of EGAM/GAMs

One of the restrictions of the hybrid MHD-kinetic approach presented in section 3.1 follows from the fluid-like representation of the velocities of all species in the form (134) which means that the ion inertia, both for thermal ions and EPs, is calculated in the cold plasma approximation, and thus provides no systematic guidance on how the effects of FLR can be incorporated for thermal and EPs. An alternative approach is to use the full GK equations for thermal ions and EPs and the quasineutrality condition in the original form, equation (130). In this straightforward approach one uses the full GK theory to find the perturbed distribution functions, $f_{\alpha,m}$ and, respectively, the densities of the ions and EPs, $n_{\alpha,m}$; $\alpha = (\mathrm{i}, \mathrm{h})$, in terms of the potential harmonics, ϕ_m, $m = 0, 1, \ldots$ The electron density is typically taken in the Boltzmann form $n_m = e\phi_m/T_\mathrm{e}n_0$ with $m \neq 0$, unless the electron kinetic effects are included. The $m = 0$ component of the electron density is usually assumed to be zero, but see comments in section 2.12. The solubility condition for the resulting system of equations for ϕ_m defines the local EGAM/GAM dispersion relation. This direct and formally most accurate approach was used, e.g. in [50, 192–194]. This approach is illustrated here using the direct separation of the harmonics in the potential and the distribution functions in each order, as in the section 2.6, and differences with other formulations commented on.

The high energy particles are described by the GK equation similar to equation (54) but allowing the anisotropic equilibrium $F_{0\mathrm{h}}(\mathcal{E}, \mu, \mathbf{r})$ for high energy particles:

$$f_\mathrm{h} = e\phi\frac{\partial F_{0\mathrm{h}}}{\partial\mathcal{E}} + g_\mathrm{h}, \tag{137}$$

$$\left(\omega - \hat{\omega}_\mathrm{dh} + \frac{\mathrm{i}v_\|}{qR_0}\frac{\partial}{\partial\theta}\right)g_\mathrm{h} = -\omega e\phi\frac{\partial F_{0\mathrm{h}}}{\partial\mathcal{E}}J_0^2(k_\perp v_\perp/\omega_\mathrm{ch}). \tag{138}$$

Here,

$$\hat{\omega}_\mathrm{dh} = -\omega_\mathrm{dh}\,\sin\,\theta = -\frac{k_\mathrm{r}\left(v_\perp^2/2 + v_\|^2\right)}{R\omega_\mathrm{ch}}\,\sin\,\theta, \tag{139}$$

and $\omega_\mathrm{ch} = eB/m_\mathrm{ic}$ is the high energy particle cyclotron frequency; in what follows it is assumed that the EPs have single charge and are of the same species as the bulk ions.

Separating the perturbations of the potential and distribution function into the $m = 0$ and $m = 1$ components, similarly to (73) and (67), $\phi = \phi_0 + \phi_\mathrm{s}\cos\theta + \phi_\mathrm{s}\sin\theta$, and $f_{\mathrm{i,h}} = f_{0(\mathrm{i,h})} + f_{\mathrm{c(i,h)}}\cos\theta + f_{\mathrm{s(i,h)}}\sin\theta$, one can obtain from equations (137)–(139)

$$g_{\mathrm{h}0} = \frac{\omega_\mathrm{dh}\omega}{2\Delta_\mathrm{h}}e\phi_\mathrm{s}\frac{\partial F_{0\mathrm{h}}}{\partial\mathcal{E}}J_0^2 - \frac{\omega^2 - v_\|^2/q^2R_0^2}{\Delta_\mathrm{h}}e\phi_0\frac{\partial F_{0\mathrm{h}}}{\partial\mathcal{E}}J_0^2 - \mathrm{i}\frac{\omega_\mathrm{d}v_\|}{2qR_0\Delta_h}e\phi_\mathrm{c}\frac{\partial F_{0\mathrm{h}}}{\partial\mathcal{E}}J_0^2, \tag{140}$$

$$g_{\mathrm{hs}} = -\frac{\omega^2}{\Delta_\mathrm{h}}e\phi_\mathrm{s}\frac{\partial F_{0\mathrm{h}}}{\partial\mathcal{E}}J_0^2 + \frac{\omega\omega_\mathrm{dh}}{\Delta_\mathrm{h}}e\phi_0\frac{\partial F_{0\mathrm{h}}}{\partial\mathcal{E}}J_0^2 - \mathrm{i}\frac{\omega v_\|}{qR_0\Delta_\mathrm{h}}e\phi_\mathrm{c}\frac{\partial F_{0\mathrm{h}}}{\partial\mathcal{E}}J_0^2, \tag{141}$$

$$g_{\mathrm{hc}} = \mathrm{i}\frac{\omega v_\|}{qR_0\Delta_\mathrm{h}}e\phi_\mathrm{s}\frac{\partial F_{0\mathrm{h}}}{\partial\mathcal{E}}J_0^2 - \mathrm{i}\frac{\omega_\mathrm{dh}v_\|}{qR_0\Delta_\mathrm{h}}e\phi_0\frac{\partial F_{0\mathrm{h}}}{\partial\mathcal{E}}J_0^2 - \frac{\omega^2 - \omega_\mathrm{dh}^2/2}{\Delta_\mathrm{h}}e\phi_\mathrm{c}\frac{\partial F_{0\mathrm{h}}}{\partial\mathcal{E}}J_0^2, \tag{142}$$

where the resonance propagator for the high energy particles is $\Delta_\mathrm{h} = \omega^2 - v_\|^2/q^2R_0^2 - \omega_\mathrm{dh}^2/2$. One can see here that, similar to the expression (68), the transit and toroidal resonances are coupled in Δ_h.

Also included here are the $\cos\theta$ parts of the perturbed potential and distribution function that can be coupled via the asymmetric (in $v_\|$) equilibrium function of the EPs, $\langle v_\|\partial_\mathcal{E}F_{0\mathrm{h}}\rangle_\mathrm{h} \neq 0$. The second order sidebands, $\phi_{\mathrm{2s,2c}}, g_{\mathrm{2s}}, g_{\mathrm{2c}}$, are neglected assuming the standard small parameter in the GAM theory: $f_2/f_1 \sim \phi_2/\phi_1 \sim \phi_1/\phi_0 \sim \omega_\mathrm{di}/\omega \sim k_\mathrm{r}\rho_\mathrm{i} < 1$. From the quasineutrality condition for the $m = 0$ component, and taking into account that for the electrons the $m = 0$ density perturbation $\tilde{n}_{\mathrm{e}0} = 0$, one has the equation

$$\phi_0\left(n_{0\mathrm{i}}L_{00}^\mathrm{i} + n_{0\mathrm{h}}L_{00}^{\mathrm{h}1} + n_{0\mathrm{h}}L_{00}^{\mathrm{h}2}\right) - \phi_\mathrm{s}\left(n_{0\mathrm{i}}L_{0\mathrm{s}}^\mathrm{i} + n_{0\mathrm{h}}L_{0\mathrm{s}}^\mathrm{h}\right) + \mathrm{i}\phi_\mathrm{c}n_{0\mathrm{h}}L_{0\mathrm{c}}^\mathrm{h} = 0 \tag{143}$$

$$L^{\rm i}_{00}=\frac{1}{T_{0\rm i}}\left(-\left\langle F_{0\rm i}\left(1-J_0^2\right)\right\rangle+\left\langle F_{0\rm i}\frac{\omega_{\rm d}^2}{2\Delta}J_0^2\right\rangle\right) \quad (144)$$

$$L^{\rm h1}_{00}=\left\langle\frac{\partial F_{0\rm h}}{\partial\mathcal{E}}\left(1-J_0^2\right)\right\rangle_{\rm h} \quad (145)$$

$$L^{\rm h2}_{00}=-\left\langle\frac{\omega_{\rm dh}^2}{2\Delta_{\rm h}}\frac{\partial F_{0\rm h}}{\partial\mathcal{E}}J_0^2\right\rangle_{\rm h} \quad (146)$$

$$L^{\rm i}_{0\rm s}=\frac{1}{T_{0\rm i}}\left\langle F_{0\rm i}\frac{\omega\omega_{\rm d}}{2\Delta}J_{0^2}\right\rangle \quad (147)$$

$$L^{\rm h}_{0\rm s}=-\left\langle\frac{\omega\omega_{\rm dh}}{2\Delta_{\rm h}}\frac{\partial F_{0\rm h}}{\partial\mathcal{E}}J_0^2\right\rangle_{\rm h} \quad (148)$$

$$L^{\rm h}_{0\rm c}=-\left\langle\frac{v_\parallel\omega_{\rm dh}}{2qR_0\Delta_{\rm h}}\frac{\partial F_{0\rm h}}{\partial\mathcal{E}}J_0^2\right\rangle_{\rm h}. \quad (149)$$

The first term in the $L^{\rm i}_{00}$ expression is the ion inertia and the second term corresponds to the perturbed pressure of the thermal ions in (134). The $L^{\rm i}_{0\rm s}$ term corresponds to the perturbed electron pressure (134). Respectively, the $L^{\rm h1}_{00}$ and $L^{\rm h2}_{00}$ terms are due to the pressure and inertia of the EP related to the ϕ_0, and $L^{\rm h}_{0\rm s}$, $L^{\rm h}_{0\rm c}$ are related to the pressure perturbations due to the $\phi_{\rm s}$ and $\phi_{\rm c}$ sidebands.

Equations for the potential sidebands $\phi_{\rm s}$ and $\phi_{\rm c}$ are found from the quasineutrality conditions for the $m=1$ components and have the form

$$\phi_{\rm s}\left(\frac{n_{0\rm e}}{T_{0\rm e}}+n_{0\rm i}L^{\rm i}_{\rm ss}+n_{0\rm h}L^{\rm h}_{\rm ss}\right)+\phi_0\left(n_{0\rm i}L^{\rm i}_{\rm s0}+n_{0\rm h}L^{\rm h}_{\rm s0}\right)+{\rm i}\phi_{\rm c}n_{0\rm h}L^{\rm h}_{\rm sc}=0, \quad (150)$$

$$\phi_{\rm c}\left(\frac{n_{0\rm e}}{T_{0\rm e}}+n_{0\rm h}L^{\rm h}_{\rm cc}\right)-{\rm i}\phi_0 n_{0\rm h}L^{\rm h}_{\rm c0}+{\rm i}\phi_{\rm s}n_{0\rm h}L^{\rm h}_{\rm cs}=0. \quad (151)$$

Here,

$$L^{\rm i}_{\rm ss}=\frac{1}{T_{0\rm i}}\left\langle\left(1-\frac{\omega^2}{\Delta}J_0^2\right)\right\rangle \quad (152)$$

$$L^{\rm h}_{\rm ss}=-\left\langle\frac{\partial F_{0\rm h}}{\partial\mathcal{E}}\left(1-\frac{\omega^2}{\Delta_{\rm h}}J_0^2\right)\right\rangle_{\rm h} \quad (153)$$

$$L^{\rm i}_{\rm s0}=\frac{1}{T_{0\rm i}}\left\langle\frac{\omega\omega_{\rm d}}{\Delta}F_{0\rm i}\right\rangle \quad (154)$$

$$L^{\rm h}_{\rm s0}=-\left\langle\frac{\omega\omega_{\rm dh}}{\Delta_{\rm h}}\frac{\partial F_{0\rm h}}{\partial\mathcal{E}}J_0^2\right\rangle_{\rm h} \quad (155)$$

$$L^{\rm h}_{\rm sc}=-\left\langle\frac{\omega v_\parallel}{R\Delta_{\rm h}}\frac{\partial F_{0\rm h}}{\partial\mathcal{E}}J_0^2\right\rangle_{\rm h} \quad (156)$$

$$L^{\rm h}_{\rm cc}=-\left\langle\frac{\partial F_{0\rm h}}{\partial\mathcal{E}}\left(1-\frac{\omega^2-\omega_{\rm dh}^2/2}{\Delta_{\rm h}}J_0^2\right)\right\rangle_{\rm h}$$

$$L^{\rm h}_{\rm c0}=-\left\langle\frac{\omega_{\rm dh}v_\parallel}{qR_0\Delta_{\rm h}}\frac{\partial F_{0\rm h}}{\partial\mathcal{E}}J_0^2\right\rangle_{\rm h} \quad (157)$$

$$L^{\rm h}_{\rm cs}=-\left\langle\frac{\omega v_\parallel}{qR_0\Delta_{\rm h}}\frac{\partial F_{0\rm h}}{\partial\mathcal{E}}J_0^2\right\rangle_{\rm h}. \quad (158)$$

The averages over the respective distribution function are defined as

$$\langle\ldots\rangle_{\rm h}=\frac{1}{n_{0\rm h}}\int(\ldots)\,{\rm d}^3v, \quad (159)$$

$$\langle\ldots\rangle=\frac{1}{n_{0\rm i}}\int(\ldots)\,{\rm d}^3v. \quad (160)$$

The terms $L^{\rm i}_{00}$ and $L^{\rm i}_{0\rm s}$ in equation (143) are the main terms defining the basic GAM dispersion equation. The term $L^{\rm i}_{0\rm s}$ determines the contribution of the electron temperature. The main order contribution from EP is given by the $L^{\rm h2}_{00}$ term, which scales to the main order GAM terms as the pressure of high energy particles to the thermal pressure: $L^{\rm i}_{00}/L^{\rm h2}_{00}\sim n_{0\rm h}T_{0\rm h}/n_{0\rm i}T_{0\rm i}$. The FLR effects of the high energy particles are described by the $L^{\rm h1}_{00}$ term, which is generally smaller than the bulk ion inertia as $n_{0\rm h}/n_{0\rm i}<1$. The addition of the high energy particle to the sideband coupling is generally small as $n_{0\rm h}/n_{0\rm i}<1$ so that the amplitude of the sideband $\phi_{\rm s}$ is mostly defined by the electron temperature, $\phi_{\rm s}/\phi_0\sim\left(T_{0\rm e}/T_{0\rm i}\right)\omega_{\rm d}/\omega$. Additional corrections due to the high energy particles are also typically small, $\left(n_{0\rm h}/n_{0\rm e}\right)\left(T_{0\rm e}/T_{0\rm h}\right)k_{\rm r}^2\rho_{\rm h}^2<1$. As can be seen from equation (151), due to the asymmetry of the distribution function $\left\langle v_\parallel F_{0\rm h}\right\rangle\neq0$, the EPs may couple to the $\phi_{\rm c}$ sideband normally omitted in the standard GAM treatments, though the amplitude of the $\phi_{\rm c}$ sideband would normally be small: $\phi_{\rm c}/\phi_0\sim\left(n_{0\rm h}/n_{0\rm e}\right)\left(T_{0\rm e}/T_{0\rm h}\right)\left(v_{\rm Th}/\omega R_0\right)\sim\left(n_{0\rm h}/n_{0\rm e}\right)\left(T_{0\rm e}/T_{0\rm h}\right)\left(T_{0\rm h}/T_{0\rm i}\right)^{1/2}<1$.

Equations (143)–(151) form the most complete kinetic model that describe local EGAM/GAMs in the main order, i.e. in neglect of the dispersion effects. Though, some dispersive effects, both from thermal and energetic ions, can be obtained from equations (143)–(151) by expanding to the higher order, $\sim(k_{\rm r}^4\rho_{\rm i}^4,k_{\rm r}^4\rho_{\rm h}^4)$, their retention would not be self-consistent, because of the omitted terms due to the second harmonics $\phi_{2\rm c}$, $\phi_{2\rm s}$ and $g_{2\rm s},g_{2\rm c}$, which are formally of the same order, $\left(\omega_{\rm d}^4/\omega^4,\omega_{\rm dh}^4/\omega_{\rm dh}^4\right)\sim(k_{\rm r}^4\rho_{\rm i}^4,k_{\rm r}^4\rho_{\rm h}^4)$, and typically larger numerically, as explained in section 2.6. Since the second harmonics of $\phi_{2\rm c}$, $\phi_{2\rm s}$ and $g_{2\rm s},g_{2\rm c}$, are not included here, for consistency, only the first order expansion has to be kept in the ion Larmor radius term $\left\langle F_{0\rm i}\left(1-J_0^2\right)\right\rangle\simeq-k_{\rm r}^2\rho_{\rm i}^2/2$, becoming equivalent to the cold ion inertia in equation (134). Additional corrections from EP are normally small as explained above, however, when resonant damping effects from thermal ions (which have additional small parameters) are included, the additional effects from EPs may become important, especially in plasmas with large fractions of EP. An analytical dispersion equation based on equations similar in structure to (143)–(151) was derived in [193, 194] but neglecting the toroidal corrections to the resonances, and assuming the symmetric bump-on-tail distribution function for the EPs so that $\left\langle v_\parallel\partial_{\mathcal{E}}F_{0\rm h}\right\rangle_{\rm h}=0$ and coupling to the $\phi_{\rm c}$ sideband was not present.

Formally, it is also possible to use for the EPs the kinetic solution in the form of the formal series (60). As was discussed in section 2.6, treatment of resonant terms with this approach is difficult to implement technically because of the absence of small parameters to cut-off the infinite series. For EPs with an

explicit optimal ordering $\omega \simeq v_{Th}/qR_0$, it is even more problematic since resonant effects cannot be treated as small perturbations and the infinite sequence of resonances $\omega \simeq lv_\parallel/qR_0$, $l = 1, 2, \ldots$ would have to be included. Moreover, the parameter $\xi_h = \omega_{dh} qR_0/v_\parallel \sim qk_r\rho_h$ can be large for EPs and the infinite series in equation (60) with $J_n(\xi_h) J_{n'}(\xi_h)$ cannot be truncated. Typically in most works only the $l = 1$ terms are included for EPs neglecting the magnetic drift resonances $\omega \simeq v_\parallel/qR_0 \gg \omega_d$, or the opposite limit $\omega \simeq \omega_d \gg v_\parallel/qR_0$ is considered [50]. Our approach allows the analysis of the resonant interaction in the optimal ordering $\omega \simeq v_{Th}/qR_0 \simeq \omega_{dh}$ for EPs.

Below, the simplest formulation of the GAM/EGAM dispersion equation in the main order is given, similar to [156, 195, 196] but extending resonances to the optimal ordering $\omega \simeq v_T/qR_0 \simeq \omega_d$ for both thermal ions and EPs.

In the main order the $m = 0$ EP particle density is due to ϕ_0 only and is given by the expression

$$\frac{\delta n_{h0}}{\delta\phi_0} \simeq n_{0h} L_{00}^{h2} = -\frac{n_{0h}}{2}\left\langle \frac{\omega_{dh}^2}{\omega^2 - v_\parallel^2/q^2R_0^2 - \omega_{dh}^2/2}\frac{\partial F_{0h}}{\partial \mathcal{E}}\right\rangle_h. \tag{161}$$

Together with the bulk ions contributions L_{00}^i and L_{0s}^i one has

$$\frac{en_{0i}k_r^2 v_{Ti}^2}{2T_{0i}}\left(-1 + \frac{\omega_{GAM}^2}{\omega^2}\right) + n_{0h}L_{00}^{h2} = 0. \tag{162}$$

In the expanded form one has a general local EGAM/GAM dispersion equation in the form

$$\begin{aligned} &-1 + \frac{1}{v_{Ti}^2R_0^2}\left\langle \frac{\left(v_\parallel^2 + v_\perp^2/2\right)^2}{\omega^2 - v_\parallel^2/q^2R_0^2 - \omega_d^2/2}F_{0i}\right\rangle \\ &\quad + \frac{T_{0e}}{T_{0i}}\frac{n_{0i}}{n_{0e}}\frac{\omega^2}{v_{Ti}^2R_0^2}\left\langle \frac{\left(v_\parallel^2 + v_\perp^2/2\right)}{\omega^2 - v_\parallel^2/q^2R_0^2 - \omega_{dh}^2/2}F_{0i}\right\rangle^2 \\ &\quad - \frac{n_{0h}}{n_{0i}}\frac{T_{0i}}{v_{Ti}^2R_0^2}\left\langle \frac{\left(v_\parallel^2 + v_\perp^2/2\right)^2}{\omega^2 - v_\parallel^2/q^2R_0^2 - \omega_{dh}^2/2}\frac{\partial F_{0h}}{\partial \mathcal{E}}\right\rangle_h = 0. \end{aligned} \tag{163}$$

The EGAM/GAM dispersion equation in the form similar to (162) was given in [156, 195, 196] with the difference that the toroidal resonance correction due to $\omega_{dh}^2/2$ was omitted in the resonance denominator. In expression (163) the transit and toroidal resonances damping on thermal and energetic ions are included. Our formalism also allows simple treatment of the magnetic drift resonance driven modes [50], which is described in section 3.6.

3.3. Selected examples of EP driven GAMs for different EP distributions

In fusion plasmas, various sources of EPs are expected. Here, an overview is presented of some specific numerical and analytical results for the GAM like modes driven by EPs with some common distribution functions considered in the literature.

In the original EGAM paper [45], the authors used the pressure coupled MHD-kinetic model to investigate instability for the anisotropic slowing-down distribution function in the form

$$f_{0h} = \frac{1}{v^3 + v_{cr}^3}\exp\left(-\frac{P_\phi}{e\Delta\Psi} - \frac{(\Lambda - \Lambda_0)^2}{\Delta\Lambda^2}\right) \tag{164}$$

where Λ and P_ϕ are the pitch-angle and toroidal momentum. The perturbed distribution function $\tilde{f}_h$ was found from the lowest order DKE

$$\frac{d\tilde{f}_h}{dt} = -\frac{d\mathcal{E}}{dt}\frac{\partial f_{0h}}{\partial \mathcal{E}}. \tag{165}$$

Here, f_{0h} is the equilibrium distribution function of the EPs, $\mathcal{E}$ is the energy, and

$$\frac{d\mathcal{E}}{dt} = e\mathbf{v}_d \cdot \mathbf{E}_0 = -m\left(v_\parallel^2 + v_\perp^2/2\right)\mathbf{v}_{E0}\cdot\nabla \ln B, \tag{166}$$

where $\mathbf{E}_0 = -\nabla\tilde{\phi}_0$ is the electric field due to the $m = 0$ component of the perturbed potential. The general solution of equation (165) was obtained by integration over the particle trajectories that, in principle, includes both passing and trapped particles. The perturbation of the pressure of the bulk plasmas was taken to be isotropic with some effective adiabatic index γ, similar to equation (17).

The numerical solution of equation (134) together with (165) reveals three EGAM roots that sensitively depend on the ratio of the EP to bulk plasma pressure $y = (p_{\parallel h} + p_{\perp h})/2\gamma p_{th}$ and the ratio of the passing particles transit frequency $\omega_{b0} = v_h/qR_0$ to the GAM frequency, $Z = \omega_{b0}/\omega_{GAM}$. For $Z = 1$ and low values of EP pressure, $y \ll 1$, the thermal bulk GAM frequency is modified, roughly consistent with equation (136), and remains stable. Two new roots appear for finite values of y ($y \simeq 0.2$) with the real frequencies well below ω_{GAM}. With a further increase of y, one of two new roots become unstable leading to the EGAM instability. For values of Z larger than some critical value $Z > Z_{cr}$, ($Z_{cr} = 1.4$ for the DIII-D parameters used in [45]), the behaviour changes. There are still three roots, but the unstable root originates from the GAM bulk mode, whose frequency decreases with EP pressure as shown in figure 14.

Thus, the frequency of the unstable EGAM is always below the ω_{GAM}. EGAMs are destabilized by the inverse distribution of the EPs, $\partial f_{0h}/\partial\mathcal{E} > 0$ and the contribution of EPs to the total diamagnetic current is negative so that $\omega_{EGAM} < \omega_{GAM}$, contrary to equation (136). The EGAM for $Z = 1.8$ is a perturbative destabilization of the GAM and, using the terminology of [194], can be called an EGAM from GAM, while the case with $Z = 1$, the EGAM is a result of the singular perturbation due to high energy particles.

In [195, 196] analytical calculations are presented based on a model similar to equation (161) but omitting the ω_{dh}^2 terms in the resonant denominator. The 'clipped' distribution function was used to illustrate the effect of the loss region and to explain fast excitations of EGAMs during counter NBI (against the plasma I_p). The distribution function of the NBI was assumed in the form

$$F_{0h} = n_{0h}(r) f(u) g(\Lambda), \tag{167}$$

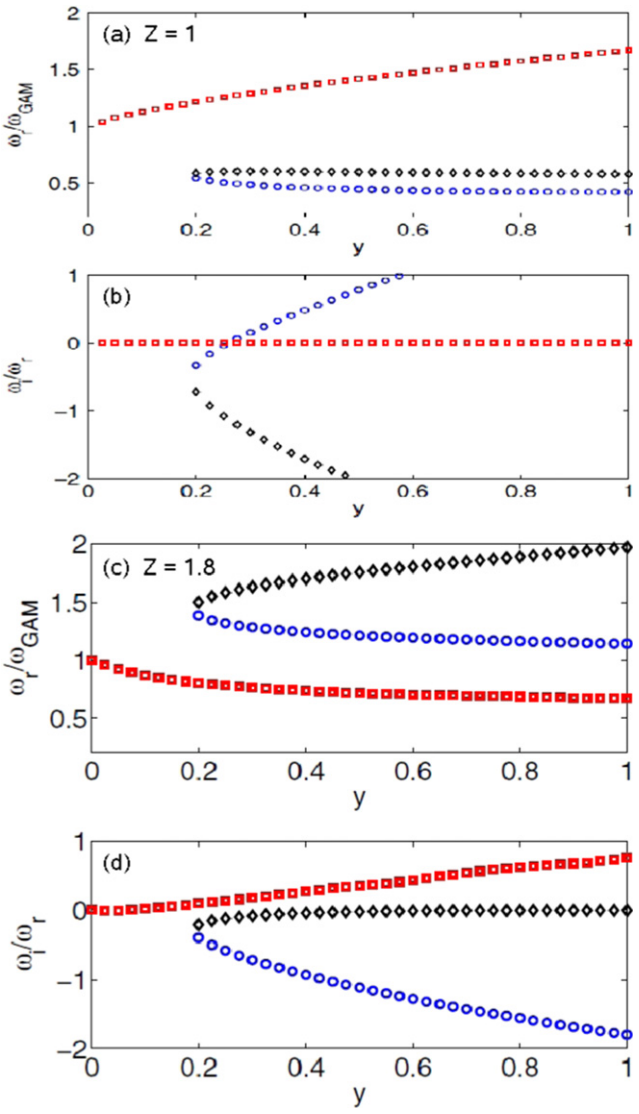

Figure 14. Real and imaginary part of the eigen-frequencies as function of $y = \left(p_{\|\mathrm{h}} + p_{\perp\mathrm{h}}\right)/2\gamma p_{\mathrm{th}}$ for $Z = \omega_{\mathrm{b0}}/\omega_{\mathrm{GAM}} = 1$ (*a*) and (*b*) and $Z = 1.8$ (*c*) and (*d*). Colours indicate separate modes. Adapted figure with permission from [45], Copyright (2008) by the American Physical Society.

$$f(u) = \delta(u - u_0)/u_0^2, \tag{168}$$

$$g(\Delta) = \frac{3}{8\pi\Delta_\Lambda}\left[1 - \left(\frac{\Lambda - \Lambda_0}{\Delta_\Lambda}\right)^2\right] \times H\left(\Lambda - \Lambda_0 + \Delta_\Lambda\right) H\left(\Lambda_0 + \Delta_\Lambda - \Lambda\right) H\left(\Lambda - \Lambda_{\mathrm{c}}\right), \tag{169}$$

where $\Lambda = u_{\|}/u$ is the pitch angle, Λ_{c} is the loss boundary to mock up the loss of EP, Δ_Λ is the width of the distribution function in the pitch angle, which is clipped by the Λ_{c} value, $\Lambda_0 - \Delta_\Lambda < \Lambda_{\mathrm{c}} < \Lambda_0 + \Delta_\Lambda$, and H is the Heaviside function.

The theory in [195, 196] also takes into account that the equilibrium distribution of high energy particles depends on the canonical angular momentum subtracted by the bounce average of the mechanical momentum, $P_\phi - m_{\mathrm{i}}\overline{R_0 u_\phi}$. This dependence produces an extra term in equation (162) with the radial gradient of EPs density.

The authors of [195, 196] have studied the beam mode with $\omega \simeq \omega_{\mathrm{b}} = u_0\Lambda_{\mathrm{c}}/qR_0$. It was shown that the beam mode has negative energy for $\omega_{\mathrm{GAM}} > \omega > \omega_{\mathrm{b}}$ so it can be destabilized by the positive dissipation due to the resonant energy exchange. The dissipation turns positive when the loss region is present for the high energy neutral beam injected counter to the plasma current. In [195, 196] it was proposed that the loss region for the counter injection provides a mechanism for the asymmetry in the EGAM excitation for the co- and counter injected neutral beams observed in DIII-D [44].

The simpler slowing-down distribution function in the form

$$F_{0\mathrm{h}} = \frac{c_0(r)H\left(E_{\mathrm{b}} - E\right)}{E^{3/2} + E_{\mathrm{cr}}^{3/2}}\delta\left(\Lambda - \Lambda_0\right), \tag{170}$$

$$c_0 = \sqrt{2(1 - \Lambda_0 B_0)}n_{\mathrm{b}}\left(r\right) / \left(4\pi B \ln\left(E_{\mathrm{b}}/E_{\mathrm{c}}\right)\right) \tag{171}$$

was analysed in [156] also using the model equation (161) and neglecting the toroidal resonance. Such a distribution function allows full analytical integration in equation (161) so that the final dispersion equation for EGAMs is obtained in the form

$$-1 + \frac{\omega_{\mathrm{GAM}}^2}{\omega^2} + N_{\mathrm{b}}\left[C\ln\left(1 - \frac{\omega_{\mathrm{tr,\,b}}^2}{\omega^2}\right) + D\left(\frac{1}{1 - \omega_{\mathrm{tr,\,b}}^2/\omega^2} - 1\right)\right] = 0, \tag{172}$$

where $\omega_{\mathrm{tr,\,b}} = \sqrt{2E_{\mathrm{b}}\left(1 - \Lambda_0 B_0\right)}/qR_0$ and $C = (2 - \Lambda_0 B_0)(5\Lambda_0 B_0 - 2)/(2(1 - \Lambda_0 B_0)^{5/2})$,

$$N_{\mathrm{b}} = \frac{\sqrt{1 - \Lambda_0 B_0}q^2}{4\ln\left(E_{\mathrm{b}}/E_{\mathrm{c}}\right)}\frac{n_{\mathrm{b}}}{n_{\mathrm{c}}}. \tag{173}$$

The authors of [156] find two unstable branches. For $\omega_{\mathrm{GAM}} < \omega_{\mathrm{tr,b}}$ there is a GAM-like branch with the real frequency close to the GAM frequency, with the instability condition $\Lambda_0 B > 2/5$. For $\omega_{\mathrm{GAM}} > \omega_{\mathrm{tr,b}}$, there is a beam branch with the real frequency close to $\omega_{\mathrm{tr,b}}$ and an instability threshold which depends on EP density.

In [197] the dispersion equation (162), again in neglect of the toroidal resonance term $\omega_{\mathrm{dh}}^2/2$, was analysed for the distribution function that is not yet completely slowed down:

$$F_{0\mathrm{h}} = \frac{c_0 H\left(E_{\mathrm{b}} - E\right) H\left(E - E_{\mathrm{L}}\right)}{E^{3/2} + E_{\mathrm{cr}}^{3/2}}\delta\left(\Lambda - \Lambda_0\right), \tag{174}$$

where $E_{\mathrm{L}} = E_{\mathrm{b}}\exp\left(-2\gamma_{\mathrm{ct}}\right)$, is the energy of the time dependent lower end of the distribution function, γ_{c} is the slowing down rate, $c_0 = \Gamma/4\pi\gamma$, and Γ is the beam flux. For this distribution an analytical dispersion equation was derived

$$-1 + \frac{\omega_{\mathrm{GAM}}^2}{\omega^2} + \frac{\pi}{\sqrt{2}}B_0 q^2\frac{c_0}{n_{0\mathrm{i}}} \times \left[C\left(\ln\left(1 - \frac{\omega_{\mathrm{b}}^2}{\omega^2}\right) - \ln\left(1 - \frac{\omega_{\mathrm{L}}^2}{\omega^2}\right)\right) + D\left(\frac{1}{1 - \omega_{\mathrm{b}}^2/\omega^2} - \frac{1}{1 - \omega_{\mathrm{L}}^2/\omega^2}\right)\right] = 0, \tag{175}$$

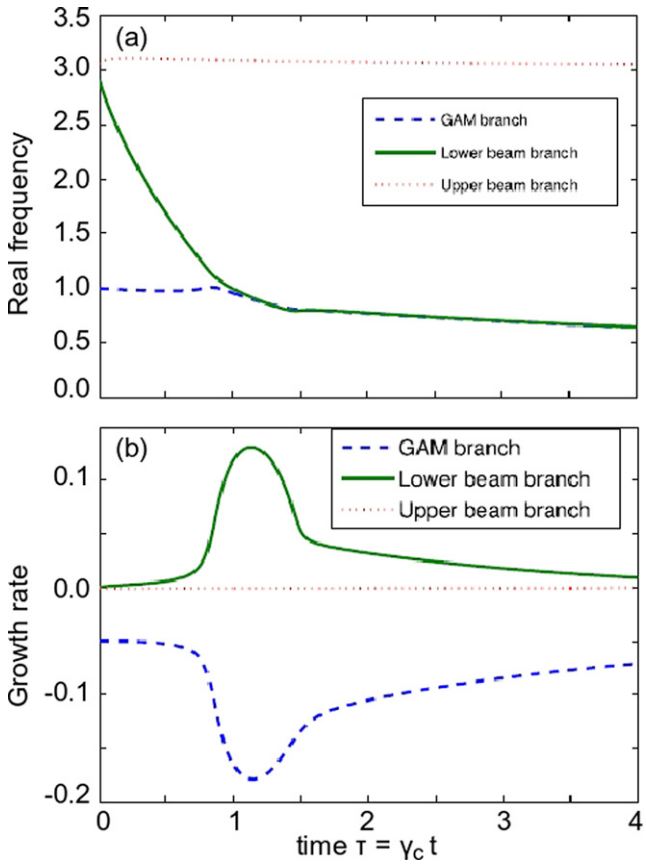

Figure 15. (*a*) Real and (*b*) imaginary part of the EGAM frequency vs time $\tau = \gamma_c t$, for a not fully slowed down EP beam with pitch angle $\Lambda_0 B_0 < 2/5$. Adapted from [197], with the permission of AIP Publishing.

where $D = \Lambda_0 B_0 (2 - \Lambda_0 B_0)^2 / 2(1 - \Lambda_0 B_0)^{5/2})$, and ω_b and ω_L are transit frequencies defined for E_b and E_L respectively. The solution of the dispersion equation (175) shows that there are three modes here: the GAM branch $\omega \simeq \omega_{GAM}$, the lower beam branch $\omega \simeq \omega_L(t)$, and the upper beam branch $\omega \simeq \omega_b$. Note that the ω_L is time dependent. It is shown that the lower beam branch with $\omega_b > \omega_{GAM} t$ may become unstable. The real frequency and growth rates are shown in figure 15 as a function of time $\tau = \gamma_c t$, for $\Lambda_0 B_0 > 2/5$. It was found in [197] that the behaviour of all three modes for $\Lambda_0 B_0 < 2/5$ is qualitatively similar.

The results in [45, 195] were obtained by using the fluid theory for bulk plasma (thermal) ions. Therefore kinetic effects in the thermal ions distributions were not included. A small amount of damping in model form was used in [197] but was found not so essential. The more general case, when the kinetic effects were considered both for thermal and high energy particles, was considered in [192, 194] for a double bump distribution function in the form

$$f_k = \frac{n_k}{2}\left(\frac{m_k}{2\pi T_i \tau_k}\right)^{3/2}\left[\exp\left(-\frac{m_k\left(v_\parallel - \overline{v}_\parallel\right)^2 + 2\mu_k B}{2T_i\tau_k}\right) + \exp\left(-\frac{m_k\left(v_\parallel + \overline{v}_\parallel\right)^2 + 2\mu_k B}{2T_i\tau_k}\right)\right], \quad (176)$$

where k (kinetic) stands for high energy particles, and $\tau_k = T_k/T_i$, the ratio of EP spread in energy to the thermal temperature, is a measure of the width of the bump $v_\parallel$. For this distribution function the contributions of the thermal and EP species to the full kinetic model, such as in section 3.2, can be reduced to the plasma dispersion functions. In [194] the emergence of EGAMs from initially damped modes was investigated in detail using an analytical dispersion relation for different plasma and EP parameters. The emergence of an unstable EGAM root in this model is shown in figure 16(*a*) for the EGAM from GAM case, when the thermal GAM mode becomes unstable with the addition of EPs, and in figure 16(*b*) for the Landau EGAM case, when the initially damped mode becomes unstable. Whether one or other situation occurs depends on the values of various parameters of thermal plasma and EPs [194]. It is interesting to note that in this model the EGAM frequency is close to half of the GAM frequency, as was also found in numerical simulations with global nonlinear code GYSELA [192].

Two different types of modes modified by the presence of EPs were also found in [198]. The frequency of the branch related to the original GAM grows with the EP density n_h, with a scaling similar to equation (136). At some critical density $n_{h,cr} \simeq 1\%$–2%, two new branches appear, with the lower frequency branch being unstable. For higher electron temperatures, the solutions on different branches bifurcate. The frequency of the GAM related branch starts to decrease with n_h and this branch becomes unstable, while the two other branches remain stable, figure 17. It seems that this bifurcation is similar to that observed in [45], see figure 14, and is related to the value of the ratio $\omega_{GAM} q R_0 / v_b$. It has been noted in [198] that the bifurcation point coincides with the condition that the contribution of the hot particles changes its sign. This is consistent with the arguments leading to the expression (136).

3.4. Reactive EGAMs

The reactive EGAM is a simper case of an EP driven instability by a cold beam-like EP distribution when the dispersion relation can be derived from the fluid theory, and, appears as high order polynomial in ω with all real coefficients. Therefore, the unstable roots appear in complex conjugate pairs. As is typical for all reactive instabilities, the reactive EGAM instability appears as a result of the interaction of the negative and positive energy modes. It is noted that the negative energy mode was shown to be destabilized by the positive dissipation due to the resonant wave absorption in [195], which is an alternative to the reactive EGAM destabilization mechanism. Despite the fact that reactive EGAMs present some idealized situation, they transparently illustrate important physics and it is useful to consider them in some detail.

Though in the case of the cold beam distribution function for EPs it is possible to derive the dispersion relation for reactive EGAMs from fluid theory, as was done in [190, 191], here a simple derivation is presented based on the MHD-kinetic formulation that can be easy generalized to include kinetic effects such as finite temperature of the EP beam.

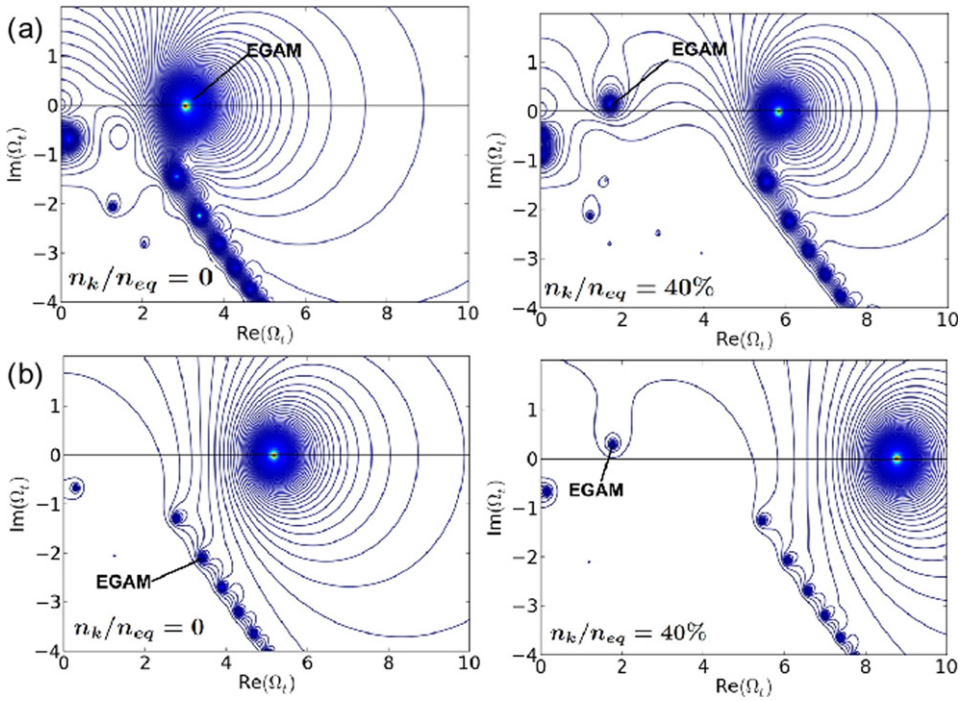

Figure 16. Contour representations of the analytic dispersion relation roots in the complex plane for (left) 0 and (right) 40% fast ion concentrations with $T_i/T_e = 1$, $\tau_k = 1$, $\overline{v}_\parallel/v_i = 2.8$ for (*a*) $q = 1.6$ and (*b*) $q = 3$. Adapted from [194], with the permission of AIP Publishing.

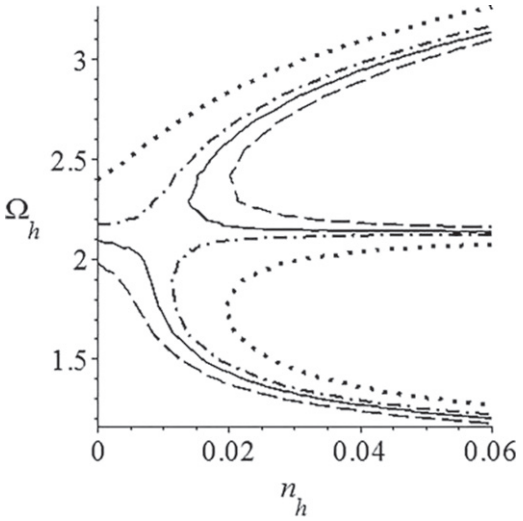

Figure 17. Plot of geodesic frequency as a function of the hot ion density n_h for different electron temperatures $\tau_e = 1$, 1.4, 1.6, and 2 (dotted, dash-dotted, solid, and dashed lines, respectively). Adapted from [198], with the permission of AIP Publishing.

The quasineutrality condition in the form of equation (134) is used where the perturbed pressure of high energy particles will be calculated from the DKE. In ($v_\parallel$, $v_\perp$) variables the lowest order DKE has the form

$$\frac{\partial \widetilde{f}}{\partial t}+v_\parallel \mathbf{b}\cdot\nabla\widetilde{f}+\mathbf{v}_d\cdot\nabla\widetilde{f}+\mathbf{v}_E\cdot\nabla\ln B\left(v_\parallel\frac{\partial f_0}{\partial v_\parallel}+v_\perp^2\frac{\partial f_0}{\partial v_\perp^2}\right)=0, \tag{177}$$

where $\widetilde{f}$, f_0 are the perturbed and equilibrium distribution function of high energy particles, here the index 'h' has been omitted. In neglect of toroidal resonances, $v_\parallel \mathbf{b}\cdot\nabla \gg \mathbf{v}_d\cdot\nabla_\perp$, the leading order solution of (177) can be obtained similarly to equation (50) in the form

$$\widetilde{f}_s = \frac{2\omega}{\omega^2 - v_\parallel^2/q^2R_0^2}\frac{ck_r\widetilde{\phi}_0}{B_0R}\left(v_\parallel\frac{\partial f_0}{\partial v_\parallel}+v_\perp^2\frac{\partial f_0}{\partial v_\perp^2}\right), \tag{178}$$

where f_s is the $\sin\theta$ component of the perturbed distribution function of EPs. This form allows an easy evaluation of the contribution of EPs with cold beam like distributions, such as performed in [190, 191]. Taking the equilibrium distribution in the form,

$$f_0 = \frac{n_h}{2\pi v_\perp}\delta\left(v_\parallel - V_b\right)\delta\left(v_\perp\right), \tag{179}$$

where v_b is the cold beam velocity, one obtains for the $\sin\theta$ component of the pressure tensor of high energy particles

$$\left(p_{\parallel h}+p_{\perp h}\right)_s = -m_h n_h v_b^2\frac{ck_r\widetilde{\phi}_0}{\omega B_0R_0}G\left(\omega\right), \tag{180}$$

where

$$G(\omega) = 8\omega^2\left(\frac{1}{\omega^2-\omega_b^2}+\frac{1}{2}\frac{\omega_b^2}{\omega^2-\omega_b^2}\right) = \frac{4\omega^2(2\omega^2-\omega_b^2)}{\left(\omega^2-\omega_b^2\right)^2} \tag{181}$$

and where $\omega_b^2 = v_b^2/q^2R_0^2$. For the bulk plasma ions, equation (178) gives the expression for the thermal pressure

$$\left(p_\parallel + p_\perp\right)_s = -\frac{7}{2}m_i n_{0i} v_{Ti}^2\frac{ck_r\widetilde{\phi}_0}{\omega B_0R}. \tag{182}$$

Combining equations (180) and (182) in the quasineutrality condition (134) one obtains the dispersion relation

$$\omega^2 = \frac{7}{4}\frac{v_{Ti}^2}{R_0^2}(1-\alpha) + \alpha\frac{v_b^2}{R_0^2}G(\omega), \tag{183}$$

where $\alpha = n_h/(n_{0i}+n_h)$ and $m_h = m_i$ was assumed.

Equation (183) can be viewed as a prototypical local dispersion relation for reactive EGAMs. A similar equation was obtained in [190] from the fluid theory with somewhat different coefficients in the expression (181) for $G(\omega)$. The biquadratic equation (183) has two branches, upper and lower frequencies EGAMs in the terminology of [190], that can be roughly identified with ω_{GAM}^2 and ω_b^2 frequencies. The frequency of the upper EGAM branch increases with the density of high energy particles, figure 18(top (a)). This branch remains stable in fluid theory: figure 18 (top (c)), but is weakly damped in the kinetic theory [190], see comments below. The lower EGAM branch can be destabilized by high energy particles. For $\omega_b < \omega_{GAM}$ the upper mode frequency starts at ω_{GAM} at $n_h = 0$ and increases with the fast particle fraction consistent with the relation (136). The real frequency of the lower branch starts at ω_b and decreases with $n_h = 0$, while its growth rate has no threshold and increases with n_h, as shown in figures 18 (bottom (b) and (d)).

For $\omega_b > \omega_{GAM}$, the real frequency of the unstable EGAM starts at ω_b and decreases with the EP density n_h. In the fluid model, the reactive instability onset has a threshold at some finite n_h, while the kinetic theory predicts that the instability has no threshold with weak growth rate increasing with n_h; possibly as a result of the dissipation due to GAM damping. It is interesting that both fluid and kinetic theory predict the upper threshold with n_h, figures 18 (bottom (b) and (d)); as is also typical for many reactive instabilities.

One can note a certain analogy of the reactive EGAMs with the lower and upper frequency branches in an anisotropic pressure plasma, compared with equation (22), where the lower frequency branch can be destabilized for a certain value of anisotropy.

The authors of [190] also compared the results of fluid and kinetic theory. In case of a beam with a finite temperature T_h, such as

$$f_{0h} = n_h A \exp\left(-m_i\frac{(v_\parallel - v_b)^2 + v_\perp^2}{2T_h}\right), \tag{184}$$

the perturbed pressure of high energy particles can be expressed in terms of the plasma dispersion functions. The latter includes the finite beam temperature effects leading to Landau damping due to energy spread in the beam distribution. The main result here is that the frequency of the upper GAM branch is modified by high energy particles but remains stable; this branch is not affected by the kinetic effects, see figure 18 (top). The lower branch has two complex conjugate roots in the fluid theory, corresponding to the reactive EGAM. The extent to which the finite spread of high energy beam affects the instability depends on the ω_b/ω_{GAM} ratio. For $\omega_b/\omega_{GAM} < 1$ and low q, the results of the kinetic and fluid theory are very close for the unstable branch which has no threshold in high energy particle pressure. For $\omega_b/\omega_{GAM} > 1$ and larger q, the kinetic effects are more pronounced, extending the instability region and eliminating the threshold (in high energy particles pressure) which was predicted in the fluid theory, as shown in figure 18 (bottom). In all cases, the real frequency of the unstable mode is below ω_{GAM} consistent with results of [45].

An example of the reactive EGAM for a cold slowing down distribution is also provided in the form [190]

$$f_0(\mathcal{E},\Lambda) = \frac{m_i^2|v_\parallel|n_f}{2\pi\mathcal{E}}\delta(\mathcal{E}-\mathcal{E}_0)\delta(\Lambda-\Lambda_0). \tag{185}$$

The reactive EGAM frequency and growth rates in this case are shown in figure 19 for DIII-D parameters.

3.5. Global profile effects and EGAM radial eigenmode structure

Before a discussion of the global profile effects in EGAM theory it is useful to recall the mechanisms that lead to the formation of the GGAM eigenmodes. In the ideal MHD theory the GGAM occurs near the local maximum of the continuum GAM frequency [12, 13, 164] that usually require negative shear. In this case, the global eigenmode is formed due to the coupling to the EM $m = 2$ harmonic which has a global character. The analytical theory of such GGAMs was developed in [162, 168, 170, 196]. The GGAM MHD solutions were also obtained for the monotonic local GAM frequency for some special plasma parameter profiles [161, 163]. These theories do not include the dispersion due to 'finite ion Larmor effects'. The latter are absent in MHD and require the kinetic theory. As discussed in section 2.7, the dispersion corrections to the GAM frequency arise from three different effects: the ion sound Larmor radius, $k_r^2\rho_s^2 = k_r^2 T_e/(m_i\omega_{ci}^2)$; the actual ion Larmor radius effects, $k_r^2\rho_i^2 = k_r^2 2T_i/(m_i\omega_{ci}^2)$; and the 'apparent' ion Larmor radius effects due to finite magnetic drift frequency, $\omega_d^2/\omega^2 \simeq \omega_d^2/\omega_{GAM}^2 \simeq k_r^2\rho_i^2$. The latter effects are also called FOW effects as they originate from the radial excursions of particles due to the magnetic drift. As it is described in section 2.7, up to the fourth order expansion in ω_d^4/ω^4 is required so that the second order $m = 2$ sidebands have to be included.

As discussed in section 2.11, while the dispersion effects define the radial propagation of GAMs [11], e.g. in the form of the radial Airy functions [16], they do not define a unique eigenmode frequency. Additional profile effects need to be considered, such as the profile of the local GAM frequency, the localization of the GAM drive either from linear (e.g. due to EPs) or nonlinear effects (due to drift wave turbulence). Accordingly, there are several effects that may affect the radial localization and radial structure of the EP related GAMs, such as the MHD coupling to the global EM $m = 2$ mode similar to the standard GGAMs, the radial variation of the EP source (beam) together with radial variations of other (bulk) plasma parameters, and EP FOW effects. It is noted that while the analysis of the global $m = 2$ coupling requires a fully EM theory, the dispersion effects due to FLR and FOW effects are often considered in electrostatic models. Barring full numerical simulations within the global GK model, it is difficult to present a uniform model where all the above

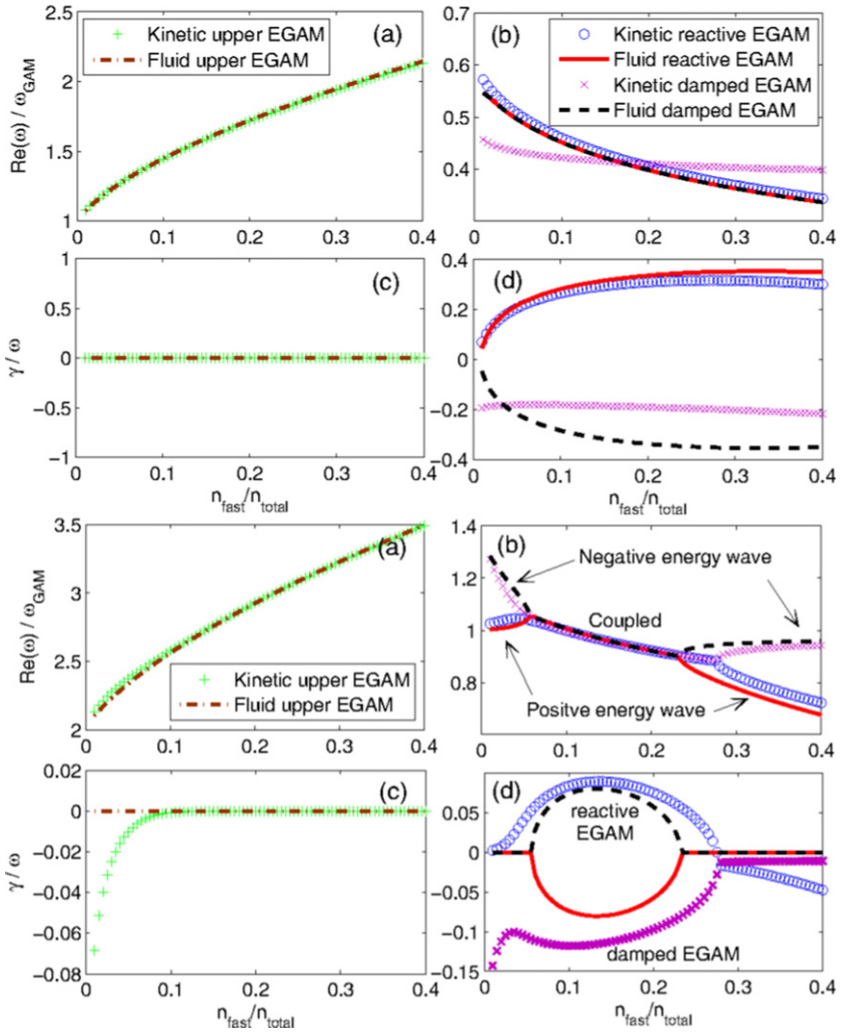

Figure 18. Real frequency (*a*), (*b*) and growth rate (*c*), (*d*) versus fast ion density for multi-fluid model with comparison to kinetic theory, for (top) $q = 4$ and (bottom) $q = 2$ and GAM. Lines represent the fluid and symbols the kinetic results. Adapted figure with permission from [190], Copyright (2016) by the American Physical Society.

effects are included and their relative importance determined. Thus, we are confined here to brief comments on the theoretical results as presented in the literature and to discuss their limitations.

In addition to the local solution (in the limit of zero orbit width of EPs), Fu [45] presented the global generalization for EGAMs by including the effects of the FOW of the EPs using the model equation in the form

$$\frac{\mathrm{d}}{\mathrm{d}r}\frac{\langle P_{\perp \mathrm{h}} + P_{\parallel \mathrm{h}}\rangle}{\rho R_0^2} q^2 \rho_{\mathrm{h}}^2 W\left(\frac{\omega}{\omega_{\mathrm{b}}}\right)\frac{\mathrm{d}}{\mathrm{d}r}E_{\mathrm{r}} + \left(\omega^2 - \omega_{\mathrm{EGAM}}^2\right)E_{\mathrm{r}} = 0, \tag{186}$$

where $W\left(\omega/\omega_{\mathrm{b}}\right)$ is the kinetic integral due to the width of the EP orbits, (no explicit expression was given), and ω_{EGAM} is the local expression for EGAM frequency. Similar to equation (107), expansion of (186) near $\omega^2 - \omega_{\mathrm{EGAM}}^2 = 0$ gives the solution in terms of the Airy function, with the characteristic radial width of the propagating eigenmode as $\Delta_{\mathrm{r}} \sim (\beta_{\mathrm{h}}/\beta_{\mathrm{th}})^{1/3} L_\omega^{1/3} (q\rho_{\mathrm{h}})^{2/3}$.

Equation (186) was analysed in [45] for the case of counter injected beam with the parameters of DIII-D experiments [44] and a global EGAM mode was found with the eigenmode maximum at $r/a \simeq 0.2$ and $\omega_{\mathrm{r}}/\omega_{\mathrm{GAE}}(0) \simeq 0.63$ and $\omega_{\mathrm{i}}/\omega_{\mathrm{r}} \simeq 0.5$.

The model equation for the global EGAM in a plasma with a spatially broad EP beam was proposed in [199] in the form

$$-\frac{e}{m_{\mathrm{i}}} n_{\mathrm{h}} \frac{1}{\omega_{\mathrm{ci}}^2}\frac{\partial}{\partial r}\mathscr{E}_{\mathrm{r}}\frac{\partial}{\partial r}\phi_0 + n_{\mathrm{h0}} = 0, \tag{187}$$

where

$$\mathscr{E}_{\mathrm{r}} = -1 + \omega_{\mathrm{GAM}}^2/\omega^2 - \frac{1}{2} D \rho_{\mathrm{i}}^2 \frac{\partial^2}{\partial r^2}, \tag{188}$$

and ϕ_0 is the $m = 0$ component of the perturbed potential, and n_{h0} is the $m = 0$ perturbed density of the EPs, and the D is the dispersion parameter from equation (83). It is easy to see that equation (187) has the structure of equation (162) with the addition of the second order term due to the thermal ions Larmor radius. The kinetic EP $m = 0$ response in this model was further generalized to include the higher order finite orbit

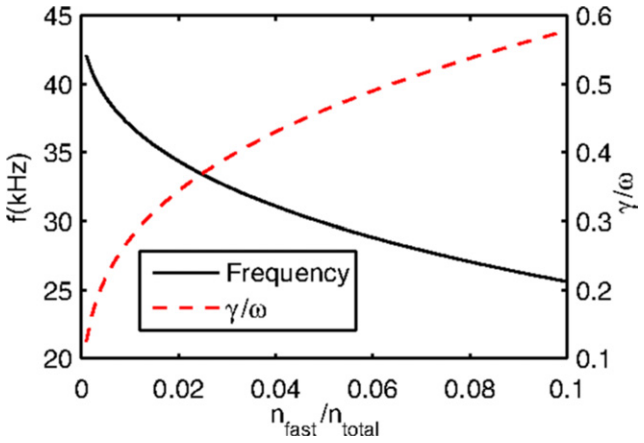

Figure 19. Real frequency and growth rate of the reactive EGAM using DIII-D parameters on flux surface $s = 0.4$. Reproduced figure with permission from [190], Copyright (2016) by the American Physical Society.

effect

$$n_{\mathrm{h}0}(r) \simeq n_{\mathrm{b}}(r)\left(\mathscr{E}_{\mathrm{h}} - \frac{1}{2}H\rho_{\mathrm{b}}^2\frac{\partial^2}{\partial r^2}\right)\frac{\partial^2}{\partial r^2}\phi_0, \tag{189}$$

where $n_{\mathrm{b}}(r)$ is the EP beam density, and $\mathscr{E}_{\mathrm{h}}$, H are some functions of the EP beam parameters. The numerical analysis of the eigenmode equation (187) with (189) in [156] shows that the eigenmode is localized near the maximum of the EGAM drive. It was also shown that mode tunnelling to the GAM continuous spectrum results in the continuum damping that may lead to the EGAM instability threshold.

Equations (186), (187) and (189) have a similar structure to the GAM eigenmode equation [11] of the type of equation (107), which is explicitly written in [156, 199] for EGAMs including the higher order in $\upsilon_{Ti}^2/(\omega^2 q^2 R_0^2)$ corrections due to the ion sound coupling.

One should note that the higher order dispersion term D in equation (187) comes from effects related to the $m = 2$ sidebands which were not included in the derivations of the EP particle response $n_{\mathrm{h}0}$ in equation (187). To our knowledge most publications omit the $m = 2$ effects in calculations of the EP response. It is not clear how the $m = 2$ dispersive terms due to EP will compare with the higher order terms represented by the H function in equation (189).

It is noted, however, that the global structure of the reactive EGAMs in [191] was studied within the fluid theory and included the $m = 2$ sidebands of the parallel velocity of the EPs. The eigenmode equation was derived where the second order radial derivative, responsible for the mode localization, included the $m = 2$ terms. The global EGAM was obtained with a frequency close to the *maximum of the local frequency*, both for the monotonic profile where the local frequency maximum is at the plasma centre, and the non-monotonic (reversed shear case) profile with an off-centre position of the local EGAM frequency, see figure 20. It was found that the EGAM for the counter beam injection is notably more unstable compared to the co-injection direction—see figure 21. It was also shown that in the presence of EPs, the EGAM continuum can

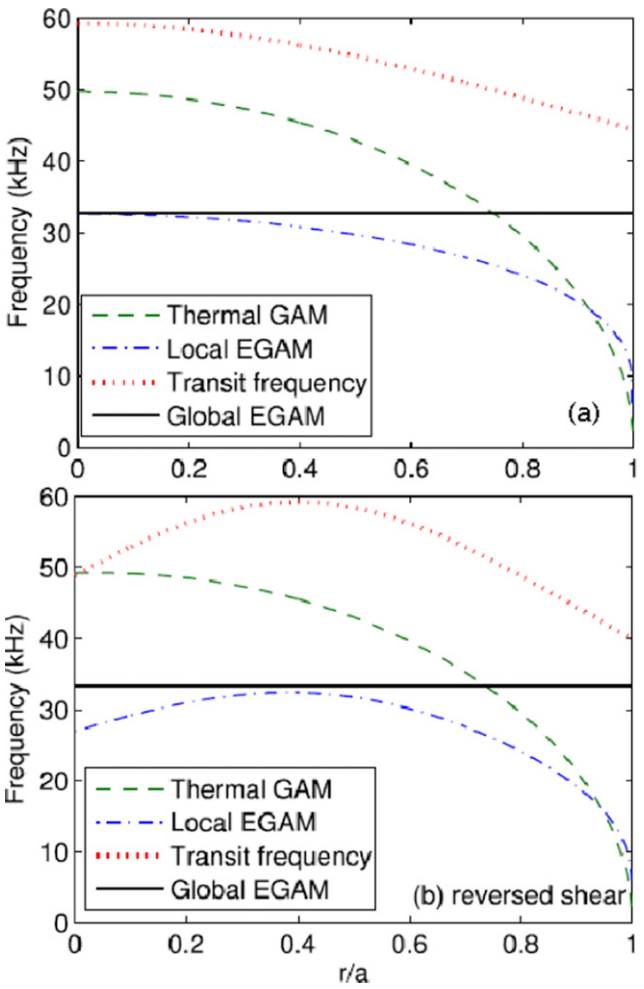

Figure 20. The thermal GAM continuum, the transit frequency as a function of radius, the local EGAM frequency and the global EGAM frequency for (*a*) monotonic and (*b*) reversed shear cases. Adapted from [191]. © IOP Publishing Ltd. All rights reserved.

have an off-axis maximum even when $q(r)$ and radial profiles of plasma parameters are monotonic, so that an EGAM eigenmode may form near the maximum point [191].

In [168] the local EGAM dispersion relation was obtained by considering EM coupling of $m = 0$ and $m = 2$ harmonics (within the model equations similar to (108) and (109) and included the $m = 0$ and $m = 2$ current contributions from the EPs

$$\mathbf{J}_{\mathrm{h}\perp} = e\int \mathbf{v}_{\mathrm{d}}\widetilde{f}_{\mathrm{h}}\,\mathrm{d}^3\mathbf{v}. \tag{190}$$

Note that the current coupling of MHD and kinetic effects of high energy particles is different from the pressure coupling scheme described in section 3.1; the comparison of the current and pressure coupling approaches is discussed in [200, 201]. The perturbed distribution function for the EPs in [168] is found from the DKE; both $m = 0$ and $m = 2$ components of the radial electric field are included. It is shown that in the local approximation, and for the slowed-down EP distribution function in the form

$$f_{0\alpha} = n_\alpha(r)\,\delta(\chi - \chi_\alpha)\,\frac{\eta(\upsilon_\alpha - \upsilon)}{\upsilon^3}, \tag{191}$$

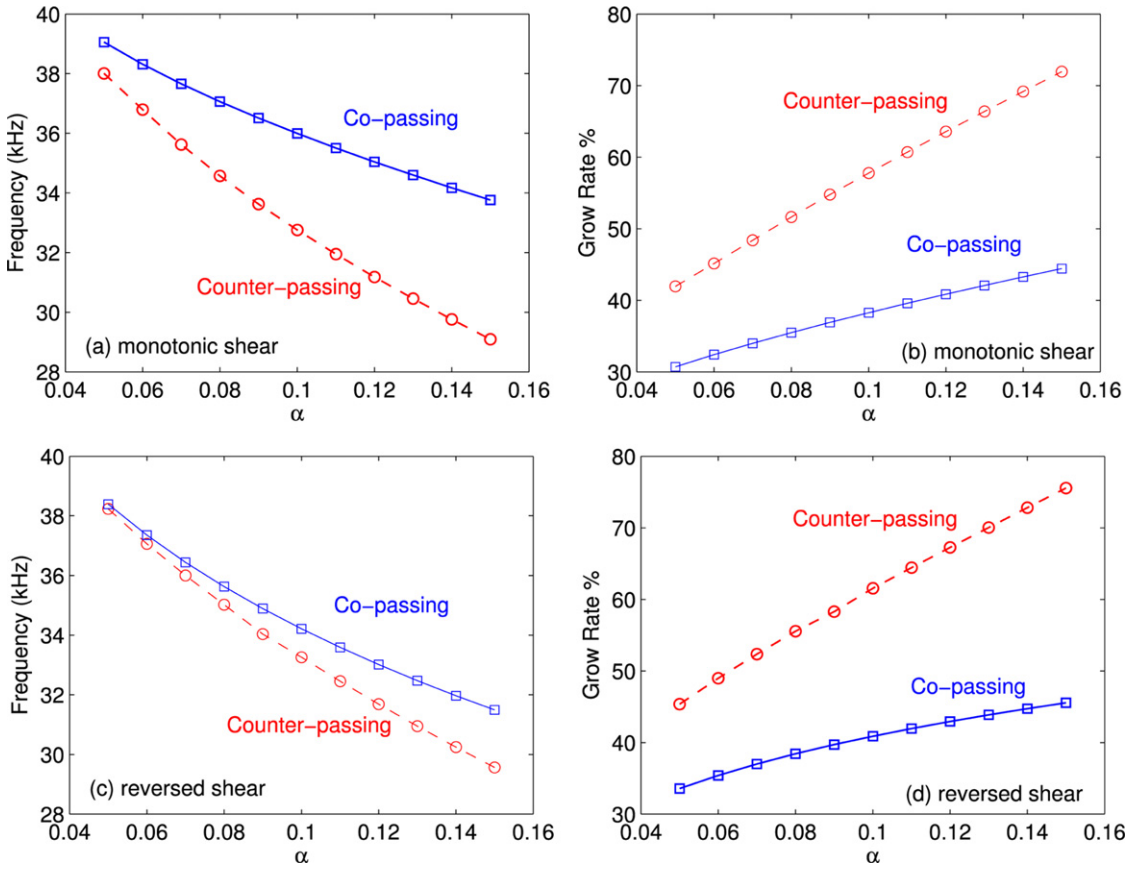

Figure 21. (*a*) Frequency and (*b*) growth rate for the monotonic case with counter-passing (red circles) and co-passing (blue squares) fast ions, scanned over fast ion proportion $\hat{\mathrm{I}}\pm$. (*c*), (*d*) The same scan for the reversed shear case. The scan domain is restricted to satisfy the condition. Adapted from [191].

where $n_\alpha(r)$ is the particle density, $\chi = v_\parallel/v$ is the pitch angle, $\eta(v_\alpha - v)$ is the step function, that there are two local EGAM branches. For low plasma pressure, only one of the branches is unstable, while for higher pressure, $\overline{\beta} = \beta/(1+\beta) = 17\%$, $\beta = c_s^2/v_A^2$, both branches have finite growth rates. It was also shown that the inhomogeneity of the energetic ion density favours the larger growth rate for the counter-injected energetic ions—the result is also shown in [195].

3.6. EP induced GAMs driven by magnetic drift resonances

The majority of analytic calculations of the EP driven GAM instabilities consider the resonant interaction of EPs at the transit resonance $\omega \simeq v_\parallel/qR_0$ and neglect the effect of the magnetic drift frequency, assuming that $\omega_d qR_0/v_\parallel \ll 1$. At best, the role of the magnetic drift, labelled as a FOW effect, is considered perturbatively, assuming the ordering $\omega_d/\omega \ll 1$, e.g. in the calculations of the dispersion effects in the GAM. This approximation is similar to the theory of collisionless GAM damping due to transit resonances $\omega \simeq v_\parallel/qR_0$, when most works adopt an auxiliary ordering $\omega \simeq v_\parallel/qR_0 \gg \omega_d$ thus excluding the modification of the transit resonances due to the magnetic drift. An exact solution of the GK equation in the form of the formal series (60) is valid for arbitrary values of the $\omega_d qR_0/v_\parallel$. However, practical calculations with this series for large values of the $\omega_d qR_0/v_\parallel$ parameter are difficult due to the coupling of an infinite number of transit resonances $\omega \simeq lv_\parallel/qR_0$, $l = 1, 2, \ldots$, since the strength of this coupling is determined by the values of the $J_l(\omega_d qR_0/v_\parallel)J_{l'}(\omega_d qR_0/v_\parallel)$ coefficients. The authors of [116] have proposed an alternative treatment of the resonant particles (ions) for the regime $\omega_d qR_0/v_\parallel \simeq qk_r v_{Ti}/\omega_{ci} \gg 1$ to describe the collisionless damping of the GAM due to magnetic drift resonance $\omega \simeq \omega_d$, see section 2.8.

The authors of [50, 115] considered the regimes $\omega \simeq \omega_d$ for *EPs* and show that magnetic drift effects resonance may lead to the excitation of the GAM modes. Since the treatments of [50, 115] are somewhat different these results are presented separately.

The authors of [50] consider equation (55) in the formal limit $q \to \infty$ and write its solution as

$$g = -\frac{\omega}{\omega - \omega_{dh}} J_0 \frac{\partial F_{0h}}{\partial \mathcal{E}} \phi(\theta), \tag{192}$$

where the potential was represented as a sum of many poloidal harmonics

$$\phi(\theta) = \sum_m \phi_m \exp(im\theta). \tag{193}$$

The dispersion equation is obtained as a solubility condition for the matrix form of the quasineutrality conditions for a system of poloidal harmonics. The numerical solution for the cold

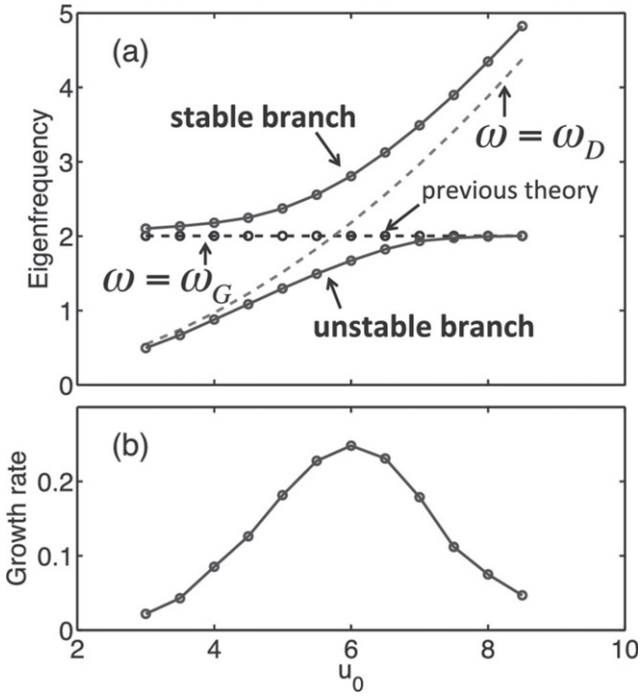

Figure 22. Real frequency and growth rate of the EGAM due to crossing of the EGAM with the EP driven beam mode $\omega = \omega_D$. Adapted from [50], with the permission of AIP Publishing.

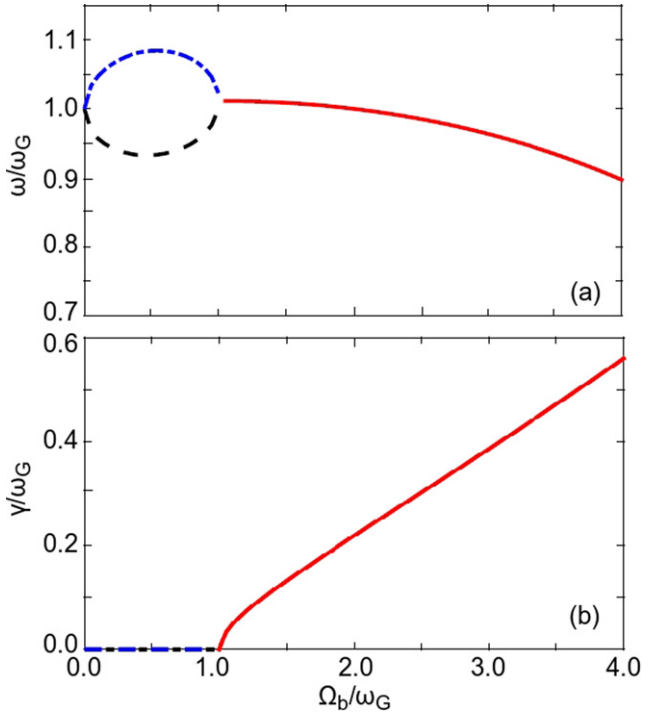

Figure 23. Normalized (a) real frequency ω/ω_G and (b) growth rate γ/ω_G vs normalized magnetic drift frequency Ω_b/ω_G. Adapted from [115], with the permission of AIP Publishing.

beam-like distribution function

$$F_{0h} = \frac{n_{0h}}{2\pi u_0^2}\delta(u-u_0)\,\delta(\Lambda-\Lambda_0) \tag{194}$$

indicates the beam instability near the crossing of the beam mode $\omega \simeq \omega_{dh}$ and the GAM mode with $\omega \simeq \omega_{GAM}$, as shown in figure 22. The lower branch with $\omega < \omega_{GAM}$ becomes unstable. The eigen-function has substantial finite m harmonics so it is peaked off the $\theta = 0$ point.

The authors of [115] have considered the GAM destabilization by the EP with a distribution function in the form

$$F_{0h} = \frac{n_b}{\sqrt{2\,(1-\Lambda_0 B_0)}4\pi \ln\left(E_b/E_c\right)}\frac{H\,(E-E_b)}{E^{3/2}+E_c^{3/2}}\,(\Lambda-\Lambda_0)\,, \tag{195}$$

and have also considered the limit $q \to \infty$, where equation (55) gives for the perturbation of the EP particles

$$f_h\,(\theta) = -e\phi\,(\theta)\,\frac{\omega_d\,(\theta)}{\omega-\omega_d\,(\theta)}\frac{\partial F_{0h}}{\partial \mathcal{E}}. \tag{196}$$

Contrary to [50], the authors of [115] included only the $m = 0$ harmonic of the potential, so that the main equation is similar to (162) with the EP density response in the form

$$n_{h0} = -e\phi_0 \oint \mathrm{d}\theta \frac{\omega_d\,(\theta)}{\omega-\omega_d\,(\theta)}\frac{\partial F_{0h}}{\partial \mathcal{E}}. \tag{197}$$

The average integral over θ is taken, by assuming that the response is localized and expanding the $\omega_d(\theta)$ function near $\theta \simeq 0$. In the result, an analytic dispersion equation was derived that shows the instability for $\Lambda_0 B_0 > 2/3$ and $\Omega_b/\omega_{GAM} > 1$, as shown in figure 23, with $\Omega_b = \omega_d\,(E = E_b)$.

We note that as discussed in sections 2.6 and 3.2, the transit and magnetic drift resonances are coupled in the $m = 1$ order, e.g. the last term in equation (163) includes both transit and magnetic drift resonances due to the EPs. It would be important to compare the results of the approaches in [50, 115] with the method presented in section 3.2.

3.7. Comments on trapped particles and electron current effects

Most analytical treatments of EGAMs consider the effects of passing EPs assuming that their velocity is constant, $v_\parallel = \text{const.}$, neglecting the effects of trapped particles. A general expression for the EP response including passing and trapped particles was given in [45], but the specific influence of trapped particles was not studied. Elfimov has considered the effects of EP and GAM destabilization in the analytical theory by integrating the DKE over the exact ion trajectories using the Jacobi function representation for trapped and passing particles [202–204]. The instability criteria was determined for a specific EP distribution which has a maximum at the trapped and un-trapped boundary and with high energy tail of several hundred keV. Another result here [202, 203] is the modification of the neoclassical polarization factor by the EPs. Using a similar approach, Elfimov [204] also considers the EGAMs destabilization due to un-trapped resonances of NB energetic ions with $v_\parallel \simeq (1.2\text{–}1.5)\omega R_0 q$. Such EGAMs have a maximum growth rate in the frequency range near the slowing-down transit frequency, cf [198].

In addition to the ion beam flows, the contribution of the electron current and drift effects has also been investigated, so

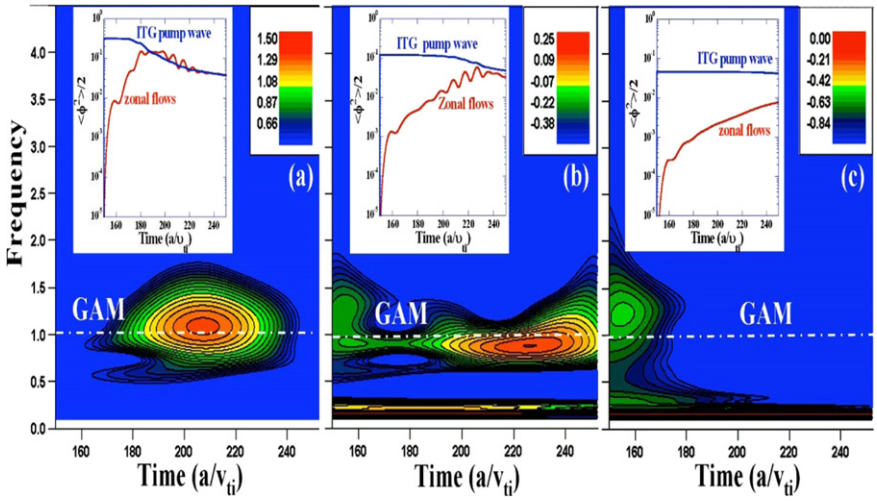

Figure 24. Wavelet energy analyses for nonlinear excitation of GAMs by ITG waves of different amplitudes (*a*) $|e\phi/T_i|^2/2 = 0.3$; (*b*) 0.12; and (*c*) 0.047. Standard cyclone base case parameters are used except $q = 2.6$. Adapted from [215].

that more general conditions for the GAM instabilities were derived [202, 205, 206].

4. GAM generation and other nonlinear effects

In this section we review some analytical and numerical results concerning GAM coupling to plasma turbulence, in particular, nonlinear GAM generation from turbulence, and discuss other nonlinear effects that may affect the GAM dynamics. First, we discuss some examples of GAM generation in nonlinear turbulence simulations of the ITG driven instabilities. These simulations demonstrate that the nonlinear development and saturation of the ITG modes is accompanied by the occurrence of intense fluctuations in the GAM frequency range. Such GAM fluctuations are well correlated with the measured RS suggesting that the turbulent RS is a source of the GAMs.

The RS provides a direct nonlinear contribution to the radial current in equation (7) thus affecting the GAM dynamics. Another channel for the turbulence to affect GAM dynamics is to drive the $m = 1$ pressure perturbation. In fact, modulations of plasma pressure induced by modulations of transport (either energy or particles) represent a wide class of several related phenomena that may result in the GAM excitation. Such mechanisms are intrinsically related to the phenomena of spontaneous generation of poloidal and toroidal plasma rotation (plasma spin-up), and damping of poloidal plasma rotation in toroidal systems, a subject that was extensively discussed in the neoclassical theory of plasma rotation and transport [7, 207–210]. In the literature, the related mechanisms are often referred as Stringer spin-up [6, 211]. In the context of GAM generation, Stringer spin-up was considered in [6]. Subsequent generalizations included effects of anomalous transport [212], and were specifically considered as the GAM generation mechanism [24, 213] and were referred to as the dynamic shearing (DS) mechanism. We review here the classical Stringer spin-up mechanism and its DS variation. We also present a simple analytical model for the Stringer spin-up GAM instability induced by transport modulations due to the parametric decay of the DWs. The section concludes with a general discussion of the relative importance of the RS and DS drive and their possible interactions. The experimental evidences illustrating nonlinear behaviour, GAM drive and interactions are reviewed in sections 14, 11.1 and 15.

4.1. GAM generation in nonlinear fluid simulations of ITG driven turbulence

Earlier analytical work demonstrated the excitation of GAMs during the relaxation of plasma rotation towards the neoclassical equilibrium [8, 23]. Such oscillations are transient and eventually die out as a result of GAM damping due to the collisionless (wave–particle) and collisional processes. Sustained GAM excitation by nonlinear processes was clearly shown in a number of simulations [183, 214–217]. As an example, figure 24 [215] shows the GAM mode born out of a finite amplitude ITG mode with a clear correlation of induced GAM mode intensity with the amplitude of the ITG pump mode.

Three-dimensional fluid simulations of flux-driven electrostatic ITG turbulence [183, 214] show a GAM range frequency peak in the $m = n = 0$ components of the flow velocity, see figure 25. It is interesting to note that in the ITG saturated state, the for $m = n = 0$ GAM peak in rotation are somewhat below the linear GAM frequency and remain constant across a relatively wide radial region, figure 25, while in the linear growth stage the ITG produces a transient GAM excitation close to the linear GAM frequency. Qualitatively similar features of nonlinearly sustained GAM modes were demonstrated in other 3D fluid ITG simulations [102, 216, 217], which also show the GAM peak frequency below the linear GAM frequency, radially uniform, and seemingly sandwiched between the linear GAM and ion sound modes frequencies, such as shown in figure 26. These simulations also show that the GAM frequency remains constant across radial regions of the order of $\sqrt{a\rho_i}$ with step-like transitions in between [217].

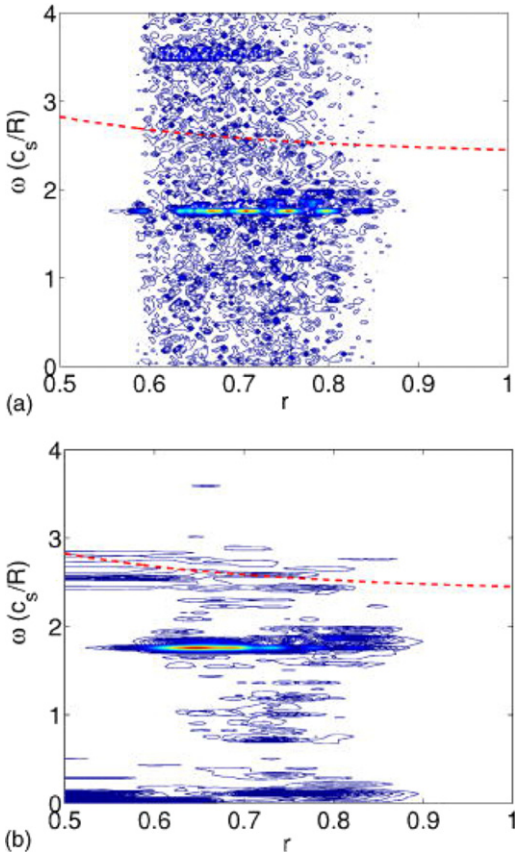

Figure 25. Simulation radial spectra of the $(n = 0, m = 0)$ component of (a) RS and (b) squared poloidal flow velocity in turbulent stationary state. Both spectra show a well localized peak around the same $\omega \sim 1.74(c_s\hat{a}/R_0)$, lower than the linear GAM frequency (dashed line). Adapted from [183], with the permission of AIP Publishing.

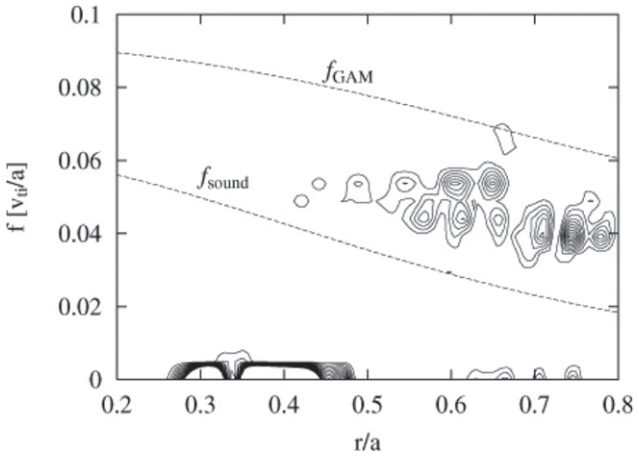

Figure 26. Radial variation of ZF frequency spectra. Dashed lines show the GAM and parallel SW frequencies for the (1, 0) mode. Adapted from [102], with the permission of AIP Publishing.

The plateau in the radial profiles of the GAM frequency were also identified in other simulations with a global two-fluid EM turbulence code CENTORI [103] for the conditions of MAST, and were interpreted as a result of the GAM damping at the transit ion sound resonances. The overall profile of

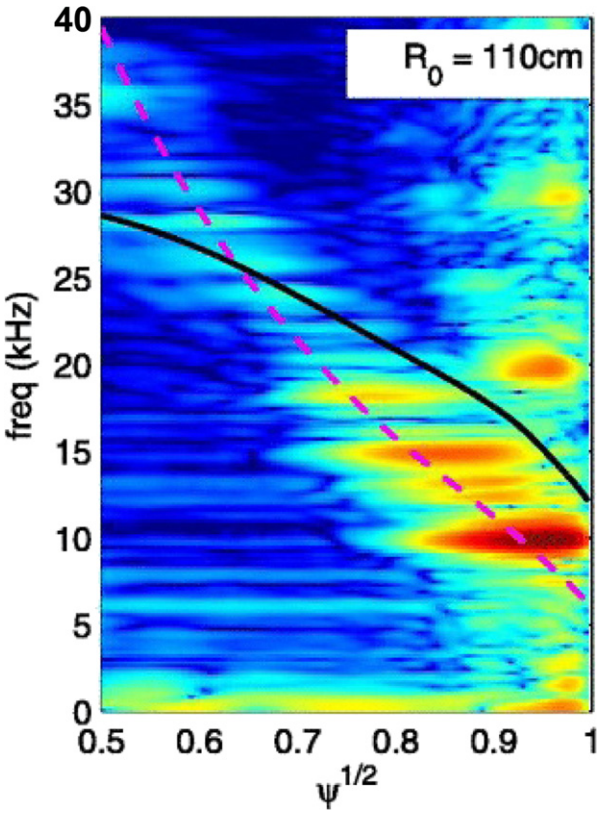

Figure 27. Simulated radial profile of the density fluctuation power for $R_0 = 110$ cm from [103] for MAST conditions. Black line shows the sound speed transit frequency $f_{cs} = c_s/(2\pi R_0)$, the magenta dashed line is the local GAM frequency based on [122]. Adapted from [103], with the permission of AIP Publishing.

the GAM frequency, overlaid through the plateaux centroids were found in good agreement with the local GAM frequency prediction for the shaped tokamak from [122], as shown in figure 27. These simulations show excellent agreement with MAST experimental data, cf figure 56 in section 7.7.

4.2. GAM generation by Reynolds stress

Substantial RS was directly measured in simulations demonstrating the GAM born out of turbulence, e.g. figure 25(a) [183], with a peak of the $m = n = 0$ component of the RS at the same GAM (nonlinear) frequency as the $m = n = 0$ poloidal rotation. Similar results on RS were shown in other papers [217]. Therefore, the prevailing thought is that the finite frequency GAMs are driven directly by the poloidally symmetric $m = 0$ component of the RS, similar to the low frequency ZFs [53].

A simple analytical model of GAM generation by RS is based on the parametric decay instability of finite amplitude DWs [218, 219], induced by the symmetry breaking GAM perturbation. Briefly outlined below are the main ideas of this model which is also useful to describe the DS, or more generally a transport modulation mechanism.

Weakly nonlinear theory of GAM generation by RS were formulated using the wave kinetic equation formalism [218, 220], and the parametric instability of the coherent pump wave

[11, 218]. Generally the results from both approaches are similar but the condition for the resonant wavevector of an unstable GAM mode can be different [218]. In the coherent pump wave model one considers a large amplitude DW with $\mathbf{k} = (k_\theta, k_\mathrm{r}, k_z)$, $k_\theta = m/r_\mathrm{s}$, $m \gg 1$,

$$\widetilde{\phi}^\mathrm{p} = \phi_{m,k_\mathrm{r}}(t)\exp(-\mathrm{i}m\theta + \mathrm{i}k_\mathrm{r}r) + \phi_{-m,-k_\mathrm{r}}(t)\exp(-\mathrm{i}m\theta - \mathrm{i}k_\mathrm{r}r), \quad (198)$$

that generates the GAM eigenmode consisting of an $m = 0$ perturbation

$$\overline{\phi} = \overline{\phi}_{0,q}(t)\exp(\mathrm{i}q_\mathrm{r}r), \quad (199)$$

and $m = \pm 1$ components

$$\widehat{\phi} = \left(\widehat{\phi}_{1,q_\mathrm{r}}(t)\exp(\mathrm{i}\theta) + \widehat{\phi}_{-1,q_\mathrm{r}}(t)\exp(-\mathrm{i}\theta)\right)\exp(\mathrm{i}q_\mathrm{r}r). \quad (200)$$

The interactions of the drift pump wave $\widetilde{\phi}^\mathrm{p}$ with the $\overline{\phi}_{0,q}$ and $\widehat{\phi}_{1,q_\mathrm{r}}$ GAM perturbations produce two types of the DW sideband satellites. The $\widetilde{\phi}^{\mathrm{s}1}$ satellite is formed due to the $\widetilde{\phi}^\mathrm{p}$ and $\overline{\phi}_{0,q}$ interaction:

$$\widetilde{\phi}^{\mathrm{s}1} = \exp(\mathrm{i}q_\mathrm{r}r) \times \left[\phi_{m,k_\mathrm{r}+q_\mathrm{r}}\exp(\mathrm{i}m\theta + \mathrm{i}k_\mathrm{r}) + \phi_{-m,-k_\mathrm{r}+q_\mathrm{r}}\exp(-\mathrm{i}m\theta - \mathrm{i}k_\mathrm{r}r)\right], \quad (201)$$

and $\widetilde{\phi}^{\mathrm{s}2}$ is due to $\widetilde{\phi}^\mathrm{p}$ and $\widehat{\phi}$ interaction:

$$\widetilde{\phi}^{\mathrm{s}2} = \exp(\mathrm{i}q_\mathrm{r}r) \times \left[\phi_{m+1,k_\mathrm{r}+q_\mathrm{r}}\exp(\mathrm{i}m\theta + \mathrm{i}\theta + \mathrm{i}k_\mathrm{r}r) + \phi_{-m+1,-k_\mathrm{r}+q_\mathrm{r}}\exp(-\mathrm{i}m\theta + \mathrm{i}\theta - \mathrm{i}k_\mathrm{r}) + \phi_{m-1,-k_\mathrm{r}+q_\mathrm{r}}\exp(\mathrm{i}m\theta - \mathrm{i}\theta - \mathrm{i}k_\mathrm{r}) + \phi_{-m-1,-k_\mathrm{r}+q_\mathrm{r}}\exp(-\mathrm{i}m\theta - \mathrm{i}\theta - \mathrm{i}k_\mathrm{r})\right]. \quad (202)$$

Therefore, the total potential is

$$\phi = \overline{\phi} + \widehat{\phi} + \widetilde{\phi}, \quad (203)$$

where $\widetilde{\phi} = \widetilde{\phi}^\mathrm{p} + \widetilde{\phi}^{\mathrm{s}1} + \widetilde{\phi}^{\mathrm{s}2}$ are the DW perturbations. As is standard in the parametric interaction theory, the amplitude of the pump wave is assumed to be large $\phi^\mathrm{p} \gg (\phi^{\mathrm{s}1}, \phi^{\mathrm{s}2}, \overline{\phi}, \widehat{\phi})$ so its amplitude remains constant in time, while the $(\phi^{\mathrm{s}1}, \phi^{\mathrm{s}2}, \overline{\phi}, \widehat{\phi})$ amplitudes are evolving in time. Therefore, the parametric decay theory is linear in $\overline{\phi}$, $\widehat{\phi}$, and $\widetilde{\phi}^{\mathrm{s}1}$, $\widetilde{\phi}^{\mathrm{s}2}$ and nonlinear in $\widetilde{\phi}^\mathrm{p}$. The latter requires that the $\widetilde{\phi}^\mathrm{p}$ variable is real, i.e. $\phi^*_{m,k_\mathrm{r}} = \phi_{-m,-k_\mathrm{r}}$, while in general for the satellites $\phi^{\mathrm{s}1,\,\mathrm{s}2}_{k_\theta,k_\mathrm{r}+q_\mathrm{r}} \neq \phi^{\mathrm{s}1,\,\mathrm{s}2}_{-k_\theta,-k_\mathrm{r}+q_\mathrm{r}}$.

Similar to the potential, the total density is represented as

$$n = n_0 + \hat{n} + \widetilde{n}, \quad (204)$$

where n_0 is the equilibrium density, $\hat{n}$ the $m = 1$ GAM component, and $\widetilde{n}$ includes all the DW components. Note that the $m = 0$ density component of the GAM is absent, $\overline{n} = 0$, and all $m \neq 0$ components are Boltzmann, $\hat{n}/n_0 = e\widehat{\phi}/T_\mathrm{e}$, and $\widetilde{n}/n_0 = e\widetilde{\phi}/T_\mathrm{e}$.

The $m = 0$ component of the quasineutrality equation (7) can now be written as

$$q_\mathrm{r}^2\frac{\partial}{\partial t}\overline{\phi}_{0,q} + \omega_\mathrm{ci}\frac{T_\mathrm{e}}{en_0}\frac{q_\mathrm{r}}{R_0}\left(\hat{n}_{-1,q} - \hat{n}_{1,q}\right) - R_{0,q} = 0, \quad (205)$$

where $R_{0,q}$ is the $m = n = 0$ component of the RS

$$R_{0,q} = \frac{c}{B_0}\overline{\left\{\phi, \nabla_\perp^2\phi\right\}}. \quad (206)$$

Calculations of the $m = n = 0$ RS are standard [221] and only involve $\widetilde{\phi}_{\pm k_\theta,\pm k_\mathrm{r}+q_\mathrm{r}}$ satellites:

$$R_{0,q} = \frac{c}{B_0}\overline{\left\{\phi, \nabla_\perp^2\phi\right\}} = \frac{c}{B_0}\left[q_\mathrm{r}^3 k_\theta\left(\widetilde{\phi}_{-k_\theta,-k_\mathrm{r}}\widetilde{\phi}_{k_\theta,k_\mathrm{r}+q_\mathrm{r}} - \widetilde{\phi}_{k_\theta,k_\mathrm{r}}\widetilde{\phi}_{-k_\theta,-k_\mathrm{r}+q_\mathrm{r}}\right) + 2k_\mathrm{r}k_\theta q_\mathrm{r}^2\left(\widetilde{\phi}_{-k_\theta,-k_\mathrm{r}}\widetilde{\phi}_{k_\theta,k_\mathrm{r}+q_\mathrm{r}} + \widetilde{\phi}_{k_\theta,k_\mathrm{r}}\widetilde{\phi}_{-k_\theta,-k_\mathrm{r}+q_\mathrm{r}}\right)\right]. \quad (207)$$

The $m = \pm 1$ components of the perturbed density are found from the ion continuity equation

$$\frac{\partial\hat{n}_{\pm1,q_\mathrm{r}}}{\partial t} - 2(\overline{\mathbf{v}}_E\cdot\nabla\ln B)_{\pm1} - 2\left(\widetilde{n}\widetilde{\mathbf{v}}_E\cdot\nabla\ln B\right)_{\pm1} - \hat{R}_{\pm1,q_\mathrm{r}} = 0, \quad (208)$$

where the dispersive corrections of the order of $\rho_\mathrm{s}^2(r_\mathrm{s}^{-2} + q_\mathrm{r}^2)$ were neglected.

The first term in equation (208) is the standard linear GAM term due to the compressibility of the poloidal flow, as in equation (34), section 2.4. The third term describes the modulation of particle transport due to the compressibility of the nonlinear particle flux $2\left(\widetilde{n}\widetilde{\mathbf{v}}_E\cdot\nabla\ln B\right)_{\pm1}$ which will be discussed below. The last term, $\hat{R}_{\pm1,q_\mathrm{r}}$, is the $m = 1$ component of the RS. This term will also lead to the nonlinear modulations of plasma density $\hat{n}_{\pm1,q_\mathrm{r}}$, but is generally smaller than the compressibility of the nonlinear particle flux.

The $\widetilde{\phi}_{\pm k_\theta,\pm k_\mathrm{r}+q_\mathrm{r}}$ satellites which are required for the RS in (207) are found from the ion density equation (27) where the ion sound corrections related to the ion parallel velocity are neglected, assuming large safety factor q:

$$\frac{\partial\widetilde{\phi}_{\pm m,\pm k_\mathrm{r}+q}}{\partial t}\left(1 + k_\pm^2\rho_\mathrm{s}^2\right) \pm \mathrm{i}k_\theta v_*\widetilde{\phi}_{\pm m,k_\mathrm{r}+q} \mp q_\mathrm{r}k_\theta \times\frac{c}{B_0}\overline{\phi}_{0,q_\mathrm{r}}\widetilde{\phi}_{\pm m,\pm k_\mathrm{r}} = 0, \quad (209)$$

where $k_\pm^2 = k_\theta^2 + (\pm k_\mathrm{r} + q_\mathrm{r})^2$. Here, the density convection due to the $m = 0$ GAM perturbation, $\overline{\mathbf{v}}_E\cdot\nabla\widetilde{n}$, is the main order term for the interaction of the pump DW with the GAM mode perturbation; the contributions of the RS and $\widetilde{n}\widetilde{\mathbf{v}}_E\cdot\nabla\ln B$ terms to this equation are generally smaller. The dispersive corrections $\sim k_\pm^2\rho_\mathrm{s}^2$ are important here as they define the resonant radial wavevector for the unstable GAM.

To find explicit expressions for the DW satellites one assumes GAM perturbations in the form $(\overline{\phi}_{0,q}(t), \widehat{\phi}_{\pm1,q_\mathrm{r}}(t)) \sim \exp(-\mathrm{i}\Omega t)$. The pump wave amplitude is constant so one

has for $\phi_{m,k_r}(t) = \exp(-i\omega_0 t)$, and $\phi_{-m,-k_r}(t) = \phi^*_{m,k_r}(t) = \exp(i\omega_0 t)$ where ω_0 is the eigen-frequency of the drift mode,

$$\omega_0 = \frac{\omega_*}{1+k^2}, \tag{210}$$

$\omega_* = -k_\theta c T_e n_0'/eB_0 n_0$, $k^2 = k_\theta^2 + k_r^2$. Therefore the sidebands have time dependence of the form

$$\widetilde{\phi}_{\pm m,\pm k_r+q} \sim \exp\left(-i\Omega t \mp i\omega_0 t\right), \tag{211}$$

and from (209) one finds

$$\phi_{\pm m,\pm k_r+q} = \pm i \frac{q_r k_\theta}{(\Omega \pm \omega_0)\left(1+k_\pm^2\right) \mp \omega_*} \overline{\phi}_{0,q_r} \widetilde{\phi}_{\pm m,\pm k_r}. \tag{212}$$

Using these expressions in (207) one obtains the RS in the form

$$\begin{aligned} R_{0,q_r} &= i q_r^4 k_\theta^2 \overline{\phi}_{0,q_r} \left|\widetilde{\phi}_{m,k_r}\right|^2 \left(\frac{2D_0}{D_0^2 - D_1^2}\right) \\ &+ 2i k_r k_\theta^2 q_r^3 \overline{\phi}_{0,q_r} \left|\widetilde{\phi}_{m,k_r}\right|^2 \left(-\frac{2D_1}{D_0^2 - D_1^2}\right) \\ &= 2i q_r^4 k_\theta^2 \overline{\phi}_{0,q_r} \left|\widetilde{\phi}_{m,k_r}\right|^2 \frac{\Omega\left(1+k^2+q_r^2-4k_r^2\right)}{D_0^2 - D_1^2}, \end{aligned} \tag{213}$$

where

$$D_+ = (\Omega + \omega_0)\left(1+k_+^2\right) - \omega_* = D_0 + D_1, \tag{214}$$

$$D_- = (\Omega - \omega_0)\left(1+k_-^2\right) + \omega_* = D_0 - D_1, \tag{215}$$

and

$$D_0 = \Omega\left(1+k^2+q_r^2\right) + 2k_r q_r \omega_0, \tag{216}$$

$$D_1 = 2\Omega k_r q_r + \omega_0 q_r^2. \tag{217}$$

Using expression (213) for the RS, from (208) and (205) one obtains the final dispersion equation for the GAM modified by the nonlinear contribution from the RS

$$\Omega^2 - 2\frac{c_s^2}{R_0^2} + 2q_r^2 k_\theta^2 \rho_s^4 \left|\frac{e\widetilde{\phi}_{m,k_r}}{T_e}\right|^2 \frac{\Omega^2\left(1+q^2+k^2-4k_r^2\right)}{D_0^2 - D_1^2} = 0. \tag{218}$$

The amplitude of the nonlinear correction here (the last term) is fairly small, so the only situation when it may be effective is the resonant regime when $\Omega \simeq \omega_{GAM} = \sqrt{2}c_s/R_0$ and $D_0 \simeq \pm D_1$, corresponding to the resonance between the GAM and one of the sidebands, $(\Omega \pm \omega_0)(1+k_\pm^2) \mp \omega_*\Omega \simeq 0$ [218]. The resonant condition imposes a constraint on the value of the radial wavevector of the GAM mode that can be excited. For the case with $k_r = 0$, from $D_0 \simeq D_1$ one has an estimate for q_r: $\Omega \simeq \sqrt{2}c_s/R \simeq q_r^2 \rho_s^2 \omega_0$. The higher order dispersive corrections $(k^2 + q_r^2)\rho_s^2 \ll 1$ were neglected here. The nonlinear GAM growth rate can be found by taking $\Omega = \omega_{GAM} + \delta\omega$, and expanding (218) near ω_{GAM} from which one obtains for the growth rate

$$(\delta\omega) = \pm i q_r c_s k_\theta \rho_s \left|\frac{e\widetilde{\phi}_{m,k_r}}{T_e}\right|. \tag{219}$$

It is also assumed here $(q^2 + k^2 - 4k_r^2)\rho_s^2 \ll 1$.

In the resonant parametric decay case only one sideband is included, so it is often referred to as the three-wave interaction, contrary to the four-wave interaction models for ZF generation where the linear eigenmode is degenerate with $\Omega \simeq 0$, so that both sidebands should be included. For the case of a broad wave spectrum, when the wave kinetic equation is used, the resonance between the DW group velocity $v_{gr} = \partial\omega_0/\partial k_r$ and the GAM mode is considered, so the resonance condition is $q_r v_{gr} = \omega_{GAM}$.

A similar model was considered for the GAM generation by ITG modes [219]. It was shown also that EM effects in finite β-plasmas provide a stabilizing effect [222] due to the addition of the Maxwell stress. Nonlinear excitation of GAMs due to three-wave decay was also considered in the kinetic theory for the DW [11], collisionless trapped electron mode (TEM) [223], and toroidal Alfvén modes [224].

The parametric GAM drive by DWs was generalized to include the radial propagation in a non-uniform plasma and dispersion effects [142, 148, 225, 226]. The analysis in [142, 148] has shown that nonlinearly excited GAMs propagate at a group velocity much larger than that predicted by linear theory, and also show the nonlinear shift of the GAM frequency due to the finite amplitude of the DW pump wave. The non-local theory of [225] has shown that the resonant three-wave interaction of the DW, GAM and drift sideband determine the mode localization and the resonant GAM frequency, thus converting the local continuum mode into the global discreet mode. Multiple resonant modes of this type can co-exist.

4.3. Stringer spin-up and GAM instability

The GAM represents the linear oscillatory eigenmode of (mostly) poloidal plasma rotation, and thus the problem of GAM generation is inherently related to a more general phenomena of the generation of poloidal and toroidal plasma rotation. Earlier works [7, 207] have pointed out that the radial diamagnetic current induced by plasma diffusion in toroidal geometry results in the instability of the poloidal rotation. The phenomena, which has been later called as Stringer spin-up, relies on the $m = 0$ radial diamagnetic current induced by the $m = 1$ oscillations of plasma pressure that are supported by Pfirsch–Schlüter type diffusion fluxes. This mechanism of the radial current is the same as in GAM dynamics, given by the first term in equation (7). In fact, the basic GAM dispersion relation describing the GAM instability also appears in the context of a study of the poloidal Stringer spin-up driven by the turbulent anomalous transport [6, 211]. It is instructive to review the Stringer spin-up mechanism as a proxy for various models of GAM generation by plasma turbulence.

Essentially, the GAM instability driven by the Stringer spin-up is the GAM eigenmode made unstable by the presence of the equilibrium plasma flow $v_\parallel^0$ that is poloidally non-uniform $v_\parallel^0 = v_\parallel^0(\theta)$. Such a flow, along the magnetic field, can be supported by the poloidally non-uniform plasma sources and plasma diffusion, e.g.

$$\frac{1}{r}\frac{\partial}{\partial r} D(\theta) \frac{\partial n}{\partial r} + \frac{1}{qR_0}\frac{\partial}{\partial\theta} n v_\parallel^0(\theta) = S(r,\theta). \tag{220}$$

The equations for oscillations on the background of such equilibrium are analogous to the GAM equations (7), (222) and (10):

$$-2\frac{cT}{B}\mathbf{b}\times\nabla\hat{n}_1\cdot\nabla\ln B-\frac{en_0c}{B_0\omega_{ci}}\frac{\partial}{\partial t}\nabla_\perp^2\tilde{\phi}_0=0. \quad (221)$$

$$\frac{\partial\hat{n}_1}{\partial t}=-n_0\nabla\cdot\overline{\mathbf{v}}_E-n_0\nabla_\parallel\hat{v}_{\parallel_1}. \quad (222)$$

$$m_in_0\left(\frac{\partial\hat{v}_{\parallel_1}}{\partial t}+\overline{\mathbf{v}}_E\frac{\partial v_\parallel^0(\theta)}{r\partial\theta}\right)=-T\nabla_\parallel\hat{n}_1. \quad (223)$$

The only modification here is the addition of the second term on the left-hand side of (223) which becomes a driving term for the GAM instability in Stringer spin-up. For simplicity, the isothermal plasma case is assumed.

Solving equations (221)–(223) one finds the dispersion equation [6]:

$$-\mathrm{i}\omega\left[-\omega^2+2c_s^2(1+1/2q^2)/R_0^2\right]=2c_s^2v_{\parallel s}^0/qR_0^2r, \quad (224)$$

where $c_s^2=T/m_i$ and $v_{\parallel s}^0=(2\pi)^{-1}\int_0^{2\pi}v_\parallel^0(\theta)\sin(\theta)\mathrm{d}\theta$. On can see that this is the basic GAM dispersion relation modified by the presence of the inhomogeneous parallel flow, $v_\parallel^0$ which makes the GAM unstable. In general, the instability occurs for either sign of $v_{\parallel s}^0\lessgtr 0$ although the growth rates are different [6]. Therefore, the poloidal spin-up investigated in [6, 211] in the context of the L–H transition is in fact the instability of the GAM oscillation. The inhomogeneous parallel flow may be caused by the poloidal non-uniformities of the anomalous transport, plasma sources, and/or magnetic geometry. A similar model of the Stringer spin-up in the divertor X-point configuration was considered in [212].

4.4. GAM generation by dynamic shearing of turbulence and transport modulations

The central point of GAM generation via Stringer spin-up is the diamagnetic radial current induced by poloidal variations of plasma pressure caused by the perturbation of the Pfirsch–Schlüter parallel flow. The symmetry breaking perturbation, the second term in equation (223), provides a positive feedback on the GAM $\overline{\mathbf{v}}_E$ perturbation leading to the instability. One can envisage that the GAM may affect the anomalous transport resulting in poloidally varying plasma perturbations driving the radial current. Such a mechanism of GAM excitation was generically called the diamagnetic drive [14, 24, 227]. One specific realization of this mechanism was suggested as turbulence shearing by the time dependent $m=0$ GAM flow, i.e. dynamic shearing.

The basic model of the DS mechanism was formulated in [213] for the isothermal GAM by an analogy with Stringer spin-up. The main equation is the density evolution in the form

$$\frac{\partial\hat{n}_1}{\partial t}+n_0\nabla\cdot\overline{\mathbf{v}}_E+n_0\nabla_\parallel\hat{v}_{\parallel_1}=S-\nabla\cdot\Gamma\equiv\hat{F}(\theta,r,t). \quad (225)$$

Here, $\hat{F}(\theta,r,t)$ is the nonlinear driving term depicting modulations of the density transport. The poloidally non-uniform $\hat{F}(\theta,r,t)$ drive induces the density perturbation. The up–down asymmetry in the density perturbation is required, $\hat{n}_1\sim\sin\theta$, to affect the GAM, so it is assumed that

$$\hat{F}(\theta,r,t)=f_s(r,t)\sin\theta. \quad (226)$$

Using the arguments of the wave action conservation and shearing of fluctuations by the GAM poloidal flow, the driving term $f_s(r,t)$ was obtained [213] as a function of $\overline{\mathbf{v}}_E$ in the form

$$f_s(r,t)=u_{DS}\left(\int^t\mathrm{d}t\frac{\partial^2}{\partial r^2}\overline{\mathbf{v}}_E\right). \quad (227)$$

hence the DS name. Assuming strongly ballooning radial transport $\Gamma_r=\Gamma_0(1+\cos\theta)$, the DS coefficient u_{DS} was estimated in the form

$$u_{DS}\simeq 3k_\theta^2\rho_s^2s\frac{\Gamma_0}{n_0}, \quad (228)$$

where s is the magnetic shear. The corresponding GAM growth rate was obtained as

$$\gamma\simeq\frac{1}{2}k_r^2R_0u_{DS}. \quad (229)$$

In the DS model described above [213], the assumption of strong ballooning of the anomalous transport is essential. More generally, the transport modulation mechanism does not necessarily require the ballooning assumption. However, the important element of this mechanism is the compressibility of the anomalous transport flux resulting in poloidally non-uniform pressure perturbations.

One can illustrate the main features of such a mechanism with the example of the density transport by the DW. It is often assumed that for simple (neutrally stable) DWs, with the adiabatic electron response, $\tilde{n}/n_0=e\tilde{\phi}/T_e$, the particle transport is identically zero due to the identity $\tilde{\mathbf{v}}_E\cdot\nabla\tilde{n}=0$. More accurately, the condition $\tilde{\mathbf{v}}_E\cdot\nabla\tilde{n}=0$ for adiabatic electrons refers to the divergent-free particle flux, $\nabla\cdot\left(\tilde{n}\tilde{\mathbf{v}}_E\right)=0$, which is only true for the case of a uniform magnetic field. In fact, for a non-uniform magnetic field one has

$$\nabla\cdot\mathbf{\Gamma}=\nabla\cdot\left(\tilde{n}\tilde{\mathbf{v}}_E\right)=\tilde{\mathbf{v}}_E\cdot\nabla\tilde{n}-2\tilde{n}\tilde{\mathbf{v}}_E\cdot\nabla\ln B. \quad (230)$$

Thus, the particle flux in the inhomogeneous magnetic field is compressible and can induce finite asymmetric density variations even for the adiabatic density response due to the last term in (230). The corresponding $m=1$ density perturbations can be found as

$$-\mathrm{i}\Omega\left(\hat{n}_{1,q_r}-\hat{n}_{-1,q_r}\right)-2\frac{cn_0}{B_0R_0}q_r\overline{\phi}_{0,q_r}-2\frac{ecn_0}{B_0R_0T_e}\times q_r\left(\phi_{m,k_r}\phi_{-m,-k_r+q_r}+\phi_{-m,-k_r}\phi_{m,k_r+q_r}\right)=0, \quad (231)$$

where the last term describes the nonlinear transport modulations. The structure of this term is similar to one of the components of the RS (207) and can be calculated using (212). Using (231) in the basic GAM equation (7) one obtains the GAM dispersion relation which includes the GAM instability due to RS

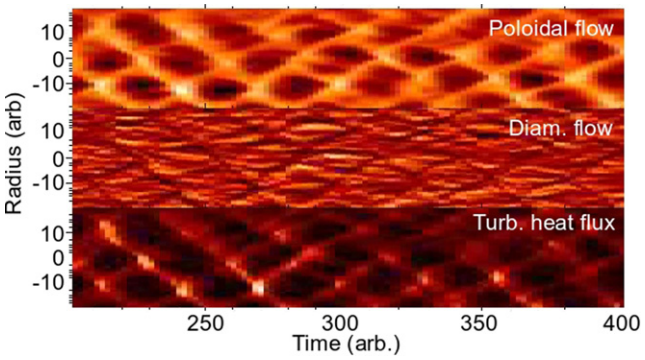

Figure 28. Contour plots of GAM poloidal flow velocity (top), ion diamagnetic velocity (middle), and turbulent ion heat flux (bottom) versus time and minor radius in a fluid turbulence simulation. Adapted with permission from [227].

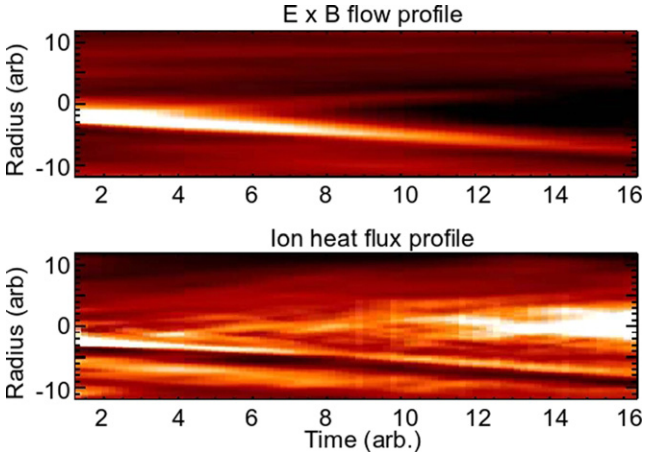

Figure 29. $E \times B$ flow (top) and turbulent heat flux (bottom) for the time evolution of an initially isolated single GAM peak. Adapted with permission from [227].

drive and transport modulations

$$\Omega^2 - 2\frac{c_s^2}{R^2} + 2q_r^2 c_s^2 k_\theta^2 \rho_s^2 \left|\frac{e\widetilde{\phi}_{m,k_r}}{T_e}\right|^2 \frac{\Omega^2\left(1+q^2+k^2-4k_r^2\right)}{D_0^2 - D_1^2}$$
$$+ 4\mathrm{i}\frac{q_r k_\theta c_s^4}{R_0^2 \omega_{ci}} \left|\frac{e\widetilde{\phi}_{m,k_r}}{T_e}\right|^2 \frac{D_1}{D_0^2 - D_1^2} = 0. \qquad (232)$$

Here, the first two terms describe the standard linear GAM oscillation with $\omega_{GAM} = \sqrt{2}c_s/R_0$. The third term is the RS from (218), and the last term is a nonlinear drive due to the transport modulations. The contribution of the RS to the quadratic dispersion relation is real, while that of the transport modulations is imaginary. The nonlinear corrections to the GAM frequency driven by transport modulations can be obtained from (232), again, by considering the resonant case $\omega = \omega_{GAM} + \delta\omega$, so that

$$\delta\omega = \pm(-\mathrm{i})^{1/2}\omega_{GAM}\left(\frac{q_r k_\theta \rho_s^2}{2}\right)^{1/2}\left|\frac{e\widetilde{\phi}_{m,k_r}}{T_e}\right|. \qquad (233)$$

It is important to note that in this simple model, the RS drive via the modulational instability results in the appearance of only the imaginary part of the GAM frequency, while the transport modulations produce the imaginary part of the GAM frequency and modify the real part thus broadening the GAM eigenmode.

In the above model, when the neutrally stable DW is considered, the GAM growth rate (233) is smaller than that due to RS (219). One can expect that for ITG type turbulence with significant energy transport, the pressure modulations can be much larger. Correlations of turbulence, plasma transport and the GAM were detected in many experiments, as reviewed in detail in section 15. Any up-down asymmetrical pressure variations, $\delta p_s \sim \sin\theta$ will drive the radial current that will feedback to the $m = 0$ GAM mode. From equation (10) one can obtain the following maximum estimate for the GAM growth due to the diamagnetic drive

$$\gamma \simeq \frac{\delta p_s}{p_0}\frac{c_s^2}{R_0 \overline{\mathbf{v}}_E}. \qquad (234)$$

Here, δp_s is the amplitude of up–down pressure asymmetry perturbation, and $\overline{\mathbf{v}}_E$ is the amplitude of the GAM induced poloidal rotation. Strong correlations of GAMs with anomalous energy transport and up–down asymmetrical pressure fluctuations were demonstrated in the 3D simulations of the ITG driven turbulence [24], as shown in figures 28 and 29. For a discussion of similar effects observed in GK simulations see section 5.

The contributions of the RS and the diamagnetic drive were directly measured in 3D fluid ITG turbulence simulations [24] where it was concluded that the diamagnetic drive can be as important as RS and is dominant in certain regimes, e.g. the plasma edge with strong temperature gradients. It was suggested that the diamagnetic drive is also a cause of strong modulations, transport suppression by GAMs, and GAM bursts observed in nonlinear fluid simulations [227–229].

Generally, poloidal modulations of plasma pressure resulting in the radial current driving the GAM can be induced by other interactions of various modes and excitations that might be present in a tokamak. Such mechanisms are briefly discussed below and further in section 11.4.

The GAM drive due from a magnetic-island induced BAE mode has also been considered [230]. In this model the axisymmetric radial current inducing the GAM is 'slaved' to the amplitude of the primary BAE mode. The driven GAM amplitude is two orders of magnitude smaller that of the BAE, which is roughly consistent with observations of axisymmetric modes accompanying Alfvén island modes in HL-2A tokamak [231]. An indirect GAM excitation mechanism was also suggested [232] in which poloidal variations of the plasma pressure are induced by cyclotron heating, which is naturally non-uniform due to piling up of non-resonant particles at the low-field side. The external excitation of GAMs is discussed further in section 11.

4.5. Nonlinear self-interactions in GAMs

The nonlinear self-interaction of GAMs has attracted some attention due to the observation of second GAM harmonics in both experiment [233] and numerical simulations [234]. These

effects and the related issue of the generation of low frequency ZFs by GAMs were theoretically analysed in several papers [143, 220, 235–238]. Here, the main ideas and some results are briefly reviewed.

Based on a fluid approach [235], it was concluded that GAMs do not generate second harmonics in the radial electric field while producing the second harmonics of the perturbed density. The standard GAM is a low frequency process and thus fluid theory is sufficient as an adequate framework [235] for analysis. However, it is instructive to consider nonlinear terms also using kinetic theory to extend the consideration to EGAMs which, in general, require a kinetic approach, and also to make connections to the arguments based on kinetic theory as in [234, 237, 238].

It was emphasized that the so-called parallel nonlinearity is important in the self-interaction of GAMs [234]. The term 'parallel nonlinearity' can be confusing as it refers to a specific form of the GK equation and more general than the commonly assumed parallel momentum transfer term due to the parallel electric field, $qE_\parallel \partial f/\partial v_\parallel$. Here, the standard DKE is used, which is more transparent compared to the Hamiltonian form of the GK theory but fully appropriate for the main order nonlinear effects in neglect of the FLR effects. Also provided is the fluid interpretation of the relevant effects.

Writing the nonlinear DKE in the phase space conserving form as follows

$$\frac{\partial f}{\partial t} + \nabla \cdot \left(\frac{\mathrm{d}\mathbf{R}}{\mathrm{d}t} f\right) + \frac{\partial}{\partial v_\parallel}\left(\frac{\mathrm{d}v_\parallel}{\mathrm{d}t} f\right) + \frac{\partial}{\partial v_\perp^2}\left(\frac{\mathrm{d}v_\perp^2}{\mathrm{d}t} f\right) = 0, \tag{235}$$

where $\mathbf{R}$ is the guiding centre coordinate, the total drift velocity is defined as

$$\frac{\mathrm{d}\mathbf{R}}{\mathrm{d}t} = v_\parallel \mathbf{b} + \mathbf{v}_E + \mathbf{v}_\mathrm{d}, \tag{236}$$

and the evolution of the $v_\perp$ and $v_\parallel$ are defined by the equations

$$\frac{\mathrm{d}v_\parallel}{\mathrm{d}t} = \frac{q}{m}\mathbf{E}\cdot\mathbf{b} + \frac{1}{2}v_\perp^2 \nabla\cdot\mathbf{b} + v_\parallel \mathbf{v}_E \cdot \nabla \ln B, \tag{237}$$

$$\frac{\mathrm{d}v_\perp^2}{\mathrm{d}t} = -v_\perp^2 v_\parallel \nabla\cdot\mathbf{b} + v_\perp^2 \mathbf{v}_E \cdot \nabla \ln B. \tag{238}$$

The phase space conservation here has the form

$$\nabla \cdot \left(\frac{\mathrm{d}\mathbf{R}}{\mathrm{d}t}\right) + \frac{\partial}{\partial v_\parallel}\left(\frac{\mathrm{d}v_\parallel}{\mathrm{d}t}\right) + \frac{\partial}{\partial v_\perp^2}\left(\frac{\mathrm{d}v_\perp^2}{\mathrm{d}t}\right) = 0. \tag{239}$$

The second term in this equation is analogous to the parallel nonlinearity terms discussed in [234]. Note that the form of the 'parallel nonlinear' terms may change depending on the choice of independent variables, for example instead of $(v_\perp, v_\parallel)$ other pairs are used, e.g. $(v_\parallel, E = mv^2/2)$ or $(v_\parallel, \mu = v_\perp^2/2B)$ as in [234].

In the fluid limit, $\omega \gg \omega_\mathrm{d} = k_\mathrm{r} v_\mathrm{dr}$, in the linear (first order) approximation, one has

$$\frac{\partial f^{(1)}}{\partial t} = -\left(v_\parallel \frac{\partial f_0}{\partial v_\parallel} + v_\perp^2 \frac{\partial f_0}{\partial v_\perp^2}\right) \overline{\mathbf{v}}_E \cdot \nabla \ln B, \tag{240}$$

where f_0 is the equilibrium distribution function, and $\overline{\mathbf{v}}_E$ is the poloidal flow velocity due to the $m = 0$ GAM potential perturbation, cf with equation (44). In the first nonlinear order, and zeroth order in $\left(\omega_\mathrm{d}/\omega, v_\parallel \nabla_\parallel/\omega\right) \ll 1$, one has from (235)

$$\frac{\partial f^{(2)}}{\partial t} = -\nabla\cdot\left(\mathbf{v}_E f^{(1)}\right) - \frac{\partial}{\partial v_\parallel}\left(\frac{\mathrm{d}v_\parallel}{\mathrm{d}t} f^{(1)}\right) - \frac{\partial}{\partial v_\perp^2}\left(\frac{\mathrm{d}v_\perp^2}{\mathrm{d}t} f^{(1)}\right). \tag{241}$$

It is easy to see here that the nonlinear density perturbation in the GAM is finite and is due to the convective perpendicular nonlinearity related to the $\mathbf{E}\times\mathbf{B}$ drift

$$\frac{\partial n^{(2)}}{\partial t} = -\nabla\cdot\left(\mathbf{v}_E^{(1)} n^{(1)}\right) - \nabla\cdot\left(\mathbf{v}_E^{(2)} n_0\right), \tag{242}$$

where $n^{(1)}$ and $\mathbf{v}_E$ are the total density and $\mathbf{E}\times\mathbf{B}$ drift velocity due to the linear GAM. In this form of the DKE the 'parallel nonlinearity', the second and third terms on the right-hand side of equation (241), do not contribute to the nonlinear density perturbation $n^{(2)}$. In the linear approximation, the GAM density perturbation has only an $m = 1$ component, $n^{(1)} = \hat{n}$, and the potential has $m = 0$ and $m = 1$ parts, $\phi^{(1)} = \overline{\phi} + \widehat{\phi}$. Thus, the second order density perturbation is

$$\frac{\partial n^{(2)}}{\partial t} = -\overline{\mathbf{v}}_E\cdot\nabla\hat{n} + 2\hat{n}\overline{\mathbf{v}}_E\cdot\nabla\ln B + 2\hat{n}\hat{\mathbf{v}}_E\cdot\nabla\ln B - \mathbf{v}_E^{(2)}\cdot\nabla n_0 + 2n_0\mathbf{v}_E^{(2)}\cdot\nabla\ln B, \tag{243}$$

where the superscript for the linear terms is now dropped. This structure is similar to that in [235] except the term with the second order electric field and density gradient $\mathbf{v}_E^{(2)}\cdot\nabla n_0$ which was not included in [235].

The first term in (243) is dominant, $\overline{\mathbf{v}}_E\cdot\nabla\hat{n}/\hat{n}\overline{\mathbf{v}}_E\cdot\nabla\ln B \sim R/r > 1$, and the third term is small with respect to the second one for long wavelength GAM modes, $\hat{n}\hat{\mathbf{v}}_E\cdot\nabla\ln B/\hat{n}\overline{\mathbf{v}}_E\cdot\nabla\ln B \sim \omega_\mathrm{d}/\omega \sim k_\mathrm{r}\rho_\mathrm{i}$. Taking the GAM radial field in the form $E_{\mathrm{r}0} = -\partial\overline{\phi}^{(1)}/\partial r = E_0\cos\omega t$, one can write the linear density perturbation as

$$\hat{n} = -2n_0\frac{c}{B_0}\frac{E_0\sin\omega t}{\omega}\frac{\sin\theta}{R_0}, \tag{244}$$

thus obtaining for the second order nonlinear density perturbations

$$n^{(2)} = n_0\left(\frac{c}{B_0}\right)^2 E_0^2 \frac{\cos 2\omega t}{2\omega^2 R_0 r}\cos\theta + n_0\left(\frac{c}{B_0}\right)^2 E_0^2\frac{\cos 2\omega t}{\omega^2 R_0^2}\sin^2\theta. \tag{245}$$

Only the contribution from the first two terms from (243) is shown here. Note that the poloidal dependence of the nonlinear density perturbations in (245) is different from the linear polarization ($\hat{n}\sim\sin\theta$). The coupling to the linear term will come from the third order term in (243) which produces the $\sin\theta$ components (as well as the third order harmonics $\sim 3\theta$). The density gradient term in (243), omitted here, also will contribute.

In the considered order, the density perturbation in (243) does not affect the electric field because these perturbations

are automatically ambipolar and do not produce an electric current. The non-ambipolar contribution to the density resulting in the nonlinear current (and electric field) perturbations, have to be found from the higher order in magnetic drift and parallel velocity when the time derivative $\partial/\partial t$ in the equations (235) and (241) is replaced with $\partial/\partial t + v_{\rm d}\partial/\partial r + v_\parallel \nabla_\parallel$ and the resulting equation is solved to the first order in $(\omega_{\rm d}/\omega, v_\parallel\nabla_\parallel/\omega)$. Alternatively, one can find the nonlinear pressure and parallel viscosity perturbations from (241) and use it in the equation for the electric field, similar to (19). The equation for the nonlinear electric field has the form

$$\frac{2c}{B}\nabla\left(p^{(2)}+\frac{1}{4}\pi_\parallel^{(2)}\right)\cdot\mathbf{b}\times\nabla\ln B-\frac{en_0c}{B_0\omega_{\rm ci}}\frac{\partial}{\partial t}\nabla_\perp^2\phi^{(2)}=0. \tag{246}$$

The second order pressure perturbations were not considered in the quasineutrality equation in [235], thus resulting in the conclusion that the second order electric field is absent, $E_{\rm r}^{(2)}=0$. Below, we discuss how the nonlinear electric field is produced by the second order perturbations in pressure (and parallel viscosity).

The expression for the nonlinear perturbed pressure has a structure similar to (243),

$$\frac{\partial}{\partial t}p^{(2)}=-\nabla\cdot\left(\overline{\mathbf{v}}_E p^{(1)}\right)+\frac{4}{3}\left(p^{(1)}+\frac{1}{4}\pi_\parallel^{(1)}\right)\overline{\mathbf{v}}_E\cdot\nabla\ln B+\cdots, \tag{247}$$

and the combination of the perturbed pressure and viscosity that defines the nonlinear electric field in the quasineutraliy equation (246) is given by the equation

$$\frac{\partial}{\partial t}\left(p^{(2)}+\frac{1}{4}\pi_\parallel^{(2)}\right)=-\nabla\cdot\left(\overline{\mathbf{v}}_E\left(p^{(1)}+\frac{1}{4}\pi_\parallel^{(1)}\right)\right)+\frac{3}{2}\left(p^{(1)}+\frac{1}{2}\pi_\parallel^{(1)}\right)\overline{\mathbf{v}}_E\cdot\nabla\ln B. \tag{248}$$

The main order nonlinear pressure perturbations have a structure similar to density (245)

$$p^{(2)}=\frac{5}{6}p_0\left(\frac{c}{B_0}\right)^2E_0^2\frac{\cos 2\omega t}{\omega^2R_0r}\cos\theta+\frac{17}{6}p_0\left(\frac{c}{B_0}\right)^2E_0^2\frac{\cos 2\omega t}{\omega^2R_0^2}\sin^2\theta \tag{249}$$

and the combination of pressure and viscosity that defined the radial electric field from (248) is

$$p^{(2)}+\frac{1}{4}\pi_\parallel^{(2)}=\frac{7}{8}p_0\left(\frac{c}{B_0}\right)^2E_0^2\frac{\cos 2\omega t}{\omega^2R_0r}\cos\theta+\frac{25}{4}p_0\left(\frac{c}{B_0}\right)^2E_0^2\frac{\cos 2\omega t}{\omega^2R_0^2}\sin^2\theta. \tag{250}$$

Here, the terms due to the mirror force and the second order electric field are omitted. Therefore, the main order nonlinear electric field, produced by nonlinear pressure perturbations, from the first term on the right-hand side of (250), is defined by the equation

$$\nabla_\perp^2\phi^{(2)}=\frac{7}{8}\frac{cc_{\rm s}^2}{\omega^3R_0^3}\sin 2\omega t\sin 2\theta\left(\frac{\partial}{\partial r}\left(\frac{E_0^2}{r}\right)-\frac{E_0^2}{r^2}\right). \tag{251}$$

Since the polarization, $\sim\sin 2\theta$, of the nonlinear electric field in (251) is different, it is a 'slaved' perturbation, that would not couple effectively to the primary $m=0$ eigenmode. The next order electric field, determined by the second term in (250), has the poloidal structure $\sim\sin^3\theta$, and only the terms similar to the third term in (243) will produce an electric field with an $m=0$ component.

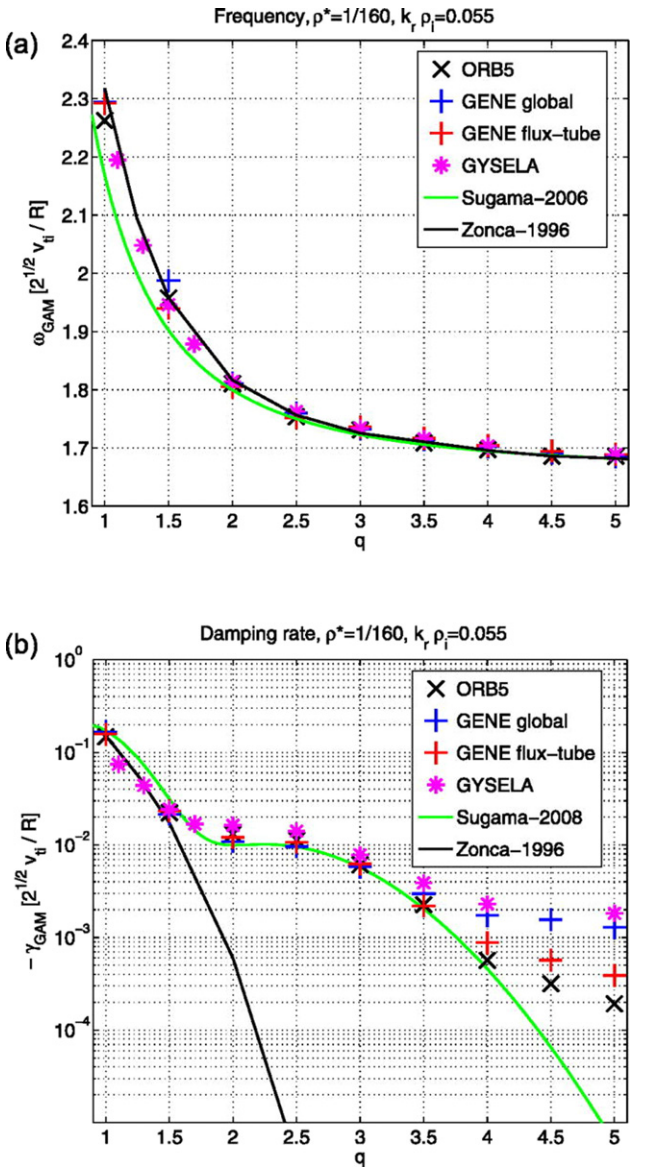

Figure 30. Frequency (*a*) and damping rate (*b*) vs safety factor q, from ORB5 (black crosses), GENE global (blue crosses), GENE flux-tube (red crosses), and GYSELA (magenta stars) for small value of $k_{\rm r}\rho_{\rm i}=0.055$. Explicit analytical formula results of Sugama-2006 [75] and Sugama-2008 [76] are shown in green, and the numerical solution of the dispersion relation from [5] in black. Adapted from [138], with the permission of AIP Publishing.

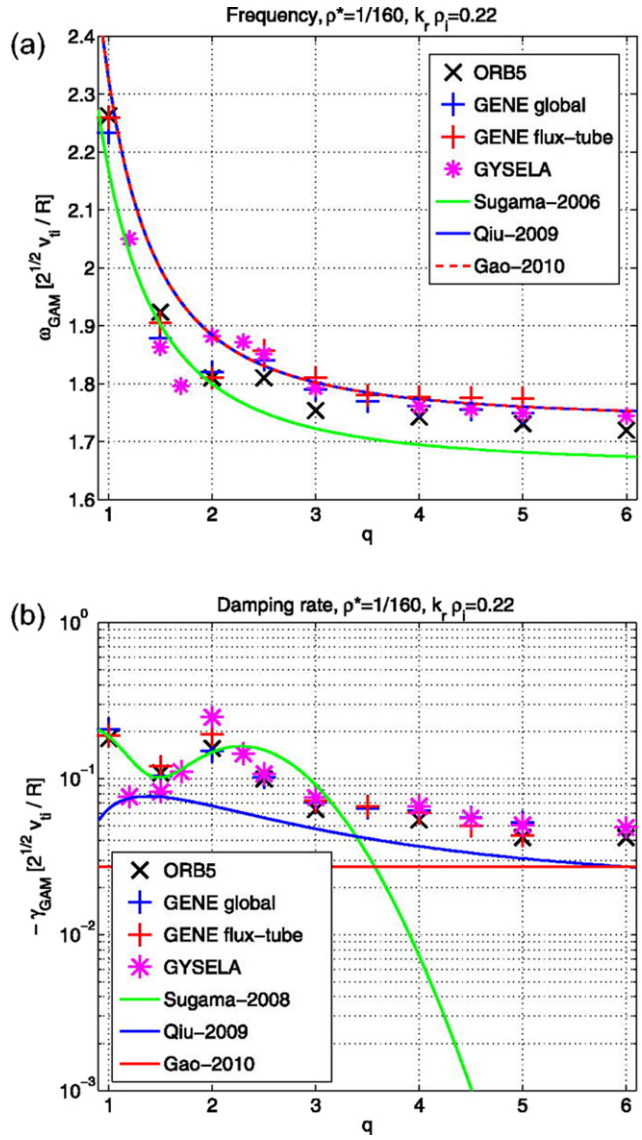

Figure 31. The same as for figure 30 for $k_r\rho_i = 0.22$. Adapted from [138], with the permission of AIP Publishing.

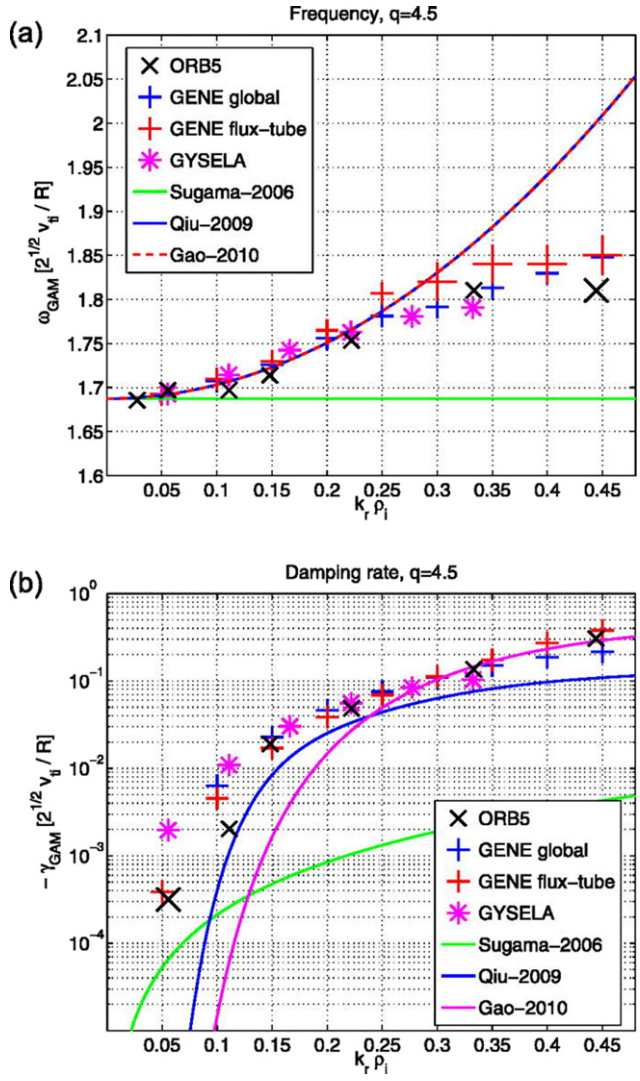

Figure 32. Frequency and damping rate of E_r vs $k_r\rho_i$, from ORB5 (black crosses), GENE global (blue crosses), GENE flux-tube (red crosses), and GYSELA (magenta stars) as a function of wavevector, compared with analytical theories of Sugama-2006, Qiu-2009, and Gao-2010. Adapted from [138], with the permission of AIP Publishing.

Note that the $m = 0$ part of the nonlinear density perturbation, from the second term in (249), $n^{(2)} \sim E_0^2$, will generate the next order nonlinear $\sin\theta$ density sideband, which will eventually couple to the $m = 0$ nonlinear electric field. Such terms were pursued via the kinetic theory in [237] by treating the ω_d and $v_\parallel\nabla_\parallel$ in the same order. However, the nonlinear density correction found in [237] is identically zero for the symmetric, in $v_\parallel$, distribution function, as pointed out in [238], where the next order corrections due to geometric asymmetry in trajectories of passing particles was included.

The EGAM could be much more effective in producing nonlinear second order harmonics of the electric field coupled to the initial $m = 0$ mode, when the EP distribution function is asymmetric and produces the $\cos\theta$ density and pressure perturbation as in equation (142). Then the convective nonlinear term in (248) would produce the $\sin\theta$ perturbation directly coupled to the $m = 0$ electric field. Second harmonic generation by an EGAM was studied in [239].

Some comments are in order regarding the possibility of the generation of a low frequency ZF by GAMs. Coupling of nonlinear perturbations of the electric field to the $m = 0$ mode has been interpreted as evidence of the ZF generation by GAMs [237–239]. This is different from the usually understood mechanism of ZF generation via modulational or parametric instabilities [221] in which the ZF perturbation becomes unstable and grows (exponentially in the linear stage) at the expense of the energy of the pump wave. The exponential instabilities 'ZF from GAMs' were not demonstrated in [237–239] and are not guaranteed by the simple presence of the nonlinear effects. The nonlinear terms (from GAMs) in the $m = 0$ ZF equation may lead to a nonlinear frequency shift (finite nonlinear frequency) for the ZF resulting in stable ZFOs, or they may be important for the saturation of ZFs (driven by other mechanism), or they may determine the shape of nonlinear oscillations and other similar effects, but

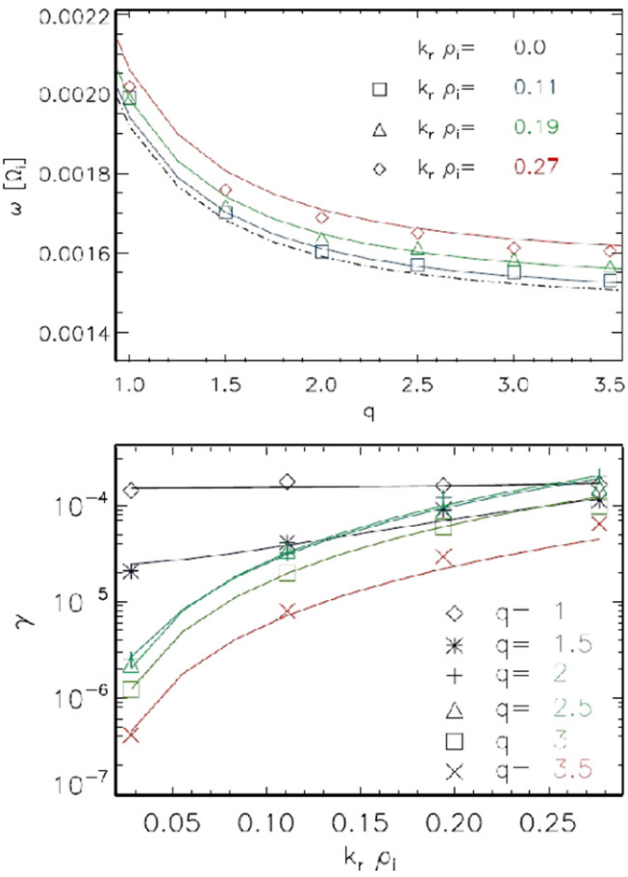

Figure 33. (Top) GAM frequency as a function of the safety factor for several values of the wavenumber. Theory lines are from [11, 74, 111]. (Bottom) GAM damping as a function of wavenumber k_r for several values of the safety factor, theory lines are from [75, 76]. Adapted from [140], with the permission of AIP Publishing.

not necessarily mean ZF instability (generation). Conversely, the absence of the direct nonlinear terms does not mean the absence of the instability and ZF generation. For example, in the standard RS mechanism of ZF generation by DWs, the nonlinear RS on the plane DW of the primary pump mode is identically zero (because of symmetry) and becomes finite to drive the ZF only after the symmetry breaking ZF test mode perturbation is introduced, as is apparent from the expression (207). It is worth noting that nonlinear effects of the RS from GAMs were not considered in [237–239]. The possibility of ZF generation by GAMs via the modulational instability from RS was analysed in [236], where it was shown that GAMs do not lead to the ZF instability but merely produce the nonlinear frequency shift $\delta\Omega$ from the linear GAM frequency, with $\delta\Omega^2 \sim |\phi_{\rm GAM}|^2 > 0$. Some indirect mechanisms of ZF generation and GAM self-interaction's via the coupled dynamics of turbulence, ZF and GAMs [143, 146, 147, 220] are discussed in section 17.

5. Gyrokinetic simulations of GAMs and EGAMs

In section 4, the results of some 3D nonlinear fluid simulations of GAMs were discussed. These simulations have provided good physics insights on some GAM features, including a convincing demonstration of the generation of GAMs in ITG driven turbulence, some global characteristics such as radial GAM localization, and signatures of coupled dynamics and interactions between GAMs, turbulence and anomalous transport dynamics. However, the fluid models used in nonlinear simulations are simplified and are not able to fully describe the ion FLR effects and GAM dispersion from higher order toroidal (FOW) effects. The closures used in some fluid simulations to account for the wave–particle interactions are only approximate and do not describe the full complexity of the nonlinear kinetic effects expected to be relevant in realistic conditions. Nonlinear kinetic effects may directly affect the nonlinear dynamics and mode saturation, such as the saturation of EP driven modes due to flattening of the distribution function of resonant EPs. Therefore, GK simulations are important tools that provide a confirmation of theoretical models, and, extend modelling towards realistic tokamak conditions. In this section an overview of some of the results from such simulations is given.

5.1. Verification and benchmarking of the linear GAM dynamics

In this section, numerical studies devoted to verification of the GAM frequency and damping rates in linear GK codes will be described. In general, the real GAM frequency is well reproduced in numerical simulations with uniform profiles and in the long wavelength limit, $k_r\rho_i \to 0$. However, when the dispersion due to FLR and higher order transit resonances are included, and in the general case of the nonuniform profiles, the agreement becomes less obvious. The latter is especially true for effective damping rates which are affected by the radial propagation and phase-mixing (PM) which is energy conserving. The radial propagation is due to the GAM dispersion with the density and temperature gradients bringing additional complexity. Thus, the dispersion and radial profiles need to be accounted for to describe the GAM amplitude decay in realistic non-uniform plasmas. The problem becomes even more intricate because the higher order theories involving higher harmonics are cumbersome, there are different expressions in the literature, and in the case of $m > 2$ the dispersion relations generally require pure numerical evaluations, cf [79, 112]. These issues have motivated dedicated efforts to compare analytical theory and GK numerical simulations [138, 140, 193, 240, 241].

The linear simulations using the GK code NEMORB with flat density and temperature profiles [240] have shown that in the high q limit the GAM frequency fits well with the dispersionless explicit expression from [75] (also derived in the high q limit), while for the lower values of q the agreement improves for the expressions from [5, 192] obtained for general q.

Extensive verification and benchmarking of three different GK codes and analytical theory in appropriate regimes have been performed [138]. As per [138] definitions, verification is understood as running a code in particular regimes where analytical solutions are available and with comparison to analytical predictions, while benchmarking means comparison of results from different codes under the same set of parameters and within regimes where the underlying physics in the codes

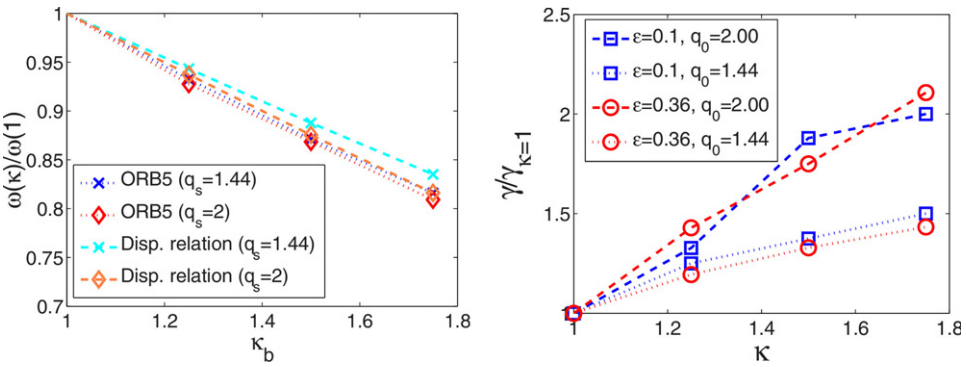

Figure 34. GAM frequency (left) and damping rate (right) as a function of the edge elongation κ_b. The dotted lines are from numerical simulations, dashed lines are from theoretical dispersion relation. The inverse aspect ratio is $\epsilon = 0.1$ (a), $\epsilon = 0.1$ and $\epsilon = 0.36$, evaluated at $r/a = 0.5$. The values are normalized to those for the circular case $\omega(1)$ and $\gamma(1)$. Adapted from [243], with the permission of AIP Publishing.

is the same. The results of the Lagrangian ORB5, the Eulerian GENE and the semi-Lagrangian GYSELA were compared for linear properties of GAMs. Flat temperature and density profiles were considered. A set of analytical expressions for the real frequency [75, 76, 116], plus an expression for non-circular geometry [117, 242], and solutions of the dispersion equation [5], were compared. The GAM damping has been compared with theoretical results from [75, 76, 116, 117, 242].

The GAM frequency and damping were measured for periodic perturbations initially excited with a fixed value of the radial wave vector in two cases: the long wavelength regimes, $k_r\rho_i = 0.055$, and the finite wavelength with $k_r\rho_i = 0.22$. It is important to note that the above theoretical expressions for the GAM frequency, though partially overlapping in some regions of parameters, were generally derived with different assumptions and approximations regarding the dispersion, values of q and elongation. Here, we comment only on selected results regarding the q dependence, elongation and dispersion, and refer to [138] for more details.

For small value of the wavevector, $k_r\rho_i = 0.055$ the results for the frequency and growth rate are shown in figure 30. The frequency dependence is generally well reproduced by all three codes and agrees well with theory, see figure 30(a). Note that while Sugama-2006 [75] has provided an explicit expression for the real frequency in the asymptotic limit of large but finite q, the exact numerical solution of the dispersion relation from Zonca-1996 [5] for arbitrary q is used in figure 30. This is likely the reason for a small difference in the real frequency between Zonca-1996 and Sugama-2006 in figure 30(a). The theoretical calculations of the real frequency in these papers did not include any dispersion effects.

The mode damping in these simulations starts to diverge from the theory for large q, cf figure 30(b). The dispersion relation from [5] does not include the second harmonics of the transit resonances, $\omega \simeq 2v_\parallel/qR_0$, which are important for larger q, as discussed in section 2.7 and which were analytically included in the damping rate Sugama-2008 [76]. This explains the divergence between Zonca-1996 and Sugama-2008 results in figure 30(b) for large values of q. One can also observe a difference between numerical results and Sugama-2008 result at even larger values of q. This is possibly due to the effects of the higher harmonics, $m > 2$, which were not included in [75, 76]. Effects of the higher harmonics were included and compared with the results of direct numerical simulations in [78, 79, 112], see the discussion in section 2.7 and figures 6 and 7.

For larger values of $k_r\rho_i = 0.22$ the numerical results, compared with theoretical expressions from [75, 116, 117] without elongation ($e = 1$), are shown as a function of q in figure 31. The dependence of the frequency and growth rate on the wavevector for constant q are further shown in figure 32. The results from all three codes are generally in good agreement with each other, but differ from theory, which are also different from each other. The difference between the theoretical results are expected because the expression for the real frequency in [75] does not include the effects of $m = 2$ harmonics, therefore no dispersion, while the expressions in Qiu-2009 [116] have some other inaccuracies in the dispersion terms for frequency, as discussed in section 2.7.

It is important to note that the above result did not consider the effects of propagation in non-uniform plasmas. The effects of dispersion including GAM radial propagation and damping were specifically studied in [140]. Here, the linear global dynamics was studied with GK simulations using the ORB5 code for different equilibrium profiles and nonuniform temperature. For the uniform temperature, small aspect ratio $\epsilon = a/R_0 = 0.1$ and circular geometry case, it was shown that the real frequency including the dispersion effect was found to agree with the result of the analytical theory in [11, 74, 111], see figure 33 (top). The linear GAM damping was found to be in agreement with the analytical results from Sugama [75, 76], see figure 33 (bottom). The radial GAM acceleration and the related evolution of the radial wave vector was investigated for the case of non-uniform temperature profiles, demonstrating a significant increase of the radial group velocity bringing it closer to the values observed in the experiments—see section 9.6. Taking into account PM effects, a good agreement of numerical results with the closed form analytical expression from [11, 74, 111] was found. In particular, the change in the direction of propagation for large values of τ_e was confirmed, in agreement with the analytical theory. These results suggest that proper account of the PM process may reduce

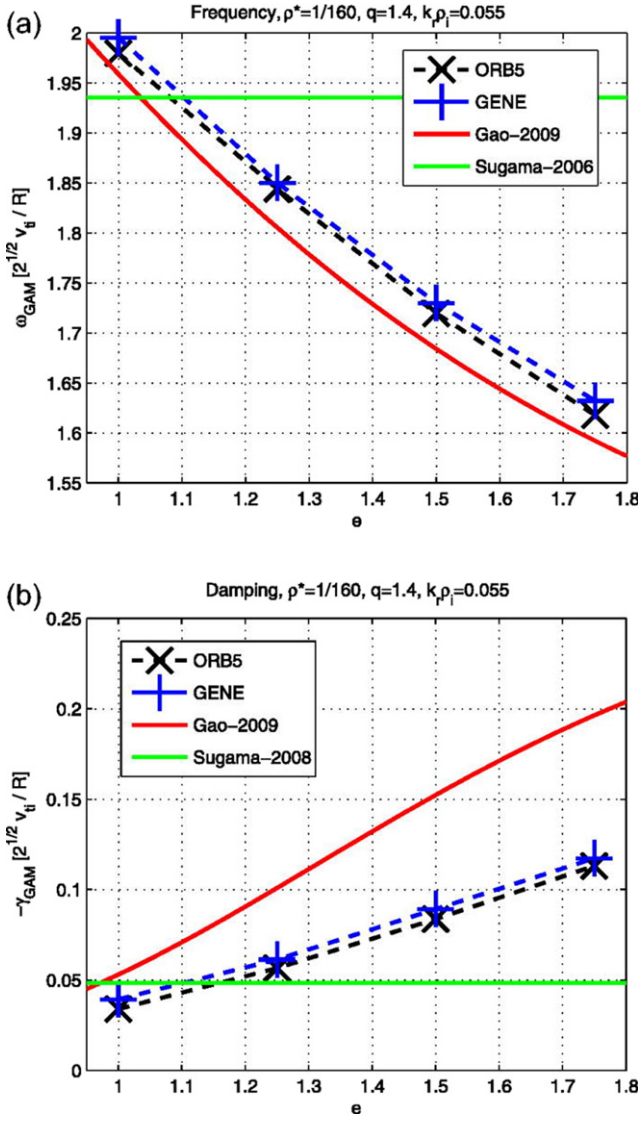

Figure 35. (*a*) Frequency and (*b*) damping rate of E_r from ORB5 (black crosses), and GENE global (blue crosses) as a function of elongation parameter e. Analytical expressions of Gao-2009 (red), and values from Sugama-2006, 2008 (green) are shown for comparison. Adapted from [138], with the permission of AIP Publishing.

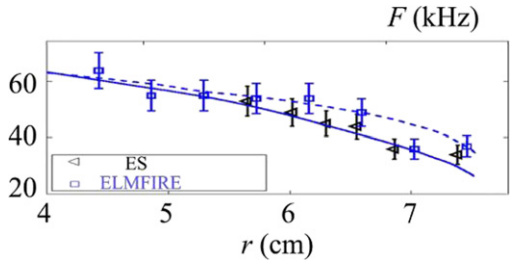

Figure 36. Radial profiles of GAM frequency from enhanced scattering diagnostic on FT-2. Solid and broken lines are analytical GAM theory predictions (Gao) [248] for initial and relaxed profiles. Adapted from [249].

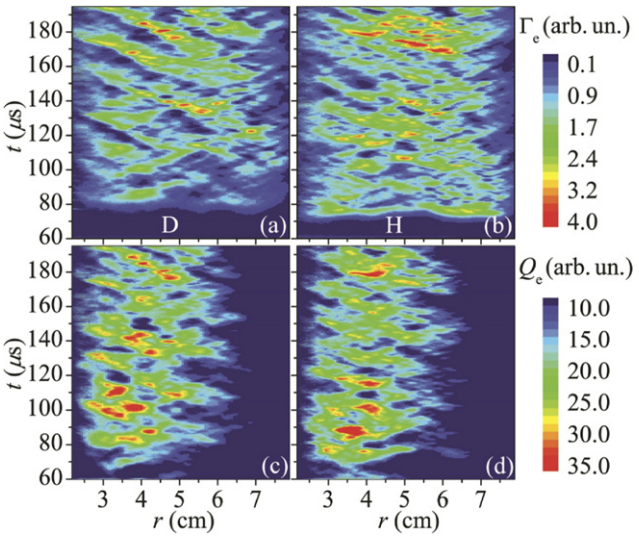

Figure 37. Temporal and spatial distributions of the electron particle Γ_e (*a*) D- and (*b*) H-discharges, and energy Q_e fluxes (*c*) D- and (*d*) H-discharges from ELMFIRE global simulations. Adapted from [250].

the gap between the value of the GAM velocity observed in experiments/simulations and linear and quasi-linear theories.

The dependence on elongation was studied with the ORB5 and GENE codes. Figure 34 show the effect of elongation on the frequency and growth rate compared to those of the cylindrical case from ORB5 simulations along with the comparison with theoretical dispersion relation [243]. The comparison of ORB5 and GENE results [138] are shown in figure 35 as compared with the analytical expressions from Gao-2009 [242]. For the comparison the values from Sugama-2006, 2008, [75, 76] which have no elongation dependence are shown as well. Note that the expressions of Gao-2009 and Sugama-2006 for the real frequency are identical in the absence of elongation for elongation parameter $e = 1$, except that the $1/q^2$ correction to the frequency is assumed small and shown in Gao-2009 as the expansion.

Also simulations with drift-kinetic electrons have been performed and compared with the case of adiabatic electrons [138]. Effects of the finite electron mass have been studied as a measure of the importance of the kinetic electrons vs the approximation of the adiabatic electrons usually used in the analytical theory. Large differences (order of magnitude) in the growth rate are observed between the numerical simulations with kinetic and adiabatic electrons. Generally smaller influence of the kinetic electrons on the growth rate was observed in numerical simulations with GTC code [127], see figures 8 and 9. Further studies of the GAM frequency and growth rates with linear GK simulations with ORB5 performed with kinetic electrons with realistic electron/ion mass ratio, temperature profiles and elongation are reported in [241].

The effects of kinetic electrons on GAM damping were studied with full-f GK codes GYSELA and ORB5 [128]. The scaling of the GAM damping rate with the ion to electron mass ratio, the electron to ion temperature ratio, the safety factor, and the aspect ratio were investigated showing good agreement

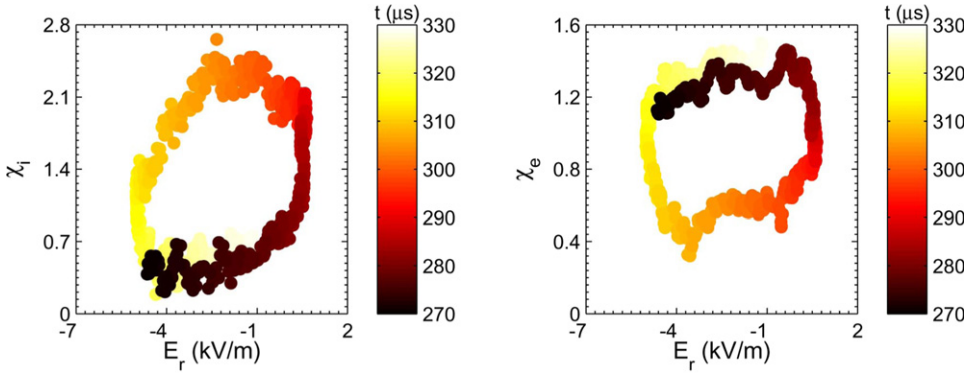

(a) Cyclic oscillations of E_r and χ_i (b) Cyclic oscillations of E_r and χ_e

Figure 38. Cyclic nature of the E_r and transport fluctuations in ELMFIRE simulations. Note that the temporal direction of the cycle is different for the electron and ion transport indicating opposite phase shifts. (*a*) Cyclic oscillations of E_r and χ_i. (*b*) Cyclic oscillations of E_r and χ_e. Reproduced courtesy of IAEA. Figure adapted from [253]. © 2015 EURATOM.

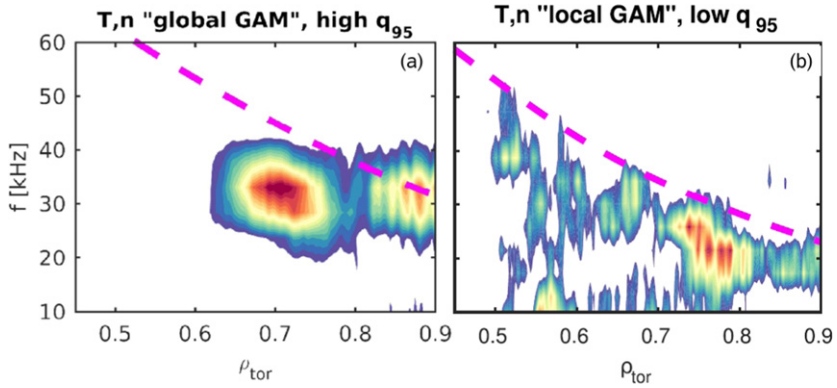

Figure 39. Power spectra of simulated $v_{E\times B}$ for (*a*) radially 'GGAM', (*b*) 'local GAM' using experimental conditions. Magenta dashed line is the analytic linear GAM frequency estimate from [117]. Adapted from [257]. © IOP Publishing Ltd. All rights reserved.

with theory in most regions of the relevant parameter space. It is worth noting that such comparisons are not straightforward, e.g. the analytical theories are typically developed for a simple harmonic eigenmode, $\exp(ik_rR)$, while in global simulations with toroidal effects and radial plasma parameters variations, the actual eigenmodes can be very different. In addition the damping rates are typically small that requires high accuracy (long runs) in simulations.

5.2. GAMs in nonlinear gyrokinetic simulations

Full global GK simulation capabilities developed in recent years have specifically addressed GAM dynamics among other phenomena for a number of experimentally relevant parameters. In this section we comment only on selected results and refer the reader to the original publications for full details.

In ORB5 simulations [244–246] the interaction of ITG turbulence, ZF and GAMs was studied as a function of plasma current and elongation effect. It was found that the radial profile of GAM amplitude is positively correlated with the q value (i.e. GAM amplitude increases with q) and, globally, inversely dependent on the total plasma. At the same time, the ion heat transport increased with the plasma current. This observation was interpreted as a result of the preferential excitation of oscillatory ZF (GAMs) rather than stationary ZFs which were proposed to be more effective in transport suppression. It was suggested that the same physics was involved in the observed dependence on elongation: the elongated equilibrium produced less GAMs and more stationary ZFs and thus lower heat transport.

TEMPEST simulations [78, 112] show GAM modes excited in the edge pedestal region of DIII-D with steep density and temperature gradients. These modes exist as radially propagating outgoing waves with a length scale determined by the temperature gradient. The latter which were found to be necessary for the radial propagation. For DIII-D conditions, GYRO simulations have shown the GAM frequency peaks in turbulent spectra and GAM induced ZF shearing in the outer region [247].

The full-f ELMFIRE GK code was used to study the turbulent transport and fluctuations in FT-2 tokamak conditions [249, 251–255]. The simulations predict the correct amplitude of GAM E_r amplitude and show the GAM frequency profile consistent with continuum GAM dispersion relation modified by the presence of impurities [248], as shown in figure 36—see section 7.4. The intensity of turbulent fluctuations and associated transport are found to correlate with large GAM intensity suggesting their connection. The radial GAM wavelength scaling in simulations was found to agree with the scaling $\rho^{2/3}L_T^{1/3}$

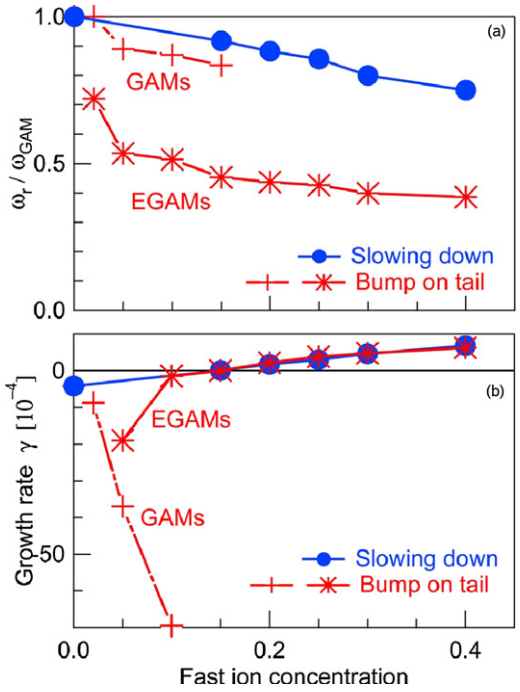

Figure 40. Dependence of (*a*) real frequency and (*b*) linear growth rate on the fast ion concentration for bump-on-tail and slowing-down distributions. Adapted from [192], with the permission of AIP Publishing.

proposed in [256]. Strong correlations of density and electron energy fluxes with GAM fluctuations are found, consistent with TEM turbulence expected in these regimes also showing the isotope scaling, see figure 37. It is interesting to note that no clear correlations between the anomalous transport and $\partial E_r/\partial r$ were found in these simulations. However the electric field E_r was found in cyclic relation with the transport as shown in figure 38.

The local and non-local nonlinear simulations have been performed with GENE code for TCV tokamak conditions [257]. By varying the discharge parameters, in particular the edge q value, two characteristic GAM regimes were reproduced as also observed in the experiments: the 'global' GAM with the radially uniform frequency and the 'local' GAM with the inhomogeneous frequency and roughly following, but noticeably below, in both cases, of the local GAM profile, see figure 39. The transition between these two regimes cannot be explained by the q values alone (see section 9.3), but seems to be a result of combination of different factors. Strong modulations of the electron and ion energy, particle fluxes and $E \times B$ velocities at GAM frequencies are observed.

The linear and nonlinear simulations of TEMs with global GTC code [258] for the parameters of HL-2A tokamak reveal GAM generation which is fed by the turbulence energy. The coupled dynamics of GAMs and turbulence exhibit typical predator–prey (PP) cycle dynamic: the GAM electric field grows while turbulence decays and the turbulence grows when the GAM decays. A comprehensive study of GAMs properties has been performed with GYSELA code for the parameters of the Tore Supra discharges in the regimes with varying collisionality. The GAM intensity is found to be larger for lower values of $\nu*$. The GAM frequency in the simulations follows the prediction of the local kinetic theory but is considerably higher than the experimental values—see section 7.5.

5.3. Linear and nonlinear dynamics of EP driven GAMs in gyrokinetic simulations

Here, numerical studies detailing linear eigenmode properties and selected nonlinear effects for EGAMs are reviewed. The linear excitation of EGAMs by EPs for bump-on-tail and slowing-down distributions in plasmas with warm bulk ions was directly demonstrated with GYSELLA simulations [192], see figure 40 which shows the behaviour of the real frequency and the growth rate of GAMs and EGAMs as a function of the EP density. These simulations have confirmed that the condition for EGAM excitation is determined by the magnitude of the (positive) derivative of the high energy particles at the resonance velocity with respect to the stabilizing Landau damping from bulk thermal ions. The critical (for EGAM excitation) density of EPs determined from the simulations was found to be in agreement with theoretical estimates.

The verification of the EGAM frequency and growth rates with the NEMORB code against the theoretical dispersion relation was reported in [193] for the case of the double-hump distribution of EP, as is shown in figure 41. For $q = 2$ this EGAM is the mode born out of the original GAM. For $q = 3$ the excited mode occurs from the initially highly damped mode, and therefore is a different branch from GAM, as shown in figure 41 (bottom). This behaviour is consistent with theoretical analysis of the relation of GAM and EGAM branches in plasmas with warm ions [193, 194] as discussed in section 3.3.

In general, good agreement between the theoretical calculations of the EGAM frequency and growth rate for a double-hump distribution are shown with several codes: NEMORB [193], figure 41, ORB5 [259], figure 42, and GYSELA [260] for different species of EP, figure 43. Likewise good agreement between the linear results from GYSELA and NEMORB was found [240].

The approach in [261] follows that of the original paper [45] with emphasis on a more general case of the EP distribution that covers the range from the initial bump-on-tail distribution to the fully slowing-down distribution for plasma parameters similar to those in DIII-D experiments [44]. The dependence of the EGAM frequency and growth rate as a function of the EP pressure, beam velocity, transverse energy (EP gyroradius), and pitch angle were studied. The correlation of the width of the EGAM eigenmode with the EPs orbit width was demonstrated, so that the eigenmode extends radially as the EP distribution was changed from bump-on-tail to fully slowing-down. It was also shown that for the case of the bump-on-tail distribution the EGAM frequency is higher (by about 25%). One of the important results is that the EGAM instability threshold for the bump-on-tail distribution is much lower.

A series of numerical studies of EGAMs were performed with a hybrid MHD-kinetic code MEGA [262–265] where the EP distribution was calculated with the δf method and current-coupling was used for the EPs. The slowing-down distribution function was used for EPs with balanced beam, as in LHD experiments [266]. These simulations confirm the basic

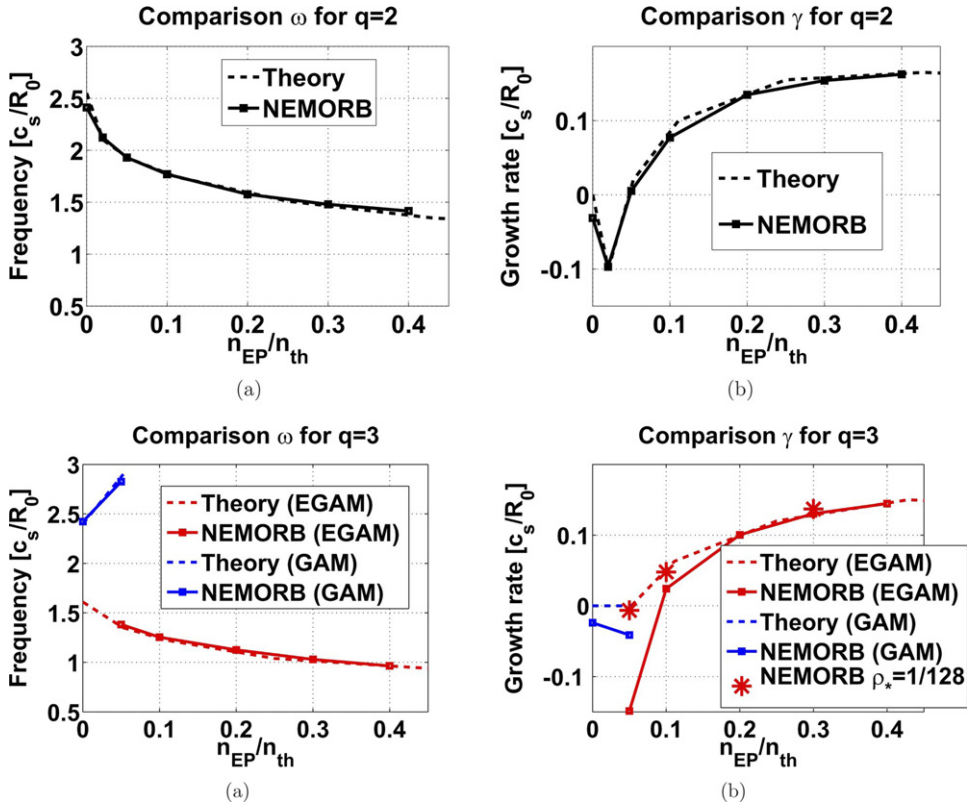

Figure 41. Comparison of frequency and growth/damping rates between NEMORB simulations with adiabatic electrons and predicted values from the dispersion relation for $q = 2$ (top) and $q = 3$ (bottom). Reproduced courtesy of IAEA. Figure adapted from [193]. © 2014 EURATOM.

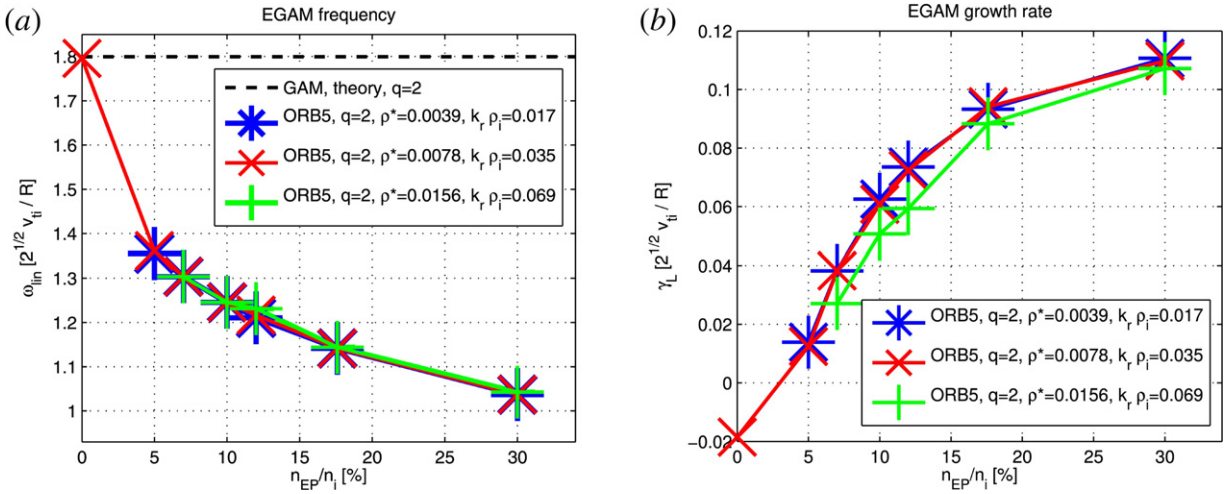

Figure 42. (*a*) Frequency and (*b*) growth rate versus EP concentration for simulations with $v_{\mathrm{bump}}/v_{\mathrm{th}} = 4$. Black dash-line shows theoretical GAM frequency from [11]. Adapted with permission from [259]. © EUROfusion Consortium Research Institutions 2017.

structure of the EGAM as a global mode with $m = 0$ poloidal velocity, $m = 1$ plasma density, and $m = 2$ magnetic field perturbations, as shown in figure 44.

The radial structure of EGAMs was also studied in [267], which reports $m = 2$ sidebands, both $\cos 2\theta$ and $\sin 2\theta$ of comparable amplitude, as well as the presence of a noticeable $\cos\theta$ component in the perturbed potential, in addition to the standard $\sin\theta$, figure 45. It is worth noting that the $m = 2$ sidebands in [262] are EM and are responsible for the global character of the EGAM, while simulations of [267] are electrostatic. Observation of the $\cos\theta$ and $\sin 2\theta$, which normally are not excited in GAMs, may be a manifestation of the effect discussed in section 3: the coupling to the $\cos\theta$ and $\sin 2\theta$ occurs as a result of the $v_{\|}$ asymmetry in the EP distribution function, as follows from equation (151) and the definition of the coupling coefficient $L^{\mathrm{h}}_{\mathrm{sc}}$ in equation (142). Similar coupling to the $\cos\theta$, and $\sin 2\theta$ density also occurs due to plasma rotation [268] and plasma radial gradients as discussed in section 2.13.

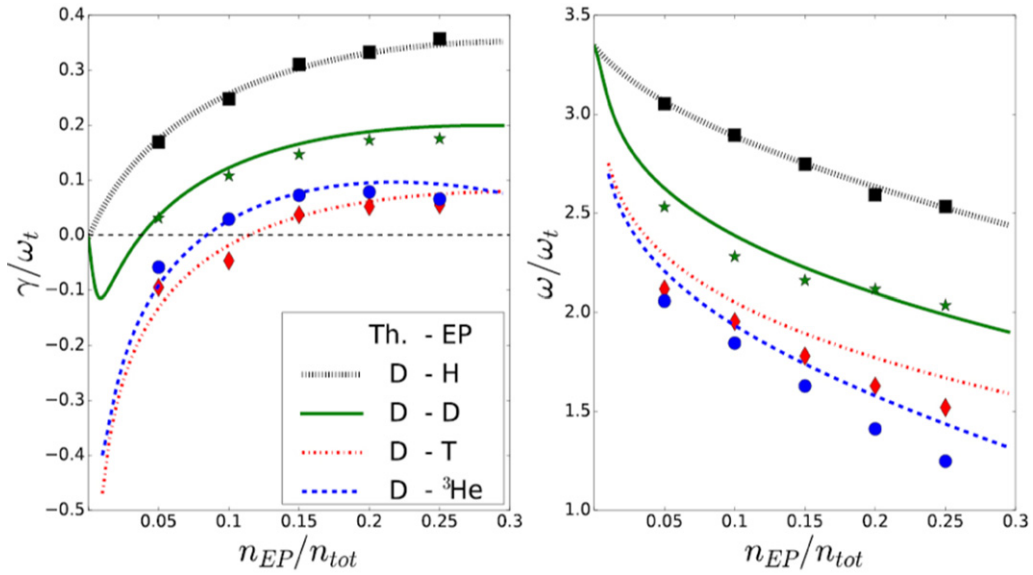

Figure 43. Frequency (left) and growth rate (right) of EGAM as predicted in [194] and as measured from GYSELA simulations (symbols) for the same parameters. Reproduced courtesy of IAEA. Figure adapted from [260]. Copyright (2018) IAEA.

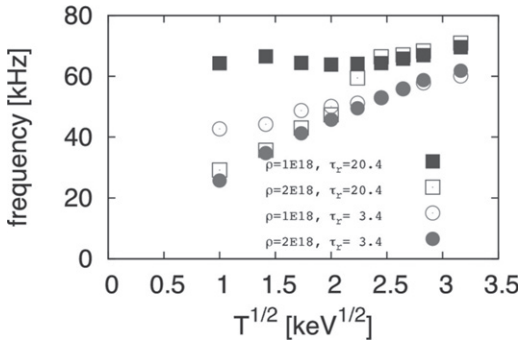

Figure 44. Perturbed variables of the EGAM in poloidal cross section: (*a*) poloidal velocity $v\theta$ (km/s), (*b*) plasma density, (*c*) poloidal magnetic field (10^{-6} T), and (*d*) radial magnetic field 10^{-6} T. The dominant poloidal mode numbers are (*a*) $m = 0$, (*b*) $m = 1$, (*c*) $m = 2$, and (*d*) $m = 2$. Adapted from [262], with the permission of AIP Publishing.

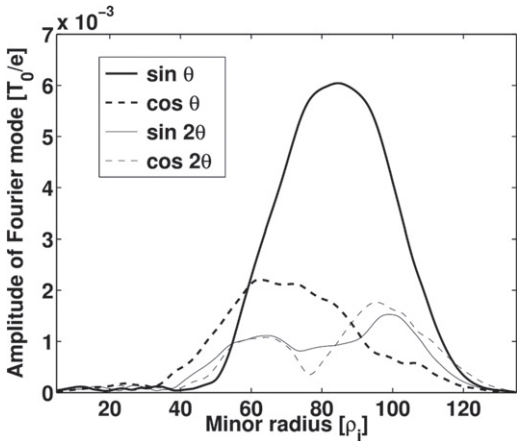

Figure 45. Radial profile of $m = 1$ (thick) and $m = 2$ (thin) poloidal components of electrostatic potential oscillation at EGAM frequency. Sine and cosine components are shown by solid and dashed lines respectively. Reproduced courtesy of IAEA. Figure adapted from [267]. © EURATOM 2017.

The extension of MHD-kinetic MEGA model included the inertia of EPs [263]. The appearance of the high frequency EGAM mode (above the GAM frequency and weakly dependent on the bulk ion temperature) was demonstrated in conditions similar to LHD experiments. This higher frequency mode is one of the EGAM eigenmodes identified as damped mode in [45]. Here, it is destabilized by the bump-on-tail EP distribution due to the resonance of passing particles. These and other results of such simulations, as well as the comparison with the experimental data, are discussed further in section 13.

High energy particles will be a substantial reservoir of free energy in fusion plasmas. Therefore, EGAMs excited by EP particle are expected to significantly affect the turbulence, energy balance and transport in a tokamak. It was suggested theoretically [269] that GAMs driven by EPs (EGAMs) can effectively heat bulk ions and thus transfer energy from EPs to thermal plasmas (GAM channelling). The energy transfer between the EP, the mode and thermal particles was investigated in detail [193] with the NEMORB code and also with the extended MEGA code where the thermal particles are also described by the kinetic equations thus including the Landau damping on thermal ions [265]. An example of the energy channelling facilitated via the excitation of the EGAMs is show in figure 46.

The role of EGAMs in plasma turbulence and transport overlaps with the general problem of instabilities and transport associated with EPs in toroidal fusion plasmas which has been a subject of intense interest and numerous publications, cf reviews [180, 270] and references therein. Here, we discuss only selected examples of EGAMs numerical simulations illustrating some nonlinear effects discussed in this review.

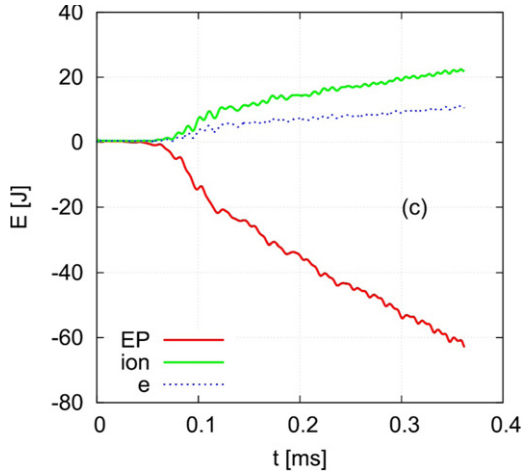

Figure 46. EGAM energy channelling: energy transfer between thermal and EP particles during EGAM activity. Reproduced courtesy of IAEA. Figure adapted from [265]. Copyright (2019) IAEA.

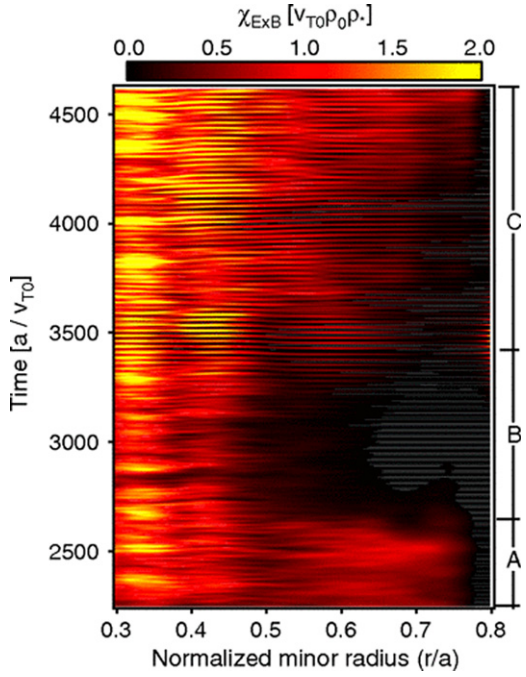

Figure 47. Contour map of thermal diffusivity modulated by EGAMs as function of time. Adapted figure with permission from [271], Copyright (2013) by the American Physical Society.

The excitation of EGAMs embedded in ITG turbulence and their effects on anomalous transport is demonstrated in [271]. The EPs excite EGAMs enhancing the transport and leading to the destruction of the transport barrier. The energy transport appears to be modulated by EGAMs, as shown in diffusivity, figure 47 and temperature gradients profiles, figures 9(*a*) and (*b*) [271], but no turbulence suppression is observed. The effects of EGAMs on the turbulence was studied further in [267] which shows the EGAM destruction of the staircase structure that existed without EPs, thereby allowing more extended radial transport that was inhibited by the staircase. In general, the heat flux is increased with the presence of EGAMs.

The three-way coupling between EGAMs and turbulence modes was also revealed via bispectral analysis [267]. The wavelet bispectra in figure 48 show the coupling of ω_1 and ω_2 modes through the third mode $\omega = \omega_1 + \omega_2$. The spectra in the top row show the interactions that occur before the EGAM is excited (top left) and in the linear EGAM stage (top right) when the interaction is mainly via the zero frequency mode, $\omega_1 + \omega_2 = 0$, as shown by the crossing of the ω_1, ω_2 line at 0. At later times, shown in the bottom row, when the EGAM is well into the nonlinear and saturated states, the crossing clearly occurs at finite $\pm\omega_{\mathrm{EGAM}}$ frequencies, indicating nonlinear interactions of turbulent modes and the EGAM zonal component, $\omega_1 + \omega_2 = \omega_{\mathrm{EGAM}}$.

The nonlinear phase space features of the EGAM excitation by resonant EPs are examined in [259, 260, 272]. It is shown in [260] that flattening of the EP distribution function in phase space occurs via the particle trapping and formation of an island in $(v_{\|}, \theta)$. The EGAM induced EP losses occur due to the interaction and overlap of the separatrix of the EGAM island and the X-point of the trapping cone, so that the losses are mostly of counter-passing particles. The analogy between beam–plasma instabilities and resonant EGAM excitation has been exploited to study the EGAM saturation [259]. The maximum value of the radial electric field is found to scale quadratically with the linear growth rate, as shown in figure 49 based on ORB5 simulations. This analogy is studied further in [272] showing that the deformation of the EP distribution is similar to the evolution of the distribution function in the 1D plasma–beam system.

6. Overview of experimental observations

In this section a collation of experimental GAM results are presented in the form of tables organised by device (following a rough chronological order of discovery) for three categories: tokamaks, helical/stellarator devices and other toroidal devices. The intent is to provide a resource of currently published work. Although GAMs are ubiquitously observed in a range of configurations and devices, reports of their absence are equally important in confirming expected parameter dependencies and in the validation of theory and numerical codes. The banner line for each device gives the machine dimensions, the main configuration, principle gas isotope, available heating schemes (OH = ohmic, NBI = neutral beam injection, ECH = electron cyclotron heating) and the principle diagnostics used in the study of GAMs. The diagnostic abbreviations are given in section 6.4.

6.1. Tokamak devices

The focus of early works was on reporting first existence and the fundamental characteristics of the GAM. Although many works were already contrasting results to theory, they also helped to highlight the deficiencies in early theory and modelling (which tended to concentrate idealized circular, large-aspect-ratio configurations) and to provide an impulse for

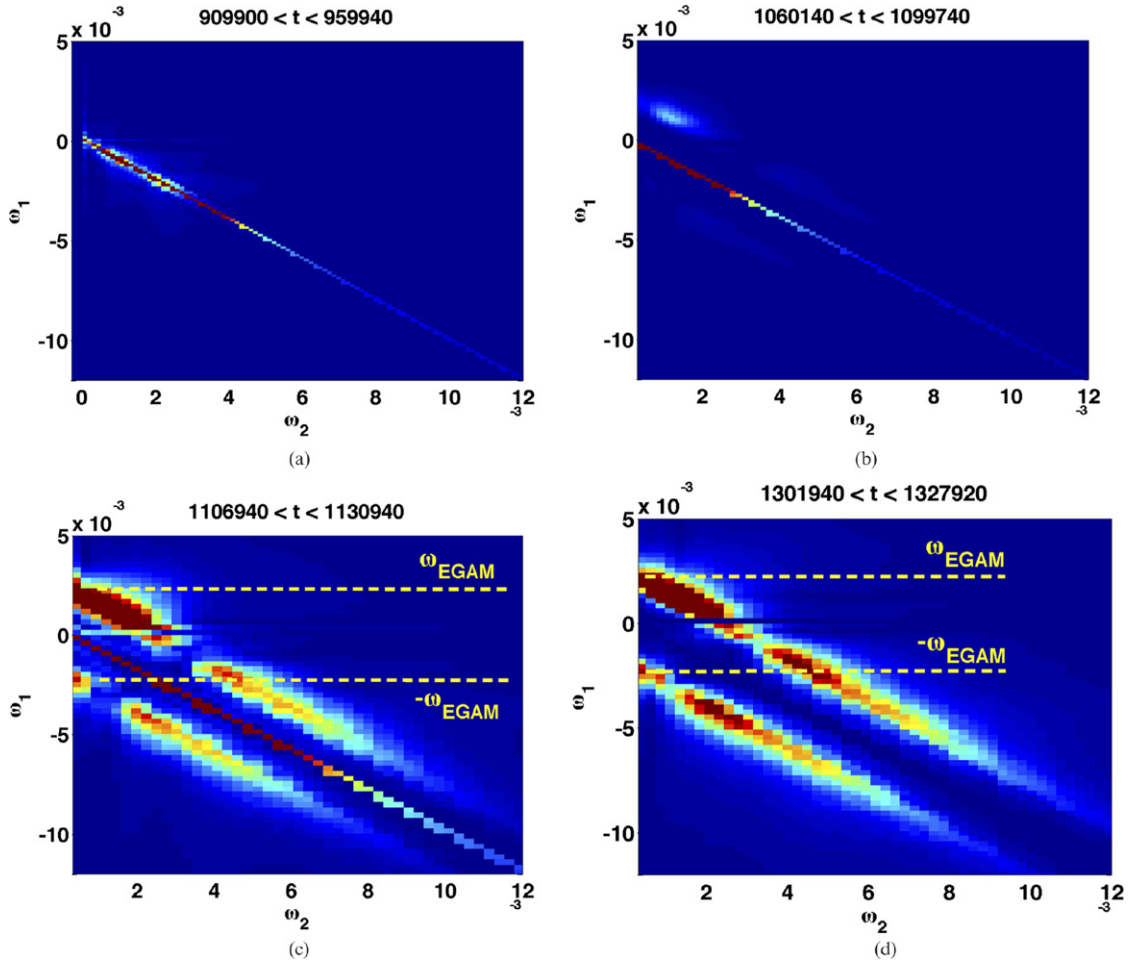

Figure 48. Wavelet bispectra showing nonlinear interactions $\omega_1 + \omega_2 = \omega$ occurring for $\omega \simeq 0$, in early (top) and late times for $\omega = \omega_{\mathrm{EGAM}}$ (bottom). Reproduced courtesy of IAEA. Figure adapted from [90]. © EURATOM 2017.

more comprehensive modelling in matching the GAM frequency and amplitude behaviour in real devices. Reports of detailed investigations followed on parameter scaling and turbulence–GAM interactions using bicoherence and non-linear data analysis techniques. Also, first indications of the non-electrostatic nature of GAMs via observations of the magnetic-halo field and multi-diagnostic approaches appeared. More recent topics include attempts at external control or excitation of natural GAMs with a view to modifying edge transport, or even triggering confinement mode transitions. The final area is the interaction of GAMs with magnetic islands—either natural MHD modes or induced edge magnetic field perturbations via RMP coils (table 7).

6.2. Stellarators and helical devices

While natural turbulence driven GAMs were initially predicted to be weaker in stellarators and helical devices compared to tokamaks [59], measurements from CHS provided some of the most convincing early GAM observations [398]. In addition, one of the earliest mentions of a GAM-like flow oscillation was from the W7-AS stellarator [399]. While the measured $f \sim 10$ kHz was close to the Winsor prediction, the measurement location was just 2 cm inside the last-closed flux surface (LCFS) where the high $\iota/2\pi = 1/q$ might be expected to strongly damp GAMs, and just before an H–L back transition, suggesting a limit cycle oscillation (LCO) [400].

While an acoustic-like mode (an $m = 2$, 20 kHz close to the GAM frequency) was reported in the U-3M torsatron using magnetic probes [401], many helical devices do not appear to show GAMs. Neither the Heliotron-J, HSX, and to-date nor W7-X devices have reported natural GAM activity, despite searching. On the other hand, core EGAMs and Alvén eigenmode driven GAMs are now substantiated in stellarators and helical devices (table 8).

6.3. Other devices

Although there is ample evidence of GAMs in the core regions of helical and stellarator devices, there appears to be a distinct absence of them in reverse field pinch (RFP) configurations. The overall low safety factor $q < 1$ (i.e. strong Landau damping), plus the presence of strong, broad-spectrum tearing mode (TM) activity leading to a chaotic or ergodic field topology (with similarities to the RMP effects in tokamaks) tends to make RFPs rather unfavourable for GAMs [424]. As such, the

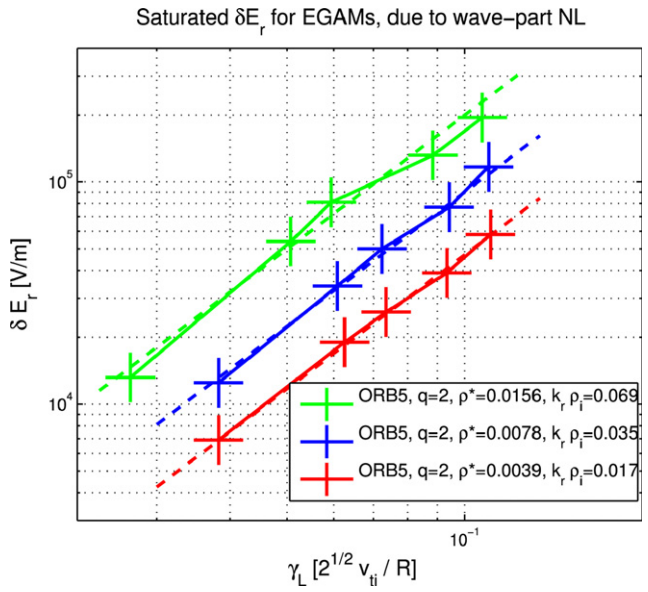

Figure 49. Maximum EGAM E_r vs linear growth rate for figure 42 for $\rho^* = 0.0039$, 0.0078 and 0.0156. Adapted with permission from [259]. © EUROfusion Consortium Research Institutions 2017.

number of specific ZF and GAM related reports is very limited. Nevertheless, ZFO signatures are beginning to appear in experiments and numerical simulations [425]. Further details of the measurements listed in table 9 are given in section 16.5.

6.4. Diagnostic techniques

What can be experimentally measured on the GAM depends on the availability and resolution of the diagnostics. The principle distinction of the GAM is the plasma potential oscillation $\tilde{\phi}$, or the corresponding radial electric field $\tilde{E}_r$, or the perpendicular plasma flow $\tilde{v}_{E\times B}$. This was the first aim of early measurements, via heavy ion beam probe (HIBP), LPs, beam emission spectroscopy (BES) and microwave reflectometry techniques. In recent years many diagnostic opportunities have evolved which now allow simultaneous multi-diagnostic measurements of multiple GAM fields, including E_r, n_e, T_e and B_θ using familiar diagnostic techniques. The following is a brief summary of the currently employed techniques and their capabilities.

HIBP measures the local electric potential $\tilde{\phi}$, the electron density $\tilde{n}_e$ and possibly magnetic field $\tilde{B}$ fluctuations with high temporal and spatial resolution. As a singly charged, accelerated (hundreds of keV) heavy ion 'primary' beam, such as K^+ or Tl^+, propagates through the plasma it experiences electron impact ionization creating doubly charged 'secondary' beams, such as K^{2+} or Tl^{2+}, which are detected externally. The position and number of sample volumes is determined by the beam trajectory and the diagnostic sophistication. Sweeping the beam injection angle increases the measurement coverage. The difference in the energy between the primary beam and the detected secondary beam is equivalent to the local ϕ at the ionization point (relative to the wall). In addition, the fluctuation of secondary beam current is proportional to $\tilde{n}_e$, though the path integral effect should be taken into account. In principle the diagnostic can give core to near edge coverage even in high temperature plasmas. Data analysis techniques, such as cross-correlation, are used to extract the GAM signature [36]. A further diagnostic development is the detection of the horizontal movement of the secondary beam which is proportional to the poloidal magnetic field. Thus a localized spectrum of $\tilde{B}_p$ can give information on the GAM's zonal magnetic field structure [406, 407]. HIBP has also been used to measure the cross-phase between $\tilde{n}_e$ and $\tilde{\phi}$ on JFT-2M [32, 317]. HIBP was one of the first GAM measurement techniques and has been employed on several devices: TEXT [30], CHS [33, 406, 407], JIPPT-IIU [36], JFT-2M [317, 318], T-10 [292, 298], TUMAN-3M [333, 428] and LHD [429].

LPs measure the potential $\tilde{\phi}_f$ (floating probe), and $\tilde{n}_e$ (biased probe). Probes offer good temporal spatial resolution, but are restricted to the far plasma edge or low power discharges and are most often mounted on fast reciprocating shafts. To interpret the probe floating potential as plasma potential requires knowledge or an assumption on the magnitude of the electron temperature fluctuations $\tilde{T}_e$. Mostly probes are used in multiple pin combinations or arrays (LPA) with both radial and poloidal/toroidal separations from which the $\tilde{E}_r \approx (\phi_1 - \phi_2)/\delta r$ is approximated. LPs have been extensively employed on many devices: DIII-D [274], HT-7 [27], H1-NF [402], T-10 [292], JFT-2M [316], HL-2A [345], IST-TOK [361], CHS hybrid probe array [408], TEXTOR [342], MAST Gunderstrup reciprocating probe [374], J-TEXT [389] and COMPASS [394].

Doppler reflectrometry/backscatter (DR/DBS) measures the propagation velocity $u_\perp = v_{E_r\times B} + v_{ph}$ of turbulent density structures moving with the plasma. Here, a microwave beam probes the plasma cutoff layer with a deliberate tilt angle to the cutoff surface so that the plasma rotation induces a Doppler frequency shift $\omega_D = u_\perp k_\perp$ in the Bragg back-scattered signal spectrum, where $k_\perp = 2k_0 N_\perp$ is the probing wavenumber with $N_\perp$ the refractive index at the cutoff location (which is obtained with ray-tracing and separate density profiles) [304]. Since the measured flow velocity contains the $E_r \times B$ velocity, fluctuations in E_r will appear directly as fluctuations in the Doppler frequency shift—with the assumption that fluctuations in turbulent phase velocity $\tilde{v}_{ph} \sim 0$. The amplitude of the back-scattered signal is also a measure of the $(\delta n/n)^2$ of the turbulence at the probed $k_\perp$. The flow and turbulence spectra are typically obtained by extracting the spectral peak frequency and amplitude as function of time using a temporally sliding FFT on the raw reflectometer data. The measurement is thus direct in the sense that the velocity is obtained directly from the Doppler shift, but is indirect in that the turbulence is used as a tracer. If there is no turbulence then there is no back-scattered signal. The need for a 'reasonable' back-scattered signal tends to restrict probing access to the plasma edge region. Pairs of DR systems separated toroidally or poloidally have also provided information on the long-range correlation (LRC) properties of the zonal/GAM flow perturbation. DR has been employed on several machines including: AUG [304], DIII-D [280, 282], Tore Supra [372], Globus-M [384, 386],

Table 7. GAM observations in tokamak devices.

DIII-D	$R/a = 1.66/0.67$ m, divertor: D_2: NBI: BES, DBS 2001: suggestions of GAM/ZF in edge [273, 274] 2002–03: first clear results/observations 28, 29, 275–277] 2006: GAM to ZF transition [278] 2007–08: basic properties [279, 280] 2008: NBI driven EGAM [44] 2009: GAM and rotation [281] 2012–13: structure and drive/damping [282], peak splitting [247], multi-field measurements [283] 2013: GAM/ZF at L–H transition [284]
HT-7	$R/a = 1.22/0.27$ m, Circ. limiter, D_2: OH: LPA 2002: low freq. ZF near GAM frequency using edge probes [27] 2010: spectral characteristics [285, 286] 2013: nonlinear coupling between multiple-KGAMs [287] 2015: using collective scattering of density [288]
TEXT	$R/a = 1.0/0.28$ m, circ.: HIBP 2003: first measurement using HIBP [30, 289] 1993: retrospective—quasicoherent modes as possible GAMs [39, 290]
T-10	$R/a = 1.5/(0.27–0.30)$ m, circ. lim., D_2: OH, ECH: CR, HIBP, MPA, LPA 2003: low freq. potential mode—possible GAM [41] 2005–13: edge and core continuum GAM [34, 291–293] 2016: He puffing effect [294] 2015: MHD effect on GAM [295] 2015–17: core GGAM [294, 296–298] 2017: GAM–turb. interaction [299, 300] 2018: GGAM scaling [301], ECRH driven [302, 303]
AUG	$R/a = 1.65/0.5$ m, Div., D_2: NBI, ECRH, ICRH: DR, PCR, MPA 2004–05: first observations [31, 304] 2008: parameter scaling [26, 305] 2011: GAMs across L–I–H-mode transition [306] 2015: GAM modulation of WCM in I-mode [307] 2015: RMP impact on GAM [308] 2016: frequency scaling comparison to models [309], mode structure and propagation [310–312] 2016: core EGAM [313] 2018: envelope analysis [314] 2019: non-linear transfer [315]
JFT-2M	$R/a = 1.31/0.35$ m, divertor, NBI & ECH: HIBP, LPA 2005: non-linear coupling [316] 2006: eigenmode GAM and radial propagation [317] 2006: turbulence and turbulent flux modulation [318] 2006: non-linear coupling [233, 319, 320] 2006: L–H trans. [321] 2009: eigenmode GAM close to the separatrix [322] 2013–14: GAMs at L–H trans. [323, 324] 2018: GAM drive: RS vs DS [325]
JIPPT-IIU	$R/a = 0.91/0.23$ m: circ. limiter: OH & NBI: HIBP 1997: retrospective—quasicoherent modes as possible GAMs [40] 2005–7: [36, 326–328] 2010–12: core GAMs [329–331]
TUMAN-3M	$R/a = 0.52/0.24$, circular OH & NBI: HIBP 2005: first edge GAM profiles [35] 2011: GAM over L–H transition [332, 333] 2013–16: isotope impact [334, 335]

Table 7. (Continued)

TEXTOR	$R/a = 1.75/0.48$ m, circular: PCR, LPA 2006: frequency and isotope scaling [336, 337] 2007: radial extm. and mag. island interaction [338] 2009: GAM structure and turb. interaction [339] 2010: GAM structure, bicoherence with LP [340] 2011: LRC of GAMs [341], radial propagation and γ scaling [342] 2012: ACFM analysis method, GAM amp. profile [343] 2013: isotope effect on GAM LRC [344]
HL-2A	$R/a = 1.65/0.4$ m, circ. limiter: OH, H_2: LPA, MPA 2006–10: basic obs. [141, 345–350] 2013: EGAM [231] 2013: GAM/ZF with ECRH [351] 2016: synchronization of GAM & magn. fluctuations [352, 353] 2017: coexisting GAMs [354] 2018: GAMs and density limits [355] 2018: L–H transition [356]
JET	$R/a = 3.0/1.25$ m, divertor, D_2: NBI, ICRH: DBS 2006: ICRH driven core GGAM [12, 13] 2013–16: GAMs using probes and DR [357, 358] 2018: GAM scaling studies [359] 2018: L–H transition [360]
ISTTOK	$R/a = 0.46/0.09$ m, circ. limiter: LPA 2008–9: long range correlations [361, 362] 2012: impact of plasma biasing [363] 2018: shearing [364]
EAST	$R/a = 1.88/0.45$ m, divertor, LHCD, ICRF, ECRH: DBS 2011: GAM only at low density and high q. Does not appear to play a role in L–H transition. No GAM in H-mode [365] 2013: GAMs in probe V_f [366] 2015: various GAM analysis methods with DR data [367] 2018: structure [368] 2018: GAM in weak H-mode [42] 2019: No GAMs in I-mode [369]
JT-60U	$R/a = 3.37/0.84$ m, divertor, NBI, ECH, LHCD 2012: EGAM [370]
NSTX	$R/a = 0.85/0.68$ m, NBI: GPI 2011: plausible observation [371]
Tore Supra	$R/a = 2.39/0.72$ m, circ. lim. ICRH: DR 2012: scaling [372] 2015: GAM scaling compared with modelling [373]
MAST	$R/a = 0.85/0.65$ m, divertor: LP 2012: RMP impact and fluid simulations [374, 375] 2018: radial wavenumber estimates [376]
Alcator C-Mod	$R/a = 0.68/0.21$ m, divertor, ICRH: GPI 2013: GAMs and WCMs in I-mode [377] 2015–17: GAM–ZF coupling [378, 379]
TCV	$R/a = 0.88/0.25$ m, multi-X-point, ECR heated 2013–4: multi-field measurements [380–382] 2018: GAMs in SOL [383] 2019: triangularity scan [157]

Table 7. (Continued)

Globus-M	$R/a = 0.36/0.24$ m spherical tok.: OH 2014: scaling and localization [384, 385] 2015–16: multi-diagnostic measurements [386, 387]
FT-2	$R/a = 0.55/0.08$ m, circular, H_2: OH: Doppler UHR BS 2013: structure [255] 2015: DR meas. with comparisons to ELMFIRE gk code [388] 2016: isotope effect [250]
J-TEXT	$R/a = 1.05/0.26$ m, circ. limiter, OH: probes 2015: GAMs suppressed with RMPs [389] 2016: GAMs enhanced with biasing H-mode [390] 2015–17: GAMs, MHD islands and enhanced RS [391, 392] 2019: effect of RMPs on GAMs [393]
COMPASS	$R/a = 0.56/0.2$ m, divertor, NBI: probes 2017: EM GAMs [394]
SINP	$R/a = 0.3/0.075$, circular, OH 2017: parameter scaling studies [395] 2018: effect of plasma biasing [396]
STOR-M	$R/a = 0.46/0.12$ m, circular, OH: LPA 2018: GAM-like oscillation suppressed by RMPs [397]

TJ-II [417], TUMAN-3M [35, 387], FT-2 [428], JET [358], EAST [42, 368], HL-2A [430], FT-2 [255] and W7-AS [399].

Poloidal correlation reflectometry (PCR) measures the propagation velocity of density turbulent structures using correlation time delay analysis of poloidally displaced microwave reflectometer beams. Similar to DR/DBS, this techniques also uses the turbulence as a tracer for the $v_{E_r\times B}$. However, as the reflectometer beams are at normal incidence rather than tilted the reflected signal is stronger than for DR/DBS and thus can be used at lower turbulence levels. The poloidal separation between the beam pairs needs to be smaller than the poloidal correlation length of the turbulence, which is usually achieved with an array or close cluster of antennas. Pairs of standard normal incidence reflectometers at wide toroidal and poloidal separations have also registered long range correlations if they are aligned on the same field-line by varying the q profile. PCR has been employed on: TEXTOR [337], T-10 [292] and AUG [314].

BES also measures the perturbation propagation velocity $u_\perp$ of large scale turbulence structures. This was one of the first diagnostics used for GAM identification on DIII-D. The emission intensity $\tilde{I}/I \propto \tilde{n}_e/n_e$ along a heating or diagnostic neutral beam is optically imaged (usually with a fibre array) onto a 2D radial-poloidal plane. Using image processing techniques the structure flow v_θ and v_r velocity fields are extracted and further processed. As with DR it is assumed that the turbulent structures move with the local $E_r \times B$ velocity. A degree of signal averaging and/or conditioning, as well as sufficient turbulence (several percent), is usually necessary to overcome detector (photon) noise, etc. BES has been employed on: DIII-D [276] and TEXTOR (Li-BES) [343].

2D gas puff imaging (GPI) measures light intensity emission from locally injected neutral gas puffing due to electron impact excitation. The emission is sensitive to T_e and n_e as $I = An_e^{\alpha_n}T_e^{\alpha_T}$, but is principally most sensitive to $\tilde{n}_e$ fluctuations. From the 2D viewing image velocimetry analysis of structures gives information on the turbulent flow velocities. The 2D map essentially gives multi-point measurements from which mode structures and nonlinear energy transfer directions can be obtained. Employed on Alcator C-Mod [377] and TEXTOR [431] on ZFOs.

Upper-hybrid-resonance DBS measures the turbulence propagation velocity in the Doppler shift in the back-scattered. The technique is similar to DR except that the microwave probe beam is back-scattered from the upper-hybrid resonance layer. In order to access the upper-hybrid cutoff the probe beam is launched from the tokamak high-field side. Due to the technical constraints the technique has so far only been employed on FT-2 [255].

ECE and correlation ECE measures radiative electron temperature fluctuations from the electron cyclotron emission. The GAM is expected to have a pressure sideband, which in principle could have a measurable $\tilde{T}_e$ component. To extract $\tilde{T}_e$ the plasma should be optically thick to avoid contamination from the density fluctuations $\tilde{n}_e$, which for the tokamak plasma edge requires reasonably high densities and strong GAMs. For typical horizontal ECE lines of sight (LoS) the measured signals will be close to the node of the $m = 1$ pressure sideband. Vertical viewing ECE LoS would be of particular interest. Even in optically thin plasmas, ECE can provide information on the $m = 1\,\tilde{n}_e$ component. When combined with a normal incidence reflectometer with the same probing LoS information on the GAM's cross-phase angle α_{nT} between the density and temperature fluctuations may be obtained [283]. (C)ECE has been employed on: TCV [381], DIII-D [283] and LHD [432] for LRC of edge modes.

Magnetic probe arrays measure the external $\tilde{B}$ component of the GAM. As part of the standard diagnostic suite many

Table 8. GAM observations in helical devices.

H-1 heliac	$R/a = 1.0/0.22$ m, 3 period flexible heliac, ICRH: LPA 2002: GAM-like oscillations [402, 403] 2006: spectral transfer [37, 404]
W7-AS	$R/a = 2.0/0.17$ m, 5 period stellarator 2004: edge flow oscillations suggestive of GAMs [399]
CHS	$R/a = 1.0/0.2$ m, $l = 2$, $m = 8$: HIBP, LPA 2006–8: natural core GAM, eigenmodes, intermittent [38, 398, 405, 406] 2007: zonal magnetic field [407] 2010: RS at L–H trans, [408]
LHD	$R/a = 3.75/0.6$ m, $l = 2$, $m = 10$: HIBP, mag. probe, interf., ECE 2010–11: EGAM in reversed magnetic shear [266, 409] 2015: high frequency EGAM [410] 2013: no natural GAM observed [411, 412] 2016–17: subcritical GAM excitation [413–415]
TJ-II	$R/a = 1.5/0.22$ m, 4 period heliac, ECH: DRefl. 2012: core flow oscillation [416] 2015: AE driven core GAM & EGAMs [417] 2016: core GAM candidate [418, 419] 2018: ECRH enhanced LRC of ZFO [302]
TJ-K	$R/a = 0.60/0.10$ m, $l = 1$, $m = 6$ torsotron: LPA 2009: possible GAM in energy trans. [420] 2010: no coherent GAM observed [421] 2015: low freq. $m = 6$ edge density mode (reflecting six-fold magnetic field structure) with ZF scaling [422]
HSX	$R/a \sim 1.4/0.1$–0.2 m 4-period quasi-helical stellarator, ECH: LPA 2011: no GAM during biasing, but increased LRC and bi-coherence [423]

Table 9. Observations in RFP devices.

RFX-mod	$R/a = 2.0/0.46$ m, ohmic: LPA 2011: absence of ZF LRC [426]
MST	$R/a = 1.5/0.50$ m, ohmic: LPA 2019: low freq. < 10 kHz, edge ZFO—not thought to be a GAM [427]

devices are equipped with a range of poloidal and toroidal arrays of Mirnov coils (B_θ) as well as B_r coils, which are usually mounted closer to the plasma boundary. These coils allow the GAM *halo field* structures (poloidal and toroidal) to be measured. Less common are magnetic coils mounted on reciprocating probes which can provided internal or radial structure measurements. Inside the plasma HIBP has also been used to measure the GAM *zonal* poloidal magnetic field B_θ on CHS up to 200 kHz [407]. Magnetic coil arrays have recently employed on several devices: JT-60U [370], DIII-D [283], TCV [382, 383] AUG [307, 311], Globus-M [386] and EAST [433].

Tangential phase contrast imaging (TPCI) measures the integrated electron density fluctuations, however, spatial resolution is achieved via toroidal geometry and spatial filtering of the signal. The tangent point to the LoS chord gives the radial localization. In TCV radial profiles were obtained by vertically shifting the plasma column [380].

Other diagnostics have also been employed, including a variety of 'exotic', i.e. non-standard diagnostics, such as camera arrays of XUV detectors ($I_{XUV} \propto n_e$) in EAST [433] suggesting the possibility of future tomographic reconstructions. Also on EAST solid-state neutral particle analyser detectors with toroidal LoS (tangent point gives radial localization) have been used to monitor energetic ion losses at the GAM frequency, as well as soft x-ray (SXR) cameras ($\propto n_e$ & T_e) for ZFOs [433]. D_α emission has also been used on Globus-M. Although the emission depends on n_e, T_e as well as neutral density, fluctuations are expected to be dominated by $\tilde{n}_e$ [386]. Line integrated $\tilde{n}_e$ signals from edge and core FIR interferometer chords were also used on JT-60U [370]. Collective scattering using a CO_2 laser with multiple detectors has also been used on HT-7 [288].

7. GAM characteristics

This section reviews the basic characteristics of the GAM and its identification in experiments and simulations. Experimental results are presented together with the corresponding theory and simulations with the aim to assess the degree of convergence (or not) between them. Starting with evidence for the acoustic nature of the GAM in the simplest geometry, i.e. a limited, circular poloidal cross section in large

aspect ratio devices dominated by toroidal (tokamak) geodesic curvature, in section 7.1, where the continuum GAM frequency should scale with the local sound speed c_s (as $\sqrt{T}$ and inversely with the ion mass m_i) and inversely with the major radius R_0. The basic GAM amplitude behaviour follows in section 7.2. Even in the simplest of geometries additional dependencies are predicted, such as the electron to ion temperature ratio $\tau_e = T_e/T_i$ and collisionality ν—see table 3. Theory also indicates the important role of equilibrium pressure anisotropy $p_\parallel \neq p_\perp$ (section 2.3) and this is discussed further in section 7.3. The expected isotope dependence and effective ion mass m_{eff} are addressed in section 7.4, and the more complex effect of impurities in section 7.5. The complexity increases with the introduction of plasma shaping (elongation κ, triangularity δ, Shafranov shift Δ, inverse aspect ratio ϵ_o, etc) in section 7.6. Further, the presence of a poloidal divertor introduces a flux surface separatrix with one or more B-field nulls (X-points) which strongly modifies the edge poloidal (up–down) symmetry. The impact of non-limiter shapes is discussed in section 7.7. Subsequent sections will then address the GAM's modal structure, it is radial structure and localization, propagation, and the impact of plasma rotation.

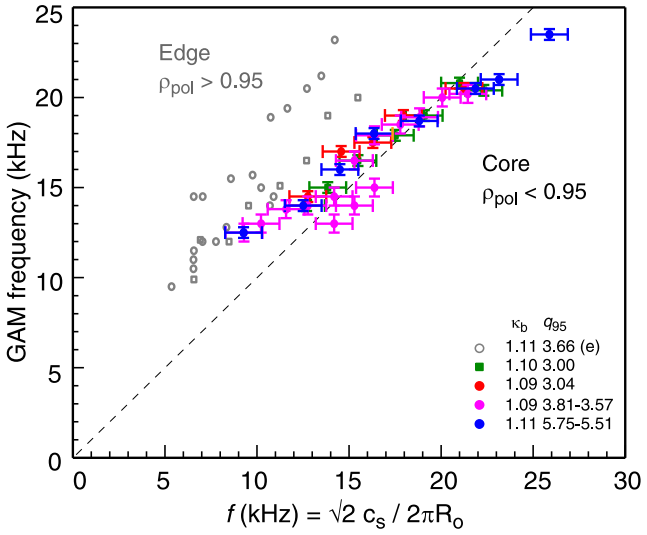

Figure 50. Measured GAM frequency vs 'Winsor' scaling $f_{GAM} = \sqrt{2}c_s/(2\pi R_0)$ with $c_s = \sqrt{(T_e + T_i)/m_i}$ from experiment for core (solid) and far edge (open) GAMs with various q_{95} in ohmic, circular, limiter AUG plasmas. Reproduced from [305]. © IOP Publishing Ltd. All rights reserved.

7.1. Acoustic nature

The foremost characteristic of the basic turbulence driven GAM is its acoustic nature, namely its frequency should scale with the plasma sound speed c_s with no strong Alfvénic (i.e. density) dependence. (Note BAE type modes and ACs, which are not strictly GAMs—cf section 2.12—are not considered here.) The sound speed c_s for a single species, fully ionized plasma, where both ions and electrons are warm is given by

$$c_s = \sqrt{(\gamma_e Z_i T_e + \gamma_i T_i)/m_i}, \tag{252}$$

where $\gamma_{e,i}$ are the electron and ion adiabatic indexes, Z_i the ion charge (= 1 for hydrogen isotope plasmas) and m_i the ion mass [11, 99, 434]. The relative contributions of the ion and electron components can vary depending on the experimental conditions. Since the GAM frequency depends on the temperature, which varies with radius, the GAM is expected to have a local behaviour with a radial continuum frequency dependence. Indeed all experimental results show this basic dependence on temperature [61]—see also the various examples within this section. However, subtle variations are observed in the exact scaling.

As discussed in section 2.1, Winsor, using an ideal single fluid MHD model for both species, obtained for a circular plasma cross-section

$$\omega_{GAM} = \sqrt{2}c_s/R_0 = \sqrt{\gamma(\tau_e + 1)}v_{Ti}/R_0 \tag{253}$$

with $v_{Ti} = (2T_i/m_i)^{1/2}$ the ion thermal velocity, $\tau_e = T_e/T_i$, and $\gamma = 5/3$ the specific heat ratio for a monoatomic gas. Here, the weak safety factor q dependence is neglected. Note the $\sqrt{2}$ factor appears due to the definitions of c_s and v_{Ti} used. Later, Hallatschek and Biskamp [24] employing two-fluid equations obtained $\omega_{GAM} = \sqrt{\tau_e + 5/3}v_{Ti}/R_0$, where the electrons are isothermal (since the $\tilde{T}_e$ relaxation is fast so as to maintain a constant temperature), hence $\gamma_e = 1$, while $\gamma_i = 5/3$.

More sophisticated MHD [65] and the kinetic models [11, 54, 99, 108, 121], see section 2.2, give an expression of the form $\omega_{GAM} = \sqrt{\tau_e + 7/4}v_{Ti}/R_0$, i.e. collisionless ions with $\gamma_i = 7/4$, that takes into account an anisotropy of the *perturbed* pressure, while $\gamma_e = 1$ for the electrons, which remain isotropic. It is important to note that $\gamma_i = 7/4$ is obtained for the case when the *equilibrium* ion pressure is isotropic. More on the theory of the anisotropic pressure in the equilibrium is given in section 2.3 and in the experiment in section 7.3. Further, extended fluid models [80] predict that with increasing ion collisionality ν_i the ion adiabatic γ_i coefficient reduces from a collisionless 7/4 to an isotropic 5/3 result. GK models show a reduction to an isothermal fluid-like value of 1 when using a number only conserving Krook operator [131], or, to 5/3 with a more correct NEC operator [132]. In either case it is noted that increasing collisionality can also significantly reduce the GAM frequency [131]. Table 3 summarizes the equation forms for the GAM frequency predicted by the main MHD and kinetic models, which include a range of effects. The somewhat special case of the EGAM frequency is discussed in sections 3 and 13.

From the experiment, taking the simplest case of limited circular plasmas in large aspect ratio devices, one finds overall good agreement with the basic Winsor model. As an example, figure 50 shows the measured continuum GAM frequency for a range of AUG ohmic, ECR and NBI heated circular ($\kappa_b \sim 1.1$) limiter plasmas vs the model $f_{GAM} = \sqrt{2}c_s/(2\pi R_0)$ with experimental $c_s^2 = (T_e + \gamma_i T_i)/m_i$ (neglecting $q > 2.5$ and $Z_{eff} = 1$) [305]. For GAMs in the near edge/core region ($\rho_{pol} < 0.95$: closed symbols) an isothermal $\gamma_i = 1$ appears to give the best fit to the frequency.

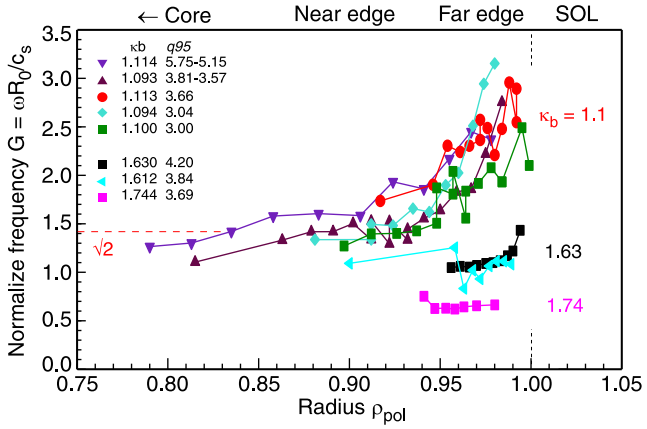

Figure 51. Radial profiles of the measured GAM frequency $G = \omega_{GAM}R_0/c_s$ normalized to experimental $c_s^2 = (T_e + \gamma_i T_i)/m_i$ with $\gamma_i = 1$, $Z_{eff} = 1$ and $m_i = m_D$ from AUG limiter and divertor plasmas with various q_{95} and κ_b. Reproduced from [305]. © IOP Publishing Ltd. All rights reserved.

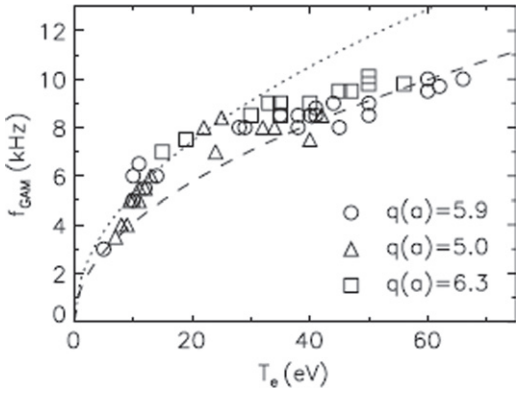

Figure 52. Measured GAM frequency vs electron temperature T_e from LP $\tilde{V}_f$ in circular TEXTOR edge ($r/a = 0.95$–0.97) for various $q(a)$. Curves are single-fluid predictions with $\gamma = 1$ (dashed) and $\gamma = 5/3$ (dotted). Reproduced from [342]. © IOP Publishing Ltd. All rights reserved.

However, towards the more collisional AUG far edge ($\rho_{pol} > 0.95$: open symbols) the GAM frequency begins to deviate from the expected $\sqrt{2}$ scaling. This is shown more clearly by the radial profiles in figure 51 where the measured GAM frequency is normalized $G = \hat{\omega} = \omega_{GAM}R_0/c_s$ (with a specified $\gamma_i = 1$) to remove the temperature dependence. Here, the scale factor rises $G \to 3$ towards the last-closed-flux surface, even though the flux surfaces remain circular—although Shafranov shifted [305]. For these (lower temperature) far edge GAMs a $\gamma_i = 7/4$ tends to give a better fit, particularly for NBI and ECR heated plasmas. Similar results obtained using a reciprocating LP in TEXTOR are shown in figure 52 for various edge $q(a)$ values. The curves are for the Winsor scaling $f_{GAM} = c_s\sqrt{2 + q^{-2}}/(2\pi R_0)$ with $c_s = (\gamma(T_e + T_i)/m_i)^{1/2}$, assuming $T_e = T_i$ and $Z_{eff} = 1$. Despite the use of a one-fluid γ the higher T_e points (more core), nevertheless, show the GAM frequency best follows $\gamma = 1$ while the lower T_e at the (more collisional) edge tend to the higher $\gamma = 5/3$ [342].

Other circular cross-sectional tokamaks also tend to favour a $\gamma_i = 1$ adiabatic index. Table 10 summarizes the best fit model scale factor G to experimental results from various devices for GAMs in the outer core and inner edge regions of circular boundary elongation $\kappa_b < 1.1$ limiter plasmas. Since varying definitions are used in the literature it is necessary to specify also the γ_i used. Aside from the three JIPP T-IIU [36, 327], SINP [395] and TCV [382] cases where the ions were particularly cold $T_e \gg T_i$, a $\gamma_i = 1$ was preferred. There is also a notable variation in G between ~ 1 and $\sqrt{2}$, with lower values appearing for cases where ions were cold or where $T_i \approx T_e$ was assumed. Unfortunately a more detailed analysis of additional dependencies, such as the inclusion of Shafranov shift corrections which may help to raise G values, is difficult since not all of the necessary parameters are given in the literature. Clearly more careful and detailed experiments are required.

Nevertheless, in this direction a couple of model comparison studies have been made. Continuum GAMs ($\rho = 0.75$–0.95) in ICRF heated, Tore Supra deuterium discharges were compared [373] with GK simulations using the GYSELA code for low and high collisionality ν^* conditions, as well as with various analytic models: including: an empirical $f_{GAM} = c_s/(2\pi R_0)$ model with $\gamma_i = 1$; the Windsor fluid model, the Sugama kinetic model [75] in the fluid limit of high q and the Gao kinetic model [117]—cf table 3. At low ν^* the empirical model gave the best fit over the whole radial profile, while at high ν^* the empirical model fitted well for the edge while moving slightly towards a model that included impurities and equilibrium parameters for the core region. For the high ν^* case the GK simulations (very close to the Sugama model) over-predict the GAM frequency. With the Gao model (see below), which includes finite aspect ratio $\epsilon = r/R_0$ and Shafranov shift gradient Δ', the Sugama prediction is reduced by $(1 - 3\epsilon^2/4 - \Delta'^2/8 - 5\epsilon\Delta'/8)$, i.e. by some 5%–10% towards the experimental values. Further parameters were also tested (e.g. impurities—see sections below) but a perfect match was not achieved [373].

Similarly for DIII-D, radial profiles of the GAM frequency for core ($0.5 < \rho < 0.9$) continuum and eigenmode GAMs in moderate κ divertor plasmas were compared to various models [283]. Again the best overall fit was found to be $\omega_{GAM} = c_s/R_0$, with $\gamma_i = 1$, as previously reported in low density, high T_e NBI heated discharges [277, 280, 435]. Models which included q or a $\sqrt{2}$ scale factor, or with $\gamma_i = 7/4$, notably over predicted [283]. Also from DIII-D, an effective adiabatic index $\gamma = (p_e + 7p_i/4)/(p_e + p_i + p_f)$ which includes the fast ion pressure p_f was used in the NOVA code to calculate the GAM continuum for modelling measurements [44].

Table 10 also includes measurements from the near edge/core regions of moderately elongated limiter shapes as well as more strongly elongated divertor shapes. The overall behaviour is similar to the circular cases. This maybe partly explained by the decreasing local κ with minor radius r/a. The tendency to a $G \to \sqrt{2}$ towards the core of diverted elongated configurations is also displayed in figure 51 for AUG data. The role of the elongation κ, X-points and q_{95} on the far-edge GAMs is discussed further bellow.

Table 10. Experimental best fit values reported for GAM scale factor $G = \omega_{GAM} R_0/c_s$ with specified ion adiabatic index γ_i from various devices at radial position r/a or ρ, elongation κ, and inverse aspect ratio $\epsilon_o = a/R_0$. Triangularity δ generally not available. Unless stated, $Z_i = 1$ and $m_i = m_{isotope}$ assumed. The categories are circular limiter, moderate elongated limiter and shaped divertor.

Device	G	γ_i	r/a, ρ	κ	ϵ_o	Notes
FT-2	$\sqrt{2}$	7/4	< 0.94	Circ.	0.14	[255] with $Z_i = 3.5$, ELMFIRE
HL-2A	~ 1	1	0.92	Circ.	0.24	[347], $T_i \approx T_e$, H_2
HT-7	~ 1	1	0.85	Circ.	0.22	[285], $T_i \approx T_e$, D_2
JIPP TII-U	1	—	< 0.5	Circ.	0.25	[36, 327], cold T_i
SINP	1	—	~ 0.86	Circ.	0.25	[395], cold T_i
T-10	1.15	1	0.73	Circ.	0.20	[34], also GGAM [302]
TEXTOR	$\sqrt{2}$	1	0.96	Circ.	0.27	[337, 342], H, D & He
Tore Supra	~ 1	1	~ 0.85	Circ.	0.30	[373] $T_i \approx T_e$, with Δ' & Z_{eff}
AUG	$\sqrt{2}$	1	< 0.95	< 1.1	0.30	[305] Lim. D_2 core
AUG	> 2	1	> 0.95	1.1	0.30	[305] Lim. Edge
TCV	1.1	—	0.95	1.4	0.28	[382] Lim. cold T_i, eigenmode
COMPASS	~ 1	7/4?	0.85	> 1.5	0.36	[394] Lim. eigenmode
JET	~ 1	1	0.97	1.4	0.42	[358, 359] Div. LSN D_2
TCV	$< \sqrt{2}$	1	0.6–0.9	1.52	0.28	[383] Div.
AUG	$\sqrt{2}$	1	< 0.95	1.63	0.30	[305] Div. LSN, core, D_2
EAST	$\sqrt{2}$	1	0.94	1.64	0.24	[368] Div.
MAST	$< \sqrt{2}$	0	0.95	1.55	0.76	[374] DNull with M_t rotation
DIII-D	~ 1	1	0.5–0.9	~ 1.8	0.40	[280, 283, 435] USN
Globus-M	$< \sqrt{2}$	7/4	0.85	1.8	0.67	[385] USN, Gao formula

As so many devices have reported a best scaling with $c_s^2 = (T_e + T_i)/m_i$ it has been termed the standard experimental or empirical scaling. Nevertheless, there remain significant variations in G between 1 and $\sqrt{2}$, which cannot be accounted for by measurement error bars, nor the chosen γ_i alone. As discussed in the following sections there are additional factors, such as impurity Z_{eff}, isotope m_{eff}, rotation M_t as well as the Shafranov shift and q effects to be considered—values of which are not always available in the publications. Inclusion of these effects, however, is also no guarantee of universal convergence. Table 10 is thus a starting point indicating the need for more detailed multi-device comparisons.

7.2. GAM amplitude

Both the GAM amplitude and frequency are important parameters in determining its impact on turbulence moderation. If the GAM frequency is lower than the inverse turbulence decorrelation time $f_{GAM} < 1/\tau_d$, which is generally the case in the plasma edge, and has a sufficiently large amplitude A_{GAM}, e.g. a physical poloidal displacement larger or comparable to the turbulence poloidal structure size, plus a radial wavelength narrower or comparable to the turbulence radial structure size; then its $E_r \times B$ shearing rate may be effective in turbulent eddy shearing, and thus in moderating cross-field particle transport. The GAM radial structure and shearing are described in subsequent sections 9 and 15.

Typically for turbulence driven GAMs the coherent edge spectral peak is 1–2 orders of magnitude above the incoherent background flow fluctuation level; AUG [304], DIII-D [435] and JET [358]. For tokamak devices the GAM oscillatory velocity amplitude (peak-to-peak) generally ranges from 0.2 to 1.0 km s^{-1}; AUG [26], TEXTOR [339], DIII-D [277], Tore Supra [372, 373], COMPASS [394], HL-2A [141, 347], TCV [382], JFT-2M [318], although in some devices, such as JET, values of $A_{GAM} \sim 3$ km s^{-1} (ptp) are reported [358], and in TUMAN-3M during particularly intense GAM bursts amplitudes of > 6 km s^{-1} have been observed [335]. Similar, or larger magnitudes have been reported for core GAMs in JIPPT-IIU (up to 300 V_{ptp} potential) [327].

In general, the GAM amplitude appears larger in tokamaks than in helical devices, cf $\delta E_r < 0.7$ kV m^{-1} in the H-1 heliac [436]. This has been attributed to the larger magnetic field inhomogeneity (edge ripple) in helical devices [61], although differences in experimental conditions may also play a role. Theoretically, the helical magnetic ripple strengthens the damping rate of the GAM [123]. Concerning the EGAM amplitude behaviour, this is discussed in more depth in section 13.

In spatial terms such potential or velocity magnitudes translate to poloidal displacements of several cm. The (ptp) $A_{GAM} \sim$ 0.2–0.8 km s^{-1} in AUG correspond to poloidal displacements $A_{GAM}/\omega_{GAM} \sim 0.4$–1 cm, which are comparable to the density turbulence eddy size [26].

From the radial gradient of the GAM (rms) velocity perturbation one can estimate an equivalent shearing rate $\omega_{E\times B} = \partial v_\theta/\partial r$, or indirectly from the GAM width or its radial wavenumber, $\gamma_{E\times B} = k_r\sqrt{\langle v_{GAM}^2\rangle}$. Estimates have been made from several devices [141, 277, 282, 306, 337, 347, 357, 363] and generally find $\omega_{E\times B}$ rates of the order of 10^5 s^{-1} comparable, within a factor of 2–3, to the turbulence decorrelation rate

$1/\tau_d$. Even when applying a frequency dependent downward correction to account for the oscillatory GAM being less effective than a static velocity shear (see section 15.1) the effective shearing rate is still significant [337]. In FT-2 a GAM (rms) amplitude of $v_{GAM} \approx 1.7$ km s^{-1} was measured, corresponding to an $E \times B$ shearing rate of $\tilde{\omega}_{E\times B} = k_{GAM} v_{GAM} \approx 442$ kHz. Applying a shearing reduction factor of $H \approx 0.5$ this gave an effective shearing rate $\omega_{eff} \approx 271 \pm 50$ kHz, which was again very close to the turbulence growth rate [388]. Therefore the GAM should have a sufficient amplitude to mediate the edge turbulence. This positive role is supported by other measurements demonstrating that the GAM can directly affect the turbulence, described in section 15.2 on the GAM modulation of the turbulence.

In real experiments the GAM flow oscillation is not static but sits on top of a mean (equilibrium driven) $E_r \times B$ rotation. Generally, experiments report relative flow oscillations of several tens of percent [26, 277, 339, 358, 372, 382, 394]. In some reports it has reached up to 100% or more of the background rotation velocity, cf Globus-M [385]. In one extreme case, the GAM oscillation was up to two times the mean $E \times B$ velocity (i.e. $E_r \sim 3$ kV m^{-1}) at the GAM radial peak location in TUMAN-3M [335]. The background rotation also generates a mean $E \times B$ flow shear which generally adds to the GAM shearing. The relative magnitude of these two shearing rates varies greatly and can be an important factor in confinement (e.g. L–H) mode transitions, cf section 18. In a related vein, the GAM magnitude, like the mean $v_{E\times B}$, is not constant on a flux surface. Variations of some 20% or more have been reported on TEXTOR, with the GAM being larger at the mid-plane compared to the top in ISTTOK [363]. These asymmetries are discussed further in section 8.2.

The GAM amplitude and its behaviour is essentially an expression of the drive (via nonlinear turbulence coupling—sections 11, 14, or EPs—section 13) and the damping mechanisms (section 12). The GAM magnitude increases with heating power and can even reach one order of magnitude larger in an NBI heated L-mode compared to ohmic—due to stronger E_r gradients and vorticity in the L-mode edge [304], or pressure gradient [358]. Other parameter dependencies, such as plasma shaping, isotope, etc, are discussed in the respective sections below, as well as the issue of thresholds in the GAM appearance—see section 11.2 and GAM amplitude modulation (AM) and intermittency in section 15.3.

7.3. Equilibrium pressure anisotropy

Anisotropy in the background or equilibrium plasma pressure $\chi = p_\perp/p_\parallel \neq 1$ can occur in experimental conditions with strong external drive, such as with NBI or ICRF heating. As discussed in section 2.3 pressure anisotropy has an impact on both the GAM frequency and amplitude. As indicated by the GK modelling results in figure 4 for a low β plasma an increasing parallel temperature anisotropy reduces both the GAM frequency and the collisionless damping rates. Experimentally, pure ohmic heating should lead to isotropic temperatures. Hence equilibrium anisotropy was not found to be an important factor for the GAM frequency behaviour in ohmic Tore Supra discharges [373]. Nevertheless, strong pressure anisotropy has been observed in several devices (JET, MAST, LHD) with neutral beam driving parallel anisotropy $\chi < 1$ or RF heating driving perpendicular anisotropy $\chi > 1$. Thus anisotropy should be important for the GAM behaviour in strongly heated plasmas. Unfortunately there are, as yet, no detailed experimental studies of the GAM frequency and amplitude dependence on anisotropy.

A second, and perhaps a more interesting effect of pressure anisotropy is the prediction from MHD theory of the formation of two branches in the dispersion relation—cf equation (22). The higher frequency branch ω_+^2 is associated with the GAM, while the lower frequency branch ω_-^2 is a zonal mode (i.e. a ZFO). As discussed in section 17, GAMs and ZFOs have been routinely observed simultaneously, but a link to pressure anisotropy has not yet been made. This would be an interesting topic for future investigation.

Finally, it is important to note that the effects of equilibrium anisotropy are intrinsically related to the EGAM, in particular to so-called reactive EGAMs that are caused, not by resonant interactions due to EPs (reactive, or dissipative EGAMs), but rather due to the appearance of new branches which become reactively unstable. See further discussion in section 13.

7.4. Isotope and effective mass m_{eff}

The so-called isotope effect is the improvement in plasma confinement with increasing isotope mass, from hydrogen to deuterium to helium. It has long been a topic of investigation from the perspective of transport studies, cf [437] and references therein. Concerning the role of ZFs there have been several recent investigations [344, 438, 439].

Specifically, for the GAM frequency the expected inverse dependence on the ion mass m_i has been confirmed in several machines. A particularly clear example from TEXTOR of the change in the GAM frequency scaling with helium (He), deuterium (D) and hydrogen (H) plasmas is shown in figure 53 [337]. The lines show the expected pure isotope frequency scaling—which fit well the fairly pure H and He data. In between are predominantly deuterium points with varying H/D ratios [336].

Similar behaviour is reported for ISTTOK where the GAM frequency decreases with isotope mass as $f_{GAM} \propto 1/\sqrt{m_i}$ [440]. Likewise in AUG the GAM frequency increased by 30%–40% when changing the plasma fuelling from deuterium to hydrogen, matching the expected c_s scaling [309]. Changing from D to H plasmas in the Globus-M spherical tokamak produced a GAM frequency up-shift [385] in good agreement with the large ODW formula of Guo [248]. Likewise in TUMAN-3M a corresponding D to H frequency up-shift was observed, although the increase was less than expected, which was attributed to a 20% H contamination [335]. Here, the isotope purity will result in an effective ion mass $m_{eff} = (\sum_i m_i n_i)/(\sum_i n_i)$ correction. Good agreement with the Guo formula was also found in FT-2—once impurities were included (see below)—for ohmic H and D plasmas [255]. A detailed study of the isotope impact on both the GAM

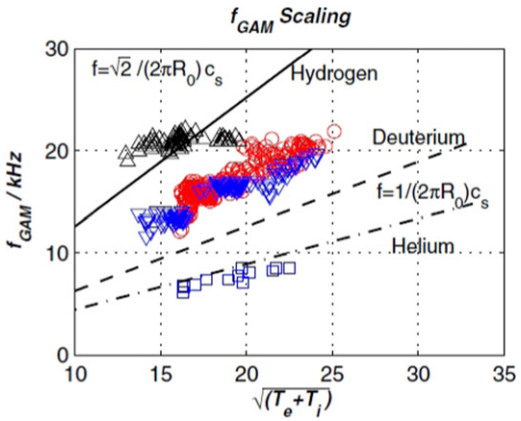

Figure 53. Measured GAM frequency vs $\sqrt{T_e + T_i}$ between $0.8 \leqslant r/a \leqslant 0.9$ for ohmic H (△), He (□) and D (○, ▽) plasma with varying H/D ratio (colours) in circular limited TEXTOR. Reprinted figure with permission from [337], Copyright (2006) by the American Physical Society.

and turbulence properties with using Doppler UHR backscatter was performed in FT-2 with comparisons to ELMFIRE global GK simulations [250].

For the GAM amplitude the results are also consistent across various machines. In FT-2 the frequency up-shift was accompanied by a decrease in amplitude in H compared to D plasmas [385]. Likewise, in AUG GAMs are generally weaker in H compared to D [441], as in TUMAN-3M [335], and in FT-2 where the GAM 'contrast' is higher in D compared to H, with lower local $\chi_{\rm eff}$ thermal diffusivity [250, 388]. Comparisons of GAM amplitude and radial wavelength in FT-2 with ELMFIRE GK simulations also showed good agreement [442]. Helium puffing into a deuterium plasma in T-10 was seen to reduce both the GAM frequency and amplitude, but unfortunately produced such a strong perturbation in the edge T_e and n_e that it is not possible to identify a clear isotope effect [294]. Also in JET the GAM amplitude is $\sim 20\%$ larger in D than in H plasmas [358].

Finally, in TEXTOR a decrease in the long-range-correlation between toroidally spaced LP (V_f) arrays was observed from H to D dominated plasmas [344]. Here, the signals were dominated by $f \approx 10$ kHz—attributed to GAMs—and lower amplitude 1 kHz oscillations. Similar behaviour was observed with correlation reflectometry [443] and Li-beam spectroscopy [343]. There was also evidence of changes in the poloidal k spectra which was attributed to a decrease in the ZF amplitude.

7.5. Impurities and effective charge $Z_{\rm eff}$

The impact of impurity ions is two-fold; impurities raise the effective collisionality which affects the GAM damping and drive, and impurities raise both the effective charge $Z_{\rm eff}$ and the effective ion mass $m_{\rm eff}$. For warm (kinetic) electrons, increasing $Z_{\rm eff}$ raises $\omega_{\rm GAM}$ while increasing $m_{\rm eff}$ lowers $\omega_{\rm GAM}$ as per equation (252). However, as $m_{\rm eff}$ increases faster than $Z_{\rm eff}$ the net result is that the GAM frequency tends to decrease. In addition, impurities generally enhance radiation with commensurate reductions in ion and electron temperatures and thus also $\omega_{\rm GAM}$.

A GAM dispersion relation including impurity ions (single species) was derived from a kinetic model [248] and shows a roughly linear decrease in the GAM frequency with increasing effective charge $Z_{\rm eff}$ (due mainly to an increase in the polarization current carried by the impurity ions), as well as a significant impact on the GAM damping, which initially increases with $Z_{\rm eff}$ (due to impurity polarization currents) and then decreases (due mainly to the effect of the curvature drift of impurity ions). A similar non-monotonic behaviour for the GAM damping vs ion collision rate $\nu_{\rm i}$ was obtained with a GK model including kinetic effects from combined collisions and impurities [444]. With increasing $Z_{\rm eff}$ the peak damping rate moves towards lower collision rates. That is, induced collisions tend to decrease the GAM frequency, but can increase the GAM damping at low $\nu_{\rm i}$ and decrease the damping at high $\nu_{\rm i}$. These simulation results were consistent with GAM frequency shifts observed in HL-2A during ECR heating induced impurity releases [351].

The effects of $Z_{\rm eff}$ in multi-ion species plasmas have also been investigated using linear GK equations and non-Maxwellian ion energy distributions [445]. Both the GAM frequency (linearly) and the damping rate (nonlinearly) were found to fall with increasing $Z_{\rm eff} = \sum_{j={\rm b,i}} q_j^2 n_j / \sum_{j={\rm b,i}} q_j n_j$, where b, i refer to bulk and impurity ion respectively, and the degree of non-Maxwellian-ness of the ion distribution function (e.g. indicating the presence of energetic tails). The combined effect of impurity (charge) and toroidal rotation was also analytically investigated [446], where it was found that without rotation, impurities decrease the GAM frequency and increase the GAM collisionless damping rate (due to polarization current). When including toroidal rotation the rate of frequency and damping change is slower as the rotation increases, particularly at large impurity concentrations. Generally, trace impurity levels were found to have little effect on the GAM, except at large toroidal rotations where additional drifts induced by toroidal rotation begin to play a role.

Experimentally there are three main sets of recent results. For hydrogen plasmas in (circular) FT-2, radial profiles of the edge GAM frequency were compared [255] with a simplified kinetic formula (derived from the work of Guo [248]):

$$\omega_{\rm GAM}^2 = \frac{2}{R_0^2\, m_{\rm i}} \left(\gamma_{\rm i} T_{\rm i} + Z_{\rm i} T_{\rm e}\right). \tag{254}$$

With $m_{\rm i} = m_{\rm H}$ and $Z_{\rm i} = 1$ for H^+ and $\gamma_{\rm i} = 7/4$ the formula over-predicts the experimental values, but if assuming cold ions $T_{\rm i} = 0$ then it under-predicts. Only once the O^{8+} impurity component was taken into account ($Z_{\rm eff} \sim 3.5$) could the (inner edge) GAM frequency be matched. For comparison with ECR heated edge GAMs in HL-2A a similar impurity compensated formula (also derived from Guo) was used [351]:

$$\omega_{\rm GAM}^2 = \frac{2T_{\rm i}}{R_0^2\, \bar{m}_{\rm i}} \left(\gamma_{\rm i} + \tau_{\rm e} - \gamma_{\rm i}(Z_{\rm z} - 1) f_{\rm z}\right), \tag{255}$$

with $\gamma_i = 7/4$, $\tau_e = T_e/T_i$, $f_z = n_z/(n_i + Z_z n_z)$ and $\bar{m}_i = (m_i n_i + m_z n_z)/(n_i + Z_z n_z)$ the average ion mass. The impurity Z_z and bulk ions are assumed to have the same temperature. Only by including a (dominant carbon C^+) impurity fraction of $f_z = 0.12$ could the temporal evolution of the measured frequency be matched.

Impurities were also found to be important in attempting to match Tore Supra edge GAM frequencies to models [373]. In Tore Supra the main impurities are carbon and oxygen. By assuming impurities and bulk ions to have the same temperature, then following [248], a similar equation as (255) was obtained $\omega^2_{GAM} = (2/R_0^2)(\gamma_i T_i/m_1 + T_e/m_2)$ with effective mass of ions $m_1 = (m_{bulk} + \alpha_{imp} m_{imp})/(1 + \alpha_{imp})$ and $m_2 = m_{bulk}$ and $\alpha_{imp} = n_{imp}/n_{bulk}$ and $\gamma_i = 7/4$. Although the GAM frequency dependence on Z_{eff} can be significant, with $T_i = T_e$ and $Z_{eff} = 2 = m_z/m_i$ it was found that the frequency downshift was less than 10% which, while important, was still not enough to account for discrepancies between experiment and predictions. Agreement would require an unrealistic Z_{eff} of 4–6, depending on ν^*.

Overall, the inclusion of impurity effects appears to be important, but not always sufficient. It should also be noted that most other experiments have not considered impurity effects in their reported results. In recent AUG results with an all tungsten wall [309], $Z_{eff} \sim 1.3$ and thus should have only a small effect. However, earlier AUG results with a partial carbon wall where $Z_{eff} \geqslant 2.5$ [304] may need reevaluating.

7.6. Plasma shape

Both theory and experiment show a significant impact of the magnetic configuration on both the GAM frequency and amplitude. As early as 2005 both AUG [304] and DIII-D [435] observed a decreasing GAM frequency with increasing vertical cross-sectional elongation κ. While the elongation is by far the most dominant shape parameter, the triangularity δ, inverse aspect ratio $\epsilon = a/R_0$, plasma centre Shafranov shift Δ, together with radial gradients $s_\kappa = (r/\kappa)\nabla_r \kappa$, magnetic shear $s_q = (r/q)\nabla_r q$, and $\Delta' = \nabla_r R_0$ are all relevant parameters. The role of the safety factor q is discussed in section 7.8.

The GAM theory presented so far has concentrated on the ideal circular cross-sectional tokamak plasma geometry. However, as early as 2005 models also began to be extended to more experimentally relevant non-circular shapes. Some of the first MHD analytic models [447, 448] used a Solov'ev type equilibrium with a finite ϵ, an elongation κ and an up-down symmetric triangularity δ to obtain a general dispersion description of the form

$$\omega^2_{GAM} = \frac{c_s^2}{R_0^2}\left(\frac{2\,g_2}{E^2} + \frac{g_1}{q^2}\right), \tag{256}$$

where $E \propto \kappa$ describes the elliptic flux surface deformation and g_1 and g_2 are general equilibrium geometric factors of the order of 1, which vary slightly with the magnetic flux radius and δ [447]. Equation (256) essentially has an $\omega_{GAM} \propto \sqrt{1 + \kappa^{-2}}$ dependence.

First global numerical simulations also appeared in 2006 with linear GK PIC GYGLES and nonlinear electrostatic ORB5 codes with an elongated D-shape equilibrium matching the TCV configuration [244]. A little later Angelino, starting with the Braginskii equation, modelled the role of κ on both the GAM frequency and damping to obtain [243],

$$\omega^2_{GAM} = (\tau_e + \gamma_i)\frac{v^2_{Ti}}{R_0^2}\left[\frac{8}{3 - 2\kappa + 3\kappa^2} + \frac{1}{q^2}\right] \tag{257}$$

with $v_{Ti} = (T_i/m_i)^{1/2}$, $\gamma_i = 1$ and κ the local elongation. The model results compared quite favourably with ORB5 GK simulations. The role of elongation on linear damping is discussed in section 12.

Using an MHD model, Wahlberg [157, 167] obtained for a non-circular cross section with finite κ and average δ,

$$\omega^2_{GAM} = \omega_s^2\left[2 + \frac{1}{q^2} - 2(\kappa - 1) - \frac{r}{2}\frac{d\kappa}{dr}\right]. \tag{258}$$

Also within the framework of an ideal MHD model, Sorokina *et al* [449] used a Miller equilibrium with variable δ, κ and local $\epsilon = r/R_0$ to derive the relation,

$$\omega^2_{GAM} = \frac{2\omega_s^2}{\kappa^2 + 1}\left(2 + \frac{(\kappa^2 + 1)}{2q^2} - \frac{3\epsilon^2}{2}\frac{3\kappa^2 + 1}{\kappa^2 + 1} + \epsilon\delta\,\frac{5\kappa^2 - 1}{2(\kappa^2 + 1)} + \delta^2\,\frac{17\kappa^2}{16(\kappa^2 + 1)}\right), \tag{259}$$

where $\omega_s = c_s/R_0$. This formula has a strong $\omega_{GAM} \propto \sqrt{2/(\kappa^2 + 1)}$ inverse dependence, an inverse parabolic dependence on ϵ and a weak, roughly linear dependence on δ. This formula is qualitatively similar to that of Gao-2008 [450, 451] derived using a GK approach with cold electrons,

$$\omega^2_{GAM} = \frac{7}{4}\frac{v^2_{Ti}}{R_0^2}\frac{2}{(\kappa^2 + 1)}\left(1 + \frac{23}{49}\frac{(\kappa^2 + 1)}{2q^2} - \frac{3\epsilon^2}{4}\frac{3\kappa^2 + 1}{2\kappa^2 + 2}\right)^2. \tag{260}$$

The model was subsequently extended to include a finite electron temperature $\tau_e = T_e/T_i$ in both zero (shown below) and large drift orbit limits (small differences in the form and placement of the s_κ term), Gao-2011 [122],

$$\omega^2_{GAM} = \frac{v^2_{Ti}}{R_0^2}\left(\frac{7}{4} + \tau_e\right)\left(\frac{2}{\kappa^2 + 1}\right)\left(1 - \frac{s_\kappa}{2}\frac{7 + 2\tau_e}{7 + 4\tau_e}\right) \times \left[1 - \epsilon^2\frac{9\kappa^2 + 3}{8\kappa^2 + 8} - \Delta'^2\frac{\kappa^2}{4\kappa^2 + 4} + \epsilon\Delta'\frac{4\kappa^2 + 1}{4\kappa^2 + 4} + \frac{(23 + 16\tau_e + 4\tau_e^2)(\kappa^2 + 1)}{2q^2(7 + 4\tau_e)^2}\right]^2 \tag{261}$$

with local $\epsilon = r/R_0$, Shafranov shift gradient Δ' and the radial derivative of elongation $s_\kappa \approx (\kappa - 1)/\kappa$. Again, the local κ is used. Gao-2010 [117] also gives expressions for the GAM frequency and damping taking into account the dispersion effects and elongation.

These analytic formulations together with numerical simulations, using fluid models with experimentally based Miller equilibria (but without an X-point) [452] or from the HELENA

Grad–Shafranov solver [453], or using GK models [245, 246], have begun to allow detailed comparisons with experimental results.

Such an experimental example of the inverse dependence of the GAM frequency on elongation is shown in figure 54 for AUG far edge ($\rho_{\rm pol} > 0.95$) continuum GAMs [305]. With increasing boundary elongation $\kappa_{\rm b}$, from circular limiter to strongly elongated diverted (lower X-point) shape, the frequency scaling weakens. The radial dependence of the scale factor, or normalized frequency, $G = \omega_{\rm GAM} R_0/c_{\rm s}$ on $\kappa_{\rm b}$ was shown in figure 51. Various heuristic models were tested against the edge data set, but the best tested was a simple model including only $\kappa_{\rm b}$ and the inverse aspect ratio $\epsilon_{\rm o} = a/R_0 \sim 0.3$

$$\omega_{\rm GAM} = \frac{c_{\rm s}}{R_0} 4\pi \left(\frac{1}{1+\kappa_{\rm b}} - \epsilon_{\rm o} \right) \tag{262}$$

with $c_{\rm s}$ given by equation (252)—see figure 14 in [305]. However, for $\kappa_{\rm b} = 1$ this reduces to $\omega_{\rm GAM} \approx 2.5 c_{\rm s}/R_0$ which too strong to describe the core GAM behaviour.

A more comprehensive study [309] of the GAM frequency scaling in AUG shaped plasmas, including core and edge databases with limiter and divertor configurations, undertook comparisons with Winsor (258), Angelino (257), Conway (262) and Gao-2011 (261) models. All of the models which included shape parameters were found to be equally good (or equally bad), but the Gao model, although under-predicting, produced the least scatter. The conclusion being that all the models capture the basic inverse κ dependence but equally miss other dependencies. These models, however, consider only linear dispersive effects. Nonlinear effects where the GAM amplitude or drive (possibly also q dependent) are predicted to pull the GAM frequency, may also be significant—see section 4. The GAM frequency in AUG being always larger than Gao's prediction would be consistent with nonlinear GK predictions of a positive frequency upshift [11, 142], or with nonlinear MHD predictions [454, 455]—which can either give up or down-shifts depending on relative strength of the turbulence drive to the oscillation stabilization [456]. This is a topic of ongoing research. The effect of q on the GAM amplitude is discussed more fully in the context of collisionless damping in section 12.1.2.

The only other machine that has reported a κ scan is COMPASS on the GAM amplitude dependence [394]. As was observed in DIII-D [435] and AUG [26], the GAM strengthens with increasing κ in diverted COMPASS plasmas. A fuller discussion of the amplitude dependence on shape and q parameters appears in section 12.1.2 on damping. Nevertheless, several machines have attempted to reconcile GAM frequencies from strongly shaped, fixed κ, plasmas with one or more of the popular analytic models. Here, just the continuum GAM results are summarized, leaving the more involved ultra-wide eigenmode GAM behaviour to section 9.3. These results are listed in the second and third sections of table 10.

Continuing with COMPASS, in strongly shaped $\kappa_{\rm b} \geqslant 1.8$ limiter (continuum like GAM) and diverted configuration (narrow edge eigenmode like with magnetic sideband) the GAM frequency ($r/a \sim 0.88$) scales as $\omega_{\rm GAM} \approx c_{\rm s}/R_0$ [394]—although with some data scatter. A unity scaling also appears for GAMs in the near-edge of JET ohmic discharges in hydrogen and deuterium with lower-single-null (LSN) divertor configuration [359], and as noted above, in a variety of upper-single-null (USN) diverted DIII-D plasmas the core and edge continuum ($\rho = 0.6$–0.9) GAM $\omega_{\rm GAM} \approx c_{\rm s}/R_0$ [277, 280, 283, 435]. On the other hand, near-edge GAMs in EAST double-null ohmic/L-mode plasmas scale closer to $\sqrt{2}$ with $\gamma_{\rm i} = 1$ [368]. Based on the published details it is difficult to say if GAMs in these devices really show no shape dependence in the near-edge, or if the scaling is just fortuitous.

Where results have been matched against numerical simulations or GK analytic predictions which include shape parameters then the agreement appears to be good—such as in TCV L-mode, limited plasmas, the edge GAM scaling (with significant data scatter) as $\omega_{\rm GAM} = 1.1 c_{\rm s}/R_0$ was in close agreement with ORB5 GK simulations [382]. The 1.1 scale factor was much stronger than the Gao prediction but not so far from the Angelino prediction. In the Globus-M spherical tokamak upper single null configurations the edge continuum GAM frequency was significantly lower than the Winsor prediction, but somewhat closer to the Gao-2011 large drift orbit prediction for both deuterium and hydrogen [385]. Likewise, in MAST the edge GAM frequency matches a modified Gao-2010 prediction reasonably well, once rotation corrections had been applied [374].

The triangularity δ is a parameter that has not been widely studied experimentally. GAMs have been measured in strongly shaped TCV plasmas at high $\kappa = 1.4$ and $\delta = +0.4$ [382], and more recently a wide δ scan was performed to investigate the frequency dependence, as shown in figure 55 where the normalized edge GAM frequency $f_{\rm GAM}/c_{\rm s}$ is plotted against average $\delta_{\rm a}$ while keeping other parameters roughly constant. The dependence is almost linear, and of particular interest, continues to decrease with negative triangularity. While some analytic formulations, such as that of Sorokina, equation (259) which includes δ terms, indicate a weak positive frequency dependence, a comparison with the MHD formulation of Wahlberg which also retained κ, Δ and their radial gradients showed a more reasonable agreement [157]. The sign and magnitude of δ was recently found to have a significant impact on the core turbulence in TCV [457], specifically a reduction of turbulent electron temperature fluctuations and correlation lengths with negative δ was observed. It would be valuable to extend these studies towards the edge and to compare with the respective GAM properties, particularly if the improved confinement observed in negative triangularity shapes proves to be a viable fusion reactor operational scenario [457, 458].

Overall, shape parameters are important for the edge, but perhaps less so for the core. This needs to be investigated further. The $\gamma_{\rm i}$ dependence on radius and specifically collisionality also needs further study. In the next section we address the impact of the flux surface X-point on GAMs close to the separatrix.

7.7. Limiter vs divertor—role of the X-point

The formation of a field null (flux surface X-point) in the poloidal divertor configuration profoundly impacts the edge

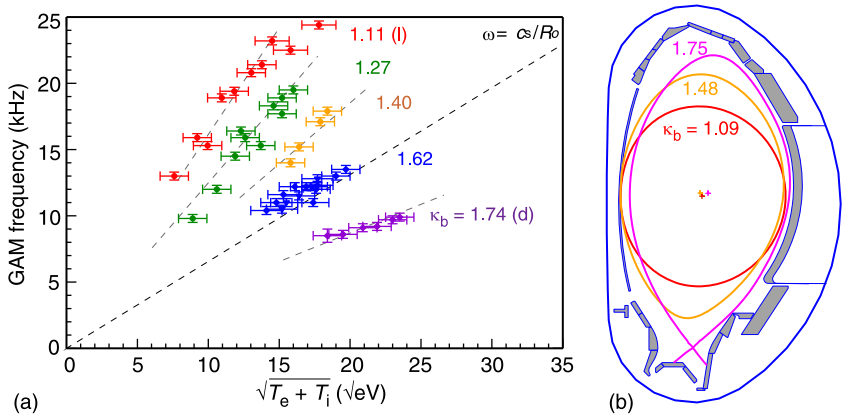

Figure 54. Measured edge GAM ($\rho_{pol} > 0.95$) frequency vs square-root temperature for increasing boundary elongation κ_b with limiter and divertor shapes in AUG. Reproduced from [305]. © IOP Publishing Ltd. All rights reserved.

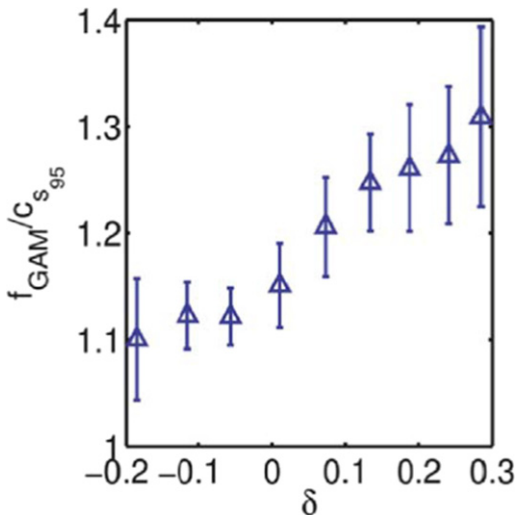

Figure 55. Measured edge ($\rho = 0.95$) GAM frequency normalized to c_s vs edge triangularity δ in an up–down symmetric, $\kappa = 1.4$ ohmic limiter TCV discharge. Reproduced from [157]. © IOP Publishing Ltd. All rights reserved.

plasma shape. It changes the up-down symmetry, it generally raises the flux surface triangularity, as well as creating a poloidal flow stagnation point. Experimentally the X-point is seen to have a distinct effect on the edge GAM, its frequency and amplitude behaviour, its radial extent, and its localization compared to limiter configurations. However, the X-point appears to have less impact on more core localized GAMs whose behaviour is similar to that in limiter configurations. There has been little theoretical work on the X-point impact on the GAM.

A series of studies have been made in AUG comparing limiter and divertor configurations [26, 305, 309]. In AUG divertor configurations the edge density profile forms a distinct pedestal, while the temperatures retain typical L-mode linear profiles. For high $1.4 < \kappa_b < 1.75$ the GAM is observed only within this steepened density gradient region, $0.95 < \rho_{pol} < 1.0$, between the pedestal top and the separatrix [304, 305]. In low κ_b limiter configurations the pedestal is weak and the density profile is more parabolic. Here, the GAM now reaches deep into the plasma. For AUG conditions this can be as far as $\rho_{pol} \sim 0.75$, limited only by the q profile. This is similar to COMPASS where the GAM appears further in for limiter configurations but is more edge localized for divertor configurations [394].

To the outside the GAM generally reaches to the LCFS in AUG limiter configurations, while in divertor configurations there is a tendency for the GAM to be suppressed just inside of the separatrix [26]. Likewise, in DIII-D [435] and JET [358] GAMs are not observed close to the separatrix. This may be due to a weakened drive as the kinetic profiles flatten towards the base of the pedestal, or a combined effect of enhanced mean $E_r \times B$ flow shear around the separatrix, or stronger collisionless damping due to the enhanced q values close to the separatrix.

In AUG divertor configurations the GAM frequency is generally higher compared to limiter plasmas with the same κ_b—cf figure 7 in [309]. In limiter configuration the GAM amplitude decreased with increasing elongation, but less so in divertor configurations [26]. A detailed example is shown in figure 12 of [309]. The GAM damping rates appear to be lower in divertor compared to limiter, and are generally dominated by collisional damping—i.e. the GAM is generally stronger—see section 12.

Current analytic models are not well suited to X-point equilibria. For edge GAM modelling in asymmetric shapes only numerical simulations with fine-grain magnetic equilibria of realistic experimental conditions have been tried. Some examples include a two-fluid model with a special algorithm to generate smooth local equilibria from course-grained experimental CLISTE solver [452]. Although the X-point could only be approximated, a reasonable prediction of the GAM frequency in diverted AUG plasmas was obtained. To simulate the ITER shape and conditions an MHD equilibrium was used with the ORB5 GK code, where it was observed that GAMs are likely to be weak due to strong damping in ITER [246].

Figure 56 shows a particularly fine example of a successful simulation of an near-edge GAM in a strongly shaped, small aspect ratio, double-null (i.e. up–down symmetric) MAST configuration. The figure compares potential fluctuation spectra from an low-field-side (LFS) LP 4 cm inside LCFS of an

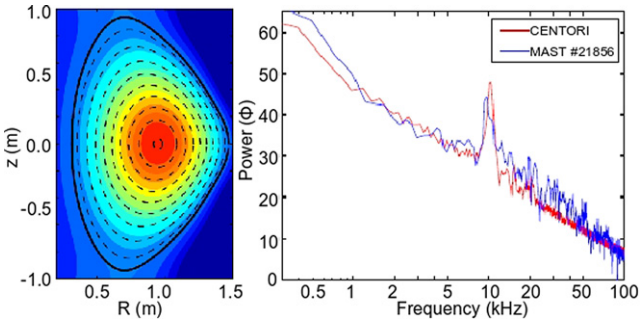

Figure 56. Comparison of experimental LP $\tilde{\phi}$ spectra from 4 cm inside MAST LCFS shot #21856 and matched CENTORI simulations. Reprinted from [103], with the permission of AIP Publishing.

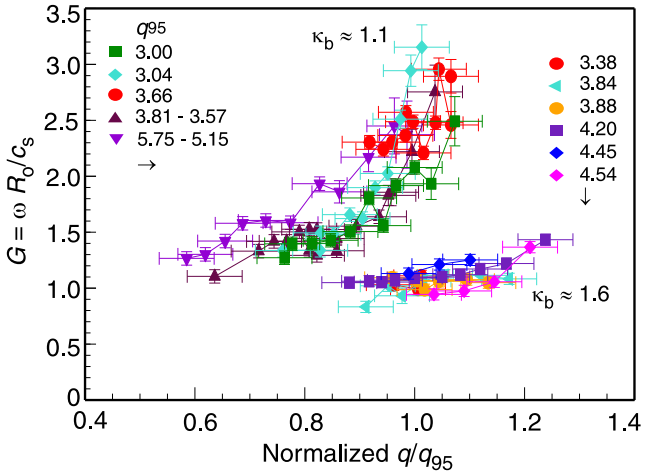

Figure 57. Normalized measured edge GAM frequency $G = \hat{\omega} = \omega_{GAM} R_0/c_s$ vs q/q_{95} with experimental $c_s^2 = (T_e + T_i)/m_i$ for AUG circular limiter $\kappa_b \approx 1.1$ and elongated divertor $\kappa_b \approx 1.6$ plasmas. Reproduced from [305]. © IOP Publishing Ltd. All rights reserved.

ohmic plasma with matched numerical simulations from the global toroidal, two-fluid, EM turbulence code CENTORI [103]. Unfortunately, the simulation grid could only extend up to 95% of the flux surface due to numerical limitations and thus could not fully resolve the X-points and separatrix. Nevertheless, performing R_0 scans the code showed the GAM diminishing with increasing R_0, as well as recovering radial step-like frequency plateaus [103, 375].

7.8. Safety factor q and the ion sound wave

Both fluid and GK theory predict a coupling of the GAM to the parallel ion SW, which appears as a correction to the GAM frequency of the form $(1 + 1/2q^2)^{1/2}$—cf sections 2.2 and 2.5, which results in a weak inverse frequency dependence on the local q. Since the safety factor is usually $q > 2$ in the tokamak edge this term is often neglected. Nevertheless, experiments do show a significant frequency variation with q.

Early DIII-D measurements showed an inverse frequency dependence consistent with the q correction, although with a somewhat stronger dependence than q^{-2} [435]. In Tore Supra radial profiles the edge GAM frequency were also found to fit better to a c_s/R_0 scaling with the inclusion of a $(1 + 1/2q^2)$ correction [372].

However, parameter scans from AUG show an opposite trend with the edge GAM frequency increasing with the local q, as shown in figure 57 where the normalized GAM frequency $G = \hat{\omega} = \omega_{GAM} R_0/c_s$ is plotted vs the normalized q/q_{95} for a range of q_{95} and selected κ_b [305]. At high boundary elongation $\kappa_b \sim 1.6$ the G sensitivity to q is weak, but with decreasing κ_b the sensitivity increases, following an overall behaviour of $G \propto (2.5 - 3.0) \times (q/q_{95})^2/\kappa_b^2$. Part of the apparent flat sensitivity at high κ_b maybe due to the strong variation of local κ with radius which compensates the local q radial variation—cf figures 4 and 11 in [305], suggesting a stronger role of the s_q and s_κ radial derivatives. For example, large κ and s_κ, which are particularly relevant to the far-edge, are expected to enhance the parallel dynamics, while a large s_q makes the ion response more adiabatic [453].

In summary, there is good progress in matching experimental measurements and analytic predictions for a wide range of plasma conditions. Nevertheless, there remain several unresolved issues; the expected $\sqrt{2}$ frequency scale factor for circular plasma is not universally observed. A more detailed cross-machine validation would help to resolve possible Δ', q and ϵ effects in these cases. In addition, strong frequency deviations close to the LCFS maybe result from ion adiabatic index γ_i variations with collisionality. In theory, large q should reduce ω_{GAM}, but its impact also appears to have a κ dependence. In particular s_q and s_κ dependencies need further attention. The strongest shape factors are elongation, aspect ratio and Shafranov shift which act to reduce the GAM frequency, while triangularity acts to increase it. Experimentally, elongation has been well studied, triangularity less so, but untested so far is the aspect ratio dependence. Heating beams and ICRF can induce significant pressure anisotropy $\chi = p_\perp/p_\parallel$ which also changes γ_i. Isotope purity affects the effective mass m_{eff}, while high Z impurities also affect the effective charge Z_{eff}. There is much experimental work to be done here. Various parameters have been investigated individually, or in combinations, but there lacks a comprehensive cross-checking of results and theory. Here, it would be most instructive to build a proper multi-parameter, cross-machine database to test against current model predictions. The good agreement of experiments with numerical modelling is encouraging, but analytic models including X-points need to be developed.

8. GAM modal structure and sidebands

In axisymmetric magnetic configurations theory predicts (see table 2) that the flow/E_r oscillation should have a toroidal $n = 0$ and poloidal $m = 0$ mode structure while the pressure sideband should have a standing-wave $n = 0, m = 1$ (or higher) structure with $\tilde{n}_e \propto -\nabla \cdot \tilde{v}_\perp$, in a non-rotating plasma. Confirmation of the mode structure is a principle means of identifying the GAM in experiments and numerical simulations. Sections 8.1 and 8.2 review the modal evidence. In addition to flow/potential and density measurements, GAMs have also

been observed in other plasma parameters, including electron temperature and magnetic field. Generally the $\tilde{n}_e$ oscillation is the dominant component of the pressure sideband, while a $\tilde{T}_e$ oscillation appears as a sub-dominant component—these measurements are reviewed together with simultaneous multi-field measurements in section 8.3. In the simple fluid picture the GAM is purely electrostatic. However, inclusion of the $J \times B$ term leads to B-field coupling and the creation of an $m = 2$ magnetic sideband signature. Experimentally this becomes particularly evident with plasma shaping and finite plasma pressure β. These effects are addressed in section 8.4. The issue of a magnetic sideband, however, is complicated by the coupling between the GAM and MHD islands—this topic is discussed in a latter section 16.1. Theoretically the GAM is expected to exist only on closed flux surfaces, as is generally observed. However, recent evidence suggests possible field coupling across the separatrix into the open field-line region of the scrape-off-layer (SOL). This is discussed in section 8.5.

8.1. Toroidal and poloidal mode structure

The GAM $E_r \times B$ flow and potential perturbations should have an $m = n = 0$ mode structure, while the pressure sideband should have an $m = 1, n = 0$ structure in circular geometry. Using multi-point measurements with poloidal and toroidal separations can give the mode amplitude and phase distribution via correlation techniques. For example, a LRC measured on the same flux surface but not field-line, with a zero phase shift at the GAM frequency, would imply an $m = n = 0$ structure.

The potential mode structure was measured in T-10 using multiple correlation reflectometers (CR) with various poloidal separations (LFS and HFS), together with LP arrays. The high poloidal cross-correlation and corresponding cross-phase shifts close to zero indicate an $m \sim 0$ [292]. Similar LRC between HIBP and LP arrays at the GAM frequency were reported [303]. Pairs of Doppler reflectometers have also been used on several devices; HL-2A [345, 430], AUG [43], DIII-D [282], EAST [42], with both toroidal and poloidal separations showing LRC in the GAM flow perturbation with zero cross-phase shift, consistent with an $m = n = 0$ structure.

Similar results were obtained using a range of other diagnostic techniques: HIBP on JFT-2M [318], BES on DIII-D [435], paired poloidal CR antennas on TEXTOR [337] and between CR at the machine top and Li-beam at the mid-plane [343] (here the slight phase-shifts could be attributed to radial mismatches—consistent with predicted linear phase shift as function of minor radius [277, 318]), also using floating potential from LP arrays on HT-7 [285], J-TEXT [390] and SINP [395].

The density component of the pressure sideband oscillation is predicted to have a $\sin\theta$ dependence related to the potential as [53]:

$$\frac{\tilde{n}_{GAM}}{n} = -\sqrt{2}\, k_r \rho_i \left(\frac{e\,\tilde{\phi}_{GAM}}{T_e} \right) \sin(\theta), \qquad (263)$$

where k_r is the GAM radial wavenumber, ρ_i the ion gyroradius and $\tilde{\phi}_{GAM}$ the GAM potential. This relation was locally confirmed in JFT-2M [317]. Overall, the density perturbation is generally reported as being significantly smaller than the potential perturbation. In JET the GAM potential to density ratio was around 10, roughly consistent with expectations [357], while in ISTTOK the potential was 5 times larger than density just inside the LCFS [361]. In JIPPT-IIU, where the GAM $\delta\phi < 200$ V was strongest in the core, the δn was negligible [36]. Likewise, in T-10 while the GAM potential was significant (up to $\delta\phi = 100$ V for ohmic, increasing by a factor of 2 with ECRH) the density oscillations were smaller [292].

The poloidal distribution of the density sideband has been measured in TEXTOR with CR showing the GAM density perturbation is larger at the machine top compared to the mid-plane, consistent with an $m = \pm 1$ structure [337]. The $m = 1$ structure was also confirmed by a $\pi/2$ cross-phase between Li-beam density perturbations at the machine bottom and CR flow perturbations at the top [343]. A notable set of mode measurements were obtained in circular HL-2A using two-point correlation analysis of toroidally (37.5°) and poloidally (2.7°) separated LP array data around the outer mid-plane. As shown by the joint spectra in figure 58, a clear $m/n \sim 1/0$ mode for I_s and $m/n = 0/0$ mode for V_f fluctuations was obtained for the $f = 9.8$ kHz edge GAM [349]. With flux surface shaping, and in particular with field-null X-points, GAM harmonic and satellite spectral peaks have been observed consistent with (theory predicted) higher m modes for the pressure. X-points may also reduce the $m = 1$ mode amplitude in the edge by spreading the energy to the higher orders via up–down symmetry breaking.

8.2. Poloidal asymmetries

While the GAM flow oscillation has a poloidally symmetric $m = 0$ mode structure, the magnitude of the oscillation is not expected to be constant on a flux surface. Firstly, the turbulence amplitude and structure size (correlation length) have a strong poloidal dependence, notably an in–out asymmetry due to unfavourable field-line curvature. This asymmetry is reduced during L–H confinement mode transitions with a preferential $E_r \times B$ shear suppression on the LFS. Secondly, the mean $E_r \times B$ velocity, and its shearing rate $\omega_{E\times B} = \partial v_\perp / \partial r$ vary significantly with poloidal angle due, primarily, to equilibrium effects such as flux surface expansion, which in divertor configurations can lead to velocity stagnation close to a separatrix X-point. Consequently the turbulence driven ZFs will follow the RS dependence. In nonlinear GK simulations of ITG-like turbulence in circular flux surface the mean zonal shearing displayed significant poloidal dependence, being much stronger on the LFS compared to the high-field-side (HFS), i.e. turbulence ballooning leads to ballooning of RS, with a commensurate reduction of the local turbulence radial correlation lengths [459].

Turbulence structure effects were suspected in recent $E_r \times B$ flow measurements from circular Tore Supra plasmas where poloidal asymmetries in the flow were greatly in excess of equilibrium (flux surface expansion) effects [460]. Here, the formation of poloidal convective cells (PCC) was suggested as

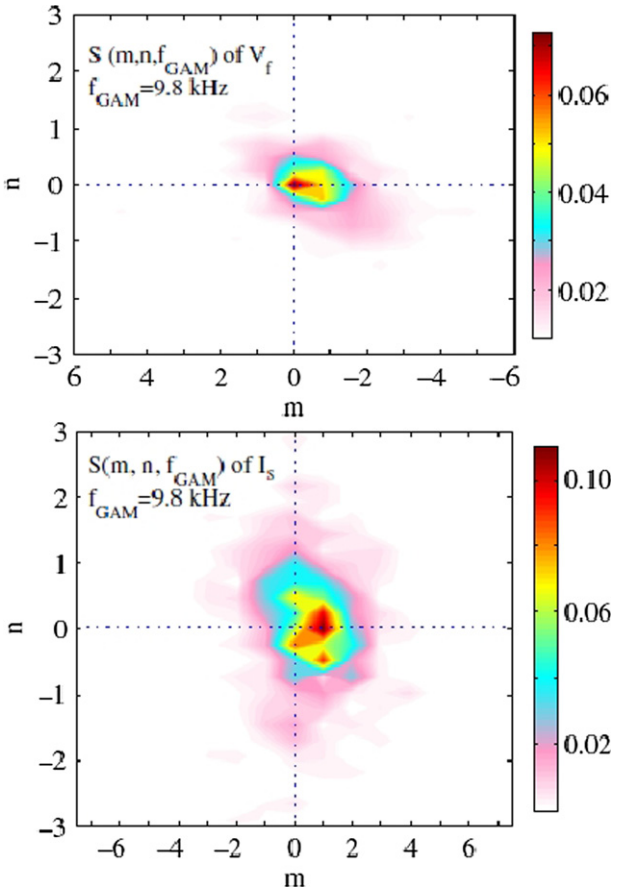

Figure 58. Joint $S(m, n, f_{\mathrm{GAM}})$ spectra of HL-2A mid-plane LP $\tilde{V}_{\mathrm{f}}$ (top) and $\tilde{I}_{\mathrm{s}}$ (bottom) as function of mode number at $f = 9.8$ kHz GAM frequency in low density $n_0 = 1.6 \times 10^{19}$ m^{-3}, ohmic $q_{95} \sim 3.5$ plasma. Reproduced courtesy of IAEA. Figure from [349]. Copyright (2009) IAEA.

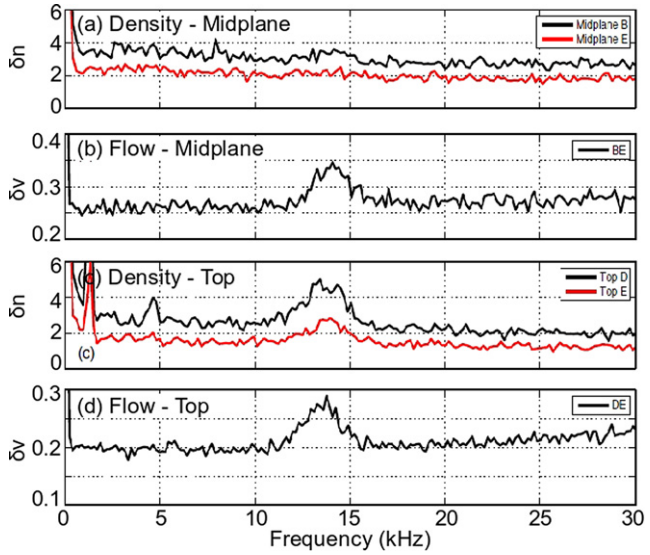

Figure 59. Density $\delta\phi$ (a) and (c) and flow δv (b) and (d) spectra from the mid-plane (a) and (b) and top (c) and (d) of TEXTOR edge showing no GAM in density at the mid-plane and a stronger GAM in flow at the mid-plane. Reproduced from [339].

a possible contributor. This was investigated using GK modelling which included convective cells, ZFs and GAMs. It was found that PCCs could be generated due to the compressional effects of ZF and poloidal asymmetries in RS due to the turbulence ballooning [461].

Although several devices have reported the GAM magnetic sideband distribution using poloidal arrays of magnetic coils (see section 8.4), measurements of the GAM flow magnitude as function of poloidal angle are scarce due to restricted diagnostic access, especially from the tokamak HFS. Nevertheless, the GAM spectra has been measured using correlation reflectometry at the LFS mid-plane and at the top of TEXTOR. As seen in figure 59, in the density fluctuation the GAM only appears at the top, consistent with an $m = 1$ mode structure, while the velocity fluctuation spectral peaks are stronger at the mid-plane, suggesting the flow oscillation is not a rigid body motion but experiences perpendicular compressibility.

Top and LFS mid-plane GAM measurements were also made in the circular Tore Supra using two poloidally displaced Doppler reflectometers. Here, the GAM behaviour was more subtle. When the mid to top mean $v_\perp$ flow asymmetry was particularly strong (a factor of 3) then the GAM peak magnitudes were similar while the background flow fluctuations $f < f_{\mathrm{GAM}}$ were larger at the mid-plane. When the asymmetry was weak (factor of 1.5) then the GAM was stronger at the top, while the background fluctuations were similar [462]. In ISTTOK the GAM potential amplitude δV was $\sim$20% larger at the mid-plane compared to the top [361].

Flux surface variations in the GAM flow magnitude will consequently impact the effective GAM shearing rate, enhancing or diminishing poloidal asymmetries in the (mean/zonal) $E \times B$ shearing rate. Overall, its impact on the turbulence and on GAM driven radial particle fluxes, and consequent drive of poloidal rotation, will have a poloidal dependence.

The measurement of GAM poloidal asymmetries in shaped/diverted plasmas needs further investigation, as well as modelling of such plasmas. Discrepancies in correlation and $\tilde{v}$ cross-phase measurements in DIII-D using multiple DR channels separated toroidally and polidally (above and below the LFS mid-plane) have been noted, which suggest that the GAM radial wavenumber k_{r} has a poloidal dependence—which could be expected in an elongated and up–down asymmetric plasma [282]. This is also a fruitful topic for future research.

8.3. Temperature and multi-field measurements

Although theory predicts a GAM pressure sideband, there was an early presumption that this was dominated by a density fluctuation component. Nevertheless, two devices, DIII-D and TCV, report measurable $\tilde{T}_{\mathrm{e}}$ values. Using a horizontal correlation ECE (CECE) diagnostic the GAM $\tilde{T}_{\mathrm{e}}$ (long wavelength $k_\perp < 1$ cm^{-1}) was found to be rather weak in DIII-D ohmic plasmas with a poor signal-to-noise ratio. However, in NBI heated L-modes $\tilde{T}_{\mathrm{e}}$ became significant. Magnitude-wise the GAM $\tilde{T}_{\mathrm{e}}/T_{\mathrm{e}} \sim \tilde{n}_{\mathrm{e}}/n_{\mathrm{e}}$, or even larger, as shown in figure 67 [283]. Combining the CECE diagnostic with a reflectometer

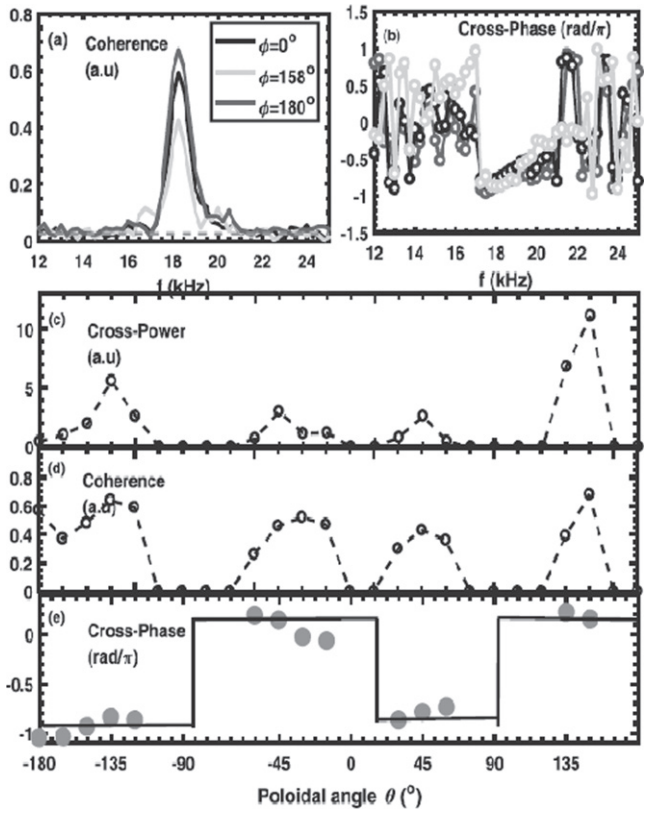

Figure 60. (*a*) Coherence and (*b*) cross-phase spectra between $\tilde{v}_\perp$ from DR at LFS mid-plane and toroidal array of Mirnov coils, and (*c*) and (*d*) GAM cross-power, coherence and cross-phase with B_θ poloidal array in EAST. Reprinted from [463], with the permission of AIP Publishing.

also provided a measure of the density–temperature $\tilde{n}_e$–$\tilde{T}_e$ cross phase angle $\alpha_{nT} \sim 140°$ at the GAM frequency. This confirms that the GAM pressure perturbation is not solely due to n_e. Since the pressure sideband should have an $m = 1$ structure with up–down anti-nodes this would suggest that either the GAM n_e or T_e perturbation should be minimal, or out of phase at the tokamak LFS mid-plane. Unfortunately poloidal measurements of $\tilde{T}_e$ or α_{nT} are currently not available to confirm the expected mode structure. This could be addressed, perhaps, using a vertical CECE/reflectometer diagnostic or SXR cameras to measure the GAM $\tilde{T}_e$ and $\tilde{n}_e$ at the top of the machine.

CECE was also used on TCV for $\tilde{T}_{rad}$, in combination with TPCI for $\tilde{n}_e$, DR for $\tilde{v}_{E\times B}$ and an extensive set of Mirnov coils for $\tilde{B}_\theta$ [380–383]. Airy-like radial profiles of $\tilde{T}_{rad}/T_{rad}$ (of which $\sim 80\%$ was due to $\tilde{T}_e$ and the rest due to $\tilde{n}_e$) show the broad eigenmode GAM peaking near the edge with a relative magnitude of 0.6%, then decaying slowly towards the core [381]. The coherent GAM was clearly identified in all diagnostics, but some discrepancies were noted in the measured radial wavenumber: 1.7–2.1 cm^{-1} from TPCI, while 0.9 cm^{-1} from CECE.

Minor disagreements were also noted between simultaneous GAM measurements in DIII-D where, in addition to the CECE and reflectometers, flow measurement using DBS/DR, long wavelength n_e from BES at the LFS mid-plane, as well as B_θ from Mirnov coil array at machine wall were available. All diagnostics showed a GAM peak, but not necessarily maximum at the same radial location [283].

Globus-M has also deployed a range of diagnostics for GAM measurements in ohmic divertor configuration plasmas; E_r from poloidal DR and mid-plane LPA, n_e from LPA, B_θ from Mirnov coil array, and multi-chord D_α spectrometers as a proxy for n_e (T_e dependence in the D_α was expected to be weak). All diagnostics showed a clear GAM peak. The poloidal structure of the D_α signal was consistent with an $m/n = 1/0$ mode [386] (although $m = 0$ quoted in [387]), while velocity fluctuations from poloidal correlation Doppler reflectometry confirm and $m = 0$ flow structure.

Many of the smaller, low power tokamaks have also employed extensive arrays of LPs (and ball-pen probes in COMPASS [394]) for simultaneous n_e and T_e measurements—results of which are presented elsewhere.

8.4. Magnetic signature (electromagnetic component)

In the fluid picture the GAM is electrostatic with no significant magnetic signature. Indeed, the absence of a magnetic signature (measured at the tokamak mid-plane using Mirnov coils) was presented as evidence that early GAM measurements where not simply low-order MHD modes, cf [304, 339]. However, as discussed in the theory section 2.12 on EM effects the inclusion of the $J \times B$ term leads to B-field coupling and the creation of a magnetic signature, which should become particularly evident with plasma shaping and increasing plasma pressure β.

Experimentally, the magnetic component has been measured in several devices. Using an HIBP diagnostic in CHS an oscillatory core zonal magnetic field around 50 kHz at $r/a \sim 0.6$ was observed [407]. Unfortunately with this single point measurement no information on the mode structure could be obtained. Generally, the term zonal field refers to the magnetic component localized to the GAM location within the plasma, while the term halo field is the tail that may extend outward to the plasma edge, and thus be observable with external Mirnov coils.

Correlation analysis of toroidal and poloidal arrays of Mirnov coil signals in EAST show, in figure 60, a clear B_θ magnetic halo component with $m \approx 2$ (sin 2θ) standing wave and $n = 0$ structure during 0.8–2 MW RF heated L-mode plasmas [463]. The coherence (between an LFS DR $\tilde{v}_\perp$ and poloidal array of Mirnov coils) goes to zero near the upper and lower divertors ($\theta = \pm 90°$) and mid-planes ($\theta = 0, 180°$) with corresponding cross-phase jumps. Nevertheless, the D-shaped plasma cross-section distorts the ideal structure with possible $m = 4$ and $m = 5$ Fourier components, as per [167]. The standing wave structure is consistent with theory [171, 173], and has similarities with TCV [382] and with EGAM measurements in JET [12]. The B_θ amplitude was 10^{-6} T, somewhat smaller than the predicted value of 10^{-5} T, possibly due to the vacuum distance between the coils and the plasma. Also observed in EAST, NBI driven core localized $0.5 < \rho \leqslant 0.8$ EGAMs display a standing wave with $m = 2$ plus an $m = 4$ side-lobe [433]. The mode is not poloidally anti-symmetric but

has a $\delta B_\theta \propto \sin 2(\theta - \theta_o) + \epsilon f(\theta, \theta_o)$ dependence where θ is poloidal angle and $\epsilon f(\theta, \theta_o)$ the effect of poloidal asymmetry and elongation. The parameter θ_o is a function of the ion beam pitch-angle and energy.

TCV is equipped with an extensive set of B_θ magnetic coils mounted between the carbon tiles. Three sets of toroidal arrays, at, above, and below the HFS mid-plane, confirms the $n = 0$ structure. From the poloidal coil set a clear $|m| = 2$ standing wave structure is observed for limiter L-mode discharges [382]. A comparison of the poloidal structure was made with theory [166] for circular cross-section:

$$\tilde{B}_\theta \propto \sin(\omega_{\mathrm{GAM}} t)\sin(2\theta). \tag{264}$$

Although this is a simplified approximation for the real TCV plasma geometry which had pronounced edge triangularity it, nevertheless, gave reasonably good structure agreement. This result complements the pure $m = 2$ magnetic structure for core localized EGAMs observed in JT-60U [370].

For circular limiter plasmas in AUG, the $\tilde{B}_\theta$ from a poloidal set of Mirnov coils was always strongest at the top and bottom of the vessel [311]. In radially wide continuum GAMs, double spectral peaks at 15 and 20 kHz were observed in the Mirnov signals (corresponding to two different radial GAM peak locations), varying from coil to coil in relative peak strength depending on the distance between the coil and plasma edge. In divertor configurations the GAM is radially narrow showing only one dominant frequency at all poloidal locations. Magnitude-wise the $\tilde{B}_\theta$ distribution had a strong HFS anti-node. In all cases there was a clear dominant $m = 2$ poloidal structure, although not with a pure ideal symmetry—see figure 9.17 in [311]. In particular, the presence of an X-point appears to introduce additional higher $m > 2$ harmonics. A 10 kHz GAM magnetic field was also observed in I-mode plasmas with a poloidal mode number $m = 1$ [307], however, it is not clear if this is purely related to the USN I-mode configuration or if it could be more generic.

Principally Mirnov coils are most sensitive to GAM features which are closest to the plasma edge—and to the coil. Taking into account the variable radial distance between the GAM and a poloidal coil array in DIII-D, estimates of $\tilde{B}_r/B_0$ strength indicated that the GAM was 9 times stronger on the HFS compared to the LFS mid-plane, suggesting an anti-ballooning nature for the GAM—which is not fully understood [283].

COMPASS reports similar measurements as AUG and TCV. Only in divertor configurations was the magnetic component (both $\tilde{B}_\theta$ and $\tilde{B}_r$) strong enough to measure with Mirnov coils and saddle loops [394]. There is no clear $n = 0$ mode in limiter configurations, but it appears in the divertor configuration. Figure 61 shows the poloidal structure of the amplitude and phase shift of the B_θ and B_r components. The poloidal $m = 2$ non-rotating standing-wave structure is evident, but is more complex with amplitude distortions (from the ideal circular structure) at the top and bottom HFS with additional phase jumps. Generally B_θ is an order of magnitude larger than the B_r component. Like in AUG, the GAM has a single narrow spectral peak in divertor configurations but is spectrally broader in limiter configurations.

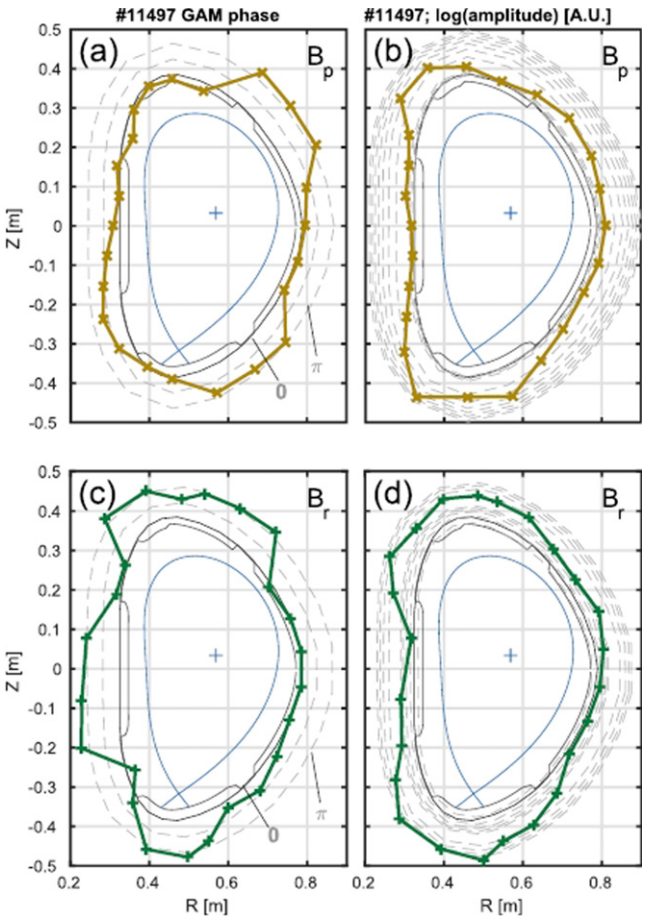

Figure 61. Poloidal structure of B_θ (top) and B_r (bottom) for phase shift (*a*) and (*c*) and amplitude (*b*) and (*d*) in COMPASS. Reproduced courtesy of IAEA. Figure from [394]. © EURATOM 2017.

Likewise, in the D-shaped plasmas of Globus-M compact spherical tokamak the toroidal and poloidal Mirnov coil arrays showed an distorted poloidal $m = 2$ standing wave with a broader HFS span in B_θ [386, 387]. The toroidal structure was less clear with a strong distortion, termed 'anti-ballooning effect' [387] similar to DIII-D observations.

8.5. Cross separatrix coupling and GAM signatures in the SOL

In theory the GAM should exist only on closed flux surfaces. Indeed, nearly every tokamak device has reported the absence of GAM related flow oscillations in the open field lines of the SOL outside the last-closed-flux surface (LCFS) of limiter, or the separatrix of divertor configurations. As one example, in T-10 limiter discharges there is no sign of GAMs in LP signals on any flux surface that intersects a plasma facing component surface [292].

However, recent results from TCV suggest a possible field coupling of the GAM across the separatrix into the open field-line SOL region may occur. Observations from LPs close to the LSN divertor strike points and D_α emission signals show an oscillation around the GAM frequency in the radial particle flow [383]. Significant coherence was observed between

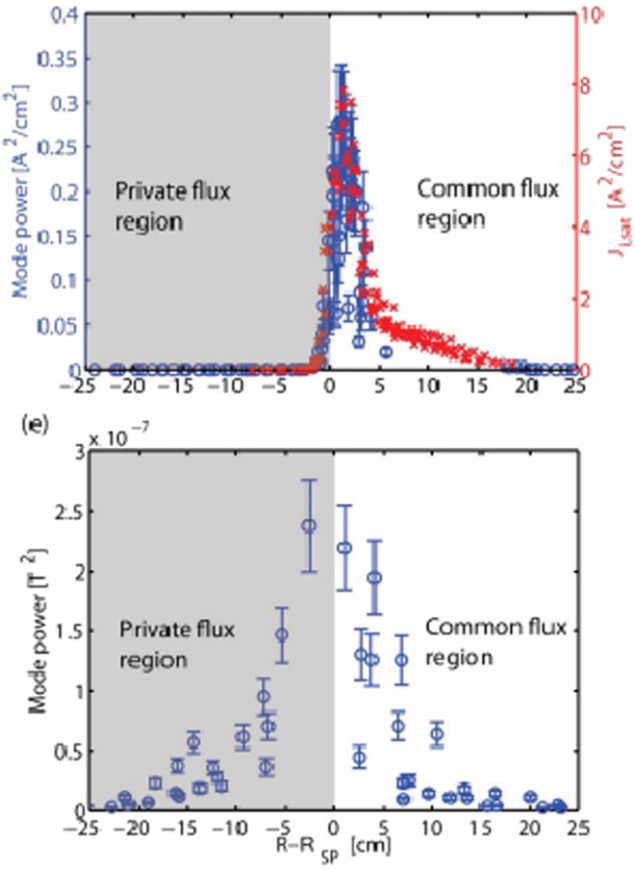

Figure 62. Radial profile of spectral power at the GAM frequency from (top) divertor Langmuir $\tilde{I}_{sat}$ probes and (bottom) $\tilde{B}_\theta$ Mirnov coils in LSN L-mode TCV discharge #54490. Reproduced from [383]. © 2018 Ecole Polytechnique Federale de Lausanne.

$\tilde{B}_\theta$ Mirnov signals and SOL Langmuir $\tilde{I}_{sat}$ signals around the separatrix, with zero cross-phase. The radial profiles in figure 62 appear to show the GAM mode power in an LSN divertor L-mode peaking just outside the outer strike-point in the common flux region. Errors in the equilibrium strike point locations were not discussed in the paper, but may be expected to be of the order of a few mm. Nevertheless, strike point sweeps show the GAM signature moving from probe to probe in a fashion consistent with the separatrix position. In the example shown, the SOL I_{sat} GAM frequency matches that of an eigenmode GAM observed in TPCI measurements inside the plasma separatrix. The precise SOL profile behaviour depended strongly on the divertor flux surface expansion and the dominant heat flux strike point. In addition, GAM signatures were not observed in SOL regions of limiter configurations.

Although nonlinear global GK simulations were able to reproduce some experimental features, there is no clear theory explanation for the observations, other than a possible coupling of the GAM halo magnetic field to the SOL generating a particle flux modulation which then travels to the divertor probes.

In summary, the toroidal and poloidal structure of the GAM flow and density component of the pressure sideband are confirmed by measurement. There are notable poloidal asymmetries in the sideband, reflecting the poloidal distribution of the turbulence amplitude and the consequent RS drive. There are direct measurements of a T_e component, as well as suggestive α_{nT} cross phase angles indicating a significant $\tilde{T}_e$ role in the pressure sideband. Magnetic sidebands with a complex, but appropriate poloidal structure are observed, and there is a suggestion of possible cross-field coupling of the edge GAM into the open-field lines of the SOL.

9. GAM radial structure

A fundamental feature of the GAM is its zonal structure. The zonal 'ring' nature of the GAM and its spatial localization is reflected in its frequency and amplitude radial profiles. The zones are seen as one or more amplitude peaks, sometimes accompanied by frequency plateaus. First the GAM localization, i.e. core or edge, is discussed section 9.1 and then its radial/zonal extent in section 9.2. These features are linked via the pressure ∇P profile to the GAM drive and the q profile to the GAM collisionless damping. In many cases the GAM frequency remains constant over an extended radial region, forming a series of steps or plateaus. As opposed to the smooth frequency continuum, these GAM radial structures are often referred to as global or eigenmode GAMs. However, note there is varying usage of the eigenmode and global terminology, particularly between experimental and theory reports, and possible confusion with the global GGAM associated with an off-axis maxima in the continuum GAM frequency. Eigenmode-like structures predicted to arise from a variety of mechanisms, kinetic and EM, as discussed in the theory sections 2.11, 2.12 and 3.5. These mechanisms are summarized in table 5. The experimental observations of eigenmode GAMs and their transition to and from continuum GAMs are reviewed in section 9.3, with multiple eigenmode GAMs in section 9.4, and the ultra-wide GGAMs in section 9.5. Unlike the stationary ZF, theory predicts that the GAM can propagate radially, and even accelerate. This is discussed in section 9.6.

9.1. Radial localisation

With few exceptions, the turbulence driven GAM is observed in the plasma edge region of tokamak devices with the last closed flux surface, or separatrix for divertor configurations, defining the outer boundary. The GAM is often found to be suppressed just inside the separatrix in higher density and heated L-mode discharges—which may be due to stronger collisional damping [282, 304, 435]. The presence of an X-point may also play a role in suppressing the GAM just inside the separatrix.

The GAM inner boundary depends on the shape of the kinetic profiles which set both the GAM drive and damping. For the drive the density and temperature gradients are determinant. In AUG divertor configurations the development of a density pedestal acts as a strong inner barrier [305] where the reduction in ∇n_e at the pedestal top essentially limits the drive scale length (cf [63]). For limiter configurations the n_e profile is more parabolic (weak pedestal) and the GAM extends inward,

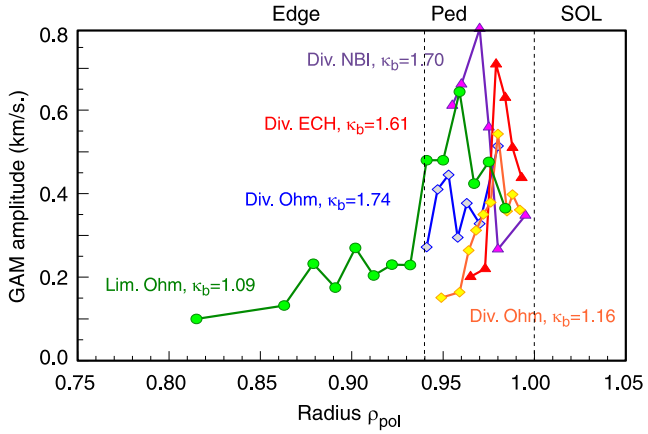

Figure 63. Measured GAM amplitude profiles for selected limiter and divertor configurations in AUG edge with $q_{95} \sim 3.7$. Adapted from [26]. © IOP Publishing Ltd. All rights reserved.

as shown in figure 63. Here, the GAM inner boundary is now set primarily by the q profile which determines the GAM collisionless Landau damping (see section 12.1.2). The role of Landau damping is nicely illustrated in the results from Tore Supra at high and low collisionality $\nu^* = \nu_{ei}/(\epsilon\omega_{be}) \propto qn_eT_e^2$ with nominally identical drive [373]. Despite the (expected) overall weaker GAM amplitude at high ν^* close to the LCFS, the GAM profile is, nevertheless, wider and extended inward due to a lower *collisonless* damping.

An exception to the edge localization is the JIPP T-IIU tokamak. Although GAMs are observed in the edge ($r/a > 0.7$), they were found to be significantly stronger in the plasma core [326]. Possible causes were proposed, including the dominance of streamers in the edge which might suggest a turbulence regime effect, or a ν^* effect. Collisionless damping is also a good candidate, however, the core GAM preference was observed for both low density 1×10^{19} cm^{-3}, moderate $q \sim 4.3$, ohmic heated plasmas with $T_e \gg T_i$ (where the higher τ_e weakens the Landau damping $\gamma \propto \exp[-(q^2 + T_e/T_i)]$), as well as in NBI heated discharges with $T_i > T_e$ and DW dominated turbulence plasmas [329]. The explanation thus remains open.

In stellarators and heliotrons the inverse $q = 2\pi/\iota$ profile leads to GAMs being more weakly damped in the plasma core. This was observed in the CHS stellarator where the GAM peaks around $\rho \sim 0.3$ and weakening towards the edge $\rho \sim 0.6$ [61]. Likewise in the H-1 heliac the strong geodesic curvature assisted the formation of a core $\rho = 0.5$ localized GAM with moderate heating [37]. However, in the TJ-II heliac core localized GAMs were only observed with strong Alfvénic drive [416].

In the few cases of GGAMs observed in some devices with exceptionally wide structures (discussed in section 9.5) the amplitude peaking (if any) is also orientated more to the edge. The exception being EGAMs which are preferentially driven in the core region of both tokamaks and helical devices, such as CHS and LHD, due to the concentration of EPs—see section 13.

9.2. Radial zonal structure

A defining feature of the GAM is its radial structure, forming one or more well defined zonal (flux surface) rings. These are usually identified as a clear velocity or $\tilde{E}_r$ amplitude variation with a central peak. Most devices report single symmetric (Gaussian-like) peaks, although peaking towards the outerside of the zonal ring is also observed. An example from AUG is shown in figure 63 with a series of GAM velocity amplitude A_{GAM} radial profiles from L-mode plasmas with various applied heating levels in limiter and divertor configurations [26]. For divertor configurations the profiles show single narrow radial amplitude GAM peaks constrained to the density pedestal region with frequencies increasing across the peak following the continuum behaviour [26, 305]. Here, the GAM peak full-width-half-maximum (fwhm) is of the order of a few cm. This is the typical magnitude reported for the GAM existence width, i.e. visibility, of edge continuum GAMs in many devices. Table 11 summarizes these results in terms of a physical Δ_r or normalized flux coordinate Δ_ρ, which generally translate to a width range of 1–5 cm. There are some exceptions of wider GAMs but these correspond to conditions with shallower temperature gradients. In terms of machine size the various widths correspond to a modest $\Delta/a \approx 2\%$–15%.

As well as the observed gradient dependency [305], a shape dependence has also been reported from AUG. In limiter configurations the GAM Δ_r (fwhm) decreased with increasing elongation from ~4 cm at $\kappa \sim 1.1$ to 1 cm at $\kappa > 1.4$, while with divertor configurations Δ_r never exceeded 2 cm [310, 311]. An isotope dependence was also noted in ISTTOK where $\Delta_r(1/e) \sim 12.4$ mm for hydrogen and ~13.5 mm for deuterium [440].

The GAM visibility range should, theoretically, be determined by the drive and damping profiles, i.e. the ∇P, q, etc. However, for the individual zonal rings there is no clear prediction, but are expected to have widths ranging from a few tens of ion gyro-radii ρ_i to mesoscales [53]. The so-called mesoscale length, $\sqrt{a\rho_i}$ or $\sqrt{L_x\rho_i}$, bridges between the turbulence scale ρ_i and the machine scale a or the kinetic profile gradient length L_x where x is density or temperature [53, 61]. The concept of a mesoscale comes from transport considerations where ZFs may have system size scales in the poloidal/toroidal direction but lengths as short as the turbulence scale in the radial direction [53]. For typical plasmas conditions this mesoscale is a few cm, i.e. several tens of ion gyro-radii—consistent with the reported magnitude of experimental zonal widths.

The low cm range is also the magnitude measured in several devices for the GAM coherence length L_{GAM} or its radial wavelength λ_r. On T-10, for example the GAM $\lambda_r \sim 3$–5 cm [292], while in JET the $\lambda_r \sim 2.4$ cm was found to be similar to the GAM existence width [358]. In DIII-D a $(1/e)$ radial correlation length of $L_{GAM} \sim 2$–3 cm [29] and in AUG the GAM λ_r, obtained from radial cross-correlation DR measurements, was found to be typically twice that of the GAM width [310, 311]. Likewise for FT-2 where $\lambda_r \sim 2$–4 cm was a factor of 2 larger than the $\Delta_r \sim 1.2$–1.9 cm. In TEXTOR a range of lengths were reported: a $\Delta_r = 4$ cm wide peak using Li-beam

Table 11. Experimental values for GAM radial existence or visibility width Δ_r (or Δ_ρ in italic) for various devices. The categories refer to experimental radial structure of continuum, eigenmode or global extent. The Δ/a indicates approximate widths as percentages of the device minor radius a.

Device	Type	Δ (cm)	Δ/a (%)	Notes
AUG	Cont.	1–5	2–10	DR edge (fwhm) [26, 310, 311]
AUG	Eigen	2–5	4–10	DR edge, stairs [305, 315]
CHS	Cont.	1–2	5–10	HIBP edge [398]
COMPASS	Eigen	2–3	10–15	LP edge [394]
DIII-D	Cont.	8–9	14	BES edge [435]
DIII-D	Eigen	*0.08–0.2*	8–20	DR edge [282, 283]
DIII-D	Global?	*0.4*	40	DR core, double GAM [247, 283]
EAST	Cont.	*0.07*	7	DR, eigen in H-mode 3% [42]
FT-2	Cont.	1.2–1.9	15–23	UHRS, $\lambda_r = 2$–4 cm [250, 255]
HL-2A	Cont.	3–4	8–10	DR edge [430, 464]
HT-7	Cont.	< 2	2.5	LP [285]
ISTTOK	Cont.	*0.5–1.0*	6–15	LP [363, 364]
JET	Eigen	2–4	2–3	DR edge. $\Delta_r \sim \lambda_r$ [358, 360]
JFT-2M	Eigen	4–5	14	HIBP edge (fwhm) [317, 325]
JIPPT-IIU	Cont.	3–5	13–20	HIBP stairs over edge/core [36]
JIPPT-IIU	Global?	21	$>$90	HIBP, NBI [331]
TCV	Cont.	*0.15*	15	TPCI edge [380]
TCV	Eigen	*0.15–0.2*	15–20	TPCI [380, 382, 383]
TEXTOR	Cont.	5–7	10–15	CR [339], LP [342], LiB [343]
TEXTOR	Eigen	8–13	16–27	CR, satellites [339]
TUMAN-3M	Cont.	2	8–9	DR [335]
Tore Supra	Cont.	*0.08–021*	8–21	DR [372, 373]
T-10	Cont.	*0.1–0.25*	10–25	HIBP, CR, LP [292]
T-10	Global?	19–20	$\sim$70	HIBP 296, 298, 301]

[343], a $\lambda_r \sim 9$–13 cm using LPs [342, 465], and a radial correlation length $L_{GAM} = 11$ mm using CR [339]. Nevertheless, all the measured values exceed wavelength predictions of the order of ρ_s [217, 219]. Generally the GAM decays radially before completing a wavelength.

9.3. Radial eigenmodes and staircases

Single-fluid MHD models describe the GAM as a singular radially narrow mode with a frequency that scales with local parameters creating a continuum of frequencies over the GAM's radial extent. This is the conventional picture most commonly reported in early experiments with ohmic or low power L-mode heating. However, as noted in section 2.4, the inclusion of factors such as FOW effects due to particle radial drifts, or FLR effects due to finite temperature leads to GAM dispersion effects. This introduces two new phenomena; the formation of an extended radial (non-local) eigenmode structure, and radial propagation of the GAM.

The FLR/FOW effects together with a finite temperature gradient lead to phase-mixing (PM), which distorts the radial structure of the continuum GAM leading to local frequency locking and flattening of the ω_{GAM} profile. As discussed in section 2.11 the GAM dispersion relation can be written in the form of an eigenmode equation (107) with an Airy function solution for the potential $\phi(r) = \mathrm{Ai}((r_0 - r)/\lambda_{Ai})$ where the Airy scale $\lambda_{Ai} = \rho_i^{2/3} L_\omega^{1/3}$ with $L_\omega = |\nabla\omega^2_{GAM}/\omega^2_{GAM}| \sim L_T$ the scale length of the GAM continuum frequency spectrum [108, 155, 156]. From this model the GAM is should propagate down the temperature, or GAM frequency gradient with a radial dimension that scales with L_ω. Theory also suggests that non-local effects should be weak for small $\rho_* = \rho_i/a \propto \sqrt{T_i}/(|B|a)$ [217]. Table 11 indicates that GAMs identified as having an eigenmode-like radial structure are more prevalent in the larger machines with, despite the larger a and B_T, higher ohmic I_p and additional heating. While this is suggestive, unfortunately current published results do not allow more than a cursory statement. To properly establish a ρ_i or a ρ_* dependency requires a more detailed multi-device analysis.

Figure 63 shows a GAM A_{GAM} radial profile for an AUG L-mode plasma in a circular limiter configurations [26]. The lack of a strong pedestal and shallower gradients allow the GAM to extend inward displaying a secondary peak and a (modulus) Airy function profile—but, contrary to the model above, reversed in radius. Tore Supra also report reversed Airy-like amplitude profiles [372]. Likewise for TEXTOR where the amplitude profile peaks towards edge with a tail extending inward. The GAM peak was also seen to move inward with decreasing mean density [339]. Interestingly, a radial shift in the profile between mid-plane and top was reported, being more inward at the mid-plane [341]. In all cases, across each of the amplitude peaks the GAM frequency remains constant, forming a series of steps or a staircase-like structure.

On FT-2 the GAM radial wavelength was compared with corresponding experimental Airy scale lengths. Using a dual-channel UHR scattering diagnostic the GAM $\lambda_r = 2.4$ cm was

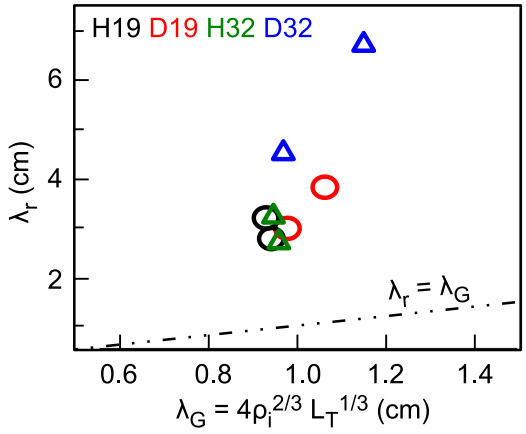

Figure 64. Measured GAM λ_r vs model $\lambda_G = 4\lambda_{Ai}$ wavelength using experimental L_T and ρ_i for various isotopes and plasma currents in FT-2. The symbols refer to plasma isotope and plasma I_p in kA. Adapted from [466]. CC BY 3.0.

substantially larger than its measured $L_{GAM} = 0.7$ cm correlation length [255]. As shown in figure 64 for various plasma isotope, the wavelength is also significantly larger than a wavelength $\lambda_G = 4\lambda_{Ai}$ derived from the Airy length at the GAM peak [466, 467]. In TUMAN-3M the measured $\Delta_r \sim 0.5$ cm (fwhm) was closer to the Airy length $\lambda_{Ai} = 0.38$ cm, but still larger [335].

The measured zonal widths for identifiable eigenmode structured GAMs from various devices are also summarized in table 11. As for the continuum GAMs, there is some spread in the reported values across device size and plasma conditions, but overall the eigenmodes appear consistently wider with $\Delta/a \sim 15\%$–25%. These values match surprisingly well results from ion fluid ITG simulations, cf figure 26 [102] where the eigenmode Δ_r/a scales with $\sqrt{\rho_*}$ over the range 10%–30%—cf figure 3 in [217]. Here, the eigenmode GAM frequency is constrained between the respective continuum f_{GAM} and f_{SW} (harmonic) branches, as shown in figure 26. A similar picture of GAM frequency steps in radius appears in the modelling of Hallatschek where the GAM coupling to the parallel SW leads to frequency jumps as the GAM continuum frequency crosses the successive SW branches with decreasing q—cf figure 5 [14].

Sometimes a single edge eigenmode is observed, such as the 5 cm wide eigenmode shown in figure 65 for JFT-2M, or the 2–3 cm eigenmode in COMPASS [394], the 5 cm eigenmode inside the pedestal radius in AUG [315], or, as in figure 66 for TCV, it is combined with regions of continuum behaviour [468]. Eigenmode GAMs are common in TCV, peaking at the edge but extending inwards to a significant portion of the plasma radius [382, 383, 468]. The eigenmode f_{GAM} scales very closely as c_s/R_0 at the A_{GAM} peak location [380]. During q_{95} scans (by ramping I_p at constant B_T) in diverted $\kappa = 1.52$, high triangularity $\delta = 0.5$–0.6 plasmas, as shown in figure 66 the GAM was seen to transition from a continuum to an eigenmode as q decreased [383, 468]. Subsequent I_p ramp experiments in TCV also compared f_{GAM} with a simplified Gao formula [117] including elongation and q terms, finding some agreement at the outer GAM boundary where the

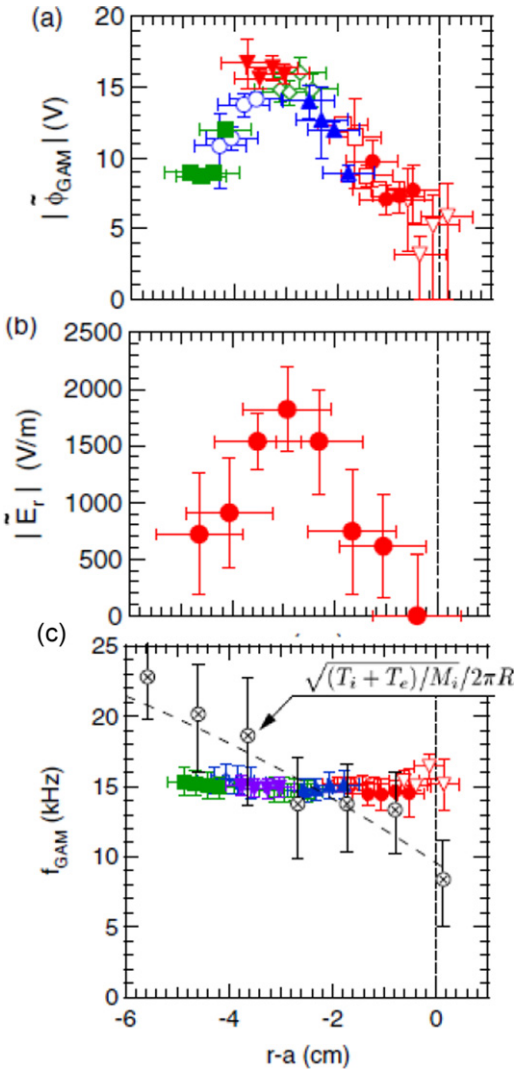

Figure 65. Radial profiles of experimental (*a*) GAM $\tilde{\phi}$, (*b*) $\tilde{E}_r$ and (*c*) f_{GAM} for eigenmode GAM in JFT-2M with 0.7 MW NBI. Colours mark different shots. The GAM peak aligns with f_{GAM} crossing the continuum frequency. Adapted from [317]. © IOP Publishing Ltd. All rights reserved.

GAM amplitude peaked [383]. Local and global nonlinear GK simulations with the GENE code for continuum and eigenmode conditions were also performed. Local flux-tube simulations always produced continuum behaviour independent of input profiles, while global simulations were found to be fairly consistent with the experiment, reproducing either continuum or eigenmode as appropriate [257]. The simulations also revealed that q was not the cause of the transition but a co-incident rise in the T_e and n_e profiles [383].

A consistent picture emerges with similar results from a range of machines, including JFT-2M where in figure 65 the frequency of a $\Delta_r \sim 5$ cm wide eigenmode crosses the predicted continuum GAM frequency around the GAM peak amplitude [317]. Similar for Globus-M where the eigenmode frequency matches the Gao continuum prediction at the GAM peak location [384], and for eigenmode GAMs in CHS [398] and on JET where the eigenmode frequency also matches the continuum frequency at the GAM peak [358].

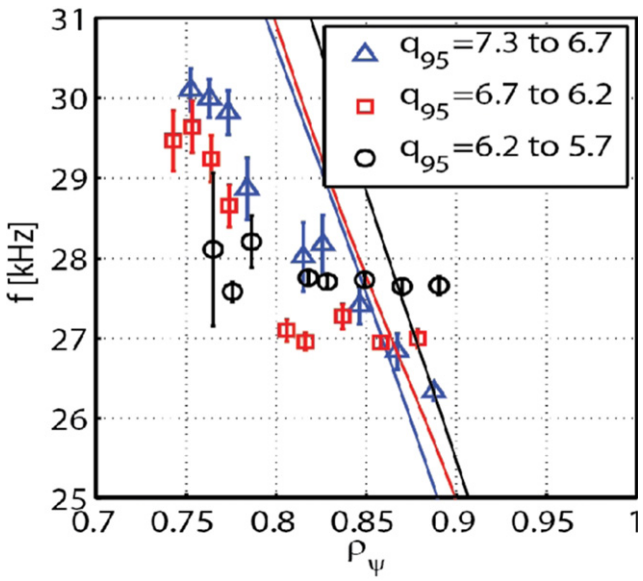

Figure 66. Measured GAM frequency $f_{\rm GAM}$ radial profiles during q_{95} ramps in TCV. Lines are predicted $f_{\rm GAM} = c_{\rm s}/(2\pi R_0)$ with experimental $T_{\rm e} = T_{\rm i}$ values. Reproduced from [468]. CC BY 3.0.

In some cases there are multiple eigenmodes appearing as a sequence of zonal rings, such as in JIPPT-IIU where a series of rings, each a few cm wide, cover the whole plasma cross-section—cf figure 4 in [36]. In both AUG limiter and divertor configurations multiple frequency plateaus are observed, increasing in width with decreasing location across the minor radius (i.e. with an increasing L_T) [26, 305]. It should be noted that resolving small staircase steps from a continuum behaviour is also an issue of diagnostic capability and measurement resolution. Around the zonal boundaries it is common to observe two spectral GAM peaks (note this is distinct from GAM spectral peak spitting due to low frequency modulation (FM), which is discussed in section 15.3) at the same radial location, suggesting a degree of overlapping GAM zonal rings [305].

Figure 67 shows $f_{\rm GAM}$ and $A_{\rm GAM}$ radial profiles from DIII-D discharges during (*a*) an NBI/ECR heated phases with dual eigenmode GAMs at 21 kHz and 24 kHz across the plasma core region, and (*b*) lower temperature ohmic phases with a wide continuum GAM [283]. Overlaid are a series of curves representing various GAM frequency predictions which are described in [283]. The continuum GAM follows the simple $f_1 = c_{\rm s}/(2\pi R_0)$ with $c_{\rm s}^2 = (T_{\rm e} + T_{\rm i})/m_{\rm i}$ rather well. For the dual eigenmode cases the radii where their frequencies cross the continuum f_1 curve again coincide rather closely with the positions of GAM maxima—marked by the vertical dashed lines—shown in the corresponding $A_{\rm GAM}$ profiles from various diagnostics. Note β corrections are not included. For comparison, curve $f_4 = (\sqrt{\pi + \ln q + 4.41}\, v_{Ti})/(2\pi q R_0)$ (where v_{Ti} is ion thermal velocity assuming $T_{\rm i} \gg T_{\rm e}$) is that of the eigenmode model of Gao [108]. This curve has some agreement with the 24 kHz case at $r/a = 0.65$, which is close to the $q = 2$ rational surface.

9.4. Multiple GAMs

Multiple or overlapping GAM zones have been reported from several devices, as in figure 67 for DIII-D [283] as well as AUG [305], HL-2A [354] and HT-7 [285, 287]. Figure 68 shows an example using LP arrays in the edge region of a low density HT-7 ohmic discharge [287] where two eigenmode GAMs, separated by ∼6 kHz, are seen to coexist simultaneously across the same radial extent. The higher frequency GAM peaks further in than the low frequency GAM. But in both cases, the GAM amplitude peaks coincides with the GAM frequency approaching or crossing the continuum frequency prediction, and where the GAM radial wavenumber $k_{\rm r}$ approaches or crosses zero. The topic of the GAM radial wavenumber and propagation is discussed in the next section 9.6, however, the results are consistent with the predictions of the kinetic description of GAMs where the small physical scales around the GAM peak leads to conversion of the continuum GAM to a radially propagating eigenmode via FLR effects [11, 121, 434].

In short, a succession of GAMs are excited different radii which then propagate radially and are seen to overlap. The transition from a continuum to an eigenmode appears to occur when temperatures are sufficiently high that ion FLR and profile gradients become important leading to a coupling across broad radial regions. The coincidence of the GAM amplitude maximum and the crossing of the eigenmode GAM frequency with the continuum GAM frequency confirms this as the coupling (drive) location.

9.5. Global GAMs

A few devices have reported ultra-wide eigenmode GAMs covering almost the whole of the plasma minor radius—see table 11—and due to their extent are called global eigenmode GAMs. From the theory side the term GGAMs is well understood—see sections 2.12 and 3.5—and occur near a local off-axis maxima in the GAM continuum frequency, which can form due to negative magnetic shear or high core plasma pressure. Here, the global nature results from the crucial coupling to the non-local EM $m = 2$ harmonic which has a global character. GGAMs are generally associated with EGAMs—see section 13.1. Nevertheless, there are also a few cases where a global eigenmode structure appears without a clear EP source. Figure 69(*b*) shows an ultra-wide global eigenmode stretching from $0.2 < \rho < 0.94$ in a sequence of low density ohmic T-10 discharges [296, 298, 301, 469]. Here, the GAM has a constant (non-chirping) $f_{\rm GAM} \sim 18$ kHz which does not follow the local continuum frequency, but does align with the continuum frequency prediction at the outer zonal edge. The frequency was observed to track the edge continuum GAM frequency $\omega_{\rm GAM} = \sqrt{2\,T_{\rm e}/m_{\rm i}}/R_0$ with $T_{\rm e}$ taken at $\rho = 0.7$ over a range of $I_{\rm p}$ and $\bar{n}_{\rm e}$ discharges. The $\rho = 0.7$ corresponds to the GAM drive location identified from the $+\pi/2$ cross-phase between the potential and density fluctuations (using HIBP) at the GAM frequency [296]. There was no indication of a local GAM continuum frequency maxima, and thus no direct

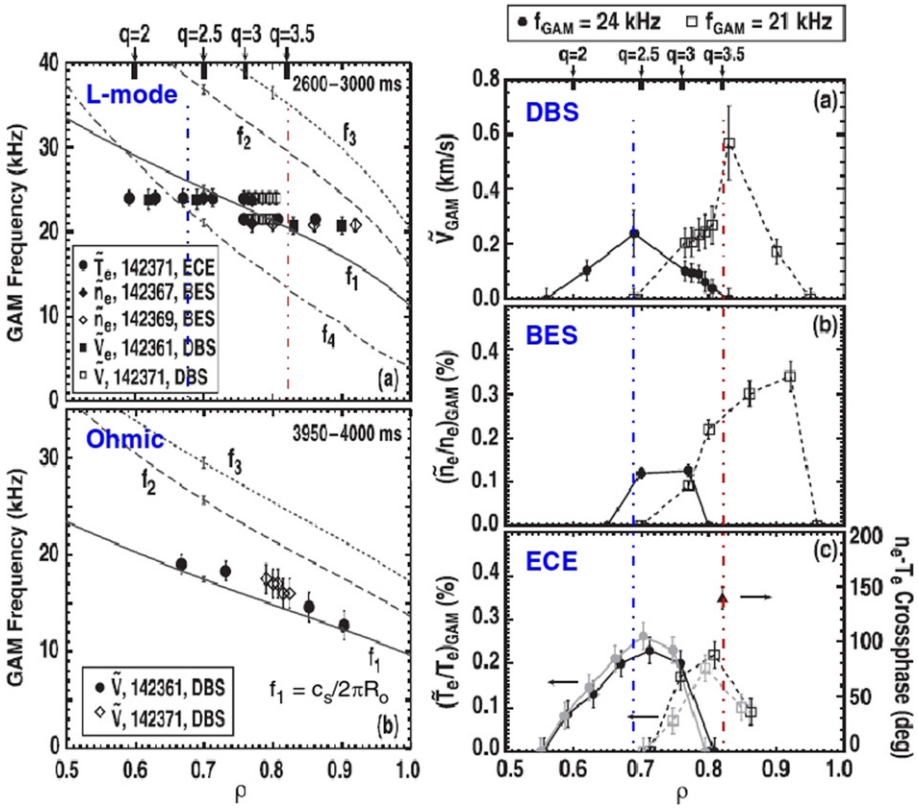

Figure 67. (Left) Measured frequency profiles for (*a*) core eigenmode during NBI/ECH L-modes and (*b*) continuum GAMs during lower temperature ohmic phases at same $\bar{n}_e$, I_p, q_{95}, etc. (Right) Radial profiles of (*a*) velocity $\tilde{v}$ from DR/DBS, (*b*) density $\tilde{n}/n$ from BES, and (*c*) $\tilde{T}_e/T_e$ from ECE, plus nT-cross-phase for eigenmode GAM in DIII-D. Adapted from [283], with the permission of AIP Publishing.

link to GGAM theory. However, it was suggested that the GAM was driven by DW turbulence at the edge with the GAM propagating radially inward [296]—consistent with standard eigenmode GAM theory. An intriguing companion to this eigenmode GAM in T-10 is the observation of GAM 'satellite' modes tracking the main GAM with a slightly higher constant difference frequency. Both modes display an $m = 0$ poloidal mode structure [296]. TEXTOR also reports the coexistence of a continuum GAM and a slightly lower frequency satellite mode with a constant (plateau) frequency with radius—see figure 4 of [339].

Core continuum/staircase GAMs ($r/a \sim 0.2$) with intense broad frequency peaks 20–50 kHz were also reported in low density ohmic plasmas in JIPP-TIIU using HIBP [330]. When applying NBI heating with increasing power the GAM converts to weaker, constant frequency GAM centred on 35 kHz, extending across almost the whole plasma minor radius, as shown in figure 69(*a*) [331]. With 0.5 MW NBI heating the core ion temperature was raised such that $T_i > T_e$ which strengthens the ion Landau damping, and thus weakens the GAM amplitude compared to the ohmic phase. A link to a maximum in the GAM continuum frequency was not established, but similarities to the simulations of eigenmode GAMs by Miyato [217] were noted, consistent with a propagating turbulence driven eigenmode. Nevertheless, an EP driven GAM cannot be ruled out.

As shown in figure 67, DIII-D also observes exceedingly wide eigenmode GAMs in several diagnostics as far in as $r/a \sim 0.6$ at the LFS mid-plane with high $q_{95} > 5$ during NBI and ECR heating [283]. As with the JIPP-TIIU results, it was noted that the appearance of the eigenmode GAM occurred at higher temperatures while the continuum GAM was present in lower temperature discharges; consistent with theoretical expectations of finite ion Larmor radius effects. These GAMs are not identified as GGAMs, despite their semi-global extent and strong $\tilde{B}_\theta$ EM signatures.

9.6. Radial propagation and acceleration

One of the main differences between stationary ZFs and GAMs is that ZF are non-dispersive and thus not expected to propagate radially, while GAMs may [144]. Radial propagation appears in the GAM dispersion due to several factors, including FOW and FLR effects. For example, FLR modifies the GAM dispersion relation from $\omega^2 = \omega_0^2$ to a linear dispersion of the form $\omega^2 = \omega_0^2(1 + Dk_r^2\rho_i^2)$ where ω_0 is the continuum GAM frequency, $D \sim \mathcal{O}(1)$, and k_r the GAM radial wavenumber cf [63, 140]. For $k_r\rho_i \ll 1$ the GAM linear group velocity $v_{gr} = \partial\omega/\partial k_r = D\omega_0\rho_i^2 k_r$, cf equation (84), which is typically outward (consistent with the picture of the GAM continuum from radial temperature profiles). Namely, in the presence of a ∇T_e the GAM propagates where $\omega < \omega_0$ and is evanescent where $\omega > \omega_0$ [16, 108, 155]. This is discussed more fully in the theory section 2.7 on dispersion effects.

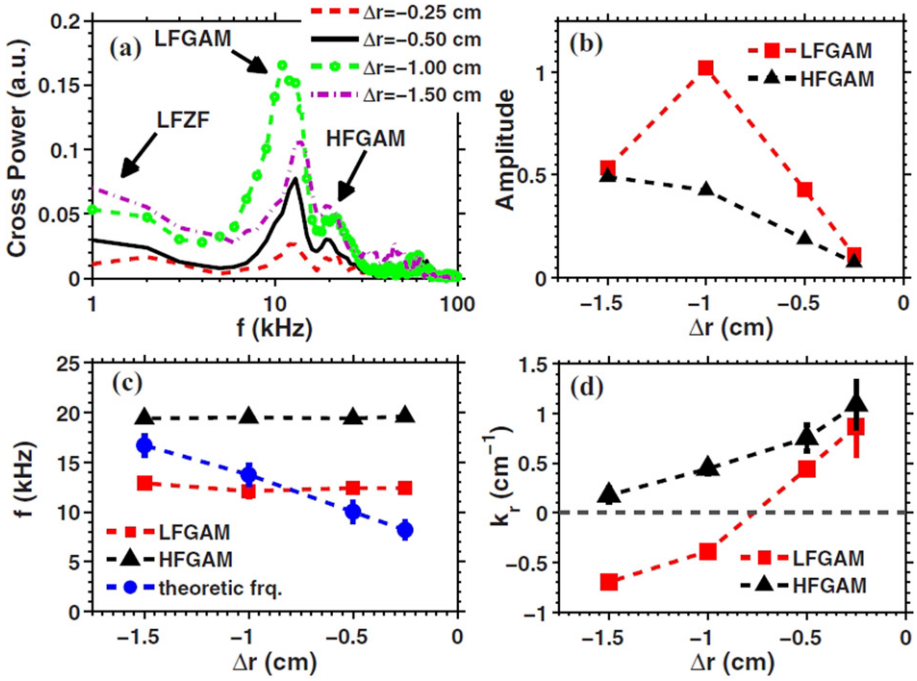

Figure 68. (*a*) Cross-power spectra for various LP radial separations Δr, (*b*) GAM amplitude A_{GAM}, (*c*) frequency f_{GAM} and (*d*) radial wavenumber k_{r} profiles as functions of Δr from the LCFS in HT-7. Reproduced courtesy of IAEA. Figure from [287]. Copyright (2013) IAEA.

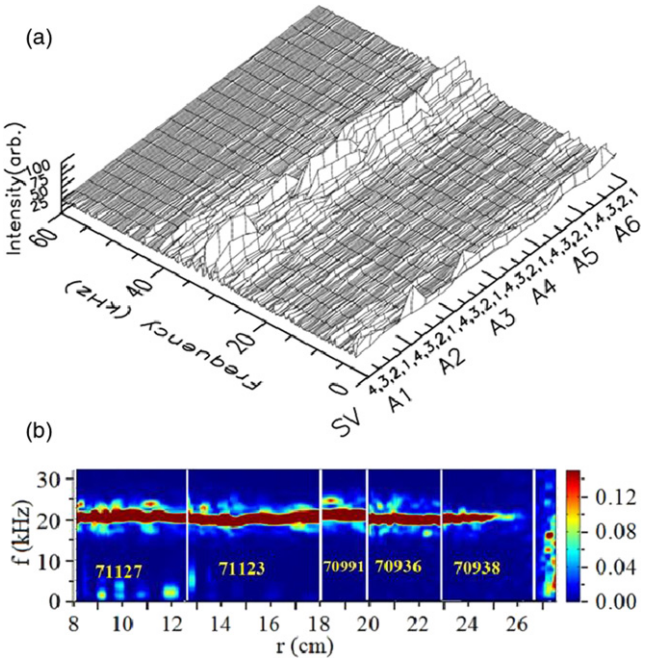

Figure 69. (*a*) Fourier spectra of potential fluctuations vs HIBP sample volumes (channel) covering the minor radius from edge (A1) to core (A6) from NBI heated JIPP-TIIU low density plasma. Reproduced courtesy of IAEA. Figure from [331]. Copyright (2012) IAEA. (*b*) Radial reconstruction of HIBP potential fluctuation spectra from T-10 low density 1×10^{19} m^{-3} ohmic plasams. Adapted from [301], with permission from JSPF.

However, a selection rule for the radial propagation direction has also been derived [145]. By including (DW) turbulence in the GAM dispersion relation (wave-kinetic equation, WKE) the GAM radial wave pattern could be varied, forming either a standing wave or inward or outward propagating waves depending on the value of the peak turbulence wavenumber. Related to this are WKE modelling results suggesting large amplitude GAMs can trap clumps of turbulence, which then propagate radially with the GAM [470], leading to a deterioration of an edge transport barrier [471]. The GAM propagation has also been linked with the formation of turbulence avalanches [472]. Here, global ORB5 GK simulations of TCV discharge conditions with a wide eigenmode show radially inward propagating avalanches with a frequency roughly coinciding with the GAM frequency at its outermost (edge) location. A similar linkage was observed in global GK simulations with EPs where outward radial propagating avalanches were synchronized to a core EGAM—see figure 93 [271].

The WKE model has recently been extended to a kinetic description showing that the GAM phase velocity and the WK advection resonate, creating a radially moving zonostrophic instability [473]. In [145] the propagation direction is set by the up–down poloidal asymmetry of the turbulence intensity (cf also 118, 454, 455, 474]), while in [473] it arises from the direction of the background $E \times B$ shear (related to a turbulence eddy tilting angle [475]).

Experimentally GAMs are seen to propagate both outward and inward, although the reports are predominantly of an outward propagation. These are summarized in table 12 for the various devices. Generally, radial propagation velocities range from some hundred m s^{-1} to a few km s^{-1} with corresponding radial wavenumbers of the order of 0.3–3 cm^{-1}. The sign indicates the direction with positive being outward. There appears to be some dependency on the measured fluctuation parameter. For example, in TEXTOR figure 70 shows

Table 12. Experimental values for GAM radial propagation in terms of k_r and v_r for various devices. A plus sign indicates outward propagation. C = continuum, E = eigenmode. Also indicated is the relative measurement location, inside or outside of the GAM peak.

Device	v_r(km s^{-1})	k_r(cm^{-1})	Position
AUG	−1.25	−0.7	In (E) [310, 311]
COMPASS	+0.70	+1.7	Out (E) [394]
DIII-D	+(0.7–1.67)	+(1.93–0.89)	Out (E) [282, 283]
DIII-D	+0.72	+1.44	Out (C) [283]
FT-2	+1.2	+2.6	Out [255]
HL-2A		+(0.72–1.8)	Out [141, 285, 476]
HL-2A		−0.3/+0.7	In/out [354, 430]
HT-7		−0.7/+1.0	In/out [285, 287]
ISTTOK		+1.5	Out 362–364, 440]
JET		+2.6	Out [358, 359]
JFT-2M		+0.94	Outside [317]
TCV		+(1.7–2.1)	Out (E) [380, 382, 383]
TCV		±0.9	In/out, CECE [380]
TEXTOR	+0.6	+0.7	Out [342]
T-10		1.2–6	Out, edge [292]
T-10	+2/+7		Out, edge/core [303]

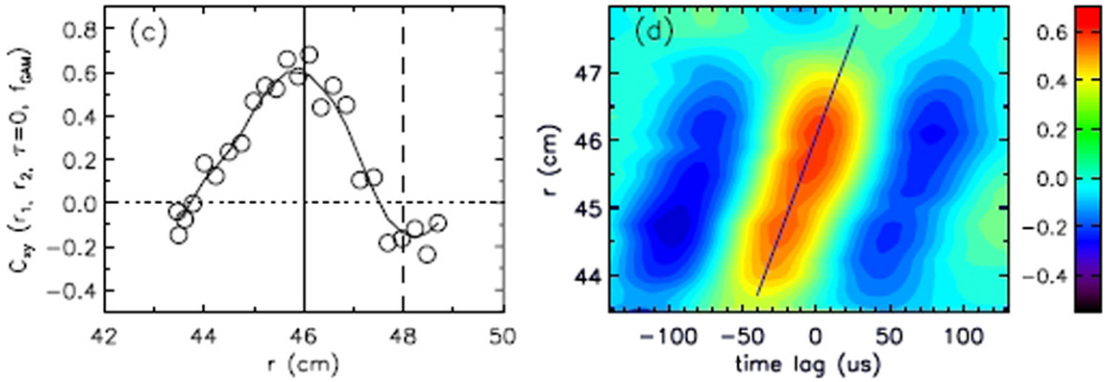

Figure 70. Cross-correlation profiles (radial and time-delay) of band-pass filtered 3–15 kHz LP $\tilde{V}_f$ reference at $r = 46$ cm (GAM peak) showing outward GAM propagation in TEXTOR edge. Adapted from [342].

an outward propagating GAM structure measured across the GAM peak using cross-correlation of reciprocating LP $\tilde{V}_f$. The structure propagation velocity $v_r = \delta r/\delta\tau = +0.6$ km s^{-1} is also very close to the measured phase velocity $v_{ph} = f_{GAM} \times \lambda_r = +0.52$ km s^{-1} where the GAM wavelength $\lambda_r \approx 9$ cm or $k_r \approx +0.7$ cm^{-1} [342]. Also using LPs on COMPASS the eigenmode GAM propagates outward, away from the GAM peak, at $v_r = +0.6$–0.8 km s^{-1} (comparable to TEXTOR) when using potential fluctuations, but was slower for T_e fluctuations. The radial wavenumbers (and thus $v_r = 2\pi f_{GAM}/k_r$) also depended on the signal used. For plasma potential $k_r \approx +1.7$ cm^{-1}, but was larger for V_f at $k_r \approx +2.7$ cm^{-1} and even larger for T_e at $k_r \approx +5.7$ cm^{-1} [394].

The majority of reports are of an outward propagation: in JET [358], in ISTTOK [440], in DIII-D (where $\Delta\rho_{tor} \approx 0.15$ or radial correlation length of $L_{GAM} > 6$ cm which is significantly larger than the turbulence correlation length) [282], and also in T-10 where the phase-velocity across an eigenmode falls from +7 km s^{-1} in the core to $v_r \approx +2 \pm 0.5$ km s^{-1} in the edge [303]. However, potential–density cross-phase measurements on T-10 also suggest the possibility of a standing-wave structure for the global eigenmode GAM [296, 298]. In HL-2A local $S(k_r, k_\theta, f)$ spectra were obtained using LP arrays with poloidal, toroidal and radial separations [141, 285, 476] from which a $k_\theta = k_\phi = 0$ and $k_r\rho_i \approx 0.04$–0.09 are obtained with localized 'GAM packets' propagating radially outward with similar phase and group velocities of $\approx +0.25$ km s^{-1} and a roughly linear dispersion relation. A similar $k_r \sim +0.68$ cm^{-1} was obtained from radially separated DR channels [430].

Most measurements appear to have been made close to the GAM peak position, although the actual position is is not always explicitly stated. In fact the position of the measurement relative to the GAM maxima appears to be critical. In table 12 an attempt has been made to indicate the relative measurement positions as inside of or outside/around the peak. Where explicit values are not available educated guesses have been made.

Referring to figure 67 for DIII-D where the radial velocity was measured at $\rho = 0.78$ using correlation DBS. For the

24 kHz GAM, $v_r = +1.67$ km s^{-1} just outside its radial maxima, but is lower for the 21 kHz GAM $v_r = +0.70$ km s^{-1} inside of its maxima. In both cases the propagation was outward. This is similar to JFT-2M measurements using HIBP where the propagation is outward at the GAM peak amplitude, while radially inside of the peak the propagation is weak and somewhat inwards—cf figure 5(c) in [317]. The radial wavenumbers were of the order of $k_r = +0.94 \pm 0.05$ cm^{-1}, or $k_r\rho_i = 0.201$ [318], consistent with theory prediction for ZF $k_r\rho_i < 1$ [277]. Further outside of the GAM peak the behaviour is more standing wave like rather than propagating—consistent with simulations from Hallatschek [24] and Miyato [102]. Velocity reversals in JFT-2M were reported close to the separatrix [325] with reference to the possible role of reflection at the separatrix boundary creating standing-wave structures [322, 325].

In the edge region of TCV an outward $k_r = +2$ cm^{-1} was measured using TPCI for a broad eigenmode GAM [382, 383], but outward and inward propagation was observed at different plasma radii using CECE [380]. From FT-2 there are mixed reports, in [255] there is an outward propagation of $v_r = +1.2 \pm 0.1$ km s^{-1} and $k_r \sim +2.6$ cm^{-1} away from the GAM maximal amplitude. While other reports [250, 466, 467] hint at an inward propagation, in agreement with ELMFIRE GK simulations, around and inside of the GAM peak. In figure 2 of [467] there are suggestions of a velocity reversal across the GAM radial maximal. DR correlation measurements in AUG give an inward propagation of -1 to -2 km s^{-1} inside of the GAM peak location for low κ shapes with both broad eigenmode and continuum GAMs in limiter configurations. However, with increasing elongation the GAM transitioned to a narrow single eigenmode with no discernible propagation. Likewise, no propagation was evident for GAMs in divertor configurations [311].

These results suggest a propagation away from the GAM peak. Indeed some of the clearest results supporting this come from HT-7 [287] and HL-2A [354]. Both show dual eigenmode GAMs, as in figure 68 for HT-7, where the lower frequency GAM is always stronger than the higher frequency one. With decreasing minor radius the GAM k_r falls from $+1$ cm^{-1} (outward propagation) to -0.7 cm^{-1} (inward propagation). The respective GAMs radial peaks coincide with locations where $k_r \approx 0$, consistent with conversion from continuum to kinetic/eigenmode GAM [11, 78].

It is tempting to conclude that propagation is always away from the GAM drive (maximum GAM amplitude) but there remain some measurement inconsistencies that need to be addressed with further measurements and theory development. There is also the question of whether the GAM accelerates radially. Palermo investigated the radial acceleration of GAMs due to a temperature gradient using GK simulations. Effects of PM via the continuum frequency spectrum leads to the GAM radial wavenumber (and thus frequency) to evolve in time resulting in the radial velocity increasing with time [140]. As yet, there are no experimental measurements of an acceleration. This will require simultaneous multi-point correlation measurements.

In summary, the GAM spatial peak is localized to regions of maximum turbulence drive (steep pressure gradient and weak velocity shearing) and minimal collisional damping (low density and high temperature) and low collisionless damping (high q). Radially the GAM displays one or more nested zonal rings of widths of the order of the mesoscale $\sqrt{a\rho_i}$. The zonal rings become broader towards the core with increasing L_T scale length. There are some significant inconsistencies between measured and predicted wavelengths which require a more detailed multi-machine database. Both continuum and eigenmode behaviour are observed. The cause of transitions from one to another is not fully resolved, but kinetic effects appear to be primary. For eigenmodes the radial wavevector changes sign at the GAM radial maxima where the eigenmode frequency crosses the expected continuum GAM frequency. This is not entirely consistent with theory and modelling which suggest the eigenmode should lie inside of the continuum frequency profile. The GAM is thus seen to propagate radially away from the GAM spatial peak. Radial acceleration is predicted, but not yet measured. Concerning the nested zonal rings, an open question is whether the zonal rings oscillate in phase, and whether the modulation of the GAM amplitude is radially correlated across the zonal boundaries. The resolution and sensitivity of the various diagnostics is an important factor in the 'visibility' of the GAM. The use of HIBP in JIPP-IIU, CHS and T-10 for example (see section 6.4) has revealed core GAM activity, where other diagnostics have failed to reach. Likewise the diagnostic radial resolution sets the ability to resolve small eigenmode steps and staircases in an overall continuum behaviour. It is not clear if there is a hard boundary between pure continuum and eigenmode step behaviour or a gradual transition.

10. Plasma rotation effects

The analysis of the GAM behaviour so far has considered the GAM flow oscillation to be a non-rotating standing wave. However, the plasma is never truly stationary but has a finite mean $E_r \times B$ velocity, which can be several km s^{-1} in the edge even in ohmic conditions due to pressure gradients or spontaneous (turbulence) rotation effects. With applied torque due to NBI the plasma rotation can become a substantial fraction of the sound speed. Rotation leads to a poloidal stratification of the plasma on a magnetic surface, resulting in a shift of the GAM frequency (from the static value) and a modification of the damping. Rotation can also drive marginal GAMs unstable which would otherwise be stable. With strong NBI (supra-thermal ions) the rotation can exceed a critical threshold and there is a cross-over from a 'moderate' rotational impact on the turbulence driven GAM to the generation of an EGAM. The EGAM drive mechanism is discussed in sections 3 and 13.

10.1. Frequency

The effect of toroidal and/or poloidal rotation on the continuum GAM has been extensively investigated theoretically using an MHD (electrostatic) framework in the large aspect ratio, circular plasma geometry. As an example of many,

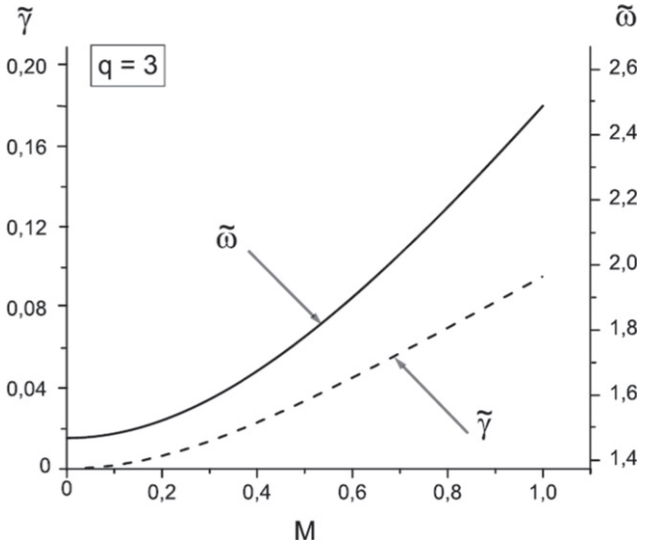

Figure 71. Simulation normalized GAM$_+$ frequency $\tilde{\omega}_+ = \omega R_0/c_s$ (solid) and normalized growth rate $\tilde{\gamma}_- = \tilde{\omega}_-$ of ZFO/GAM$_-$ (dotted) vs toroidal Mach number M for $q = 3$. Reprinted from [268], Copyright (2010), with permission from Elsevier.

Lakhin [165, 268] modelled the toroidal rotation effect with an ideal single fluid MHD framework in the low $\beta \sim \epsilon^2$, isodense magnetic surfaces, and large aspect ratio limit to obtain:

$$\omega_\pm^2 = \frac{c_s^2}{2R_0^2}\left\{2 + \frac{1}{q^2} + 4M_t^2 \pm \left[\left(2 + \frac{1}{q^2} + 4M_t^2\right)^2 + \frac{2M_t^4}{q^2}\right]^{1/2}\right\}, \quad (265)$$

where $M_t = \Omega_t R_0/c_s$ is the toroidal Mach number. The effect of adding rotation to the dispersion relation is to create two branches of continuum modes. The (+) branch is a rotationally modified (stable) GAM which smoothly links to the usual GAM at $M_t = 0$, while the (−) branch is a new lower frequency (unstable) continuum ZFO $\gamma_- = \omega_-$. At $M_t = 0$ this branch becomes the zero-frequency SZF. In the case of slow (sub-sonic) toroidal rotation $M_t^2 \ll 1$ the equation for the high frequency GAM reduces to $\omega_+^2 = (c_s/R_0)^2(2 + 1/q^2 + 4M_t^2)$.

Similar expressions for the dispersion relation have also been derived in [166, 477–482], all of which show the frequency of both modes increasing with the Mach number, as does the growth rate $\gamma_- = |\omega_-|$ of the lower mode. Figure 71 shows the normalized frequency $\tilde{\omega} = \omega R_0/c_s$ from the Lakhin model vs toroidal Mach number for both roots for a representative $q = 3$ [268].

For a predominant mean poloidal rotation $M_p = u_p B_t/(B_p c_s) < 1$ a similar dispersion relation form was also obtained [483], with the exception that three roots are now obtained: ω_0 and $\omega_\pm$. The first branch is the same as for the stationary case $\omega_0 = 0$ (suggesting that a finite frequency ZFO requires the centrifugal force associated with the toroidal rotation); the low frequency branch ω_- appears now as a SW like mode, while the ω_+ is a GAM. Very similar conclusions were reached, also using an MHD model, from the more complex behaviour with combined toroidal and poloidal rotation [479, 480, 484]. It should be noted that the precise properties of the various branches, notably the stability and nature, depends strongly on the tokamak plasma equilibrium; specifically, adiabatic models give two GAMs, while isothermal gives a GAM and a ZFO.

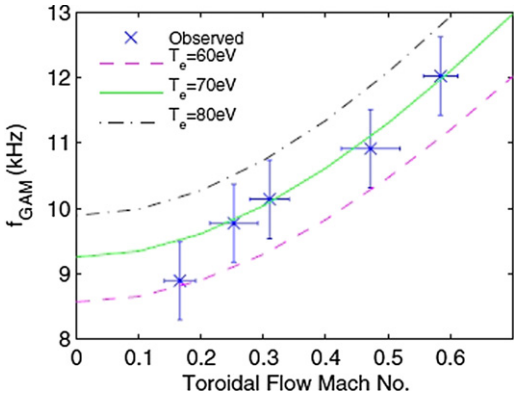

Figure 72. Measured GAM frequency vs toroidal flow Mach number at $R = 1.42$ m ($r/a = 0.61$), $q = 6$ in ohmic MAST (points) edge compared with simulation values from the Lahkin model with Gao corrections for $T_e = 70 \pm 10$ eV. Reproduced from [374]. © IOP Publishing Ltd. All rights reserved.

Further extensions to the above models include the addition of finite plasma pressure to give a β correction, $\omega_{GAM}^2 = \omega_0^2/(1 + \beta)$ [165, 485], or kinetic effects with an isothermal MHD rotating equilibria [482], as well as GGAM eigenmodes [165] and the global structure of the SZF with rotation [486].

As well as a frequency up-shift, the rotation creates sine and cosine components in the density sideband perturbation resulting in a small propagating wave in the poloidal direction superimposed on the GAM standing wave—in contrast to the pure poloidal standing wave in a static plasma [483].

From the experiments, the rotation effect on edge continuum GAMs in low-density, ohmic L-modes was investigated in MAST (small aspect ratio) using externally applied RMPs [374, 375]. Applying RMPs led to a spin-up of the edge plasma (parallel Mach number M varied between -0.2 to -0.6 measured with a reciprocating Gunderstrup probe) and a corresponding upshift in the GAM frequency, as shown in figure 72. A comparison with the Larkin model, equation (265), provided good agreement, once a correction factor for the finite aspect ratio and elongation (from Gao [117]) was included, as shown by the lines in the figure for the measured T_e range.

10.2. Damping and amplitude

The kinetic effects of toroidal rotation on the GAM collisionless damping were investigated using a GK framework in the large aspect ratio circular plasma limit by Guo [487, 488]. The GAM dispersion relation including toroidal rotation Ω_t,

to leading terms gives frequency and (collisionless) damping

$$\omega_{\rm GAM}^2 = \frac{v_{Ti}^2}{R_0^2}\left(7/4 + 2M^2 + \frac{M^4}{(1+\tau_{\rm e})^2} + \frac{2M^2}{1+\tau_{\rm e}}\right) + \cdots$$
$$\gamma_{\rm c.l.} \approx -(q^2/2)\,\omega_{\rm GAM}\,D_{\rm i} \quad (266)$$

where $D_{\rm i}$ is imaginary part of the dispersion function. As with the MHD models there is a significant frequency up-shift with $M = \Omega_{\rm t} R_0/v_{Ti}$, and an initial increase followed by a decrease in the damping when the rotation exceeds a critical value. The model was used to interpret observations of the GAM amplitude behaviour in DIII-D and AUG with increasing NBI power which suggest a qualitative consistency with the model predictions [487].

Similar investigations using a modified GK equation showed a dramatic decrease in the Landau damping with rotation, i.e. stronger GAM in rotating plasmas, independent of the flow orientation [489]. Likewise, the inclusion of an equilibrium radial electric field in the GK framework [490] resulted in multiple branches of zonal eigenmodes, including a GAM, SW and a ZFO, similar to the fluid model with poloidal mass flow. Both the GAM frequency and collisionless damping rates increase with strengthening $E_{\rm r}$ velocity (which was expressed in terms of a poloidal Mach number), while the ZFO frequency and damping slightly decrease. A tentative comparison was also made with AUG experimental results but with contradictory behaviour to the Guo model above [490].

With combined anisotropic pressure and an equilibrium radial electric field it was found that when $p_{\|}$ was larger than $p_{\perp}$ then $E_{\rm r}$ had a stronger effect on the GAM frequency and damping [90]. But, overall, the pressure anisotropy effect on $\omega_{\rm GAM}$ and $\gamma_{\rm c.l.}$ dominated the $E_{\rm r}$ rotation effect. The implication being that the control of the GAMs maybe achieved via selective perpendicular heating of the ions, for example using ICRF.

Concerning the effect of rotation on collisional GAM damping, a fluid model was used [491] which shows that, while increasing toroidal rotation can result in a frequency up-shift, as with other MHD models, it had only a weak (increase) effect on the collisional damping. A more stronger impact on the GAM growth rate, however, was found in the MHD model of [481]. A sequence of studies were performed using the GK equation for collisional and collisionless damping with either toroidal or poloidal rotation [492–494]. In a similar vein the GK equation was also used for a detailed study of the role of impurities (cf section 7.5) in modifying the toroidal rotation effect on the GAM frequency and damping [446]. This last study shows a varying effect that depends on the level of impurity. Trace impurities were found to enhance the rotation effect (due mainly to additional drifts induced by the toroidal rotation) on the GAM frequency and damping, particularly for high rotation; while significant impurity levels weakened the rotation effect.

In the MAST experiments with RMP modified rotation the up-shift in the GAM frequency was accompanied by a reduction in both the GAM amplitude and the GAM bicoherence (a measure of the GAM nonlinear drive) with a threshold-like response [374]. Here, the GAM reduction was thought to result from a loss of drive due to the GAM interacting with the RMP imposed field (of sufficient magnitude), which may form a resonance with the GAM in the rotating plasma frame when $\omega_{\rm GAM} \sim \omega_{\rm RMP} = nMc_{\rm s}/R_0$. For the MAST conditions this occurred when $M = 0.6$, above which the GAM was completely suppressed.

In the COMPASS tokamak the direction of the applied NBI heating appeared to play a role in the GAM amplitude—slightly enhancing it over ohmic conditions when the injection was in the co-current direction, but strongly suppressing the GAM amplitude when in the counter-current direction [394]. Similar observation ware reported for EGAMs in DIII-D [44] and JT-60U [370]. Two possible influences were proposed for the effect: the GAM growth rate is influenced by an interaction with fast (resonant particle) ions depending on the pitch angle distribution; and an electron current velocity combined with the ion flow increases the GAM growth rate over the Landau damping. As discussed below, both mechanisms were found to be plausible.

Figure 73 shows a sequence of poloidal flow spectra from an L-mode torque-scan in DIII-D where the core rotation was reduced from $v_\theta \sim 300$ km s^{-1} to ~ 200 km s^{-1} by stepping 3 MW of NBI from pure co-injection to 3/4-co, 1/4-counter, and balanced injection [281]. As the central rotation is reduced the edge GAM shifts up in frequency and is diminished in amplitude until, with balanced torque, it disappears and is supplanted by a stronger, broad low-frequency feature. (The discharge subsequently transitioned to H-mode from which it was speculated that the lower frequency flow perturbations were more effective in triggering the L–H transition.) The initial up-shift of the GAM frequency can be attributed to an increase in the edge $T_{\rm e}$, but the transition from a coherent GAM to a spectrally broad ZFO appears to be a rotational effect on the GAM/ZFO growth rate. With balanced beams the reduced rotation may actually stabilize the GAM allowing the turbulence drive to transfer to the unstable ZFO.

10.3. Driven

With moderate NBI energies the ion velocity is typically subthermal, $v_{\rm NBI} \ll v_{Te}$, due to electron collisions, i.e. a slowed down ion distribution function. However, with strong NBI (suprathermal) injection there is a cross-over from a moderate impact on the turbulence driven edge GAM to the generation of a core EP EGAM—intrinsically an EP mode—which is discussed in section 13. In the COMPASS case [394] the NBI did not generate an EGAM but modified the pre-existing ohmic GAM. The resulting GAM was weaker with co-injection, but slightly enhanced with counter-injection NBI compared to ohmic. This is similar to TEXTOR results where GAMs were not observed with co-injection tangential NBI, but were with small counter injection (i.e. deceleration of the toroidal rotation) [495].

The COMPASS results were interpreted with the aid of two models. The first is the ideal MHD model of Kolesnichenko [168] where the GAM dispersion is derived in the presence

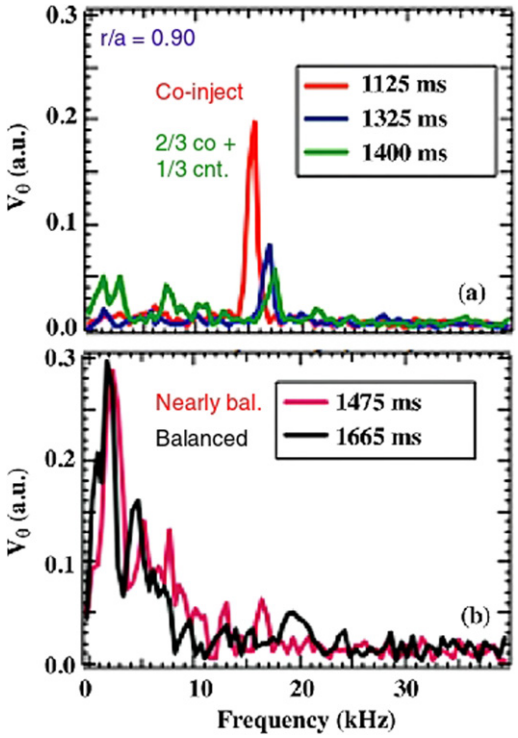

Figure 73. Poloidal flow spectra in USN divertor DIII-D edge $r/a = 0.9$ (edge $n_e \sim 1.5 \times 10^{19}$) showing GAM frequency shift with variation of external NBI drive. Reproduced courtesy of IAEA. Figure from [281]. Copyright (2009) IAEA.

of energetic ions (coupled to the MHD equations via the current) and finite β coupling. The dispersion relation has several potential modes/branches, but the one of interest here is the continuum GAM. With a strongly peaked ion beam pitch angle distribution it was found that energetic ions can significantly decrease the local GAM frequency, and, that the drive is strongest with counter-injection. This is qualitatively consistent with the COMPASS observations; but other effects are also present.

When the beam ions are slowed towards the critical velocity $v_0 \approx 5.5\, Z_{\rm eff}^{1/3} \sqrt{T_e/m_i}$ then pitch-angle scattering due to ion–ion collisions becomes important. This effect is considered in the model of Elfimov [206] which uses a full-DKE to study the effect of an NBI induced parallel electron current and particle flux on the natural GAM. When the induced electron current velocity is larger than the GAM sideband phase velocity, $v_{e0} > \omega_{\rm GAM} R_0 q$ then the natural GAM can become unstable. This is particularly favoured during tokamak current ramp-up and with counter-NBI. Again, this flux model was found to be in qualitative agreement with the COMPASS measurements where ion and electron fluxes may increase or decrease the GAM growth rate for counter and co-NBI respectively, as observed experimentally. In a further development of the model [205] qualitative agreement with the COMPASS observations was also found, but it was noted that two other effects could be important. With counter NBI the electron distribution is shifted in such a way as to make inverse Landau damping more effective. Also, the NBI driven rotation could enhance or diminish the GAM growth rate. This can be contrasted with the GK model predictions for anisotropic pressure where collisionless Landau damping is reduced with increasing $\chi = p_\perp/p_\parallel$ [86].

The effects of energetic passing particles (fast ions) on the GAM was also modelled using a hybrid kinetic-fluid model in a large aspect ratio, circular low β plasma [496]. Again, as with the Elfimov model, the dispersion relation gave two branches, one is the EGAM (stable but resonantly excited by the EPs) and the other is the natural GAM which can be unstable. The EPs were found to shift the bulk pressure p_0 outward across the flux surfaces leading to poloidal density inhomogeneities. This modifies the GAM frequency $\omega = \omega_0(1 + \chi' Y)^{1/2}$ where $\chi' \sim \mathcal{O}(1)$ and $Y = (p_\parallel + p_\perp)/(2\gamma p_0)$. Similar results were also obtained with a hybrid kinetic-fluid model for oblique NBI plasma fluxes where the GAM phase resonance can be important at critical velocity (hot bump-on-tail model) [198]. Again two unstable modes appear: the standard GAM and an EGAM, as shown in figure 17 and discussed in section 3. The simulations reproduced the GAM frequency continuum behaviour in DIII-D.

In summary, the toroidal rotation induced centrifugal force creates pressure non-uniformities, leading to the formation of new roots in the GAM dispersion relation: the standard GAM, and a second lower frequency GAM/ZFO. With poloidal rotation an additional SW branch is formed. In both cases the rotation up-shifts the mode frequencies. The intrinsic stability and form of the modes is sensitive to the equilibrium. Sub-thermal rotation can also drive a normally stable edge GAM unstable. The effect of rotation on the GAM damping is more subtle with threshold effects evident. Both theory and experiment show the GAM may be reduced or enhanced by rotation. For super-thermal particle injection a core localized EGAM is created.

11. GAM drive

The observed natural GAM amplitude is the result of multiple mechanisms involving the level of (turbulence) drive, the degree or effectiveness of the coupling to the GAM, the back reaction of the GAM on the drive (e.g. on turbulence shearing/moderation), the rate of energy transfer out of the GAM back into the turbulence or non-GAM/ZFO flow fluctuations, and finally the rate at which energy is lost to collisional or Landau collisionless damping, dissipation and other mechanisms including continuum damping, phase-mixing (PM), etc. This is a complex story which is addressed in several sections. Beginning with the GAM drive this section covers 4 topics from the experimental perspective: (i) RS and DS drive in section 11.1; (ii) thresholds and gradients in section 11.2; (iii) MHD interaction in section 11.3—with further aspects in section 16.1; (iv) external drive mechanisms, such as plasma biasing to enhance edge E_r, as well as AC modulation mechanisms to modulate the edge potential are discussed in section 11.4. The somewhat simpler GAM damping and dissipation mechanisms follow in section 12, with EPs (both internal born (RF driven) and NBI injected) driven GAMs in section 13, and finally the nonlinear turbulent transfer mechanism in section 14.

11.1. Dynamic shearing and Reynolds stress

Even in the absence of collisional and collisionless (linear) damping, a continuum GAM will still decay due to PM. Thus to maintain and drive the GAM an external energy source is needed. As discussed in section 4 there are two different mechanisms presented in the literature through which the GAM may be driven by turbulence. The first is turbulent RS [53] directly driving the $m = 0$ radial current. RS directly enters via the quasineutrality condition (7). The second is the so-called DS mechanism. Here, the GAM is excited via a feedback loop where the GAM flow oscillation 'dynamically' shears the turbulent eddies, which modulates the radial particle flux Γ_r (transport) which, due to the inhomogenous magnetic field, generates up–down asymmetric $m = 1$ pressure perturbations, and Stringer–Winsor like torque on the plasma column, that drives the $m = 0$ radial current in the GAM [24, 213, 227]. In the DS formulation the GAM is preferentially excited in high q regions that satisfy the condition $q^2 > q_c^2 \sim LR_0^{-1}k_{\perp 0}^{-2}\rho_s^{-2}s^{-1}$ [213]. More generally, the DS mechanism may be viewed as a 'diamagnetic drive' [24, 227]. The theory behind both mechanisms is described in detail in section 4.

While Sasaki [456] noted that both RS drive [53] and DS induced Winsor drive [213] could be important, the evidence for RS appears, overall, to be convincing. In HL-2A the turbulent RS was measured using LP arrays and rake probes and was found to be strongly correlated with the formation of simultaneous multiple shear flows; a ZFO (<5 kHz) and GAM ($f \sim 12$–18 kHz) [476]. The radial particle flux was significantly reduced near the LCFS and at the GAM radial maxima.

For FT-2 conditions the ELMFIRE code was used to simulate discharges. Here, the nonlinear energy transfer from the turbulence to the flows through the Reynolds force was balanced by the collisional dissipation. A temporal relationship between the oscillating flow, Reynolds force $\Pi_{r\theta} = -\langle \tilde{E}_r \tilde{E}_\theta \rangle / B^2$, and turbulent particle flux $\Gamma_r = \langle \tilde{E}_\theta \tilde{n} \rangle / B$ was found to be consistent with the fundamental physics picture of the GAM modulating the turbulent transport on the time scale of the mode. The experimental results also suggest an anti-correlation between the GAM amplitude and the turbulent fluctuations [254].

A direct evaluation of the comparative strength of RS and DS drive was recently made in JFT-2M [325]. In this case the results indicate that RS dominates over any drive from DS. Following the derivation of Kobayashi [325], the rate of change in the GAM kinetic energy, $K_G = |\tilde{v}_{E\times B}|^2$, is given by

$$\gamma_K = \frac{\partial_r K_G}{K_G} = \gamma_{RS} + \gamma_{DS} - \gamma_L, \tag{267}$$

where γ_K is balanced by the RS drive plus DS drive minus the linear (collisional or collisionless) damping rate γ_L. The various rates for x are defined as $\gamma_x = 2|\hat{F}_x||v_{E\times B}|^{-1}\cos(\theta_{F_x} - \theta_{E\times B})$, with the forces given by $\hat{F}_{RS} = -r^{-1}\partial_r r \hat{\Pi}_{r\theta}$ and $\hat{F}_{DS} = \mathrm{i}c_s^2/(4\pi^2 f_{GAM} R)\, r^{-1}\partial_r r(\hat{\Gamma}_r/\hat{n})$ respectively.

Using HIBP on JFT-2M to measure $\tilde{\phi}$ with conditional averaging triggered by a magnetic signal, the modulational pattern of RS and Γ, plus the energy exchange could be evaluated. For an ohmic eigenmode GAM of several cm width,

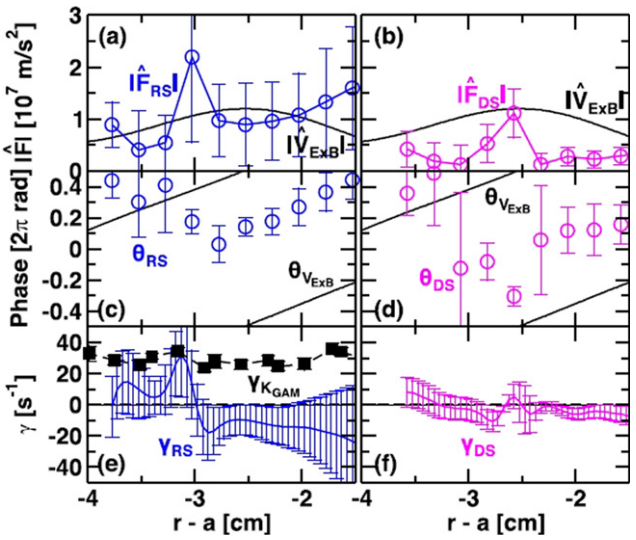

Figure 74. Profiles of (*a*) and (*b*) modulation amplitude $|\hat{F}|$, (*c*) and (*d*) modulation phase, and (*e*) and (*f*) growth rates for RS and DS forces, respectively. Also in (*e*) over-plotted is the GAM kinetic energy effective growth rate in JFT-2M. Reprinted figure with permission from [325], Copyright (2018) by the American Physical Society.

the peak γ_{DS} was found to be small compared to $\gamma_{RS} \sim 3 \times 10^4\ \mathrm{s}^{-1}$, as shown in figure 74 [325]. The collisionless and collisional damping rates $\gamma_{c.l.} \sim 1 \times 10^4\ \mathrm{s}^{-1}$ and $\gamma_{col} \sim 50\ \mathrm{s}^{-1}$ respectively are also slightly smaller than predicted growth rate.

As a final point, configuration effects, such as magnetic shear $\hat{s}$, on the RS were discussed in [497] where simulations showed a strong polidal asymmetry in the RS. The role of the X-point in breaking poloidal symmetry of $\hat{s}$ was noted—circular plasmas have up–down asymmetric RS, while divertor configuration is more complex with high RS in a narrow radial strip localized to the X-point. Breaking the poloidal symmetry of $\hat{s}$ induces tilting of the turbulent structures (via X-point resistivity or limiter) which leads to an extra (positive or negative) contribution to flux surface averaged RS. However, what this means for the GAM drive remains to be answered.

11.2. Gradients and threshold effects

Several devices report that the GAM amplitude increases in L-mode with applied heating power [292, 304, 306, 435] with the implication that the greater heat flux enhances the turbulence magnitude and then via nonlinear coupling drives the GAM harder. For gradient driven turbulence, such as ITG or electron drift wave turbulence, the density fluctuation level is expected to scale with the gradient, e.g. $\tilde{n}/n \sim (k_\perp L_n)^{-1}$ where $L_n = |n/(\mathrm{d}n/\mathrm{d}r)|$ is the density gradient scale length. In TEXTOR the GAM δv and δn fluctuation levels both decreased with increasing density gradient length L_n (shallower gradients)—cf figure 16 in [339] for a series of low density ohmic discharges. The GAMs were most pronounced for steep edge gradients $L_n \leqslant 0.1$ m, with long wavelength $k_\perp \rho_s < 0.2$ drift-ballooning modes appearing to be the dominant turbulence mode.

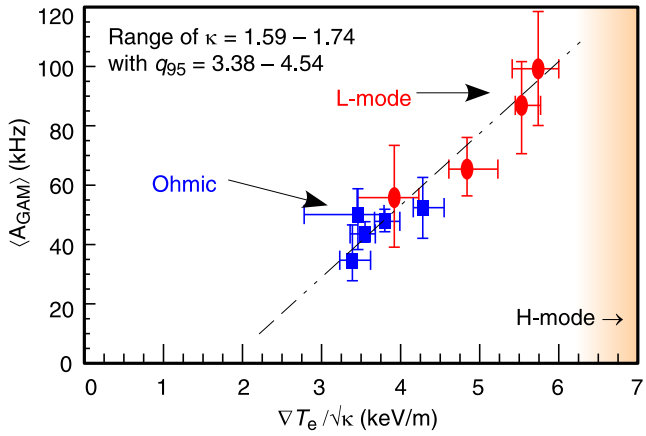

Figure 75. Scaling of mean (radially averaged) GAM amplitude in AUG vs normalized ETG $\nabla T_e/\sqrt{\kappa}$ for elongated, diverted ohmic and L-mode discharges at moderate q_{95}. Adapted from [26]. © IOP Publishing Ltd. All rights reserved.

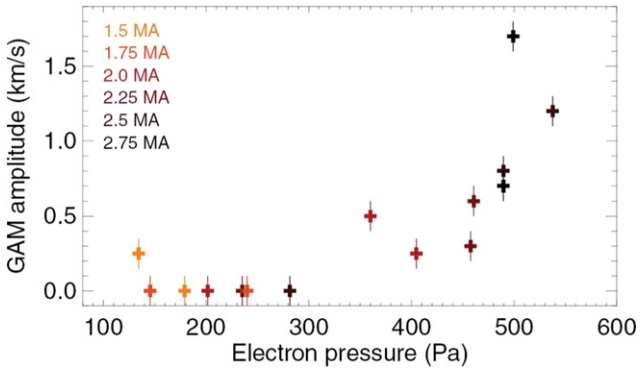

Figure 76. GAM amplitude vs electron pressure at GAM peak radius in JET. Reproduced courtesy of IAEA. Figure from [358]. © 2016 EURATOM.

At low collisionalities TEM type turbulence, driven primarily by the (electron) temperature gradient, can be dominant. Figure 75 shows the mean GAM amplitude $\langle A_{GAM}\rangle$ (averaged over the GAM spatial peak) as a function of temperature gradient normalized to elongation $\nabla T_e/\sqrt{\kappa}$ for a selection of low density ohmic and L-mode shots with a restricted $\kappa_b = 1.64 \pm 0.05$ and $q_{95} \sim 3.9 \pm 0.4$ divertor configuration [26]. Above a certain onset threshold the GAM amplitude increases linearly with the gradient right up to the L to H-mode transition. Due to increasing turbulent transport the stronger GAM is accompanied by a corresponding decrease in the global energy confinement time τ_E. The GAM onset threshold value also appears to depend on geometrical and other turbulence parameters. For lower κ_b the threshold also moves to lower ∇T_e values.

A similar threshold behaviour effect was observed in JET divertor discharges, as shown in figure 76 of GAM peak amplitude vs pedestal electron pressure P_e (used as a proxy for the pressure gradient) for a range of I_p [358]. In this study the GAM drive was the dominant factor since both I_p and $\bar{n}_e$ were sufficiently low that collisionless and collisional damping were small in the edge. Spatially, the GAM amplitude profile is also seen to follow the $1/L_T$ and $1/L_n$ inverse scale length profiles across the edge region. This is similar to AUG divertor shapes where the radial inside boundary for the GAM aligns with the density pedestal top, and thus where $1/L_n$ decreases [305]. The role of the nonlinear transfer rates are discussed in section 14.

11.3. MHD interaction

The importance of the role of Alfvén eigenmodes to the GAM was introduced in section 2.12 and the excitation of GAMs by TAEs was explicitly discussed and modelled by Todo [498] and by Qiu [224, 499]. Using GK theory, the condition for the spontaneous excitation of a GAM by TAEs was derived as $\omega_0^2 > v_A^2/(4q^2R_0^2)$, where ω_0 is the real frequency of the TAE pump wave and v_A the Alfvén speed. If the TAEs (driven for example by EPs) are of sufficient amplitude then they can overcome the GAM onset threshold (due to collisionless damping and nonlinear coupling) and stimulate the GAM via three-wave parametric decay process involving the TAE pump wave (ω_0, k_0), the TAE lower sideband (ω_s, k_s) and the GAM (ω_{GAM}, k_{GAM}).

Due to its high rotational transform, GAMs are not normally observed in TJ-II. However, in appropriate L-mode configurations an $f \sim 105$ kHz, $m = 6$ global Alfvén eigenmode and an $f \sim 14$ kHz low frequency mode (magnetic) is observed in the core ($\rho \sim 0.65$) together with an $f \sim 20$ kHz flow oscillation lasting some tens of ms. The combination is highly suggestive of an AE nonlinear mode coupling to a GAM [417].

In the broader context of MHD modes there are also theory considerations suggesting that nonlinear interactions between two unstable neoclassical tearing modes (NTMs) can create GAM-like flow oscillations. Using numerical simulations of fully toroidal reduced MHD equations in a circular equilibrium with high β and electron viscosity [500], two radially separated NTMs modified the perpendicular flow around the islands structures creating a GAM-like flow oscillation. Similar work on the generation of secondary GAMs via non-linear coupling with beta-induced Alfvén eignemodes induced by plasma flow around the magnetic island [230]. Here, the GAM has the same mode structure and frequency as the primary BAE. A fuller discussion on the interaction of MHD islands with GAMs appears in section 16.1.

11.4. Externally driven GAMs

In addition to the turbulence and EGAMs, theory suggests some alternate mechanisms may also be effective in stimulating or enhancing edge GAMs. As early as 2005, Itoh *et al* outlined the various sources for driving GAMs—principally dynamical poloidal asymmetry [213]. A further development [501] introduced a framework describing the turbulent plasma response (and ZF) in space and time to a local source, i.e. force, perturbation. For a resonant sinusoidal oscillating source the model predicts modulation of the turbulence envelope, coupled to a modulated ZF. In principle, the source perturbation could be generated by an externally controlled perturbation, such as a localised heat deposition (i.e. pressure gradient modulation, or

momentum), or a magnetic perturbation (plasma equilibrium), or even an externally induced E_r via probe or limiter biasing.

11.4.1. Modulated external fields. The motivation for externally driving GAMs is the possibility to control the degree of localized flow shearing of the turbulence, and thus transport, and perhaps even trigger a confinement mode transition. Here, GAMs may be more advantageous than ZFs since they can be generated without momentum input by exploiting a resonance with an oscillating perturbation of the plasma equilibrium.

Two approaches have been proposed. The first considers the possibility of using external magnetic perturbation coils modulated at the GAM frequency to induce a resonant global (equilibrium) plasma displacement [502]. Using an MHD model it was shown that a quadrupole field ($m = 2$) with up–down and in–out anti-symmetry would induce a rotation in an elliptical plasma column. This dynamic perturbation of the equilibrium acts as a source for the GAM. An estimation of the efficiency using DIII-D parameters seemed realistic with power requirements of $P = E_{GAM}\omega_{GAM}/Q < 1$ kW for a resonance factor $Q \sim 20$. Similar estimates were also obtained when considering ion–ion collisions and continuum damping due to PM [137]. MHD fluid simulations for large aspect ratio, circular plasmas were also performed [503]. Applying an oscillation current at the standard GAM frequency in two external coils on LFS above and below mid-plane with 90° phasing, creates a time varying $\nabla B_{coil} = J_+ + J_-$ which induces an E_{coil} field and a narrow radial annulus of oscillating poloidal flow with a maximum around the LFS mid-plane. The amplitude of the flow oscillation is linearly proportional to the coil current. When the frequency is resonant with the standard GAM then an enhanced zonal ring flow is formed. Experiments were proposed for DIII-D [502] but results are not reported to date.

The second approach is to excite GAM flows using edge localised resonant heating (such as ECRH or ICRF) modulated at the expected GAM frequency [503, 504]. Again, MHD fluid simulations show that applying a localized heating with a particular resonant configuration—specifically with a positive half cycle applied to the upper half of the plasma poloidal plane—produces an $m = 1$ temperature perturbation which induces a poloidal flow with an amplitude linearly proportional to the heating power. The required power needs to be sufficient to overcome the natural GAM damping. Estimates for typical DIII-D parameters suggests power levels less than a kW would be required, which is experimentally feasible. Attempts to drive GAMs have been made in several devices, including DIII-D, AUG and TCV, however, to-date there are no reports of either successful excitation or the enhancement of edge GAMs.

11.4.2. DC plasma biasing. External DC biasing of the plasma edge, using limiters or large probes inserted into the edge, can change the mean E_r radial profile and thus enhance or diminish the $E \times B$ sheared flows, as well as inducing tilting and anisotropization of the turbulent eddies. Both effects may in turn change the energy transfer from the small to the large scale turbulence structures [426, 505].

In the case of stationary or low frequency ZFs, several DC biasing experiments support this picture of (mean and fluctuating) flow shear stretching of eddies. In the TJ-II stellarator the application of DC plasma biasing induced a spontaneous edge transition with an amplification in the LRC of LP floating potential V_f (proxy for flow) perturbations—which was interpreted as evidence for the development of low frequency ($\sim$ 1–2 kHz) ZFOs [506, 507]—and accompanied by an increase in low frequency (at the expense of high frequency) broadband turbulence. Likewise, in the TEXTOR tokamak the LRC in edge V_f increased (ZFO-like $f < 5$ kHz—not GAM) during a biased induced H-mode [344, 431, 465, 508]—which is interpreted as an enhanced energy transfer from the turbulence into large scale ZF structures. In the HSX stellarator biasing also led to an increase in the bicoherence of poloidal electric field fluctuations and an increase in the LRC of probe floating potential fluctuations [423].

The impact of plasma biasing on the GAM has been less studied. Nevertheless, there are data from at least three devices. Negative biasing in ISTTOK using an emissive $LaBa_6$ electrode, inserted 15 mm inside the limiter radius, significantly increased the mean edge $E \times B$ shear flow, resulting in reduced ambient turbulence (AT) and a consequent suppression of the edge GAM [363]. However, positive biasing resulted in only a modest increase in the mean shear flow, but an increased long-range-correlation $\sim$ 1 m (ZF-like structures) in probe V_f fluctuations. For reference, without biasing the GAM shear rate $\gamma_{E\times B} \approx \Delta V_f/\Delta r^2 B$ was a factor of 2–3 times smaller than the mean shear rate, but was comparable to the decorrelation rate of the fluctuations.

Likewise, in J-TEXT, positive biasing was found to increase either the GAM or ZFO amplitude (they appear to be in competition) [390]. The radial particle flux Γ_r (obtained from LPs) was reduced during biasing and the discharge took on the appearance of an H-mode with increased density and confinement. In ohmic conditions the $E \times B$ shearing rate was less than the turbulence decorrelation rate, but with biasing the sum of both the mean and GAM/ZFO shearing rate together exceeded the turbulence rate and the turbulence was reduced. A similar effect was also observed in SINP, where a roughly linear increase in the GAM-like mode amplitude with applied external electrode positive biasing was found [396].

There is a clear parallel between the role of the edge E_r shear in the H-mode and the reports above where a negative bias enhanced mean $E \times B$ shear results in a reduced GAM amplitude, and thus GAM oscillatory shearing—i.e. the GAM plays less of a role in turbulence reduction. However, with positive bias a modest mean flow shear increase appears to drive the GAM and thus its flow shear role. This picture is consistent with GK simulations which show that a strong E_r (as in the H-mode tokamak edge pedestal region) substantially enhances the collisionless decay rate of the GAM [79].

11.4.3. AC plasma biasing. While DC plasma biasing using limiters or external electrodes can significantly modify the mean edge E_r radial profile resulting in an indirect enhancement or suppression of the GAM, there is also the possibility of

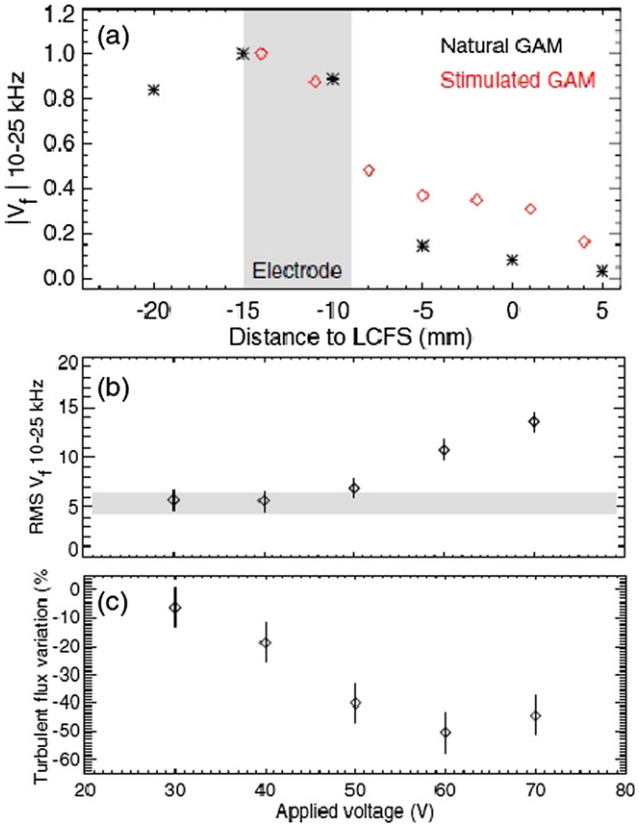

Figure 77. (*a*) Radial profiles of GAM frequency filtered normalized potential fluctuation $|V_{\rm f}|$ for applied AC bias $V_{\rm bias} = 0$ and 70 V (peak)/15 A at 15 kHz GAM frequency, (*b*) RMS $V_{\rm f}$ and flux $\Gamma_{\rm r}$ at $r - a = 5$ mm (SOL) vs bias voltage in ISTTOK. Reproduced courtesy of IAEA. Figure from [364]. © 2017 EURATOM.

directly driving or amplifying the GAM flow oscillation using modulated bias voltages at the GAM frequency.

Building on modelling work on the effect of GAM suppression of turbulence [428], numerical simulations have been performed using reduced two-fluid hydrodynamic Braginski equations, modified to include an external electric field [509]. The simulations show that an oscillating field close to the tokamak wall (i.e. in the plasma SOL) at the GAM frequency, and of sufficient strength, was cable of suppressing turbulence. The turbulence cell reduction was not due to shearing but through a resonant interaction between the GAM and the turbulence which reduces the turbulence growth rate. There was a critical field strength for the effect which depends on $T_{\rm e}$ and $n_{\rm e}$.

So far there is only one successful experimental attempt reported from the ISTTOK tokamak [364]. With an AC biasing electrode inserted at the GAM maximal radial location and driven at the natural GAM frequency, the natural GAM was enhanced by a factor of 7 or more. Figure 77 shows normalized band-pass filtered $V_{\rm f}$ level for natural and stimulated GAMs. The GAM amplitude increases with applied bias, beyond a threshold, coincident with a factor of 2 enhancement in the GAM shearing rate and a commensurate decrease in the cross-field particle flux into the SOL [364].

In summary, there are multiple drive mechanisms for the GAM. For the turbulence drive both direct drive of three-wave turbulence coupling via RS and indirect excitation by DS via a modulational instability. Experimentally both mechanisms exist together and may be equally important. In common with many turbulence effects the GAM displays an onset threshold with the turbulence amplitude, represented by the kinetic profile radial gradients. Internally the GAM may also be driven by MHD interactions, while externally there are possibilities to drive or modify the natural GAM with modulated edge plasma biasing, magnetic perturbations or localized plasma heating.

12. GAM damping

The GAM amplitude in steady-state is the result of an energy balance between sources (such as the turbulence or EP drive) and sinks (such as linear damping and energy transfer back into the turbulence, as well as non-linear damping effects which act as amplitude saturation mechanisms). This is summarized in the following table 13. This section reviews the GAM dissipation, for which there are several linear mechanisms, such as collisionless parallel and toroidal ion Landau damping, collisional (ion) damping and electron non-adiabatic effects, which were introduced in section 2.8. In addition, there is continuum damping due to PM. PM can combine with Landau damping leading to an enhanced damping rate, which is especially pronounced in the presence of a temperature gradient.

12.1. Overview of linear damping mechanisms

12.1.1. Continuum damping and phase-mixing. Continuum damping is intrinsic to the experimental GAM and arises directly from the radial gradients of the temperatures $\nabla_{\rm r} T$ which, while providing a drive for the turbulence, also results in PM as the GAM frequency goes radially out-of-phase over adjacent flux surfaces. As discussed in section 2.11, PM distorts the radial structure of the GAM leading to a decay in the GAM amplitude proportional to the local gradient of the GAM frequency. In the absence of other damping mechanisms—collisional and collisionless—the continuum damping rate sets the minimum threshold which the GAM drive must exceed for the GAM to be sustained. It was also shown that the enhanced damping due to coupling to the continuum may result in a finite threshold for the EGAM excitation by EPs [199]. The experimental observation of drive thresholds was discussed in section 11.2.

As discussed below there remain significant discrepancies between experimental observations of the GAM amplitude behaviour and predictions from individual collisional and collisionless damping models. However, theory suggests that PM may combine with collisionless Landau damping resulting in an enhanced (PL) damping mechanism; possibly raising the effective damping in realistic tokamak conditions by an order of magnitude [139, 151]. It may also be expected that the GAM existence will be strongly impacted in the steep edge temperature gradients regions of enhanced confinement regimes, such as I-mode and H-mode. Indeed, order of magnitude comparisons of characteristic drive rates $\gamma_{\rm DR}$ from nonlinear coupling and combined PM-Landau damping rates $\gamma_{\rm PL}$ were found

Table 13. Simplified overview of drive and damping mechanisms: from [53].

Ampl.	= drive $\gamma-$	linear damping $-$	non-linear damping
		Collisional $\gamma_{\rm col}$	Tertiary instabilities (KH)
		Collisionless $\gamma_{\rm c.l.}$	Scattering & trapping of wave packets
			System dynamics, LCO, bursts, etc

to be consistent with experimental observations of GAMs in L-mode, I-mode and H-mode [139].

12.1.2. Collisionless Landau damping. Landau damping is a kinetic effect arising from wave particle interactions, which can occur even in a spatially uniform plasmas, i.e. without density or temperature gradients. The basic theory of collisionless damping was reviewed in section 2.8. Several formulas were derived under various conditions and constraints, starting with the exponential damping rate $\gamma \propto \exp(-q^2)$ obtained from the DKE in the large aspect ratio limit with circular flux surfaces by Lebedev [9], Zonca [5] and Sugama [75]—so-called zero orbit width models. Further expressions were obtained for FOW conditions. These are summarized in table 4.

However, plasma shape introduces additional corrections, usually via the GAM frequency which, as discussed in section 7.6, has strong shape dependencies. An example is the form derived by Angelino (2008) who showed using linear ORB5 GK simulations that the damping rate increased with the plasma elongation κ, together with an inverse aspect ratio ϵ. Also, good agreement (cf figure 14 in [243]) between ORB5 and the kinetic formulation was obtained when the plasma shape dependence, such as elongation, was included in the real frequency

$$\omega_{\rm GAM}^2 = (\tau_{\rm e}+\gamma_{\rm i})\frac{v_{Ti}^2}{R_0^2}\left[\frac{8}{3-2\kappa+3\kappa^2}+\frac{1}{q^2}\right]$$
$$\gamma_{\rm kin} = \omega_{\rm GAM}\,\exp(-(\omega_{\rm GAM}qR_0/v_{Ti})^2/2). \qquad (268)$$

Plasma shaping effects were extensively investigated by Gao in a series of papers. Separating the real and imaginary terms of equation (86) and reforming one obtains the form proposed in [108] (Gao-2008)

$$\gamma_{\rm c.l.} = \frac{-\sqrt{\pi}}{2}\frac{v_{Ti}}{R_0}\frac{(R_0\,\omega_{\rm GAM}/v_{Ti})^6}{7/4+\tau_{\rm e}}q^5 \times \exp\left[-(qR_0\,\omega_{\rm GAM}/v_{Ti})^2\right] \qquad (269)$$

valid under the assumption of $\gamma \ll \omega$ (real) and high q. This was derived in the limit of small GAM radial wavenumbers, $k_{\rm r} \to 0$, (termed small ODW in [122]) and leading order terms. The effect of plasma shape (specifically κ) again enters via $\omega_{\rm GAM}$, where increasing κ lowers the GAM frequency and correspondingly raises the collisionless damping [242]. The inclusion of finite ODW effects, e.g. finite GAM radial $k_{\rm r} > 0$ may become important for $q > 2$ [131, 240]. Sugama and Watanabe included FOW effects in their GK approach in circular shape to obtain equation (88) [75, 76]. Gao also considered the so-called large ODW limit expansion for shaped plasmas, deriving the following analytic formula from the GK equation [117, 122] (Gao-2010)

$$\gamma_{\rm c.l.} = -\frac{v_{Ti}}{R_0}\frac{4\kappa^2\sqrt{7/4+\tau_{\rm e}}}{\hat{k}^2(\kappa^2+1)^{3/2}}\left(1+\frac{2\kappa^2+5}{4\kappa^2+4}s_\kappa-\frac{27\kappa^2+9}{8\kappa^2+8}\epsilon^2 - \frac{7\kappa^2+4}{4\kappa^2+4}\Delta'^2+\frac{9\kappa^2}{4\kappa^2+4}\epsilon\Delta'\right) \times \exp\left[-\frac{\sqrt{7/4+\tau_{\rm e}}}{\hat{k}}\sqrt{\frac{2\kappa^2}{\kappa^2+1}}\left(1+\frac{3\kappa^2+4}{4\kappa^2+4}s_\kappa - \frac{9\kappa^2}{8\kappa^2+8}\epsilon^2-\frac{3\kappa^2+2}{4\kappa^2+4}\Delta'^2+\frac{4\kappa^2+1}{4\kappa^2+4}\epsilon\Delta'\right)\right], \qquad (270)$$

where $\hat{k} = k_{\rm r}\rho_{\rm i}$. This form has a qualitatively different behaviour to that of the low $k_{\rm r}$ limit. In [117] it was claimed that the difference arises from a change in the resonant mechanism from a low-order harmonic transit resonance to high-order harmonic resonance contributions, with the result that the damping rate becomes independent of q. The two Gao formulas are popular expressions that have been used by several authors for experimental comparisons, as discussed below in section 12.2.

12.1.3. Collisional damping. Collisional damping is expected to become important in the tokamak plasma edge where $q \gg 1$ and the collisionless damping becomes less important, that is $\gamma_{\rm col} > \gamma_{\rm c.l.}$. Damping due to the ion–ion collisions occurs as result of the collisional relaxation of the anisotropy of the perturbed pressure and, as discussed in section 2.10, is therefore amenable to the fluid description within the two-pressure model. Generally the collisional damping rate scales linearly with the ion–ion collision frequency, such as in the form obtained by Novakovskii [8] $\gamma_{\rm col} = -4/7\nu_{\rm i}$ equation (96) where $\nu_{\rm i} = 4.80\times10^{-2}\sqrt{1/2}\,n_{\rm e}\ln\Lambda_{\rm i}^{3/2}\ {\rm s}^{-1}$ (for deuterium). Table 4 gives several expressions for $\gamma_{\rm col}$ obtained using different collision operators. The forms obtained by Gao (99) and Li (100) in particular have been tested in experimental comparisons. Note that none of the collisional formulas contain any shape dependence.

12.2. Experimental results

There is substantial evidence from several experimental devices for the role of both collisionless and collisional damping. DIII-D [282, 435], AUG [26, 309] and JET [358] all show an increasing GAM amplitude at low density (low collisionality) with increasing q, consistent with a collisionless Landau damping effect. This is supported by GK all-order FOW numerical simulations from the TEMPEST code [78],

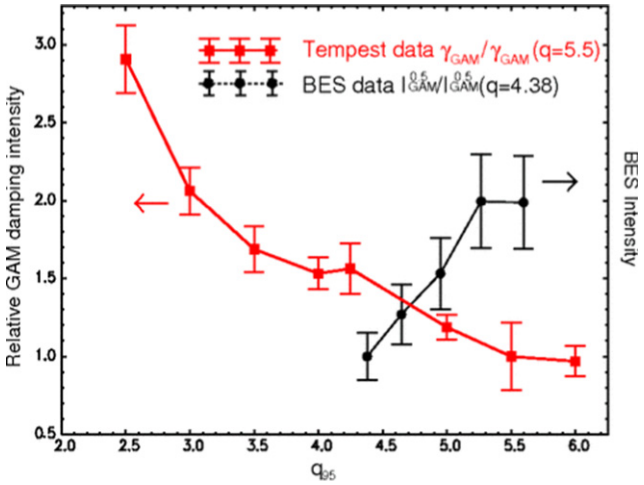

Figure 78. GAM damping rate from TEMPEST code (red) and integrated GAM amplitude from BES measurement (black) vs q_{95} during I_p high current ramp in diverted DIII-D edge $r/a = 0.9$ [435]. Adapted figure with permission from [78], Copyright (2008) by the American Physical Society.

which show, in figure 78, the correlation of a decreasing damping rate with increasing edge GAM amplitude as q_{95} is varied during I_p current ramps in USN divertor, high $\kappa = 1.75$, DIII-D discharges. However, at very high q_{95}, see figures 4 and 6 in [435], the GAM amplitude decreases again—possibly due to changes in turbulence drive or other shape effects.

With increasing density the edge GAM is suppressed in AUG, consistent with a now dominant collisional damping [305]. Likewise, in diverted plasmas in HL-2A during gas-puffing, collisional damping appears to determine the edge GAM amplitude [354, 430]. In T-10 the GAM was found to exist only below a local density of $n_e \sim 2 \times 10^{19}$ m^{-3}—a clear indicator of an upper bound for collisional suppression of the GAM.

Several detailed studies have been undertaken comparing the GAM amplitude behaviour with various damping models. The first, from Tore Supra [373], used DR to obtain A_{GAM} profiles in low and high ν_{ii} circular plasmas. These were compared with simulations from the global full-f flux-driven GK GYSELA code. An interpretation of the A_{GAM} behaviour requires knowledge of both sources and sinks. The source is related to the turbulence intensity. Lacking good $\delta n/n$ experimental profiles, linear growth rates were estimated from local GK GENE code simulations. The GAM was found to be more intense in the low ν_{ii} case than in the high ν_{ii} one, which is consistent with the estimated source and damping of the mode. The result suggests that the GAM damping was dominated by collisional effects while Landau damping was negligible. Nevertheless, the GAM amplitudes in the simulations were weaker than in the experiments. This was attributed to an underestimation of the turbulence intensity. A simple evaluation of the GAM source and damping ratio S/γ (using an energy equilibrium model: $\partial A/\partial t + \gamma A = S$), in both experiments and simulation, confirmed the GAM intensity scales consistently with the local fluctuation level δn.

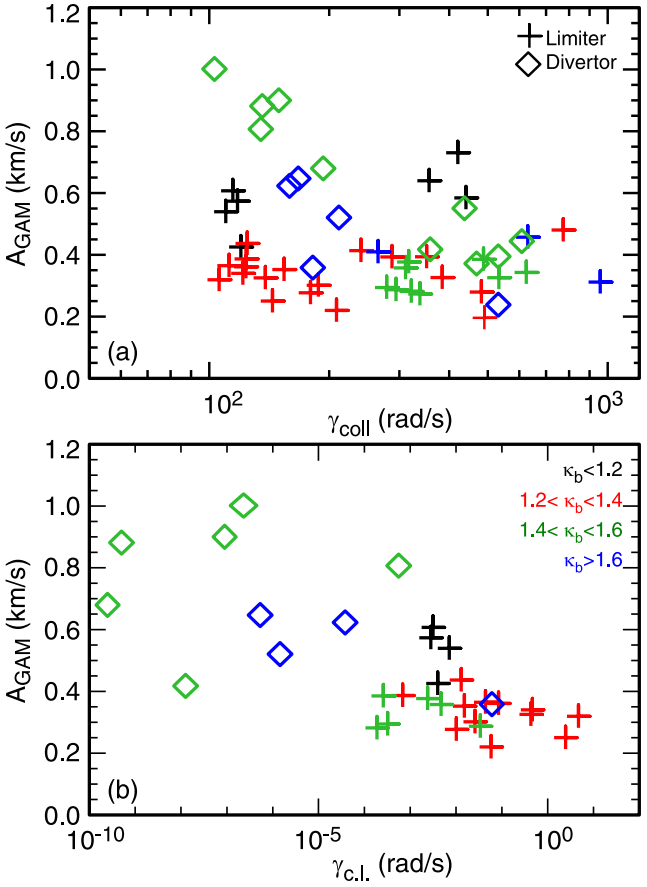

Figure 79. GAM amplitude in AUG vs (*a*) Gao collisional (98), and (*b*) collisionless for $k_r = 0$ (269) damping rates for limiter (crosses) and divertor (diamonds) configurations. Adapted from [309]. © IOP Publishing Ltd. All rights reserved.

Doppler reflectometry was also used in AUG to investigate the role of plasma shaping, specifically the boundary elongation κ_b, and q on the GAM amplitude A_{GAM} for both limiter and divertor configurations [26]. Using a database with similar $\nabla T_e/\sqrt{\kappa_b}$ (to separate the turbulence drive effect) different dependencies were found for limiter and divertor configurations. In limiter plasmas A_{GAM} decreased inversely with increasing κ_b, but not in divertor plasmas at low q. Nevertheless, a common behaviour of increasing A_{GAM} with increasing q was observed—consistent with Landau damping.

Behavioural discrepancies where noted in SINP where the GAM amplitude was independent of $q_{edge} = 1.5$–6 in low density limiter circular plasmas [395]. However, the effect of the T_e/T_i ratio could be influential here. According to Watari [99] the GAM damping rate should be smaller if $T_e > T_i$. This appears to be the case for SINP and is also supported by JIPP T-IIU results in ohmic heated low density plasmas (where T_e and T_i decouple and $T_e > 3T_i$ [36]). Here, very intense core GAMs and weak ZFO were observed when $1 \ll T_e/T_i$ [329–331].

The AUG study was further extended [309] with detailed experimental parameter scans and comparisons to various analytic expressions, including Gao's collisional model (98), and collisionless $k_r \to 0$ model (269), Sugama's FOW collisionless model (88) [75, 76] and Gao's large ODW model (270). As an example of the analysis performed figure 79 [309] shows the

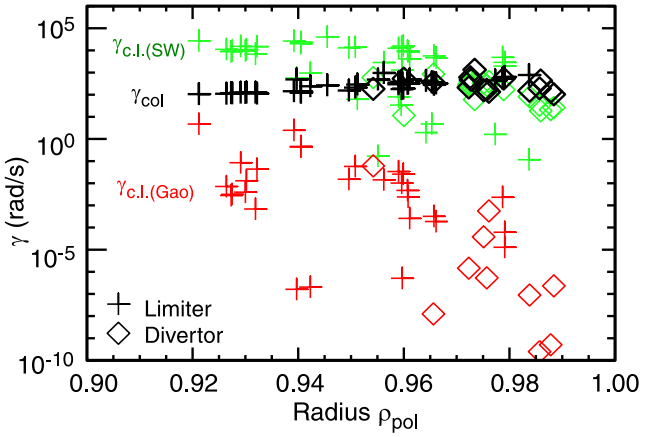

Figure 80. Computed damping rates vs normalized radius ρ_{pol} using experimental input parameters from AUG: (black) Gao collisional γ_{col} (98), (red) Gao collisionless $\gamma_{c.l.}$ for $k_r = 0$ (269), (green) Sugama collisionless $\gamma_{c.l.}$ with FOW corrections (88). Adapted from [309]. © IOP Publishing Ltd. All rights reserved.

GAM amplitude A_{GAM} (with a constant $\nabla T_e/\sqrt{\kappa_b}$) vs the Gao collisional γ_{col} (98) and collisionless $\gamma_{c.l.}$ (269) damping rates using local experimental values for limiter and divertor shapes with various boundary κ_b. For the divertor data-points there is a clear decrease in A_{GAM} with increasing γ_{col}, while the limiter points are more flat at high collisionality. Against collisionless damping there is also a general decreasing tend, but the spread in the divertor points is much greater.

The collisional damping rates are generally orders of magnitude larger than the collisionless values, however, as shown in figure 80 [309] the collisionless $\gamma_{c.l.}$ vary enormously depending on the model and radial position. Using experimental values for the data-set of figure 79, collisional γ_{col} was found to dominate over the $k_r \to 0$ collisionless $\gamma_{c.l.}$ in the outer plasma edge. Towards the core the collisionless $\gamma_{c.l.}$ rose to became comparable, or greater than the collisional γ_{col}. Overall, including finite ODW effects raises the collisionless $\gamma_{c.l.}$ making it more important towards the core for both limiter and divertor cases. The role of the GAM k_r appears more significant in divertor configurations where the GAM radial extent is generally narrower. Decreasing k_r brings both FOW $\gamma_{c.l.}$ (88) and (270) towards the small ODW $\gamma_{c.l.}$ (269) in the edge. The conclusion was that collisional damping plays a dominant role for divertor configurations at high q in the plasma edge, while collisional and collisionless damping play equal roles for limiter configurations at low q towards the plasma core.

Similar studies on JET also used DR to build a database of GAM amplitude dependencies on line averaged plasma density $\bar{n}_e$, plasma current I_p and divertor target geometry in ohmic hydrogen and deuterium plasmas [358, 359]. At high I_p the GAM amplitude A_{GAM} increases with $\bar{n}_e$—essentially steepening edge ∇n_e and thus turbulence drive—up to a point where collisional damping becomes effective and A_{GAM} falls. With decreasing $I_p \propto 1/q_{95}$ the roll-over point moves to lower $\bar{n}_e$ due to enhanced collisionless damping, until the GAM is extinguished. Holding $\bar{n}_e$ constant reveals an initial rise then suppression of the GAM with increasing I_p. Comparing the measurements against the (NEC) collisional γ_{col} of Li equation (100) and the collisionless small OWD (269) and large ODW (270) $\gamma_{c.l.}$ models of Gao reveals discrepancies [359]. The collisional γ_{col} was predicted to be universally dominant in the edge, but in the experiments it was only found to be effective at low I_p and high $\bar{n}_e$. The collisionless damping behaviour is complicated by the interrelated drive dependencies, nevertheless, the observed GAM suppression at high I_p is in agreement with collisionless models, although the estimated damping rates appeared to be too small to explain the measurements. In JET the GAM radial wavenumber was estimated at $k_r \sim 2.6\,\mathrm{cm}^{-1}$ suggesting large ODW effects should be important. The observed discrepancy in predicted γ maybe due to fact that in the JET edge $\nu_{ii} \leqslant \omega_b = v_{Ti}/qR_0$, implying that the collisionless formulas may not be applicable.

In another experimental approach [255, 510] a Lorenzian profile was fitted to the GAM spectral peak P_G in FT-2, assuming a dissipative oscillator driven by a random force (such as RS):

$$P_G = \frac{A_{turb}^2}{(\omega - \omega_{GAM})^2 + \gamma_o^2} \tag{271}$$

to obtain a radial profile of the GAM γ_o experimental damping rate of the order of 20–30 ms^{-1}. Reasonable agreement was found with a damping profile using the sum of a collisional $\gamma_{col} \sim 4\nu_i/7$ and a Landau $\gamma_{c.l.} \sim \omega_{GAM}\exp(-q^2)$ damping rate (including impurities with $Z_{eff} \sim 3.5$ [248]), except at the tokamak edge where it was speculated that the γ_{col} was a factor of 2 too small due to the neglect of significant ion-neutral collisions in the edge. Similarly, in DIII-D the GAM spectral peak widths were measured at $\sim$ 200–300 Hz, giving $\Delta f/f \sim$ 1%–2%. Assuming an exponential Landau damping form this translates to an upper bound for $\gamma_{GAM} <$ 100–150 Hz (i.e. 6–10 ms^{-1}) [282].

In summary, collisional damping appears to dominate at the plasma edge, but collisional and collisionless damping appear to be equally important away from the edge. The collision rate affects not only the GAM damping but also reduces the GAM frequency as well as changing the ion adiabatic index γ_i dependency. The GAM visibility is, nevertheless, still a question of the balance between damping and drive.

13. Energetic particle GAMs

As reviewed in section 3, EPs can also be a source of drive for the GAM. A GAM-like instability with a toroidal mode number $n = 0$ was first observed in the core region of ion cyclotron resonance heated (ICRH) plasmas in JET [12, 13], as shown in figure 81. Unlike the turbulence driven GAM, the mode had a significant magnetic component from which the toroidal mode number of zero was confirmed by a toroidal array of Mirnov coils. The GAM had chirping frequencies which suggest that the mode is driven by fast ions. Since the GAM was observed around a local maximum of the GAM continuum induced by the reversed magnetic shear where the safety factor profile has a local minimum, the GAM was interpreted as a GGAM driven by fast ions.

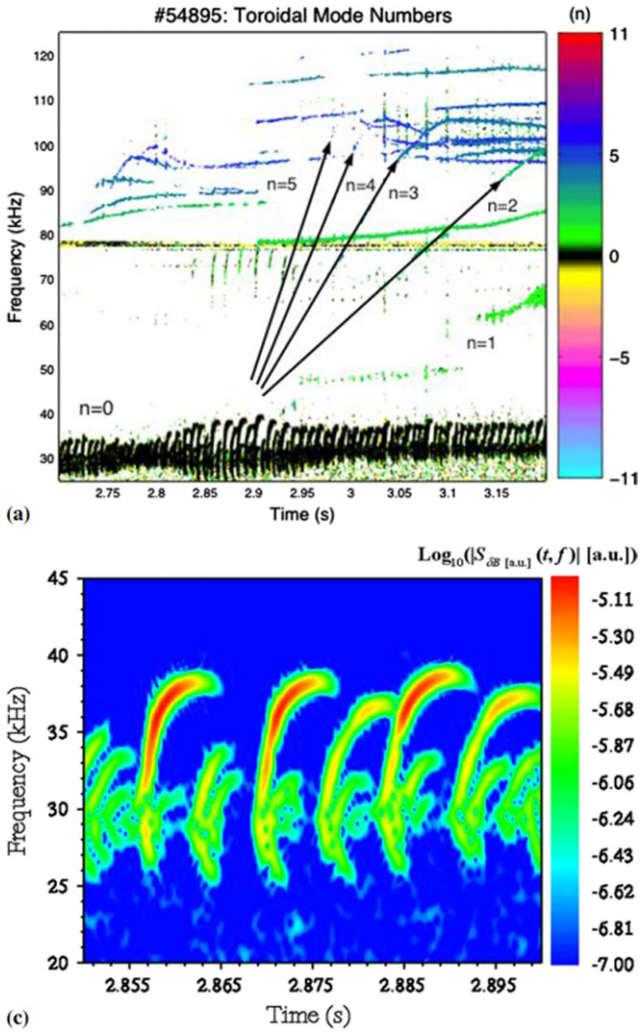

Figure 81. Toroidal mode analysis and spectrogram of magnetic fluctuations in the JET tokamak. Reproduced courtesy of IAEA. Figure from [12]. Copyright (2006) IAEA.

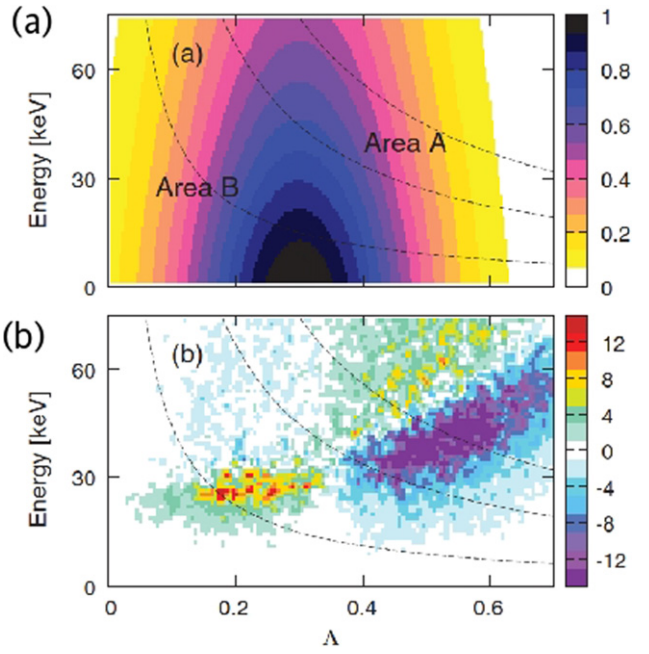

Figure 82. (*a*) Initial EP distribution function in (Λ, E) space used in a numerical simulation, where $\Lambda = \mu B/E$ with μ the adiabatic invariant, and E the ion energy. Dashed curves mark constant μ. (*b*) Resultant simulated energy transfer rate from EGAM to fast ions. Reprinted figure with permission from [512], Copyright (2013) by the American Physical Society.

Core, $n = 0$ chirping modes were also observed in NBI heated plasmas in DIII-D. However, the experiment clearly displayed mode frequencies significantly lower than the expected standard GAM frequency by a factor of approximately 2 [44]. The frequency discrepancy was explained when taking the EPs into account, and was thus termed an EGAM [45] as described in section 3. Subsequently EGAMs were widely observed in NBI plasmas in LHD [266, 409, 410], JT-60U [370], HL-2A [231], AUG [313], and EAST [433]. Table 14 summarizes the main features of the EGAMs reported from various devices. Several where observed in reversed magnetic shear conditions, but the JET case is clearly linked with a GGAM structure and with frequencies above the continuum. In the following subsections the driving mechanism and characteristics of the EGAM and EP driven GGAM are reviewed.

13.1. Driving mechanisms

Fast ions with parallel velocities close to the GAM phase velocity can resonate with the GAM. Numerical simulations, taking into account kinetic fast ions, show that the fast ions lose energy in the region where the gradient of the energy distribution is positive along curves on which the adiabatic invariant is constant, as shown in figure 82 [512].

In LHD a similar behaviour in the energy distribution was observed with a neutral particle analyzer [513]. As shown in figure 83, the ions in the higher energy region (150–170 keV, where the energy of the neutral beam is 175 keV) decrease and those in the lower energy region (110–150 keV) increase. That is, the fast ions lose energy during the growth of the EGAM, thus implying an energy transfer from the fast ions to the EGAM. As noted in section 3 and summarized in table 6, theoretical analysis [195] also suggests the possibility of a dissipative EGAM excitation due to the negative energy mode instability (with the positive energy loss) and the EP distribution decreasing with the energy.

In HL-2A an EP driven GAM was observed in ohmic plasmas in which no fast ions existed [231, 511], but there were energetic electrons generated by magnetic re-connection during TM activity. An important feature of these observations is the presence of an $m = 2$ mode detected in Mirnov coils which was well correlated with $n = 0$ and $m = 2$ EGAM activity, figure 84, thus pointing to a global nature for the EGAM in this case. This unconventional EGAM is accompanied by TMs and BAEs, showing nonlinear three wave coupling interactions between the EGAM, TM and BAE, as demonstrated in figure 85; with $f_{\mathrm{EGAM}} = f_{\mathrm{BAE2}} - f_{\mathrm{TM}}$, $f_{\mathrm{EGAM}} = f_{\mathrm{BAE1}} + f_{\mathrm{TM}}$, and $f_{\mathrm{EGAM}} = f_{\mathrm{BAE1}} + f_{\mathrm{BAE2}}$. Similar EGAM/Alfvén-like $n = \pm 1$ modes with frequency splitting were reported from

Table 14. Reported observations of EGAM/EP-GGAMs by experiment. f_{GAM} is the expected continuum GAM frequency, f_{t} the EP transit frequency, eigen = eigenmode structure.

Device	Source	Features
AUG	NBI	Chirp $f_0 \sim f_{\mathrm{t}}$, $m = 2$ EM [313]
DIII-D	NBI	Chirp $f < f_{\mathrm{GAM}}$, $m = 2$ EM, rev. shear [44]
EAST	NBI	No-chirp $f < f_{\mathrm{GAM}}$, core eigen, $m = 2$ & 4 EM [433]
HL-2A	Ohmic	No-chirp $f < f_{\mathrm{GAM}}$, eigen, $m = 2$ EM. Fast elec., TM + BAEs [231, 511]
JET	ICRF	Chirp $f > f_{\mathrm{GAM}}$, Rev. shear, GGAM, $m = 2$ EM [12, 13]
JT-60U	NBI	$f < f_{\mathrm{GAM}}$, eigen, $m = 2$ EM, rev. shear [370]
LHD	NBI	Chirp $f \gtrless f_{\mathrm{GAM}}$, eigen, cnt-NBI [410]
LHD	NBI	No-chirp, rev./weak shear [266, 409]
TJ-II	ECH	Chirp $f < f_{\mathrm{GAM}}$, core eigen, $n = 1$, candidate EGAM [418]

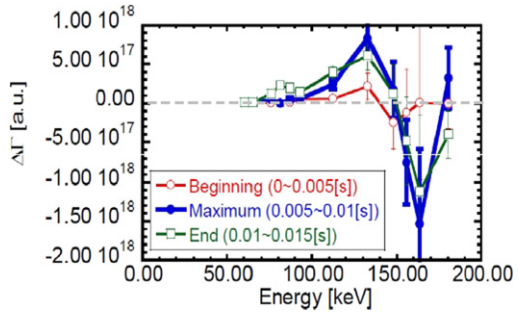

Figure 83. Variation in energy distribution measured by neutral particle analyzer during EGAM burst in LHD. Reproduced with permission from [513].

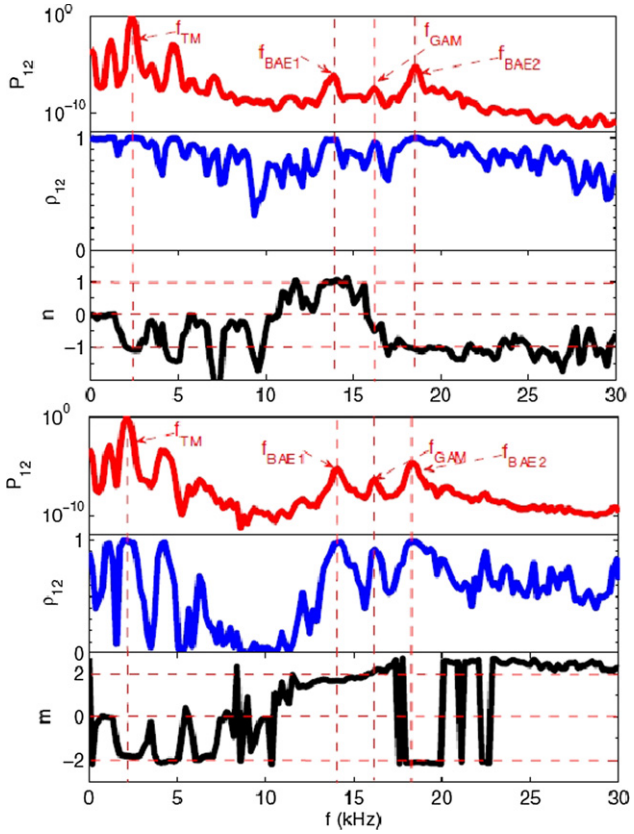

Figure 84. Cross-power spectra, correlation coefficient and mode numbers from (top) toroidal Mirnov signals of TM ($n = -1$), BAE1 ($n = 1$), BAE2 ($n = -1$) and EGAM ($n = 0$), and (bottom) poloidal Mirnov signal of TM ($m = -2$), BAE1 ($m = 2$), BAE2 ($m = -2$) and EGAM ($m = 2$) in HL-2A. Reproduced courtesy of IAEA. Figure from [231]. Copyright (2013) IAEA.

ICRF heated TEXTOR plasmas in the presence of large 2/1 TMs or external magnetic perturbations [514].

It was suggested that the EGAMs in the HL-2A case were generated by the energetic electrons at the passing-trapped boundary, as a result of passing electron scattering into the trapped region due to the anomalous Doppler instability. This picture is supported by ECE and SXR signals during periods of sawtooth activity [231]. It is also consistent with theoretical analysis [125] indicating that marginally trapped electrons produce the largest contribution. Another destabilization mechanism for such modes may be related to the direct contribution of the electron current generated by the TM activity [202, 205, 206]. Potentially, three wave coupling may also play a role in the mode generation.

The mechanism of the EGAM drive has also been confirmed by numerical simulations [512] and expanded by taking into account the GAM continuum [156], as well as the effects of finite ion Larmor radius and guiding-centre drift orbit width [199, 515], and also a bump-on-tail velocity distribution function [194, 195, 197, 496].

EGAMs are generally observed in low density plasmas (typically 1×10^{19} m^{-3} or less). Since the anisotropy in the velocity space of the EP is more easily sustained in low density and collisionless plasmas, the observation of the GAM in low density plasmas is consistent with an EP driving mechanism.

13.2. Frequency chirping

One of the common features of the EP driven GAM is a frequency up-chirping, as shown in the example from JET in figure 81—see also table 14. As described in [180, 516] the frequency chirping corresponds to the nonlinear evolution of the velocity distribution via a wave–particle interaction, which is described by the hole–clump creation model of Berk and Breizman [517]. The hole–clump creation has been observed in various experiments during the excitation of the EGAM, cf figure 83 [513] from LHD, and in numerical simulations, such as those shown in figure 82(*b*) [512].

According to the hole–clump creation model, which is described more fully in section 3, since the initial frequency

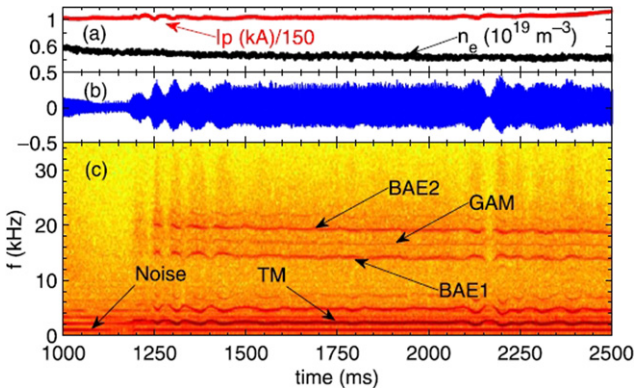

Figure 85. Discharge evolution of (*a*) plasma current I_p & core density, (*b*) poloidal Mirnov signal, and (*c*) spectrogram in HL-2A. Reprinted from [511], Copyright (2013), with permission from Elsevier.

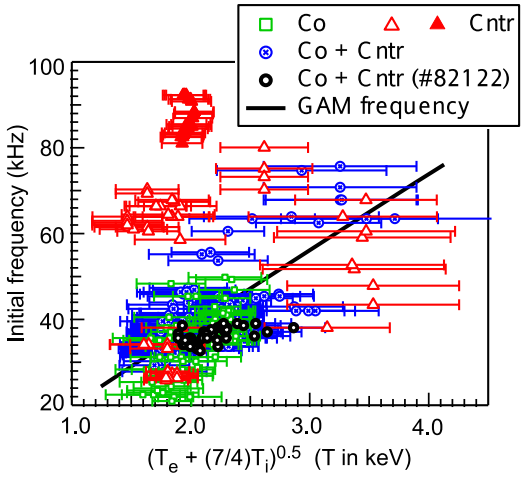

Figure 86. EGAM frequency higher than the GAM frequency. Temperature dependence of measured EGAM frequency in LHD. Reproduced courtesy of IAEA. Figure from [410]. Copyright (2015) IAEA.

of the chirping mode reflects the linear characteristics of the instability, the observed initial EGAM frequency is expected to coincide with the standard GAM frequency [1, 54]. However, the frequency of the EGAM observed in DIII-D was significantly lower than that of the expected standard GAM [44]. Similar results have been observed in other devices; JET [13], LHD [410], JT-60U [370], HL-2A [231] and AUG [313]. This frequency discrepancy can be explained when taking into account the form of the distribution function of the EPs [45, 156, 192, 194, 197, 496, 512]. As described in section 3, EPs can either modify a natural GAM or destabilize a new branch of the GAM dispersion relation. In both cases the destabilized EGAM has a frequency lower than the standard GAM *when* the velocity distribution function of the EPs has the form of a slowing-down distribution, cf figure 14 in section 3.

On the other hand, it is also observed experimentally that the frequency of the EGAM can become *higher* than the standard GAM frequency, as shown for example in figure 86 [410]. In these cases the higher frequency can be explained if one considers a *non-slowing-down* velocity distribution function with a significant beam component, e.g. a bump-on-tail [197, 263, 410], as shown in figures 87 and 15, where it is shown that the frequency can be reached by the transit frequency of the passing EPs.

Although the frequency chirping is a predominant feature, there are also cases where the frequency does not chirp. Such cases have been observed in reversed or weak magnetic shear configurations in LHD [266, 409] and in ohmic plasmas in HL-2A [231]. In both cases other MHD modes or Alfvén eigenmodes existed simultaneously, and thus additional mode coupling may affect the behaviour of the EGAM.

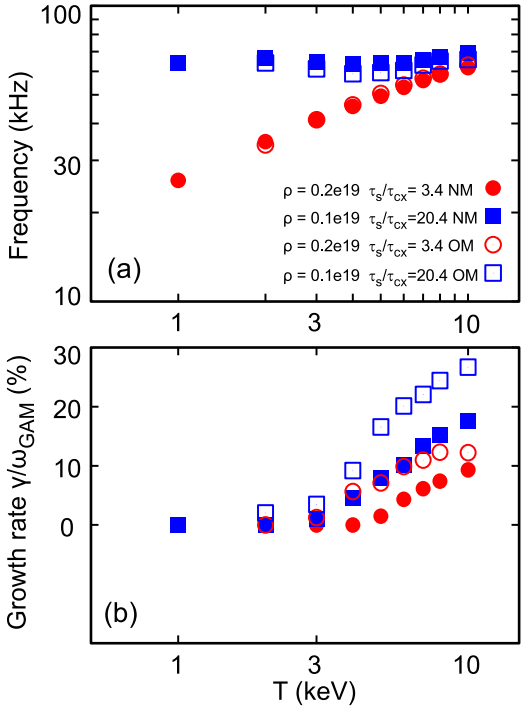

Figure 87. Numerical simulation using hybrid DK and MEGA MHD fluid code of (*a*) EGAM frequency and (*b*) growth rate vs temperature (for new and old models). ρ is bulk plasma density and τ_s/τ_{cx} is the slowing down over charge-exchange time, based on LHD experiments. Adapted from [263], with the permission of AIP Publishing.

13.3. Spatial structure

The EGAM usually exists close to the plasma central region [12, 13, 44, 266, 313, 409] unlike the turbulence-driven GAMs which tend to be excited near the edge region in tokamaks. The mode width extends to a few tens of percent of the plasma minor radius. In JET, cross-correlation analysis between SXR signals and a Mirnov coil indicates that the GAM is localized near the plasma core (figure 88). The structure is associated with a minimum in the q profile leading to a local maximum in the GAM continuum, thus the GAM is interpreted as a GGAM, as described in section 9, induced by EPs [12, 13]. Likewise, in DIII-D, BES shows that the electron density fluctuation associated with the GAM also exists in the core region (figure 89). Similar to JET, the GAM extends across the reversed magnetic shear region. However, the predicted GAM continuum from the NOVA code is monotonic, suggesting the observed

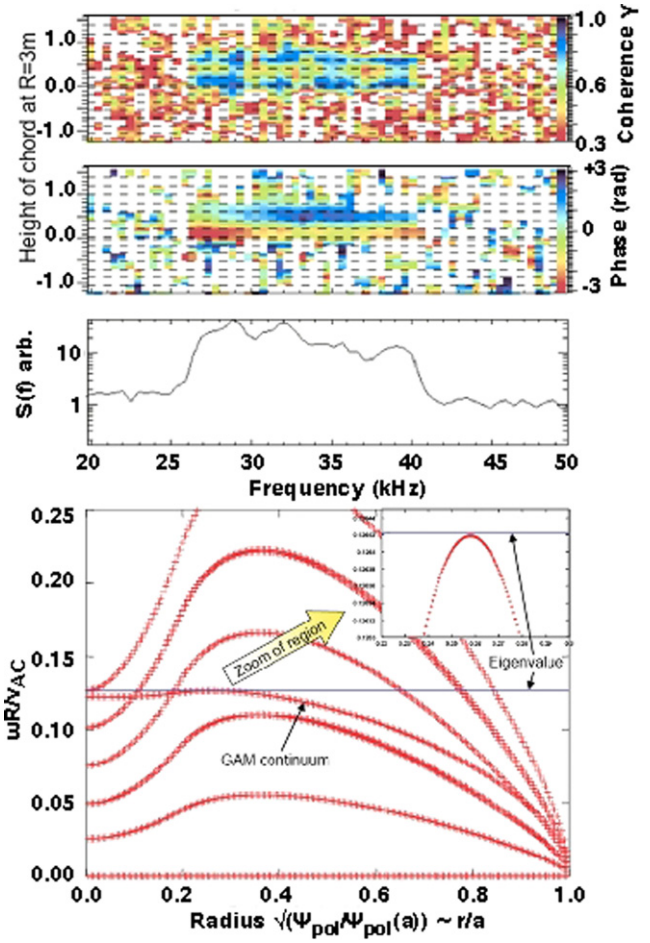

Figure 88. Radial profiles of EP induced GAM in JET, (*a*) and (*b*) cross correlation amplitude and phase between a Mirnov coil and SXR horizontal camera array signals, (*c*) Mirnov coil frequency spectrum, and (*d*) radial profile of $n = 0$ continuum modes from CASTOR code. Reproduced courtesy of IAEA. Figure from [12]. Copyright (2006) IAEA.

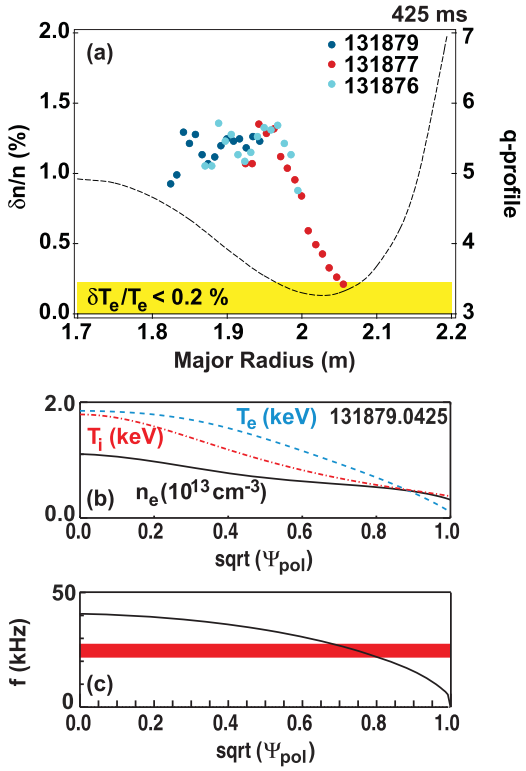

Figure 89. Radial profiles of EP induced GAM in DIII-D. (*a*) Density fluctuation amplitude associated with the GAM measured using BES $\tilde{n}/n$ plus safety factor q, (*b*) ion T_i and electron T_e temperature and density n_e. The radial coordinate is $\sqrt{\Psi_{pol}}$ of the poloidal flux, (*c*) the $n = 0$ GAM continuum from the NOVA code (black) with observed GAM frequency range (red band). Reprinted figure with permission from [44], Copyright (2008) by the American Physical Society.

GAM profile is not be determined entirely by the local maximum of the GAM continuum [44], but may reflect the radial distribution of the fast ions [45].

In addition, in the LHD heliotron the rms amplitude of the electric potential fluctuation associated with the EGAM can reach several hundreds of volts with peak values of a few kV—more than the mean core potential—which is much larger than for the turbulence-driven GAMs [410]. The large amplitude is attributed to the high energy of the fast ions. Associated with the core EGAM, an abrupt GAM has also recently been reported with a magnitude exceeding that of the seeding EGAM [518].

The spatial structure of the EGAM has been investigated in detail. Since the EGAM has a significant magnetic component its mode numbers have been easily confirmed by analysis of the phase delay between signals of toroidal and poloidal arrays of Mirnov coils. The observed poloidal mode number of the magnetic halo field fluctuation is $m = 2$ [231, 313, 370, 433], which agrees with theoretical predictions [171].

Although it is not easy to measure the mode structures of the density and electric potential perturbations near the central region of high temperature plasmas, radial profiles have been obtained using BES on DIII-D [44] as well as HIBP on LHD [410]. They agree with the structures of the standard GAM: $m = 1$ for the density fluctuation and $m = 0$ for the electric potential fluctuation. For example, from LHD figure 90 shows the spatial structures of the electric potential and density fluctuations. The electric potential structure is up–down symmetric, and the density fluctuation is up–down anti-symmetric, thus in agreement with poloidal mode numbers $m = 0$ and $m = 1$ respectively.

Although the poloidal structures of the EGAMs are usually up–down symmetric, the symmetry can be broken [413, 433]. In LHD the amplitudes of density fluctuations associated with the EGAMs sometimes become up–down asymmetric [413]. In EAST the observed poloidal magnetic field fluctuation is tilted (i.e. the m mode structure not up–down but rotated in the poloidal plane) with a mode amplitude that is asymmetric or varies in the poloidal direction [433]. The tilting and asymmetry of the amplitude are determined by the pitch angle and energy of the energetic ions. In addition, the co-existing lower frequency mode with the poloidal mode number of $m = 2$ causes the asymmetry in the amplitude of the EGAM.

In ASDEX Upgrade the temporal evolution of the radial structure of the chirping EGAM has been studied using SXR measurements [313]. The radial profile of the EGAM shrinks during the chirping. The shrinkage can be explained by the

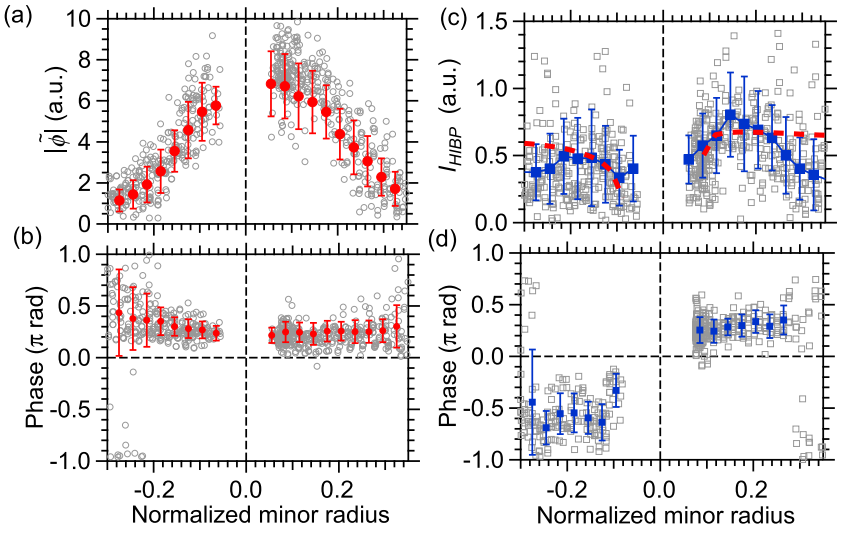

Figure 90. Radial profiles of (*a*) and (*c*) amplitude and (*b*) and (*d*) phase associated with the EGAM. (*a*), (*b*) Correspond to the electric potential, and (*c*) and (*d*) correspond to the density fluctuation in LHD. Reproduced courtesy of IAEA. Figure from [410]. Copyright (2015) IAEA.

changing resonance condition in the velocity space of fast ions as follows: during the chirp-up, the energy range in which fast ions resonate with the EGAM increases. Since the magnetic moment is conserved, the pitch angle of the resonant fast ion decreases. Thus, the passing particles having narrower drift orbit width drive the EGAM. Since the mode structure of EGAMs is sensitive to the EP distribution, the narrower orbit width of the interacting fast ions leads to the shrinkage of the mode structure.

Most of the theories take into account the resonance between the transit motion of the fast ions and the EGAM, i.e. $\omega_{\mathrm{GAM}} \sim \omega_{\mathrm{h}}$ (hump). In addition, the EGAM can resonate with the magnetic drift of the fast ions $\omega_{\mathrm{GAM}} \sim \omega_{\mathrm{D}} \gg \omega_{\mathrm{h}}$ [50]. The resonance causes poloidal asymmetry of the density fluctuation and the electric potential fluctuation. The asymmetry depends on the radial wave number of the EGAM and the direction of magnetic drift of the EPs, and, as a result of the resonance, humps in the poloidal structures appear. This poloidal asymmetry leads to an increase in the parallel wave number, which in turn may enhance the Landau damping of the GAM by the bulk ions.

13.4. Influence on particle and heat transport

In principle GAMs, including EGAMs, do not directly induce the fluctuation-driven radial particle flux $\langle \Gamma_{\mathrm{r}} \rangle = \langle \tilde{n} \times \tilde{v}_{\mathrm{r}} \rangle = \langle \tilde{n} \times \tilde{E}_{\mathrm{p}}/B_{\mathrm{t}} \rangle$ in the main order, as they do not possess a poloidal electric field fluctuation. But they can impact affect particle and heat transport via other routes.

In DIII-D an enhancement of fast ion losses [519] is observed during the EGAM excitation, as shown in figures 91(*a*) and (*b*). Trajectory calculations based on the pitch angles and gyroradii of the lost ions, measured by a lost ion probe, reveals that confined counter-passing ions become unconfined trapped particles because of their interaction with the EGAM is accompanied with a change in their pitch angles (see figure 91(*c*)).

A drop in the neutron emission at the EGAM burst is also observed in DIII-D, as shown in figure 92(*b*). This result is interpreted as a loss of the fast ions induced by the EGAM [44]. Thus a deterioration in the performance of future fusion reactors may result from an EGAM induced loss of fast ions, which otherwise should contribute to self-heating of the fusion plasma.

The influence of the EGAM on turbulent transport has been investigated theoretically. GK simulations using the GYSELA code indicate that the EGAM transports packets of turbulence in the radial direction, even across a transport barrier, as shown in the two simulation phases in figure 93 [271].

Analytic investigations of the interaction between DW type turbulence and the EGAM in the phase space also indicates that the turbulence can be trapped at the local maximum of the radial electric field associated with the EGAM, as shown in figure 94 [470, 471]. Note that whether the turbulence is trapped at the local maximum or the local minimum depends on the dispersion relation of the turbulence. In the case that the EGAM propagates in the radial direction, the trapped DW turbulence is transported by the EGAM ballistically. The EGAM having a semi-macro scale can transport the micro turbulence to places where the turbulence is originally stable, and thus contribute to the formation of spatial structures in the plasma by modifying the turbulent heat and particle transport as a non-local effect.

From the point of view of energy transport the EGAM may contribute to bulk ion heating, in a manner similar to alpha particle channelling [520]. At first sight this process does not seem to be straightforward. The EGAM is excited through inverse Landau damping of fast ions. Thus its phase velocity is comparable to the velocity of the EPs, but much faster than the velocity of the bulk ions. Hence the energy exchange between the EGAM and the bulk ions is not efficient. Nonetheless, since the amplitude of the EGAM is large ($\sim$ kV) the ion Landau damping can still contribute to ion heating [269]. In addition, the generation of higher harmonic f_{EGAM} EGAM resonances,

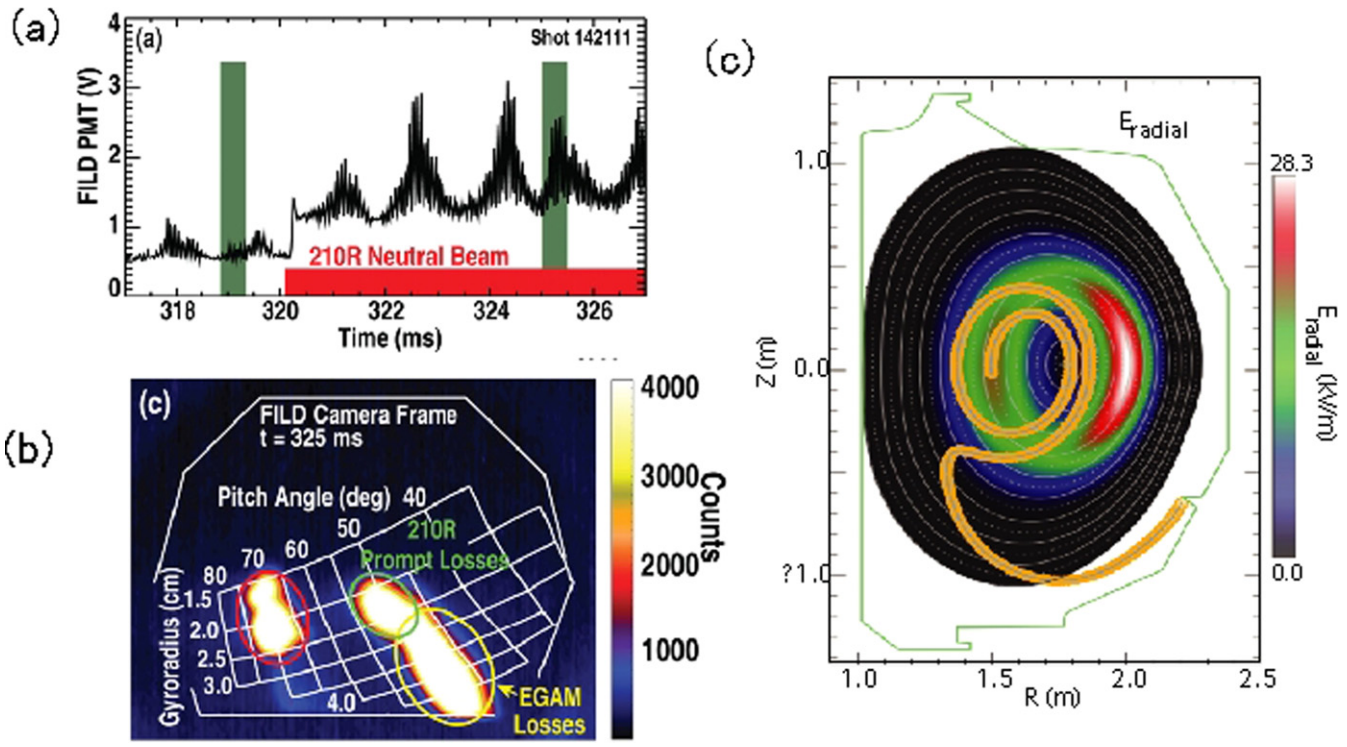

Figure 91. Loss of EPs during EGAM excitation. (*a*) Temporal evolution and (*b*) pitch angle-gyroradius distribution of beam loss signal measured by a fast ion loss detector (FILD). (*c*) A loss orbit calculated by a full particle-orbit following code SPIRAL. Reproduced courtesy of IAEA. Figure from [520]. Copyright (2012) IAEA.

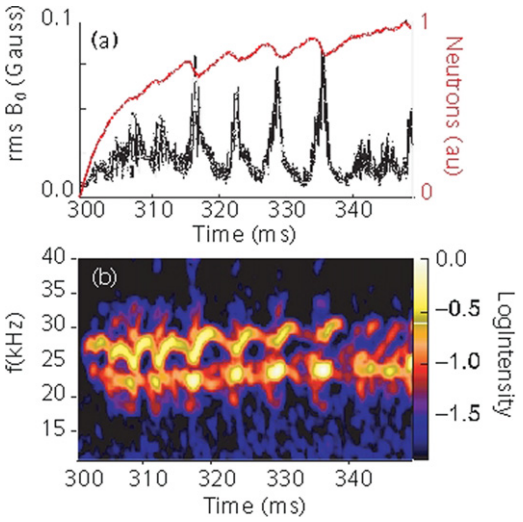

Figure 92. (*a*) Poloidal magnetic field $\tilde{B}_{\rm pol}$ fluctuation and neutron emission and (*b*) $\tilde{B}_{\rm pol}$ spectrogram during EGAMs in DIII-D. Reprinted figure with permission from [44], Copyright (2008) by the American Physical Society.

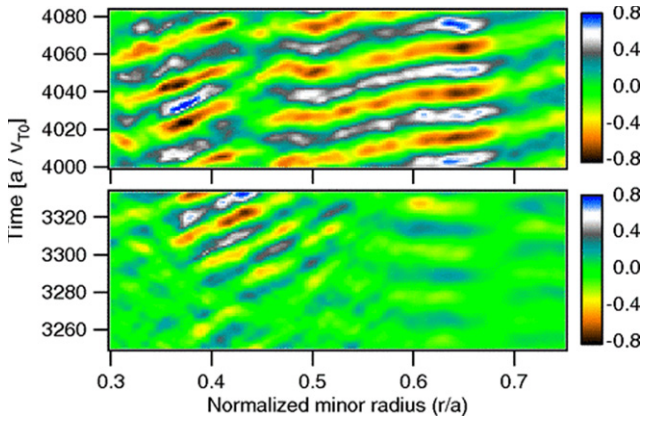

Figure 93. Temperature gradient R_0/L_T oscillation due to modulation of turbulent transport by the EGAM during two simulation phases. Reprinted figure with permission from [271], Copyright (2013) by the American Physical Society.

$f_{\rm EGAM} = l \cdot f_{\rm tr,bulk}$, may take place, where $f_{\rm tr,bulk}$ is the transit frequency of the bulk ions and l is an integer. According to numerical simulations [265] the energy transfer from the EGAM to the bulk ions via the sideband resonance with $l = 2$ is visible.

Another possibility for energy channelling from the EGAM to the bulk ions is an enhancement of the ion Landau damping. It is predicted that the resonance between the EGAM and magnetic drift of fast ions produces an asymmetry in the poloidal structure of the electric potential fluctuations associated with the EGAM [50]. As a result the parallel wavenumber of the EGAM increases and the ion Landau damping is significantly enhanced. See also [521].

Although the energy transfer from the EGAM to bulk ions has not yet been confirmed in experiments, an increase in the ion temperature has been observed during the EGAM excitation [513] which may indicate such an energy channel. In future fusion reactors α-particle heating by energetic fusion

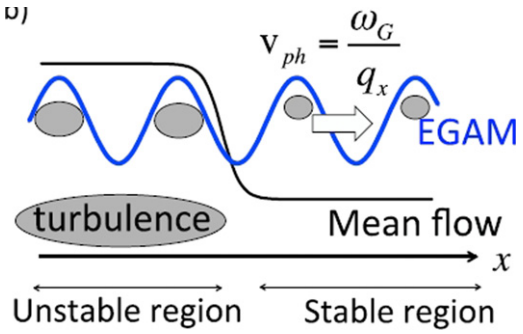

Figure 94. Conceptual view of turbulence trapping by the EGAM, Reproduced from [471]. CC BY 4.0.

products is expected to be a dominant heating method. However, it will mainly heat the electrons and the bulk ions are only indirectly heated via collision with the electrons. The energy channelling from the fast ions to the bulk ions via the EGAM may, however, contribute to an efficient ion heating in fusion reactors, and thus should be verified experimentally.

As noted above the EGAM can also resonate with the magnetic drift of the fast ions leading to poloidal asymmetries in the density and potential fluctuations [50]. In quasi-linear theory this breaking of the up–down anti-symmetry of the EGAM poloidal eigenfunction allows for a finite toroidal momentum flux. That is, the formation toroidal momentum transport from the fast ions to the bulk ions via the EGAM—the so-called GAM momentum channelling [51]. The magnitude of the EGAM induced momentum flux can be significant, compared to external momentum input sources or turbulent residual stress (intrinsic rotation). This channelling effect is yet to be confirmed experimentally, but it does suggest the possibility that EGAMs could be used as a mechanism for controlling toroidal rotation.

13.5. Fractional resonance and sub-critical instability

The amplitude of the fluctuations associated with the EGAM can in some cases become very large, at which point the EGAM may induce some interesting nonlinear phenomena. One phenomenon is when the frequency of the chirping EGAM reaches twice that of the standard GAM frequency, and, if the EGAM amplitude is sufficiently large, then a second GAM is excited at the standard GAM frequency (which is the half frequency of the chirping EGAM) [264, 414, 518, 522]. The transit frequency of the fast ions is the same as the EGAM frequency in the initial phase. Further, when the *electric field* amplitude associated with the EGAM rises sufficiently then the drift orbits of the fast ions become significantly perturbed by the EGAM with the result that the fast ions can resonate with a GAM at half the unperturbed transit frequency. Thus the fractional frequency resonance excites the GAM nonlinearly [264, 522], indicating a new energy path between EPs and the GAM through nonlinear processes.

In addition, the secondary excited GAM can have a larger amplitude than the initially excited EGAM [414, 518]. In this phenomenon the growth rate of the secondary excited GAM suddenly increases when the amplitude of the initial GAM exceeds a certain threshold. This phenomenon is interpreted as the excitation of a sub-critical instability, i.e. a GAM triggered by the EGAM [415, 523, 524]. Sub-critical instabilities are a working hypothesis to explain the onset of abrupt phenomena such as sawteeth oscillations and disruptions in laboratory plasmas, as well as solar flares in astrophysical plasmas [525]. The study of the abrupt excitation of the GAM shows not only new energy channel between EPs and the GAM but also an experimental path for exploring the trigger problem of abrupt phenomena.

In summary, it is seen that GAMs can be excited by EPs. The features of this EGAM, such as its frequency and spatial structure, are similar to those of the natural GAM, but are modified by the presence of EPs. It has been demonstrated that EGAMs can deteriorate the confinement of EPs via wave–particle interactions. In addition, the EGAM is predicted to affect the transport of bulk plasma via its influence on the turbulence and via direct heating and toroidal momentum input. Thus EGAMs may significantly affect the performance of fusion reactors and hence a deeper understanding of the EGAM will be an important task from the viewpoint of fusion reactor development. In addition, the behaviour of the EGAM reflects nonlinear dynamics in the phase space. New phenomena such as fractional resonances and sub-critical instabilities have been found. Hence the study of wave–particle interaction during the EGAM excitation may provide opportunities to further explore nonlinear science.

14. Nonlinear turbulence energy transfer

Of particular importance is the relationship between the GAM and plasma confinement. There are two aspects here; a demonstration that the GAM gives or receives energy from the turbulence, discussed in this section, and secondly that the GAM directly impacts the turbulent transport, which is discussed in the next section 15.

14.1. Nonlinear interactions in experiments

The principle excitation mechanism for the standard or natural GAM is by nonlinear turbulence interactions, such as via the radial gradient in the turbulent RS $\nabla_r \langle \tilde{v}_r \tilde{v}_\theta \rangle$ which can nonlinearly couple energy from the background, or ambient, high wavenumber turbulent fluctuations to low ($k_\theta \approx 0$) poloidal wavenumber ZFs [18, 274, 526, 527]. Calculation of RS requires multi vector field measurements, which are not always accessible. In the absence of direct RS measurements an alternative approach is to measure the bicoherence between high frequency density fluctuations and low frequency electrostatic potential or velocity fluctuations [47, 277]. Bispectral analysis is a third-order spectral technique where the signal energy is decomposed, not into a one-dimensional frequency spectrum $\hat{P}(f)$, but into a two-dimensional spectrum $\hat{B}(f_1, f_2)$ involving a triplet of three related frequencies $f_1 + f_2 = f_3$ [528]. Regions of common $\hat{B}(f_1, f_2)$ spectral intensity then indicate three-wave couplings within the turbulence [529, 530].

Typically the normalized squared auto and cross-bicoherence spectra $b^2_{xyz}(f_1, f_2)$ are used, with xyz indicating the signal triplet, together with the partial summed bicoherence $b^2_\Sigma(f_3)$ as an indicator of the interaction strength of a certain frequency—for example the GAM frequency—with all other fluctuation frequencies, and the total summed bicoherence b^2_Σ as a measure of the total nonlinear activity in the spectrum. Definitions and further details of the method are provided in appendix B.1.

The technique has been widely applied to plasma turbulence studies. For example early 1993 bicoherence analysis of probe potential fluctuations in ohmic TEXT plasmas [39] identified a quasi-coherent (QC) 20 kHz (low m) plasma potential mode inside the edge velocity shear layer ($r/a = 0.95$) coupling to small-scale broad-band fluctuations $f > 40$ kHz. The mode was not identified as a GAM, but could be a possible candidate, considering later TEXT observations [30].

Specifically in the context of ZFs, as early as 2002 a clear coupling between an edge GAM and broad-band fluctuations was demonstrated in HT-7 using cross-bicoherence analysis of poloidal velocity, radial velocity and floating potential fluctuations from LP arrays [27]. The choice of $\langle \tilde{v}_r \tilde{v}_\theta \tilde{V}_f \rangle$ was made on the assumption that the ZF results from DW induced momentum transport. In the HT-7 data an inverse cascade was measured which suggests the GAM was driven by the turbulence.

A series of detailed bicoherence studies of edge GAM/ZFs were performed in JFT-2M using reciprocating LPs [316, 319, 320, 531]. Figure 95 shows an example JFT-2M squared auto-bicoherence $b^2(f_1, f_2)$ spectra of floating potential fluctuations $\tilde{V}_f$ [319]. The GAM coupling to the high frequency broad-band turbulence >20 kHz appears as narrow ridges at $f_3 = f_1 + f_2 = \pm f_{GAM}$ (10 kHz) extending above the GAM frequency—confirming the three-wave coupling basis. The auto-biphase spectrum also shows distinct ridges at $f_3 = f_{GAM}$. The biphase at the GAM frequency $f_3 = f_{GAM}$ is roughly constant, consistent with all the turbulent modes experiencing the same E_r of the GAM, but is otherwise random at the background fluctuation frequencies [319, 320]. Similar biphase results were obtained from LP $\tilde{V}_f$ in HT-7 [285] and from HIBP $\tilde{\phi}$ in T-10 [300].

Much pioneering work has also been performed on HL-2A [347, 348] where a general scaling of the summed auto-bicoherence $b^2_\Sigma(f_{GAM})$ at the GAM frequency with the relative GAM amplitude $\tilde{\phi}^2_{GAM}/\tilde{\phi}^2_f$ was observed in some discharges (consistent with JFT-2M observations [319] and with theory predictions of DW turbulence [53, 532]), but not in others. In these later cases there may have been a particular sensitivity to the auto-correlation time of the turbulence. This is discussed later in section 15.2. Other work from the Hefei/SWIP groups includes radial profiles of $b^2_\Sigma(f_{GAM})$ [354], I-phase and bispectrum [356, 533], as well as many papers by Zhao [345, 353, 476, 534, 535] and others [346].

Bicoherence coupling of GAMs has now been observed in many devices. DIII-D [277], and JIPPT-IIU where wavelet cross-bicoherence (potential and density from HIBP) show broad turbulence coupling to the core GAM [329], as well as auto-bicoherence of flow perturbations $\tilde{u}_\perp$ from Doppler

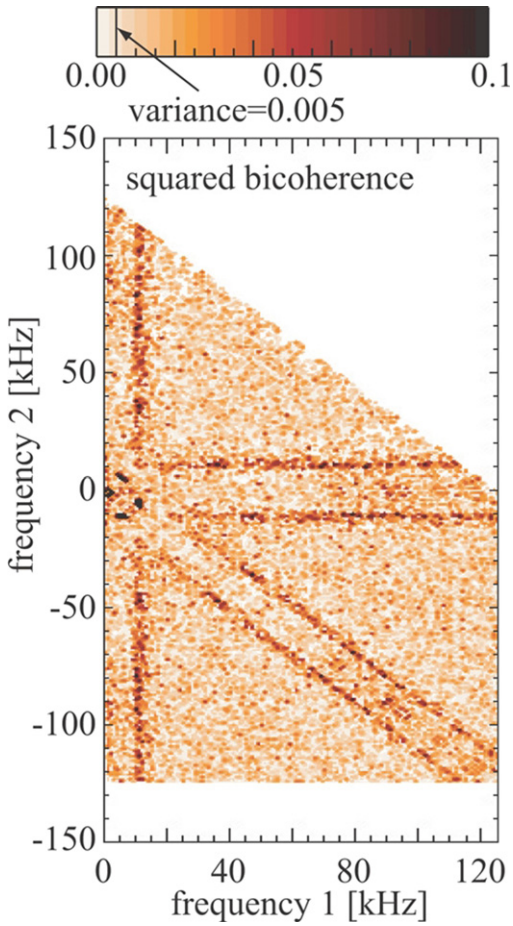

Figure 95. Auto-bicoherence b^2 vs frequencies f_1 and f_2 from LP floating potential fluctuations from edge region of JFT-2M. Reproduced from [319].

reflectometry on EAST [368], AUG [315] and likewise on T-10 [299] (only for edge GAM) and also on TUMAN-3M (although there are no clear stripes in $b^2(f_1, f_2)$ due to the bursty nature of GAM, the summed bicoherence $b^2_\Sigma(f_3)$ displays a peak at the GAM frequency) [335]. Using LP arrays on TEXTOR a stronger auto-bicoherence b^2 was found in $\tilde{V}_f$ than in $\tilde{I}_{sat}$, as might be expected at the tokamak mid-plane, but was comparable to the cross-bicoherence $b^2_{V_f, V_f, I_{sat}}$ [340]. In COMPASS wavelet bicoherence of LP floating potential and ball-pen probe plasma potential signals also showed broad-band 100–500 kHz high frequency turbulence nonlinear coupling to the GAM. However, the bicoherence was stronger in the floating potential V_f than in the plasma potential ϕ, suggesting a non-negligible contribution from the temperature component [394]. Also from LP $\tilde{V}_f$ in HT-7, a significant nonlinear coupling between coexisting multiple edge GAMs at different frequencies was observed, particularly between two close GAMs and a low frequency ZFO [287].

Cross-bicoherence of Doppler reflectometer signals in Globus-M, together with diagnostic modelling, suggests the bicoherence arises from an amplitude modulation (AM) of the backscattered signal (primarily low-k density fluctuations) at the GAM frequency. These were similar to auto-bicoherence

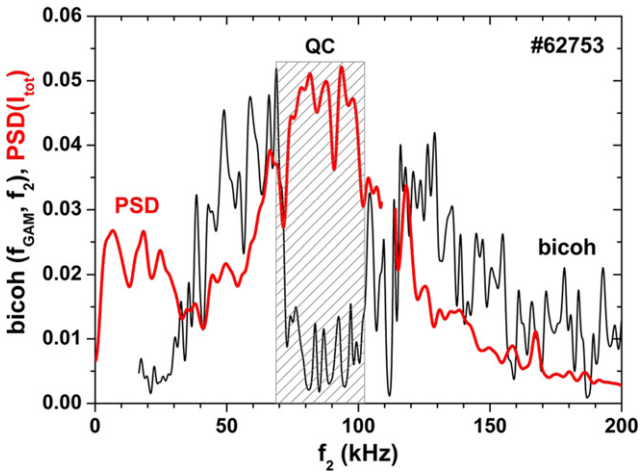

Figure 96. Density–potential cross-bicoherence $b^2_{\phi n_e n_e}$ at $f_1 = f_{GAM}$, and n_e spectral power from HIBP fluctuations from the edge region ($\rho = 0.9$) of T-10. Reproduced courtesy of IAEA. Figure from [300]. Copyright (2017) IAEA.

results of n_e fluctuations from normal incidence reflectometry on FT-2 [388].

An intriguing set of observations from T-10 ohmic discharges using HIBP shows the interaction of an edge localized QC mode (70–120 kHz) and a radially broad GGAM (17 kHz) [300]. Both density b^2_{nnn} and potential $b^2_{\phi\phi\phi}$ auto-bicoherences as well as the potential–density cross-bicoherence $b^2_{\phi nn}$ show coupling to the GAM over non-contiguous bands of high frequency fluctuations. As shown in figure 96 the frequency range of the reduced b^2 coupling to the GAM coincides with the QC frequency band, implying that the QC mode interferes with the nonlinear coupling process. The actual mechanism is not yet clear but it is highly suggestive that the effect (possibly EM) is not in the spatial but in the wavenumber domain. On the topic of EM effects, the auto-bicoherence of HIBP toroidal deflection φ ($\propto B_{pol}$) shows no three-wave coupling, although cross-bicoherences involving φ, e.g. $b^2_{\varphi nn}$, do show weak coupling. For low β conditions the magnetic sideband of the GAM is not expected to be measurable, and indeed there was no GAM observable in either the HIBP φ or Mirnov coil signals, nevertheless, the $b^2_{\varphi nn}$ coupling points towards an EM link with the edge turbulence [300].

The bicoherence measurements reported are generally made at the radial maxima of the GAM. In the recent study of inter-GAM nonlinear couplings it was suggested that the intensity of the respective couplings may depend strongly on the driving GAM amplitude [287, 351]. Recent Doppler reflectometry measurements on AUG show an alignment in the radial profiles of the flow auto-bicoherence $b^2_\Sigma(f_{GAM})$ (GAM coupling) and the GAM amplitude A_{GAM}, both peaking at the same radial position [315]. Together with flow-density cross-phase measurements, which reverse across the GAM spatial peak (see also JFT-2M results [317]), this suggests that the GAM is driven at a the location of maximum turbulence and nonlinear coupling and then spreads inward and outward as the GAM propagates towards the zonal boundaries. It was noted earlier that as the GAM weakens towards the core in AUG, the broad-band flow (rms) fluctuation level increases [305]. This is now seen to also follow an increasing total b^2_Σ nonlinear activity, even while the density fluctuation level falls towards the core [315].

All of the above results are from L-mode conditions. In contrast, during edge limiter biasing experiments in the HSX stellarator, enhanced (compared to ohmic) cross and auto-bicoherence in E_θ and E_r fluctuations from LPs were found at low frequencies [423]. However, there was no evidence of GAM oscillations. These results are similar to the diffuse low-frequency enhanced b^2 observed in CCT, PBX-M and DIII-D devices during H-mode transition experiments [527] in a region of enhanced edge E_r—again consistent with turbulent RS driven edge shear flow.

14.2. Energy transfer

Although the bicoherence indicates the strength of the nonlinear couplings between the GAM and the background turbulence it does not give the direction of the energy transfer, namely, from the turbulence to the GAM (drive) or from the GAM back to the turbulence (dissipation). For this other techniques have been employed, these include: (i) the power transfer function (PTF) technique developed by Ritz [536] and refined by Kim [537] which produces a 2D map—similar to the bispectrum—of the energy transfer rate $T_k(k_1, k_2)$ (magnitude) and its direction (sign) between different scales. The method essentially computes 2nd and 3rd order moments to derive linear and quadratic transfer functions between two fields. The method can also be extended to two vector fields, e.g. the radial and poloidal components of $\tilde{E}$ [538, 539]. (ii) The kinetic energy transfer (KET) method of Holland [279] is a multi-field vector technique which also computes an energy transfer rate $T^y_n(f', f)$ using 3rd order moments of the density n, velocity v_y and density gradient $\nabla_y n$ fluctuations, where y is the poloidal direction. (iii) In the amplitude correlation technique (ACT) [540] a time-delayed correlation is computed between two frequency bands of a single field. With suitable choice of filter frequency bands this can indicate the magnitude (from the peak correlation) and direction (from the sign of peak time delay) of energy movement within the spectrum. (iv) The amplitude envelope analysis. Here, the cross-phase angle (or correlation time lag) between the GAM flow oscillation and the envelope of the high frequency density (or flow) turbulence is computed. This popular technique is discussed further in section 15 on transport. Fuller details of the techniques are given in appendix B.2.

All of these techniques have been widely applied to both ZF and GAM studies, with the general conclusion that the direction of the energy flow is from the high frequency density turbulence $f > f_{GAM}$ into the lower frequency flow fluctuations.

Using LPs in the H-1 heliac the spectral energy transfer in probe V_f fluctuations was calculated using the single-field Ritz/Kim PTF method showing a clear energy gain at low frequencies and a corresponding energy loss at the high frequencies, i.e. an inverse energy cascade [541, 542]. Further, the generation of ZFs was correlated with the energy input and confinement mode [543]. Consistent with the PFT estimation,

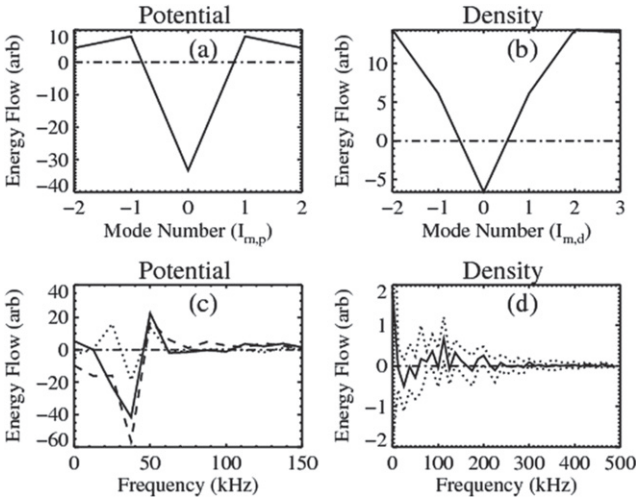

Figure 97. Nonlinear energy flow in mode-number (top) and frequency (bottom) domain for potential and density using HIBP in JIPPT-IIU core, showing energy moving from turbulence >50 kHz to the GAM. Reproduced courtesy of IAEA. Figure from [329]. Copyright (2010) IAEA.

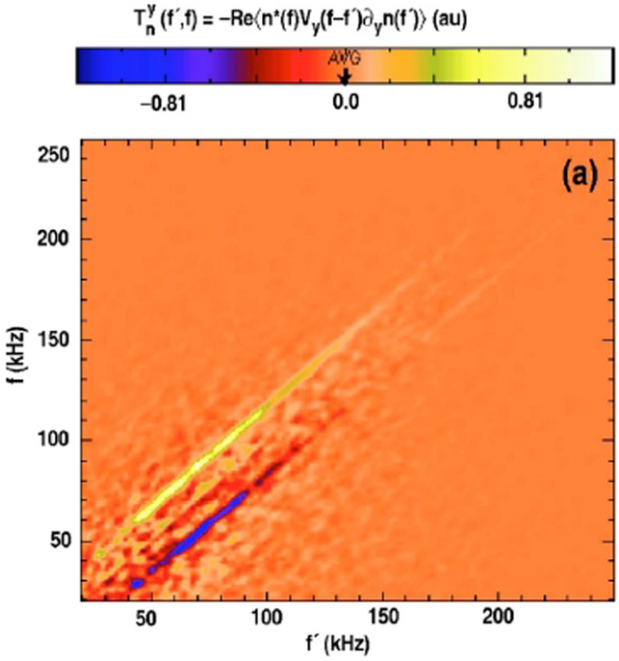

Figure 98. Nonlinear energy transfer rate $T_n^y(f', f)$ for edge density fluctuations f and poloidal gradient of density fluctuations at f' using BES on DIII-D, showing high frequency $\tilde{n}(f > 40$ kHz) gain energy from low frequency $\nabla n(f < f f_{\mathrm{GAM}})$ mediated by the 18 kHz GAM. Reprinted from [279], with the permission of AIP Publishing.

the ACT method also showed significant correlation (nonlinear coupling magnitude) and negative time delay (direction), indicating the low frequency band <15 kHz (ZF/GAM) received energy from the high frequencies 20–50 kHz (turbulence). The same PTF method (with wavelet cross-bicoherence) was applied to potential and density fluctuations from HIBP in JIPPT-IIU low density ohmic plasmas. A broad turbulence coupling to the core GAM was observed with energy flow, as shown in figure 97, from high frequency $f > 50$ kHz, high m potential fluctuations to the low frequency ($m = 0$) GAM [329].

In HL-2A the KET method was applied to LP data to study RS and turbulence energy (TE) behaviour in ohmic and ECR heated plasmas. A net frequency-resolved energy transfer was obtained by integrating the 2D $T_v^{\perp}$ map over selected GAM and ZF areas, from which it was observed that high frequency turbulence transfers to both the low frequency ZF and GAM. When raising the applied heating power the net normalized $T_v^{\perp}/\langle \tilde{v}_{\perp}^2 \rangle$ for both the GAM and ZF were observed to initially increase, but the GAM $T_v^{\perp}/\langle \tilde{v}_{\perp}^2 \rangle$ then saturates and decreases [544].

In the broader turbulence picture, similar behaviour was reported from the LMD-U linear device where the PTE method also showed an inverse cascade with energy flow from high to low fluctuation frequencies [539]. Likewise for LP poloidal array data from the TJ-K torsatron. Further, the spectral transfer was also seen to decrease with increasing collisionality [545].

An apparent exception to this trend appears in the original Holland paper [279]. With his KET method applied to BES data from the DIII-D edge, the 2D plot in figure 98 was obtained for the nonlinear energy transfer rate $T_n^y(f', f)$ which shows two ridges at $f = f' \pm f_{\mathrm{GAM}}$. Both the upper and lower ridges indicate that high frequency $\tilde{n}_{\mathrm{e}}(f > 40$ kHz) fluctuations gain energy from the low frequency $\nabla_y n_{\mathrm{e}}(f < f_{\mathrm{GAM}})$ fluctuations mediated by the $f_{\mathrm{GAM}} = 18$ kHz GAM. The roughly equal magnitude of the two ridges implies that the GAM (velocity) convection drives a forward turbulent energy transfer from frequencies below the GAM to frequencies above the GAM. Such an energy transfer effect from a GAM to the turbulence via the poloidally asymmetric pressure perturbations was identified in Landau-fluid simulations [102, 216]. However, Hamada [329] also compared the Holland KET method to the Ritz/Kim PTF method and likewise observed two $\pm f_{\mathrm{GAM}}$ ridges in the density–potential cross-bispectrum $\langle n_{\mathrm{e}} n_{\mathrm{e}} \phi^* \rangle$). With the KET method the ridges have opposite polarity (which was interpreted by Holland as density fluctuation energy moving back and forth between n_{e} and gradient fluctuation through the interaction with the GAM) while the PTF method had the same polarity. The difference was attributed to the use of velocity (by Holland) and potential (by Hamada) [329].

In order to test Holland's energy transfer direction interpretation, a KET $T_n^{\theta}(f_1, f_2)$ analysis was performed on model n_{e}, $\partial_{\theta} n_{\mathrm{e}}$ and v_{θ} broadband fluctuation signals with additional simulated AM or phase/FM at the GAM frequency [141]. As discussed below (section 15.2), based on the modulational instability model an AM of the density turbulence (direct regulation effect) is expected to result during the GAM growth cf [233]. On the other hand, the velocity shearing action of the GAM would result in a FM of the turbulence, cf [277]. What the simulations indicate is that the only mechanism for energy to transfer from low to high frequencies is via GAM velocity shearing induced FM, while the GAM may gain energy via three-wave interactions induced by AM during the GAM generation/growth [141]. As noted below, which mechanism appears to dominate depends on the measurement

location. At the GAM radial peak (energy injection radius) the GAM is growing (AM) with energy from the turbulence, but away from the peak the GAM is shearing (FM) the turbulence and thus moving energy from low frequencies (long wavelengths/large structures) back to high frequencies (short wavelengths/small structures).

In summary, bispectral and energy transfer analysis techniques confirm the three-wave coupling of high-frequency/short-wavelength turbulence to the low frequency $m = 0$ GAM flow oscillation. The degree of nonlinear coupling (b^2) scales with the GAM magnitude with respective radial profiles that are aligned. Frequency resolved energy transfer measurements confirm high frequency (density) turbulence drives the GAM/ZFO flow. Radial measurements of density-flow cross-phase, however, indicate that the spectral energy flow direction varies across the GAM spatial peak. The GAM gains energy at the radial peak, but then redistributes the energy from low frequency density fluctuations back to high frequencies via GAM velocity shearing. This topic is discussed further in the following section 15 on transport.

15. GAM impact on transport

Due to their $m = n = 0$ structure GAMs (and ZFs in general) cannot extract energy directly from the equilibrium profile gradients and thus do not contribute directly to radial (energy or particle) transport. Nevertheless, GAMs can impact transport in several ways. The oscillatory flow shearing action of the GAM can help to break-up or inhibit the formation of large radial turbulent structures; the GAM can also act as an energy sink via Landau damping and dissipation; and it can modulate and even moderate the cross field transport via the pressure fluctuations. The theory models concerning transport impact can be summarized as follows—cf [53]

- Non-linear energy transfer via RS and three-wave coupling leads to DW turbulence mediation—see section 4.2.
- GAM perpendicular velocity shearing (with spatial and temporal pattern) of turbulence eddies moves turbulence energy to higher k_r where it is dissipated—see section 15.1.
- GAMs scatter DW packets into the stable high k_r domain [53, 63].
- GAMs are involved in the modulation of radial transport Γ_r, and also of sources, via the modulational/parametric instability—see sections 4.5 and 15.2.
- EGAMs change pitch angle scattering of fast EPs. EGAMs may also transport turbulence packets radially via trapping, as well as modify bulk ion energy and momentum via channelling—see section 13.4.

15.1. Shear flow suppression

The basic theory of $E \times B$ shear flow suppression proposed in the early 1990s [546] was extended to include the effect of time-varying flows [46]. Using a one-field fluid model an effective shearing rate $\omega_{\text{eff}} = \omega_E^{(0)} H$ was derived where $\omega_E^{(0)}$ is the stationary $E \times B$ shearing rate (ω_E without oscillation) and H is an oscillatory reduction factor

$$H = \frac{((1+3F)^2 + 4F^3)^{1/4}}{(1+F)\sqrt{1+4F}} \tag{272}$$

with $F = \omega_f^2/\Delta\omega_T^2$ the squared ratio of fluctuating flow frequency to the turbulence decorrelation rate. The argument being that the fast time-varying velocity shear of a GAM is less effective in regulating DW turbulence since they have similar frequency ranges, i.e. a smaller effective velocity shear, because the flow changes before the turbulent eddies become distorted enough to reduce their correlation properties. Nevertheless, the effective shearing action is still non-negligible. Indeed, it has also been claimed that due to the broader turbulence spectrum and the lower c_s in the tokamak edge, compared to the core, that the GAMs are just as effective in shearing as the stationary ZFs [14].

A similar argument was given by Kim and Diamond [547] in demonstrating the importance of *random* ZF shear (as opposed to a coherent oscillatory shear) on the turbulence reduction. Noting that a random ZF has a finite correlation time τ_{ZF} which enhances the decorrelation of nearby fluid elements (although less efficiently than a mean shear flow) resulting in a turbulent decorrelation time $\tau_D = (\tau_\eta/\tau_{ZF}\Omega_{rms}^2)^{1/2}$, where τ_η is the turbulent scattering time and Ω_{rms} the rms shear rate). It was further argued that the spatial structure of the flow pattern is as important as its frequency spectrum. That is, the GAM can impose a complex spatial-temporal pattern on the turbulence and transport through the shearing mechanism with the result that the comparison of a linear growth rate and a shearing rate becomes non-trivial [254].

In general, the GAM/ZFO shear does not exist alone but together with an equilibrium mean shear. Hahm [46] suggested the calculation of an effective shearing rate that combines the mean and temporally varying components, while discounting the impact of the latter. Ignoring the spatial complexity of the shear flow, the condition turbulence moderation thus becomes [388]

$$\omega_{\text{eff}} = |\tilde{\omega}_s H + \bar{\omega}_s| > \gamma, \tag{273}$$

where $\bar{\omega}_s$ and $\tilde{\omega}_s$ are the mean and fluctuating components of the shear rate $\omega_s = (r/qB)\partial_r((q/r)\partial_r\phi)$ and H the oscillatory shear reduction factor of equation (272) with $F = (\omega_{GAM}/\gamma)^2$ where γ is the turbulence growth rate or inverse correlation time. This effective shearing formula was applied to edge GAMs in ohmic FT-2 plasmas. With $H \approx 0.5 \rightarrow \omega_{\text{eff}} \approx 271 \pm 50$ kHz this is close to the predicted turbulence growth rate, as well as to growth rates from matched ELMFIRE GK simulations [254, 388].

As noted in section 7.2, equivalent GAM shearing rates have been estimated in several other devices, either directly from the radial gradient of the GAM rms velocity $\omega_{E\times B} = \partial v_\theta/\partial r$, or indirectly from the GAM spectral width or radial wavenumber, $\gamma_{E\times B} = k_r\sqrt{\langle v_{GAM}^2\rangle}$. Not all have applied a reduction factor, for example in DIII-D an effective GAM shearing rate $\omega_s = \mathrm{d}v_\theta/\mathrm{d}r = 0.3 \times 10^5$ s^{-1} was measured with a turbulence decorrelation rate of $1/\tau_c \approx 1 \times 10^5$ s^{-1}—comparable and thus relevant for turbulence moderation [277].

Likewise for later DIII-D results [282]. In AUG the mean and GAM (without correction) shear rate of 10^5 s^{-1} was found to be comparable, within a factor of 2–3, to the turbulence decorrelation rate $1/\tau_c$ [306]. Similar results were obtained for IST-TOK [363] and JET [357]. In TEXTOR a correction factor was calculated and applied to the GAM, but the resulting effective shearing rate was still found to be significant [337]. Only in HL-2A was the GAM $\omega_{E\times B} = k_r v_{\theta,\mathrm{GAM}}$ (with frequency correction applied, but without mean shear) found to be smaller than the turbulence growth rate: $\omega_{\mathrm{eff}} \approx 3\times10^4 < \gamma \sim \tau_c^{-1} \approx 1\times10^5$ s^{-1} [141, 347].

As a final comment, numerical simulations suggest that, while time-varying and stationary flow shears alone can generate similar turbulence suppression effects, when coexisting they may become mutually exclusive if their magnitudes become comparable [548]. For certain parameter ranges it appeared that the dominant component could diminish the other.

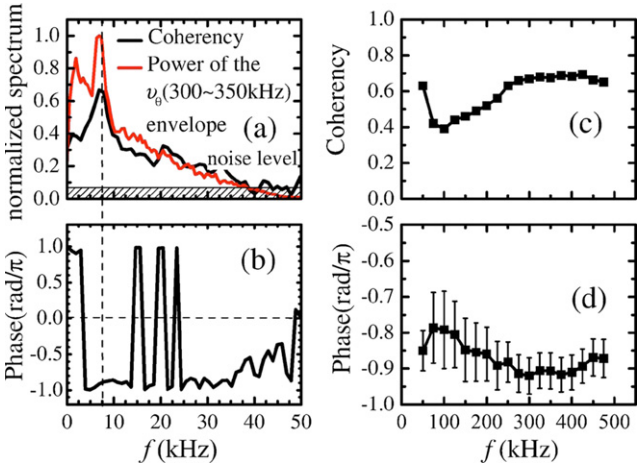

Figure 99. (*a*) Coherence $\gamma(f)$ and (*b*) cross-phase $\alpha(f)$ spectra between E_r and Env(E_r) for band-pass range 300–350 kHz; (*c*) coherency $\bar{\gamma}$ and (*d*) $\bar{\alpha}$ at GAM frequency as a function of envelope Env(E_r) filter frequency (centre) with fixed 50 kHz bandwidth in HL-2A. Reprinted from [141], with the permission of AIP Publishing.

15.2. Turbulence modulation

According to the parametric or modulational theory of ZF generation [221] the GAM should be accompanied by a modulation of the turbulence amplitude envelope (the so-called envelope formalism) at the GAM frequency [53]. This offers two diagnostic opportunities: firstly the measurement of such a modulation would demonstrate that the GAM impacts the turbulence, and secondly (and inversely) the envelope of the density fluctuations can be used for detecting the GAM even when the density fluctuation itself shows no direct oscillation at the GAM frequency [233, 307]. The envelope detection technique has been successfully employed for GAM studies on several devices. The favoured analysis approach is to apply a Hilbert transform to the band-pass or high-pass filtered ($f > f_{\mathrm{GAM}}$) turbulent signal to create the analytic signal, the modulus of which is the amplitude envelope $\mathrm{Env}[A](t) = |A(t) + \mathrm{i}\mathcal{H}[A(t)]|$. If a complex amplitude fluctuation signal (real and imaginary parts) is available from the diagnostic then the envelope modulus can be formed directly.

One of the first applications was on DIII-D using BES measurements of high frequency ($100 < f < 200$ kHz) density turbulence. Envelope modulation depths of the order of $|\tilde{n}|_{\mathrm{GAM}}/n \sim 10\%$ at the GAM frequency were measured [277]. For lower band filter frequencies the modulation was less clear, indicating that the oscillatory flow shear has more effect on turbulence frequencies above the GAM frequency, cf [46]. Similar results have been obtained from JFT-2M [317] using HIBP, [233, 319, 320] and on T-10 [292], HT-7 [286–288], HL-2A [141, 476, 534, 535] and TEXTOR [340] using LPs, on LHD [266] using HIBP, and on TUMAN-3M [335] and AUG [314, 315] using reflectometry.

Further, the turbulence envelope can then be cross-correlated with the E_r flow fluctuations. Here, a high coherence would indicate a modulation of the turbulence by the GAM, or vice versa. Together with the sign of their relative cross-phase this elucidates the nature of the non-linear interaction and the direction of the energy transfer.

Using arrays of LP V_f and I_s signals from HL-2A a significant GAM coherence of $\gamma \sim 0.7$ between E_r (flow) and Env(E_r) (turb.) signals with a cross-phase of $\alpha \approx -\pi$ radians (i.e. the flow turbulence delays the GAM) was observed, as shown in figures 99(*a*) and (*b*). Similar phase values were obtained for Env(E_r) and ϕ signals, but for E_r and the probe Env(I_s) (density), the coherence was low and α was closer to $-\pi/2$ [141]. Scanning the envelope filter range, figures 99(*c*) and (*d*), confirms it is the very high turbulence frequencies which satisfy the three-wave coupling criteria $f_2 - f_1 = |f_{\mathrm{GAM}}|$. Similar results were also obtained for V_f signals with strong coherence at ZFO and GAM peaks [535].

The temporal correlation between the turbulence envelope and the flow can be used to determine which of them is the 'drive'. On DIII-D a multi-field cross correlation $\gamma_{v,n^2}(f) = |\langle\tilde{v}^*(f)\,\tilde{n}^2(f)\rangle|/\sqrt{\langle|\tilde{v}(f)|^2\rangle\,\langle|\tilde{n}^2(f)|^2\rangle}$ was applied to BES edge data [279]. In the frame of a predator-prey (PP) type oscillation a finite coherence between the velocity and turbulence intensity $\tilde{n}^2$ is expected. The cross-phase $\alpha(f)$ indicates which is the predator (leads) and which is the prey (lags). For DIII-D a significant $\gamma \sim 0.3$ at the GAM frequency was observed with a cross-phase close to $\alpha = +\pi/2$ indicating that the edge GAM velocity oscillation leads the turbulence intensity oscillation—which was opposite to that expected from an analytic PP model and from GYRO GK simulations [279]. It has been suggested that the $\pi/2$ cross-phase with the GAM leading could be due to nonlinear damping of the GAM [421]. In the same DIII-D paper [279], using an energy transfer analysis the GAM was found to modulate both the turbulence intensity and to drive a forward transfer of fluctuation energy from the low ($\leqslant$40 kHz) to the high ($\geqslant$105 kHz) frequencies (see previous section 14.2). It was concluded from this that the GAM shearing may be a relevant saturation mechanism for the edge turbulence.

Although this subsection was introduced with the modulational instability, there are in fact two candidates for explaining

the turbulence envelope observations. Both involve the GAM $E \times B$ velocity [266]. Either the measured frequency spectrum can be distorted (broadened) by the Doppler shift due to GAM velocity oscillation [29], or there is dynamic shearing (DS) of the turbulence (cf [213]) by the GAM induced $E \times B$ velocity [233, 317]. To test the GAM modulation explanations synthetic model E_r signals with variable amplitude and phase modulation indexes were employed [141, 354]. The tests indicate that a pure AM—such as would be expected from DS—results in a cross-phase between E_r and Env(E_r) of $\alpha = 0$ or $\pm\pi$, while for a pure phase modulation or FM, i.e. Doppler modulation, the cross-phase is $\pm\pi/2$. A complex mixture AM and FM results in a phase somewhere in-between, but tending to π radians.

The HL-2A bispectral and envelope modulation measurements of $\alpha \sim \pi$ point towards the GAM mainly gaining energy from the high-frequency ambient turbulence (AT) through amplitude (envelope) modulation at the GAM generating location (i.e. at the radial peak), but as the GAM propagates radially the cross-phase shifts to $\approx -\pi/2$, consistent with velocity shearing and a reduction of the AT [354]. Likewise, in JFT-2M radial profiles of the E_r and Env(n)$_{f>60\text{kHz}}$ coherence and cross-phase show the phase decreasing from $+\pi/2$ towards 0 at the GAM spatial maxima [317]. A similar $\alpha = 0$ was obtained in Globus-M using DR flow and amplitude signals, indicating (moderate-k) turbulence modulated at the GAM frequency [386]. In AUG the E_r and Env(A) cross-phase varied linearly with radius over $\pm\pi$ across the GAM spatial peak [315]. On the other hand, a cross-phase shift between E_r and the Env(δn) using collective scattering in HT-7 is close to $\pi/2$, indicating phase shift is caused by phase modulation by the GAM—i.e. velocity shearing of the turbulence by the GAM [288]. Although it should be noted that the radial localization of the measurement was poor with a scattering volume of $r/a \sim 0.45$–0.75, i.e. including GAM peak and wings.

15.3. GAM modulation and intermittency

Even in steady plasma conditions the GAM is rarely contiguous and stable. Multiple devices report a slow (few tens to hundreds of Hz) modulation of both the GAM amplitude and frequency. Figure 100 shows an example frequency–time spectrogram of plasma potential fluctuations in T-10 using HIBP [292]. Here, the 22 kHz edge GAM appears as a train of quasi-regular 2–4 ms long peaks with a repetition or modulation frequency of 0.2–1 kHz. The modulation of the GAM frequency by some ± 2 kHz is also particularly evident. However, the GAM does not disappear entirely between the peaks but is simply modulated by some 50% in amplitude.

Similar behaviour was seen in AUG with a 50% GAM amplitude A_{GAM} temporal modulation at $f_{\text{mod}} = 0.2$–0.5 kHz. With an average GAM spectral peak two orders of magnitude above the background the GAM is indeed far from being suppressed entirely. Compared to T-10 the modulation in AUG was more regular and sinusoidal, as if the GAM was 'breathing' [304]. Likewise in Tore Supra the GAM was continuously modulated in both A_{GAM} and f_{GAM}, cf figure 11 in [372] (using the double-MUSIC analysis method), at some

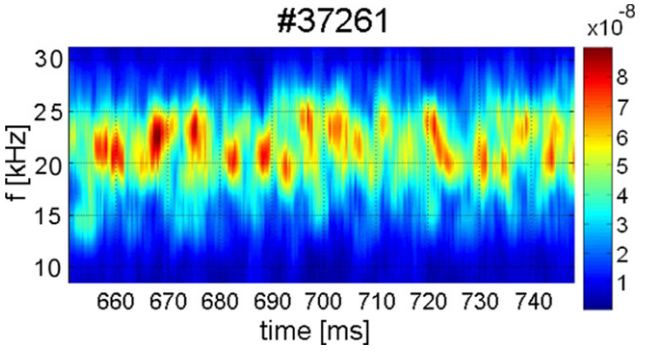

Figure 100. Power spectrogram of plasma potential from HIBP in T-10 showing edge GAM amplitude/FM with ~2–4 ms long intermittent bursts. Intensity modulation is ~50%. Reproduced from [292]. © IOP Publishing Ltd. All rights reserved.

100 Hz. As with T-10, the f_{GAM} modulation depth was several kHz. In some devices the modulation can be particularly strong, as in HL-2A where the GAM amplitude modulation approached 100% [549].

In many devices the GAM appears more as a sequence of well defined short bursts of a few GAM cycles with lengthy gaps between, as in JIPP T-IIU low density ohmic plasmas using HIBP and wavelet analysis where the 50 kHz core GAM potential bursts grow and die in some 250 μs aligned with shorter bursts (<100 μs) of high frequency density fluctuations [327]. ISTTOK reports strong edge GAM intermittence with a $\sim$ 100 μs burst lifetime (in both potential and toroidal LRC) [361, 363]. In TUMAN-3M the disparity between the quasi-periodic burst length 0.2–0.4 ms and the 200 Hz (5 ms) repetition is notably pronounced [335]. Other examples of GAM bursts are shown in figures 121 (HL-2A) and 119 (TUMAN-3M).

Table 15 lists reported (and deduced) values for a range of GAM modulation and intermittency parameters from various devices. Overall the GAM burst lifetime ranges from $t_{\text{lt}} > 100$ μs to a few milliseconds (scaling with the machine size) and is generally consistent with the inverse of the GAM spectral peak fwhm width Δf_{pk} (see below). Nevertheless, categorizing the modulation vs bursting behaviour is not always clear-cut.

Possible diagnostic effects for the GAM intensity modulation, such as radial movement in the measurement position relative to the GAM peak due to density or equilibrium variations, or temperature variations could be discounted in most cases. This leaves a plausible explanation that the GAM intensity envelope is being time modulated by a low frequency ZF. Such an interpretation is supported by an extensive set of measurements.

The modulation of the GAM amplitude, the GAM frequency and the flow and density turbulence levels appear to be interrelated. Figure 101 [315] shows an example flow spectrogram and time traces of the frequency-integrated spectral power over the GAM spectral peak (12–18 kHz) $P_{f_{\text{D}}(\text{GAM})}$ and the high frequency ($f > 18$ kHz) incoherent fluctuations $P_{f_{\text{D}}(\text{HF})}$ from a low density, ohmic AUG shot. The GAM intensity, GAM frequency and the ambient flow and density turbulence are all modulated at a dominant $f_{\text{mod}} = 47$ Hz while

Table 15. GAM modulation: type, GAM frequency (kHz), spectral peak fwhm Δf_{pk} (kHz), burst lifetime t_{lt} (ms), burst repetition or modulation frequency f_{mod} (Hz), AM depth (%), short τ_S and long τ_L auto-correlation times (ms).

Device	Type	f_{GAM}	Δf_{pk}	t_{lt} (ms)	f_{mod} (Hz)	AM	τ_S	τ_L (ms)
AUG [304, 315]	Mod.	14–20	0.3–0.5	—	40–100	>50	0.19	1.3
CHS [33, 398]	Burst	16.5	∼1	∼0.5	>200	—	—	—
DIII-D [282]	Cont.	∼15	0.3–0.5	—	—	—	<0.06	0.2–0.9
Globus-M [385, 387]	Burst	23–28	2–6	0.2–0.4	200	—	—	0.2
HL-2A [349]	Mod.	9.8	∼4	0.25	> 2500	>60	—	—
HL-2A [25]	Mod.	8.5	∼3	—	∼500	—	—	0.7
ISTTOK [361, 363]	Burst	20	<10	∼0.1	5000	>50	—	—
JET [357]	Mod.	4	2	1.5	250	10	—	1.3
JET [358]	Mod.	10	<0.3	—	400–800	>50	—	5
JFT-2M [316, 318]	Mod.	10.5	<1	—	800	—	—	—
JIPP-TIIU [327]	Burst	∼45	> 5	0.2	>3000	>50	—	—
SINP [395]	Burst	20.5	2.5	—	—	—	—	0.34
T-10 [292]	Mod.	∼20	3–4	2–4	170	∼50	—	—
Tore Supra [372]	Mod.	8–12	∼ 3	—	∼100	>50	—	—
Tore Supra [373]	Mod.	12–15	1–2	—	—	—	—	0.1–0.3
TUMAN-3M [335]	Burst	∼32	< 2	0.2–0.4	200	>50	—	∼0.1

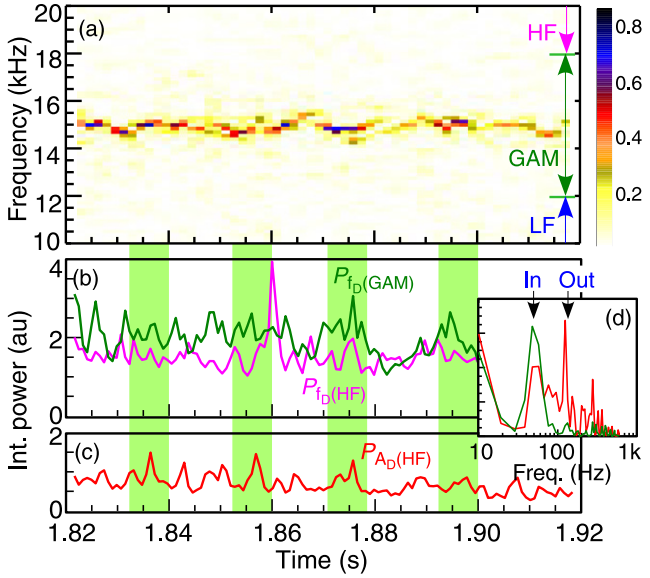

Figure 101. (*a*) Spectrogram of f_D flow fluctuations showing GAM behaviour with AM and FM, (*b*) frequency integrated spectral power for f_D between 12–18 kHz (green) and 18–80 kHz (purple), (*c*) *A* (red), and (*d*) corresponding spectra at GAM radial maxima from AUG ohmic shot. Adapted from [315]. CC BY 3.0

the ambient density fluctuations $P_{A_D(HF)}$ also show significant higher harmonics. Generally the GAM flow intensity $P_{f_D(GAM)}$ is in anti-phase with the incoherent flow fluctuations $P_{f_D(HF)}$ at the main f_{mod}, while the GAM flow and ambient density fluctuations $P_{A_D(HF)}$ are in-phase correlated at the main modulation frequency but phase-shifted at other frequencies. That is to say, when the GAM peak is reduced the broad-band flow spectrum is enhanced, suggesting that the turbulence energy moves within the flow spectrum. However, as should be expected, the GAM intensity follows the density turbulence level.

Similar anti-phase behaviour between GAM and broadband LP V_f fluctuations is observed in ISTTOK [362] and JET [357], as well as in DR flow perturbations in TUMAN-3M [335], FT-2 [466]. In Globus-M the GAM intensity modulation in $\tilde{E}_r$ from DR was in anti-phase with $\tilde{B}_\theta$ and $\tilde{n}_e$ from D_α emission, with two characteristic time scales; a 0.4 ms (quasi-periodic bursts with a ZFO like 2.5 kHz) and a slower 3 ms (equilibrium time scale 300 Hz) oscillation [385, 387].

The envelope analysis technique has also been employed on several devices for studying the interaction of GAMs and turbulence. Figure 102 shows a particularly clear example from HL-2A of the envelope of LP V_f fluctuations filtered around the GAM peak (10–12 kHz) being modulated in-phase with a low frequency ZFO (<2 kHz) while the envelope of the HF (>200 kHz) V_f turbulence (not shown) is out of phase with the ZFO and the GAM envelope [25, 349]. Earlier reports from JFT-2M show a similar low FM of the GAM, but also demonstrate the ZF nature and structure of the modulating mode [316]. In CHS the intermittent coupling between the broadband turbulence (50 kHz) and the GAM (19 kHz) was seen to be moderated by the phase of the $\lesssim$1.5 kHz ZFO [405]. Using wavelet spectra and conditionally averaged bicoherence (triggered on the ZFO phase) the strongest b^2 at $f_1 + f_2 = \pm 0.5$ kHz lines were observed when the ZFO phase was at a minimum, i.e. when the ZF was opposing the bulk flow rotation.

As noted in table 15 the GAM amplitude varies from practically continuous (as in DIII-D), to moderate AM depths of some 50% or so, to extreme modulation where the GAM appears as distinct intermittent bursts. It is notable that the majority of intermittent burst reports come from the small machines with low ohmic plasma currents I_p, while clear continuous GAM modulation appears to be the province of the larger L-mode heated machines. Intermittency is usually an indication of nearness to a critical condition, in this case, nearness to the GAM excitation threshold, cf [146]. Thus, the GAM bursting may simply reflect a lower GAM drive in the

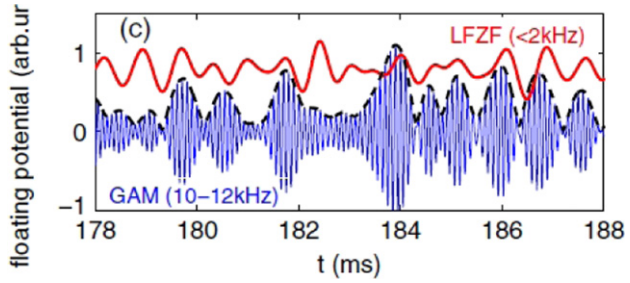

Figure 102. Time traces of edge GAM amplitude envelope (10–12 kHz) and ZFO (<2 kHz) showing a continuous GAM with AM $\gtrsim$50% in HL-2M. Reprinted figure with permission from [25], Copyright (2009) by the American Physical Society.

smaller, low power devices. Another factor may be the structure of the underlying AT, that is the turbulence radial correlation length relative to the GAM radial extent—i.e. shearing rates—in the various devices. This possible correlation has yet to be studied.

To quantify the GAM temporal behaviour the auto-correlation of the flow, potential or E_r fluctuation, which has been filtered around the GAM frequency, has been used. Figure 103 [282] shows an example time-delayed auto-correlation and corresponding probability distribution function of velocity fluctuations (from DR) band-pass filtered for a 15 ± 5 kHz GAM in DIII-D. Generally the auto-correlation shows a fast initial decay (within a single GAM cycle), defined here as τ_S (short), followed by a slower (long) exponential-like decay $\rho = A\exp(-|\Delta t|/\tau_L)$. In some reported cases the correlation takes a more Gaussian shape, in which case only the τ_L is quoted.

The initial fast drop comes primarily from uncorrelated background fluctuations and noise, which is minimized by band-pass filtering the signal. The short decay is particularly noticeable for weak GAMs or with an insufficiently narrow filter bandwidth. Fitting to a range of AUG L-mode data shows for a single dominant GAM, $\tau_S^{-1} \sim f_{GAM}$, but this can decrease by a factor of 2 or more $\tau_S^{-1} \ll f_{GAM}$ in the presence of two close frequency GAMs creating frequency beating—for example at the GAM zonal edges [315]. From the reciprocality of the temporal correlation and Fourier spectrum, the secondary slower (long) decay should be inversely related to the width of the GAM spectral peak. For the reported AUG shots the fwhm of the GAM power spectral peak was found to scale as $\Delta f_{pk} = 0.5/\tau_L$. As seen from table 15 this behaviour appears to hold for many devices.

Essentially the GAM spectral width reflects the temporal dynamics of the GAM and may arise from either a slow FM of the GAM (mean) frequency—as might be expected from ZF interaction, or from the intrinsic decay (lifetime) of the GAM itself [372]. For the two JET cases in table 15 with $\tau_L = 1.5$ ms (corresponding to roughly 6 GAM periods) [357], and 5 ms (50 GAM periods) [358], both decays are significantly longer than the AT decay time $\tau_D \sim 10$ μs. (Which incidentally highlights the need to perform temporal averages over sufficient time periods.) Such slow decays suggest that the GAM damping dominates over the turbulence dynamics.

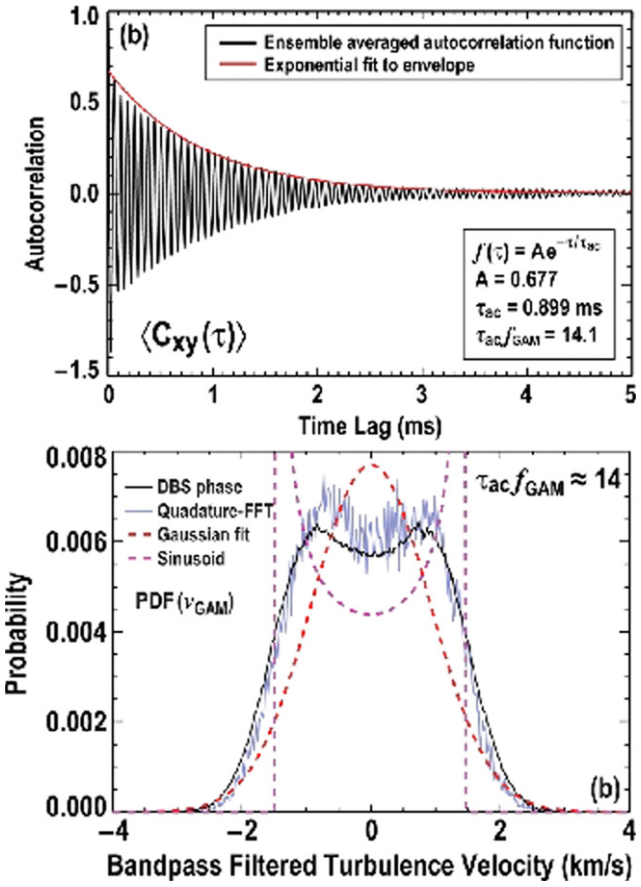

Figure 103. (*a*) Autocorrelation and (*b*) probability distribution of band-pass filtered ($f_{GAM} \pm 5$ kHz) velocity fluctuations for strongly coherent 15 kHz GAM in a $q_{95} \sim 4.5$, high density, 4.4 MW NBI, limiter, L-mode DIII-D shot #142121. Adapted from [282], with the permission of AIP Publishing.

In the SINP tokamak the decay rate (≈5–8 GAM periods) $\tau_L \sim 0.34$ ms $\gg \tau_D \sim 6$–8 μs was consistent with GAM damping rates according to the Guo-2010 prediction where τ_L scaled with q_{edge} [395]. In Tore Supra both τ_L and f_{GAM} varied with collisionality in such a way that their product $\tau_L \times f_{GAM}$ scaled roughly with ν^* [373]. However, in the continuous GAM case of DIII-D the measured τ_L (4–15 GAM periods and constant across the GAM eigenmode radius) appeared to be inconsistent with the narrow GAM spectral peak [282]. A corresponding τ estimated from the upper bound of the GAM damping rate in DIII-D was an order of magnitude too large. However, in this case a narrow spectral peak and a short auto-correlation time τ_L would be consistent with a short coherence time for the GAM drive and a weak damping for the GAM.

A short, intermittent GAM drive could explain many of the bursty GAM observations. However, AM alone, whether exponential growth/decay or 100% pulse modulation, does not explain the GAM FM. A plausible explanation is that the train of GAM bursts are not phase-locked in time. Each GAM pulse is essentially a brand new GAM oscillation with a new phase. Such FM/phase-modulation is evident in the examples of figures 100 and 101 and in much of the literature. Matched numerical simulations of Tore Supra using the GYSELA code

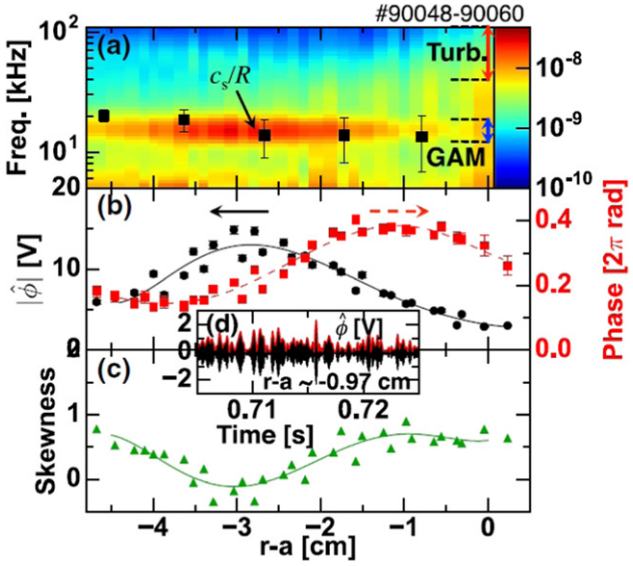

Figure 104. Radial profiles of (*a*) the frequency dependent potential power spectrum density, (*b*) the GAM amplitude and phase, (*c*) the skewness of GAM amplitude, and (*d*) the time evolution of the GAM potential fluctuation and its envelope at $r - a \sim -1$ cm. Reprinted figure with permission from [325], Copyright (2018) by the American Physical Society.

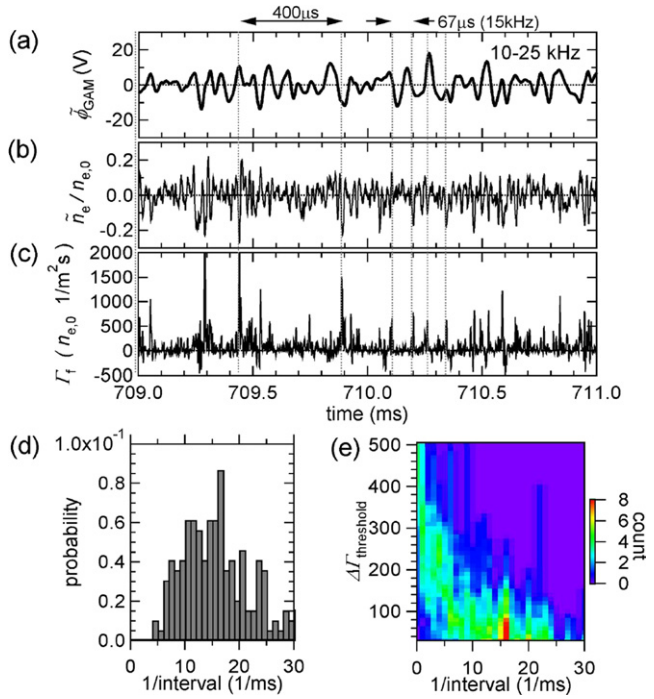

Figure 105. (*a*) Filtered $\tilde{\phi}_f$, (*b*) $\tilde{n}_e/n_{e0}$ for $f > 30$ kHz and higher (*c*) Γ_r in JFT-2M L-mode edge, (*d*) distribution function of transport bursts (*e*) histogram of burst interval discriminated by pulse height threshold $\Delta\Gamma_{thr}$. Reproduced courtesy of IAEA. Figure from [318]. Copyright (2006) IAEA.

show the phase of the GAM radial propagation experiencing a sequence of sporadic phase jumps at points of GAM low intensity—due to variations in the radial gradient of the GAM frequency—leading to a temporal and spatial desynchronization of the GAM [373]. A detailed analysis of the GAM time traces for the published cases from the various devices would be a useful exercise.

The radial propagation of the GAM also appears to be an important ingredient in the intermittency story. The nature of the GAM intermittency was investigated in JFT-2M using potential measurements from HIBP. The skewness (3rd moment) of the intermittent GAM amplitude was found to be close to $Sk \approx 0$, i.e. a Gaussian distribution, at the radial maxima of an eigenmode GAM, but rises $Sk > 0$ (positive spikes) towards the inner and outer GAM boundary/edges, as shown in figure 104 [325]. At the maxima location the Gaussian statistics behaviour aligns with a maximum in the RS force. Away from the maxima the GAM is no longer driven but purely propagating, creating the observed eigenmode structure, with more filament-like behaviour [325]. Again consistent with an intermittent particle flux behaviour at the edge. In AUG the GAM spectral peak width Δf_{pk} varies inversely with the GAM amplitude [315] with similar behaviour in Tore Supra where $\tau_L \sim 0.2 \pm 0.1$ ms at the GAM maxima decreases with the GAM amplitude. In short, as the GAM propagates away from the injection position it decays and spectrally broadens, becoming more intermittent in nature.

The experimental evidence thus strongly supports the predicted interaction between the GAM/ZF and the turbulence amplitude [550], from modelling results [551], etc. However, not all modelling results are so supportive. Simulations of the nonlinear interaction between GAMs and ZFOs using GK theory with FOW effects, predict that, while 'sub-critical' GAMs could drive ZFs, however, the ZF had a negligible effect on the GAM dynamics (up to parallel nonlinearity time scales). More specifically, ZFs are not expected to modulate the GAM [237]. This is clearly an area for further study.

15.4. Particle & energy transport

At first sight the GAM may not appear to have a direct impact on the turbulent radial particle transport flux $\Gamma_r = \langle \tilde{n}_e \tilde{v}_r \rangle = \langle \tilde{n}_e \tilde{E}_\theta / B_t \rangle$ since the GAM has no $\tilde{E}_\theta$ component. However, the GAM does have an effect via the density modulation. Using HIBP in JFT-2M to measure both n_e and E_θ, the turbulent density fluctuations were found to be modulated by the GAM potential fluctuations, resulting in a bursty or intermittent electrostatic local particle transport Γ_r, as shown in figure 105 [318]. The measured average $\langle \Gamma_r \rangle$ was of the same order as the particle flux derived from an estimated particle confinement time $\tau_p \approx 5\tau_E$. Also the probability distribution of the inverse time interval of the intermittent Γ_r bursts, peaks around $1/15$ ms, comparable to the GAM frequency thus indicating that the flux is also modulated by the GAM. Similar results were obtained in TEXTOR using LPs where the intermittent $\Gamma \sim \langle \tilde{I}_{sat} \tilde{E}_\theta \rangle$ histogram also peaked at the GAM frequency [340].

A clear correlation between the local particle transport and the magnitude of zonal structures was also evident in the IST-TOK edge. Figure 106 [361] shows the mean fluctuation driven particle flux $\langle \Gamma_{E\times B} \rangle = \mathrm{Cov}_{n,E_\theta}(\tau = 0)$ (of intermittent transport events) decreasing with increasing toroidal long-range

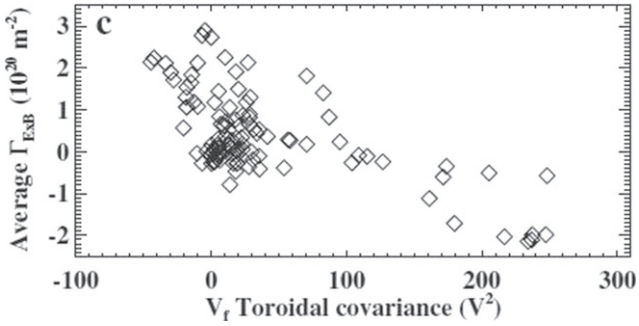

Figure 106. Radial particle flux vs toroidal covariance of $\tilde{V}_f$ at the GAM peak location ($r - a = -1.5$ cm) in ISTTOK. Reprinted from [361], with the permission of AIP Publishing.

covariance of GAM frequency dominated potential fluctuations measured using LPs. The result indicates that the local radial transport is linked, in anti-phase, with the amplitude of large scale potential fluctuations (10–25 kHz GAM). Unfortunately due to the short GAM lifetime the radial transport modulation at the GAM frequency could not be demonstrated, just a modulation at the intermittency frequency.

The GAM amplitude in HL-2A was also observed to be in anti-phase with the radial particle flux Γ_r with an intermittent burst period of 80–120 μs, comparable to the GAM frequency [349]—again indicating that the particle flux was regulated by the GAM. Similarly, in T-10 using HIBP the particle flux associated with an $f > 100$ kHz QC mode can be seen to in anti-phase with the GAM amplitude [297]. Further, in HL-2A using forked LPs a 13% reduction in Γ_r (due to broad-band 20–100 kHz AT) was measured during intermittent bursts of strong GAM activity, as shown in figure 107, compared to periods of weak GAM activity [549]. As with ISTTOK, the Γ_r was also found to decrease with increasing GAM strength (measured from Cov($\tau = 0$) between poloidally separated probe V_f). The flux reduction was correlated with a factor of three increase in the effective GAM $E \times B$ shearing rate $\omega_{E\times B}$ to become comparable with the turbulent decorrelation rate ω_D. The particle flux was calculated from $\Gamma_r(f) = (2/B_\phi)\sqrt{|P_n|\,|P_{E_\theta}|}\,\gamma_{nE_\theta}(f)\,\cos(\alpha_{nE}(f))$. A detailed analysis of the various terms indicates that reductions in the density turbulence level $|P_n|$ and the coherence γ_{nE} both play equally significant roles, while the electric field/potential fluctuation level $|P_{E_\theta}|$ and their cross-phase α_{nE} are much less significant. Taken together, the results indicate that the GAM plays a significant role in moderating the AT in L-mode conditions. Its impact is via suppression of the density turbulence and their correlation—as suggested by numerical simulations [552].

Heat transport is of course interrelated with particle transport [553]. Of particular importance is the GAMs role in suppressing or promoting radial steamers and avalanches which expel heat and particles [472, 554]. General ballistic events, as well as wave-trapping of turbulence in the EGAM electric field leading to turbulence spreading were discussed in relation to EGAMs in section 13. EGAMs may also impact heat transport via bulk ion heating (the GAM channelling effect) and enhanced Landau damping.

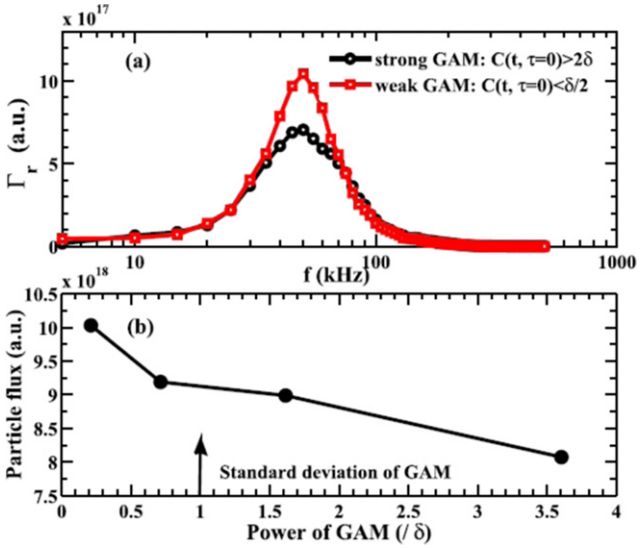

Figure 107. (*a*) Radial particle flux Γ_r spectrum during 'strong' and 'weak' GAM activity, and (*b*) total Γ_r vs GAM intensity in HL-2A L-mode edge $r/a \sim 0.95$. Reprinted from [549], with the permission of AIP Publishing.

In summary, the GAM plays a significant role in edge turbulence moderation. This is demonstrated by comparable velocity shearing and turbulence decorrelation rates, as well as modulation of AT at the GAM frequency. The GAM appears to gain energy from the high-k density turbulence at the GAM spatial maxima, but as it propagates radially it begins to shear and reduce the low-k turbulence, thus moving energy back to the high k turbulence. By reducing and decorrelating the density fluctuations the GAM also moderates the radial particle transport. The GAM displays both AM and FM, consistent with a low frequency ZF interaction. Strong modulation leads to intermittency, suggesting closeness to the GAM critical onset threshold. As the GAM propagates from the injection position it decays faster and spectrally broadens, becoming more intermittent in nature. In some devices the GAM decay appears consistent with strong GAM damping, while for others a GAM drive with short coherence and weak GAM damping seems appropriate.

16. GAMs in 3D field structures

Ideally the tokamak has an axi-symmetric magnetic field—and hence an $n = 0$ GAM toroidal structure—but in practice a number of magnetic field effects, including toroidal field ripple (due to the finite number of toroidal field coils), (non)-resonant magnetic field perturbation (RMP) coils, as well as MHD modes can lead to three dimensional magnetic field structures. The stellarator of course has the ultimate 3D field structure.

16.1. MHD islands—GAM drive

The interaction of GAMs with MHD modes (static and rotating) is multi-fold. An island chain may create a GAM-like

oscillation, or it may enhance and/or entrain a natural edge GAM, or it may suppress and destroy the natural GAM.

Early measurements from T-10 report an GAM localized around the $q = 2$ surface and to be strongly associated with the presence of an $m/n = 2/1$ (m and n are the poloidal and toroidal mode numbers respectively) MHD island [292]. With varying plasma current and B_t the GAM spatial peak moved with the $q = 2$ radius. Across the radial extent of the island chain the GAM also had a finite structure, while outside the island region no GAM was observed. It is not stated if the MHD mode was rotating or static, or if the measurements are associated with the O or X-point of the island. As will be shown these are relevant to the observations.

In TEXTOR the dynamic ergodic divertor (DED) was used to generate and lock large (non-rotating) $m/n = 2/1$ islands of some $w \approx 8$–10 cm width around $r/a \approx 0.6$, allowing poloidal CR antenna arrays at the machine top (island O-point) and mid-plane (island X-point) to observe a strong GAM across the plasma edge $0.65 < r/a < 0.83$, outside of the island [338]. With the locked island the GAM amplitude was enhanced by factor of 2 over the no-island case. Close to the island separatrix/boundary the GAM was diminished and secondary spectral peaks appeared. Around the island O-point there was clear evidence of a (poloidally correlated) flow oscillation consistent with the GAM structure.

The TEXTOR observations appear to be consistent with a resistive MHD model [555] where a small amount of magnetic energy is transformed into kinetic energy which can generate significant oscillating velocity fields at the island separatrix of tearing-like modes. In this model, spontaneous ZFs are generated when the control parameter $\Delta' w \geqslant 1$ exceeds a critical threshold, where Δ' is the step in the logarithmic gradient of normalized magnetic flux $\hat{\psi}(r)$ across the island separatrix and w the saturated island width. It was suggested that the formation of the enhanced ZFs (i.e. velocity shearing) may help to mitigate the cross-field transport due to the island chain.

Likewise, simulations with the (EM non-Boussinesq two-fluid turbulence) NLET code show the formation of a GAM surrounding the island structure due to a modulation of the diamagnetic velocity resulting from the temperature profile flattening (across the island) and steepening at the island separatrix [556]. However, there was no indication of a 'micro-GAM' inside the island structure.

A recent review on the multi-scale interactions between magnetic islands and turbulence [557] summarizes the ZF—island interaction as follows. Essentially a ZF is forced to pass around the island surface creating sheared flows around the reconnected separatrix due to flow stagnation around the island O-point. Such sheared flows around static islands have been observed in several experiments; LHD [558], TJ-II [559] and HL-2A [560]. The flow forms corrugations which oscillate, creating a GAM-like behaviour (termed a magnetic island induced GAM) corresponding (although the structure is not specified) to the standard GAM induced by toroidal geodesic curvature. Further, the oscillatory flows can back-react on the magnetic island making it oscillate—the so-called magnetic island seesaw phenomena [561]. It is also suggested that the rotation of magnetic islands can be regulated by the self-generated ZF [562]. At the extreme, the velocity shearing associated with the GAM can also restrict the island radial structure and thus limit the growth of the MHD mode.

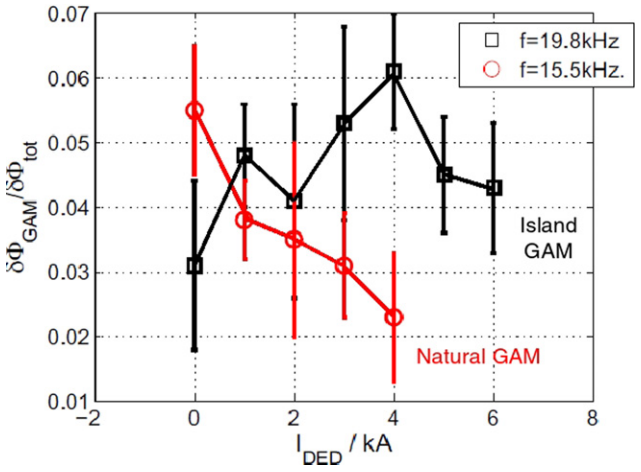

Figure 108. Relative reflectometer phase (density) fluctuation level $\tilde{\phi}_{GAM}/\tilde{\phi}_{tot}$ vs I_{DED} (RMP strength) in top region of TEXTOR for natural edge GAM $f = 15.5$ kHz; $0.380 \leqslant r \leqslant 0.385$ m (red) and RMP induced GAM $f = 19.8$ kHz; $0.345 \leqslant r \leqslant 0.350$ m (black). Reprinted from [563], with permission from JSPF.

In another set of TEXTOR experiments a strong spectral peak in the density fluctuations $\tilde{n}$ appeared at the expected $f = 19.8$ kHz GAM frequency close to the separatrix O-point of an RMP induced $m/n = 5/2$ island. The perturbation grew with the RMP strength (I_{DED}) as shown in figure 108 [563]. However, a comparison of density and velocity spectra only showed an increase in the $\tilde{n}$ peak and not in $\tilde{v}$, suggesting the mode structure is more complicated than a simple GAM.

16.2. Islands and GAM entrainment

The flow and turbulence behaviour can be divided into three distinct spatial regions: inside the island separatrix, around the island boundary, and spatially (radially) well away from the island chain.

Inside the island separatrix the turbulence interaction is predicted to create a coherent vortex flow, represented by low (m, n) stable modes [557, 564], etc. Indications of a vortex-like flow rotation have been observed experimentally in TEXTOR [563].

During a series of experiments in J-TEXT with static $m/n = 3/1$ and $4/1$ RMPs the induced islands are located very close to the plasma edge (a couple of cm inside of the separatrix), coinciding with the natural GAM spatial peak. Even with modest RMP strengths the GAM amplitude was reduced at all radii across the edge, but particularly inside the island region [391]. In addition, the E_r reverses from negative to positive across the island (as seen in other experiments, cf figure 110, [308]), the edge toroidal velocity increases, turbulent RS is enhanced, leading to increased RS gradients at the island inner and outer boundary, consistent with reduced broad-band V_f fluctuations (AT) inside the island, but enhanced at the inner and outer island separatrix [391, 392].

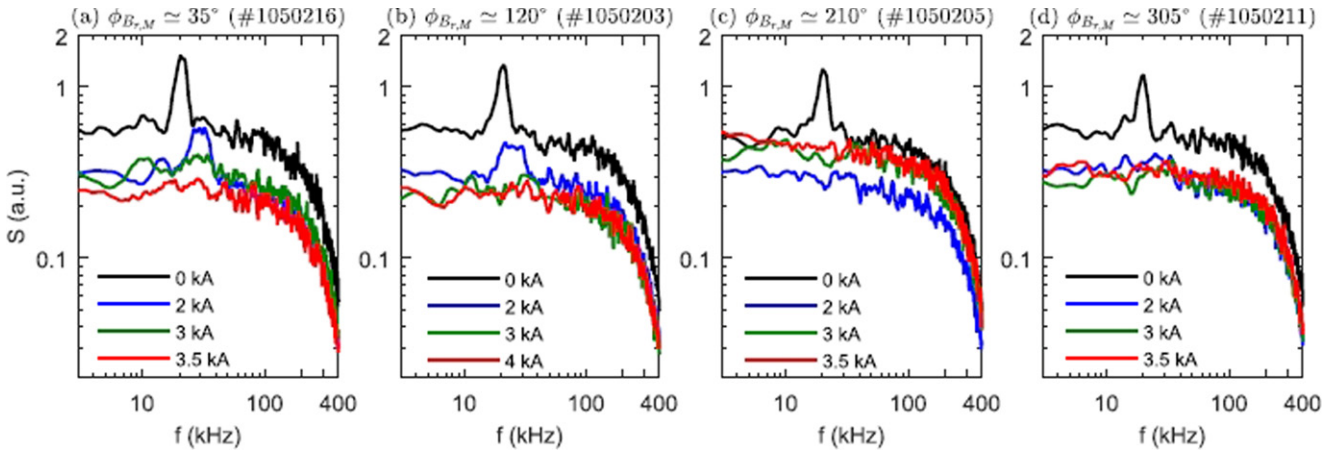

Figure 109. $\tilde{E}_r$ power spectra $S(f)$ from DR at $\rho \approx 0.93$ for increasing RMP currents with four RMP phases Φ in J-TEXT. Reproduced courtesy of IAEA. Figure from [393]. Copyright (2019) IAEA.

Identical behaviour was observed in HL-2A with the application of $m/n = 3/1$ or $4/1$ RMPs where the E_r reversed to positive across the induced island at $q = 3$ and 4 respectively. The broad band turbulence decreased inside island but increased at the island boundaries. In addition the mean turbulence wavenumber $\langle k_\theta \rangle$ increased together with the toroidal (co-current) velocity, mostly towards the outer island boundary [565].

In another set of J-TEXT experiments the dominant applied RMP component resonated at the $q = 2$ surface exciting an $m/n = 2/1$ magnetic island which could be rotated poloidally by changing the toroidal phase of the RMP field. In this instance the natural GAM was well outside the island region but, nevertheless, was affected by the RMP. Figure 109 [393] shows four $\tilde{E}_r$ spectra at the GAM spatial peak $\rho \approx 0.93$ with increasing RMP coil current at four RMP toroidal phases Φ. At large RMP coil currents the GAM is completely suppressed—see next section, but for a moderate RMP strengths the GAM frequency is up-shifted and varies in amplitude with the RMP Φ, consistent with the imposed RMP $2/1$ field structure—although in a somewhat complex manner. While the plasma rotation showed little difference at the island O- and X-point, the turbulence level was significantly reduced at the O-point, due presumably to reduced local temperature gradient. In addition, for certain RMP coil currents the nonlinear coupling of AT was considerably enhanced at both the island O and X-point [393].

A similar frequency up-shifting of GAM flow perturbations was observed in MAST using probes [374]—where it was attributed to an increase in the edge plasma Mach number, as well as in AUG using DR [308]. Figure 110 [308] shows the effect of an edge 'resonant' $n = 2$ with dominant $m \approx 12$–14 MP on the $E_r \times B$ flow and n_e fluctuation spectra at the GAM maximal location ($\rho_{pol} \approx 0.99$) in an AUG low density, ECRH discharge. With increasing RMP (B-coil) current I_B the E_r well slowly decreases and a magnetic sideband forming at the GAM frequency in LFS mid-plane Mirnov coil $\tilde{b}_r$ signals (GAMs in AUG generally display no $\tilde{b}_r$ signature but often a $\tilde{b}_{pol}$ component [311].) Once the MP strength exceeds a certain threshold, the E_r well shrinks, and the GAM flow peak weakens and up-shifted in frequency from 14.6 kHz to 15.9 kHz with an enhanced magnetic sideband (with constant T_e). Overall, the broadband $\tilde{E}_r$ falls while the $\tilde{n}_e$ is enhanced. Spatially, the GAM extends across the negative E_r shear region, rising in frequency with the local temperature in a staircase fashion with GAM maxima close to the stair inner edge. With RMPs the mode extends radially deeper, but peaks further out, closer to the E_r minimum.

The entrainment of an edge ($m/n = 0/0$) natural GAM with an applied ($m/n = 6/2$) static RMP magnetic field has been studied in HL-2A ECR heated L-mode plasmas. Using multiple arrays of multi-pin LPs and magnetic Mirnov coils, a strong $f \approx 10.5$ kHz GAM in V_f fluctuations was observed, together with an ($m/n = 6/2$) potential mode, (so-called meso-scale electric field fluctuations (MSEFs)), plus an ($m/n = 6/2$) magnetic perturbation, all oscillating at the same 'GAM' frequency [352, 353]. Toroidally separated LPs confirm the GAM $n = 0 \pm 0.2$ and finite $k_r = 3.5 \pm 0.2$ cm^{-1} zonal structure (poloidal m number not given), while cross correlation of probe V_f (close to the GAM spatial peak) and magnetic signals from a toroidal array of 10 Mirnov coils show a clear $m/n = 6/2$ structure at the $q = 3$ surface. The implication being that there were two simultaneous potential modes at the same frequency with the later being created by the RMP applied field. The temporal evolution of the MSEFs and the magnetic fluctuations also show the frequency entrainment and phase locking between the GAM and the $m/n = 6/2$ magnetic fluctuations (but only during the ECRH phase). This result was interpreted as the GAMs and magnetic fluctuations transferring energy through nonlinear synchronization. Such a nonlinear synchronization may also contribute to the formation of a simultaneous low-frequency ZF and a reduction of the turbulence level—as suggested by bispectral analysis. A simultaneous core $m/n = 4/2$ mode at the $q = 2$ surface did not lock to the GAM as it was spatially too far away from the natural GAM radial peak in the edge, even though the mode frequencies are close.

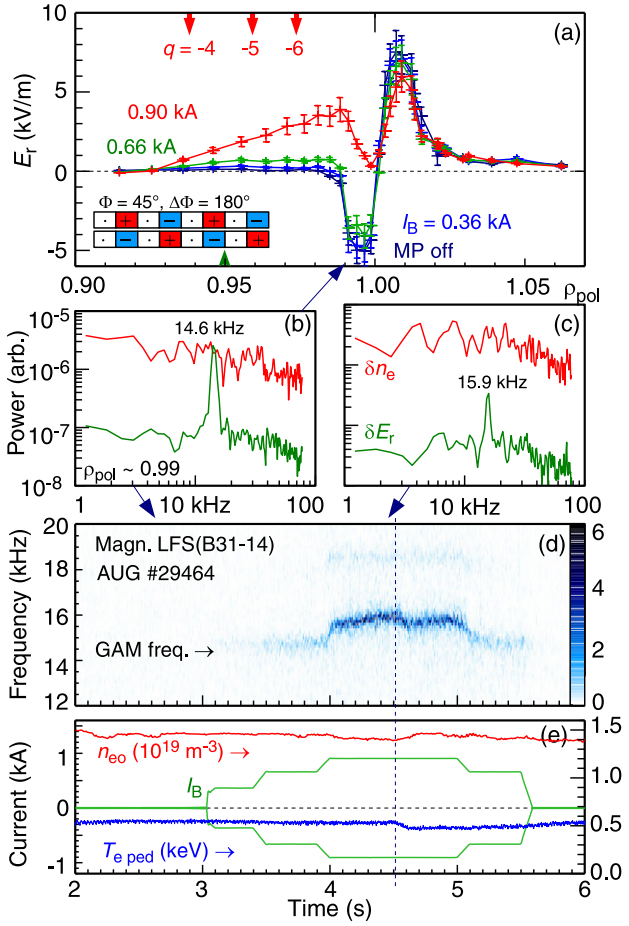

Figure 110. (*a*) Edge E_r profiles in 0.55 MW ECRH (-2.5 T, 0.8 MA, $q_{95} = -5.2$) AUG L-mode with increasing $n = 2$, 'resonant', odd-parity, MPs, (*b*) and (*c*) $\tilde{E}_r$ and $\tilde{n}_e$ spectra at $\rho_{pol} \approx 0.99$ without and with RMP, (*d*) LFS Mirnov spectrogram and (*e*) core n_{eo}, edge T_e and MP coil I_B time traces. Adapted from [308]. © IOP Publishing Ltd. All rights reserved.

16.3. Ergodic & stochastic fields—GAM suppression

With the formation of strong edge MHD modes the GAM, however, is suppressed. In T-10 the interaction of low $m \approx$ 2–3 MHD modes and GAMs in ohmic plasmas was studied using HIBP and magnetic probe arrays. The edge GAM (of $\delta\phi \sim$ 10–100 V amplitude) was suppressed with the onset of large MHD (with a $\delta\phi \approx 40$ V component and wide radial extent of 4–6 cm). The GAM recovered after the MHD mode decayed [295]. Likewise, in TUMAN-3M the GAM was strongly damped during bursts of MHD activity [332].

While externally applied magnetic perturbations of moderate magnitude can lead to GAM enhancement and/or entrainment, large perturbation amplitudes have the opposite effect. Sufficiently strong RMPs cause magnetic field ergodization which has the effect of destroying the toroidal and poloidal structure of the GAM. In TEXTOR with an RMP induced $m/n = 6/2$ mode the GAM both shrank in radial extent and decreased in amplitude with increasing DED strength I_{DED} [566]. In another experiment with an $m/n = 5/2$ RMP, the natural $f = 15.5$ kHz edge GAM (around $0.380 \leqslant r \leqslant 0.384$ m) gradually disappeared with increasing RMP strength—as shown in figure 108—as the ergodic region radially expanded, reducing the long field-line connection length [563]. However, at the RMP induced $m/n = 5/2$ island radius ($0.345 \leqslant r \leqslant 0.350$—which was well inside of the natural GAM location), there was a concurrent increase in the *density* fluctuations at the expected $f = 19.8$ kHz GAM frequency. These fluctuations do not appear to be caused by a change in the turbulence but are believed to be due to parallel currents on the rational surface caused by the RMP—i.e. a magnetic island induced 'GAM'.

Fluid model simulations of GAM oscillations using the 3D ATTEMPT code with TEXTOR-like RMP parameters show the plasma response to the RMP are currents with in-phase and out-of-phase components (which act to screen out the RMP field) depending on the collisionality and the plasma β [567, 568]. When switching on the RMP the GAM changes its character. First it is amplified by the out-of-phase component of the induced plasma current coupling to the GAM via Maxwell stress (resulting in significant modifications to the GAM amplitude and frequency). But, with increasing RMP amplitude the GAM is then diminished as the screening effect breaks-down, particularly at the rational surfaces where the RMP field is strongest [568].

A series of supporting effects, also reported from TEXTOR, include a reduction in the RS (from LPA) across the edge velocity shear region with increasing I_{DED} (for both 6/2 and 3/1 RMP modes resonant at $q \approx 3$ surface) [569], a shift from a GAM to a ZFO; decreasing long-range-correlation (LRC) at the GAM frequency, and a corresponding increase in the low frequency turbulent flux when the GAM is suppressed [426]. A similar reduction in the summed bicoherence Σb^2 at the GAM frequency (i.e. the GAM drive/amplitude)—consistent with the reduced RS—in LP floating potential V_f fluctuations was observed, as shown in figure 111 for an $m/n = 6/2$ RMP configuration [340]. Reducing the mode number from $m/n = 6/2$ to $3/1$ also led to a lowering of the GAM suppression threshold. In these cases the gradual suppression of the GAM with increasing I_{DED} (RMP strength) was attributed to damping of the GAM by resistivity due to finite $k_\parallel \neq 0$ and nonzero B_r components [426]. Finally, GAM-like oscillations (global mode) in the STOR-M tokamak are completely suppressed around the last closed flux surface (where profiles are strongly steepened and confinement improves) with the application of a static ($m/n = 2/1$) RMP field [397].

16.4. Non-axisymmetric field configurations

There are distinctly fewer experimental observations of natural GAMs in stellarators and helical devices compared to tokamaks, however, these measurements appear to show that the GAMs have similar properties as to those in axisymmetric systems. Early CHS measurements show a core mode frequency scaling consistent with basic fluid GAM predictions [38, 398, 405, 406], although unfortunately there are no measurements of the mode structure for the GAM, only for a low frequency zonal flow oscillation (ZFO), which shows an $n = 0$ mode structure. However, for EGAMs in the LHD an $m = 0$

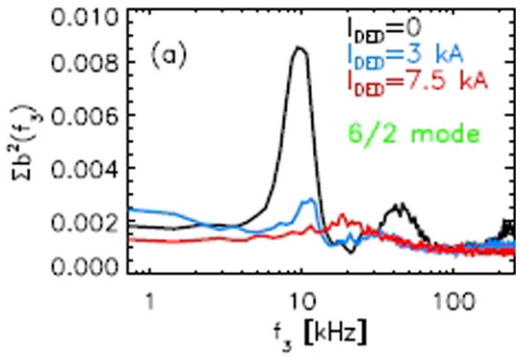

Figure 111. Probe V_f auto-bicoherence $\Sigma b^2(f_3)$ spectra for an $m/n = 6/2$ RMP with increasing DED coil current in TEXTOR. Adapted from [340]. CC BY 3.0

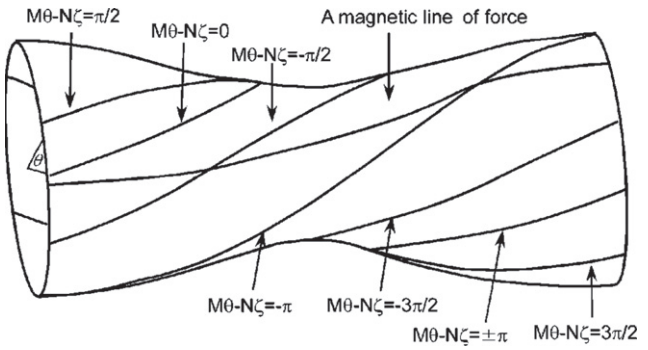

Figure 112. Schematic of a single helicity helical system showing representative flux surface for an $M = 2, N = 10$ helical system for one toroidal pitch ($0 < \varphi < 2\pi/N$). Density perturbations follow the lines $M\theta - N\varphi = 2l\pi \pm \pi/2$, Reprinted from [99], with the permission of AIP Publishing.

mode structure for the electric potential fluctuation and $m = 1$ mode structure for the density fluctuation has been measured, as shown in figure 90 [410].

Prompted by these early results the GAM dispersion relation was derived from the DKE with a three-dimensional equilibrium [99, 570, 571] (and later with FOW effects [572]) which is applicable to a broad range of field configurations, including helical systems with multi-helicity, such as quasi-toroidal or quasi-helical systems. Starting with the linearized DKE and expressing the magnetic field in terms of Fourier components: $B^2 = \sum_{m,n} B_0^2(1 + \delta_{m,n}\cos(m\theta - n\varphi))$, in terms of the poloidal and toroidal angles, a generalized dispersion relation of the form

$$D = \omega^4 - \omega^2 \sum_{m,n} \omega_{G,m,n}^2 F_{m,n} = 0 \tag{274}$$

is obtained where $\omega_{G,m,n}$ is defined as the Fourier component of the base GAM frequency $\omega_G = v_T/R_0$ and $F_{m,n}$, likewise the Fourier component sum of the radial driving current. Equation (274) can be solved easily for the real frequency $\mathrm{Re}\,\omega^2$ and imaginary growth rate $\gamma = -\mathrm{Im}\,\omega$. For practical purposes, after some approximations the real frequency can be simplified to,

$$\omega_{GAM}^2 \approx \frac{c_s^2}{R_0^2} \sum_{m,n} \frac{m^2\,\delta_{m,n}^2(\psi)}{4(l_\psi/2\pi R_0)^2} \tag{275}$$

where $\delta_{m,n}(\psi)$ represents the geodesic curvature of the (m, n) ripple component at the flux surface ψ. The term l_ψ^2 is defined as radial wavenumber index and can be approximated as the circumferential poloidal flux surface path length.

For a single helicity plasma, e.g. a circular flux surface cross section tokamak with low β, the magnetic field has a single dominant Fourier component—the toroidal ripple (geodesic curvature) $\delta_{1,0}(\psi) \sim 2(r/R_0)$. Taking $l_\psi = 2\pi r$, one obtains the familiar GAM frequency $\omega_{GAM}^2 = 2c_s^2/R_0^2$. For non-circular tokamaks the ellipticity κ introduces an $(m = 2, n = 0)$ and the triangularity an $(m = 3, n = 0)$ Fourier component. In contrast, a mixed helicity system, such as the CHS device, has both a toroidal ripple $\delta_{1,0}$ and a helical ripple $\delta_{2,8}$.

Several interesting points were drawn from the model, for example the GAM frequency is expected to be higher in helical devices compared to tokamaks, and that the damping rate will be stronger in multi-helicity magnetic configurations. Nevertheless, if $T_e > T_i$, as in the limiter CHS discharges, then the damping rates are predicted to be small. Concerning the sideband structure, in a helical system the density perturbation is predicted to form maxima and minima along the lines of $(m\theta - n\varphi) = \pm\pi/2$ respectively, as shown in figure 112 [99].

To specifically study the GAM behaviour in helical magnetic configurations numerically the neoclassical transport code FORTEC-3D (applicable to axi and non-axisymmetric magnetic geometries), which solves the DKE of the first order using the δf method, was developed [573]. These global simulations indicate that the GAM couples across neighbouring flux surfaces due to FOW effects. Using the LHD geometry (which has a separatrix) the GAM frequency was found to decrease and its damping rate to increase when the magnetic axis was shifted inward (the LHD-IS configuration), so as to increase the sideband Fourier components of magnetic field and decrease the radial drift of helical ripple trapped particles. This suggests the possibility of controlling both the neoclassical transport level and the GAM oscillation (or the ZF) in helical plasmas.

Figure 113 shows an example simulated E_r spectrum against normalized radius for a moderate $\iota_0/2\pi = 1/q = 0.34$ LHD configuration [573]. Here, the GAM is found to be strongly damped in the edge region where $q < 1$, together with the appearance of a finite low frequency ZFO in the core. Also in the LHD geometry the GAM appeared to be insensitive to collisional effects due to the overwhelming enhancement of collisionless damping by the magnetic field ripple [123]. Similar results were obtain in [54, 574, 575] from analytic derivations for the GAM dispersion together with GK simulations in a helical system, as presented in section 2.8. It was noted that the radial drift of particles trapped in the helical ripples impacts both the residual ZF level and long wavelength ZFOs. Consequently, there are no experimental reports to-date of natural GAMs appearing in LHD.

The collisionless plasma response to a potential perturbation in general stellarator geometry was treated in [54, 55] where it was found that the residual ZF does not reach a steady

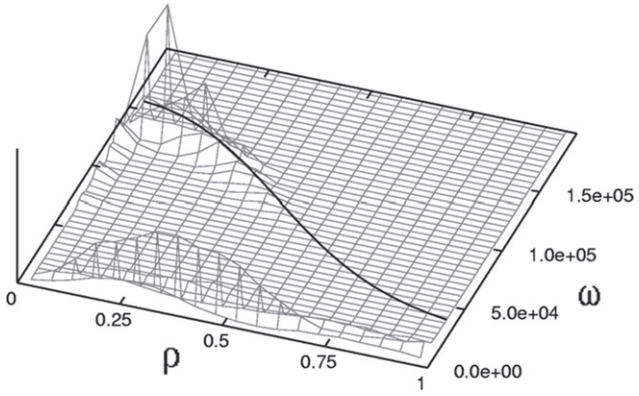

Figure 113. Simulated E_r power spectrum as a function of radius for a $\iota_0/2\pi = 1/q_0 = 0.34$ LHD case using FORTEC-3D code. The solid line is analytic $\omega_{GAM} = \sqrt{7/4}v_{Ti}/R_0$. Reproduced courtesy of IAEA. Figure from [573]. Copyright (2005) IAEA.

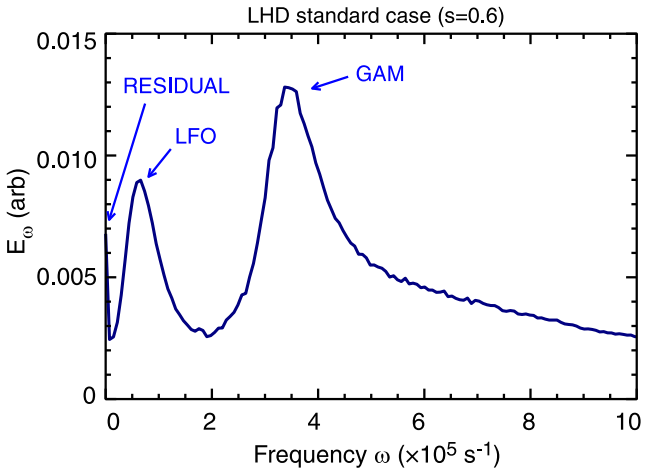

Figure 114. Radial electric field E_r fluctuation spectrum from the EUTERPE GK code for an LHD plasma, showing the zero-frequency SZF residual, a low frequency oscillation LFO and a GAM. Reproduced from [57]. © IOP Publishing Ltd. All rights reserved.

level but oscillates with a low frequency due to the radial drift of the locally trapped particles—a feature particularly prevalent in stellarator geometry with strong helical ripples. The theory was subsequently extended in [57] where the low frequency ZFO (labelled LFO) also undergoes a Landau damping [54], which is highly sensitive to the magnetic geometry via the radial drift frequency $\tilde{\omega}_d = k_r\tilde{v}_d$ (proportional to the geodesic curvature) of the trapped particles [576]. This LFO frequency scales as,

$$\omega_{LFO}^2 = \Lambda_2/(\Lambda_1 + \Lambda_0), \tag{276}$$

where Λ_0 is the classical polarization, Λ_1 a quantity related to the neoclassical polarization, and $\Lambda_2 \propto \sum_a n_{0a}e_a^2/T_a \ldots$ (where $a = e, i$) the ZF frequency due to the trapped particle contribution, defined in [55]. Here, all the Λ terms essentially scale with c_s^2 giving the ZFO mode an acoustic nature.

In general, GAMs (due to passing ion dynamics) and ZFOs (due to tapped particle drifts) are observed in a variety of GK simulations in a wide range of W7-X, TJ-II, LHD configurations [57, 576–580], etc. In the comparative studies [57, 576] using the GENE (flux-tube version) and EUTERPE (global PIC code using the full stellarator geometry), the ZFO and GAM behaviour was substantively different between the LHD and W7-X configurations. The potential oscillations in LHD were predominantly GAM-like while in W7-X they were predominantly ZFO-like, due principally to the different q_a values and consequent Landau damping rates. Figure 114 [57] shows an example spectrum of simulated E_r fluctuations from the EUTERPE code for the standard LHD configuration (LHD-SC) where the GAM dominates over the stationary SZF residual and the ZFO (LFO). More recent W7-X simulations using the hybrid CKA-EUTERPE MHD/GK PIC code indicate that a core localized GAM can appear if the ι is reduced by the induction of a plasma current via ECCD at low magnetic shear $s < 0.5$ [579].

Due to its high rotational transform ι and large ripple, GAMs are normally expected to be heavily damped in TJ-II. For example, linear global GK simulations (3D EUTERPE code) predict GAM frequencies $f \sim 50$ kHz in the standard (low iota) TJ-II configuration, but with strong collisionless damping [581]. For this configuration the predicted frequencies were also in reasonable agreement with analytic tokamak predictions [54, 108]. Discrepancies, nevertheless, appeared at higher ι where fluid and kinetic models are believed to become inaccurate for non-axisymmetric configurations. As with corresponding tokamak simulations, non-linear GK EUTERPE simulations (complemented by CAS3D-K and analytic calculations) for TJ-II also show fast damped GAMs and longer lasting ZFOs with a finite RH residual ZF [580, 582]. Performing a multivariate fit to the CAS3D-K simulations for TJ-II resulted in $\omega_{GAM} \propto T^{0.49\pm0.1}\iota^{0.49\pm0.04}\kappa_G^{0.85\pm0.13}$, where κ_G is the geodesic curvature. For the amplitude: $A_{GAM} \propto T^{-0.60\pm0.1}\iota^{0.03\pm0.06}\kappa_G^{0.46\pm0.17}$. Interestingly the amplitude was found to have a very low dependency on ι, in contrast to tokamaks and heliotrons where the damping scales as $1/q$. Also notable is that the ZFO frequency and amplitude have opposite κ_G scaling to that of the GAM [582].

While early measurements of potential fluctuations across the TJ-II edge, with LRC properties, showed no distinctive GAM peak [584] plus more recent global low frequency flows [585] (as expected for low q), there are several later reports of candidate GAMs in the core. For example, low frequency E_r oscillations were triggered by the transition of the core radial electric field E_r during density ramp experiments from the positive E_r (electron-root) to the negative E_r (ion-root) [586]. This transition is unique to non-axisymmetric systems and arises from the intrinsic nonambipolar nature of the neoclassical radial particle flux in non-axisymmetic systems. E_r is determined so as to satisfy the ambipolar condition [587]. Because the neoclassical particle flux is a nonlinear function of E_r, multiple roots for the ambipolar condition appear under certain density and temperature conditions. As a result, a sudden change in the E_r occurs between the roots [588]. Linear GK simulations of the temporal evolution of the E_r transition using the global, δf, particle-in-cell code EUTERPE revealed a short-lived GAM oscillation at the positive to negative E_r transition [586].

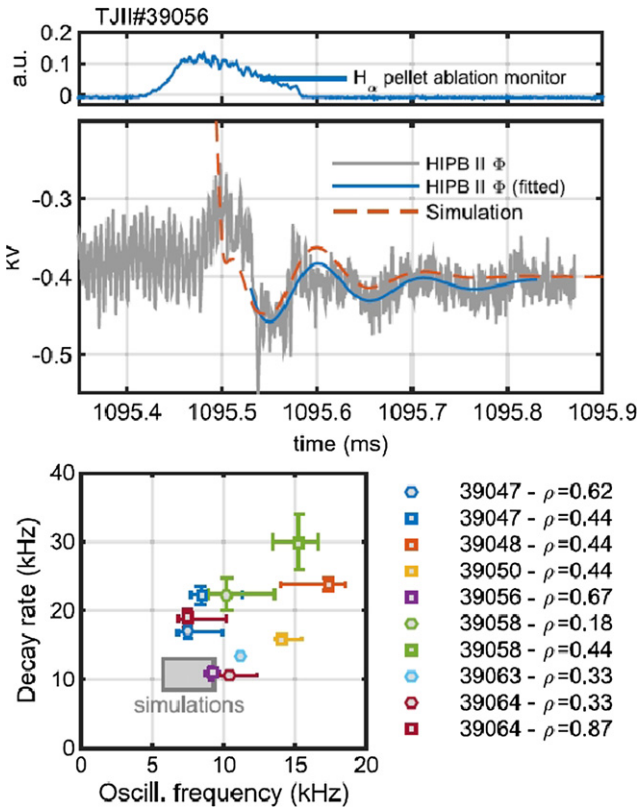

Figure 115. Time traces of (a) H_α emission and (b) HIBP potential Φ plus GK simulation, during a pellet-induced transient in TJ-II, (c) oscillation damping rate vs frequency with measured (symbols) and simulated (box) values for several radii and experimental profiles. Reproduced from [584]. CC BY 4.0

In appropriate L-mode conditions an $f \approx 105$ kHz, $m = 6$ global Alfvén eigenmode and an $f \approx 14$ kHz low frequency mode (magnetic) has been observed in the TJ-II core ($\rho \approx 0.65$) together with an $f \approx 20$ kHz flow oscillation lasting some tens of ms. The combination is highly suggestive of an AE nonlinear mode coupling to a GAM. Alternatively, the GAM may possibly be sufficiently driven by fast electrons generated by the ECR heating at low density [417]. A similar damped $\geqslant 10$ kHz oscillation was observed in low density, NBI heated discharges with $T_e > T_i$, after a pellet injection triggered a fast transient in the potential ψ (measured with HIBP and DR), as shown in figure 115 [583]. The figure also shows excellent reproduction by matched GK simulations, cf also [580]. The results would suggest that natural GAMs can exist in TJ-II—if they have sufficient drive.

A distinctive GAM-like mode was also observed in the TJ-II core using HIBP and bolometry during counter NBI heating with an intermediate magnetic well configuration. The mode appeared in both the electric potential and density with a frequency $f \approx 40$ kHz, scaling with the ion sound speed. The mode is not Alfvénic and has a global structure $\rho \approx 0.8 \pm 0.2$ [418]. The candidate is an EGAM. However, an $n = 1$ toroidal structure was deduced from the toroidal correlation of bolometer signals [419], which is different from the usual $n = 0$ toroidal structure obtained in tokamaks. Nevertheless, recent kinetic-MHD modelling indicates that non-axisymmetric $n \neq 0$ zonal modes can exist in rotating plasmas [482]. As with the axisymmetric $n = 0$ case, the $n \neq 0$ ZFs acquire finite frequencies in rotating plasmas. However, in static plasmas their electric and magnetic field perturbations are zero and thus these modes are strictly hydrodynamic.

16.5. RFP configurations

There appears to be an absence of GAMs in RFP devices. Ideally the RFP magnetic equilibrium is axisymmetric, i.e. tokamak-like. However, the dynamo process which leads to the reversed toroidal field at the edge, and the low overall $q < 1$, also allows ideal kink and tearing modes (TMs) to form. The core is dominated by saturated $m = 1$ kink modes with single or multiple helicity creating a stellarator-like helical axis [425, 589], while in edge region has strong TM activity, leading to chaotic field structures. In the RFX-mod device, for example, long-range-correlations in $\tilde{v}$ flows (observed in various devices as a marker of ZF structure) was noted as being absent [426]. It is thought that the presence of ergodic magnetic field lines and strong TM activity in the edge (as indicated by Poincaré plots [424]) prevent the formation of the GAM current flow—a phenomenon also noted in ergodic field experiments in TEXTOR and the suppression of GAMs with strong RMPs in other tokamak experiments where edge magnetic field ergodisation occurs—see section 16.3.

Nevertheless, a low frequency ZFO (<10 kHz) was recently reported in the confined edge plasma region of the Madison Symmetric Torus (MST) RFP device when running with very low q [427]. The E_r fluctuations (from LPs) had an $m/n = 0/0$ mode structure and narrow radial extent, however, it was not identified as a GAM since the peak mode frequency was below the ion–ion collision frequency of ~ 3 kHz. GK simulations for this low edge q configuration predict the strong excitation of a RHR and ZFOs [590]. But the low q should be detrimental for GAMs, and thus their absence is at least consistent.

In summary, moderate amplitude MHD island chains may induce and enhance GAM-like flow oscillations, or entrain a natural edge GAM. However, with large MHD modes or applied magnetic perturbations the GAM is suppressed. For non-axisymmetric field configurations trapped particle drifts create a new branch of GAM-like low-frequency oscillations. In addition $n \neq 0$ modes may be supported.

17. GAM and ZFO transitions

No discussion of GAMs can be complete without broaching the topic of zero (SZF) and low frequency ZFO and their coexistence, competition, and transition to standard high frequency GAMs. In essence there are two types of ZFs: (a) the quasi-zero-frequency stationary ZF, here termed SZF (although in the literature a variety of terms appear, including zero-frequency ZFZF, zero-mean-frequency ZMF, low-frequency LFZF, etc); and (b) the finite frequency GAM. The difference lies in the plasma response to a flow perturbation and in the absence or presence of a pressure sideband. The first section 17.1 therefore begins with a discussion of the plasma

Table 16. Parameter dependencies for the stationary zero-frequency zonal flow (SZF) and the GAM. cf [53, 60, 61]. Terms are defined within the text.

Parameter	SZF ω_0	GAM $\omega_\pm$
Pol. velocity v_θ	$-E_r/B$	$-E_r/B$
Response	Incomp.	Comp.
	$\nabla \cdot v \approx 0$	$\nabla \cdot v \neq 0$
Parallel $k_\parallel$	—	$(qR_0)^{-1}$
Tor. velocity v_ϕ	$-2qv_\theta \cos\theta$	$q^{-1}v_\theta \cos\theta$
Frequency	$\omega \sim 0$	$\omega \sim \omega_t$
p-sideband	—	$m = 1$
Radial λ_r	$\sim \sqrt{a\rho_s}$	$\sim \sqrt{a\rho_s}$
Radial vel. v_r	Small	$\sim \frac{1}{2}\omega k_r \rho_i^2$
Damping	Predom. lin.	Lin. + nonlin.

response to a flow perturbation. The SFZ has a zero mean frequency but can be collisionally broadened up to around the ion–ion collision frequency ν_{ii}. However, due to various mechanisms the SZF can acquire a finite mean (peak) frequency to become a low frequency ZFO, (section 17.2) and may eventually even transition into a GAM. A ZFO and a GAM can also simultaneously coexist. Section 17.3 considers the ZFO/GAM competition for the turbulence drive. Finally, this section finishes with a discussion of the nonlinear interaction of GAMs and ZFs.

17.1. SZFs and GAMs

Table 16 summarizes the main parameters expected for the zero-frequency stationary SZF and the standard high frequency transit-ion GAM. The SZF and the GAM share many features, but the principle difference is in the plasma response to a perturbation in the poloidal flow. Since the poloidal rotation is compressible in a toroidal device, there are two ways to compensate a poloidal flow perturbation: (i) generate a toroidal (zonal) flow so that the perpendicular flow divergence can be compensated by the parallel flow gradient, $\nabla \cdot v_\perp \simeq -\nabla_\parallel v_\parallel$ without pressure sidebands being excited. This process is slow, i.e. $\tau^{-1} \sim \nu_{ii}/\epsilon^\gamma$, where γ depends on the collisionality regime—basically RH residual and neoclassical damping that establishes the neoclassical level of the poloidal flow, potentially modified by the turbulent effects [553]; (ii) however, if the flow perturbation is fast then $\nabla \cdot v_\perp$ cannot be compensated by the toroidal rotation quick enough and thus poloidally asymmetric pressure sidebands form, so that $\partial \hat{p}/\partial t + p_0 \nabla \cdot v_\perp = 0$, which causes a radial current, which will be compensated by a polarization current, and hence a GAM. So, if the perturbation source (e.g. turbulent RS) is fast, one should get a GAM and not an SZF. In fact it is rather difficult to avoid GAMs in toroidal systems as one starts to produce a poloidal ZF with RS or whatever.

In a nutshell, in axisymmetric systems such as a tokamak, slow sources (turbulent or otherwise) can drive toroidal rotation, while fast sources should drive GAMs. An alternative perspective is the GAM as a relaxation process to establish the poloidal and toroidal rotations in the tokamak. Note, if the source fluctuates then the system may never become stationary, and the result is GAM pulsations. This is an area that needs further study, particularly the connections to neoclassical theory, e.g. trapped particles.

17.2. Low frequency ZF oscillations

In earlier sections several mechanisms were introduced where the GAM/ZF dispersion relation may acquire an additional low-frequency branch. Modes in these branches are called ZFO. The mechanisms include: (i) diamagnetic drifts ω_{*1} from temperature gradients (section 2.13), (ii) pressure anisotropy $\chi = p_\perp/p_\parallel$, generated by NBI or ICRF heating (section 2.3), (iii) equilibrium plasma rotation $M_t = v_t/c_s$, from intrinsic or external NBI or RMPs (section 10), and (iv) radial drifts of trapped particle orbits due to toroidal/helical field ripple (section 16.4). In the first three mechanisms (i)–(iii) the GAM dispersion relation splits into two branches of finite frequency continuum modes $\omega_\pm$, cf equations (119), (20) and (22), where the upper branch ω_+ is a modified standard GAM while the lower frequency branch ω_- is a ZFO mode that bridges to the stationary SZF when the effect is removed.

All the mechanisms introduce a form of asymmetry, via the kinetic gradients, an additional velocity or a pressure anisotropy. Each removes the degeneracy of the zero-frequency SZF mode. There are common themes as well as differences, for example rotation and drifts are related, although drift effects require strictly two-fluid theory to model. Anisotropy is different from rotation, but it does bring in some inhomogeneity from the equilibrium, similar to drift effects.

Only trapped particle drift effects, case (iv), are somewhat different. The story of trapped particles has been mostly ignored in GAM theory, but there are important connections, such as to the damping of poloidal rotation. Indeed, a ZFO with an acoustic frequency scaling but bounded by the particle bounce frequency ω_b of helically trapped particles is a particular feature of stellarators—where they are named LFO—see section 16.4. The magnitude of the drift effect is predicted to depend greatly on the degree of stellarator configuration optimization. As shown in the simulation example of figure 114 [57], the ZFO/LFO may also simultaneously coexist with the residual and a standard turbulence driven GAM. In stellarator simulations the presence of an ambient radial electric field also appears to have the same effect on the ZFO/LFO frequency as for the GAM in a poloidally rotating tokamak plasma, but with enhanced damping [591]. Recent GK simulations [592] have also addressed the issue of trapped particle (ions) interacting with a resonant wave in generating a ZFO with a frequency close to the ion precession frequency. As yet, there are no experimental reports of a trapped particle ZFO. Also chronically missing are experimental measurements of the pressure sideband presence and structure in tokamak SZF/ZFO cases.

Table 17 summarizes, in order of increasing frequency, the relationship of GAMs and ZFOs within the broader hierarchy of poloidal flows in toroidal devices. A zero-mean-frequency SZF may become a finite-mean-frequency ZFO with the addition of one or other form of asymmetry. And, as described in the previous section, the ZFO, as soon as it acquires a sufficiently large enough frequency $\omega \gtrsim \nu_{ii}/\epsilon^\gamma$ should transform

Table 17. Hierarchy of poloidal flows in toroidal devices in order of increasing perturbation frequency. ω_b = ion bounce, $\omega_t \sim (c_s/R_0, c_s/qR_0)$ ion transit, $\omega_{t,fp}$ = fast particle transit frequencies.

Type	Freq.	Drive/damping
Mean	0	Neoclassical poloidal damp. $\nu_{ii}/\epsilon^{\gamma}$
SZF	$\omega \approx 0$	Coll. broadened, nonlinear RS drive
↓		
ZFO[a]	$\omega_- < \omega_+$	Drift/anisotropy/rotation. linear drive
↓	$\omega < \omega_b$	Trapped particle: LFO
GAM	$\omega_+ \sim \omega_t$	Nonlin. turb. RS + DS drive
	$\omega \sim \omega_{t,fp}$	Fast particle drive: EGAM

[a]Note: if ZFO/LFO $\omega_- > \nu_{ii}/\epsilon^{\gamma}$ then the mode is GAM-like, otherwise ZF-like.

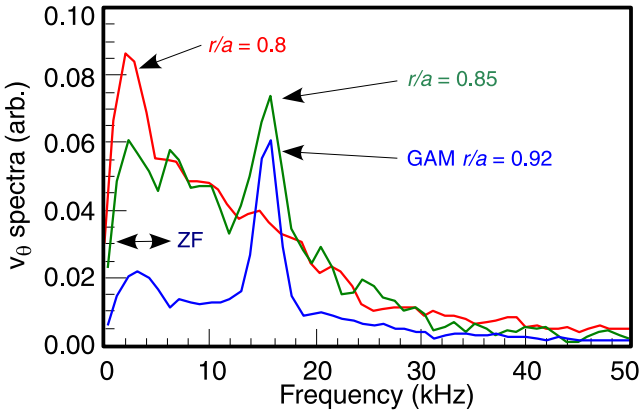

Figure 116. Poloidal flow spectra at three edge radial locations from DIII-D, 5 MW NBI heated, $q_{95} = 6.5$, USN, L-mode discharge. Adapted figure with permission from [278], Copyright (2006) by the American Physical Society.

to become essentially GAM-like with a pressure sideband, cf [478]. However, it should be stressed that the boundaries are far from hard and that experimentally it maybe challenging to distinguish a ZFO from a GAM in the transition region when pressure-sidebands and parallel flow/sound-waves are both acting.

17.3. Coexistence and transitions

Figure 116 shows a classic example using BES of the change in the poloidal flow fluctuation spectrum across the edge region of DIII-D [278]. The spectra at three radial r/a locations for NBI heated, USN, L-mode discharges at high $q_{95} = 6.5$, show the amplitude of a low-frequency ZFO 'peak' increasing towards the core, while the GAM amplitude decreases—consistent with the role of the q profile in damping the edge GAM, but not the more core localized SZF/ZFO. At some radial position the GAM and ZFO are seen to coexist. A similar enhanced SZF together with a strong edge GAM was observed in HL-2A during ECR heating when q_{95} was reduced from 5.5 to 4.5 [430], and lower [535]. Here, the GAM amplitude exceeds that of the SZF in the edge but then weakens as the SZF strengthens towards the core.

The finite frequency of the ZFO feature in the NBI heated DIII-D example was noted by Ren who compared the ZFO and GAM frequencies with an anisotropic pressure model (section 2.3) [85]. In this model (with homogeneous average pressure) the two mode frequencies are linked by $\omega_- = 1/q\sqrt{3/14}\omega_+$. With a $q = 3.5$ taken from the experiment a good agreement was obtained with the observed $\omega_-/2\pi \sim 2$ kHz and $\omega_+/2\pi = 15$ kHz values. In this example it was assumed that the NBI induced a dominant pressure anisotropy rather than a rotation effect, where the two roots are also linked, e.g. $\omega_+^2 = \omega_-^2(1 + 2q^2 + 4q^2M_t^2)$ for $M_p = 0$ [480]. Note that both the rotation and anisotropy formulations give $\omega_- \propto \omega_+$ and thus an acoustic and geodesic frequency scaling. The only missing element in this comparison is a confirmation of the $\tilde{p}$-sideband nature.

Nevertheless, the effect of plasma rotation is clearly seen in the DIII-D edge flow spectra in figure 73 which show the disappearance of the GAM with decreasing toroidal torque and the appearance at the same edge radial location of a broader ZFO. This case has not yet been modelled. There are also several other observations (reported in section 18.1) of the GAM being replaced by a ZFO where the plasma conditions are changing rapidly as the discharge approaches an L to H-mode transition.

The turbulence type also appears to play a role in the dominance of ZFO over a GAM. In JIPP T-IIU the core flow spectra transitioned from a GAM to an SZF/ZFO when the dominant turbulence was apparently changed from TEM to ITG using either strong gas puffing or heating with ICRF fast wave or NBI [328]. Here, it was concluded that ITG turbulence is more effective in generating ZFs.

Table 18 summarizes experimentally reported cases where more than one spectral feature was evident simultaneously at the same radial region—not too close to the edge and not so far in as to be core. Where a clear ZFO peak is observed together with a GAM (notably a feature of the larger well-heated machines), its frequency is around a factor of 10 smaller than the GAM. For the cases where no clear low frequency peak is observed (mostly small low power machines), the spectrum continues to rise towards zero-frequency SZF. For example in HL-2A discharges see figure 2, or figure 2(a) in [25], or in low ohmic heated HT-7 discharges [287]. However, HL-2A also report GAM only cases [345]. Note in the case of the larger machines AUG [31, 304] and JET [358] neither a ZFO or SZF was evident in the edge. Here, the low frequency spectra are flat below the GAM frequency in the edge, cf figure 2, or tending to $1/f$-like towards the core.

17.4. GAM/ZF competition

Since both the GAM and the ZF are driven by turbulence there is the issue of competition in the nonlinear transfer leading to the dominance of one or other mode. This GAM vs SZF/ZFO competition was investigated in strongly ECR heated L-mode plasmas in HL-2A cf figure 4 of [544]. The frequency resolved nonlinear turbulent energy transfer was measured using multi-field (plasma potential and density) cross-bispectral and energy transfer techniques (RS profiles) applied to LP array signals. It was observed that the turbulence drives both GAMs (10 kHz) and ZFOs (1–2 kHz). With increasing heating power both the GAM and ZFO initially grow, but then the GAM intensity saturates and then

Table 18. Experimental frequencies (kHz) for a stationary SZF, a low frequency ZFO (ω_-) and a high frequency GAM (ω_+), either coexisting or transitioning.

Device	SZF	ZFO	GAM	Notes
CHS	<1		16.5	Core coexistence [33]
C-Mod	<3		20	I-mode [379]
DIII-D	—	2	$\sim$15	Radial location [278, 593]
DIII-D	—	2–3	15–19	NBI torque/rotation [281]
EAST	0–4		20	Weak H-mode [42]
HL-2A	0.1–4		10	ECRH, low I_p [25, 544]
HL-2A	0.5–3		12–17	ECRH & q reduction [430, 535]
HT-7	<1		10	ECRH [287]
ISTTOK	<6		15–25	Sign of DC bias E_r [363]
JIPP TII-U	$1/f$		$\sim$35	Change of turb. with heating [328, 329]
JFT-2M		$\sim$1	15	Coexistence [317, 318]
J-TEXT	0.5–2		16.8	Biased H-mode/E_r [390]
MAST	<1		9–12	RMP application [374]
TEXTOR		1–2	10	DC bias E_r [344, 431, 465, 508]
TJ-II		1–2	$\sim$20	Core, drive and q [417]

decreases while the ZFO continues to grow linearly [544]. This was claimed as being consistent with a shear mode competition model [594] which involves two predators and one prey model using nonlinear mode competition via coupling of higher order wave-kinetics to describe the coexistence of GAMs and ZFO. Note also that the model predicts that as the input power is increased the energy goes first into a ZFO only state, and then into a GAM only state, i.e. there is a threshold for the GAM excitation—consistent with AUG and ISTTOK measurements for a critical ∇T_e below which no GAM was observed—see figure 75 [26]. The model also suggests a hysteresis-like behaviour during power ramp-up and down.

17.5. Nonlinear GAM processes

Related to the issue of coexisting multiple GAMs and/or simultaneously together with ZFs is the question of the GAM's ability to nonlinearly create stationary ZFs or higher GAM harmonics. The driving of ZFOs is of course of particular interest since their lower frequencies may have a stronger impact on turbulent transport.

As discussed in section 4.5 there are conflicting theory and modelling results on this topic. Early fluid simulations of ITG turbulence close to a critical threshold show packets of radially propagating GAMs leading to an accumulation of residual ZF [146]. Later considerations showed that GAMs are not capable of generating a ZF via the RS drive [236]. Other models of nonlinear coupling between GAMs and ZFs in the higher order show ZFs transiently driven by the self-interaction of GAMs [143]. One example has two radially counter propagating GAMs, generated by reflection at the plasma boundary, interacting to transiently excite a stationary SZF mode. Subsequent developments extended the model to general conditions of symmetry breaking with either pairs of GAMs with different phase velocities forming a radial standing wave which induces a ZFO (in this case the strength of the ZFO grows with the amplitude of the GAMs), or a standing wave formed by symmetry breaking of the AT [595].

Models based on GK theory suggest that a stationary ZF could be generated nonlinearly by a finite amplitude GAM when crucial first order FOW effects due to magnetic field gradients or curvature drifts where included [237]. See section 4.5 for further comments on the validity of this model. Nevertheless, the main implication of this model is that it might be possible to excite a stationary ZF from a finite-amplitude GAM, even in conditions (such as the high q edge) where it would normally be below the threshold for its own spontaneous excitation by turbulence. This work was recently extended to show that in fact second order FOW effects must also be included [238]. With some assumptions a simple formula for the ZF amplitude $\delta\phi_Z$ as a function of the GAM amplitude $\delta\phi_G$ and k values was derived. A comparison of predicted values and measurements from HT-7 were of the right order of magnitude.

The nonlinear self-interaction of GAMs may have other effects as well as exciting ZFs, for example an up-shift in the GAM frequency as the GAM amplitude increases [143, 220]. Such effects were proposed as possible causes for model discrepancies with experimental results from AUG [309]. This is a particular area where much work is needed on the further validation of models and more specific comparisons with experimental results. In addition to the nonlinear frequency pulling effect, models also suggest higher GAM harmonics may also be excited [220]. Figure 117 shows the derived analytically amplitudes $e\phi/T$ for the GAM and its second harmonic—which is significantly weaker but still measurable, and, as shown in the comparison to JFT-2M experimental results [233] in reasonable agreement.

In summary, rotation, diamagnetic drift and anisotropy can open up a second low frequency branch in the GAM dispersion relation. With increasing strength this may convert a zero-mean-frequency SZF to a finite-mean-frequency ZFO, which may further convert to a GAM with a pressure sideband. Both SZF/ZFO and GAMs can coexist at the same location with dominance changing with q, heating, etc. Further, they are in competition for the nonlinear turbulence energy transfer which

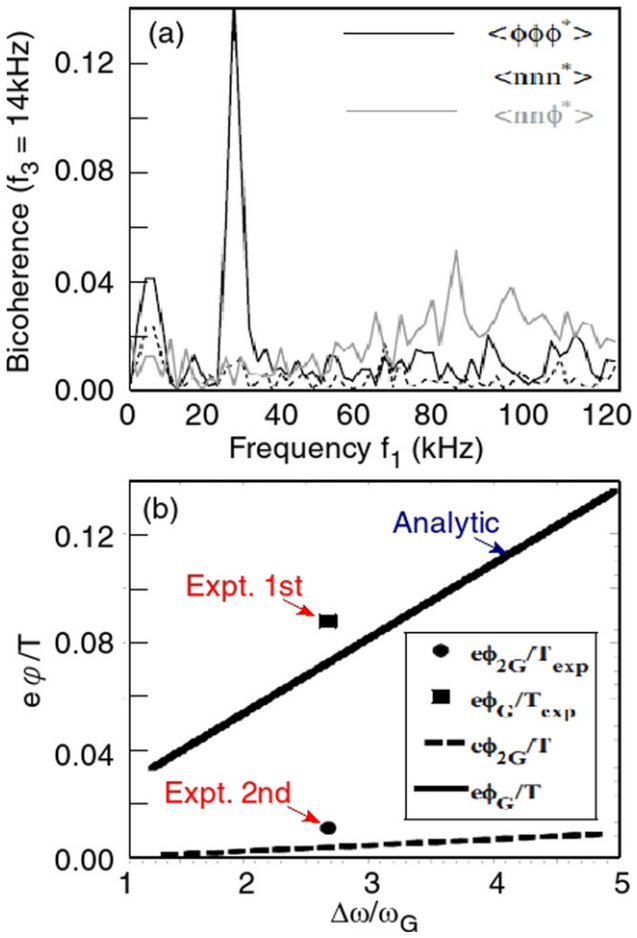

Figure 117. (*a*) Bicoherence spectra at $f_3 = 14$ kHz showing 2nd GAM harmonic around 30 kHz, in JFT-2M. Adapted from [233]. and (*b*) analytic saturated fundamental and 2nd harmonic amplitudes $e\phi/T$ vs normalized GAM width $\Delta\omega/\omega_{\rm GAM}$, with experimental points. Adapted from [220], with the permission of AIP Publishing.

may lead to the preferential suppression of one or other. Nonlinear GAM self-interaction is predicted to 'pull' the GAM frequency, and may also possibly excite a 2nd harmonic GAM, or even a stationary SZF. A trapped-ion ZFO is predicted to exist, but remains to be confirmed experimentally.

18. GAMs and confinement mode transitions

18.1. L–H transition

It is generally understood that the L-mode to H mode confinement transition results from a feedback loop involving a localized enhancement of the edge $E_{\rm r}$ velocity shear which reduces the local turbulence and thus transport, which in turn enhances the pressure gradients and hence to stronger shearing [546, 596]. Many studies show that the L–H bifurcation can be very rapid, occurring on the turbulence decorrelation time scale. Although there are several mechanisms that could lead to triggering the L–H transition, cf [531], it is the role of turbulence driven flows that is of interest here.

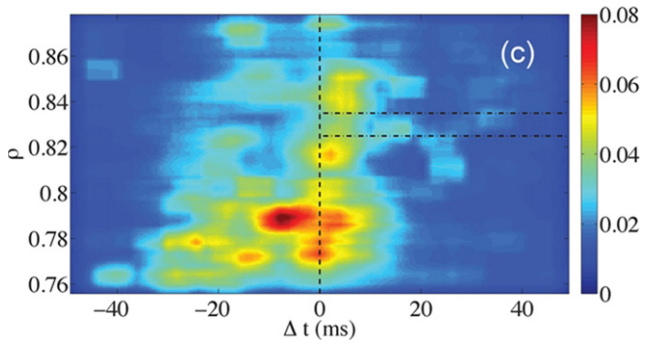

Figure 118. Contour plot of mean bicoherence b^2_Σ as a function of normalized radius ρ and time relative to L–H transition in TJ-II. Reproduced courtesy of IAEA. Figure from [531].

While RS driven flows $\langle\tilde{v}_{\rm r}\tilde{v}_\theta\rangle$ seem too small in L-mode to create a critical shear alone (cf [64]), when combined with a 'baseline' equilibrium mean flow shear, RS flows may take the role of a trigger. RS is indeed observed to increase prior to the L–H transition in many experiments. For example, probe measurements in HT-6M [597] and CHS [408] show a spike in RS with finite radial extent. Likewise in TEXTOR bias induced H-modes a clear stretching, tilting and splitting of turbulent eddies was observed with GPI [598] inside the separatrix. The consequent increase in RS and $E_{\rm r} \times B$ shearing rate was accompanied by an enhanced $\sim$1.3 kHz ZFO and a weaker GAM. The picture is thus of an close interaction among sheared flows, eddy structures, RS, and ZFs across the confinement transition [431]. Also using GPI a transient spike in RS driven ZFs was measured a few mm inside the separatrix of C-Mod at the L–H transition [599]. Here, the transient flow preceded the final turbulence suppression and the subsequent rise in the pressure gradient driven $E_{\rm r}$ shear. Similar results were obtained in DIII-D using BES [600].

Bispectral analysis has been widely used as a proxy for RS driven shear flow, as in DIII-D where a spike was observed in the total b^2_Σ, equation (B.6), from probes inside the separatrix just before the L–H transition [526]. In this case the change came mainly from the SZF frequencies. Figure 118 shows a recent example from TJ-II where a b^2_Σ peak during spontaneous and bias induced H-modes is seen to propagate outwards as the confinement barrier forms [530, 601]. Other examples include turbulence energy transfer measurements in EAST [602]. In each case the conclusion drawn was that the H-mode was triggered via nonlinearly generated shear flow.

18.2. GAM-ZFO role

A recent overview paper [603] compares and summarises results on the role and occurrence of GAMs and ZFOs in promoting (or hindering) the H-mode transition. As noted in section 17 GAMs and ZFOs can coexist, compete and even suppress one another depending on equilibrium conditions. The changing plasma conditions during the L to H-mode transition are thus particularly relevant to the GAM/ZFO evolution.

As shown in figure 73 a strong L-mode edge GAM in DIII-D with co-current NBI induced rotation was suppressed and replaced by a low frequency ZFO when reducing the torque with counter-current NBI, just before transitioning to H-mode. Here, it was proposed that the lower frequency of the ZFO was more effective than the GAM in shearing the turbulence and thus in triggering the L–H transition [281]. The missing L–H transitions co-injection NBI were provided later [284]. Again, at low density the L-mode GAM evolved into ZFO together with increased long wavelength $\tilde{n}/n$ in the pedestal region as the L–H transition approached. However, at higher densities the GAM was simply diminished leaving a broad flat or $1/f$-like flow spectrum [284]. There were also notable behaviour changes with varying B_t.

In JFT-2M with NBI heating, approaching the L–H transition the 15 kHz eigenmode GAM was replaced by a $\sim$1 kHz ZFO. However, with additional ECH power the 10 kHz GAM continued up to the L–H transition [321]. After the L–H transition only weak, low-frequency broad-band potential fluctuations <5 kHz were observed. Although this is suggestive of possible ZFs, there was no significant bicoherence in either potential or density fluctuations during subsequent H-mode inter-edge localized mode (ELM) phases. Power ramps in JET using NBI heating at various densities first show the GAM is maintained up to the L–H transition at fairly low densities, but is reduced (damped) prior to the transition at higher densities. This was thought to be due to changes in the induced toroidal plasma rotation due to the NBI torque [360].

Concerning the role of the T_e/T_i ratio in maintaining the GAM, or not, up to the L–H transition, Watari [99] predicted that the GAM damping rate should be smaller for $T_e > T_i$. This appears to be supported by results from JIPP T-IIU in ohmic heated low density plasmas—a condition where T_e and T_i decouple and $T_e > 3T_i$ [36]. Similarly they also observe very intense core GAMs and weak ZFO when $1 \ll T_e/T_i$ [329–331]. There are similar observations in AUG at low densities with strong ECR electron heating where the GAM continues through the I-phase (see below) up to L–H transition [306].

During ohmic and NBI heated discharges in TUMAN-3M the GAM observed using HIBP in preceding L-mode sometimes continues into the H-mode, only decaying $\sim$1 ms after the L–H transition, as shown in figure 119, with a frequency dropping from 30 to 20 kHz with a notable anti-correlation between the GAM amplitude and the higher frequency $f > f_{GAM}$ turbulence level. In other similar discharges, however, the GAM ceased some $\sim$1 ms before the transition [332, 333]. In TUMAN-3M the GAM (4.5 kV m^{-1}) is localized to just inside separatrix while in FT-2 the GAM appears is global, extending to the half minor radius with an amplitude (15 kV m^{-1})—exceeding the mean E_r [604]. The L–H transition in TUMAN-3M was always preceded by an intense series of GAM bursts (not an I-phase) of short <3 ms duration with individual GAM bursts of 0.2–1.0 ms, during which the GAM frequency either falls (HIBP) [333] or remains constant (DR) but with modulated amplitude [335]. Despite the strong GAM in FT-2, no self-sustained H-mode could be formed.

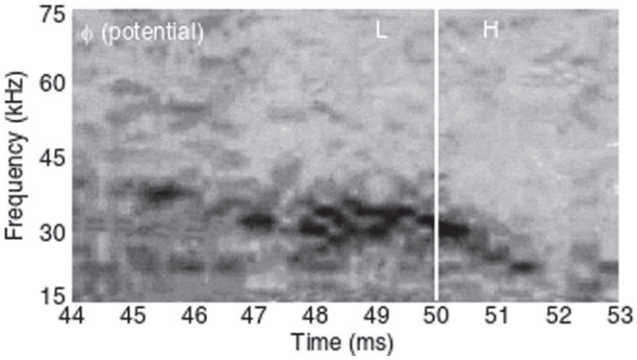

Figure 119. HIBP $\tilde{\phi}$ spectrogram of GAM evolution across low density $n_0 \sim 1.5 \times 10^{19}$ m^{-3}, ohmic L–H transition in TUMAN-3M. Adapted by permission from Springer Nature Customer Service Centre GmbH: Springer Nature, Technical Physics Letters, [333], Copyright 2012.

A simple one-dimensional numerical model of the density profile evolution with GAM induced radial E_r shear, developed by Askinazi *et al* [428, 605, 606], suggests that if the GAM amplitude and burst duration overcome a certain threshold then the peripheral shear is sufficient to push the plasma into an H-mode. The model predictions were compared with the GAM measurements in TUMAN-3M, and, using experimental values of the GAM wavelength and magnitude the transition appeared reasonable. The TUMAN-3M and FT-2 experimental configurations were also modelled using the ELMFIRE GK code. With the GAM modelled as a time and space-localized travelling wave an L–H transition occurs in TUMAN-3M if the GAM amplitude or duration exceeds certain thresholds—which depend on the plasma parameters, principally T_i [428]. In FT-2 the GAM could not promote an L–H transition, even with a higher mean E_r shear value and double the GAM amplitude and duration.

18.3. I-phase and LCOs

At heating powers below those normally required for the tokamak L–H transition the plasma may enter an intermediate state, often termed dithering [607], IM-mode [608] or (intermediate) I-phase [306]. Unlike the dynamic L–H transition the I-phase can be maintained as a non-evolving steady-state condition with an edge E_r well depth between L and H-mode and enhanced energy confinement times above that of comparable L-modes. At densities associated with the low-density-branch of the L–H power threshold, cf figure 3, the I-phase is characterized by a periodic (few kHz) modulation or bursts of the edge turbulence and E_r shear in the form of a LCO. Confirmed I-phases have been observed in multiple devices; TJ-II [609], AUG [306], DIII-D [610], EAST [365, 611, 612], HL-2A [356, 544, 613], Globus-M [385, 614], JFT-2M [323], COMPASS [615]. Similar phases were also observed in the H-1 heliac where the GAM appears to play a role in L–H transition together with the mean E_r [37, 436].

In AUG low density I-phases the GAM appears to play an role in sustaining the limit-cycle. As shown in figure 120 a cycle starts with a rising turbulence level crossing a threshold

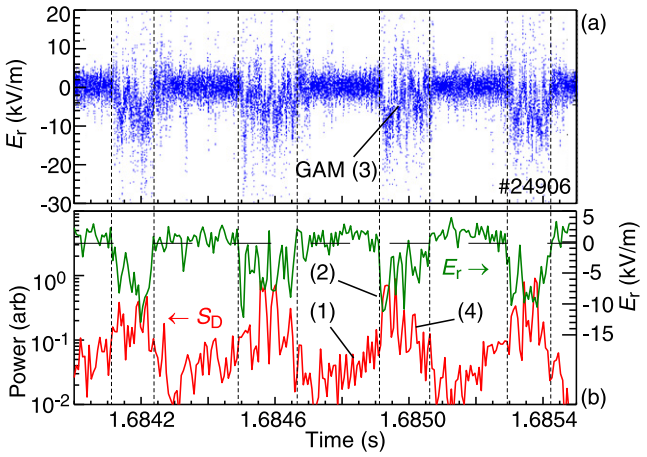

Figure 120. (*a*) Instantaneous E_r showing GAM oscillation within I-phase bursts and (*b*) smoothed E_r and turbulence level S_D showing (1) rising turbulence, (2) threshold, (3) GAM, and (4) turbulence suppression in AUG. Adapted figure with permission from [306], Copyright (2011) by the American Physical Society.

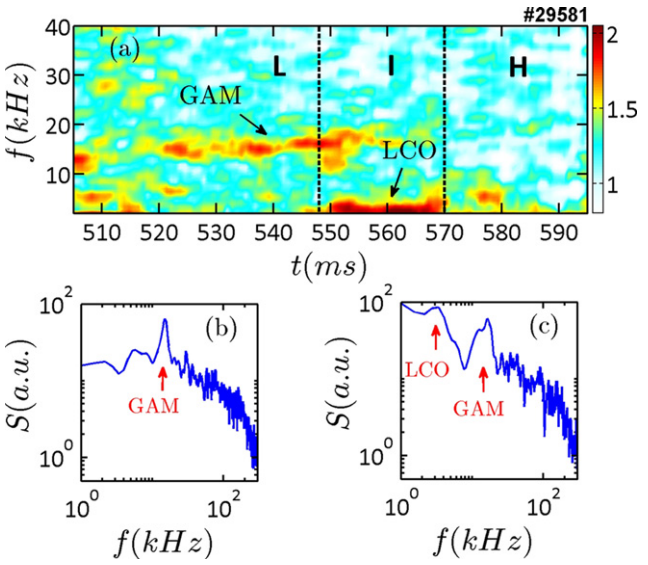

Figure 121. (*a*) Spectrogram of E_r fluctuation, (*b*) E_r power spectrum in L-mode at 537 ms with GAM and (*c*) in I-phase at 551 ms with coexistence of GAM and LCO in HL-2A. Reprinted from [356], with the permission of AIP Publishing.

which turns on an intense GAM across the narrow pedestal region with an enhanced mean E_r well. The GAM shearing begins to suppress the turbulence below a threshold value turning the GAM off. The LCO repeats with typically 50% duty cycle. With increasing NBI power the ∇p driven equilibrium velocity shear grows and overtakes the GAM shearing, at which point the GAM decays [306] and the H-mode edge barrier forms. The GAM shearing rate within the I-phase LCO bursts is substantially stronger than the mean LCO E_r shearing. With increasing density the LCO frequency and duty cycle decreases and the bursts acquire a more ELM-like nature [616, 617].

Similarly in Globus-M a QC intermittent L-mode GAM oscillation transitions to LCOs with gradual increasing GAM amplitude (up to 100%), followed by sharp amplitude decrease and disappearance at the H-mode transition [385]. The GAM oscillations were accompanied by fast changes in D_α emission which were attributed to density oscillations at the GAM frequency with an $m = n = 0$ form, and speculated could be due to fast local suppression of turbulent diffusivity caused by the GAM flow shear.

In DIII-D with co-injection NBI power close to the L–H threshold also leads to the formation of an I-phase with a ~2 kHz LCO with a similar structure as in AUG, however, the ~20 kHz GAM observed in the preceding L-mode appears to be suppressed [610]. Here, it was inferred that it is the zonal-nature of the LCO (2–3 cm wide radially localized with high toroidal coherence), or more precisely, the flow shear due to the action of the LCO that is the important factor.

First reports from HL-2A report the absence of a GAM in the L–H transition [544, 613, 618] but a possible ZFO during the initial LCO (with bicoherence at 2–3 kHz indicating nonlinear coupling). However, later studies of the GAM/ZF behaviour through the L–I–H transition, show the GAM decaying slowly during the I-phase, as seen in figure 121 [356]. Together with bispectral analysis indicating a coupling of the GAM via the background turbulence to the LCO, this suggested energy flowing from the GAM to the LCO, which facilitated the transition!

The LCO behaviour reported in EAST show low frequency 2 kHz flow oscillations prior to the L–H transition at marginal power and $q_{95} \sim 3$–4 [365, 611]. Although at these low q_{95} values GAMs are not usually observed in EAST. Bicoherence analysis also revealed a direct coupling between the edge turbulence and E_r oscillations below 4 kHz. Reviews of the LCO/I-phase phenomena [619, 620] conclude that a burst of E_r shear initiates the final I–H transition [620].

In the case of JFT-2M, HIBP measurements show the formation of bursty LCOs (4.5 kHz, $m = 0$) with NBI heating (with edge $T_i \sim T_e$). Similar to the HL-2A case, the 15 kHz GAM was reduced during the I-phase prior to the (low density, low $q_{95} \sim 2.9$) H-mode transition [323, 324]. However, interestingly, for JFT-2M the measured RS was smaller than that required to accelerate the flow during the LCO which suggests that the LCO flow modulation in JFT-2M is not turbulence driven.

In an analytic study of the GAM contribution to LCOs it was proposed that the time varying RS can excite off-resonant GAMs within the LCO burst—as per AUG observations. The process of off-resonant excitation of GAMs is where the excitation frequency is far from the natural GAM frequency [621]. From the model the off-resonant GAM oscillates not at the natural GAM frequency but at the excitation (i.e. LCO) frequency. For certain conditions the velocity contribution of the GAM can be amplified, adding to the velocity shear of the LCO. In the case of the JFT-2M conditions the off-resonant excited GAM was predicted to be small and thus plays only a limited role, consistent with observations [324].

In the early 2000s a series of simple 0D predator-prey (PP) type models were introduced to describe the nonlinear dynamics of coupled (stabilizing) ZFs and (driving) DW turbulence [622–624]. The models universally display state

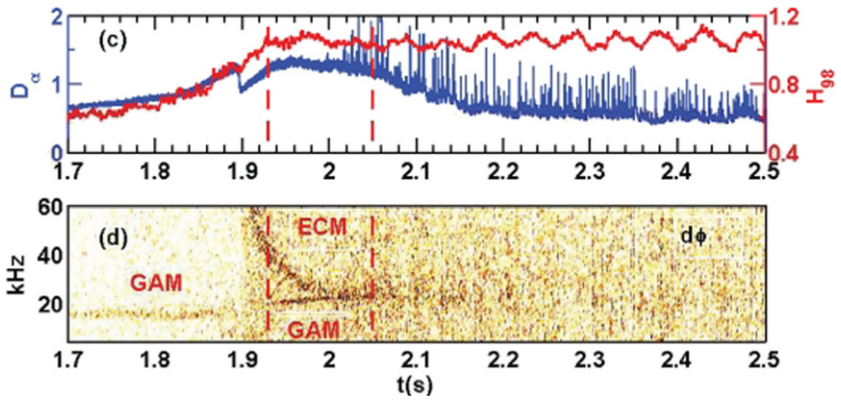

Figure 122. Time traces of D_α and H_{98} plus $u_\perp$ flow spectrogram across an L–H transition in EAST, with $n_0 \approx 3 \times 10^{19}$ m^{-3}, $q_{95} \sim 5.9$ and ∼2 MW wave heating. Reproduced courtesy of IAEA. Figure from [42]. Copyright (2018) IAEA.

transitions with critical thresholds in increasing drive, from stable flow/turbulence oscillation first to a bursty LCO then to chaotic behaviour. With appropriate parameters the models could reproduce several DIII-D experimental observations. They concluded that transient RS driven ZF/GAMs could trigger the L–H transition [624].

The PP model was subsequently developed and compared with global Landau-fluid simulations of ITG turbulence, which showed intermittent transport events associated with radially propagating GAMs near to critical gradient regimes [146]; and later to study the role of the GAM velocity shear feedback-loop in the L–H transition [144]; a 0D model with two-predators (ZF and GAM shearing actors) led to multiple states (ZF only, ZF with GAM and GAM only) where coexistence, mode competition and a sequence of transitions are obtained [594]. A 1D model with two-predators and one-prey was used to study the spatial-temporal evolution of the L → I → H-mode transition [625].

Many experimental results are seen to be consistent with such PP models with comparative measurements from HL-2A, DIII-D and EAST with GAMs and LCOs [626] and through the L–H transition in C-Mod [599]. In the case of C-Mod measurements of RS using GPI a transfer of nonlinear kinetic energy from the turbulence into the ZF via RS was obtained, sufficient to explain the initial turbulence reduction. The time sequence of the transition was as follows: first a peaking of the normalized Reynolds power, then a collapse of the turbulence, and finally a rise of the diamagnetic electric field shear as the L–H transition occurs. Measurements were compared with a one-predator, one-prey model which explicitly retains the RS flow drive [599]. A fast, forced bifurcation of turbulence and transport in electrostatic nonlinear GK XGC1 simulations [627] confirmed the underlying assumptions of the PP model, except that ion-orbit loss mechanisms were also critical to the bifurcation and work together. A synergy between RS and orbit-loss forces may help to reconcile observations that ascribe the L–H transition to orbit-loss, or neoclassical effects, or to the role of turbulent RS.

18.4. H-mode

Until recently there were no reports of GAM observations in high confinement H-mode conditions. The GAM's absence is generally attributed to reduced nonlinear drive and strong suppression of turbulence in the edge E_r shear region. However, it is also known that the edge turbulence can recover in H-modes to almost L-mode-like levels due to profile steepening, cf [628]. This effect appears to be supported by recent GAM observations in natural ELM-free H-mode conditions in the EAST tokamak.

As shown in figure 122 [42] the GAM initially disappears just before the spontaneous L–H transition as the turbulence level collapses—as is generally observed in many devices. However, in some discharge conditions with dominant RF and ECH heating the turbulence level recovers in the edge, and, when exceeding a certain value the GAM reappears with a higher frequency and a stronger intensity (and larger bicoherence) than in the preceding L-mode. This is attributed to the steeper H-mode edge gradients driving the turbulence to higher levels. In addition the GAM radial structure is seen to change from a wide continuum to a radially narrow eigenmode close to the separatrix. During this ELM-free phase the GAM is accompanied by an edge coherent mode. With the subsequent onset of ELMs the GAM is then diminished. There are hints of residual GAM bursts during the ELMy phase.

Experiments in H-1 [403, 404] report a strong GAM shear oscillation prior to an L–H transition [436], as well as a ZF sustaining the transport barrier once in H-mode [629] via spectral condensation.

H-mode confinement can also be induced with edge DC biasing. As noted, in section 11.4.2 several devices report the formation of a ZFO in the near edge region as H-modes form. In some cases these appear to be transitory, in others they are more persistent. A particular case is the steady-state ELM-free H-mode induced by positive biasing in J-TEXT where the GAM intensity was enhanced around the radial location of the edge biasing [390]. However, coinciding with the increased

edge ∇n_e in the H-mode there is a strong reduction in local edge turbulence as well as the radial particle flux $\Gamma_r(f)$ (over preceding ohmic levels), particularly around the GAM frequency. In some discharges the GAM was found to take the dominant role while in others it was replaced by an $f < 2$ kHz ZFO. The GAM and ZFO never appeared together with some form of competition evident. This ZFO vs GAM exclusiveness is consistent with observations during L–H transitions in various devices.

In either case an enhanced ZFO or GAM (via stronger gradients) in the H-mode means enhanced drive via non-linear coupling with the consequent implication is that it is not the overall level of edge turbulence per se—particularly the long wavelength fluctuations which are more closely associated with radial transport—but the short wavelength turbulence that is important to the ZFs. The GAM shearing can promote energy movement to the high k turbulence, as well as impacting the turbulence cross-phases, and thus the transport. This is an area that requires further investigation.

ELMs are an inherent feature of H-modes with steep edge pressure gradients and are often linked with the destabilization of ideal peeling–ballooning modes. During the repetitive ELM cycle the edge transport barrier/pedestal collapses back towards L-mode conditions. During such intra-ELM phases the formation of edge GAMs might occur. This has not been studied experimentally, but the role of edge ZF/GAMs in the pedestal collapse has been modelled using a non-linear three-field MHD model in the BOUT++ code where bursts of strong zonal vorticity together with geodesic curvature coupling are observed to drive GAM oscillations [630]. The model results suggest that compound ELMs will be accompanied by the strong excitation of GAM perturbations leading to a sequence of smaller secondary pedestal crashes.

Finally, in the more general context of transport barriers, in CHS a causal link was suggested between the amplitude of a core SZF which increased with the formation of an internal transport barrier (ITB) and higher frequency E_r fluctuation components which decreased [398].

18.5. I-mode and the weakly coherent mode

The I-mode is an ELM-free improved confinement regime observed in some tokamaks, notably AUG, Alcator C-Mod, DIII-D and more recently EAST. When operated with an ion $\nabla B \times B$ drift direction away from the X-point or field null of the last closed flux surface the H-mode power threshold is twice that of the favourable direction [631]. The I-mode is characterized by an H-mode like temperature (energy) barrier but an L-mode like density (particle) transport barrier. While ELMs are absent, due to the weaker edge pressure gradient, they are replaced by a weakly coherent mode (WCM) in the density and magnetic fluctuations ($f \sim 100$–300 kHz) located around the temperature pedestal top—which is thought to regulate the particle transport [377].

In Alcator C-Mod the GAM appears to be a key component in the I-mode dynamics. As shown in the example in figure 123 [377], the I-mode forms when the GAM becomes accessible, i.e. the non-linear drive exceeds the collisional damping, and terminates when the GAM is either damped-out by a transition to a high density L-mode, or when the mean velocity shear becomes sufficient to suppress the long wavelength edge turbulence and promote a transition to H-mode. Similar results were obtained in AUG I-mode conditions where the preceding (high density) L-mode phase shows no strong GAM (collisionally damped or nonlinear drive too weak), but appears when sufficiently driven in the I-mode phase, that is when $\gamma_{NL} > \gamma_{col}$ [307].

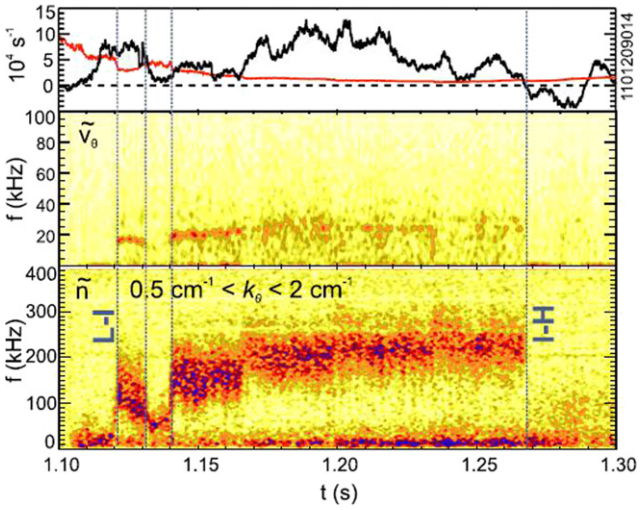

Figure 123. Time trace of (*a*) non-linear GAM drive (black) and collisional damping (red), (*b*) poloidal flow spectrogram and (*c*) low k density fluctuation spectrogram over L–I–H transition in C-Mod. Reprinted from [377], with the permission of AIP Publishing.

Non-linear studies using cross-bispectral measurements show that the GAM is coupled to the WCM with energy moving from the WCM peak to the GAM [377], and then through scattering back into lower and higher frequencies, i.e. creating the broadening of the WCM [307]. The actual origin of the WCM is, however, currently unknown. It was speculated [377, 379] that a geodesic Alfvénic mode resulting from coupling of the ZF, not only to the pressure sideband, but to global Aflvénic modes could be involved, however, this interpretation is not universal [307].

On EAST a strong GAM is reported in the preceding L-mode [369] which is then reduced and gradually supplanted by a low frequency (5–10 kHz) oscillation during the I-mode. This oscillation is observed in density, electron temperature, and indeed in nearly all diagnostics. Although the GAM was reduced at the WCM peak location, it may still be present at other radial positions, which were not probed. The low frequency oscillation did not appear to conform to either a LCO nor dithering. Bicoherence analysis did show significant non-linear three-wave coupling between the ambient/background turbulence and both the low frequency oscillation and WCM at the WCM location. Together with measurements of its toroidal symmetry this suggests the low frequency oscillation could be a ZFO. For the EAST conditions it seems that this 'ZFO' may replace the function of the GAM in the C-Mod and AUG I-modes. There are currently no reports of ZF activity during I-modes in DIII-D, nor has the WCM been detected [632].

In summary, the L–H transition is linked with a spatially localized spike in RS, often accompanied by enhanced GAM or ZFO activity. The intermediate I-phase which can form between the L and H-mode conditions is associated with a LCO involving periodic enhancement of GAM or ZFO velocity shearing and turbulence suppression. The GAM can briefly reappear in H-mode as the turbulence rebuilds with steepened edge pressure gradients. In the high density improved confinement I-mode the GAM was linked with a weakly coherent edge mode and appears in moments when the nonlinear drive exceeds the collisional damping $\gamma_{\rm NL} > \gamma_{\rm col}$.

19. Conclusions and outlook

ZFs are an intrinsic consequence of plasma turbulence and form an indispensable element in the control and mitigation of turbulent transport in magnetic confinement devices. GAMs (in all their various guises) are the oscillatory branch of the ZF phenomena and arise naturally from the geodesic magnetic curvature and compressability of poloidal flow in toroidal systems. In tokamak devices GAMs appear in the confined plasma edge region making them particularly amenable to experimental investigation by well developed diagnostic techniques. Not least due to the role of GAMs in mitigating turbulent edge transport, this has triggered great interest from experiment, theory and simulations, and indeed has lead to a phenomenal number of publications in recent years. The topic has reached a sufficiently mature state to warrant a dedicated and comprehensive review of the experimental and theoretical developments. Since the first major review of ZF and GAM physics [53] there have been tremendous advances on several fronts, which are summarized in the following. However, this progress does not mean that GAMs are now fully understood, nor that the topic has stagnated—to the contrary the field remains very active with new results proliferating every month. There is still much to be investigated. Some of the unresolved issues and opportunities for future research are also outlined below.

19.1. Summary

19.1.1. Hierarchy. The GAM is part of a broader hierarchy of flows in toroidal devices, as illustrated in table 17. Both mean neoclassical and nonlinear turbulence driven stationary (zero-mean-frequency) zonal flows (SZFs) are subject to strong poloidal damping with an incompressible plasma response. For the standard natural ω_+ GAM (also driven by nonlinear turbulence) the flow resonates with passing/transit ions at a frequency that elicits a compressible response, and thus a pressure sideband. In between the SZF and the GAM is a branch of low frequency ZFO generated by various linear mechanisms, which may have a compressible or incompressible response depending on their frequency. The GAM is basically a bulk plasma pressure phenomena. FLR and FOW effects add dispersion, positive due to the ions, and negative due to the electrons, which partially offsets the ion positive dispersion effects. Dispersion leads to radial propagation of the GAM, in which the radial profiles of plasma parameters also play important roles. Adding fast ions initially modifies the natural GAM behaviour, but with sufficiently energetic particles (EPs) a new branch opens to form the EGAM with frequencies that typically chirp around the standard GAM frequency.

19.1.2. Zonal flow oscillations. In realistic tokamak plasmas drift effects due to finite diamagnetic gradients will also modify the GAM dispersion relation. For a density gradient ∇n this adds a frequency correction term ω_{1*}, while for a temperature gradient ∇T the dispersion relation acquires a second low frequency ZFO root ω_-. For $\omega_{1*} = 0$ the ZFO degenerates into the stationary zero-mean-frequency SZF. Similar low frequency roots are destabilized by pressure anisotropy $p_\perp \neq p_\parallel$ or by plasma rotation $\mathbf{v}$. In each case an increasing degree of asymmetry in p, ∇p or $\mathbf{v}$, raises the mode frequency of each root. Trapped ions (typically within toroidal and helical magnetic field ripple) can drift radially creating a radial current and thus also drive a low frequency flow oscillation with an acoustic and magnetic configuration scaling dependency. These kind of ZFOs are predicted and simulated, but not yet (conclusively) observed experimentally. Experimental validation is eagerly awaited.

19.1.3. ZFO/GAM transitions. While the zero-frequency SZF elicits an incompressible response where poloidal flow perturbations are compensated by a toroidal flow, the GAM response is compressible with a pressure sideband compensating the flow perturbation. For the ZFO, if its frequency is sufficiently large, $\omega_- > \nu_{\rm ii}/\epsilon^\gamma$, such as in the core of a well-heated ($\nu_{\rm ii} \ll$ 1 kHz) or strongly rotating tokamak plasma, then it will acquire an $m = 1$ pressure sideband and convert to a GAM, and thus also be subject to Landau damping. Thus, in realistic fusion plasma conditions it is questionable if a pure SZF can exist. Although ZFOs have been observed experimentally there is a critical absence of sideband structure measurements to confirm its ZF or GAM nature in specific conditions. Here, more experimental data would be valuable—for example elucidation of the ZF to GAM transition threshold and the onset of sideband formation with rotation would seem straightforward. However, around the transition where the response may be complex with a combination of parallel flow response and pressure sidebands, it may be challenging to clearly distinguish between a ZFO and a GAM.

19.1.4. Localization. The GAM is susceptible to parallel ion Landau damping, which generally restricts it to the high q tokamak edge or the low ι stellarator core regions, as well as to ion–ion collisions which damp it at high densities and/or low temperatures in the very edge. On the other hand the SZF is predominantly collisionally damped and thus tends to be core localized. Nevertheless, there are observations of core GAMs appearing under conditions where $T_{\rm e}/T_{\rm i}$ is large leading to reduced Landau damping. EP driven GAMs also tend to be localized around the EP beam interaction region.

19.1.5. Dependencies. The basic GAM behaviour is well established by experiment. Its frequency scales acoustically with $\omega_{\rm GAM} = Gc_{\rm s}/R_0$ where G is a shape dependent factor of $\mathcal{O}(1)$. Generally, modelling and simulations are advanced, drawing from both MHD/fluid and GK models. Here, the

basic dependencies have been identified and quantitative comparisons with experiments made—in several specific cases (mostly circular, low beta, etc) with good agreement. In more realistic configurations with shaping the agreement is promising, but not fully conclusive. For example, current analytic models and numerical simulations do not fully treat the presence of a field null (X-point). Numerical simulations using realistic experimental equilibria have come closest with grids reaching out to $\rho \approx 0.97$, but the GAM behaviour close to the seperatrix is still not properly resolved. There are also several other areas requiring further investigation. The sound speed c_s is a function of the ion adiabatic index γ_i and effective mass $m_{\rm eff}$. Experiments suggest that γ_i may vary between 1 (isothermal) in the core to 7/4 (dissipation-free adiabatic) in the edge, depending on plasma conditions, etc. However, the parameter variation is not firmly established. Another unknown is the effect of nonlinear GAM self-interaction where the GAM amplitude may pull its frequency either up or down by potentially significant amounts. Current modelling offers contradictory results. Finally, the plasma size impacts several parameters. The inverse aspect ratio $\epsilon = a/R_0$ enters weakly in GAM frequency models, while the major radius R_0 more strongly with an inverse $\omega_{\rm GAM} \propto c_s/R_0$ scaling. Thus in larger fusion devices, e.g. ITER and DEMO, this R_0 scaling may offset the effect of stronger plasma heating. Lowering the GAM frequency may be seen as desirable due to possible more effective velocity shearing of turbulence structures. The plasma minor radius a also enters into the so-called mesoscale which experimentally appears to set the GAM zonal width $\Delta_r \sim \sqrt{a\rho_s}$. Wider zonal layers may be expected in ITER with consequent wider turbulence shearing regions. To validate such dependencies requires a comprehensive multi-machine comparison from small to medium to large sized machines, and from low aspect ratios to tight spherical tokamaks. To be useful, such a database will need to be comprehensively populated with full sets of parameter profiles.

19.1.6. Sidebands. The $n = m = 0$ flow/potential and the $n = 0, m = 1$ density component of the pressure sideband structure have been confirmed experimentally. There are also direct measurements of a T_e component as well as suggestive α_{nT} fluctuation cross phase angles which indicate a significant $\tilde{T}_e$ role in the pressure sideband. T_i fluctuations at the GAM frequency need further investigation. The de-phasing of $\tilde{n}_{\rm GAM}$ and $\tilde{T}_{\rm GAM}$ through shearing action may also be an important factor in the GAM behaviour. Magnetic sidebands with an appropriate $m = 2$ dominant poloidal structure have been observed experimentally. With strongly shaped equilibria the poloidal structure takes a more complex form with additional harmonics and poloidal asymmetries/tilting. There are some indications that strong edge GAMs may couple across the LCFS or separatrix to the open-field lines of the SOL, driving parallel particle fluxes at the GAM frequency. The potential impact on divertor fluxes is important and thus further investigation and validation is warranted.

19.1.7. Damping. The magnitude of a GAM is essentially set by the drive and damping rates. There are extensive measurements and validation studies of the linear collisional and nonlinear Landau damping with sophisticated theory/modelling predictions. Currently the overall agreement is far from perfect. Less studied is the role of continuum damping and phase-mixing (PM) due to finite temperature gradients. Here, predictions are advanced but, as yet, no experimental comparison studies have considered this effect.

19.1.8. Nonlinear turbulence drive. The existence of three-wave coupling between ambient high-frequency turbulence and the various low-frequency ZF modes has been demonstrated via bicoherence analysis of experimental and numerical simulation signals. Experimentally the total (frequency summed) bicoherence b^2_Σ, as a measure of the total nonlinear coupling, scales with the GAM amplitude $A_{\rm GAM}$, consistent with Reynold stress (RS) (turbulent structure tilting) being the dominant drive mechanism. Nevertheless, observations of modulation of the turbulence strength and radial cross-field particle transport at the GAM frequency suggest that dynamic flow shearing (DS) also plays a significant role in the GAM–turbulence interaction.

19.1.9. Energy flow. The turbulence energy flow has both spectral and spatial aspects. Using a variety of data analysis techniques, experiments support the standard picture of energy moving from the high-frequency/short-wavelength turbulence to the low frequency $m = 0$ ZFO and GAM flow oscillations. There is also evidence that the GAM and ZFO compete for the turbulent energy transfer—which one dominates appears to depend on specific plasma/device conditions. Spatially the $A_{\rm GAM}$ follows the b^2_Σ radial profile with both showing maxima aligning with the location of maximum turbulence, i.e. max $\nabla p(r)$ pressure gradient and minimal mean (equilibrium) velocity shear $\nabla v_{E_r \times B}$. This is supported by measurements of the flow $\tilde{v}$ and turbulence $\tilde{n}_e$ cross-phase $\alpha \approx 0/\pi$, implying modulation of the GAM amplitude consistent with DS. Thus the GAM is driven spatially where the turbulence energy is injected. As the GAM propagates away from the radial maxima (both inward and outward—depending on conditions) the $\alpha \to \pi/2$ implying frequency/phase modulation, consistent with GAM velocity shearing, and thus turbulence moderation either side of the GAM peak. Spectrally, the impact of the ZF/GAM shear flow is to help break up the low-k density turbulence structures and thus move energy back to the higher-k turbulence region, and dissipation.

19.1.10. Nonlinear GAM self-interaction. Several effects arising from GAM nonlinear self-interaction have been predicted by theory. These include a frequency pulling effect correlated with the GAM amplitude. Benchmarking studies of the GAM frequency show unresolved discrepancies between experiment and theory/model predictions, which at least leave room for nonlinear effects. More precise studies on the GAM frequency–amplitude interrelation are required. Another nonlinear RS self-interaction effect is the creation of higher GAM harmonics and SZFs. These are suggested by theory and appear at least to be partially supported by experiment. This opens the possibility of a particularly interesting concept of

driving SZF/ZFOs, and thus impacting turbulent transport, in conditions and regions where they would normally be damped.

19.1.11. Total GAM suppression. In plasma regions or conditions with strong damping or weak drive due to below-excitation threshold gradients, measurements indicate the coherent GAM oscillation is replaced by an overall enhancement of broad-band incoherent flow perturbations. This is not inconsistent with theory where, even if the GAM resonance is lost, the geodesic forcing still occurs at all frequencies. In such cases the enhanced random velocity shearing might still be a significant. Another factor is the width of turbulence wavenumber spectrum. If the turbulence spectrum is narrowed, i.e. the k-spectra cascade is truncated for whatever reason, then the three-wave coupling condition may no longer be satisfied for the GAM, leaving the turbulence energy to go entirely into a low frequency ZFO. Further, the formation of strong pressure gradients in the edge or ITB regions lead to strong mean $E \times B$ velocity shearing—which experimentally also appears to reduce the GAM. Further, corresponding steep edge temperature gradients will also increase PM and continuum damping and thus impacting the GAM existence in enhanced confinement regimes. More detailed studies of the mean and oscillatory flow shear interdependence in these conditions are warranted.

19.1.12. Energetic particle GAMs. EGAMs form a direct energy path from EPs to the turbulence. They cause radial transport of the EPs, they may affect micro-turbulence by their shear flow, and in addition they may heat ions directly through the so-called GAM-channelling. Theory also indicates potentially significant induced toroidal momentum (so-called GAM momentum channelling)—as yet to be confirmed experimentally. For fusion reactors, EPs resulting from fusion products and EGAMs are particularly noteworthy subjects. Hitherto, EGAMs are observed in low density plasmas where the anisotropy in the velocity space of the EPs is sustained. An outstanding question is whether EGAMs can be excited in fusion reactor conditions at higher densities. Nevertheless, there are strong indications that they can since the energy of the fusion products will be much higher than the temperature of the bulk plasma, and the slowing-down time will be longer than in present plasmas. Further fusion grade experiments and numerical simulations are expected.

19.1.13. External drive. While GAMs are primarily associated with turbulence or EPs, there are other mechanisms that can also potentially drive GAMs. External drive techniques, such as modulation of the temperature profile via localized electron cyclotron resonance heating, or via vertical kicks to the equilibrium using external magnetic perturbation coils have been proposed, but as yet have not proven to be effective in experiments. On the other hand, modulation of the edge E_r/potential via limiter or probe biasing has been shown to be effective in amplifying GAMs in small machines. An external control of the GAM magnitude would offer a potential mechanism for influencing the edge transport and confinement, but its application to fusion grade experiments remains an interesting challenge.

19.1.14. Radial propagation. With the inclusion of dispersion effects the GAM is expected to propagate radially. Early theory predicted an outward propagation, down the T_e gradient. However, experiments as well as numerical simulations show the GAM to propagate both inward and outward. In conditions where a clear A_{GAM} peak or drive region can be identified, the GAM appears to propagate away from it. In particular, observations of the local GAM k_r and flow-turbulence cross-phases reversing sign across the GAM maxima appear conclusive. Nevertheless, the presence of boundaries (separatrix and pedestals) may also lead to standing-wave structures forming. In general, the description of the GAM as an eigenmode with a local k_r is expected to be insufficient, in particular in elongated and up–down asymmetric plasma shapes and with large radial gradients of plasma parameters. A radial acceleration of the GAM is also predicted, but as yet not measured. Propagating GAMs have also been indicated as a possible mechanism for density turbulence spreading and radial propagation via so-called turbulence trapping effects. These remain fruitful topics for future research.

19.1.15. Continuum vs eigenmodes. Theory predicts the GAM may take one of several forms: (i) a radial continuum with $\omega_{GAM} \propto c_s$, described by fluid or kinetic models as a singular narrow mode with a frequency scaling with the local parameters; or (ii) a radial eigenmode where $\omega \sim$ const. formed by profile gradients with PM, FOW (radial drifting of orbits) or FLR (temperature) effects and radially propagating GAM-packets, or (iii) a global eigenmode (GGAM) formed by the GAM coupling to a non-localized $m = 2$ magnetic sideband and/or electrostatic $m = 2$ modes around an off-axis maxima in the continuum frequency. Experimentally all three forms are observed. Generally, with increasing temperature the continuum breaks into one or more extended rings (staircases) of frequency plateaus and amplitude peaks. Plateau widths are in the mesoscale range but scale with the profile scale lengths L_T. The discrimination of small staircase steps from a pure continuum is an issue of diagnostic and measurement resolution. EGAMs always display a global nature, but turbulence driven GGAMs are more rare. Radially overlapping multiple eigenmode GAMs have also been observed experimentally. In such cases the eigen-frequency matches or crosses the continuum frequency at the GAM amplitude maxima. The complex interplay of the GAM generation and sources, profile effects, such as damping due to propagation, and the formation of (especially multiple) eigenmodes are not yet well understood. In particular the GAM width is poorly predicted. On the measurement side the exact mechanism of the GAM generation and its spatial localization is also not yet established over the full range of experimental conditions. Much more work is required here.

19.1.16. Transport. The GAM impact on transport and confinement is a critical issue. Primary is the GAM contribution to the velocity shearing of turbulent radial structures—moving energy from low-k to high-k—in which the GAM shearing rate, strength and radial extent are relevant. Spatially the GAM shearing appears not at the GAM radial maxima, but to either

side as the GAM propagates. Concerning the cross-field particle transport flux $\Gamma_r = \langle \tilde{E}_\theta \tilde{n}_e \rangle / B$, the GAM modulates the high frequency $\tilde{n}_e$ turbulence and the relative turbulent $E - n$ cross-phase. Transport modulations in turn may drive the GAM through DS. Much of the radial transport appears in the form of intermittent bursts, a feature commonly associated with nearness to criticality. Criticality is also apparent in the onset ∇p threshold for the GAM drive—observed both experimentally and theoretically. It has also been noted that zonal structures may trigger NTMs and radial transport avalanches leading to intermittent heat flux events. The role of GAMs in promoting or hindering avalanches and streamers (eigenmode GAMs vs velocity shearing, and the type of edge turbulence, i.e. ITG vs TEM-like) requires further investigation. With EGAMs there are other potential effects including bulk ion heating (GAM channelling) as well as turbulence wave-trapping and spreading. These also require further experimental investigation.

19.1.17. GAM modulation. A related transport effect is the low frequency temporal modulation of the GAM intensity and frequency. The larger machines generally show small to moderate (50%) modulation of the GAM amplitude at a few tens to hundreds of Hz, often synchronized with a modulation or chirping of the GAM frequency—which is highly suggestive of modulation by a ZFO. In smaller devices the tendency is to a more bursty GAM nature with short, intermittent bursts of GAM activity lasting a few GAM cycles. A particularly salient observation is that the GAM modulations/bursts become phase decorrelated in time, that is each burst is a new GAM. Comparing the GAM flow auto-correlation time τ and spectral width Δf_{pk} gives insights in the GAM drive and decay rates (linear and nonlinear damping). In most cases the GAM dynamics appear to be dominated by the damping rate rather than the turbulence dynamics. However, the database of observations is not conclusive. An intermittent turbulence drive on the other hand would be more consistent with the bursty GAM observations and the temporal de-phasing.

19.1.18. Confinement modes. A much discussed topic is the role of the GAM/ZFO velocity shear in assisting the mean $E_r \times B$ flow shear to trigger a high confinement H-mode bifurcation. The evidence for such a role is compelling. Of less importance perhaps is whether it is a GAM or a ZFO, since the predominance of one or the other, their mutual exclusiveness or competition or transformation from one to another, appears to be machine or plasma dependent. Once in H-mode the edge turbulence reduction and strong mean equilibrium velocity shearing generally reduce the GAM to below detection levels. Nevertheless, with sufficient drive/suitable conditions GAMs are observed to reappear in weak, as well as bias induced ELM-free H-modes. Of particular interest are numerical simulations showing GAMs forming in the intra-ELM cycle where the plasma edge momentarily falls back into L-mode with consequent increased edge turbulence. This has yet to be studied experimentally. The possibility of GAM shearing playing a role in the ELM cycle (an LCO similar to the I-phase) is a question of time scales. Nevertheless, an interesting topic for investigation. For the improved confinement I-mode regime the GAM appeared to be critical in some devices in maintaining the weakly-coherent-mode and the favourable edge transport conditions. However, not all devices are in agreement. More measurements, particularly of the full edge flow spectrum, are required to confirm the role of GAMs or ZFOs.

19.1.19. Non-axisymmetric. In non-axisymmtric field configurations, such as stellerators and helical devices, an extra level of complexity is added to the GAM dispersion relation. Nevertheless, the GAMs observed to-date are qualitatively similar to those in tokamaks. There are some stellarator specifics, such as the loss of the up–down asymmetry in the sideband—which now rotates with the helical pitch. The intrinsic nonambipolarity in non-axisymmetric systems leads to electron and ion roots. The switching of roots changes the E_r profile and shearing—and tentatively appears to impact the ZF behaviour. Toroidal rotation is distinctly slower in stellarators and consequently has a lesser role in the GAM/ZFO behaviour. Not least is the stronger edge ripple and the formation of trapped particle driven ZFOs and GAMs. Observations of such modes and their sideband structure are eagerly awaited, and likewise for evidence of the predicted $n \neq 0$ modes. Still at an early stage of understanding is the formation of GAMs by magnetic islands, and GAM entrainment by external magnetic perturbations. Notably missing are 3D measurements of the GAM mode structure in these conditions.

19.2. Outlook

In the previous section various specific issues, in terms of missing or desirable new measurements and analytic theory or numerical simulations, were highlighted. In this section more general issues concerning future directions in the field of GAM studies as well as limitations and problems are discussed

- A range of high quality diagnostics have been used in the study of ZFs, but, often lacking are comprehensive sets of simultaneous measurements of the flow oscillations, their structure (as well as their sidebands to confirm the ZFO or GAM identity), together with high-k measurements of the ambient flow and density turbulence, its properties and structure. This is a demanding task experimentally. In principle these diagnostic capabilities are currently available for the tokamak edge, but require work to deploy together.
- Improved diagnostic capability, particularly for detecting GAMs in low turbulence core and edge conditions is always desirable. For the core only HIBP is reliably deployed. It is possible that significant ZFO/GAM activity is being missed, as well as under reporting of the GAM's radial extent. Finer radial resolution may reveal more staircase structures. Extending the existing, well developed edge diagnostic techniques to probing the difficult transition region between edge and core is demanding, nevertheless, it is here that the physics of ZFOs may be advanced.
- The GAM/ZFO role in the L to H-mode transition, as well as a possible role in the ELM cycle was noted

above. However, future tokamak fusion devices may operate in alternate ELM-free H-mode scenarios, as well as so-called 'advanced' discharge scenarios with significant core plasma current drive leading to enhanced q and steeper kinetic profile gradients, even to the formation of ITBs. Such conditions maybe rather favorable for GAMs.

- GAMs are a multifaceted phenomena which appear in different conditions. Many of the experimental tasks noted above still require theoretical explanations/understanding. Although analytical models are instructive and provided insights on many GAM features and behaviour, they are limited. The role of comprehensive nonlinear gyro-kinetic simulations remains paramount.
- ZF and GAM theories require better integration. The interaction, coupling and transitions between GAMs and ZFs needs further study. Fundamentally it is all a question of plasma rotation (poloidal and toroidal) which can be stationary, stable oscillatory, with some linearly unstable branches, and can be driven nonlinearly by drift wave instabilities. The theory needs to address the role of compressibility vs toroidal rotation in ZFs and role of trapped particles (neoclassical effects) on GAMs.
- Real confinement devices have complex geometries, such as X-points and strong up–down asymmetries. Recently there is renewed interest in negative triangularity shapes. These configurations are very difficult to model analytically, while numerical simulations require particularly demanding grid resolutions.
- The coupling of GAMs into the SOL region is not well understood theoretically. The impact of possible GAM driven SOL flows on the divertors may be rather important.
- A related question is whether radially structured SZF/ZFOs may form just inside the tokamak separatrix in low collisionality conditions. Such ZFs could significantly affect the mean equilibrium $E_r \times B$ flow shear across the LCFS, with a consequent impact on L–H transition physics. This is a question for both experiment and simulations. Nevertheless, careful discrimination between SZF/ZFOs and $\langle p \rangle$ diamagnetic flows, which may result from avalanches, streamers and transport events that have nothing to do with ZFs [53] is required.
- In general, the role of ZFOs vs SZF needs thorough investigation, both experimentally and numerically, particularly in conditions, such as strongly rotating core plasmas, where the ZFO may play the turbulence control role mechanism rather than the SZF.
- The topic of GAM/EGAM self-interaction, nonlinear and phase-space structures, saturation and effects on transport is an underdeveloped area of investigation.
- Energetic fusion alpha-particle driven EGAMs are predicted to be critical features in the next step devices. Fully understanding the EGAM drive and channelling capabilities should be a priority topic.
- The nature of the GAM eigenmode structure remains unclear. Theory presents a series of models which are not fully consistent with experiment. In particular, the eigenmode width is not well predicted. Further, there is a need to understand the difference between ultra-wide eigenmodes and the theoretical global GGAMs. Are the structures determined by the drive and damping profiles alone?
- So far the GGAM has only been studied with MHD codes. Global EM GK capabilities are required to extend these studies to include, and kinetic effects, etc.
- Finally, while many critical results have been obtained on individual devices, full theory/simulation validations requires detailed cross-machine comparisons. However, these are hampered by poor reporting of the general measurement conditions and basic plasma parameter profiles. The formation of well documented cross-machine databases would greatly assist qualified parameter scaling studies.

The experimental research on ZFs was once characterized [53] as still in its youth. In the last years, advances in studies of GAMs as the oscillatory branch of the ZF phenomena arising in toroidal systems, show that the field has advanced in years to quite a maturity—but the topic is far from closed with much to still resolve. GAMs offer many opportunities for basic turbulence studies as well as nonlinear phenomena in general. GAMs, both low frequency core (ZFOs) and high frequency edge will remain relevant in progressing the performance of current and future magnetic confinement devices.

Acknowledgments

We would like to thank our many collaborators for their contributions over the years to our understanding of the physics of the GAM, including (alphabetically): A. Biancalani, X. Garbet, K. Hallatschek, P. Hennequin, V. Ilgisonis, A. Krämer-Flecken, V.P. Lakhin, P. Lauber, F. Palermo, B.D. Scott, C. Silva, P. Simon, and E. Sorokina. We would also like to acknowledge H. Berk, V. Bulanin, S. Coda, T. Estrada, A. Fujisawa, J.P. Graves, R. Hager, T.S. Hahm, Y. Hamada, P. Helander, E. Holzhauer, Z. Huang, K. Itoh, T. Kobayashi, M. Lesur, G.R. McKee, A. Melnikov, A. Mishchenko, Y. Nagashima, T. Nishizawa, M. Sasaki, A. Shimizu, A. von Stechow, K. Toi, G.R. Tynan, L. Vermare, C. Wahlberg, H. Wang, T. Watari, A. Yashin, D. Zarzoso, W. Zholobenko, and S. Zoletnik for fruitful discussions. Our apologies to those we may have forgotten. Finally, we are particularly grateful to X. Garbet, F. Palermo, A. Krämer-Flecken and H. Zohm for reading and commenting on draft versions of the manuscript, as well as to the anonymous referees for their incisive and constructive comments. We also thank the numerous authors cited in this work for permission to reproduce their figures. This work was partly supported by NSERC Canada and was also partly carried out within the framework of the EUROfusion Consortium and has received funding from the Euratom research and training programme 2014–2018 and 2019–2020 under Grant Agreement No. 633053. The views and opinions expressed herein do not necessarily reflect those of the European Commission.

Appendix A. GAM as diagnostic

In principle, measurements of the GAM properties might also be used as a diagnostic for other plasma parameters. Several possible applications have been suggested, including:

GAM spectroscopy: for continuum GAMs, and at the spatial peak of eigenmode GAMs where $k_r \to 0$ is predicted and the eigen-frequency should align with the local GAM continuum frequency, the GAM frequency may provide a measure of the local ion sound speed c_s. And, when combined with additional information on the local T_i, T_e and n_e kinetic profiles the sound speed may then provide a measure of the ion composition, i.e. the effective mass m_{eff}. This technique was termed GAM spectroscopy [256].

Similarly, Alfvén spectroscopy using energetic-particle driven modes has been adopted by measuring the frequency and mode numbers of Alfvén eigenmodes, which are determined by the safety factor and the mass density [633]. For example, the temporal evolution of the minimum of the safety factor q_{min} in reversed shear configurations can be deduced [634]. Since the EGAM is an acoustic wave the parameter dependence of its frequency is different from that of Alfvén eigenmodes (with a dependence on the mass density, but a weak dependence on the safety factor). Thus from the simultaneous observation of Alfvén cascades and EGAMs it may be possible to deduce q_{min} and the mass density [70].

The caveat of course is the additional requirement of knowledge of the plasma shape, as there are many parameters that affect the natural GAM frequency in a realistic shaped plasma. Nevertheless, in fixed geometry conditions, such as in ITER, where the shape and q will be tightly controlled parameters, GAM spectroscopy may provide valuable information. Although in this case GAM frequency shifts might be attributed primarily to mass changes, such as isotope ratios, the role of impurity dilution (in a D_2 plasma) still needs to be accounted for. For the EGAM, the influence of the velocity space distribution of the EPs also needs to be considered.

q profile: in cases where a GAM and an ion acoustic mode (IAM) exist simultaneously, then from the ratio between the lowest frequency of the IAM (SW) $\omega_{SW} \approx c_s/(qR_0)$ and the GAM frequency (which is not strongly dependent on q) one might extract the safety factor of toroidal plasmas [635]. In such conditions when both a GAM and an IAM may be excited, for example in the plasma edge of tokamaks (high q) where the IAM is expected to have a slower damping rate than the ZFO, then bispectral analysis techniques can be used as an indicator of the coupling behaviour for co-existing modes. In the case of a coexisting GAM and a low-frequency ZFO (in a rotating plasma), the respective frequencies are predicted to be linked, e.g. $f_{ZFO} = 1/q\sqrt{3/14}f_{GAM}$ [85], thus allowing the q (profile) to be simply extracted from the frequency ratio.

Surface location: the GAM $m = n = 0$ mode structure and narrow radial extent can be exploited as a means of identifying the radial location (to an accuracy to a few gyroradii) of a specific iso-magnetic surface through long-range-correlation measurements of the flow perturbation [636]. Further, on the assumption that the GAM exists only on closed flux surfaces this may also be used as a rough locator for the tokamak last closed flux-surface or separatrix position (noting that the GAM may be suppressed close to the separatrix due to increasing collisionality) [322].

Appendix B. Data analysis methods

B.1. Bispectral analysis

Bispectral analysis is a well established technique for investigating nonlinear processes in turbulent systems, cf [528], and can directly indicate three-wave couplings in plasma drift-wave type turbulence, cf [529, 530]. Similar to the standard (second-order correlation) cross power spectrum:

$$\hat{P}_{xy}(f) = \langle X(f)\, Y^*(f) \rangle \tag{B.1}$$

the general cross-bispectrum (i.e. third-order correlation) is defined as

$$\hat{B}_{xyz}(f_1, f_2) = \langle X(f_1)\, Y(f_2)\, Z^*(f_3) \rangle\,, \tag{B.2}$$

where X, Y, Z are the Fourier transforms of time signals x, y and z with $f_3 = f_1 + f_2$, and * the complex conjugate. The angled brackets indicate ensemble (time) averaging. Note that three-wave coupling is a wavenumber space phenomena $k_3 = k_1 + k_2$—when using the frequency space this assumes the k-matching as a constraint [347, 637]. The squared bicoherence and biphase spectra are further defined as

$$b^2_{xyz}(f_1, f_2) = |\hat{B}_{xyz}(f_1, f_2)|^2 / \langle X(f_1)\, Y(f_2) \rangle \left\langle Z(f_3)^2 \right\rangle \tag{B.3}$$

$$\theta_{xyz}(f_1, f_2) = \tan^{-1}\left(\mathrm{Im}\, \hat{B}_{xyz}(f_1, f_2) / \mathrm{Re}\, \hat{B}_{xyz}(f_1, f_2) \right). \tag{B.4}$$

For the auto-bispectra and bicoherence $X = Y = Z$ [27]. In the cross bispectrum the ordering of the signal triplet is important. In GAM–turbulence studies common signal combinations include b^2_{vvn} (flow–flow–density) or $b^2_{\phi n_e n_e}$ (potential–density–density). The choice depends on the model being tested.

Two commonly used indicators of the nonlinear coupling strength are the f_3 normalized summed squared bicoherence spectrum and the total normalized summed squared bicoherence

$$b^2_\Sigma(f_3) = \sum_{f_3 = f_1 + f_2} b^2(f_1, f_2)\, / N(f_3) \tag{B.5}$$

$$b^2_\Sigma = \sum_{f_1} \sum_{f_2} b^2(f_1, f_2)\, / N_{tot}, \tag{B.6}$$

where $b^2_\Sigma(f_3)$ gives a measure of the interaction of the match frequency f_3 with all other frequency components, and the total squared bicoherence b^2_Σ summed over all frequencies as a measure of the total nonlinear activity [347, 530].

B.2. Energy transfer methods

The bispectrum is a real quantity which indicates the strength of the nonlinear couplings within the turbulence, but not the

direction of the energy transfer. For this other techniques are employed.

B.2.1. Power transfer function. This technique developed by Ritz [536] and modified by Kim [537] gives the nonlinear coupling as well as the direction of the energy transfer between different spatial scales. The method uses the Hasegawa–Mima model (single-field turbulence description) [638] to give an energy flow equation in the form

$$\partial P_k/\partial t \approx \gamma_k P_k + \sum_{k_1,k_2} T_k(k_1,k_2), \tag{B.7}$$

where $P_k = \langle X_k X_k^* \rangle$ is the spectral power of some signal $x(k,t)$ at wavenumber $k = k_1 + k_2$. The equation is reformed and solved for the fluctuation linear growth/damping rate γ_k and the nonlinear energy transfer rate $T_k(k_1,k_2)$, with the aid of auto and cross power spectra (2nd-order moments), auto and cross bispectra (3rd-order moments) and 4th order moments of x_k [537]. The method was first demonstrated on DIII-D data on ZFs [639].

A similar derivation [538, 539] (assuming three-wave coupling conditions $k_3 = k_1 + k_2$ and $f_3 = f_1 + f_2$) was obtained for the energy transfer function in the frequency domain

$$F(\omega_1,\omega_2) = [k_\mathrm{r}(\omega_1) + k_\mathrm{r}(\omega_2)]\,\mathrm{Im}\,\langle \tilde{E}_\theta(f_1)\,\tilde{E}_\mathrm{r}(f_2)\,\tilde{E}_\mathrm{r}^*(f_3)\rangle. \tag{B.8}$$

Here, $\langle E_\theta E_\mathrm{r} E_\mathrm{r}^* \rangle$ is essentially the poloidal—radial flow cross-bispectrum.

B.2.2. Kinetic energy transfer. This multi-field (more than one vector field) method developed by Holland [279] takes the continuity equation for an incompressible flow and reformulates it in frequency space to give an expression for the evolution of the turbulence energy $\partial \langle |\tilde{n}_\mathrm{e}(f)|^2 \rangle / \partial t$ as the sum of a linear and nonlinear terms involving a coupling parameter

$$T_n^\alpha(f,f') = -\mathrm{Re}\,\langle \tilde{n}_\mathrm{e}^*(f)\,\tilde{v}_\alpha(f-f')\partial_\alpha \tilde{n}_\mathrm{e}(f')\rangle. \tag{B.9}$$

The parameter T_n^α is essentially a cross-bispectrum which quantifies the rate at which energy is transferred between, in this case density fluctuations (subscript n), at frequency f and poloidal or radial (superscript α) density gradient fluctuations at frequency f', mediated by the poloidal velocity $v_\alpha(f - f')$ fluctuation at a particular spatial location. Holland also recast T in terms of the cross-bicoherence and biphase spectra $\langle n_\mathrm{e} v_y \nabla_y n_\mathrm{e}\rangle$ for poloidal (y-direction) velocity and gradient fluctuations and shows their equivalence (with some nuances) using experimental and simulation data. In standard bispectral notation, $T_n^y(f_1,f_2) = -\mathrm{Re}\,\langle n_\mathrm{e}^*(f_3)\,v_y(f_1)\,\partial_y n_\mathrm{e}(f_2)\rangle$, where $f_3 = f_1 + f_2$. Another multi-field method using Fourier transforms of the electron continuity and momentum equations to give KET rates in the frequency domain results in a similar equation as Holland's [640, 641]. For example, for density fluctuations the transfer rate is given by

$$T_n^\perp(f_3,f_1) = -\mathrm{Re}\,\langle n_\mathrm{e}^*(f_3)\,(\vec{u}_\perp(f_2)\cdot\nabla_\perp)\,n_\mathrm{e}(f_1)\rangle\,. \tag{B.10}$$

B.2.3. Amplitude correlation technique. A related method proposed by Crossley [540] computes the time-delayed cross correlation

$$C(\tau) = \left\langle x^2_{\Delta f_1}(t)\cdot x^2_{\Delta f_2}(t+\tau)\right\rangle \tag{B.11}$$

between two frequency bands Δf_1 and Δf_2 of the same signal (e.g. low and high frequency band-pass ranges below and above the GAM frequency). The sign of the peak correlation time delay then gives the direction of energy flow between the two frequency bands. The PTF and ACT methods have been compared using LP data of ZFOs in H-1 [542, 543].

B.2.4. Envelope correlation analysis. In another related multi-field approach the energy transfer direction is implied from the cross-phase angle (or correlation time lag) between the flow vector and the envelope of the high frequency filtered turbulence scalar. This method draws on the parametric model of ZF generation which states that the GAM flow modulation should also be accompanied by a corresponding modulation of the driving turbulence amplitude envelope at the GAM frequency [53, 221], even though the density fluctuation spectrum itself shows no oscillation at the GAM frequency. A common approach is to compute a Hilbert transform of a band-pass or high-pass filtered ($f > f_\mathrm{GAM}$) scalar turbulent signal to create the analytic signal, the modulus of which gives the amplitude envelope $\mathrm{Env}[A](t) = |A(t) + \mathrm{i}\mathcal{H}[A(t)]|$. The envelope can then be correlated with a flow or potential signal using standard techniques.

ORCID iDs

A.I. Smolyakov https://orcid.org/0000-0002-4975-2743

References

[1] Winsor N., Johnson J.L. and Dawson J.M. 1968 Geodesic acoustic waves in hydromagnetic systems *Phys. Fluids* **11** 2448
[2] Grimm R.C. and Johnson J.L. 1973 Stability analysis of low-pressure axisymmetric toroidal plasma simulations *J. Comput. Phys.* **11** 591–605
[3] Grimm R.C. and Johnson J.L. 1975 Fluid simulation of a low-pressure axisymmetric toroidal plasma using natural coordinates *J. Comput. Phys.* **17** 192–208
[4] Mikhailovsky A.B. 1973 'Drift' instabilities distorting the magnetic surfaces of tokamak-type toroidal systems *Nucl. Fusion* **13** 259
[5] Zonca F., Chen L. and Santoro R.A. 1996 Kinetic theory of low-frequency Alfvén modes in tokamaks *Plasma Phys. Control. Fusion* **38** 2011–28
[6] Hassam A.B. and Drake J.F. 1993 Spontaneous poloidal spin-up of tokamak plasmas: reduced equations, physical mechanism, and sonic regimes *Phys. Fluids* B **5** 4022
[7] Stringer T.E. 1969 Diffusion in toroidal plasmas with radial electric field *Phys. Rev. Lett.* **22** 770
[8] Novakovskii S.V., Liu C.S., Sagdeev R.Z. and Rosenbluth M.N. 1997 The radial electric field dynamics in the neoclassical plasmas *Phys. Plasmas* **4** 4272
[9] Lebedev V.B., Yushmanov P.N., Diamond P.H., Novakovskii S.V. and Smolyakov A.I. 1996 Plateau regime dynamics of the relaxation of poloidal rotation in tokamak plasmas *Phys. Plasmas* **3** 3023

[10] Chen L 2009 Alfvén waves: a journey between space and fusion plasmas *Plasma Phys. Control. Fusion* **50** 124001

[11] Zonca F. and Chen L. 2008 Radial structures and nonlinear excitation of geodesic acoustic modes *Europhys. Lett.* **83** 35001

[12] Berk H.L., Boswell C.J., Borba D., Figueiredo A.C.A., Johnson T., Nave M.F.F., Pinches S.D. and Sharapov S.E. (JET Contributors) 2006 Explanation of the JET $n = 0$ chirping mode *Nucl. Fusion* **46** S888

[13] Boswell C.J., Berk H.L., Borba D.N., Johnson T., Pinches S.D. and Sharapov S.E. 2006 Observation and explanation of the JET chirping mode *Phys. Lett.* A **358** 154–8

[14] Hallatschek K. 2007 Nonlinear three-dimensional flows in magnetized plasmas *Plasma Phys. Control. Fusion* **49** B137–48

[15] Gorelenkov N.N. *et al* 2007 Predictions and observations of global beta-induced Alfvén-acoustic modes in JET and NSTX *Plasma Phys. Control. Fusion* **49** B371–83

[16] Sasaki M., Itoh K., Ejiri A. and Takase Y. 2008 Radial eigenmodes of geodesic acoustic modes *Contrib. Plasma Phys.* **48** 68

[17] Greene J.M., Johnson J.L., Weimer K.E. and Winsor N.K. 1971 Inertial and resistive effects in toroidal systems *Phys. Fluids* **14** 1258

[18] Diamond P.H. and Kim Y.B. 1991 Theory of mean poloidal flow generation by turbulence *Phys. Fluids* B **3** 1626

[19] Waltz R.E., Kerbel G.D. and Milovich J. 1994 Toroidal gyro-Landau fluid model turbulence simulations in a nonlinear ballooning mode representation with radial modes *Phys. Plasmas* **1** 2229

[20] Beer M.A., Cowley S.C. and Hammett G.W. 1995 Field-aligned coordinates for nonlinear simulations of tokamak turbulence *Phys. Plasmas* **2** 2687

[21] Lin Z., Hahm T.S., Lee W.W., Tang W.M. and White R.B. 1835 1998 turbulent transport reduction by zonal flows: massively parallel simulations *Science* **281** 1835–7

[22] Lin Z., Hahm T.S., Lee W.W., Tang W.M. and Diamond P.H. 1999 Effects of collisional zonal flow damping on turbulent transport *Phys. Rev. Lett.* **83** 3645

[23] Hinton F.L. and Rosenbluth M.N. 1999 Dynamics of axisymmetric and poloidal flows in tokamaks *Plasma Phys. Control. Fusion* **41** A653–62

[24] Hallatschek K. and Biskamp D. 2001 Transport control by coherent zonal flows in the core/edge transitional regime *Phys. Rev. Lett.* **86** 1223

[25] Liu A.D. *et al* 2009 Characterizations of low-frequency zonal flow in the edge plasma of the HL-2A tokamak *Phys. Rev. Lett.* **103** 095002

[26] Conway G.D. (ASDEX Upgrade Team) 2008 Amplitude behaviour of geodesic acoustic modes in the ASDEX Upgrade tokamak *Plasma Phys. Control. Fusion* **50** 085005

[27] Xu G.S., Wan B.N. and Song M. 2002 In search of zonal flows using cross-bispectrum analysis in the boundary plasma of the Hefei tokamak-7 *Phys. Plasmas* **9** 150

[28] Jakubowski M., Fonck R.J. and McKee G.R. 2002 Observation of coherent sheared turbulence flows in the DIII-D tokamak *Phys. Rev. Lett.* **89** 265003

[29] McKee G.R., Fonck R.J., Jakubowski M., Burrell K.H., Hallatschek K., Moyer R.A., Nevins W., Rudakov D.L. and Xu X. 2003 Observation and characterization of radially sheared zonal flows in DIII-D *Plasma Phys. Control. Fusion* **45** A477–85

[30] Schoch P.M., Connor K.A., Demers D.R. and Zhang X. 2003 Zonal flow measurements using a heavy ion beam probe *Rev. Sci. Instrum.* **74** 1848

[31] Conway G.D., Scott B., Schirmer J., Reich M. and Kendl A. (ASDEX Upgrade Team) 2004 Direct measurement of zonal flows and geodesic acoustic mode (GAM) oscillations in ASDEX Upgrade using Doppler reflectometry *Proc. 31st EPS Conf. Plasma Phys.* (London) (ECA) vol 28Gp P4.124 (http://epsppd.epfl.ch/London/start.htm)

[32] Ido T. *et al* 2004 Electrostatic fluctuation and fluctuation-induced particle flux during formation of the edge transport barrier in the JFT-2M tokamak *Proc. 20th IAEA Fusion Eng. Conf.* (Villamoura) IAEA-CN-116 EX/4–6Rb (http://www-naweb.iaea.org/napc/physics/fec/fec2004/papers/ex_4-6rb.pdf)

[33] Fujisawa A. *et al* 2004 Identification of zonal flows in a toroidal plasma *Phys. Rev. Lett.* **93** 165002

[34] Vershkov V.A., Shelukhin D.A., Soldatov S.V., Urazbaev A.O., Grashin S.A., Eliseev L.G. and Melnikov A.V. (T-10 Team) 2005 Summary of experimental core turbulence characteristics in ohmic and electron cyclotron resonance heated discharges in T-10 tokamak plasmas *Nucl. Fusion* **45** S203–26

[35] Bulanin V.V., Petrov A.V., Rozhansky V.A. and Yefanov M.V. 2005 Revealing of geodesic acoustic mode oscillations in TUMAN-3M tokamak via Doppler reflectometry *Proc. 32nd EPS Conf. Plasma Phys.* (Taragona) (ECA) vol 29Cp P4.051 (http://epsppd.epfl.ch/Tarragona/start.htm)

[36] Hamada Y., Nishizawa A., Ido T., Watari T., Kojima M., Kawasumi Y., Narihara K. and Toi K. (JIPPT-IIU Group) 2005 Zonal flows in the geodesic acoustic mode frequency range in the JIPP T-IIU tokamak plasmas *Nucl. Fusion* **45** 81

[37] Shats M.G., Xia H. and Yokoyama M. 2006 Mean $E \times B$ flows and GAM-like oscillations in the H-1 heliac *Plasma Phys. Control. Fusion* **48** S17

[38] Fujisawa A. *et al* 2006 Properties of turbulence and stationary zonal flow on transport barrier in CHS *Plasma Phys. Control. Fusion* **48** A370

[39] Tsui H.Y.W., Rypdal K., Ritz C.P. and Wootton A.J. 1993 Coherent nonlinear coupling between a long-wavelength mode and small-scale turbulence in the TEXT tokamak *Phys. Rev. Lett.* **70** 2565–8

[40] Hamada Y., Nishizawa A., Kawasumi Y., Fujisawa A. and Iguchi H. (JIPP T-IIU Group) 1997 Plasma potential fluctuations and large quasi-coherent modes observed by a heavy ion beam probe on the JIPP T-IIU tokamak *Fusion Eng. Des.* **34** 663–6

[41] Melnikov V.A. *et al* 2003 Observation of the specific oscillations with frequencies near 20 kHz by HIBP, reflectometry and Langmuir probes in T-10 *Proc. 30th EPS Conf. Plasma Phys.* (St.Petersburg) (ECA) vol 27Ap P3.114 (https://epsppd.epfl.ch/StPetersburg/)

[42] Zhou C. *et al* 2018 Investigation of the geodesic acoustic mode in EAST H-mode operation using Doppler backscattering systems *Nucl. Fusion* **58** 106009

[43] Conway G.D., Angioni C., Poli E., Ryter F., Sauter P., Scott B., Happel T. and Vicente J. (ASDEX Upgrade Team) 2010 Behaviour of mean and oscillating $E \times B$ plasma flows and turbulence interactions during confinement mode transitions *Proc. 23rd IAEA Fusion Eng. Conf.* (Daejon) IAEA-CN-180 EXC/7–1 (http://www-naweb.iaea.org/napc/physics/FEC/FEC2010/papers/exc_7-1.pdf)

[44] Nazikian R. *et al* 2008 Intense geodesic acousticlike modes driven by suprathermal ions in a tokamak plasma *Phys. Rev. Lett.* **101** 185001

[45] Fu G.Y. 2008 Energetic-particle-induced geodesic acoustic mode *Phys. Rev. Lett.* **101** 185002

[46] Hahm T.S., Beer M.A., Lin Z., Hammett G.W., Lee W.W. and Tang W.M. 1999 Shearing rate of time-dependent $E \times B$ flow *Phys. Plasmas* **6** 922

[47] Diamond P.H. *et al* 2000 In search of the elusive zonal flow using cross-bicoherence analysis *Phys. Rev. Lett.* **84** 4842

[48] Hahm T.S. 2002 Physics behind transport barrier theory and simulations *Plasma Phys. Control. Fusion* **44** A87–A101

[49] Scott B. 2003 The geodesic transfer effect on zonal flows in tokamak edge turbulence *Phys. Lett.* A **320** 53

[50] Sasaki M., Kasuya N., Itoh K., Hallatschek K., Lesur M., Kosuga Y. and Itoh S.-I. 2016 A branch of energetic-particle driven geodesic acoustic modes due to magnetic drift resonance *Phys. Plasmas* **23** 102501

[51] Sasaki M., Kasuya N., Itoh K., Kosuga Y., Lesur M., Hallatschek K. and Itoh S.-I. 2017 Toroidal momentum channeling of geodesic acoustic modes driven by fast ions *Nucl. Fusion* **57** 036025

[52] Rosenbluth M.N. and Hinton F.L. 1998 Poloidal flow driven by ion-temperature-gradient turbulence in tokamaks *Phys. Rev. Lett.* **80** 724

[53] Diamond P.H., Itoh S.-I., Itoh K. and Hahm T.S. 2005 Zonal flows in plasma—a review *Plasma Phys. Control. Fusion* **47** R35–R161

[54] Sugama H. and Watanabe T.-H. 2006 Collisionless damping of zonal flows in helical systems *Phys. Plasmas* **13** 012501

[55] Mishchenko A., Helander P. and Könies A. 2008 Collisionless dynamics of zonal flows in stellarator geometry *Phys. Plasmas* **15** 072309

[56] Ghizzo A. and Palermo F. 2015 Shear-flow trapped-ion-mode interaction revisited. I. Influence of low-frequency zonal flow on ion-temperature-gradient driven turbulence *Phys. Plasmas* **22** 082303

[57] Helander P., Mishchenko A., Kleiber R. and Xanthopoulos P. 2011 Oscillations of zonal flows in stellarators *Plasma Phys. Control. Fusion* **53** 054006

[58] Itoh K., Itoh S.-I., Diamond P.H., Hahm T.S., Fujisawa A., Tynan G.R., Yagi M. and Nagashima Y. 2006 Physics of zonal flows *Phys. Plasmas* **13** 055502

[59] Fujisawa A. *et al* 2007 Experimental progress on zonal flow physics in toroidal plasmas *Nucl. Fusion* **47** S718

[60] Itoh K. *et al* 2008 Physics of zonal flows *AIP Conf. Proc.* **1013** 106

[61] Fujisawa A. 2009 A review of zonal flow experiments *Nucl. Fusion* **49** 013001

[62] Numerous Authors 2006 Special section on experimental studies of zonal flows and turbulence *Plasma Phys. Control. Fusion* **48** S1–S205

[63] Qiu Z., Chen L. and Zonca F. 2018 Kinetic theory of geodesic acoustic modes in toroidal plasmas: a brief review *Plasma Sci. Technol.* **20** 094004

[64] Zhao K.J., Dong J.Q., Li J.Q. and Yan L.W. 2018 A brief review: experimental investigation of zonal flows and geodesic acoustic modes in fusion plasmas *Plasma Sci. Technol.* **20** 094006

[65] Smolyakov A.I., Garbet X., Falchetto G. and Ottaviani M. 2008 Multiple polarization of geodesic curvature induced modes *Phys. Lett.* A **372** 6750–6

[66] Heidbrink W.W., Strait E.J., Chu M.S. and Turnbull A.D. 1993 Observation of beta-induced Alfvén eigenmodes in the DIII-D tokamak *Phys. Rev. Lett.* **71** 855–8

[67] Nazikian R., Kramer G.J., Cheng C.Z., Gorelenkov N.N., Berk H.L. and Sharapov S.E. 2003 New interpretation of alpha-particle-driven instabilities in deuterium–tritium experiments on the tokamak fusion test reactor *Phys. Rev. Lett.* **91** 125003

[68] Nguyen C. *et al* 2009 Excitation of beta Alfvén eigenmodes in tore-supra *Plasma Phys. Control. Fusion* **51** 095002

[69] Chen W. *et al* 2010 β-induced Alfvén eigenmodes destabilized by energetic electrons in a tokamak plasma *Phys. Rev. Lett.* **105** 185004

[70] Breizman B.N., Pekker M.S. and Sharapov S.E. (JET Contributors) 2005 Plasma pressure effect on Alfvén cascade eigenmodes *Phys. Plasmas* **12** 112506

[71] Sharapov S.E. *et al* 2006 Alfvén cascades in JET discharges with NBI-heating *Nucl. Fusion* **46** S868–79

[72] Elfimov A.G., Galvão R.M.O. and Sharapov S.E. (JET Contributors) 2010 Determination of the minimum value of the safety factor from geodesic Alfvén eigenmodes in Joint European Torus *Phys. Plasmas* **17** 110705

[73] Elfimov A.G., Galvão R.M.O., Garcia-Munoz M., Igochine V., Lauber P. and Maraschek M. (ASDEX Upgrade Team) 2011 Identification of geodesic chirping Alfvén modes and q-factor estimation in hot core tokamak plasmas in ASDEX Upgrade *Plasma Phys. Control. Fusion* **53** 025006

[74] Nguyen C., Garbet X. and Smolyakov A.I. 2008 Variational derivation of the dispersion relation of kinetic coherent modes in the acoustic frequency range in tokamaks *Phys. Plasmas* **15** 112502

[75] Sugama H. and Watanabe T.-H. 2006 Collisionless damping of geodesic acoustic modes *J. Plasma Phys.* **72** 825–8

[76] Sugama H. and Watanabe T.H. 2008 Erratum: Collisionless damping of geodesic acoustic modes [J. Plasma Phys. (2006) 72, 825] *J. Plasma Phys.* **74** 139–40

[77] Sugama H. and Watanabe T.H. 2007 Erratum: collisionless damping of zonal flows in helical systems (PoP 13, 012501 (2006)) *Phys. Plasmas* **14** 079902

[78] Xu X.Q., Xiong Z., Gao Z., Nevins W.M. and McKee G.R. 2008 Tempest simulations of collisionless damping of the geodesic-acoustic mode in edge-plasma pedestals *Phys. Rev. Lett.* **100** 215001

[79] Dorf M.A., Cohen R.H., Dorr M., Rognlien T., Hittinger J., Compton J., Colella P., Martin D. and McCorquodale P. 2013 Numerical modelling of geodesic acoustic mode relaxation in a tokamak edge *Nucl. Fusion* **53** 063015

[80] Smolyakov A. 2015 *Elements of Neoclassical Theory and Plasma Rotation in a Tokamak* (Singapore: World Scientific) pp 173–217

[81] Mazur V.A. and Mikhajlovskij A.B. 1977 Stabilization of the Alfvén wave instability in a two-component tokamak *Nucl. Fusion* **17** 193

[82] Garbet X., Falchetto G., Ottaviani M., Sabot R., Sirinelli A. and Smolyakov A. 2006 Coherent modes in the acoustic frequency range in tokamaks *AIP Conf. Proc.* **871** 342–9

[83] Chew G.F., Goldberger M.L. and Low F.F. 1956 The Boltzmann equation an d the one-fluid hydromagnetic equations in the absence of particle collisions *Proc. R. Soc.* A **236** 112

[84] Mikhailovskii A.B. and Tsypin V.S. 1984 Transport equations of plasma in a curvilinear magnetic field *Beitr. Plasmaphys.* **24** 335–54

[85] Ren H. 2014 Zonal flows in tokamaks with anisotropic pressure *Phys. Plasmas* **21** 044505

[86] Ren H. and Cao J. 2014 Geodesic acoustic mode in anisotropic plasmas using double adiabatic model and gyro-kinetic equation *Phys. Plasmas* **21** 122512

[87] Lakhin V.P. and Sorokina E.A. 2018 Low-frequency magnetohydrodynamic spectra of plasmas with anisotropic pressure in axisymmetric toroidal systems *Phys. Plasmas* **25** 072111

[88] Lakhin V.P. and Sorokina E.A. 2019 Low-frequency continuous MHD spectrum of toroidally rotating tokamak plasmas with anisotropic pressure *Plasma Phys. Rep.* **45** 179–94

[89] Ren H. 2017 Geodesic acoustic mode in a reduced two-fluid model *Plasma Sci. Technol.* **19** 122001

[90] Ming Y., Zhou D. and Wang W. 2018 Geodesic acoustic modes in tokamak plasmas with anisotropic distribution and a radial equilibrium electric field *Plasma Sci. Technol.* **20** 085101

[91] Ren H. 2015 Geodesic acoustic mode in anisotropic plasma with heat flux *Phys. Plasmas* **22** 102505

[92] Ren H. 2017 Energetic particle driven geodesic acoustic mode in a toroidally rotating tokamak plasma *Nucl. Fusion* **57** 016023

[93] Zhang M. and Zhou D. 2010 Magnetic components of geodesic acoustic modes in plasmas with anisotropic ion distribution *Plasma Sci. Technol.* **12** 6–10

[94] Sivukhin D.V. 1963 *Motion of Charged Particles in Electromagnetic Fields in the Drift Approximation* vol 1 ed M Leontovich (New York: Consultants Bureau)

[95] Morozov A.I. and Solovev L.S. 1966 *Reviews of Plasma Physics* vol 2 ed M Leontovich (New York: Consultants Bureau) p 201

[96] Hazeltine R.D. and Ware A.A. 1978 The drift kinetic equation for toroidal plasmas with large mass velocities *Plasma Phys.* **20** 673–8

[97] Ramos J.J. 2008 Finite-Larmor-radius kinetic theory of a magnetized plasma in the macroscopic flow reference frame *Phys. Plasmas* **15** 082106

[98] Smolyakov A.I. and Garbet X. 2010 Drift kinetic equation in the moving reference frame and reduced magnetohydrodynamic equations *Phys. Plasmas* **17** 042105

[99] Watari T., Hamada Y., Fujisawa A., Toi K. and Itoh K. 2005 Extension of geodesic acoustic mode theory to helical systems *Phys. Plasmas* **12** 062304

[100] Smolyakov A.I., Nguyen C. and Garbet X. 2010 Electromagnetic effects on geodesic acoustic and beta-induced Alfvén eigenmodes *Nucl. Fusion* **50** 054002

[101] Elfimov A.G., Smolyakov A.I., Melnikov A.V. and Galvão R.M.O. 2013 Second harmonic effect on geodesic modes in tokamak plasmas *Phys. Plasmas* **20** 052116

[102] Miyato N., Kishimoto Y. and Li J. 2004 Global structure of zonal flow and electromagnetic ion temperature gradient driven turbulence in tokamak plasmas *Phys. Plasmas* **11** 5557

[103] Robinson J.R., Hnat B., Thyagaraja A., McClements K.G., Knight P.J. and Kirk A. (MAST Team) 2013 Global two-fluid simulations of geodesic acoustic modes in strongly shaped tight aspect ratio tokamak plasmas *Phys. Plasmas* **20** 052302

[104] Elfimov A.G. 2009 Kinetic ion effect on geodesic acoustic Alfvén modes in tokamaks *Phys. Plasmas* **16** 034501

[105] Catto P.J. and Rosenbluth M.N. 1981 Trapped electron modifications to tearing modes in the low collision frequency limit *Phys. Fluids* **24** 243–55

[106] Tang W.M., Connor J.W. and Hastie R.J. 1980 Kinetic-ballooning-mode theory in general geometry *Nucl. Fusion* **20** 1439–53

[107] Smolyakov A.I., Nguyen C. and Garbet X. 2008 Kinetic theory of electromagnetic geodesic acoustic modes *Plasma Phys. Control. Fusion* **50** 115008

[108] Gao Z., Itoh K., Sanuki H. and Dong J.Q. 2008 Eigenmode analysis of geodesic acoustic modes *Phys. Plasmas* **15** 072511

[109] Wang L., Dong J.Q., Shen Y. and He H.D. 2011 Electromagnetic effects of kinetic geodesic acoustic mode in tokamak plasmas *Phys. Plasmas* **18** 052506

[110] Mikhailovskii A.B. 1998 *Instabilities in a Confined Plasma* (Bristol: Institute of Physics Publishing)

[111] Smolyakov A.I., Bashir M.F., Elfimov A.G., Yagi M. and Miyato N. 2016 On the dispersion of geodesic acoustic modes *Plasma Phys. Rep.* **42** 407–17

[112] Xu X.Q. *et al* 2009 Dynamics of kinetic geodesic-acoustic modes and the radial electric field in tokamak neoclassical plasmas *Nucl. Fusion* **49** 065023

[113] Mikhailovskii A.B. 1999 Beta-induced temperature-gradient eigenmodes in tokamaks: II. Kinetic theory *Plasma Phys. Rep.* **25** 838–45

[114] Bashir M.F., Smolyakov A.I., Elfimov A.G., Melnikov A.V. and Murtaza G. 2014 Electromagnetic effects on geodesic acoustic modes *Phys. Plasmas* **21** 082507

[115] Chen L., Qiu Z. and Zonca F. 2018 Short wavelength geodesic acoustic mode excitation by energetic particles *Phys. Plasmas* **25** 014505

[116] Qiu Z., Chen L. and Zonca F. 2009 Collisionless damping of short wavelength geodesic acoustic modes *Plasma Phys. Control. Fusion* **51** 012001

[117] Gao Z. 2010 Plasma shaping effects on the geodesic acoustic mode in the large orbit drift width limit *Phys. Plasmas* **17** 092503

[118] Hager R. and Hallatschek K. 2009 Radial propagation of geodesic acoustic modes *Phys. Plasmas* **16** 072503

[119] Sasaki M., Itoh K., Ejiri A. and Takase Y. 2009 Poloidal eigenmode of the geodesic acoustic mode in the limit of high safety factor *J. Plasma Phys.* **75** 721

[120] Ren H. and Xu X.Q. 2016 Analytical collisionless damping rate of geodesic acoustic mode *Nucl. Fusion* **56** 106008

[121] Gao Z., Itoh K., Sanuki H. and Dong J.Q. 2006 Multiple eigenmodes of geodesic acoustic mode in collisionless plasmas *Phys. Plasmas* **13** 100702

[122] Gao Z. 2011 Analytical theory of the geodesic acoustic mode in the small and large orbit drift width limits and its application in a study of plasma shaping effect *Plasma Sci. Technol.* **13** 15–20

[123] Satake S., Sugama H. and Watanabe T.-H. 2007 Simulation studies on the GAM oscillation and damping in helical configurations *Nucl. Fusion* **47** 1258–64

[124] Wang L., Dong J.Q., Shen Y. and He H.D. 2011 Effects of electron dynamics on kinetic geodesic acoustic mode in tokamak plasmas *Plasma Phys. Control. Fusion* **53** 095014

[125] Ehrlacher C., Garbet X., Grandgirard V., Sarazin Y., Donnel P., Caschera E., Ghendrih P. and Zarzoso D. 2018 Contribution of kinetic electrons to GAM damping *J. Phys.: Conf. Ser.* **1125** 012010

[126] Zhang S., Gao Z., Wu W. and Qiu Z. 2014 Damping of geodesic acoustic mode by trapped electrons *Plasma Sci. Technol.* **16** 650–6

[127] Zhang H.S. and Lin Z. 2010 Trapped electron damping of geodesic acoustic mode *Phys. Plasmas* **17** 072502

[128] Grandgirard V. *et al* 2019 Linear collisionless dynamics of the GAM with kinetic electrons: comparison simulations/theory *Phys. Plasmas* **26** 122304

[129] Singh R., Storelli A., Gürcan Ö.D., Hennequin P., Vermare L., Morel P. and Singh R. 2015 Geodesic acoustic modes in a fluid model of tokamak plasma: the effects of finite beta and collisionality *Plasma Phys. Control. Fusion* **57** 125002

[130] Kovrizhnykh L.M. 2003 Relaxation of plasma rotation in toroidal magnetic confinement systems *Plasma Phys. Rep.* **29** 279–89

[131] Gao Z. 2013 Collisional damping of the geodesic acoustic mode *Phys. Plasmas* **20** 032501

[132] Li Y. and Gao Z. 2015 Comparison of collision operators for the geodesic acoustic mode *Nucl. Fusion* **55** 043001

[133] Braginskii S. 1965 *Reviews of Plasma Physics* vol 1 ed M Leontovich (New York: Consultants Bureau) p 205

[134] Guo W., Wang S. and Li J. 2008 Damping effects of finite parallel thermal conductivity on zonal flows *Plasma Phys. Control. Fusion* **50** 095006

[135] Braun S., Helander P., Belli E.A. and Candy J. 2009 Effect of impurities on collisional zonal flow damping in tokamaks *Plasma Phys. Control. Fusion* **51** 065011

[136] Morris R.C., Haines M.G. and Hastie R.J. 1996 The neoclassical theory of poloidal flow damping in a tokamak *Phys. Plasmas* **3** 4513–20

[137] Hung C.P. and Hassam A.B. 2013 Phase mixing and nonlinearity in geodesic acoustic modes *Phys. Plasmas* **20** 092107

[138] Biancalani A. *et al* 2017 Cross-code gyrokinetic verification and benchmark on the linear collisionless dynamics of the geodesic acoustic mode *Phys. Plasmas* **24** 062512

[139] Palermo F., Biancalani A., Angioni C., Zonca F. and Bottino A. 2016 Combined action of phase-mixing and Landau damping causing strong decay of geodesic acoustic modes *Europhys. Lett.* **115** 15001

[140] Palermo F., Poli E., Bottino A., Biancalani A., Conway G.D. and Scott B. 2017 Radial acceleration of geodesic acoustic modes in the presence of a temperature gradient *Phys. Plasmas* **24** 072503

[141] Lan T. *et al* 2008 Spectral features of the geodesic acoustic mode and its interaction with turbulence in a tokamak plasma *Phys. Plasmas* **15** 056105

[142] Qiu Z., Chen L. and Zonca F. 2015 On fast radial propagation of parametrically excited geodesic acoustic mode *Phys. Plasmas* **22** 042512

[143] Sasaki M., Itoh K., Ejiri A. and Takase Y. 2009 Transient excitation of zonal flows by geodesic acoustic modes *Plasma Phys. Control. Fusion* **51** 085002

[144] Miki K. and Diamond P.H. 2010 Role of the geodesic acoustic mode shearing feedback loop in transport bifurcations and turbulence spreading *Phys. Plasmas* **17** 032309

[145] Sasaki M., Itoh K., Kobayashi T., Kasuya N., Fujisawa A. and Itoh S.-I. 2018 Propagation direction of geodesic acoustic modes driven by drift wave turbulence *Nucl. Fusion* **58** 112005

[146] Miki K., Kishimoto Y., Miyato N. and Li J.Q. 2007 Intermittent transport associated with the geodesic acoustic mode near the critical gradient regime *Phys. Rev. Lett.* **99** 145003

[147] Miki K., Kishimoto Y., Li J. and Miyato N. 2008 Dynamics of turbulent transport dominated by the geodesic acoustic mode near the critical gradient regime *Phys. Plasmas* **15** 052309

[148] Qiu Z., Chen L. and Zonca F. 2014 Excitation of kinetic geodesic acoustic modes by drift waves in nonuniform plasmas *Phys. Plasmas* **21** 022304

[149] Palermo F., Biancalani A., Angioni C., Zonca F., Bottino A., Conway G.D. and Poli E. 2016 A new mechanism causing strong decay of geodesic acoustic modes: combined action of phase-mixing and Landau damping *Proc. 43rd EPS Conf. Plasma Phys.* (Leuven) (ECA) vol 40Ap P1.046 (http://ocs.ciemat.es/EPS2016PAP/pdf/P1.046.pdf)

[150] Chen L. and Hasegawa A. 1974 Plasma heating by spatial resonance of Alfveén wave *Phys. Fluids* **17** 1399

[151] Biancalani A., Palermo F., Angioni C., Bottino A. and Zonca F. 2016 Decay of geodesic acoustic modes due to the combined action of phase mixing and Landau damping *Phys. Plasmas* **23** 112115

[152] Li Z., Dong J., Sheng Z., Yu M.Y. and Wang W. 2017 Radial properties of the geodesic acoustic mode *Phys. Plasmas* **24** 102507

[153] Palermo F., Poli E. and Bottino A. 2020 Complex eikonal methods applied to geodesic acoustic mode dynamics *Phys. Plasmas* **27** 032507

[154] Mikhailovskii A.B., Smolyakov A.I., Churikov A.P. and Pustovitov V.D. 2009 Large-scale oscillations in a tokamak due to strong plasma temperature gradient *Dokl. Phys.* **54** 525–8

[155] Itoh K., Itoh S.-I., Diamond P.H., Fujisawa A., Yagi M., Watari T., Nagashima Y. and Fukuyama A. 2006 Geodesic acoustic eigenmodes *Plasma Fusion Res.* **1** 037

[156] Qiu Z., Zonca F. and Chen L. 2010 Nonlocal theory of energetic-particle-induced geodesic acoustic mode *Plasma Phys. Control. Fusion* **52** 095003

[157] Wahlberg C. and Graves J.P. 2019 Singular global components and frequency shift of the geodesic acoustic continuum modes in shaped tokamaks *Plasma Phys. Control. Fusion* **61** 075013

[158] Cheng C.Z. and Chance M.S. 1986 Low-*n* shear Alfveén spectra in axisymmetric toroidal plasmas *Phys. Fluids* **29** 3695–701

[159] Fesenyuk O.P., Kolesnichenko Y.I., Wobig H. and Yakovenko Y.V. 2002 Ideal magnetohydrodynamic equations for low-frequency waves in toroidal plasmas *Phys. Plasmas* **9** 1589–95

[160] Fesenyuk O.P., Kolesnichenko Y.I. and Yakovenko Y.V. 2012 Geodesic acoustic mode frequency and the structure of Alfvén continuum in toroidal plasmas with high $q^2\beta$ *Plasma Phys. Control. Fusion* **54** 085014

[161] Ilgisonis V.I., Khalzov I.V., Lakhin V.P., Smolyakov A.I. and Sorokina E.A. 2014 Global geodesic acoustic mode in a tokamak with positive magnetic shear and a monotonic temperature profile *Plasma Phys. Control. Fusion* **56** 035001

[162] Lakhin V.P. and Sorokina E.A. 2014 Geodesic acoustic eigenmode for tokamak equilibrium with maximum of local GAM frequency *Phys. Lett.* A **378** 535–8

[163] Ilgisonis V.I., Konoval'tseva L.V., Lakhin V.P. and Sorokina E.A. 2014 Analytical solutions for global geodesic acoustic modes in tokamak plasmas *Plasma Phys. Rep.* **40** 843

[164] Huysmans G. 2005 private communication

[165] Lakhin V.P., Sorokina E.A., Ilgisonis V.I. and Konovaltseva L.V. 2015 MHD-model for low-frequency waves in a tokamak with toroidal plasma rotation and problem of existence of global geodesic acoustic modes *Plasma Phys. Rep.* **41** 975

[166] Wahlberg C. 2009 Low-frequency magnetohydrodynamics and geodesic acoustic modes in toroidally rotating tokamak plasmas *Plasma Phys. Control. Fusion* **51** 085006

[167] Wahlberg C. and Graves J.P. 2016 Magnetohydrodynamic theory of the global structure and magnetic components of the geodesic acoustic continuum modes in tokamaks *Plasma Phys. Control. Fusion* **58** 075014

[168] Kolesnichenko Y.I., Lepiavko B.S. and Lutsenko V.V. 2013 Geodesic acoustic mode in tokamaks: local consideration and eigenvalue analysis *Plasma Phys. Control. Fusion* **55** 125007

[169] Fesenyuk O.P., Kolesnichenko Y.I. and Yakovenko Y.V. 2013 Frequencies of the geodesic acoustic mode and Alfvén gap modes in high-$q^2\beta$ plasmas with non-circular cross section *Phys. Plasmas* **20** 122503

[170] Zhou T. and Wang X. 2018 Global MHD GAMs in toroidal plasmas with reversed magnetic shear *Nucl. Fusion* **58** 076006

[171] Zhou D. 2007 Electromagnetic geodesic acoustic modes in tokamak plasmas *Phys. Plasmas* **14** 104502

[172] Zhou D. 2016 The magnetic component of geodesic acoustic modes in tokamak plasmas with a radial equilibrium electric field *Phys. Plasmas* **23** 102503

[173] Ren H. 2014 Perturbation analysis of electromagnetic geodesic acoustic modes *Phys. Plasmas* **21** 064502

[174] Smolyakov A.I., Lakhin V., Sorokina E. and Ilgisonis V. 2020 On magnetic perturbations in geodesic acoustic modes *Phys. Plasmas* (in preparation)

[175] Turnbull A.D., Strait E.J., Heidbrink W.W., Chu M.S., Duong H.H., Greene J.M., Lao L.L., Taylor T.S. and Thompson S.J. 1993 Global Alfvén modes: theory and experiment *Phys. Fluids* B **5** 2546–53

[176] Heidbrink W.W., Ruskov E., Carolipio E.M., Fang J., van Zeeland M.A. and James R.A. 1999 What is the 'beta-induced Alfvén eigenmode?' *Phys. Plasmas* **6** 1147–61

[177] Elfimov A.G. 2010 Alfvén continuum deformation by kinetic geodesic effect in rotating tokamak plasmas *Phys. Plasmas* **17** 022102

[178] Gorelenkov N.N., Berk H.L., Fredrickson E. and Sharapov S.E. (JET EFDA Contributors) 2007 Predictions and observations of low-shear beta-induced shear Alfvén-acoustic eigenmodes in toroidal plasmas *Phys. Lett.* A **370** 70–7

[179] Gorelenkov N.N. *et al* 2009 Beta-induced Alfvén-acoustic eigenmodes in national spherical torus experiment and DIII-D driven by beam ions *Phys. Plasmas* **16** 056107

[180] Gorelenkov N.N., Pinches S.D. and Toi K. 2014 Energetic particle physics in fusion research in preparation for burning plasma experiments *Nucl. Fusion* **54** 125001

[181] Sgalla R.J.F., Smolyakov A.I., Elfimov A.G. and Bashir M.F. 2013 Drift effects on geodesic acoustic modes *Phys. Lett.* A **377** 303

[182] Smolyakov A.I., Diamond P.H. and Medvedev M.V. 2000 Role of ion diamagnetic effects in the generation of large scale flows in toroidal ion temperature gradient mode turbulence *Phys. Plasmas* **7** 3987–92

[183] Falchetto G.L., Ottaviani M., Garbet X. and Smolyakov A. 2007 Turbulent excitation of plasma oscillations in the acoustic frequency range *Phys. Plasmas* **14** 082304

[184] Smolyakov A.I., Janhunen S., Ilgisonis V.I., Lakhin V. and Sorokina E.A. 2017 Geodesic eigenmodes and ion temperature fluctuations in a tokamak *59th Annual Meeting APS Div. Plasma Phys.* (BAPS) vol 62DPP.YP11 (https://ui.adsabs.harvard.edu/abs/2017APS..DPPY11063S/abstract)

[185] Zielinski J., Smolyakov A.I., Beyer P. and Benkadda S. 2017 Electromagnetic electron temperature gradient driven instability in toroidal plasmas *Phys. Plasmas* **24** 024501

[186] Janhunen S., Merlo G., Jenko F., Gurchenko A., Gusakov E. and Kiviniemi T. 2020 Nonlinear symmetry breaking in electron temperature gradient driven turbulence (arXiv:2005.14581)

[187] Chakrabarti N., Guzdar P.N. and Kaw P.K. 2012 The electron geodesic acoustic mode *Phys. Plasmas* **19** 092113

[188] Anderson J., Nordman H., Singh R. and Kaw P. 2012 Electron geodesic acoustic modes in electron temperature gradient mode turbulence *Phys. Plasmas* **19** 082305

[189] Anderson J., Skyman A., Nordman H., Singh R. and Kaw P. 2013 High frequency geodesic acoustic modes in electron scale turbulence *Nucl. Fusion* **53** 123016

[190] Qu Z.S., Hole M.J. and Fitzgerald M. 2016 Energetic geodesic acoustic modes associated with two-stream-like instabilities in tokamak plasmas *Phys. Rev. Lett.* **116** 095004

[191] Qu Z.S., Hole M.J. and Fitzgerald M. 2017 Linear radial structure of reactive energetic geodesic acoustic modes *Plasma Phys. Control. Fusion* **59** 055018

[192] Zarzoso D., Garbet X., Sarazin Y., Dumont R. and Grandgirard V. 2012 Fully kinetic description of the linear excitation and nonlinear saturation of fast-ion-driven geodesic acoustic mode instability *Phys. Plasmas* **19** 022102

[193] Zarzoso D., Biancalani A., Bottino A., Lauber P., Poli E., Girardo J.-B., Garbet X. and Dumont R.J. 2014 Analytic dispersion relation of energetic particle driven geodesic acoustic modes and simulations with NEMORB *Nucl. Fusion* **54** 103006

[194] Girardo J.-B., Zarzoso D., Dumont R., Garbet X., Sarazin Y. and Sharapov S. 2014 Relation between energetic and standard geodesic acoustic modes *Phys. Plasmas* **21** 092507

[195] Berk H.L. 2010 Fast excitation of EGAM by NBI *Nucl. Fusion* **50** 035007

[196] Zhou T. 2009 MHD GAMs and kinetic GAMs driven by energetic particles *PhD Thesis* University of Texas at Austin

[197] Cao J., Qiu Z. and Zonca F. 2015 Fast excitation of geodesic acoustic mode by energetic particle beams *Phys. Plasmas* **22** 124505

[198] Camilo de Souza F., Elfimov A.G. and Galvão R.M.O. 2018 Geodesic modes driven by plasma fluxes during oblique NB heating in tokamaks *Phys. Plasmas* **25** 122507

[199] Qiu Z., Zonca F. and Chen L. 2012 Geodesic acoustic mode excitation by a spatially broad energetic particle beam *Phys. Plasmas* **19** 082507

[200] Belova E.V., Denton R.E. and Chan A.A. 1997 Hybrid simulations of the effects of energetic particles on low-frequency MHD waves *J. Comput. Phys.* **136** 324–36

[201] Park W. *et al* 1992 Three-dimensional hybrid gyrokinetic magnetohydrodynamics simulation *Phys. Fluids* B **4** 2033

[202] Elfimov A.G., Smolyakov A.I. and Galvão R.M.O. 2014 Geodesic mode instability driven by the electron current in tokamak plasmas *Phys. Lett.* A **378** 800–3

[203] Elfimov A.G. 2018 Geodesic mode instability driven during ion cyclotron heating in tokamaks *Phys. Plasmas* **25** 062516

[204] Elfimov A.G., Galvão R.M.O. and Gorelenkov N.N. 2019 Geodesic modes driven by untrapped resonances of NB energetic ions in tokamaks *Phys. Plasmas* **26** 102508

[205] Camilo de Souza F., Elfimov A.G., Galvão R.M.O., Krbec J., Seidl J., Stöckel J., Hron M., Havlicek J. and Mitosinkova K. 2017 Geodesic mode instability driven by electron and ion fluxes during neutral beam injection in tokamaks *Phys. Lett.* A **381** 3066

[206] Elfimov A.G., Camilo de Souza F. and Galvão R.M.O. 2015 Geodesic mode instability driven by electron and ion fluxes in tokamaks *Phys. Plasmas* **22** 114503

[207] Rosenbluth M.N. and Taylor J.B. 1969 Plasma diffusion and stability in toroidal systems *Phys. Rev. Lett.* **23** 367

[208] Stringer T.E. 1971 Development of ambipolar electric field and flows in toroidal plasmas *Proc. 4th IAEA Conf. Plasma Phys. Control. Nucl. Fusion* (Madison) IAEA-CN-28/F-3

[209] Galeev A.A., Sagdeev R.Z., Liu S.S. and Novakovskii S.V. 1996 Spontaneous generation of plasma poloidal rotation in tokamak in banana mode *Zh. Eksp. Teor. Fiz.* **109** 1626–33

[210] Hirshman S.P. 1978 The ambipolarity paradox in toroidal diffusion, revisited *Nucl. Fusion* **18** 917–27

[211] Hassam A.B., Antonsen T.M., Drake J.F. and Liu C.S. 1991 Spontaneous poloidal spin-up of tokamaks and the transition to the H mode *Phys. Rev. Lett.* **66** 309

[212] Strauss H.R. 1995 Poloidal rotation spin-up in divertor tokamaks *Phys. Plasmas* **2** 1229–35

[213] Itoh K., Hallatschek K. and Itoh S.-I. 2005 Excitation of geodesic acoustic mode in toroidal plasmas *Plasma Phys. Control. Fusion* **47** 451

[214] Falchetto G.L., Garbet X., Ottaviani M. and Smolyakov A. 2006 Generation of geodesic acoustic modes in ITG turbulence *AIP Conf. Proc.* **871** 324–9

[215] Li J.Q., Kishimoto Y., Miyato N., Miki K., Anderson J. and Shi B.R. 2008 Gyrofluid simulation on the nonlinear excitation and radial structure of geodesic acoustic modes in ITG turbulence *J. Phys.: Conf. Ser.* **123** p 12027

[216] Miyato N., Li J.Q. and Kishimoto Y. 2005 Study of a drift wave-zonal mode system based on global electromagnetic Landau-fluid ITG simulation in toroidal plasmas *Nucl. Fusion* **45** 425

[217] Miyato N., Kishimoto Y. and Li J.Q. 2006 Nonlocal behaviour of zonal flows in tokamak plasmas *Plasma Phys. Control. Fusion* **48** A335–40

[218] Chakrabarti N., Singh R., Kaw P.K. and Guzdar P.N. 2007 Nonlinear excitation of geodesic acoustic modes by drift waves *Phys. Plasmas* **14** 052308

[219] Guzdar P.N., Chakrabarti N., Singh R. and Kaw P.K. 2008 Excitation of geodesic acoustic modes by ion temperature gradient modes *Plasma Phys. Control. Fusion* **50** 025006

[220] Sasaki M., Itoh K., Nagashima Y., Ejiri A. and Takase Y. 2009 Nonlinear self-interaction of geodesic acoustic modes in toroidal plasmas *Phys. Plasmas* **16** 022306

[221] Smolyakov A.I., Diamond P.H. and Shevchenko V.I. 2000 Zonal flow generation by parametric instability in magnetized plasmas and geostrophic fluids *Phys. Plasmas* **7** 1349–51

[222] Chakrabarti N., Guzdar P.N., Kleva R.G., Naulin V., Rasmussen J.J. and Kaw P.K. 2008 Geodesic acoustic

modes excited by finite beta drift waves *Phys. Plasmas* **15** 112310
[223] Qiu Z., Chen L. and Zonca F. 2014 Nonlinear excitation of geodesic acoustic mode by collisionless trapped electron mode *Nucl. Fusion* **54** 033010
[224] Qiu Z., Chen L. and Zonca F. 2013 Spontaneous excitation of geodesic acoustic mode by toroidal Alfvén eigenmodes *Europhys. Lett.* **101** 35001
[225] Guzdar P.N., Kleva R.G., Chakrabarti N., Naulin V., Rasmussen J.J., Kaw P.K. and Singh R. 2009 Nonlocal analysis of the excitation of the geodesic acoustic mode by drift waves *Phys. Plasmas* **16** 052514
[226] Yu J., Dong J.Q., Li X.X., Du D. and Gong X.Y. 2012 Excitation of geodesic acoustic mode continuum by drift wave turbulence *J. Plasma Phys.* **78** 651
[227] Hallatschek K. 2008 Diamagnetic GAM drive mechanism *Proc. 22nd IAEA Fusion. Eng. Conf.* (Geneva) IAEA-CN-165 TH/P8–11 (http://www-naweb.iaea.org/napc/physics/FEC/FEC2008/papers/th_p8-11.pdf)
[228] Hallatschek K. 2009 Dependence of turbulent transport on GAMs *Proc. 36th EPS Conf. Plasma Phys.* (Sofia) (ECA) vol 33Ep P4.119 (http://epsppd.epfl.ch/Sofia/start.htm)
[229] Hallatschek K and Hager R 2010 Control of turbulent transport by GAMs *Proc. 23rd IAEA Fusion Eng. Conf.* (Daejon) IAEA-CN-180 THC/P8–4 (http://www-naweb.iaea.org/napc/physics/FEC/FEC2010/papers/thc_p8-04.pdf)
[230] Marchenko V.S., Panwar A., Reznik S.N. and Ryu C.M. 2017 Generation of geodesic acoustic mode by nonlinear coupling of magnetic island and island-driven beta-induced Alfvén eigenmode *Plasma Phys. Control. Fusion* **59** 092001
[231] Chen W. *et al* 2013 Observation of energetic-particle-induced GAM and nonlinear interactions between EGAM, BAEs and tearing modes on the HL-2A tokamak *Nucl. Fusion* **53** 113010
[232] Marchenko V.S. 2006 Excitation of the geodesic acoustic mode during ion cyclotron resonance heating *Phys. Plasmas* **13** 060701
[233] Nagashima Y. *et al* 2007 In search of zonal flows by using direct density fluctuation measurements *Plasma Phys. Control. Fusion* **49** 1611
[234] Zhang H.S., Qiu Z., Chen L. and Lin Z. 2009 The importance of parallel nonlinearity in the self-interaction of geodesic acoustic mode *Nucl. Fusion* **49** 125009
[235] Fu G.Y. 2011 On nonlinear self-interaction of geodesic acoustic mode driven by energetic particles *J. Plasma Phys.* **77** 457–67
[236] Mikhailovskii A.B., Smolyakov A.I., Churikov A.P. and Pustovitov V.D. 2009 Zonal stability of geodesic acoustic modes in a tokamak *Plasma Phys. Control. Fusion* **51** 075010
[237] Chen L., Qiu Z. and Zonca F. 2014 On nonlinear geodesic acoustic modes in tokamak plasmas *Europhys. Lett.* **107** 15003
[238] Ren H. and Xu X.Q. 2020 Excitation of zonal flow by nonlinear geodesic acoustic mode *Phys. Plasmas* **27** 034501
[239] Qiu Z., Chavdarovski I., Biancalani A. and Cao J. 2017 On zero frequency zonal flow and second harmonic generation by finite amplitude energetic particle induced geodesic acoustic mode *Phys. Plasmas* **24** 072509
[240] Biancalani A., Bottino A., Lauber P. and Zarzoso D. 2014 Numerical validation of the electromagnetic gyrokinetic code NEMORB on global axisymmetric modes *Nucl. Fusion* **54** 104004
[241] Novikau I., Biancalani A., Bottino A., Conway G.D., Gürcan Ö.D., Manz P., Morel P., Poli E. and Di Siena A. (ASDEX Upgrade Team) 2017 Linear gyrokinetic investigation of the geodesic acoustic modes in realistic tokamak configurations *Phys. Plasmas* **24** 122117
[242] Gao Z., Peng L., Wang P., Dong J. and Sanuki H. 2009 Plasma elongation effects on temperature gradient driven instabilities and geodesic acoustic modes *Nucl. Fusion* **49** 045014
[243] Angelino P. *et al* 2008 The role of plasma elongation on the linear damping of zonal flows *Phys. Plasmas* **15** 062306
[244] Angelino P., Bottino A., Hatzky R., Jolliet S., Sauter O., Tran T.M. and Villard L. 2006 Effects of plasma current on nonlinear interactions of ITG turbulence, zonal flows and geodesic acoustic modes *Plasma Phys. Control. Fusion* **48** 557–71
[245] Villard L., Angelino P., Bottino A., Hatzky R., Jolliet S., McMillan B.F., Sauter O. and Tran T.M. 2006 Plasma shape effects on geodesic acoustic *AIP Conf. Proc.* **871** 424–9
[246] Villard L., Angelino P., Bottino A., Brunner S., Jolliet S., McMillan B.F., Tran T.M. and Vernay T. 2013 Global gyrokinetic ion temperature gradient turbulence simulations of ITER *Plasma Phys. Control. Fusion* **55** 074017
[247] Shafer M.W., Fonck R.J., Mckee G.R., Holland C., White A.E. and Schlossberg D.J. 2012 2D properties of core turbulence on DIII-D and comparison to gyrokinetic simulations *Phys. Plasmas* **19** 032504
[248] Guo W., Wang S. and Li J. 2010 Effect of impurity ions on the geodesic acoustic mode *Phys. Plasmas* **17** 112510
[249] Gusakov E.Z. *et al* 2013 Anomalous transport and multi-scale drift turbulence dynamics in tokamak ohmic discharge as measured by high resolution diagnostics and modeled by full-fgyrokinetic code *Plasma Phys. Control. Fusion* **55** 124034
[250] Gurchenko A.D. *et al* 2016 The isotope effect in turbulent transport control by GAMs. Observation and gyrokinetic modeling *Plasma Phys. Control. Fusion* **58** 044002
[251] Leerink S. *et al* 2012 Multiscale investigations of drift-wave turbulence and plasma flows: measurements and total-distribution-function gyrokinetic simulations *Phys. Rev. Lett.* **109** 165001
[252] Krutkin O.L. *et al* 2019 Validation of full-f global gyrokinetic modeling results against the FT-2 tokamak Doppler reflectometry data using synthetic diagnostics *Nucl. Fusion* **59** 096017
[253] Niskala P., Kiviniemi T.P., Leerink S. and Korpilo T. 2015 Gyrokinetic simulations of interplay between geodesic acoustic modes and trapped electron mode turbulence *Nucl. Fusion* **55** 073012
[254] Niskala P., Gurchenko A.D., Gusakov E.Z., Altukhov A.B., Esipov L.A., Chôné L., Kiviniemi T.P. and Leerink S. 2018 Neoclassical and turbulent $E \times B$ flows in flux-driven gyrokinetic simulations of Ohmic tokamak plasmas *Nucl. Fusion* **58** 112006
[255] Gurchenko A.D. *et al* 2013 Spatial structure of the geodesic acoustic mode in the FT-2 tokamak by upper hybrid resonance Doppler backscattering *Plasma Phys. Control. Fusion* **55** 085017
[256] Itoh S.-I., Itoh K., Sasaki M., Fujisawa A., Ido T. and Nagashima Y. 2007 Geodesic acoustic mode spectroscopy *Plasma Phys. Control. Fusion* **49** L7
[257] Merlo G. *et al* 2018 Investigating the radial structure of axisymmetric fluctuations in the TCV tokamak with local and global gyrokinetic GENE simulations *Plasma Phys. Control. Fusion* **60** 034003
[258] Liu F., Lin Z., Dong J.Q. and Zhao K.J. 2010 Gyrokinetic simulation of turbulence driven geodesic acoustic modes in edge plasmas of HL-2A tokamak *Phys. Plasmas* **17** 112318
[259] Biancalani A., Chavdarovski I., Qiu Z., Bottino A., Del Sarto D., Ghizzo A., Gürcan Ö., Morel P. and Novikau I. 2017 Saturation of energetic-particle-driven geodesic acoustic modes due to wave-particle nonlinearity *J. Plasma Phys.* **83** 725830602

[260] Zarzoso D., del-Castillo-Negrete D., Escande D.F., Sarazin Y., Garbet X., Grandgirard V., Passeron C., Latu G. and Benkadda S. 2018 Particle transport due to energetic-particle-driven geodesic acoustic modes *Nucl. Fusion* **58** 106030

[261] Xiang X. and Fu G. 2019 Linear properties of global energetic particle induced geodesic acoustic mode with bump-on-tail distribution in tokamak plasmas *Phys. Plasmas* **26** 032509

[262] Wang H. and Todo Y. 2013 Linear properties of energetic particle driven geodesic acoustic mode *Phys. Plasmas* **20** 012506

[263] Wang H., Todo Y., Ido T. and Osakabe M. 2015 Simulation study of high-frequency energetic particle driven geodesic acoustic mode *Phys. Plasmas* **22** 092507

[264] Wang H., Todo Y., Ido T. and Suzuki Y. 2018 Chirping and sudden excitation of energetic-particle-driven geodesic acoustic modes in a large helical device experiment *Phys. Rev. Lett.* **120** 175001

[265] Wang H., Todo Y., Oasakabe M., Ido T. and Suzuki Y. 2019 Simulation of energetic particle driven geodesic acoustic modes and the energy channeling in the large helical device plasmas *Nucl. Fusion* **59** 096041

[266] Ido T. *et al* 2011 Potential fluctuation associated with the energetic-particle-induced geodesic acoustic mode in the large helical device *Nucl. Fusion* **51** 073046

[267] Zarzoso D., Migliano P., Grandgirard V., Latu G. and Passeron C. 2017 Nonlinear interaction between energetic particles and turbulence in gyro-kinetic simulations and impact on turbulence properties *Nucl. Fusion* **57** 072011

[268] Lakhin V.P., Ilgisonis V.I. and Smolyakov A.I. 2010 Geodesic acoustic modes and zonal flows in toroidally rotating tokamak plasmas *Phys. Lett.* A **374** 4872–5

[269] Sasaki M., Itoh K. and Itoh S.-I. 2011 Energy channeling from energetic particles to bulk ions via beam-driven geodesic acoustic modes-GAM channeling *Plasma Phys. Control. Fusion* **53** 085017

[270] Chen L. and Zonca F. 2016 Physics of Alfvén waves and energetic particles in burning plasmas *Rev. Mod. Phys.* **88** 015008

[271] Zarzoso D. *et al* 2013 Impact of energetic-particle-driven geodesic acoustic modes on turbulence *Phys. Rev. Lett.* **110** 125002

[272] Biancalani A., Carlevaro N., Bottino A., Montani G. and Qiu Z. 2017 Nonlinear velocity redistribution caused by energetic-particle-driven geodesic acoustic modes, mapped with the beam–plasma system *J. Plasma Phys.* **84** 725840602

[273] Coda S., Porkolab M. and Burrell K.H. 2001 Signature of turbulent zonal flows observed in the DIII-D tokamak *Phys. Rev. Lett.* **86** 4835

[274] Moyer R.A., Tynan G.R., Holland C. and Burin M.J. 2001 Increased nonlinear coupling between turbulence and low-frequency fluctuations at the L–H transition *Phys. Rev. Lett.* **87** 135001

[275] McKee G.R. *et al* 2002 Turbulence regulation and stabilization by equilibrium and time-varying, sheared turbulence flows *Proc. 19th IAEA Fusion Eng. Conf.* (Lyon) IAEA-CN-94 EX/C4–1Ra (https://www-pub.iaea.org/MTCD/publications/PDF/csp_019c/pdf/exc4_1ra.pdf)

[276] McKee G.R., Fenzi C., Fonck R.J. and Jakubowski M. 2003 Turbulence imaging and applications using beam emission spectroscopy on DIII-D (invited) *Rev. Sci. Instrum.* **74** 2014

[277] McKee G.R. *et al* 2003 Experimental characterization of coherent, radially-sheared zonal flows in the DIII-D tokamak *Phys. Plasmas* **10** 1712

[278] Gupta D.K., Fonck R.J., McKee G.R., Schlossberg D.J. and Shafer M.W. 2006 Detection of zero-mean-frequency zonal flows in the core of a high-temperature tokamak plasma *Phys. Rev. Lett.* **97** 125002

[279] Holland C., Tynan G.R., Fonck R.J., McKee G.R., Candy J. and Waltz R.E. 2007 Zonal-flow-driven nonlinear energy transfer in experiment and simulation *Phys. Plasmas* **14** 056112

[280] Schmitz L., Wang G., Hillesheim J.C., Rhodes T.L., Peebles W.A., White A.E., Zeng L., Carter T.A. and Solomon W. 2008 Detection of zonal flow spectra in DIII-D by a dual-channel Doppler backscattering system *Rev. Sci. Instrum.* **79** 10F113

[281] McKee G.R. *et al* 2009 Dependence of the L- to H-mode power threshold on toroidal rotation and the link to edge turbulence dynamics *Nucl. Fusion* **49** 115016

[282] Hillesheim J.C., Peebles W.A., Carter T.A., Schmitz L. and Rhodes T.L. 2012 Experimental investigation of geodesic acoustic mode spatial structure, intermittency, and interaction with turbulence in the DIII-D tokamak *Phys. Plasmas* **19** 022301

[283] Wang G. *et al* 2013 Multi-field characteristics and eigenmode spatial structure of geodesic acoustic modes in DIII-D L-mode plasmas *Phys. Plasmas* **20** 092501

[284] Yan Z. *et al* 2013 Relating the L–H power threshold scaling to edge turbulence dynamics *Nucl. Fusion* **53** 113038

[285] Liu A.D., Lan T., Yu C.X., Zhang W., Zhao H.L., Kong D.F., Chang J.F. and Wan B.N. 2010 Spectral characteristics of zonal flows in the edge plasmas of the HT-7 tokamak *Plasma Phys. Control. Fusion* **52** 085004

[286] Zhao H. *et al* 2010 Properties of density fluctuations induced by geodesic acoustic mode in the edge of HT-7 tokamak *Plasma Sci. Technol.* **12** 262

[287] Kong D.F. *et al* 2013 Observation of nonlinear couplings between coexisting kinetic geodesic acoustic modes in the edge plasmas of the HT-7 tokamak *Nucl. Fusion* **53** 113008

[288] Shen H.G. *et al* 2016 Investigation of zonal flows by using the collective scattering measurement of density fluctuations *Nucl. Fusion* **55** 093004

[289] Schoch P.M. 2003 Experimental evidence of zonal flows using HIBP data *Phys. Rev. Lett.* (private communication)

[290] Tsui H.Y.W., Schoch P.M. and Wootton A.J. 1993 Observation of a quasicoherent mode in the Texas experimental tokamak *Phys. Fluids* B **5** 1274–80

[291] Melnikov A.V. *et al* 2005 Investigation of the plasma potential oscillations in the range of geodesic acoustic mode frequencies by heavy ion beam probing in tokamaks *Czech. J. Phys.* **55** 349

[292] Melnikov A.V. *et al* 2006 Investigation of geodesic acoustic mode oscillations in the T-10 tokamak *Plasma Phys. Control. Fusion* **48** S87

[293] Melnikov A.V. *et al* 2013 Radial mode structure of plasma fluctuations in the GAM frequency range in OH and ECRH plasmas in the T-10 tokamak *Proc. 40th EPS Conf. Plasma Phys.* (Helsinki) (ECA) vol 37Dp P2.178 (http://ocs.ciemat.es/EPS2013PAP/pdf/P2.178.pdf)

[294] Zenin V.N., Subbotin G.F., Klyuchnikov L.A. and Melnikov A.V. 2016 Plasma potential and geodesic acoustic mode evolution with helium puffing in the ECRH regime on the T-10 tokamak *J. Phys.: Conf. Ser.* **747** 012005

[295] Eliseev L.G., Ivanov N.V., Kakurin A.M., Lysenko S.E., Maltsev S.G., Melnikov A.V., Perfilov S.V. and Zenin V.N. 2015 Study of the large-scale MHD mode and its effect on GAM in the T-10 tokamak *Proc. 42nd EPS Conf. Plasma Phys.* (Lisbon) (ECA) vol 39Ep P5.159 (http://ocs.ciemat.es/EPS2015PAP/pdf/P5.159.pdf)

[296] Melnikov A.V. *et al* 2015 The features of the global GAM in OH and ECRH plasmas in the T-10 tokamak *Nucl. Fusion* **55** 063001

[297] Eliseev L.G., Zenin V.N., Lysenko S.E. and Melnikov A.V. 2017 Measurement of geodesic acoustic modes and the turbulent particle flux in the T-10 tokamak plasmas *J. Phys.: Conf. Ser.* **907** 012002
[298] Melnikov A.V. *et al* 2017 Heavy ion beam probing-diagnostics to study potential and turbulence in toroidal plasmas *Nucl. Fusion* **57** 072004
[299] Vershkov V.A. *et al* 2017 Review of recent experiments on the T-10 tokamak with all metal wall *Nucl. Fusion* **57** 102017
[300] Melnikov A.V., Eliseev L.G., Lysenko S.E., Ufimtsev M.V. and Zenin V.N. 2017 Study of interactions between GAMs and broadband turbulence in the T-10 tokamak *Nucl. Fusion* **57** 115001
[301] Melnikov A.V. *et al* (HIBP Team) 2018 GAM and broadband turbulence structure in OH and ECRH plasmas in the T-10 tokamak *Plasma Fusion Res.* **13** 3402109
[302] Melnikov A.V. *et al* 2018 ECRH effect on the electric potential and turbulence in the TJ-II stellarator and T-10 tokamak plasmas *Plasma Phys. Control. Fusion* **60** 084008
[303] Zenin V.N., Drabinskij M.A., Eliseev L.G., Grashin S.A., Khabanov P.O., Kharchev N.K. and Melnikov A.V. 2018 The study of long range electric potential correlation on the GAM frequency on the T-10 tokamak *Proc. 45th EPS Conf. Plasma Phys.* (Prague) (ECA) vol 42Ap P2.1090 (http://ocs.ciemat.es/EPS2018PAP/pdf/P2.1090.pdf)
[304] Conway G.D., Scott B., Schirmer J., Reich M. and Kendl A. (ASDEX Upgrade Team) 2005 Direct measurement of zonal flows and geodesic acoustic mode oscillations in ASDEX Upgrade using Doppler reflectometry *Plasma Phys. Control. Fusion* **47** 1165
[305] Conway G.D., Tröster C., Scott B. and Hallatschek K. (ASDEX Upgrade Team) 2008 Frequency scaling and localization of geodesic acoustic modes in ASDEX Upgrade *Plasma Phys. Control. Fusion* **50** 055009
[306] Conway G.D., Angioni C., Ryter F., Sauter P. and Vicente J. (ASDEX Upgrade Team) 2011 Mean and oscillating plasma flows and turbulence interactions across the L–H confinement transition *Phys. Rev. Lett.* **106** 065001
[307] Manz P. *et al* 2015 Geodesic oscillations and the weakly coherent mode in the I-mode of ASDEX Upgrade *Nucl. Fusion* **55** 083004
[308] Conway G.D. *et al* (ASDEX Upgrade Team) 2015 Impact of magnetic perturbation coils on the edge radial electric field and turbulence in ASDEX Upgrade *Plasma Phys. Control. Fusion* **57** 014035
[309] Simon P., Conway G.D., Stroth U., Biancalani A. and Palermo F. 2016 Comparison of experiment and models of geodesic acoustic mode frequency and amplitude geometric scaling in ASDEX Upgrade *Plasma Phys. Control. Fusion* **58** 045209
[310] Simon P., Conway G.D., Stroth U., Manz P. and Biancalani A. (ASDEX Upgrade Team) 2015 Structure and properties of geodesic acoustic mode oscillations in ASDEX Upgrade *Proc. 12th Int. Reflectometer Workshop IRW12* (Jülich) p 1214 (https://www.aug.ipp.mpg.de/IRW/IRW12/papers/1214-IRW12-SimonP-paper.pdf)
[311] Simon P. 2017 Investigation of geodesic acoustic mode flow oscillations using Doppler reflectometry in ASDEX Upgrade *PhD Thesis* Universität Stuttgart
[312] Stroth U. *et al* 2015 Experimental turbulence studies for gyrokinetic code validation using advanced microwave diagnostics *Nucl. Fusion* **55** 083027
[313] Horváth L. *et al* 2016 Experimental investigation of the radial structure of energetic particle driven modes *Nucl. Fusion* **56** 112003
[314] Prisiazhniuk D., Conway G.D., Krämer-Flecken A. and Stroth U. (ASDEX Upgrade Team) 2018 Density fluctuation correlation measurements in ASDEX Upgrade using poloidal and radial correlation reflectometry *Plasma Phys. Control. Fusion* **60** 075003
[315] Conway G.D., Palermo F., Novikau I., Simon P. and Hennequin P. (ASDEX Upgrade Team) 2019 Observations on edge GAM-turbulence interactions in ASDEX Upgrade *Proc. 46th EPS Conf. Plasma Phys.* (Milan) (ECA) vol 43Cp P2.1091 (http://ocs.ciemat.es/EPS2019PAP/pdf/P2.1091.pdf)
[316] Nagashima Y. *et al* 2005 Observation of nonlinear coupling between small-poloidal wave-number potential fluctuations and turbulent potential fluctuations in ohmically heated plasmas in the JFT-2M Tokamak *Phys. Rev. Lett.* **95** 095002
[317] Ido T. *et al* 2006 Geodesic-acoustic-mode in JFT-2M tokamak plasmas *Plasma Phys. Control. Fusion* **48** S41
[318] Ido T. *et al* 2006 Observation of the interaction between the geodesic acoustic mode and ambient fluctuation in the JFT-2M tokamak *Nucl. Fusion* **46** 512
[319] Nagashima Y. *et al* 2006 Bispectral analysis applied to coherent floating potential fluctuations obtained in the edge plasmas on JFT-2M *Plasma Phys. Control. Fusion* **48** S1
[320] Nagashima Y. *et al* 2006 Observation of coherent bicoherence and biphase in potential fluctuations around geodesic acoustic mode frequency on JFT-2M *Plasma Phys. Control. Fusion* **48** A377–86
[321] Hoshino K. *et al* 2006 Measurement and analysis of the fluctuations and poloidal flow on the JFT-2M tokamak *Proc. 21st IAEA Fusion Eng. Conf.* (Chengdu) IAEA-CN-149 EX/2–2 (http://www-naweb.iaea.org/napc/physics/FEC/FEC2006/papers/ex_2-2.pdf)
[322] Nagashima Y. *et al* 2009 Boundary of the geodesic acoustic eigenmode in the vicinity of the magnetic separatrix *Plasma Phys. Control. Fusion* **51** 065019
[323] Kobayashi T. *et al* 2013 Spatiotemporal structures of edge limit-cycle oscillation before L-to-H transition in the JFT-2M tokamak *Phys. Rev. Lett.* **111** 035002
[324] Kobayashi T. *et al* 2014 Dynamics of edge limit cycle oscillation in the JFT-2M tokamak *Nucl. Fusion* **54** 073017
[325] Kobayashi T. *et al* 2018 Quantification of turbulent driving forces for the geodesic acoustic mode in the JFT-2M tokamak *Phys. Rev. Lett.* **120** 045002
[326] Hamada Y., Watari T., Nishizawa A., Narihara K., Kawasumi Y., Ido T., Kojima M. and Toi K. (JIPP-IIU Group) 2006 Streamers in the JIPP T-llU tokamak plasmas *Phys. Rev. Lett.* **96** 115003
[327] Hamada Y., Watari T., Nishizawa A., Ido T., Kojima M., Kawasumi Y. and Toi K. (JIPPR-IIU Group) 2006 Wavelet and Fourier analysis of zonal flows and density fluctuations in JIPP T-llU tokamak plasmas *Plasma Phys. Control. Fusion* **48** S117
[328] Hamada Y., Watari T., Yamagishi O., Nishizawa A., Narihara K., Kawasumi Y., Ido T., Kojima M. and Toi K. (JIPP-IIU Group) 2007 Change of zonal flow spectra in the JIPPT-IIU tokamak plasmas *Phys. Rev. Lett.* **99** 065005
[329] Hamada Y., Watari T., Nishizawa A., Yamagishi O., Narihara K., Kawasumi Y., Ido T., Kojima M. and Toi K. (JIPPR-IIU Group) 2010 GAM generation by drift waves in JIPP T-llU tokamak core plasmas *Nucl. Fusion* **50** 025001
[330] Hamada Y. *et al* (JIPPR-IIU Group) 2011 Detection of the kinetic geodesic acoustic mode (KGAM) near the centre region of JIPPT-IIU tokamak plasmas *Nucl. Fusion* **51** 033005
[331] Hamada Y., Watari T., Nishizawa A., Yamagishi O., Narihara K., Kawasumi Y., Ido T., Kojima M. and Toi K. (JIPPT-IIU Group) 2012 Regions of kinetic geodesic acoustic modes and streamers in JIPPT-IIU tokamak plasmas *Nucl. Fusion* **52** 063023
[332] Askinazi L.G. *et al* 2011 GAM evolution in the H-mode discharge in the TUMAN-3M tokamak *Proc. 38th EPS*

Conf. Plasma Phys. (Strasbourg) (ECA) vol 35Gp P1.115 (http://ocs.ciemat.es/EPS2011PAP/pdf/P1.115.pdf)
[333] Askinazi L.G. *et al* 2012 Evolution of geodesic acoustic mode in ohmic H-mode in TUMAN-3M tokamak *Tech. Phys. Lett.* **38** 268–71
[334] Yashin A.Y., Askinazi1 L.G., Belokurov A.A., Bulanin V.V., Lebedev S.V., Kornev V.A., Petrov A.V., Tukachinsky T.S. and Vildjunas M.I. 2013 GAM observation in the TUMAN-3M tokamak using Doppler reflectometry *Proc. 40th EPS Conf. Plasma Phys.* (Helsinki) (ECA) vol 37Dp P2.179 (http://ocs.ciemat.es/EPS2013PAP/pdf/P2.179.pdf)
[335] Bulanin V.V. *et al* 2016 GAM observation in the TUMAN-3M tokamak *Plasma Phys. Control. Fusion* **58** 045006
[336] Krämer-Flecken A., Soldatov S., Koslowski H.R. and Zimmermann O. (TEXTOR Team) 2006 Investigation of the poloidal GAM induced density fluctuation at TEXTOR *Proc. 33rd EPS Conf. Plasma Phys.* (Rome) (ECA) vol 30Ip P2.152 (http://epsppd.epfl.ch/Roma/start.htm)
[337] Krämer-Flecken A., Soldatov S., Koslowski H.R. and Zimmermann O. (TEXTOR Team) 2006 Properties of geodesic acoustic modes and the relation to density fluctuations *Phys. Rev. Lett.* **97** 045006
[338] Kramer-Flecken A., Soldatov S., Shelukhin D.A., Melnikov A.V. and Zimmermann O. (TEXTOR and T-10 Teams) 2007 Geodesic acoustic mode—radial extension and interaction with magnetic islands *Proc. 34th EPS Conf. Plasma Phys.* (Warsaw) (ECA) vol 31Fp P1.068
[339] Krämer-Flecken A., Soldatov S., Reiser D., Kantor M. and Koslowski H.R. 2009 Investigation of geodesic acoustic modes and related zonal flows at TEXTOR *Plasma Phys. Control. Fusion* **51** 015001
[340] Shesterikov I., Xu Y., Vergote M., Van Schoor M. and Van Oost G. (TEXTOR Team) 2010 Investigation of GAM zonal flows in the TEXTOR tokamak *Proc. 38th EPS Conf. Plasma Phys.* (Dublin) (ECA) vol 34Ap P1.1090 (http://ocs.ciemat.es/EPS2010PAP/pdf/P1.1090.pdf)
[341] Krämer-Flecken A., Soldatov S., Xu Y. and Zhang T. 2011 Correlation reflectometry in fusion plasmas—an application at TEXTOR *Plasma Phys. Control. Fusion* **53** 074020
[342] Xu Y. *et al* 2011 Observation of geodesic acoustic modes (GAMs) and their radial propagation at the edge of the TEXTOR tokamak *Plasma Phys. Control. Fusion* **53** 095015
[343] Zoletnik S., Bardoczi L., Krämer-Flecken A., Xu Y., Shesterikov I., Soldatov S., Anda G., Dunai D. and Petravich G. (TEXTOR Team) 2012 Methods for the detection of zonal flows using one-point and two-point turbulence measurements *Plasma Phys. Control. Fusion* **54** 065007
[344] Xu Y., Hidalgo C., Shesterikov I., Krämer-Flecken A., Zoletnik S., Van Schoor M. and Vergote M. (TEXTOR Team) 2013 Isotope effect and multiscale physics in fusion plasmas *Phys. Rev. Lett.* **110** 265005
[345] Zhao K.J. *et al* 2006 Toroidal symmetry of the geodesic acoustic mode zonal flow in a tokamak plasma *Phys. Rev. Lett.* **96** 255004
[346] Yan L.W. *et al* 2007 Three-dimensional features of GAM zonal flows in the HL-2A tokamak *Nucl. Fusion* **47** 1673
[347] Lan T. *et al* 2008 Spectral characteristics of geodesic acoustic mode in the HL-2A tokamak *Plasma Phys. Control. Fusion* **50** 045002
[348] Liu A.D. *et al* 2008 Three-dimensional spectral characteristics of low-frequency zonal flow in the edge plasma of HL-2A tokamak *Proc. 22nd IAEA Fusion Eng. Conf.* (Geneva) IAEA-CN-165 EX/P5–32 (http://www-http://www-naweb.iaea.org/napc/physics/FEC/FEC2008/papers/ex_p5-32.pdf)
[349] Cheng J. *et al* 2009 Density fluctuation of geodesic acoustic mode on the HL-2A tokamak *Nucl. Fusion* **49** 085030
[350] Dong J. *et al* 2010 Experimental study of turbulence and zonal flow in edge plasmas of the HL-2A tokamak *Plasma Fusion Res.* **5** S2014
[351] Kong D.F. *et al* 2013 Evolutions of zonal flows and turbulence in a tokamak edge plasma during electron cyclotron resonance heating *Nucl. Fusion* **53** 123006
[352] Zhao K.J. *et al* 2016 Synchronization of geodesic acoustic modes and magnetic fluctuations in toroidal plasmas *Phys. Rev. Lett.* **117** 145002
[353] Zhao K.J. *et al* 2017 Mesoscale electric fluctuations interacting with zonal flows, magnetic fluctuations and turbulence *Nucl. Fusion* **57** 076036
[354] Kong D.F. *et al* 2017 Exciting and propagating characteristics of two coexisting kinetic geodesic acoustic modes in the edge of plasma *Nucl. Fusion* **57** 044003
[355] Hong R. *et al* (HL-2A Team) 2018 Edge shear flows and particle transport near the density limit of the HL-2A tokamak *Nucl. Fusion* **58** 016041
[356] Liang A.S. *et al* 2018 Pedestal dynamics across low to high confinement regime in the HL-2A tokamak *Phys. Plasmas* **25** 022501
[357] Silva C., Arnoux G., Groth M., Hidalgo C. and Marsen S. (JET-EFDA Contributors) 2013 Observation of geodesic acoustic modes in the JET edge plasma *Plasma Phys. Control. Fusion* **55** 025001
[358] Silva C. *et al* (JET Contributors) 2016 Experimental investigation of geodesic acoustic modes on JET using Doppler backscattering *Nucl. Fusion* **56** 106026
[359] Silva C., Hillesheim J.C., Gil L., Hidalgo C., Meneses L. and Rimini F. (JET Contributors) 2018 Scaling of the geodesic acoustic mode amplitude on JET *Plasma Phys. Control. Fusion* **60** 085006
[360] Silva C., Hillesheim J.C., Gil L., Hidalgo C., Maggi C.F., Meneses L. and Solano E.R. (JET Contributors) 2019 Geodesic acoustic mode evolution in L-mode approaching the L–H transition on JET *Plasma Phys. Control. Fusion* **61** 075007
[361] Silva C., Hidalgo C., Figueiredo H., Duarte P., Fernandes H., Nedzelskiy I. and Pedrosa M.A. 2008 Experimental evidence of coupling between local turbulent transport and large scale fluctuations in the ISTTOK edge plasma *Phys. Plasmas* **15** 120703
[362] Silva C., Duarte P., Fernandes H., Figueiredo H., Nedzelskij I., Hidalgo C. and Pedrosa M.A. 2009 Characterization of geodesic acoustic modes in the ISTTOK edge plasma *Plasma Phys. Control. Fusion* **51** 085009
[363] Silva C., Duarte P., Fernandes H. and Figueiredo H. 2012 Interaction between mean and fluctuating $E \times B$ shear flows on the ISTTOK edge plasma *Plasma Phys. Control. Fusion* **54** 085013
[364] Silva C., Henriques R., Hidalgo C. and Fernandes H. 2018 Experimental evidence of turbulence regulation by time-varying $E \times B$ flows *Nucl. Fusion* **58** 026017
[365] Xu G.S. *et al* 2011 First evidence of the role of zonal flows for the L–H transition at marginal input power in the EAST tokamak *Phys. Rev. Lett.* **107** 125001
[366] Yan N. *et al* 2013 Statistical characterization of turbulence in the boundary plasma of EAST *Plasma Phys. Control. Fusion* **55** 115007
[367] Zhang X.-H. *et al* 2015 Comparison of three methods in extracting coherent modes from a Doppler backscatter system *Chin. Phys. Lett.* **32** 125201
[368] Zhang X.H. *et al* 2018 Observation of geodesic acoustic mode in EAST using Doppler backscattering system *Phys. Plasmas* **25** 092503
[369] Feng X. *et al* 2019 I-mode investigation on the experimental advanced superconducting tokamak *Nucl. Fusion* **59** 096025

[370] Matsunaga G., Kamiya K., Shinohara K., Miyato N., Kojima A. and Bierwage A. (JT-60 Team) 2012 Observation of energetic particle driven axisymmetric mode in the JT-60U tokamak *Proc. 39th EPS Conf. Plasma Phys.* (Stockholm) (ECA) vol 36Fp P2.062 (http://ocs ciemat.es/EPSICPP2012PAP/pdf/P2.062.pdf)

[371] Sechrest Y., Munsat T., D'Ippolito D.A., Maqueda R.J., Myra J.R., Russell D. and Zweben S.J. 2011 Flow and shear behavior in the edge and scrape-off layer of L-mode plasmas in national spherical torus experiment *Phys. Plasmas* **18** 012502

[372] Vermare L., Hennequin P. and Gürcan Ö.D. (Tore Supra Team) 2012 Detection of geodesic acoustic mode oscillations, using multiple signal classification analysis of Doppler backscattering signal on Tore Supra *Nucl. Fusion* **52** 063008

[373] Storelli A. *et al* 2015 Comprehensive comparisons of geodesic acoustic mode characteristics and dynamics between Tore Supra experiments and gyrokinetic simulations *Phys. Plasmas* **22** 062508

[374] Robinson J.R., Hnat B., Dura P., Kirk A. and Tamain P. (MAST Team) 2012 Interaction between a low-frequency electrostatic mode and resonant magnetic perturbations in MAST *Plasma Phys. Control. Fusion* **54** 105007

[375] Robinson J. 2012 The geodesic acoustic mode in strongly-shaped tight aspect ratio tokamaks *PhD Thesis* Department of Physics and Astronomy, University of Warwick, UK

[376] Hnat B., Gadgil S., Kirk A., Militello F. and Walkden N. (MAST Team) 2018 Experimental constraint on the radial mode number of the geodesic acoustic mode from multi-point Langmuir probe measurements in MAST Ohmic plasma *Plasma Phys. Control. Fusion* **60** 085016

[377] Cziegler I. *et al* 2013 Fluctuating zonal flows in the I-mode regime in Alcator C-Mod *Phys. Plasmas* **20** 055904

[378] Cziegler I., Tynan G.R., Diamond P.H., Hubbard A.E., Hughes J.W., Irby J. and Terry J.L. 2013 Nonlinear transfer in heated L-modes approaching the L–H transition threshold in Alcator C-Mod *Nucl. Fusion* **55** 083007

[379] Cziegler I., Hubbard A.E., Hughes J.W., Terry J.L. and Tynan G.R. 2017 Turbulence nonlinearities shed light on geometric asymmetry in tokamak confinement transitions *Phys. Rev. Lett.* **118** 105003

[380] Huang Z. *et al* 2013 Multi-diagnostic characterization of geodesic acoustic modes in the TCV tokamak *Proc. 40th EPS Conf. Plasma Phys.* (Helsinki) (ECA) vol 37Dp P2.175 (http://ocs.ciemat.es/EPS2013PAP/pdf/P2.175.pdf)

[381] Vuille V., Porte L., Brunner S., Coda S., Fasoli A., Huang Z., de Meijere C.A., Merlo G. and Vermare L. 2013 Investigation of turbulence and zonal flows for different shapes and scenarios in TCV using correlation ECE *Proc. 40th EPS Conf. Plasma Phys.* (Helsinki) (ECA) vol 37Dp P2.176 (http://ocs.ciemat.es/EPS2013PAP/pdf/P2.176.pdf)

[382] de Meijere C.A. *et al* 2014 Complete multi-field characterization of the geodesic acoustic mode in the TCV tokamak *Plasma Phys. Control. Fusion* **56** 072001

[383] Huang Z., Coda S., Merlo G., Brunner S., Villard L., Labit B. and Theiler C. (TCV Team) 2018 Experimental observations of modes with geodesic acoustic character from the core to the edge in the TCV tokamak *Plasma Phys. Control. Fusion* **60** 034007

[384] Bulanin V.V. *et al* 2014 Observation of geodesic acoustic modes in the Globus-M spherical Tokamak *Tech. Phys. Lett.* **40** 375–7

[385] Yashin A.Y. *et al* 2014 Geodesic acoustic mode observations in the Globus-M spherical tokamak *Nucl. Fusion* **54** 114015

[386] Yashin A.Y. *et al* 2015 Multi-diagnostic approach to geodesic acoustic mode study *J. Instrum.* **10** P10023

[387] Bulanin V.V. *et al* 2016 Geodesic acoustic mode investigation in the spherical Globus-M tokamak using multi-diagnostic approach *Nucl. Fusion* **56** 016017

[388] Gurchenko A.D. *et al* 2015 Turbulence and anomalous tokamak transport control by geodesic acoustic mode *Europhys. Lett.* **110** 55001

[389] Zhuang G. *et al* 2015 Overview of the recent research on the J-TEXT tokamak *Nucl. Fusion* **55** 104003

[390] Shen H.G. *et al* 2016 Observations of zonal flows in electrode biasing experiments on the joint Texas experimental tokamak *Phys. Plasmas* **23** 042305

[391] Zhao K.J. *et al* 2015 Plasma flows and fluctuations with magnetic islands in the edge plasmas of J-TEXT tokamak *Nucl. Fusion* **55** 073022

[392] Zhao K.J. *et al* 2017 Temporal-spatial structures of plasmas flows and turbulence around tearing mode islands in the edge tokamak plasmas *Nucl. Fusion* **57** 126006

[393] Jiang M. *et al* 2019 Influence of resonant magnetic perturbations and induced islands on plasma rotations and turbulence properties in the J-TEXT tokamak *Nucl. Fusion* **59** 046003

[394] Seidl J. *et al* 2017 Electromagnetic characteristics of geodesic acoustic mode in the COMPASS tokamak *Nucl. Fusion* **57** 126048

[395] Lachhvani L., Ghosh J., Chattopadhyay P.K., Chakrabarti N. and Pal R. 2017 Observation of geodesic acoustic mode in SINP-tokamak and its behaviour with varying edge safety factor *Phys. Plasmas* **24** 112501

[396] Lachhvani L., Macwan T., Ghosh J., Chattopadhyay P.K., Chakrabarty N. and Pal R. 2018 Effect of externally applied radial electric field (biased-electrode) on geodesic acoustic modes in SINP tokamak *Proc. 27th IAEA Fusion Eng. Conf.* (Gandhinagar) IAEA-CN-258 EX/P4–11 (https://nucleus.iaea.org/sites/fusionportal/Shared%20Documents/FEC%202018/fec2018-preprints/preprint0671.pdf)

[397] Basu D., Nakajima M., Melnikov A.V., McColl D., Rohollahi A., Elgriw S., Xiao C. and Hirose A. 2018 Geodesic acoustic mode (GAM) like oscillations and RMP effect in the STOR-M tokamak *Nucl. Fusion* **58** 024001

[398] Fujisawa A. *et al* 2006 Spectrograph of electric field fluctuation in toroidal helical plasma *Plasma Phys. Control. Fusion* **48** S31

[399] Hirsch M. and Holzhauer E. 2004 Doppler reflectometry with optimized temporal resolution for the measurement of turbulence and its propagation velocity *Plasma Phys. Control. Fusion* **46** 593–609

[400] Hirsch M., Akiyama T., Estrada T., Mizuuchi T., Toi K. and Hidalgo C. 2010 H-mode in helical devices *Proc.23rd IAEA Fusion Eng. Conf.* (Daejon) IAEA-CN-180 EXC/2–5Ra (http://www-naweb.iaea.org/napc/physics/FEC/FEC2010/papers/exc_2-5ra.pdf)

[401] Dreval M.B., Yakovenko Y.V., Sorokovoy E.L., Slavnyj A.S., Pavlichenko R.O., Kulaga A.E., Zamanov N.V. and Hirose A. 2016 Observation of 20–400 kHz fluctuations in the U-3M torsatron *Phys. Plasmas* **23** 022506

[402] Shats M.G. and Solomon W.M. 2002 Experimental evidence of self-regulation of fluctuations by time-varying flows *Phys. Rev. Lett.* **88** 045001

[403] Shats M.G. and Solomon W.M. 2002 Zonal flow generation in the improved confinement mode plasma and its role in confinement bifurcations *New J. Phys.* **4** 30

[404] Shats M.G., Xia H. and Punzmann H. 2006 Zonal flows, GAM, and radial electric field in the H-1 heliac *Czech. J. Phys.* **56** 1353–9

[405] Fujisawa A. *et al* 2007 Intermittent characteristics in coupling between turbulence and zonal flows *Plasma Phys. Control. Fusion* **49** 211

[406] Fujisawa A. *et al* 2008 Experimental studies of zonal flow and field in compact helical system plasma *Phys. Plasmas* **15** 055906

[407] Fujisawa A. *et al* 2007 Experimental evidence of a zonal magnetic field in a toroidal plasma *Phys. Rev. Lett.* **98** 165001

[408] Nagashima Y. *et al* 2010 Observation of edge Reynolds stress increase preceding an L–H transition in compact helical system *Plasma and Fusion Res.* **5** 022

[409] Toi K. *et al* 2010 Observation of reversed-shear Alfvén eigenmodes excited by energetic ions in a helical plasma *Phys. Rev. Lett.* **105** 145003

[410] Ido T. *et al* 2015 Identification of the energetic-particle driven GAM in the LHD *Nucl. Fusion* **55** 083024

[411] Inagaki S. *et al* 2008 Transport dynamics and multi-scale coupling of turbulence in LHD *Plasma and Fusion Res.* **3** S1006

[412] Inagaki S. *et al* 2013 How is turbulence intensity determined by macroscopic variables in a toroidal plasma? *Nucl. Fusion* **53** 113006

[413] Ido T. *et al* 2016 Abrupt excitation of intense geodesic acoustic mode in the LHD *Proc. 26th IAEA Fusion Eng. Conf.* (Kyoto) IAEA-CN-234 EX/P8–13 (https://nucleus.iaea.org/sites/fusionportal/Shared%20Documents/FEC%2016/fec2016-preprints/preprint0510.pdf)

[414] Ido T. *et al* 2016 Strong destabilization of stable modes with a half-frequency associated with chirping geodesic acoustic modes in the large helical device *Phys. Rev. Lett.* **116** 015002

[415] Lesur M. *et al* (LHD Experiment Group) 2016 Nonlinear excitation of subcritical instabilities in a toroidal plasma *Phys. Rev. Lett.* **116** 015003

[416] Estrada T. *et al* 2013 Spatial, temporal and spectral structure of the turbulence-flow interaction at the L–H transition *Plasma Phys. Control. Fusion* **54** 124024

[417] Estrada T., Ascasíbar E., Blanco E., Cappa A., Castejón F., Hidalgo C., van Milligen B.P. and Sánchez E. 2015 Limit cycle oscillations at the L–I–H transition in TJ-II plasmas: triggering, temporal ordering and radial propagation *Nucl. Fusion* **55** 063005

[418] Castejón F. *et al* 2016 Influence of magnetic well on electromagnetic turbulence in the TJ-II stellarator *Plasma Phys. Control. Fusion* **58** 094001

[419] Castejón F. *et al* 2017 3D effects on transport and plasma control in the TJ-II stellarator *Nucl. Fusion* **57** 102022

[420] Manz P., Ramisch M. and Stroth U. 2009 Physical mechanism behind zonal-flow generation in drift-wave turbulence *Phys. Rev. Lett.* **103** 165004

[421] Manz P., Ramisch M. and Stroth U. 2010 Long-range correlations induced by the self-regulation of zonal flows and drift-wave turbulence *Phys. Rev.* E **82** 056403

[422] Schmid B., Manz P., Ramisch M. and Stroth U. 2015 Investigation of the energy transfer to zonal flows at the stellarator TJ-K *Proc. 42nd EPS Conf. Plasma Phys.* (Lisbon) ECA 39E P1.160 (http://ocs.ciemat.es/EPS2015PAP/pdf/P1.160.pdf)

[423] Wilcox R.S., van Milligen B.P., Hidalgo C., Anderson D.T., Talmadge J.N., Anderson F.S.B. and Anderson M. 2011 Measurements of bicoherence and long-range correlations during biasing in the HSX stellarator *Nucl. Fusion* **51** 083048

[424] Vianello N. *et al* 2009 Transport mechanisms in the outer region of RFX-mod *Nucl. Fusion* **49** 045008

[425] Marrelli L., Martin P., Puiatti M.E., Sarff J.S., Chapman B.E., Drake J.R., Escande D.F. and Masamune S. 2021 The reversed field pinch *Nucl. Fusion* **61** 023001

[426] Xu Y. *et al* 2011 Long-range correlations and edge transport bifurcation in fusion plasmas *Nucl. Fusion* **51** 063020

[427] Nishizawa T. *et al* 2019 Direct measurement of a toroidally directed zonal flow in a toroidal plasma *Phys. Rev. Lett.* **122** 105001

[428] Askinazi L.G. *et al* 2017 Physics of GAM-initiated L–H transition in a tokamak *Plasma Phys. Control. Fusion* **59** 014037

[429] Sasaki M., Itoh K., Ido T., Shimizu A., Kobayashi T., Arakawa H., Kasuya N., Fujisawa A. and Itoh S.-I. 2018 Evaluation of measurement signal of heavy ion beam probe of energetic-particle driven geodesic acoustic modes *Plasma Fusion Res.* **13** 3403040

[430] Zhong W.L. *et al* 2015 Spatiotemporal characterization of zonal flows with multi-channel correlation Doppler reflectometers in the HL-2A tokamak *Nucl. Fusion* **55** 113005

[431] Shesterikov I., Xu Y., Tynan G.R., Diamond P.H., Jachmich S., Dumortier P., Vergote M., Van Schoor M. and Van Oost G. (TEXTOR Team) 2013 Experimental evidence for the intimate interaction among sheared flows, eddy structures, reynolds stress, and zonal Flows across a transition to improved confinement *Phys. Rev. Lett.* **111** 055006

[432] Inagaki S. *et al* 2011 Observation of long-distance radial correlation in toroidal plasma turbulence *Phys. Rev. Lett.* **107** 115001

[433] Xu M. *et al* 2018 Observation of electromagnetic GAMs excited by NBI in EAST *Nucl. Fusion* **58** 096004

[434] Qiu Z. and Chen L 2011 Kinetic theories of geodesic acoustic modes: radial structure, linear excitation by energetic particles and nonlinear saturation *Plasma Sci. Technol.* **13** 257–66

[435] McKee G.R., Gupta D.K., Fonck R.J., Schlossberg D.J., Shafer M.W. and Gohil P. 2006 Structure and scaling properties of the geodesic acoustic mode *Plasma Phys. Control. Fusion* **48** S123–36

[436] Punzmann H. and Shats M.G. 2004 Formation and structure of transport barriers during confinement transitions in toroidal plasma *Phys. Rev. Lett.* **93** 125003

[437] Bonanomi N., Angioni C., Crandall P.C., Di Siena A., Maggi C.F. and Schneider P.A. (ASDEX Upgrade Team, EUROFusion MST1 Team and JET Contributors) 2019 Effect of the isotope mass on the turbulent transport at the edge of L-mode plasmas in ASDEX Upgrade and JET-ILW *Nucl. Fusion* **59** 126025

[438] Hahm T.S., Wang L., Wang W.X., Yoon E.S. and Duthoit F.X. 2013 Isotopic dependence of residual zonal flows *Nucl. Fusion* **53** 072002

[439] Bustos A., Bañón Navarro A., Görler T., Jenko F. and Hidalgo C. 2015 Microturbulence study of the isotope effect *Phys. Plasmas* **22** 012305

[440] Liu B., Silva C., Figueiredo H., Pedrosa M.A., van Milligen B.P., Pereira T., Losada U and Losada C. 2016 Multi-scale study of the isotope effect in ISTTOK *Nucl. Fusion* **56** 056012

[441] Hennequin P 2015 Comprehensive experimental study of plasma turbulence structure and its scaling with rho* *Proc. 42nd EPS Conf. Plasma Phys.* (Lisbon) ECA-Invited Oral

[442] Niskala P. *et al* 2017 Gyrokinetic characterization of the isotope effect in turbulent transport at the FT-2 tokamak *Plasma Phys. Control. Fusion* **59** 044010

[443] Krämer-Flecken A. 2017 Observations of long-range correlation variations with isotope in TEXTOR using poloidal correlation reflectometry (private communication)

[444] Yang S., Xie J. and Liu W. 2015 Kinetic effects on geodesic acoustic mode from combined collisions and impurities *Phys. Plasmas* **22** 044502

[445] Ni G.S., Liu Y. and Liu S.Q. 2015 Collisionless damping of geodesic acoustic mode in a multi-ion plasma with superthermal ions *Contrib. Plasma Phys.* **55** 578

[446] Xie B., Guo W. and Xiang N. 2018 Impurity effect on geodesic acoustic mode in toroidally rotating tokamak plasmas *Plasma Phys. Control. Fusion* **60** 025015
[447] Shi B.R., Li J.Q. and Dong J.Q. 2005 Geodesic acoustic mode in toroidally axisymmetric plasmas with non-circular cross sections *Chin. Phys. Lett.* **22** 1179
[448] Shi B 2007 Collisionless residual zonal flow level of toroidally axisymmetric plasmas with arbitrary aspect ratio and elongation *Plasma Phys. Control. Fusion* **49** 2019–25
[449] Sorokina E.A., Lakhin V.P., Konovaltseva L.V. and Ilgisonis V.I. 2017 Geodesic acoustic modes in noncircular cross section tokamaks *Plasma Phys. Rep.* **43** 271
[450] Gao Z., Wang P., Dong J. and Sanuki H 2008 Plasma shaping effects on temperature gradient driven instabilities and geodesic acoustic modes *Proc. 22nd IAEA Fusion Eng. Conf.* (Geneva) IAEA-CN-165 TH/P8–4 (http://www-naweb.iaea.org/napc/physics/FEC/FEC2008/papers/th_p8-4.pdf)
[451] Gao Z., Wang P. and Sanuki H. 2008 Plasma shaping effects on the geodesic acoustic mode in toroidally axisymmetric plasmas *Phys. Plasmas* **15** 074502
[452] Hager R. and Hallatschek K. 2013 Geodesic acoustic mode frequencies in experimental tokamak equilibria *Plasma Phys. Control. Fusion* **55** 035009
[453] Kendl A. and Scott B.D. 2006 Flux-surface shaping effects on tokamak edge turbulence and flows *Phys. Plasmas* **13** 012504
[454] Hager R. and Hallatschek K. 2012 Nonlinear dispersion relation of geodesic acoustic modes *Phys. Rev. Lett.* **108** 035004
[455] Hager R. and Hallatschek K. 2012 The nonlinear dispersion relation of geodesic acoustic modes *Phys. Plasmas* **19** 082315
[456] Sasaki M., Itoh K., Kasuya N., Hallatschek K. and Itoh S.-I. 2013 On a nonlinear dispersion effect of geodesic acoustic modes *Plasma Fusion Res.* **8** 1403010
[457] Fontana M., Porte L., Coda S. and Sauter O. (TCV Team) 2018 The effect of triangularity on fluctuations in a tokamak plasma *Nucl. Fusion* **58** 024002
[458] Austin M.E. *et al* 2019 Achievement of reactor-relevant performance in negative triangularity shape in the DIII-D tokamak *Phys. Rev. Lett.* **122** 115001
[459] Cho Y.W., Yi S., Kwon J.M. and Hahm T.S. 2016 In-out asymmetry of zonal flow shear and turbulence reduction *Phys. Plasmas* **23** 102312
[460] Vermare L., Hennequin P., Gürcan Ö.D., Garbet X., Honoré C., Clairet F., Giacalone J.C., Morel P. and Storelli A. (Tore Supra Team) 2018 Poloidal asymmetries of flows in the Tore Supra tokamak *Phys. Plasmas* **25** 020704
[461] Donnel P., Garbet X., Sarazin Y., Asahi Y., Wilczynski F., Caschera E., Dif-Pradalier G., Ghendrih P. and Gillot C. 2019 Turbulent generation of poloidal asymmetries of the electric potential in a tokamak *Plasma Phys. Control. Fusion* **61** 014003
[462] Vermare L., Hennequin P., Gürcan O.D., Honoré C., Morel P., Storelli A., Donnel P., Garbet X. and Giacalone J.C. (Tore Supra Team) 2018 Poloidal asymmetry and dynamics of perpendicular flow in Tore Supra plasmas *Proc. 45th EPS Conf. Plasma Phys.* (Prague) ECA 42A P5.1062 (http://ocs.ciemat.es/EPS2018PAP/pdf/P5.1062.pdf)
[463] Wang M.Y *et al* 2018 Investigation of electromagnetic geodesic acoustic mode in EAST RF-heating plasma *Phys. Plasmas* **25** 102508
[464] Zhong W.L. *et al* 2015 Three dimensional measurements of geodesic acoustic mode with correlation Doppler reflectometers *J. Instrum.* **10** P10014
[465] Xu Y., Shesterikov I., Van Schoor M., Vergote M., Weynants R.R., Krämer-Flecken A., Reiser D. and Zoletnik S. (TEXTOR Team) 2011 Overview of recent results on long-range correlations and zonal flows in the edge of TEXTOR tokamak *Proc. 38th EPS Conf. Plasma Phys.* (Strasbourg) ECA 35G O4.125 (http://ocs.ciemat.es/EPS2011PAP/pdf/O4.125.pdf)
[466] Gurchenko A.D., Gusakov E.Z., Altukhov A.B., Esipov L.A., Kantor M.Y., Kouprienko D.V., Lashkul S.I. and Perevalov A. 2013 The isotope effect on the geodesic acoustic mode spatial structure and its interaction with small scale turbulence in the FT-2 tokamak *Proc. 40th EPS Conf. Plasma Phys.* (Helsinki) ECA 37D P2.181 (http://ocs.ciemat.es/EPS2013PAP/pdf/P2.181.pdf)
[467] Gurchenko A.D. *et al* 2014 The isotope effect in GAM—turbulence interplay and anomalous transport in tokamak *Proc. 25th IAEA Fusion Eng. Conf.* (St. Petersburg) IAEA-CN-221 EX/11–2Ra (http://www-naweb.iaea.org/napc/physics/FEC/FEC2014/fec2014-preprints/446_EX112Ra.pdf)
[468] Huang Z., Coda S. and de Meijere C.A. 2014 Investigation of plasma turbulence and geodesic acoustic modes using tangential phase-contrast imaging in the TCV tokamak *Proc. 41st EPS Conf. Plasma Phys.* (Berlin) ECA 38F P5.071 (http://ocs.ciemat.es/EPS2014PAP/pdf/P5.071.pdf)
[469] Melnikov A.V., Eliseev L.G., Lysenko S.E., Perfilov S.V., Shurygin R.V., Krupnik L.I., Kozachek A.S. and Smolyakov A.I. 2014 Radial homogeneity of geodesic acoustic modes in ohmic discharges with low B in the T-10 tokamak *JETP Lett.* **100** 555–60
[470] Sasaki M., Kobayashi T., Itoh K., Kasuya N., Kosuga Y., Fujisawa A. and Itoh S.-I. 2018 Spatio-temporal dynamics of turbulence trapped in geodesic acoustic modes *Phys. Plasmas* **25** 012316
[471] Sasaki M., Itoh K., Hallatschek K., Kasuya N., Lesur M., Kosuga Y. and Itoh S.-I. 2017 Enhancement and suppression of turbulence by energetic-particle-driven geodesic acoustic modes *Sci. Rep.* **7** 16767
[472] Villard L. *et al* 2019 Global turbulence features across marginality and non-local pedestal-core interactions *Plasma Phys. Control. Fusion* **61** 034003
[473] Gillot C., Dif-Pradalier G., Garbet X., Panico O., Sarazin Y., Varennes R. and Zarzoso D. 2021 Investigation of tokamak turbulent avalanches using wave-kinetic formulation in toroidal geometry *J. Plasma Phys.* **87** 905870221
[474] Hager R. and Hallatschek K. 2010 Radial propagation of geodesic acoustic modes in up-down asymmetric magnetic geometries *Phys. Plasmas* **17** 032112
[475] McMillan B.F., Jolliet S., Tran T.M., Villard L., Bottino A. and Angelino P. 2009 Avalanchelike bursts in global gyrokinetic simulations *Phys. Plasmas* **16** 022310
[476] Zhao K.J. *et al* 2013 Spatial structures and interaction of multiple sheared flow populations in tokamak edge turbulence *Nucl. Fusion* **53** 083011
[477] Wang S. 2006 Erratum: zonal flows in tokamak plasmas with tororidal rotation [Phys. Rev. Lett. 97, 085002 (2006)] *Phys. Rev. Lett.* **97** 129902
[478] Wahlberg C. 2008 Geodesic acoustic mode induced by toroidal rotation in tokamaks *Phys. Rev. Lett.* **101** 115003
[479] Ilgisonis V.I., Lakhin V.P., Smolyakov A.I. and Sorokina E.A. 2011 Geodesic acoustic modes and zonal flows in rotating large-aspect-ratio tokamak plasmas *Plasma Phys. Control. Fusion* **53** 065008
[480] Elfimov A.G., Galvão R.M.O. and Sgalla R.J.F. 2011 Rotation effect on geodesic and zonal flow modes in tokamak plasmas with isothermal magnetic surfaces *Plasma Phys. Control. Fusion* **53** 105003
[481] Yu J. and Gong X. 2013 Geodesic acoustic mode excitation by drift waves in tokamak plasmas with toroidal rotation *Nucl. Fusion* **53** 123027
[482] Graves J.P. and Wahlberg C. 2017 Generalised zonal modes in stationary axisymmetric plasmas *Plasma Phys. Control. Fusion* **59** 054011

[483] Zhou D. 2010 Zonal flow modes in a tokamak plasma with dominantly poloidal mean flows *Phys. Plasmas* **17** 102505

[484] Lakhin V.P. and Ilgisonis V.I. 2011 Continuum modes in rotating plasmas: general equations and continuous spectra for large aspect ratio tokamaks *Phys. Plasmas* **18** 092103

[485] Ren H. 2012 Effect of toroidal rotation on the geodesic acoustic mode in magnetohydrodynamics *Phys. Plasmas* **19** 094502

[486] Marusov N.A., Lakhin V.P., Sorokina E.A. and Smolyakov A.I. 2019 Global structure of stationary zonal flow in rotating tokamak plasmas *Proc. 46th EPS Conf. Plasma Phys.* (Milan) ECA 43C P4.1039 (http://ocs.ciemat.es/EPS2019PAP/pdf/P4.1039.pdf)

[487] Guo W., Ye L., Zhou D., Xiao X. and Wang S. 2015 Kinetic effect of toroidal rotation on the geodesic acoustic mode *Phys. Plasmas* **22** 012501

[488] Guo W., Ye L., Zhou D., Xiao X. and Wang S. 2016 Erratum: Kinetic effect of toroidal rotation on the geodesic acoustic mode [Phys. Plasmas 22, 012501 (2015)] *Phys. Plasmas* **23** 119901

[489] Ren H. and Cao J. 2015 Landau damping of geodesic acoustic mode in toroidally rotating tokamaks *Phys. Plasmas* **22** 062501

[490] Zhou D. 2015 Geodesic acoustic modes in tokamak plasmas with a radial equilibrium electric field *Phys. Plasmas* **22** 092504

[491] Gong X., Xie B., Guo W., Chen Y. and Yu J. 2016 Collisional damping of the geodesic acoustic mode with toroidal rotation. I. Viscous damping *Phys. Plasmas* **23** 032503

[492] Xie B., Yu J., Gong X., Guo W. and Chen Y. 2017 Collisional damping of the geodesic acoustic mode with toroidal rotation. II. Gyrokinetic formulation *Phys. Plasmas* **23** 032504

[493] Xie B., Guo W., Gong X., Yu J., Chen Y. and Cao J. 2016 Electron collisionless damping of the geodesic acoustic mode in rotating tokamak plasmas *Nucl. Fusion* **56** 124001

[494] Xie B., Guo W. and Xiang N. 2017 Collisional damping of the geodesic acoustic mode with poloidal rotation *Phys. Plasmas* **24** 052510

[495] Krämer-Flecken A. 2020 Unpublished observations of GAMs in TEXTOR with tangential cnt-NBI, but absent with co-NBI (private communication)

[496] Ren H. and Dong C. 2014 Effects of passing energetic particles on geodesic acoustic mode *Phys. Plasmas* **21** 102506

[497] Manz P. *et al* 2018 Magnetic configuration effects on the Reynolds stress in the plasma edge *Phys. Plasmas* **25** 072508

[498] Todo Y., Berk H.L. and Breizman B.N. 2010 Nonlinear magnetohydrodynamic effects on Alfvén eigenmode evolution and zonal flow generation *Nucl. Fusion* **50** 084016

[499] Qiu Z., Chen L., Zonca F. and Chen W. 2019 Nonlinear excitation of a geodesic acoustic mode by toroidal Alfvén eigenmodes and the impact on plasma performance *Nucl. Fusion* **59** 066031

[500] Chandra D., Agullo O., Benkadda S., Garbet X. and Sen A. 2013 Nonlinear dynamics of multiple neoclassical tearing modes in tokamaks *Phys. Plasmas* **20** 042505

[501] Itoh S.I. and Itoh K. 2012 Response of plasma turbulence against externally-controlled perturbations *Chin. Phys.* B **21** 095201

[502] Hallatschek K. and McKee G.R. 2012 Excitation of geodesic acoustic modes by external fields *Phys. Rev. Lett.* **109** 245001

[503] Kleva R.G. and Hassam A.B. 2013 The excitation of geodesic acoustic mode flows by a resonant magnetic field and by resonant heating *Phys. Plasmas* **20** 032508

[504] Hallatschek K. 2008 Diamagnetic GAM drive mechanism *Proc. 35th EPS Conf. Plasma Phys.* (Hersonissos) ECA 32D P1.036 (http://epsppd.epfl.ch/Hersonissos/start.htm)

[505] Stroth U., Manz P. and Ramisch M 2011 On the interaction of turbulence and flows in toroidal plasmas *Plasma Phys. Control. Fusion* **53** 024006

[506] Pedrosa M.A., Hidalgo C., Silva C., Carreras B.A., Carralero D. and Calvo I. (TJ-II Team) 2010 Long-range correlations during plasma transitions in the TJ-II stellarator *Contrib. Plasma Phys.* **50** 507

[507] Hidalgo C. *et al* 2009 Multi-scale physics mechanisms and spontaneous edge transport bifurcations in fusion plasmas *Europhys. Lett.* **87** 55002

[508] Xu Y., Jachmich S., Weynants R.R., Van Schoor M., Vergote M., Krämer-Flecken A., Schmitz O., Unterberg B. and Hidalgo C. (TEXTOR Team) 2009 Long-distance correlation and zonal flow structures induced by mean $E \times B$ shear flows in the biasing H-mode at TEXTOR *Phys. Plasmas* **16** 110704

[509] Shurygin R.V. and Melnikov A.V. 2018 Influence of an external AC electric field on plasma turbulence in the tokamak near-wall layer *Plasma Phys. Rep.* **44** 303

[510] Gurchenko A.D. *et al* 2011 Investigation of GAM dynamics and spatial structure in the FT-2 tokamak *Proc. 38th EPS Conf. Plasma Phys.* (Strasbourg) ECA 35G P2.127 (http://ocs.ciemat.es/EPS2011PAP/pdf/P2.127.pdf)

[511] Chen W. *et al* 2013 EGAM induced by energetic electrons and nonlinear interactions among EGAM, BAEs and tearing modes in a toroidal plasma *Phys. Lett.* A **377** 387–90

[512] Wang H., Todo Y. and Kim C.C. 2013 Hole-clump pair creation in the evolution of energetic-particle-driven geodesic acoustic modes *Phys. Rev. Lett.* **110** 155006

[513] Osakabe M. *et al* 2014 Indication of bulk-ion heating by energetic particle driven geodesic acoustic modes on LHD *Proc. 25th IAEA Fusion Eng. Conf.* (St. Petersburg) IAEA-CN-221 EX/10–3 (http://www-naweb.iaea.org/napc/physics/FEC/FEC2014/fec2014-preprints/446_EX103.pdf)

[514] Zimmermann O., Buratti P., Krämer-Flecken A., Koslowski H.R., Liang Y., Pinches S.D. and Sharapov S.E. (TEXTOR Team and JET EFDA Contributors) 2007 Excitation of Alfvén-like modes by large resonant magnetic perturbations in ohmic discharges *Proc. 34th EPS Conf. Plasma Phys.* (Warsaw) ECA 31F P1.121 (http://epsppd.epfl.ch/Warsaw/start.htm)

[515] Miki K. and Idomura Y. 2015 Finite-orbit-width effects on energetic-particle-induced geodesic acoustic mode *Plasma Fusion Res.* **10** 3403069

[516] Heidbrink W.W. 2008 Basic physics of Alfvén instabilities driven by energetic particles in toroidally confined plasmas *Phys. Plasmas* **15** 055501

[517] Berk H.L., Breizman B.N. and Petviashvili N.V. 1997 Spontaneous hole-clump pair creation in weakly unstable plasmas *Phys. Lett.* A **234** 213–8

[518] Ido T. *et al* 2017 Observation of subcritical geodesic acoustic mode excitation in the large helical device *Nucl. Fusion* **57** 072009

[519] Fisher R.K., Pace D.C., Kramer G.J., Van Zeeland M.A., Nazikian R., Heidbrink W.W. and García-Muñoz M. 2012 Beam ion losses due to energetic particle geodesic acoustic modes *Nucl. Fusion* **52** 123015

[520] Fisch N.J. and Herrmann M.C. 1994 Utility of extracting alpha particle energy by waves *Nucl. Fusion* **34** 1541–56

[521] Novikau I. *et al* 2020 Nonlinear dynamics of energetic-particle driven geodesic acoustic modes in ASDEX Upgrade *Phys. Plasmas* **27** 042512

[522] Kramer G.J., Chen L., Fisher R.K., Heidbrink W.W., Nazikian R., Pace D.C. and Van Zeeland M.A. 2012 Fractional resonances between waves and energetic particles in tokamak plasmas *Phys. Rev. Lett.* **109** 035003

[523] Itoh K., Itoh S.-I., Kosuga Y., Lesur M. and Ido T. 2016 Onset condition of the subcritical geodesic acoustic mode instability in the presence of energetic-particle-driven geodesic acoustic mode *Plasma Phys. Rep.* **42** 418

[524] Lesur M. *et al* 2016 Nonlinear excitation of subcritical fast ion-driven modes *Nucl. Fusion* **56** 056009

[525] Itoh S.-I., Itoh K., Zushi H. and Fukuyama A. 1998 Physics of collapse events in toroidal plasmas *Plasma Phys. Control. Fusion* **40** 879

[526] Holland C., Tynan G.R., Diamond P.H., Moyer R.A. and Burin M.J. 2002 Evidence for Reynolds-stress driven shear flows using bispectral analysis: theory and experiment *Plasma Phys. Control. Fusion* **44** A453

[527] Tynan G.R., Moyer R.A., Burin M.J. and Holland C. 2001 On the nonlinear turbulent dynamics of shear-flow decorrelation and zonal flow generation *Phys. Plasmas* **8** 2691

[528] Collis W.B., White P.R. and Hammond J.K. 1998 Higher-order spectra: the bispectrum and trispectrum *Mech. Syst. Signal Process.* **12** 375

[529] van Milligen B.P., Sánchez E., Estrada T., Hidalgo C., Brañas B., Carreras B and García L. 1995 Wavelet bicoherence: a new turbulence analysis tool *Phys. Plasmas* **2** 3017

[530] van Milligen B.P., Estrada T., Hidalgo C., Happel T. and Ascasíbar E. 2013 Spatiotemporal and wavenumber resolved bicoherence at the low to high confinement transition in the TJ-II stellarator *Nucl. Fusion* **53** 113034

[531] Ida K., Miura Y., Ido T., Nagashima Y. and Shinohara K. 2006 Studies of radial electric field formation and its effect on fluctuations and transport barriers in the JFT-2M tokamak *Fusion Sci. Technol.* **49** 122

[532] Itoh K., Hallatschek K., Itoh S.-I., Diamond P.H. and Toda S. 2005 Coherent structure of zonal flow and onset of turbulent transport *Phys. Plasmas* **12** 062303

[533] Zhong W. *et al* 2017 Dynamics of oscillatory plasma flows prior to the H-mode in the HL-2A tokamak *Plasma Sci. Technol.* **19** 070501

[534] Zhao K.J. *et al* 2007 Characteristics of geodesic acoustic mode zonal flow and ambient turbulence at the edge of the HL-2A tokamak plasmas *Phys. Plasmas* **14** 12230

[535] Zhao K.J. *et al* 2010 Turbulence and zonal flows in edge plasmas of the HL-2A tokamak *Plasma Phys. Control. Fusion* **52** 124008

[536] Ritz C.P., Powers E.J. and Bengtson R.D. 1989 Experimental measurement of three-wave coupling and energy cascading *Phys. Fluids* B **1** 153

[537] Kim J.S., Durst R.D., Fonck R.J., Fernandez E., Ware A. and Terry P.W. 1996 Technique for the experimental estimation of nonlinear energy transfer in fully developed turbulence *Phys. Plasmas* **3** 3998

[538] Nagashima Y. *et al* 2008 Nonlinear energy transfer of drift-wave fluctuation in a cylindrical laboratory plasma *Plasma Fusion Res.* **3** 056

[539] Nagashima Y. *et al* 2009 Observation of the parametric-modulational instability between the drift-wave fluctuation and azimuthally symmetric sheared radial electric field oscillation in a cylindrical laboratory plasma *Phys. Plasmas* **16** 020706

[540] Crossley F.J., Uddholm P., Duncan P., Khalid M. and Rusbridge M.G. 1992 Experimental study of drift-wave saturation in quadrupole geometry *Plasma Phys. Control. Fusion* **34** 235

[541] Xia H. and Shats M.G. 2003 Inverse energy cascade correlated with turbulent-structure generation in toroidal plasma *Phys. Rev. Lett.* **91** 155001

[542] Xia H. and Shats M.G. 2004 Spectral energy transfer and generation of turbulent structures in toroidal plasma *Phys. Plasmas* **11** 561

[543] Shats M.G., Xia H., Punzmann H. and Solomon W.M. 2004 Spectral energy transfer, generation of zonal flows and their role in confinement transitions *Fusion Sci. Technol.* **46** 279

[544] Xu M. *et al* 2012 Frequency-resolved nonlinear turbulent energy transfer into zonal flows in strongly heated L-mode plasmas in the HL-2A tokamak *Phys. Rev. Lett.* **108** 245001

[545] Schmid B., Manz P., Ramisch M. and Stroth U. 2017 Collisional scaling of the energy transfer in drift-wave zonal flow turbulence *Phys. Rev. Lett.* **118** 055001

[546] Biglari H., Diamond P.H. and Terry P.W. 1990 Influence of sheared poloidal rotation on edge turbulence *Phys. Fluids* B **2** 1

[547] Kim E.-j. and Diamond P.H. 2004 Random shearing by zonal flows and transport reduction *Phys. Plasmas* **11** L77

[548] Zhang Y.Z., Xie T. and Mahajan S.M. 2012 Analysis on the exclusiveness of turbulence suppression between static and time-varying shear flow *Phys. Plasmas* **19** 020701

[549] Geng K.N. *et al* 2018 The role of geodesic acoustic mode on reducing the turbulent transport in the edge plasma of tokamak *Phys. Plasmas* **25** 012317

[550] Hahm T.S., Burrell K.H., Lin Z., Nazikian R. and Synakowski E.J. 2000 Zonal flow measurements concept I *Plasma Phys. Control. Fusion* **42** A205–10

[551] Ramisch M., Stroth U., Niedner S. and Scott B. 2003 On the detection of Reynolds stress as a driving and damping mechanism of geodesic acoustic modes and zonal flows *New J. Phys.* **5** 12

[552] Falchetto G.L. and Ottaviani M. 2004 Effect of collisional zonal-flow damping on flux-driven turbulent transport *Phys. Rev. Lett.* **92** 025002

[553] Garbet X. 2006 Introduction to turbulent transport in fusion plasmas *C. R. Phys.* **7** 573

[554] Garbet X., Sarazin Y., Imbeaux F., Ghendrih P., Bourdelle C., Gürcan Ö.D. and Diamond P.H. 2007 Front propagation and critical gradient transport models *Phys. Plasmas* **14** 122305

[555] Grasso D., Margheriti L., Porcelli F. and Tebaldi C. 2006 Magnetic islands and spontaneous generation of zonal flows *Plasma Phys. Control. Fusion* **48** L87

[556] Hallatschek K. 2013 Action of magnetic islands on GAMs and zonal flows *Proc. 40th EPS Conf. Plasma Phys.* (Helsinki) ECA 37D P2.184 (http://ocs.ciemat.es/EPS2013PAP/pdf/P2.184.pdf)

[557] Ishizawa A., Kishimoto Y. and Nakamura Y. 2019 Multi-scale interactions between turbulence and magnetic islands and parity mixture-a review *Plasma Phys. Control. Fusion* **61** 054006

[558] Ida K. *et al* 2002 Observation of plasma flow at the magnetic island in the large helical device *Phys. Rev. Lett.* **88** 015002

[559] Estrada T., Ascasíbar E., Blanco E., Cappa A., Hidalgo C., Ida K., López-Fraguas A. and van Milligen B.P. 2016 Plasma flow, turbulence and magnetic islands in TJ-II *Nucl. Fusion* **56** 026011

[560] Jiang M. *et al* 2018 Influence of $m/n = 2/1$ magnetic islands on perpendicular flows and turbulence in HL-2A ohmic plasmas *Nucl. Fusion* **58** 026002

[561] Li J. and Kishimoto Y. 2012 Small-scale dynamo action in multi-scale magnetohydrodynamic and micro-turbulence *Phys. Plasmas* **19** 030705

[562] Nishimura S., Benkadda S., Yagi M., Itoh S.I. and Itoh K. 2008 Rotation of magnetic islands regulated by self-generated zonal flow *Proc. 35th EPS Conf. Plasma Phys.* (Hersonissos) ECA 32D P5.059 (http://epsppd.epfl.ch/Hersonissos/start.htm)

[563] Krämer-Flecken A., Xu Y., Soldatov S., Jakubowski M., Liang Y., Reiser D. and Schmitz O. 2009 Overview on turbulence and structure formation during resonant magnetic perturbations at TEXTOR *J. Plasma Fusion Res.* **8** 44

[564] Hornsby W.A., Peeters A.G., Siccinio M. and Poli E. 2012 On the dynamics of vortex modes within magnetic islands *Phys. Plasmas* **19** 032308
[565] Zhao K.J. *et al* 2016 Co-current toroidal rotation-driven and turbulent stresses with resonant magnetic perturbations in the edge plasmas of the J-TEXT tokamak *Nucl. Fusion* **56** 076005
[566] Krämer-Flecken A., Soldatov S., Reiser D. and Jakubowski M.W.(TEXTOR Team) 2008 Effect of resonant magnetic perturbations on zonal flows and ambient turbulence *Proc. 35th EPS Conf. Plasma Phys.* (Hersonissos) ECA 32D P2.016 (http://epsppd.epfl.ch/Hersonissos/start.htm)
[567] Reiser D. 2008 Zonal flow dynamics and GAM oscillations in tokamaks with resonant magnetic field perturbations *Proc. 35th EPS Conf. Plasma Phys.* (Hersonissos) ECA 32D P2.031 (http://epsppd.epfl.ch/Hersonissos/start.htm)
[568] Reiser D. and Chandra D. 2009 Plasma currents induced by resonant magnetic field perturbations in tokamaks *Phys. Plasmas* **16** 042317
[569] Xu Y. *et al* 2007 Edge turbulence during the static dynamic ergodic divertor experiments in TEXTOR *Nucl. Fusion* **47** 1696
[570] Watari T., Hamada Y., Nishizawa A., Notake T. and Takeuchi N. 2006 Zonal flows and geodesic acoustic mode oscillations in tokamaks and helical systems *Plasma Sci. Technol.* **8** 105
[571] Watari T., Hamada Y., Notake T., Takeuchi N. and Itoh K. 2006 Geodesic acoustic mode oscillation in the low frequency range *Phys. Plasmas* **13** 062504
[572] Watari T., Hamada Y., Nishizawa A. and Todoroki J. 2007 Unified linear response function for zonal flows with full finite orbit effects *Phys. Plasmas* **14** 112512
[573] Satake S., Okamoto M., Nakajima N., Sugama H., Yokoyama M. and Beidler C.D. 2005 Non-local neoclassical transport simulation of geodesic acoustic mode *Nucl. Fusion* **45** 1362–8
[574] Watanabe T.-H., Sugama H. and Ferrando-Margalet S. 2007 Gyrokinetic simulation of zonal flows and ion temperature gradient turbulence in helical systems *Nucl. Fusion* **47** 1383
[575] Watanabe T.H., Sugama H. and Nunami M. 2011 Effects of equilibrium-scale radial electric fields on zonal flows and turbulence in helical configurations *Nucl. Fusion* **51** 123003
[576] Xanthopoulos P., Mischchenko A., Helander P., Sugama H. and Watanabe T.-H. 2011 Zonal flow dynamics and control of turbulent transport in stellarator *Phys. Rev. Lett.* **107** 245002
[577] Kleiber R., Hatzky R. and Mishchenko A. 2010 Simulation of residual zonal flow levels in stellarator including a radial electric field *Contrib. Plasma Phys.* **50** 766
[578] Monreal P., Sánchez E., Calvo I., Bustos A., Parra F.I., Mishchenko A., Könies A. and Kleiber R. 2017 Semianalytical calculation of the zonal-flow oscillation frequency in stellarator *Plasma Phys. Control. Fusion* **59** 065005
[579] Kleiber R., Borchardt M., Könies A., Mischenko A., Riemann J., Slaby C. and Hatzky R. 2018 Global gyrokinetic multi-model simulations of ITG and Alfvénic modes for tokamaks and the first operational phase of Wendelstein 7-X *Proc. 27th IAEA Fusion Eng. Conf.* (Gandhinagar) IAEA-CN-258 TH/P2–4 (https://nucleus.iaea.org/sites/fusionportal/Shared%20Documents/FEC%202018/fec2018-preprints/preprint0108.pdf)
[580] Sánchez E., Calvo I., Velasco J.L., Medina F., Alonso A., Monreal P. and Kleiber R. (TJ-II Team) 2018 Oscillatory relaxation of zonal flows in a multi-species stellarator plasma *Plasma Phys. Control. Fusion* **60** 094003
[581] Sánchez E. *et al* 2013 Collisionless damping of flows in the TJ-II stellarator *Plasma Phys. Control. Fusion* **55** 014015
[582] Sánchez E., Monreal P., Calvo I. and Kleiber R. 2015 Relaxation of zonal flows in stellarator: influence of the magnetic configuration *Proc. 42nd EPS Conf. Plasma Phys.* (Lisbon) ECA 39E P4.172 (http://ocs.ciemat.es/EPS2015PAP/pdf/P4.172.pdf)
[583] Alonso J.A. *et al* 2017 Observation of oscillatory radial electric field relaxation in a helical plasma *Phys. Rev. Lett.* **118** 185002
[584] Alonso J.A., Velasco J.L., Arévalo J., Hidalgo C., Pedrosa M.A., van Milligen B.P., Carralero D. and Silva C. 2013 Dynamics of zonal-flow-like structures in the edge of the TJ-II stellarator *Plasma Phys. Control. Fusion* **55** 014001
[585] Kobayashi T., Losada U., Liu B., Estrada T., van Milligen B.P., Gerrú R., Sasaki M. and Hidalgo C. 2019 Frequency and plasma condition dependent spatial structure of low frequency global potential oscillations in the TJ-II stellarator *Nucl. Fusion* **59** 044006
[586] Velasco J.L. *et al* (TJ-II Team) 2013 Damping of radial electric field fluctuations in the TJ-II stellarator *Plasma Phys. Control. Fusion* **55** 124044
[587] Kovrizhnykh L.M. 1984 Neoclassical theory of transport processes in toroidal magnetic confinement systems, with emphasis on non-axisymmetric configurations *Nucl. Fusion* **24** 851–936
[588] Fujisawa A. 2003 Experimental studies of structural bifurcation in stellarator plasmas *Plasma Phys. Control. Fusion* **45** R1–R88
[589] Escande D. 2013 What is a reversed field pinch? *HAL Archives* hal-00909102
[590] Williams Z.R., Pueschel M.J., Terry P.W. and Hauff T. 2017 Turbulence, transport, and zonal flows in the Madison symmetric torus reversed-field pinch *Phys. Plasmas* **24** 122309
[591] Mishchenko A. and Kleiber R. 2012 Zonal flows in stellarator in an ambient radial electric field *Phys. Plasmas* **19** 072316
[592] Ghizzo A. and Del Sarto D. 2019 Transport barrier triggered by resonant three-wave processes between trapped-particle-modes and zonal flow *Plasma* **2** 228
[593] McKeeR G *et al* 2006 Characterization of zonal flows and their dynamics in the DIII-D tokamak, laboratory plasmas, and simulation *Proc. 21st IAEA Fusion Eng. Conf.* (Chengdu) IAEA-CN-149 EX/2–3 (http://www-naweb.iaea.org/napc/physics/FEC/FEC2006/papers/ex_2-3.pdf)
[594] Miki K. and Diamond P.H. 2011 Novel states of pre-transition edge turbulence emerging from shearing mode competition *Nucl. Fusion* **51** 102003
[595] Sasaki M., Itoh K., Itoh S.-I. and Kasuya N. 2012 Zonal flows induced by symmetry breaking with existence of geodesic acoustic modes *Nucl. Fusion* **52** 023009
[596] Terry P.W. 2000 Suppression of turbulence and transport by sheared flow *Rev. Mod. Phys.* **72** 109
[597] Xu Y.H., Yu C.X., luo J.R., Mao J.S., Liu B.H., Li J.G., Wan B.N. and Wan Y.X. 2000 Role of Reynolds stress-induced poloidal flow in triggering the transition to improved ohmic confinement on the HT-6M tokamak *Phys. Rev. Lett.* **84** 3867
[598] Shesterikov I., Xu Y., Hidalgo C., Berte M., Dumortier P., Schoor M.V., Vergote M. and Van Oost G. (TEXTOR Team) 2012 Direct evidence of eddy breaking and tilting by edge sheared flows observed in the TEXTOR tokamak *Nucl. Fusion* **52** 042004
[599] Cziegler I., Tynan G.R., Diamond P.H., Hubbard A.E., Hughes J.W., Irby J. and Terry J.L. 2005 Zonal flow production in the L–H transition in Alcator C-Mod *Plasma Phys. Control. Fusion* **56** 075013
[600] Yan Z., McKee G.R., Fonck R., Gohil P., Groebner R.J. and Osborne T.H. 2014 Observation of the L–H confinement bifurcation triggered by a turbulence-driven shear flow in a tokamak plasma *Phys. Rev. Lett.* **112** 125002
[601] van Milligen B.P., Kalhoff T., Pedrosa M.A. and Hidalgo C. 2008 Bicoherence during confinement transitions in the TJ-II stellarator *Nucl. Fusion* **48** 115003

[602] Manz P. *et al* 2012 Zonal flow triggers the L–H transition in the experimental advanced superconducting tokamak *Phys. Plasmas* **19** 072311

[603] Schmitz L. 2017 The role of turbulence-flow interactions in L- to H-mode transition dynamics: recent progress *Nucl. Fusion* **57** 025003

[604] BelokurovA A *et al* 2017 LH-transition dynamics in the presence of GAM and pellet-injection *Proc. 44th EPS Conf. Plasma Phys.* (Belfast) ECA 41F P1.172 (http://ocs.ciemat.es/EPS2017PAP/pdf/P1.172.pdf)

[605] Askinazi L.G. and Belokurov A.A. 2014 GAM evolution and LH-transition in TUMAN-3M tokamak *Proc. 41st EPS Conf. Plasma Phys.* (Berlin) ECA 38F P4.060 (http://ocs.ciemat.es/EPS2014PAP/pdf/P4.060.pdf)

[606] Belokurov A.A. *et al* 2019 Geodesic acoustic mode temporal parameters effect on the LH-transition initiation possibility in TUMAN-3M tokamak *Tech. Phys. Lett.* **45** 783

[607] Zohm H., Suttrop W., Büchl K., de Blank H.J., Gruber O., Kallenbach A., Mertens V., Ryter F. and Schittenhelm M. (ASDEX Upgrade Team) 1995 Investigation of the bifurcation character of the H-mode in ASDEX Upgrade *Plasma Phys. Control. Fusion* **37** 437

[608] Colchin R.J. *et al* 2002 Slow L-H transitions in DIII-D plasmas *Phys. Rev. Lett.* **88** 255002

[609] Estrada T., Happel T., Hidalgo C., Ascasíbar E. and Blanco E. 2010 Experimental observation of coupling between turbulence and sheared flows during L–H transitions in a toroidal plasma *Europhys. Lett.* **92** 35001

[610] Schmitz L., Zeng L., Rhodes T.L., Hillesheim J.C., Doyle E.J., Groebner R.J., Peebles W.A., Burrell K.H. and Wang G. 2012 Role of zonal flow predator-prey oscillations in triggering the transition to H-mode confinement *Phys. Rev. Lett.* **108** 155002

[611] Xu G.S. *et al* 2014 Study of the L–I–H transition with a new dual gas puff imaging system in the EAST superconducting tokamak *Nucl. Fusion* **54** 013007

[612] Zhao H. *et al* 2017 Zonal flow energy ratio evolution during L–H and H–L transitions in EAST plasmas *Plasma Sci. Technol.* **19** 035101

[613] Cheng J. *et al* 2013 Dynamics of low-intermediate-high-confinement transitions in toroidal plasmas *Phys. Rev. Lett.* **110** 265002

[614] Yashin A.Y., Bulanin V.V., Gusev V.K., Kurskiev G.S., Patrov M.I., Petrov A.V., Petrov Y.V. and Tolstyakov S.Y. 2018 Phenomena of limit-cycle oscillations in the Globus-M spherical tokamak *Nucl. Fusion* **58** 112009

[615] Grover O. *et al* 2018 Limit cycle oscillations measurements with Langmuir and ball-pen probes on COMPASS *Nucl. Fusion* **58** 112001

[616] Colchin R.J. *et al* 2002 Physics of slow L-H transitions in the DIII-D tokamak *Nucl. Fusion* **42** 1134

[617] Birkenmeier G. *et al* 2016 Magnetic structure and frequency scaling of limit-cycle oscillations close to L- to H-mode transitions *Nucl. Fusion* **56** 086009

[618] Cheng J. *et al* 2015 Evolutions of limit cycle oscillation in L–I–H transitions on HL-2A *J. Nucl. Mater.* **463** 455

[619] Itoh K., Itoh S.-I. and Fujisawa A. 2013 An assessment of limit cycle oscillation dynamics prior to L–H transition *Plasma Fusion Res.* **8** 1102168

[620] Tynan G.R., Cziegler I., Diamond P.H., Malkov M., Hubbard A., Hughes J.W., Terry J.L. and Irby J.H. 2016 Recent progress towards a physics-based understanding of the H-mode transition *Plasma Phys. Control. Fusion* **58** 044003

[621] Itoh K., Kobayashi T., Ido T., Itoh S.-I. and Kamiya K. 2015 Contribution of geodesic acoustic modes in the limit cycle oscillation near H-mode transition in JFT-2M plasmas *Plasma Phys. Control. Fusion* **57** 092001

[622] Malkov M.A., Diamond P.H. and Rosenbluth M.N. 2001 On the nature of bursting in transport and turbulence in drift wave-zonal flow systems *Phys. Plasmas* **8** 5073

[623] Marchenko V.S., Goloborod'ko V.Y. and Reznik S.N. 2003 Behavior of a zonal flow near the threshold *Phys. Plasmas* **10** 4913

[624] Kim E.-j. and Diamond P.H. 2003 Zonal flows and transient dynamics of the L−H Ttansition *Phys. Rev. Lett.* **90** 185006

[625] Miki K., Diamond P.H., Gürcan Ö.D., Tynan G.R., Estrada T., Schmitz L. and Xu G.S. 2012 Spatio-temporal evolution of the L → I → H transition *Phys. Plasmas* **19** 092306

[626] Tynan G.R. *et al* 2013 Turbulent-driven low-frequency sheared $E \times B$ flows as the trigger for the H-mode transition *Nucl. Fusion* **53** 073053

[627] Chang C.S., Ku S., Tynan G.R., Hager R., Churchill R.M., Cziegler I., Greenwald M., Hubbard A.E. and Hughes J.W. 2017 Fast low-to-high confinement mode bifurcation dynamics in a tokamak edge plasma gyrokinetic simulation *Phys. Rev. Lett.* **118** 175001

[628] Burrell K.H. 2001 Diagnostics for advanced tokamak research (invited) *Rev. Sci. Instrum.* **72** 906

[629] Xia H., Shats M.G. and Punzmann H. 2003 Strong $E \times B$ shear flows in the transport-barrier region in H-mode plasma *Phys. Rev. Lett.* **97** 255003

[630] Jhang H., Kaang H.H., Kim S.S., Rhee T., Singh R. and Hahm T.S. 2017 Impact of zonal flows on edge pedestal collapse *Nucl. Fusion* **57** 022006

[631] Ryter F. *et al* (ASDEX Upgrade Team) 1998 H-mode power threshold and transition in ASDEX Upgrade *Plasma Phys. Control. Fusion* **40** 725–9

[632] Marinoni A. *et al* 2015 Characterization of density fluctuations during the search for an I-mode regime on the DIII-D tokamak *Nucl. Fusion* **55** 093019

[633] Fasoli A., Testa D., Sharapov S., Berk H.L., Breizman B., Gondhalekar A., Heeter R.F. and Mantsinen M. (EFDA-JET Workprogramme Contributors) 2002 MHD spectroscopy *Plasma Phys. Control. Fusion* **44** B159–72

[634] Sharapov S.E. *et al* 2002 Alfvén wave cascades in a tokamak *Phys. Plasmas* **9** 2027–36

[635] Itoh S.-I., Nishimura S., Itoh K., Fujisawa A., Nagashima Y. and Inagaki S. 2009 Geodesic acoustic mode spectroscopy II *Plasma Fusion Res.* **4** 014

[636] Itoh K., Itoh S.-I., Nagashima Y., Yamada T., Kosuga Y. and Fujisawa A. 2018 Symmetry-breaking of turbulence structure and position identification in toroidal plasmas *Plasma Fusion Res.* **13** 1102113

[637] Itoh S.-I., Itoh K., Nagashima Y. and Kosuga Y. 2017 On the application of cross bispectrum and cross bicoherence *Plasma Fusion Res.* **12** 1101003

[638] Hasegawa A. and Mima K. 1977 Stationary spectrum of strong turbulence in magnetized nonuniform plasma *Phys. Rev. Lett.* **39** 205

[639] Kim J.S., Fonck R.J., Durst R.D., Fernandez E., Terry P.W., Paul S.F. and Zarnstorff M.C. 1997 Measurements of nonlinear energy transfer in turbulence in the tokamak fusion test reactor *Phys. Rev. Lett.* **79** 841

[640] Xu M., Tynan G.R., Holland C., Yan Z., Muller S.H. and Yu J.H. 2009 Study of nonlinear spectral energy transfer in frequency domain *Phys. Plasmas* **16** 042312

[641] Xu M., Tynan G.R., Holland C., Yan Z., Muller S.H. and Yu J.H. 2010 Fourier-domain study of drift turbulence driven sheared flow in a laboratory plasma *Phys. Plasmas* **17** 032311